

MORPHOLOGY, PROPERTIES AND REACTIVITY OF NANOSTRUCTURES

A Dissertation

Submitted to the Faculty

of

Purdue University

by

Garrett M. Mitchell

In Partial Fulfillment of the

Requirements for the Degree

of

Doctor of Philosophy

May 2020

Purdue University

West Lafayette, Indiana

**THE PURDUE UNIVERSITY GRADUATE SCHOOL
STATEMENT OF DISSERTATION APPROVAL**

Dr. Fabio H. Ribeiro, Chair

Davidson School of Chemical Engineering

Dr. W. Nicholas Delgass

Davidson School of Chemical Engineering

Dr. Rajamani Gounder

Davidson School of Chemical Engineering

Dr. Volkan Ortalan

Department of Materials Science and Engineering, University of Connecticut

Dr. Rosa Diaz Rivas

Birck Nanotechnology Center

Approved by:

Dr. John Morgan

Director, Graduate Studies

To my lovely wife, who insists that she will also become a doctor once I defend,
much to my "delight".

ACKNOWLEDGMENTS

This work was supported by the Designing Materials to Revolutionize and Engineer our Future (DMREF) program of the National Science Foundation (CBET-1437219). This work was also supported by the Multidisciplinary University Research Initiative Program of Department of Defense Office of Naval Research (Grant Number: 108329). Part of the TEM work was carried out at Florida State University, and the TEM facility at FSU is funded and supported by the Florida State University Research Foundation, National High Magnetic Field Laboratory (NSF-DMR-0654118) and the State of Florida.

The authors acknowledge funding from the U.S. Department of Energy, Office of Basic Energy Sciences, Chemical Sciences, under Grant DE-FG02-03ER15408. Garrett Mitchell acknowledges Purdue University for funding from an Andrews fellowship. We thank Jason Bates, Michael Cordon, Dr. Viktor Cybulskis, and Dr. Wen-Sheng Lee (Dow Chemical) for many useful discussions, and also thank Dr. Yury Zvinevich for assistance constructing the CSTR reactor unit.

Y.W. appreciates support from the Herbert L. Stiles Professorship and the ACRI Center Initiative at Iowa State University. F.H.R. acknowledges the partial support provided by the National Science Foundation. This paper is based on work supported in part by the National Science Foundation under cooperative agreement EEC-1647722. Any opinions, findings and conclusions or recommendations expressed in this material are those of the author(s) and do not necessarily reflect the views of the National Science Foundation.

Support for this research was provided National Science Foundation's program for Designing Materials to Revolutionize and Engineer our Future, DMREF (CBET-1437219). Use of the Advanced Photon Source is supported by the U.S. Department

of Energy, Office of Science, and Office of Basic Energy Sciences, under Contract DE-AC02-06CH11357. MRCAT operations are supported by the Department of Energy and the MRCAT member institutions.

This paper is based upon work supported in part by the National Science Foundation under Cooperative Agreement EEC-1647722. Use of the advanced photon source was supported by the U.S. Department of Energy, Office of Basic Energy Sciences, under Contract DE-AC02-06CH11357. MRCAT operations, beamline 10-BM and 10-ID, are supported by the Department of Energy and the MRCAT member institutions. The authors also acknowledge the use of the 11-ID-C beamline at the advanced photon source. XPS data were collected at the Surface Analysis Facility of the Birck Nanotechnology Center of Purdue University. Use of the Center for Nanoscale Materials (CNM), a U.S. Department of Energy, Office of Science, Office of Basic Energy Sciences User Facility, Information Technology at Purdue (West Lafayette, IN), and computational resources from the National Energy Research Scientific Computing Center is gratefully acknowledged. This material is based upon work supported, in part, by the U.S. Department of Energy Office of Science, Office of Basic Energy Sciences, Chemical Sciences, Geosciences, & Biosciences (CSBG) division. The authors acknowledge Joseph Kubal, Brandon Bukowski, and Siddharth Deshpande for valuable discussions.

This thesis is partly based upon work supported in part by the National Science Foundation under Cooperative Agreement No. EEC-1647722. Use of the advanced photon source was supported by the U.S. Department of Energy, Office of Basic Energy Sciences, under contract no. DE-AC02-06CH11357. MRCAT operations, beamline 10-BM and 10-ID, are supported by the Department of Energy and the MRCAT member institutions. The authors also acknowledge the use of the 9-BM and 11-ID-C beamline at the advanced photon source. Use of the Center for Nanoscale Materials, an Office of Science user facility, was supported by the U.S. Department of Energy, Office of Science, Office of Basic Energy Sciences, under Contract No. DE-

AC02-06CH11357. Use of the National Energy Research Scientific Computing Center is also gratefully acknowledged.

Financial support from the H. C. Brown Center for Borane Research is gratefully acknowledged. J.R.R. thanks CONACYT-SENER for financial support (Project 274314) and Dr. P. Manikandan for technical support.

The authors acknowledge Saul Lapidus (11-BM-A, Advanced Photon Source, ANL, Lemont, IL) for performing high-resolution powder diffraction experiments. Use of the Advanced Photon Source at Argonne National Laboratory was supported by the US Department of Energy, Office of Science, Office of Basic Energy Sciences, under Contract No. DE-AC02-06CH11357. Arthur Dysart thanks the U.S. Department of Energy, Office of Science, Office of Workforce Development for Teachers and Scientists, Office of Science Graduate Student Research (SCGSR) program. The SCGSR program is administered by the Oak Ridge Institute for Science and Education for the DOE under contract number DE-SC0014664.

TABLE OF CONTENTS

	Page
LIST OF TABLES	xii
LIST OF FIGURES	xvi
ABSTRACT	xxxii
1 PROBING THE THERMAL BEHAVIOR AND STABILITY OF METAL- FE ₃ O ₄ HETERODIMER NANOPARTICLES UTILIZING <i>IN SITU</i> PULSED LASER HEATING TEM	1
1.1 Abstract	1
1.2 Introduction	3
1.3 Methods Section	5
1.3.1 Sample Preparation	5
1.3.2 ILH-TEM Characterization	5
1.3.3 TEM characterization	6
1.4 Results and Discussion	6
1.4.1 Laser Heating	6
1.4.2 SAED Analysis	12
1.4.3 EELS Characterization	13
1.5 Conclusions	15
1.6 Supporting Information	16
1.6.1 DRUV-Vis Characterization	16
2 EFFECT OF COBALT ADDITION ON PLATINUM SUPPORTED ON MULTI-WALLED CARBON NANOTUBES FOR WATER-GAS SHIFT	18
2.1 Abstract	18
2.2 Introduction	19
2.3 Experimental Methods	20
2.3.1 Catalyst Synthesis	20
2.3.2 Measurements of Reaction Kinetics	21
2.3.3 Catalyst Characterization	22
2.3.4 DFT Calculations	24
2.4 Results	25
2.4.1 Measurement of Reaction Kinetics	25
2.4.2 Catalyst Characterization	27
2.4.3 DFT Results	36
2.5 Discussion	39

	Page	
2.6	Conclusions	46
2.7	Supporting Information	46
2.7.1	DFT Methods	46
3	ORIGIN OF ELECTRONIC MODIFICATION OF PLATINUM IN A Pt ₃ V ALLOY AND ITS CONSEQUENCES FOR PROPANE DEHYDROGENA- TION CATALYSIS	58
3.1	Abstract	58
3.2	Introduction	60
3.3	Experimental Section	62
3.3.1	Catalyst Synthesis	62
3.3.2	Electron Microscopy	63
3.3.3	Propane Dehydrogenation	64
3.3.4	X-ray Absorption Spectroscopy (XAS)	64
3.3.5	Resonant Inelastic X-ray Scattering (RIXS)	65
3.3.6	X-ray Photoelectron Spectroscopy (XPS)	65
3.3.7	X-ray Diffraction (XRD)	66
3.3.8	Density Functional Theory (DFT)	66
3.4	Results	68
3.4.1	Structural Characterization	68
3.4.2	Electronic Characterization	73
3.4.3	Propane Dehydrogenation	77
3.4.4	DFT	81
3.5	Discussion	84
3.5.1	Structural Model	84
3.5.2	Nature of Electronic Modification	86
3.5.3	Effect of Structure on Catalytic Performance	91
3.6	Conclusions	92
3.7	Supporting Information	93
3.7.1	Experimental	93
3.7.2	Results	97
3.7.3	Discussion	116
4	STRUCTURAL TRENDS IN THE DEHYDROGENATION SELECTIV- ITY OF PALLADIUM ALLOYS	119
4.1	Abstract	119
4.2	Introduction	120
4.3	Methods	123
4.3.1	Catalyst Synthesis	123
4.3.2	STEM/EDS	123
4.3.3	<i>In Situ</i> Synchrotron X-ray Diffraction (XRD)	124
4.3.4	<i>In Situ</i> X-ray Adsorption Spectroscopy (XAS)	125
4.3.5	Propane Dehydrogenation	126

	Page
4.3.6 Density Functional Theory	127
4.4 Results	128
4.4.1 Structural Characterization	128
4.4.2 Propane Dehydrogenation	136
4.4.3 Density Functional Theory	139
4.5 Discussion	149
4.5.1 Catalyst Structure	149
4.5.2 Selectivity Trends in Pd Alloys	149
4.6 Conclusions	154
4.7 Supporting Information	155
4.7.1 Methods	155
4.7.2 Results	158
4.7.3 Discussion	168
5 REACTIVE METAL–SUPPORT INTERACTIONS AT MODERATE TEMPERATURE IN TWO-DIMENSIONAL NIOBIUM-CARBIDE-SUPPORTED PLATINUM CATALYSTS	173
5.1 Abstract	173
5.2 Introduction	174
5.3 Methods	176
5.3.1 Synthesis of the Nb ₂ AlC phase	176
5.3.2 Preparation of Nb ₂ CT _x MXene	176
5.3.3 Preparation of the Pt/Nb ₂ CT _x catalysts	176
5.3.4 Determination of the WGS reaction kinetics	177
5.4 Results	178
5.4.1 Preparation and characterizations of the Nb ₂ CT _x support	178
5.4.2 Kinetics of the WGS reaction	179
5.4.3 Reducibility of the Pt/Nb ₂ CT _x catalysts	182
5.4.4 RMSI	185
5.5 Conclusions	189
5.6 Supporting Information	190
5.6.1 Supporting Methods	190
5.6.2 Langmuir-Hinshelwood mechanism	192
5.6.3 Supporting Figures	193
6 PROPYLENE OXIDE INHIBITS PROPYLENE EPOXIDATION OVER Au/TS-1	208
6.1 Abstract	208
6.2 Introduction	210
6.3 Experimental Methods	214
6.3.1 Catalyst Synthesis	214
6.3.2 Catalyst Characterization	215
6.3.3 Kinetic Studies of Propylene Epoxidation	217

	Page
6.4 Results and Discussion	219
6.4.1 Structural Characterization of Titanosilicates	219
6.4.2 Measurement of Reaction Kinetics of Over Au/TS-1 Catalysts	221
6.5 Conclusions	237
6.6 Supporting Information	238
6.6.1 Reactor Apparatus	238
6.6.2 XRD Patterns	238
6.6.3 Nitrogen Isotherms	238
6.6.4 Diffuse Reflectance UV Visible Spectroscopy	243
6.6.5 Additional Kinetic Data and Derivations	243
7 THREE-DIMENSIONAL ANTIMONY NANOCHAINS FOR LITHIUM- ION STORAGE	259
7.1 Abstract	259
7.2 Introduction	261
7.3 Results and Discussion	262
7.3.1 Nanoparticle Synthesis	262
7.3.2 Structural Characterization	263
7.3.3 Electrochemical Studies	265
7.4 Conclusions	269
7.5 Supporting Information	269
7.5.1 Synthesis and NMR Characterization	269
7.5.2 Discussion of Antimony Nanoparticles Synthesis via Ammonia Borane Reduction	275
7.5.3 Effect of the Sb Salt, Reducing and Capping Agents on the Architecture of Sb Nanoparticles	278
7.5.4 Structural Characterization	281
7.5.5 Electrochemical Studies	284
8 EFFECT OF SYNTHESIS METHOD, USING VARYING TYPES OF MI- CROPORE LEVEL SULFUR INFILTRATION, ON ELECTROCHEMI- CAL PERFORMANCE IN LITHIUM-SULFUR BATTERIES	291
8.1 Abstract	291
8.2 Introduction	292
8.3 Experimental Section	295
8.3.1 Synthesis of Autogenic Carbon–Sulfur Composites	295
8.3.2 Synthesis of Mechanical Carbon–Sulfur Composites	295
8.3.3 Battery Fabrication and Assembly	296
8.3.4 Electrochemical Characterization	297
8.3.5 Characterization of Carbon–Sulfur Composites	298
8.4 Results and Discussion	299
8.4.1 Influence of Synthesis on Material Properties of Carbon–Sulfur Composites	299

	Page
8.4.2 Influence of Synthesis on Electrochemical Performance of Carbon-Sulfur Composites	306
8.5 Conclusions	311
REFERENCES	313
A A SHORT DESCRIPTION OF (S)TEM IMAGING	342
B ELECTRON ENERGY-LOSS SPECTROSCOPY (EELS) AND ENERGY DISPERSIVE SPECTROSCOPY (EDS)	346
VITA	348

LIST OF TABLES

Table	Page	
1.1	Tabulated values of the integral ratio of the Fe L ₃ and L ₂ edges of the heterodimers before and after laser irradiation with included Fe reference states.	15
2.1	Comparison of WGS TOR, E _{app} , and reaction orders for the as prepared and the acetic acid treated Pt/MWCNT monometallic catalysts.	27
2.2	Results of linear combination XANES fits of the Co K edge for the as-prepared leached PtCo/MWCNT catalysts. Co foil was used as a standard for metallic Co, while CoO powder was used as reference for Co ²⁺	31
2.3	Pt L _{III} edge EXAFS data fit parameters for the PtCo/MWCNT catalysts.	34
2.4	WGS Kinetic data over the series of PtCo/MWCNT catalysts	47
2.5	ICP-AES data for PtCo/MWCNT catalysts	48
2.6	CO Chemisorption (collected at 35 °C) and WGS TOR data for PtCo/MWCNT Catalysts	49
2.7	Co K edge EXAFS data fit parameters for the PtCo/MWCNT catalysts. .	50
2.8	DFT calculated binding energies of intermediates at the CoOH/Pt interface, the sites correspond to that shown in Figure 2.7	50
2.9	DFT calculated binding energies of intermediates on various Pt-containing structures	51
3.1	XANES Edge Energies and EXAFS Fitting Parameters for 3Pt, 5Pt-5V, and 2Pt-5V: Coordination Number (CN), Bond Distance (<i>R</i>), Debye-Waller Factor (σ^2), and <i>E</i> ₀ Correction	70
3.2	EXAFS Fit for Pt-V Difference Spectra	80
3.3	Synthesis parameters for Pt and Pt-V catalysts	94
3.4	First shell EXAFS fits and XANES edge energy of Pt-V catalysts	104
3.5	Fits of the 220 reflection for 3Pt and 5Pt-5V catalysts calcined at different temperatures	109
3.6	Pt 4f XPS fitting parameters for 3Pt and 2Pt-5V	109

Table	Page
3.7 Binding energies of CO and CH ₃ on Pt (111), Pt ₃ V-1ML-Pt, Pt ₃ V-2ML-Pt and Pt ₃ V (111). Binding energies were calculated according to Table 3.8	110
3.8 Formalism used to calculate binding energies for CO and CH ₃ on Pt, Pt ₃ V shell on Pt and Pt ₃ V alloy	110
3.9 Most stable binding configurations and their corresponding binding energies for CO, C ₁ , C ₂ , and C ₃ hydrocarbon fragments adsorbed on Pt (111) and Pt ₃ V (111) surfaces.	111
3.10 H binding energy on Pt (111) and Pt ₃ V (111) referenced to H ₂ gas	113
3.11 Binding energies of CO, and CH _x , species as calculated on Pt ₃ V (111) and Pt (111) with the lattice constant of Pt ₃ V. The effect of changing the lattice constant of Pt (111) is minimal on the binding energy compared to the Pt slab constructed using the equilibrium lattice constant.	114
3.12 Work function values for the (111) face of Pt and Pt ₃ V.	116
4.1 Synthetic details of Pd and Pd alloy catalysts.	123
4.2 Number average particle size for Pd and bimetallic catalysts	129
4.3 EXAFS fitting parameters for Pd foil, Pd, Pd-Mn, Pd-Ga, and Pd-Zn	131
4.4 Reduction-Oxidation difference EXAFS fit of 1Pd-5Mn	134
4.5 Dehydrogenation rate, first order deactivation rate constants, and activity loss after 90 minutes of reaction for Pd and Pd alloy catalysts	137
4.6 Binding energies of adsorbates on Pd and Pd alloy surfaces, with more positive values indicating weaker adsorption. The binding energies of open-shell species (hydrogen, ethylidyne), are referenced to the corresponding gas phase species (H ₂ , ethane).	142
4.7 Most stable binding sites of adsorbates on Pd and Pd alloy surfaces. The numbers in parentheses refer to sites as labeled in Figure 4.6.	143
4.8 Propylene dehydrogenation activation energy barrier, propylene selectivity descriptor, and activation energy barriers for C-C bond cleavage of propynyl for Pd and Pd alloys.	146
4.9 Pd K edge EXAFS fits of Pd and Pd alloy catalysts after room temperature air exposure.	162
4.10 The <i>d</i> -band center (first moment) and <i>d</i> -band width (second moment) calculated from the pDOS of surface Pd atoms in monometallic Pd and Pd alloys	164

Table	Page
4.11 Binding energies of deep dehydrogenated intermediates with respect to gas phase reference	165
4.12 Binding energies of deep dehydrogenated intermediates on Fe (110) and their difference from Pd (111)	165
4.13 Activation energy barriers for C-C bond cleavage of propyne on Pd and Pd alloy surfaces	166
4.14 Calculated values of selectivity descriptor and propynyl C-C bond breaking barriers for Pd ₃ Zn (111) surface	171
5.1 WGS kinetics of Pt/Nb ₂ CT _x and Pt/Al ₂ O ₃	182
5.2 Quantitative evaluation of the EXAFS fit (Artemis Software)	203
6.1 Characterization data for all catalyst samples used in this study.	220
6.2 Measured reaction orders compared to those reported in literature.	223
6.3 Relation between the true reaction order and the coverages of the most abundant surface species, according to the mechanism shown in Figure 6.4 and the mechanistic assumptions resulting in Equation 6.16.	232
6.4 Apparent and PO-inhibition-corrected reaction orders and activation energies for propylene oxide formation and H ₂ oxidation determined by averaging the measured kinetic parameters for eight separate Au/TS-1 samples (0.092Au/TS-1(75), 0.019Au/TS-1(143), 0.040Au/TS-1(81), 0.030Au/TS-1(81), 0.044Au/TS-1(81), 0.033Au/TS-1(143), 0.069Au/TS-1(143), and 0.064Au/TS-1(143)).	235
6.5 Parameters used to calculate the Mears' criterion for Au/TS-1 catalysts used in this study.	246
6.6 Parameters used to calculate the Mears' criterion for Au/TS-1 catalysts used in this study.	247
6.7 Apparent reaction orders and activation energies for PO formation measured over all catalysts in this study. Activation energies were measured in the temperature range 443-483 K with a feed composition of 10% H ₂ / 10% O ₂ / 10% C ₃ H ₆ / 70% N ₂ and a space velocity of 26,000 cm ³ g _{cat} ⁻¹ h ⁻¹ in a gas-phase CSTR. Reaction orders were measured at 473 K with a feed composition of 2.5-10% H ₂ / 2.5-10% O ₂ / 2.5-10% C ₃ H ₆ / 0-0.3% PO/ Balance N ₂ and a space velocity of 26,000 cm ³ g _{cat} ⁻¹ h ⁻¹ in a gas-phase CSTR.	251

6.8	Apparent reaction orders and activation energies for propylene oxide, acrolein, acetone, ethanal, propanal, carbon dioxide, and H ₂ oxidation determined by averaging the measured kinetic parameters for eight separate Au/TS-1 samples (0.092Au/TS-1(75), 0.019Au/TS-1(143), 0.040Au/TS-1(81), 0.030Au/TS-1(81), 0.044Au/TS-1(81), 0.033Au/TS-1(143), 0.069Au/TS-1(143), 0.064Au/TS-1(143)).	252
-----	---	-----

LIST OF FIGURES

Figure	Page
1.1 (a) Schematic diagram of the experimental set up of an <i>In Situ</i> Laser heating Transmission Electron Microscope. (b) HAADF-STEM image of Pt HD system. (c-d) HR-STEM images of Pt and Fe ₃ O ₄ nanoparticles at atomic resolution.	7
1.2 TEM micrographs displaying the heterodimer wetting behavior on a carbon support membrane (a,h) Bright field (BF)-TEM images of Pt and Au heterodimers, respectively, before laser irradiation. (b-e) and (i-l) Frames taken from the <i>in situ</i> laser heating TEM movie which illustrates the wetting process of the Pt and Au, respectively, onto the Fe ₃ O ₄ . (f-g) and (m-n) HAADF-STEM images of Pt and Au heterodimers, respectively, after laser irradiation.	9
1.3 TEM micrographs displaying the heterodimer wetting behavior on a silicon nitride support membrane (a,f) Bright field (BF)-TEM images of Pt and Au heterodimers, respectively, before laser irradiation. (b-d) and (g-i) Frames taken from the <i>in situ</i> laser heating TEM movie which illustrates the wetting process of the Pt and Au, respectively, onto the Fe ₃ O ₄ . (e,j) HAADF-STEM images of Pt and Au heterodimers, respectively, after laser irradiation.	10
1.4 (a-b) SAED diffraction patterns of Au-Fe ₃ O ₄ HD on a Si ₃ N ₄ support membrane of a region of interest before and after laser irradiation, respectively. (c-d) SAED diffraction patterns of Pt-Fe ₃ O ₄ HD on Si ₃ N ₄ support membrane of a region of interest before and after laser irradiation, respectively. (e-f) EELS spectra showing Fe- L ₃ and L ₂ edges before and after laser irradiation on Au-Fe ₃ O ₄ HD on Si ₃ N ₄ support membrane, respectively. (g-h) EELS spectra showing Fe- L ₃ and L ₂ edges before and after laser irradiation on Pt-Fe ₃ O ₄ HD on Si ₃ N ₄ support membrane, respectively. . . .	13
1.5 (a-b) SAED diffraction patterns of Au-Fe ₃ O ₄ HD on a carbon support membrane of a region of interest before and after laser irradiation, respectively. (c-d) SAED diffraction patterns of Pt-Fe ₃ O ₄ HD on a carbon support membrane of a region of interest before and after laser irradiation, respectively.	14
1.6 DRUV-Vis spectra of model samples silicon nitride and amorphous carbon	17

Figure	Page
2.1 WGS TOR at 300 °C vs. Co:Pt molar ratio for the as prepared, leached and the Pt ₃ Co/MWCNT catalysts. Reaction conditions, 7% CO, 8.5% CO ₂ , 21.9% H ₂ O, 37.4% H ₂ and balance Ar.	26
2.2 XRD patterns for Pt, PtCo as prepared and PtCo leached catalysts supported on MWCNT.	29
2.3 Co K edge XANES spectra at RT after 450 °C reduction for (a) as prepared and (b) leached PtCo catalysts.	30
2.4 Pt L _{III} edge EXAFS spectra collected at RT after 450 °C reduction of PtCo/MWCNT catalysts (a) as prepared (b) leached and Pt ₃ Co/MWCNT.	33
2.5 HAADF-STEM image and X-ray EDS mapping of the Pt ₃ Co/MWCNT catalyst after reaction. In the composite EDS map, Pt is shown in Red and Co is shown in green.	35
2.6 Phase diagram of (left) bulk Co oxides (right) 1 ML of Co oxide films on Pt. WGS conditions are highlighted with + symbol (1) T = 227 °C (2) T = 327 °C. Inset in (right) shows the structure of most stable phase on Pt under WGS conditions. Green – CoOH. Grey-Pt, Pink-Co, White-H, Red – O	36
2.7 Semi-infinite CoOH ribbon on Pt. Grey - Pt, Pink - Co, White - H, Red - O of CoOH. The under-coordinated Co atoms at the interface are numbered. Adsorption energies of OH at these sites are provided in Table 2.8.	37
2.8 Stabilization effect of different systems of adsorbates: – Grey - Pt, Pink - Co, White - H, Red - O of CoOH, Blue - O; (a) OH on Pt (b) OH on Pt ₃ Co alloy (c) OH at CoOH/Pt interface (d) co-adsorbed OH and H ₂ O at CoOH/Pt interface (e) dissociation energy of H ₂ O for the different systems showing more favorable dissociation thermodynamics for CoOH/Pt system.	38
2.9 HAADF-STEM image of the Pt ₃ Co/MWCNT catalyst after reaction. . . .	52
2.10 Colorized Z-contrast STEM image of the Pt ₃ Co/MWCNT catalyst after reaction indicating placement of Pt and Co atoms.	53
2.11 X-ray EDS line-scan of the Pt ₃ Co/MWCNT catalyst after reaction	53
2.12 ($\sqrt{7}\times\sqrt{7}$) CoOH on (3x3) Pt(111) (left) top view (right) side view. Grey - Pt, Pink - Co, White - H, Red - O of CoOH. The unit cell boundaries are indicated using dashed lines. The height of the film from the top layer of Pt is 2.18 Å [66]. Some of the bond lengths are indicated in Å. d ₁ = 3.15, d ₂ = 2.9, d ₃ = 3.12, d ₄ = 2.57, d ₅ = 2.48, d ₆ = 2.16.	54

Figure	Page
2.13 Adsorption geometries; Grey - Pt, Pink - Co, White - H, Red - O of CoOH, Blue - O of adsorbate; (a) H on Pt ₃ Co (b) H ₂ O on Pt ₃ Co (c) H ₂ O on CoOH/Pt (d) H on CoOH/Pt (e) two co-adsorbed H ₂ O on CoOH/Pt.	55
2.14 Raw XRD patterns correlated with Figure 2.2 before background selection.	56
2.15 XRD background pattern collected on the MWCNT support used for correction of artifacts in the raw XRD patterns shown in Figure 2.14.	57
3.1 <i>In situ</i> Pt L ₃ edge EXAFS magnitude (solid lines) and imaginary (dashed lines) of 3Pt (black) and 2Pt-5V (red) catalysts. Spectra were collected at room temperature in He after a 30 min reduction at 550 °C in 3.5% H ₂	69
3.2 (a) <i>In situ</i> synchrotron XRD patterns of 3Pt (black), 5Pt-5V (red). Fundamental fcc lines are labeled in black. Simulated patterns of Pt with a lattice parameter of 3.89 Å (blue) and Pt ₃ V with a lattice parameter of 3.87 Å (green). (b) Expanded view of the 220 and 311 reflection for the above samples with vertical dashed lines denoting experimental peak positions. All experimental spectra were collected at 35 °C in 3.5% H ₂ after reduction at 550 °C.	74
3.3 (a) <i>In situ</i> Pt L ₃ edge XANES of 3Pt (black) and 2Pt-5V (red). Spectra were collected at room temperature in He after reduction at 550 °C in 3.5% H ₂ for 30 min and a subsequent purge in He at 550 °C. (b) High-resolution Pt 4f XPS spectra of 2Pt-5V and 3Pt after a reduction treatment in 5% H ₂ at 550 °C for 30 min. Black circles: raw data; black line: Shirley background; red lines: component fits; blue line: total fit. Background and components are offset for clarity. The vertical line denotes the peak position of the Pt 4f _{7/2} component of 3Pt and 2Pt-5V.	75
3.4 Pt L ₃ -Lβ ₅ RIXS maps of Pt (a) and Pt ₃ V (b). Spectra were collected after a reduction treatment at 550 °C in 3.5% H ₂ for 30 min. Spectra were collected at 100 °C in 3.5% H ₂ . Horizontal dashed lines denote the maximum of the inelastic scattering peak for each sample.	76
3.5 Propylene selectivity and propane conversion for 3Pt (black squares), 5Pt-5V (red circles), and 2Pt-5V (blue triangles) tested without (a) and with (b) cofed H ₂ . Reactions were performed at 550 °C at 3 psig with 2.5% propane balance N ₂ . For (b) the hydrogen concentration was 2.5%. Data points shown are at zero deactivation with each data point representing a separate test.	78

Figure	Page
3.6 Pt L ₃ edge EXAFS difference spectra for 2Pt-5V (a) and 5Pt-5V (b) (magnitude: solid black; imaginary: dashed black) and difference spectra fit (magnitude fit: solid red; imaginary fit: dashed red). A reduced scan of both 2Pt-5V and 5Pt-5V was taken at room temperature in He after reduction at 550 °C in 3.5% H ₂ ; subsequently, the samples were exposed to air for 30 min and then scanned again.	79
3.7 Binary compositional phase diagram for Pt-V. Red nodes are stable phases lying on the convex hull (black line). Blue nodes are the most stable phases for given Pt-V compositions which do not lie on the convex hull.	82
3.8 (a) pDOS for Pt (gold), Pt ₃ V (burgundy), and two epitaxial structures with one (orange) and two (crimson) layers of Pt ₃ V on Pt with the Fermi energy marked by a vertical dashed line. The inset graph shows an expanded view of near-Fermi energy unfilled states. (b) Structures corresponding to each model. (c) The d-band center and d-band width for the above structures.	83
3.9 Pt L ₃ edge XANES shift (vs Pt foil) plotted against the ratio of Pt-V to Pt-Pt coordination numbers for 3Pt and 10 Pt-V catalysts. The Pt-V to Pt-Pt ratio for the bulk Pt ₃ V phase is shown as a vertical dashed line. A linear fit of the data is shown in red.	87
3.10 Volume average particle size distributions and representative STEM images for: (a,b) 3Pt, (c,d) 5Pt-5V, and (e,f) 2Pt-5V	98
3.11 Pt-V catalyst characterization by electron microscopy. (a) HAADF STEM image of 2Pt-5V. (b) EDS map of 2Pt-5V with Pt in blue and V in yellow. (c) EDS line scan of green boxed area in b, with Pt in blue and V in Red.	99
3.12 V K edge EXAFS of 5Pt-5V after reduction at 550°C in 3.5% H ₂	100
3.13 <i>In situ</i> Pt L ₃ edge EXAFS of Pt foil (black) and 5Pt-5V catalysts calcined at 600°C (magenta), 550°C (cyan), 500°C (Blue), 450°C (green) and 250°C (Red). Scans were taken at room temperature in He after reduction at 550°C in 3.5% H ₂	101
3.14 R space EXAFS magnitude (solid black) and imaginary (dashed black) components of 5Pt-5V reduced at 200°C in 3.5% H ₂	102
3.15 <i>In situ</i> synchrotron XRD pattern of 2Pt-5V at 35 °C in He after a reduction treatment in 3.5% H ₂ at 550 °C for 30 minutes. The pattern was collected using an X-ray wavelength of 0.1173 Å.	106

Figure	Page
3.16 Multi component fits of the 220 XRD reflection for 5Pt-5V catalysts calcined at 250 °C, 450 °C, 500 °C, and 600 °C. Raw data is shown in black, component fits in red (Pt) and green (Pt ₃ V) and total fit (Pt+Pt ₃ V) in blue. Component fits have been offset for clarity. Spectra were collected at 35 °C in 3.5% H ₂ after reduction in the same atmosphere at 550 °C. .	108
3.17 Schematics of most stable binding configurations and their corresponding binding energies (with respect to Pt (111)) for CO, C ₁ , C ₂ , and C ₃ hydrocarbon fragments adsorbed on Pt ₃ V (111) and Pt (111) surfaces. .	112
3.18 Calculated C-H bond breaking energy for adsorbed propylene on Pt (111) (solid black) and Pt ₃ V (111) (solid red) referenced to gas phase propylene (dashed black).	115
3.19 X-Y axis averaged electrostatic potential for Pt (111) and Pt ₃ V (111) slab plotted along Z-axis (perpendicular to the surface of the slab).	116
4.1 <i>R</i> space Pd K edge EXAFS magnitude (solid lines) and imaginary (dashed) components of Pd catalysts. (a) monometallic Pd catalysts: Pd foil (dark blue) 2Pd (blue) and 1Pd (light blue), (b) 2Pd-3Zn (grey) and 1Pd (light blue), (c) 2.5Pd-2.5Ga (green) and 1Pd (light blue), and (d) 1Pd-5Mn (magenta) and 1Pd (light blue). Spectra were collected at room temperature in He after reduction at 550 °C in 3.5% H ₂	130
4.2 Reduction-Oxidation difference EXAFS of 1Pd-5Mn with the experimental difference magnitude (solid) and imaginary (dashed) shown in black and the difference fit shown in red.	133
4.3 (a) <i>In situ</i> synchrotron XRD pattern for 2.5Pd-2.5Ga (green) after a reduction treatment at 550 °C in 3.5% H ₂ with simulated Pd ₂ Ga pattern (black), and (b) simulated bulk patterns for Pd-Ga intermetallic compounds.	135
4.4 (left) simulations of bulk PdZn phases and (right) experimental in-situ synchrotron XRD pattern for the Pd-Zn catalyst (grey) along with simulated pattern for the β ₁ -PdZn phase.	136
4.5 Initial propylene conversion for 2Pd-3Zn (grey circles), 2Pd-3In (tan triangles), 2.5Pd-2.5Ga (green diamonds), 1Pd-5Mn (magenta inverted triangles), 2Pd-3Fe (orange hexagons), 1Pd (open dark blue squares), and 2Pd (filled dark blue squares) plotted against the initial propane conversion. Tests were performed at 550 °C in 2.5% H ₂ and 2.5% propane after pre-reducing in 550 °C in 5% H ₂	138

Figure	Page
4.6 Adsorption sites for Pd and Pd alloy slabs. Ontop sites are denoted by triangles, bridge sites by rectangles, and adsorption sites involving three or more atoms by circles. Sites marked in white involve direct bonding only to Pd atoms, while those in green indicate that the site involves a promoter atom. The black circles in Pd ₂ Ga indicate bonding at a fourfold site.	141
4.7 Reaction coordinate diagram for propylene dehydrogenation and propynyl hydrogenolysis.	148
4.8 Structural model of Pd and Pd alloy catalysts. The PdIn and PdMn catalysts have alloy shells with a Pd core, while the PdZn, PdGa and PdFe catalysts are pure phases. The unit cell of each alloy structure and the lowest energy surface are pictured beneath the respective nanoparticle models.	150
4.9 Representative ensembles of surface atoms involved in propynyl C-C bond breaking with corresponding transition state structures. (a) Pd (111) (b) Pd ₃ Mn/Pd (111) (c) PdZn (101)	153
4.10 STEM images of Pd and bimetallic Pd catalysts: (a) 1Pd (b) 2Pd (c) STEM image of 1Pd-5Mn with overlaid EDS maps for Pd (red) and Ga (Green). (d) STEM image of 2.5Pd-2.5Ga with overlaid EDS maps for Pd (purple) and Ga (yellow).	159
4.11 Simulated Pd ₂ Ga XRD patterns with different crystallite sizes (black, grey, purple, blue, light blue) compared with experimentally measured Pd-Ga catalyst (pink).	161
4.12 XANES of 1Pd (black), 2Pd-3Zn (orange), 2.5Pd-2.5Ga (green) and 1Pd-5Mn (magenta) at the K edge (a) and L ₃ edge (b) after reduction at 550 °C in 3.5% H ₂	163
4.13 Propylene most stable configurations on alloy and pure Pd surfaces . . .	166
4.14 Ethylidyne most stable configurations on alloy and pure Pd surfaces . . .	167
4.15 Transition states of propylene C-H bond breaking to form propenyl and hydrogen	168
4.16 Transition states of propynyl C-C bond breaking to form carbon and ethylidyne	169
4.17 Top view of fcc Pd ₃ Zn (111) surface	170

Figure	Page
5.1 Characterization of Nb ₂ CT _x MXene support. (a) Niobium K-edge XANES of Nb ₂ AlC, Nb ₂ CT _x MXene, NbC and Nb ₂ O ₅ . (b) Fourier transforms of the k ² EXAFS of Nb ₂ CT _x compared with the references (NbC and Nb ₂ O ₅). (c) Scanning electron microscopy micrograph of Nb ₂ CT _x MXene. (d) TEM image of Nb ₂ CT _x nanosheets. Inset: selected-area electron diffraction pattern showing hexagonal basal plane symmetry of the Nb ₂ CT _x nanosheets.	180
5.2 Kinetics of the WGS reaction over the 1% Pt/Nb ₂ CT _x MXene catalyst. (a) WGS rates normalized by the amount of platinum in the 1% Pt/Nb ₂ CT _x catalyst. The rates were measured at 300 °C with a feed composition of 6.8% CO, 21.9% H ₂ O, 8.5% CO ₂ and 37.4% H ₂ balanced by argon (standard conditions). (b) Apparent reaction orders for CO, CO ₂ , H ₂ and H ₂ O for 1% Pt/Nb ₂ CT _x . Reaction orders were determined under standard conditions, with each component varying in the following range: 4–21% for CO, 5–25% for CO ₂ , 11–34% for H ₂ O and 14–55% for H ₂ .	181
5.3 Niobium 3d XPS measurements and niobium edge XAS of Pt/Nb ₂ CT _x catalysts. (a) Niobium 3d region of <i>ex situ</i> XPS of a fresh 1% Pt/Nb ₂ CT _x sample, quasi <i>in situ</i> XPS of 1% Pt/Nb ₂ CT _x reduced at 350 and 550 °C, and <i>ex situ</i> XPS of 1% Pt/Nb ₂ CT _x reduced at 350 °C and exposed to air before analysis. (b) Quasi <i>in situ</i> XPS of the O 1s region of 1% Pt/Nb ₂ CT _x reduced at 350 °C and 550 °C. (c) Quasi <i>in situ</i> XPS of the F 1s region of 1% Pt/Nb ₂ CT _x reduced at 350 °C and 550 °C. (d) XANES spectra of the niobium K-edge of fresh Nb ₂ CT _x scanned in air, fresh 1% Pt/Nb ₂ CT _x treated with 3% H ₂ /He at 350 °C (<i>in situ</i>) and post-WGS reaction 1% Pt/Nb ₂ CT _x catalyst scanned in air. (e) Fourier transform magnitude of the k ² EXAFS of fresh Nb ₂ CT _x , reduced fresh 1% Pt/Nb ₂ CT _x and post-WGS reaction 1% Pt/Nb ₂ CT _x catalyst. All treatments were the same as those used to collect the XANES spectra.	184
5.4 <i>In situ</i> XAS and quasi <i>in situ</i> XPS of the 1% Pt/Nb ₂ CT _x catalysts. (a) <i>In situ</i> XANES spectra of the platinum L _{III} edge of the 2% Pt/Al ₂ O ₃ sample treated at 550 °C and fresh 1% Pt/Nb ₂ CT _x treated at 350 °C in 3% H ₂ /He. (b) Fourier transform magnitude of the k ² EXAFS of the 2% Pt/Al ₂ O ₃ sample treated at 550 °C and fresh 1% Pt/Nb ₂ CT _x treated at 350 °C in 3% H ₂ /He. (c) Quasi <i>in situ</i> XPS spectra of platinum 4f of Pt/SiO ₂ reduced at 550 °C and 1% Pt/Nb ₂ CT _x reduced at 350 °C.	186

Figure	Page
5.5 Electron microscopy and spectroscopy of the spent 1% Pt/Nb ₂ CT _x catalyst. (a,b) High-angle annular dark-field scanning TEM (HAADF-STEM) images of the post-WGS 1% Pt/Nb ₂ CT _x catalyst. (c,d) HAADF-STEM images of typical nanoparticles supported by Nb ₂ CT _x MXene. The majority of each particle is hanging over the vacuum to avoid niobium interference from the support. (e) EELS images acquired at several points on the particle surface, the locations of which are shown by corresponding numbers in (c) and (d,f) HAADF-STEM image showing discontinuous Nb ₂ CT _x MXene layers.	187
5.6 XRD patterns of Nb ₂ AlC MAX phase and Nb ₂ CT _x MXene	194
5.7 (a) SEM image of Nb ₂ AlC MAX. The as-synthesized Nb ₂ AlC shows the typical lamellar structure. (b) SEM image of 1% Pt/Nb ₂ CT _x after WGS reaction showing the Pt/Nb ₂ CT _x maintains the typical layered structure of MXene.	195
5.8 Arrhenius plots for WGS over 1% Pt/Nb ₂ CT _x -MXene catalyst. The WGS rates were measured in presence of 7% CO, 22% H ₂ O, 8.5% CO ₂ , 37% H ₂ , and balance Ar.	196
5.9 (a-c) HAADF-STEM images of 1% Pt/Nb ₂ CT _x after WGS reaction. (d) Particle size distribution statistics of used 1% Pt/Nb ₂ CT _x catalyst, and the average particle size is determined to be 2.6 ± 0.6 nm	197
5.10 (a) HAADF-STEM image of 1% Pt/NbC (bulk) after WGS reaction. (b) Particle size distribution statistics of used 1% Pt/NbC (bulk), and the average particle size is determined to be 13.8 ± 9.6 nm.	198
5.11 (a) Temperature programmed reduction (TPR) profile of Nb ₂ CT _x MXene. The H ₂ O peak around 340 °C can be attributed to the reduction of O and OH terminations on the surface of Nb ₂ CT _x MXene, which is consistent with the results of the quasi <i>in situ</i> XPS. Comparing with the TPR profile of Nb ₂ O ₅ , the additional H ₂ O peaks located above 600 °C can be assigned to the reduction of residual Nb ₂ O ₅ after HF etching [275]. The residue oxygen on the surface also desorbs as CO and CO ₂ [276] (b) TPR profile of commercial bulk NbC. The H ₂ O peaks at around 400 °C and 650 °C are likely due to the removal of the surface residue oxygen [277]. (c) TPR profile of commercial bulk Nb ₂ O ₅ . The peak between 800 °C and 900 °C is due to the reduction of Nb ₂ O ₅ to NbO ₂ [278].	199

Figure	Page
5.12 Quasi <i>in situ</i> XPS spectra of Nb 3d of pre-reduced 1% Pt/Nb ₂ CT _x sample (the fresh sample was reduced at 350 °C by H ₂ and then exposed to air before the quasi <i>in situ</i> XPS measurement) reduced at 350 °C and 550 °C again. These results indicate the enriched Nb ₂ O ₅ induced by subsequent air exposure is not reducible by H ₂ at 550 °C.	200
5.13 XRD patterns of spent 1% Pt/Nb ₂ CT _x catalyst after WGS reaction (red line) and Nb ₂ CT _x MXene after TPR treatment (black line).	201
5.14 (a) <i>In situ</i> XANES spectra of Pt L _{III} edge of 2% Pt/Al ₂ O ₃ sample treated at 550 °C and fresh 1% Pt/Nb ₂ CT _x treated at 350 °C and 550 °C in 3% H ₂ /He. (b) Fourier transform magnitude of the k ² EXAFS of 2% Pt/Al ₂ O ₃ sample treated at 550 °C and fresh 1% Pt/Nb ₂ CT _x treated at 350 °C and 550 °C in 3% H ₂ /He. (c) Quasi <i>in situ</i> XPS spectra of Pt 4f _{7/2} of Pt/SiO ₂ reduced at 550 °C and Pt/Nb ₂ CT _x sample reduced at 350 °C and 550 °C. (d) HAADF-STEM image of fresh 1% Pt/Nb ₂ CT _x catalyst reduced in H ₂ at 550 °C. Particle agglomerates after the high temperature (550 °C) reduction. (e) Elemental mapping of Pt. (f) Elemental mapping of Nb. A Nb deficient area is circled by the white dash line.	202
5.15 (a) HAADF-STEM image of used 1% Pt/Nb ₂ CT _x WGS catalyst. (b) Elemental mapping of Pt (c) Elemental mapping of Nb, (d) Elemental mapping of O. The area of interest (circled using white dash line) is a nanoparticle which is hanging over vacuum to avoid Nb signal from the Nb ₂ CT _x support. The EDS result suggests that uniform bulk Pt-Nb alloy is not formed.	204
5.16 (a) HAADF-STEM image of used 1% Pt/NbC bulk catalyst. (b) Spectrum of electron-energy loss acquired at a point (marked as “1”) on the particle surface. The absence of Nb M _{4,5} absorption edge with onset at 205 eV indicates no Pt-Nb surface alloy is formed for Pt supported by bulk NbC. The signal of C can be caused by carbon lacey of the TEM grid or carbon contamination of the catalysts. Note the catalyst was synthesized and treated using the same procedure with 1% Pt/Nb ₂ CT _x WGS catalyst. . .	205
5.17 (a) HAADF-STEM image of fresh 1% Pt/Ti ₃ C ₂ T _x catalyst reduced in H ₂ at 550 °C. Particles agglomerated after the high temperature (550 °C) reduction. (b) Elemental mapping of Pt and Ti. (c) Elemental mapping of Ti, (d) Elemental mapping of Pt.	206
5.18 The magnitude and imaginary part of the Fourier Transform of the k ² weighted EXAFS plot and corresponding first shell fit for Pt/Nb ₂ CT _x catalyst reduced at (a) 350 °C and (b) 550 °C. The fitting ranges are Δk = 2.7-11.7 Å ⁻¹ and ΔR = 1.6-3.2 Å. Corresponding fitting results are in Table 5.2	207

Figure	Page	
6.1	Time on stream (TOS) profile for 0.092Au/TS-1(75). Initial rate increase occurs during temperature ramp (0.0083 K s^{-1}) until reaction temperature (473 K) is reached. Returns to 10% H_2 /10% O_2 /10% C_3H_6 /70% N_2 (by volume) are represented by white boxes after the initial activation under these conditions. Reaction orders are measured by non-monotonically varying the reactant (or product) flowrate of interest while keeping the total flowrate constant ($\text{SV} = 14,000 \text{ cm}^3 \text{ g}_{\text{cat}}^{-1} \text{ h}^{-1}$ up to 25 h, then 26,000 for $\text{TOS} > 25 \text{ h}$) and varying the balance N_2 flow rate to compensate. N_2 flow at reaction temperature maintained between each experiment to maintain O_2 and moisture-free atmosphere.	222
6.2	Natural log of the net PO rate ($\text{mol g}_{\text{cat}}^{-1} \text{ s}^{-1}$ total minus $\text{mol g}_{\text{cat}}^{-1} \text{ s}^{-1}$ fed) (diamonds) and natural log of the H_2 oxidation rate ($\text{mol g}_{\text{cat}}^{-1} \text{ s}^{-1}$ H_2 consumed minus net $\text{mol g}_{\text{cat}}^{-1} \text{ s}^{-1}$ PO formed) (squares) as a function of the natural log of the total gas phase PO mol fraction over 0.030Au/TS-1(81) at 473 K with gas composition 10% H_2 /10% O_2 /10% C_3H_6 , balance N_2 and PO (PO mol fraction in feed 0–0.003) at a SV of $26,000 \text{ cm}^3 \text{ g}_{\text{cat}}^{-1} \text{ h}^{-1}$. The solid lines show the linear regressions to the data resulting in the reported reaction orders. Error bars represent one standard deviation.	225
6.3	(a) PO production rate (circles) and H_2 oxidation rate (squares) in a gas-phase CSTR as a function of space time (b) natural log of C_3H_6 conversion (circles), natural log of H_2 conversion (filled squares), and natural log of H_2 oxidation computed from the H_2 conversion by subtracting PO formation (open squares) as functions of the natural log of space time (c) natural log of PO production rate (circles) and natural log of H_2 oxidation rate (squares) as functions of the natural log of the total gas phase PO mol%. Dotted lines in (b) and (c) are linear trendlines fit to the data resulting in the reported equations, while the thick dotted line in (c) is the average of the natural log of the H_2 oxidation rates included to guide the eye. Mass of catalyst ranged from 0.080 to 0.400 g 0.10Au/TS-1(143), 473 K, 10% H_2 /10% O_2 /10% C_3H_6 / 70% N_2 (vol%) and the total flow rate was varied from 0.6 to $1.4 \text{ cm}^3 \text{ s}^{-1}$, resulting in a range of space times from 1.6 to $19 \times 10^5 \text{ h g}_{\text{cat}} \text{ cm}^{-3}$	226
6.4	Proposed reaction mechanism for propylene oxide synthesis over Au/TS-1 catalysts. S_1 is a Au site, S_2 is an Au-Ti interfacial site, and that they are neighboring sites.	230
6.5	Single-site reaction mechanism proposed by Barton and Podkolzin for hydrogen oxidation over Au/TS-1 catalysts [321].	236
6.6	Photograph of gas-phase CSTR system with heat-traced recirculation loop (left). P&ID diagram for gas-phase PFR/CSTR system (right).	239

Figure	Page
6.7 Diagram of Pyrex reactor (left). Photograph of Pyrex reactor (right). . .	240
6.8 XRD patterns for calcined (a) TS-1(75) and (b) TS-1(81) and (c) TS-1(143). Patterns are normalized to their maximum intensity and offset vertically for clarity.	241
6.9 N ₂ adsorption isotherms for TS-1(75) (circles) and TS-1(81) (squares) TS-1(143) (triangles). Isotherms are offset by 120 cm _{STP} ³ g ⁻¹ for clarity. Micropore volumes are reported in Table 6.1.	242
6.10 DRUV spectra in Kubelka-Munk units (normalized to the maximum F(R) intensity) for (a) TS-1(75) (b) TS-1(81) and (c) TS-1(143), collected (i) under ambient conditions (solid line), (ii) after dehydration at 523 K (dashed line).	244
6.11 Tauc plots for (a) TS-1(75) and (b) TS-1(81) and (c) TS-1(143) measured under dehydrated conditions (He flow, 523 K).	245
6.12 Determination of the deactivation rate constants in the initial deactivation (large dashed line, circles) and the steady-state deactivation (small dashed lines, squares) regimes for 0.092Au/TS-1(75). Note that after 24 h time on stream, the space velocity was changed from 14,000 to 26,000 cm ³ g _{cat} ⁻¹ h ⁻¹ and the reactor operating mode changed from PFR to CSTR, resulting in an increased reaction rate at 25 h time on stream. (T = 473 K, feed was 10% H ₂ /10% O ₂ /10% C ₃ H ₆ /70% N ₂ by volume).	248
6.13 Example determination of the first-order exponential decay constant for correction of steady-state reaction rates during PO order measurement on 0.063Au/TS-1(75). Data collected in CSTR mode, SV= 26,000 cm ³ g _{cat} ⁻¹ h ⁻¹ , T = 473 K, feed = 10% H ₂ /10%O ₂ /10%C ₃ H ₆ /0%-0.012% PO/Balance N ₂ over 0.063Au/TS-1(75) and represent returns to the standard condition with 0% PO co-feed. Over the time scale studied, the deactivation is approximately linear.	249
6.14 Apparent (a) H ₂ , (b) O ₂ , and (c) C ₃ H ₆ reaction orders measured over 0.092Au/TS-1(75) at 473 K and a space velocity of 26,000 cm ³ g _{cat} ⁻¹ h ⁻¹ in a gas-phase CSTR.	250
6.15 Apparent activation energies (deactivation corrected, not PO corrected) for PO formation measured over (a) 0.019Au/TS-1(143), (b) 0.040Au/TS-1(81), and (c) 0.022Au/TS-1(143) from 443-483 K with a feed composition of 10% H ₂ / 10% O ₂ / 10% C ₃ H ₆ / 70% N ₂ and a space velocity of 26,000 cm ³ g _{cat} ⁻¹ h ⁻¹ in a gas-phase CSTR.	250

Figure	Page
6.16 Example PO order measurement (a) before and (b) after correction for deactivation over time on stream. Numbers near each data point represent the non-monotonic order in which the data were collected (data points 1 and 6 represent no PO co-feed). Data collected in CSTR mode, $SV = 26,000 \text{ cm}^3 \text{ g}_{\text{cat}}^{-1} \text{ h}^{-1}$, $T = 473 \text{ K}$, feed = 10% H_2 /10% O_2 /10% C_3H_6 /0%-0.024% PO/Balance N_2 over 0.069Au/TS-1(143).	253
6.17 Propylene oxide formation rate as a function of time on stream (filled circles) and CO_2 inlet pressure (open squares) over 0.11Au/TS-1(81) with 10% H_2 /10% O_2 /10% C_3H_6 /Balance N_2 flow ($SV = 14,000 \text{ cm}^3 \text{ g}_{\text{cat}}^{-1} \text{ h}^{-1}$, $T = 473 \text{ K}$).	254
6.18 Apparent water order measured over 0.069Au/TS-1(143) at 473 K, $SV = 26,000 \text{ cm}^3 \text{ g}_{\text{cat}}^{-1} \text{ h}^{-1}$, 10% H_2 , 10% O_2 , 10% C_3H_6 , 0-0.86% H_2O /Balance N_2 in a gas phase CSTR.	255
6.19 One variation of the sequential mechanism. In this mechanism, S_1 refers to a Au site, and S_2 refers to a Ti site.	257
7.1 Illustration of the Formation of Sb Nanochains	263
7.2 Micrographs of the Sb nanochains: (a) conventional TEM image displaying the connected Sb nanochain structure; (b) HAADF-STEM image showing the hollow structure of the Sb nanochains; (c) FFT bandpass-filtered HRTEM image displaying the crystal lattice of Sb with the corresponding FFT inset (#) relating to the $[4\bar{1}1]$ Sb zone axis; (d-f) STEM-EDS elemental maps with (d) a reference HAADF-STEM image with (e) the Sb elemental map in blue and (f) the O elemental map in yellow revealing an O impurity phase.	266
7.3 Electrochemical performance of Li-ion cells fabricated using a 3D Sb nanochain anode material: (a) voltage versus (dis)charge capacity profiles (the inset corresponds to the cyclic voltammetric analysis acquired between 0.01 and 2.5 V versus Li/Li^+ at 0.1 mV s^{-1}); (b) capacity versus cycling performance for 100 cycles at 0.5 C, with a comparison between Sb nanochains and Sb supported on graphene; (c) rate capability studies of voltage versus (dis)charge capacity profiles; (d) comparison of the rate capability between Sb nanochains and Sb supported on graphene.	267
7.4 ^{11}B NMR spectrum of the progress of ammonia-borane synthesis: (a) prior to water addition (SBH: AB, 1:0); (b) 15 min. after addition of water (SBH: AB, 4.4:1.0); (c) 4 h after addition of water (SBH: AB, 0.01:1.00); and (d) 5 h after addition of water (SBH: AB, 0:1).	271
7.5 ^1H NMR (300 MHz, Tetrahydrofuran- <i>d</i> 8) Ammonia-borane	273

Figure	Page
7.6 ^{11}B NMR (96 MHz, Tetrahydrofuran- <i>d</i> 8) Ammonia-borane	274
7.7 Reaction Solution, prior to the addition of methanol. ^{11}B NMR (96 MHz, water) δ 19.03. (s).	277
7.8 ^{11}B NMR of boric acid (96 MHz, water) δ 19.06. (s).	277
7.9 TEM analysis of antimony nanoparticles synthesized using; antimony salt, reducing agent, capping agent: (a) SbCl_3 , ammonia borane, oleylamine; (b) SbCl_3 , methylamine borane, oleylamine; (c) SbCl_3 , triethylamine borane, oleylamine; (d) SbCl_3 , piperidine borane, oleylamine	279
7.10 Continued from Figure 7.9: (e) SbCl_3 , sodium borohydride, oleylamine; (f) SbF_3 , ammonia borane, oleylamine; (g) ammonia borane, SbCl_3 , PVA.	280
7.11 The crystalline structure and composition of 3D antimony-nanochains investigated using (a) powder X-ray diffraction, (b) Raman spectroscopic measurements, and (c) energy dispersive X-ray spectroscopy.	282
7.12 Homogeneous morphological investigation of 3D antimony nanochains (a), (b), (c) and crystallinity (d) examined using transmission electron microscopic technique.	283
7.13 High resolution transmission electron microscope image displays (a) & (c) the lattice fringes of crystalline antimony and (b) & (d) the corresponding fast Fourier transform of 3D antimony nanochains of the characteristic zone axes $[0\bar{1}1]$ & $[4\bar{1}1]$ of the rhombohedral antimony phase, respectively.	285
7.14 Cyclic voltammetric analysis of the 3D antimony nanochains anode material between 0.01 – 2.5 V at 0.1 mV s $^{-1}$ using 1 M LiPF_6 in ethylene carbonate (EC) and diethyl carbonate (DEC) in the volume ratio of 1:1 as electrolyte and Celgard TM 2500 separator.	286
7.15 TEM analysis of (a) pristine, (b) lithiated and (c) delithiated antimony nanochains.	287
7.16 Physical and chemical characterization of Sb/Gr composite. (a) XRD pattern; (b,c) TEM micrographs; (d) SEM image; and EDX mapping of (e) carbon and (f) Sb.	289
7.17 Electrochemical impedance spectroscopy information of 3D antimony nanochains and Sb/Gr before and after 2 nd , 100 th cycles.	290
8.1 Autogenic synthesis of carbon–sulfur composites. Carbon–sulfur composites are synthesized by controlled deposition of sulfur vapor. Heating carbon and sulfur within the autogenic reactor distributes sulfur vapor throughout the carbon substrate. Upon cooling, solid sulfur deposits on the available surface area of the carbon substrate.	296

Figure	Page
8.2 Sulfur distribution in carbon–sulfur composites. Deposition of fluid sulfur phases encourages homogeneous sulfur distribution. In the autogenic process, sulfur vapor can access and deposit onto the large surface area of small carbon micropores. In the mechanical mixing process, solid sulfur species are unable to penetrate or access pores beyond particle surfaces.	300
8.3 Controlled sulfur loading for autogenic carbon–sulfur composites. (a) As sulfur–carbon precursor ratio increases, the efficiencies of sulfur loading for the autogenic and mechanical mixing processes converge toward unity. (b) While it is constant for mechanical process, synthesis efficiency for the autogenic process is a monotonic function of final sulfur mass percent. (c) Targeted sulfur loading for different weight percent sulfur.	302
8.4 High-resolution X-ray powder diffraction of autogenic carbon–sulfur composites. (a) The characteristic diffraction features of orthorhombic sulfur (green) are absent in diffractograms of carbon–sulfur composites. (b) Diffractogram features not associated with amorphous carbon are likely attributable to experimental artifacts. High-resolution X-ray powder diffraction was conducted at beamline 11-BM at Argonne National Laboratory with a wavelength of 1–0.34 Å.	303
8.5 Isothermal nitrogen sorption of autogenic carbon–sulfur composites. (a) Specific volume of carbon precursor compared with the specific volumes of composites postsynthesis. Showing mechanical synthesis possibly has a high amount of surface sulfur. (b) Pore distribution of carbon precursor compared with the pore distributions of carbon–sulfur composites post synthesis.	305
8.6 Scanning electron micrographs of autogenic carbon–sulfur composites. Autogenic carbon–sulfur composites (left) show carbon (middle) and sulfur (right) species distributed throughout the composites.	306
8.7 Scanning transmission electron micrographs of autogenic carbon–sulfur composites. (a,c) Autogenic composites and (b,d) pure carbon generally appear the same in scanning transmission microscopy.	307
8.8 Extended galvanostatic cycling of autogenic carbon–sulfur composites. Autogenic carbon–sulfur composites, under various extent of vaporization time at a temperature of 445 °C, demonstrate a high specific capacity compared with mechanical mixing synthesis, in addition, to the high capacity demonstrated by the 30% vaporization high sulfur loading (HS) at 80 wt%. Autogenic samples are termed vaporization percentages, that is to say autogenic 30% refers to 4.9 h at 155 °C and 2.1 h at 445 °C.	309

Figure	Page
8.9 Columbic efficiencies of extended galvanostatic cycling of autogenic carbon sulfur composites. Autogenic carbon sulfur composites, under various extent of vaporization time at temperature 445 °C, demonstrate unstable columbic efficiencies.	310
8.10 Chronopotentiograms for autogenic carbon–sulfur composites. (a) After ten cycles at a current density of 3344 A kg ⁻¹ (corresponding to cycle 130), which was the last cycle at that current density. (b) Similarly, ten cycles at a current density of 84 A kg ⁻¹ (corresponding to cycle 160), which was the last cycle for that current density. Autogenic carbon–sulfur composites demonstrate high capacity and greater energy efficiency than mechanically synthesized composites.	311
A.1 Ray diagrams and sample TEM images demonstrating BF and DF TEM imaging. Dashed lines indicate electrons scattered or diffracted by the sample. Note the position of the objective aperture.	343
A.2 A ray diagram showing the elements of the electron beam in STEM mode. Dashed lines indicate deflection of the beam path by the scan coils in order to raster the electron probe across the sample surface. Faint lines indicate electrons scattered or diffracted from the sample.	344
B.1 Cartoon depicting the mechanism of incident electron deflection via excitation of an electron in an atom.	346

ABSTRACT

Mitchell, Garrett M. Ph.D., Purdue University, May 2020. Morphology, Properties and Reactivity of Nanostructures. Major Professors: Fabio H. Ribeiro and W. Nicholas Delgass.

Metal nanoparticles have long been of paramount importance in many areas such as: emission reduction in cars, hydrogen production via the water-gas shift reaction, and lithium-ion storage in batteries. For these purposes, the size and shape of the nanoparticles have been shown to play a crucial role in improving nanoparticle performance.

For characterization of nanostructures, the use of transmission electron microscopy (TEM) has been shown to be extremely useful. Via a TEM instrument, one can learn about nanoparticle properties such as: particle size, 3D morphology, chemical composition, fine structure, crystallography, even to atomic resolution. No other technique boasts such ability at such a high xyz resolution. This work includes TEM work for many different applications within catalysis and energy storage fields.

In catalytic applications, the <1 nm particle sizes often sought after generally lead to higher activity per unit mass of the catalyst, but also have the tendency to sinter due to concomitant increases in the surface free energy, leading to catalyst deactivation especially at elevated temperatures. To investigate the sintering, (Pt,Au)-iron oxide heterodimer nanoparticles were heated in the microscope with simultaneous imaging. For that purpose, the sample was irradiated with a 532 nm pulsed laser, with laser powers of 4-25 mW within a TEM microscope to investigate particle sintering as it happens. The Au and Pt phases were both found to wet over the Fe_3O_4 phase, a behavior opposite to the Strong Metal Support Interactions (SMSI - caused by oxide wetting the metal) which were expected from well-known literature reports.

This new behavior demonstrates that not only nanoparticle size, but also the support particle size can affect catalytic properties. This is shown by the fact that the size of the support oxide in these heterodimer nanoparticles is only 3 times the diameter of the active metal nanoparticles, compared to a greater than 20 times size difference for a standard metal oxide supported nanoparticle system.

Nanoparticle metal catalysts can also undergo significant catalytic improvement via the addition of promoting metals. Kinetics were measured on a series of Pt/Co on carbon nanotube support catalysts, and addition of Co was seen to improve the turnover frequency by 10 times. Leaching of the bulk Co phases, while preserving PtCo alloy structures, reduced activity by more than 18 times demonstrating the need for a Pt/CoO_xH_y interface for catalytic promotion, and showing that PtCo alloying did not produce the promotion effect.

Although, for the PtCo catalysts for WGS, the formation of a Co-oxyhydroxide phase was proved to be vital, nanoparticle alloying is also well-known to improve dehydrogenation kinetics. This was shown for a series of PtM catalysts with core/shell structures, which were found to be highly selective for propane dehydrogenation as a result of the PtM intermetallic phase. XAS studies of these materials led to the discovery that formation of a continuous PtM alloy surface layer that is 2–3 atomic layers thick was sufficient to obtain identical catalytic properties between those of the core–shell and full alloy catalysts. TEM characterization was also performed to determine the core/shell nature of these catalysts.

Another interesting morphological “tuning knob” of nanoparticle catalysts is related to Reactive metal–support interactions (RMSI). RMSI can have electronic, geometric and compositional effects that can be used to tune catalytic active sites. Generally, non-oxide supports are disregarded as unable to undergo RMSI. However, we report an example of non-oxide-based RMSI between platinum and Nb₂CT_x MXenes—a recently developed, two-dimensional metal carbide, with a dopant labeled as T. The surface functional groups can be reduced, and a Pt–M surface alloy is formed. WGS reaction kinetics reveal that these RMSI supports stabilize the relevant nanoparticles

and generate higher H₂O activation ability and thus higher rates compared with a non-reducible support or a bulk niobium carbide. This RMSI between platinum and the niobium MXene support can be extended to other members of the MXene family and opens new avenues for the facile design and manipulation of functional bimetallic nanoparticle catalysts.

Other important catalytic nanostructures are Au/TS-1 (Titanosilicalite-1, a zeolite with the MFI structure) catalysts which can be used to make propylene oxide (PO), an important industrial intermediate, and are extremely interesting due to the potential for one-pot chemical reactions, which will save on capital costs. The kinetics of propylene epoxidation over these Au/TS-1 catalysts were measured in a continuous stirred tank reactor (CSTR) free from temperature and concentration gradients. Apparent reaction orders were measured at 473 K for H₂ (0.7 order), O₂ (0.2), and C₃H₆ (0.2) for a series of Au/TS-1 catalysts with varied Au (0.02–0.09 wt%) and Ti (Si/Ti: 75–143) contents. These measured orders were consistent with those reported previously. Co-feeding propylene oxide enabled measurement of the apparent reaction order in propylene oxide (−0.4 to −0.8 order), showing, for the first time, and it was found that relevant pressures of propylene oxide reversibly inhibit propylene epoxidation over Au/TS-1, while co-feeding carbon dioxide and water has no effect on the propylene epoxidation rate. Analysis of previously proposed two-site reaction mechanisms in light of these new reaction orders for O₂ (0.4), H₂ (1), and C₃H₆ (0.4), corrected to account for propylene oxide inhibition, provides further evidence that propylene epoxidation over Au/TS-1 occurs via a simultaneous mechanism requiring two distinct, but adjacent, types of sites, and not by a sequential mechanism that invokes migration of H₂O₂ formed on Au sites to PO forming Ti sites. H₂ oxidation rates are not inhibited by propylene oxide, implying that the sites required for hydrogen oxidation are distinct from those required for propylene epoxidation. Those who intend on performing kinetics in the future are encouraged to perform a simple conversion-based τ -test, outlined in the relevant chapter of this thesis, to determine whether products inhibit reaction rates.

Yet another important field in which nanoparticle morphology research is essential is that of development of lithium-ion batteries. The current commercial graphite anode for lithium batteries is unfortunately prone to formation of lithium plating during use, from which well-documented safety issues arise. We demonstrated the use of an alternative anode, antimony, to have a measured specific capacity that is 1.6x higher than the theoretical capacity of graphite. Antimony, however, suffers from low cyclability due to large volumetric changes (150%) upon the expansion caused by lithiation. To combat this problem, several different synthesis methods to produce nanoparticles of differing structures were tested and it was found that amine boranes produce a unique 3D nanochain structure with stable particle sizes of 30 nm. These “3D nanochains” were found to have a stable charge capacity retention (98%) after 100 cycles due to their unique morphology which accommodates the lithiation expansion.

The role of sulfur nanostructures in lithium–sulfur batteries was also examined. Carbon–sulfur composites without crystalline sulfur demonstrate a high specific capacity of $\approx 1000 \text{ Ah kg}^{-1}$ after 100 cycles with a gravimetric current of 557 A kg^{-1} . This high rate capacity is found to depend on sulfur distribution which, in turn, is controlled by the synthesis pathway.

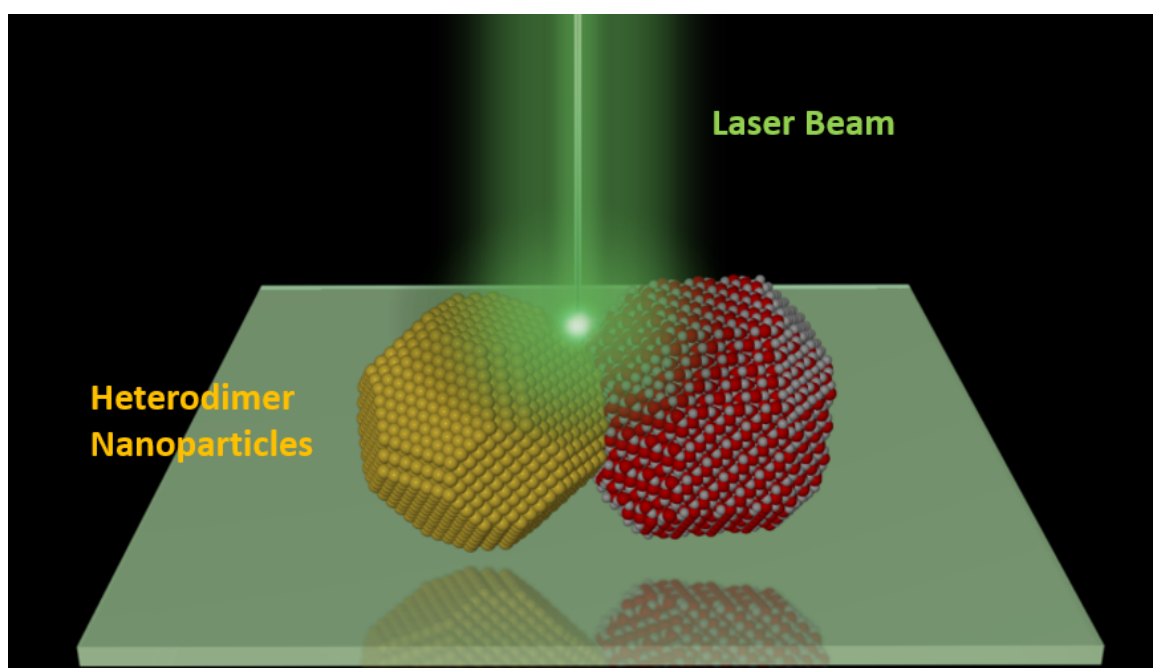
In conclusion, the morphology of nanostructures affects many different aspects of performance, rate, and stability. Further study into these details are expected to generate additional knowledge of a wide variety of interesting nanomaterials.

1. PROBING THE THERMAL BEHAVIOR AND STABILITY OF
METAL- Fe_3O_4 HETERODIMER NANOPARTICLES UTILIZING *IN SITU*
PULSED LASER HEATING TEM

Garrett M. Mitchell, Shoumya Nandy Shuvo, Subhajit Kundu, Michael J. Manto,
Chao Wang, Volkan Ortalan

1.1 Abstract

In situ laser heating with transmission electron microscopy (ILH-TEM) is utilized as a neoteric method to probe the thermal behavior and stability of metal (Pt, Au)-metal oxide (Fe_3O_4) heterodimer (HD) nanoparticles. Two different supporting membrane types are used for the laser heating: pure-carbon and silicon-nitride, requiring different amounts of laser power to induce morphological changes. Diffraction pattern analysis and Scanning Transmission Electron Microscopy-Electron Energy Loss Spectroscopy (STEM-EELS) is utilized to analyze reduction of the iron oxide under laser heating, which has differing effects depending on the support film heating mode and the heterodimer particle. A unique wetting behavior of Pt and Au onto Fe_3O_4 is observed in both heterodimers of Au and Pt. However, this wetting behavior is found to be partially reversible only in the case of the Au- Fe_3O_4 HD system, whereas for the Pt- Fe_3O_4 HD system, this wetting process was found to be irreversible under the applied experimental conditions. Understanding this wetting behavior has future implications in understanding the performance of metal nanoparticles supported on oxides at high temperature applications, such as catalysis.



1.2 Introduction

Metal nanoparticles supported on oxides have long been of paramount importance in catalysis for water purification, emission reduction in cars, the water-gas shift reaction and the methane/propane oxidation reaction [1–7]. In this regard, size and shape of the nanomaterials have been shown to play a crucial role in improving catalytic activity [8–10]. Reduction in size leads to higher activity per unit mass of the catalyst but due to concomitant increase in surface free energy, there is a higher tendency to sinter. The high temperature and reactive conditions encountered during catalysis often accelerate the sintering process, which results in a loss of active surface area of the nanoparticles, causing an undesired catalyst deactivation. An unwanted shape change may further pose a threat to the activity. Apart from the shape/size, tuning the metal-support interaction (MSI) has been a key factor in improving functionality of catalytic systems [8]. Over the past two decades, there have been plenty of studies on the bonding between gold/platinum and metal oxide supports showing not only high catalytic activities [9, 10] but also high stability [11] against sintering. Often abrupt change in activity has been observed at higher temperature [12, 13], therefore, studying the evolution of shape/size with temperature is important to correlate the high temperature catalytic activity with its respective shape/size.

To investigate this stability behavior, we employ a study involving the use of plasmonics, a growing field of nanotechnology where the interaction between the electromagnetic fields and the free electrons in metal nanostructures are being studied [14, 15]. Many exciting research directions have emerged by the virtue of the wide variety of chemical and physical processes that can be induced by light [16–19]. The advent of lasers provided a useful system to investigate and control plasmonic materials. Along with the development of the novel nanomaterial synthesis route called laser ablation [20, 21], the ability of laser pulses to heat locally in a controlled and efficient way also makes it promising for architecting nanomaterials with good precision. The synchronized use of electron microscopy and lasers resulted in the possibility of *in situ*

laser heating-transmission electron microscopy (ILH-TEM), which has enabled spatial and temporal studies of structural dynamics with nanoscale resolution [22–28]. Real time data was achieved with ILH-TEM utilizing different electron microscopy techniques, such as real-space imaging, diffraction and electron energy loss spectroscopy (EELS) [22, 23]. In order to further investigate samples after ILH-TEM imaging, scanning transmission electron microscopy (STEM) is used since it provides a unique advantage for imaging. Through the exploitation of high angle scattered electrons, detectable by a high angle annular dark field (HAADF) detector, which depends on strong atomic number (Z^2) contrast (incoherent imaging), direct interpretation of an image is possible. While HAADF-STEM imaging is very valuable in imaging localized nanoscale regions with Z-contrast, ILH-TEM imaging exploits the utilization of lasers which give rise to a profound way to study laser-matter interactions, such as a plasmonic study of nanomaterials. Therefore, utilization of both techniques offers the full potential of electron microscopy in providing direct images and precise characterization of local nanostructures in real-time to achieve a fundamental understanding of dynamic processes occurring in nanomaterials.

Here we report the use of *in situ* laser heating experiments to probe the dynamic behavior and stability of Pt-Fe₃O₄ heterodimer (HD) and Au-Fe₃O₄ HD particles. The laser heating causes the Pt particles to undergo complete wetting onto Fe₃O₄, proving evidence for strong metal support bonding (MSB). A partial dewetting after cooling is observed in the Au-Fe₃O₄ HD system while no noticeable dewetting after cooling was observed for the Pt-Fe₃O₄ HD system, which could be understood by thermodynamic analysis. Understanding the nature of how these particles behave under heating gives insights into the precise control of the metal oxide supports in rational design of a stable metal catalyst.

1.3 Methods Section

1.3.1 Sample Preparation

In this experiment, two types of materials were used: Au-Fe₃O₄ HD, and Pt-Fe₃O₄ HD with two different kinds of TEM support membranes, a copper grid with an amorphous carbon support membrane (referred to as carbon support membrane) and a Silicon-Nitride support membrane (Ted Pella, Inc.). Synthesis of Au-Fe₃O₄ HD and Pt-Fe₃O₄ HD nanoparticles were made possible by inaugurating the epitaxial growth of Fe on Au and Pt nanoparticles (NP) seeds followed by Fe oxidation in an organometallic solution synthesis [22–24]. The main objective of employing organic methods of synthesis was to ensure regulation of the nanoparticles and a controlled uniform growth of Fe₃O₄ on the exposed (111) facets of the Au and Pt seeds.

For both Au-Fe₃O₄ HD and Pt-Fe₃O₄ HD nanoparticles, the nanoparticles were dispersed in hexane (3-6 mg/mL) which was then further diluted with hexane in a separate container to avoid surplus of samples on the grid. The purpose of hexane was to prevent any agglomeration and clump formation of the nanoparticles when the sample is loaded on the grid.

1.3.2 ILH-TEM Characterization

Two drops of hexane mixed with the heterodimers were then drop casted on both the grid types before they were placed in the sample holder. *In situ* TEM images and videos were obtained by using a modified FEI Tecnai T20 200 kV. Samples were heated via pulsed frequency doubled Nd-YAG laser beam with a wavelength of 532 nm, pulse frequency of 25 kHz, and pulse duration of 1 ns. The laser was first set at a minimum power of 3 mW. After loading the holder with either grid containing HD nanoparticles (copper grid with an amorphous carbon membrane or a Si₃N₄ membrane) into the goniometer, the sample was irradiated with a laser excitation pulse starting from a minimum power of 3 mW, which then is gradually increased with a step size of 0.44 mW up until reaching to a power where the heterodimers show

some structural or positional changes via TEM. The Region of Interest (ROI) was selected in such a way as to utilize effectively the Gaussian heating profile of the laser. The samples were also imaged for only 30 minutes for each ROI (much more than the time required to induce wetting under these laser heating conditions) to ensure that the structural changes in the HD nanoparticles were induced by laser heating and not by the electron radiation required for TEM imaging. No changes in the HD nanoparticles were observed via only electron radiation in this time scale.

1.3.3 TEM characterization

SAED diffraction patterns were collected both before and after the laser irradiation. The corresponding patterns were then analyzed to index the spots to determine the materials or phases present in the sample.

HAADF-STEM images were collected at 300 kV on a FEI Titan ETEM 80-300 kV in an *ex situ* condition. STEM-EELS, as well as some of the HAADF-STEM imaging, was performed on a JEOL JEM-ARM200cF utilizing a GIF Quantum SE Imaging Filter operated in Dual-EELS mode in an *ex situ* condition as well. *Ex situ* scanning TEM (STEM) electron energy loss spectroscopy (EELS) was performed after the laser irradiation of the Au-Fe₃O₄ HD and Pt-Fe₃O₄ HD nanoparticles to probe “local” chemical nature of the nanoparticles through point scans and spectrum imaging.

1.4 Results and Discussion

1.4.1 Laser Heating

Figure 1.1 displays the experimental set up of the ILH-TEM, which was utilized to study the laser-assisted annealing of the HD nanoparticles. The setup consisted of a specialized TEM with a port of entry for the laser beam and an optical bench, wherein the laser beam was generated and processed before entry into the TEM. In regular operation of an ILH-TEM, a sample excitation laser is used to induce change

in the sample. Herein, the sample excitation laser (532 nm Nd-YAG laser operating at 25 kHz with pulse duration of ~ 1 ns) along with continuous thermionic emission mode of the ILH-TEM is utilized to carry out the laser-assisted thermal annealing study on the HD nanoparticles. The HD nanoparticles were synthesized using a wet chemical route reported elsewhere [29–31]. Fe is grown epitaxially on (111) facets of Au or Pt nanoparticles and is subsequently oxidized to form the Metal- Fe_3O_4 HDs. Figure 1.1b-d shows low magnification and atomic resolution HAADF-STEM images of a typical Pt- Fe_3O_4 HD nanoparticle sample. The spacing between the array of Pt atoms was precisely measured to be 2.2 \AA , which corresponds to the (111) plane of Pt.

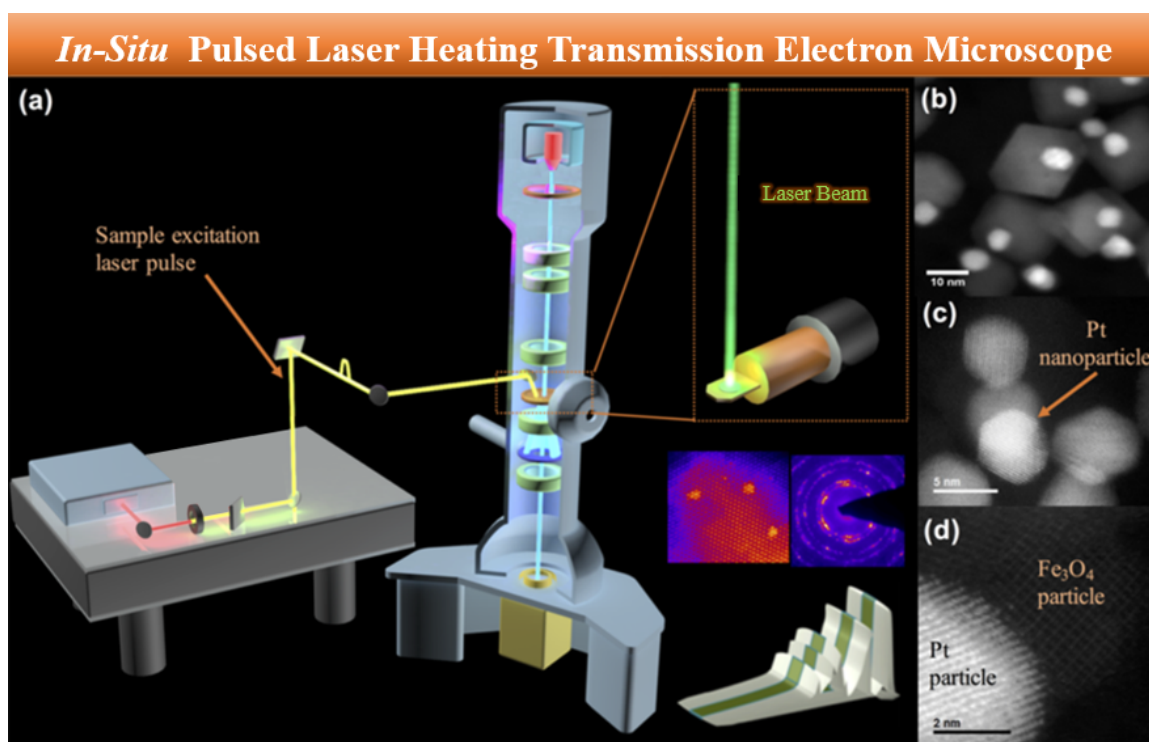


Figure 1.1. (a) Schematic diagram of the experimental set up of an *In Situ* Laser heating Transmission Electron Microscope. (b) HAADF-STEM image of Pt HD system. (c-d) HR-STEM images of Pt and Fe_3O_4 nanoparticles at atomic resolution.

Figure 1.2a shows Bright Field (BF)-TEM images of Pt-Fe₃O₄ HD nanoparticles supported on a carbon support membrane before laser irradiation. Laser irradiation of this region at a power of 7 mW (Figure 1.2b-e) reveals that the Pt nanoparticles (NPs) spread and cover the Fe₃O₄ nanoparticles at higher temperatures, which would indicate wetting of the Fe₃O₄ NPs by the epitaxial Pt NPs. The relevant particles in Figure 1.2 are color coded for clarity. In addition, the HD particles are seen to undergo sintering (Figure 1.3). After completion of the laser irradiation process, there was negligible amount of de-wetting of Pt from Fe₃O₄, indicating that such a transformation is irreversible under the experimental conditions. It can be noted that there is a cavity left by the sintering nanoparticles, this is seen for both the Si₃N₄ and the carbon film case (Figures 1.2e and 1.3d) and can be due to etching of the support by the nanoparticles. It can also be noted that there is some carbon contamination present in this system that could potentially affect the reduction process of Fe and even potentially form iron carbides [32]. However, carbon XPS studies in the literature suggest that there is no carbide formation under similar conditions [33].

Similar experiments were carried out with Au-Fe₃O₄ HD nanoparticles at a laser power of 5 mW (Figure 1.2h-l). It is well known that for an Au film grown on single crystalline Fe₃O₄, the interfacial adhesion between the Au and Fe₃O₄ is weaker compared to the Au-Au bonding, shown by the formation of 3D island shapes, following a Volmer-Weber growth mode [34, 35]. Indeed, to create a 2D film of Au on (111) Fe₃O₄ via UHV sputtering, the Au film thickness must be as high as 7 nm, at temperatures not above 200 °C. Such 2D films, however, can be created with Pt with a film thickness as low as 2 nm and are stable to a much higher temperature of 750 °C [34, 35]. However, this effect is contrary to our results for the Au-Fe₃O₄ HD system: Au particles spread onto the Fe₃O₄, wetting the Fe₃O₄ NPs at higher temperatures above 200 °C and lower film thickness than 7 nm. Also, unlike the Pt HD system, partial de-wetting of Au from Fe₃O₄ was observed after the laser irradiation was stopped. To further investigate this result, HAADF-STEM images were acquired from different regions which clearly shows the partial de-wetting of Au resulting in

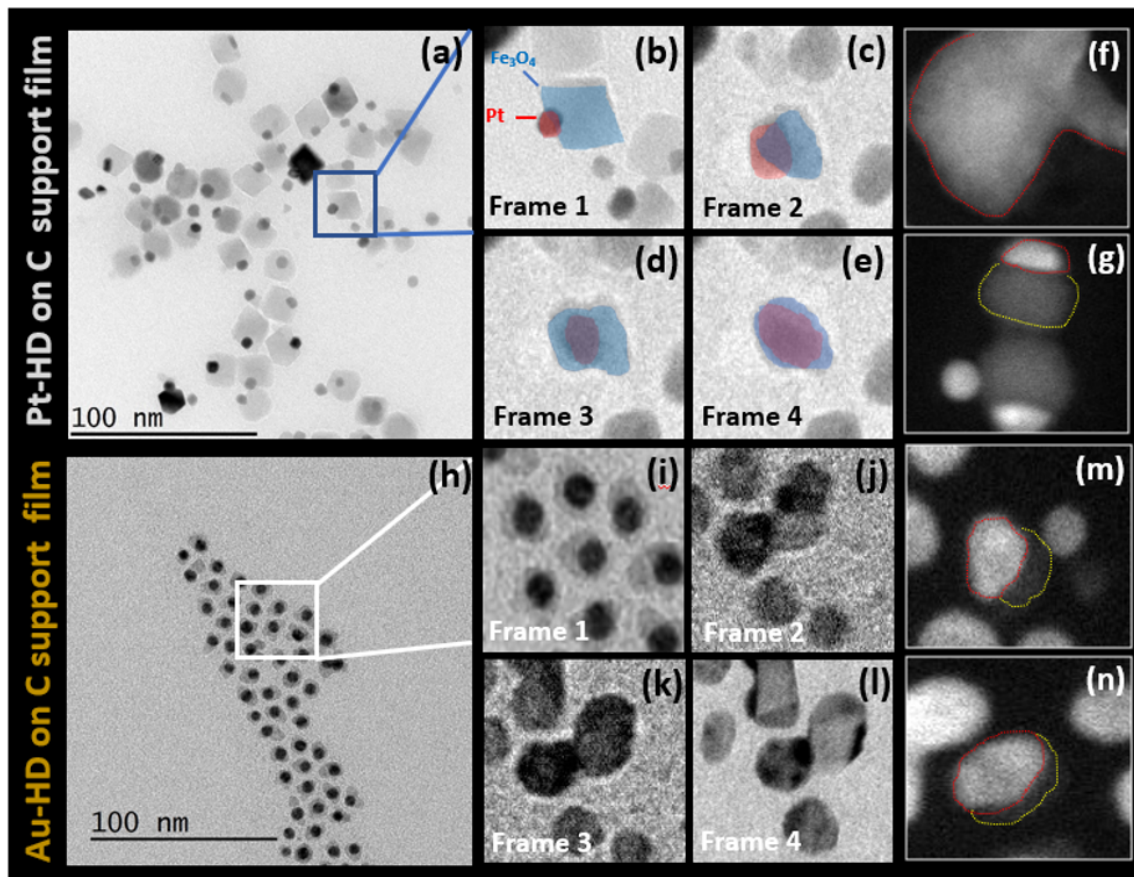


Figure 1.2. TEM micrographs displaying the heterodimer wetting behavior on a carbon support membrane (a,h) Bright field (BF)-TEM images of Pt and Au heterodimers, respectively, before laser irradiation. (b-e) and (i-l) Frames taken from the *in situ* laser heating TEM movie which illustrates the wetting process of the Pt and Au, respectively, onto the Fe_3O_4 . (f-g) and (m-n) HAADF-STEM images of Pt and Au heterodimers, respectively, after laser irradiation.

formation of two-faced Janus particles (Figure 1.2m-n). Some of the particles in TEM and STEM images are color coded for clarity.

The notable difference between the de-wetting behavior of Au and Pt onto Fe_3O_4 could be due to the difference in the strength of the Metal Support Bonding (MSB).

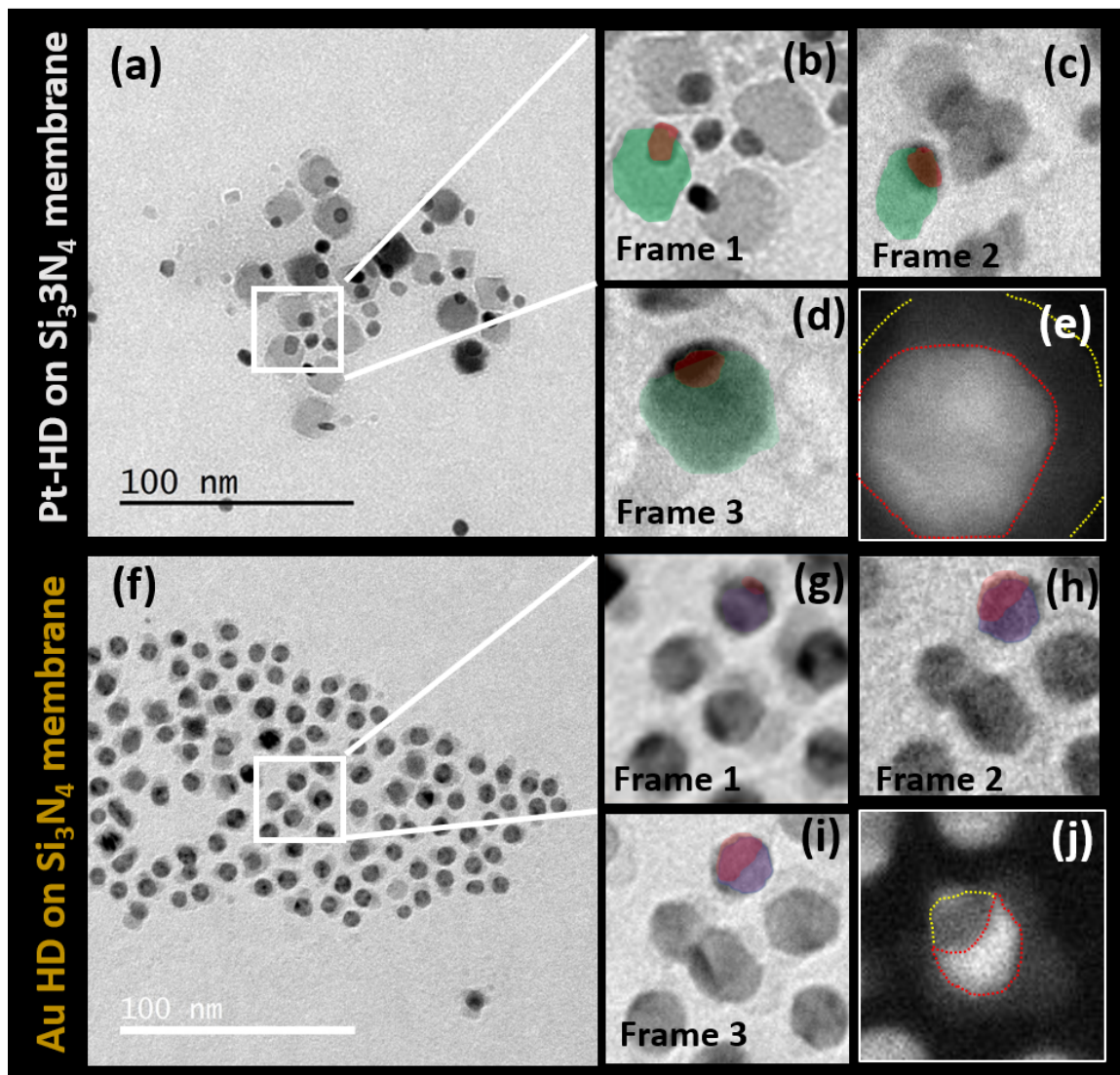


Figure 1.3. TEM micrographs displaying the heterodimer wetting behavior on a silicon nitride support membrane (a,f) Bright field (BF)-TEM images of Pt and Au heterodimers, respectively, before laser irradiation. (b-d) and (g-i) Frames taken from the *in situ* laser heating TEM movie which illustrates the wetting process of the Pt and Au, respectively, onto the Fe_3O_4 . (e,j) HAADF-STEM images of Pt and Au heterodimers, respectively, after laser irradiation.

An estimate of MSB strength under annealing conditions can be obtained using Young-Dupre equation:

$$E_{adh} = \gamma_{np}(1 - \cos\theta) \quad (1.1)$$

Where θ is the contact angle and γ_{np} is the surface energy of the supported nanoparticle.

In both the cases (Au and Pt), complete wetting of the surface of Fe_3O_4 is observed, making the contact angle, θ , equal 180° . But, since the surface energy of (111) Pt (2.489 J/m^2) is higher than Au (1.506 J/m^2) by a factor of 1.65 [36,37] the interfacial adhesion of Au is expected to be lower than Pt by a factor of 0.61. It can also be noted that Au has a lower melting point (1064°C or 1337 K) than Pt (1768°C or 2041 K) [38] Pt is also known to form many different full alloys with Fe, while Au will only form dilute solid solutions, indicating that the Pt-Fe interfacial energy is lower, or more relevant than for the Au-Fe system, therefore making the Pt-Fe wetting more stable [39,40]. Therefore, surface energy and bulk phase diagrams support the experimental result that Au will dewet from Fe_3O_4 , while Pt does not.

Pt heterodimers need more laser power (7 mW) to show viable occurrence of visible dynamics than Au heterodimers (5 mW), leading to a power ratio of 1.4:1, which is similar to the surface energy ratio of 1.65:1 showing a dependency of laser power on the surface energy of the different elements. The difference in laser power for the Pt and Au samples can also potentially be attributed to the relative absorbance power of the heterodimers. From the literature, the absorbance of Pt- Fe_3O_4 HD at 532 nm (the wavelength of the laser used in this experiment) is lower ($\sim 1.8x$) than the absorbance of the Au- Fe_3O_4 HD nanoparticles [41,42]. This effect, paired with the Pt:Au surface energy ratio of 1.65:1 (similar to the absolute melting point ratio of 1.53:1), should result in a required laser power ratio of $\sim 2.97:1$. The fact that the Pt:Au laser power ratio is only 1.4:1 on the carbon membrane, similar to the surface energy ratio, demonstrates that the laser power required to induce wetting is relatively unaffected by the absorbance differences between the Au- Fe_3O_4 HD and Pt- Fe_3O_4 HD particles.

Figure 1.3 demonstrates the result for laser heating of the HD nanoparticles on the silicon nitride (Si_3N_4) support membrane. For both the Pt- Fe_3O_4 HD and Au- Fe_3O_4 HD systems, it was observed that the laser power required to visualize any possible dynamics (such as wetting) was lower for the carbon support membrane compared to the Si_3N_4 support membrane by a factor of 2.88 averaged over the two sample types. This laser power Si_3N_4 /carbon is remarkably similar to the carbon/ Si_3N_4 DRUV-VIS Kubelica-Munk function ratio of 2.68 (shown in Figure 1.6). This indicates that the laser heating mechanism for both of these support types is dominated by laser absorption of the support and not the nanoparticles themselves. This conclusion is further made solid by the observation that the Pt/Au required laser power ratio on silicon nitride is 1.38, which is similar to ratio on the carbon membrane. If laser heating was performed mainly by direct plasmonic heating of heterodimer nanoparticles, the required Pt/Au laser power ratio would be closer to 2.97:1 as indicated in the previous paragraph. Thus, laser heating on silicon nitride is also dominated by laser absorption of the support, and not by the heterodimer nanoparticles.

1.4.2 SAED Analysis

To investigate any potential differences in chemistry between the two different support membranes, diffraction pattern analyses were carried out on both kinds (Pt- Fe_3O_4 HD and Au- Fe_3O_4 HD) of samples. Figure 1.4c-d and Figure 1.5c-d show diffraction patterns of Pt heterodimers supported on the silicon nitride and carbon support membranes respectively before and after laser irradiation. The appearance of rings indicates the presence of multiple nanocrystals of the heterodimers inside the Selected Area Diffraction (SAED) aperture. Indexing of the spots shows the presence of Pt and Fe_3O_4 crystal phases upon laser irradiation of Pt- Fe_3O_4 HD on both the silicon nitride and carbon support membrane. In this case, distinct diffraction spots corresponding to Fe were observed after laser irradiation indicating partial reduction of Fe_3O_4 to Fe after laser irradiation. This auto reduction behavior is well known

in the literature, and is known to be directly proportional to the temperature under vacuum [43].

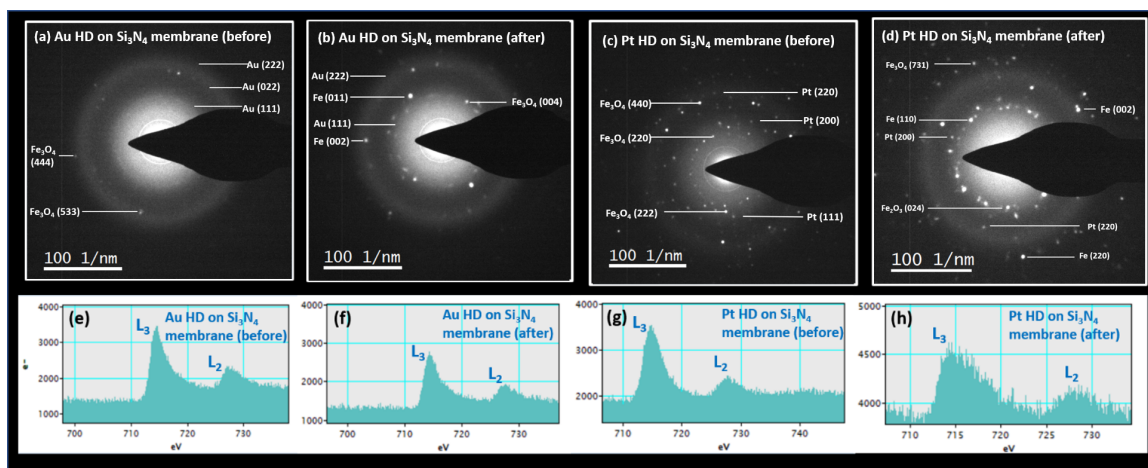


Figure 1.4. (a-b) SAED diffraction patterns of Au-Fe₃O₄ HD on a Si₃N₄ support membrane of a region of interest before and after laser irradiation, respectively. (c-d) SAED diffraction patterns of Pt-Fe₃O₄ HD on Si₃N₄ support membrane of a region of interest before and after laser irradiation, respectively. (e-f) EELS spectra showing Fe-L₃ and L₂ edges before and after laser irradiation on Au-Fe₃O₄ HD on Si₃N₄ support membrane, respectively. (g-h) EELS spectra showing Fe-L₃ and L₂ edges before and after laser irradiation on Pt-Fe₃O₄ HD on Si₃N₄ support membrane, respectively.

A very similar result was observed for the case of Au-heterodimers which has been shown in Figure 1.4a-b and Figure 1.5a-b, wherein faint spots corresponding to Fe were observed along with that of Au and Fe₃O₄ in both the systems comprising Si₃N₄ and carbon support membrane grids, indicating partial reduction of Fe₃O₄ to Fe.

1.4.3 EELS Characterization

The reduction of Fe₃O₄ after laser treatment was further investigated using STEM-EELS. Figure 1.4e-h shows the EELS spectrum of the Pt-Fe₃O₄ HD and Au-Fe₃O₄ HD samples before and after laser irradiation on a Si₃N₄ support membrane. The

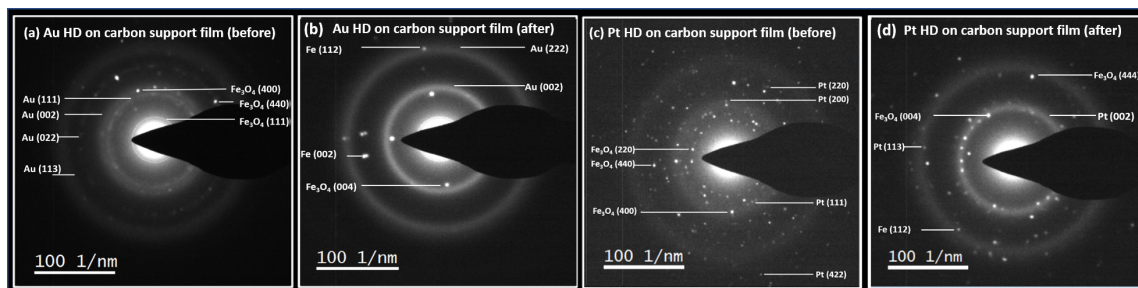


Figure 1.5. (a-b) SAED diffraction patterns of Au-Fe₃O₄ HD on a carbon support membrane of a region of interest before and after laser irradiation, respectively. (c-d) SAED diffraction patterns of Pt-Fe₃O₄ HD on a carbon support membrane of a region of interest before and after laser irradiation, respectively.

peaks were identified using the EELS atlas, Fe-L₃ edge being the more intense peak at ~ 715 eV and Fe-L₂ edge being the less intense peak at ~ 725 eV [44]. Since calculation of the oxidation state of Fe by the use of chemical shifts is not reliable when there are systems of mixed Fe oxidation states [45], the white-line intensity method was used to visualize the overall oxidation state. The peaks were first background subtracted using an inverse power law method, then deconvoluted by using the Fourier ratio method so that thickness effects were removed from the peak intensities. A double-atan function with a sharpness of 1 eV was fitted to the continuum, so that the continuum was subtracted from the white-line peaks [46]. The intensity of each peak was then measured with an energy window of 8 eV, and the resulting ratio of the L₃ intensity over the L₂ intensity was used to track the change in the average oxidation state of the Fe [47]. Reference peaks from HD nanoparticles before laser heating and from standard samples of Fe₂O₃ and metallic Fe (bulk form) were obtained for comparison to demonstrate that the white line intensity ratio will reduce upon reduction. However, since these bulk structures do not have the same fine structure as the HD nanoparticles, their white line intensity values cannot be directly compared to those in the HD systems. A tabulated form of the quantification data in Table 1.1 shows

the white line intensity ratios of Fe L₂ and L₃ edges of the reference samples of Fe and Fe₂O₃ and the HD before and after laser irradiation. It can be clearly seen that after laser treatment, the Pt-Fe₃O₄ HD system undergoes a more rigorous reduction as the white line intensity ratio undergoes a larger percent change of 63% compared to the Au-Fe₃O₄ 13% change in peak ratio, as well as having a higher percent difference from the initial HD white line intensity peak ratio than the carbon support membrane. This behavior can partly be explained by the fact explanation for why the Au-Fe₃O₄ HD wetting is semi-reversible where the Pt-Fe₃O₄ HD wetting is not, fine-structure changes that would change the white-line intensity ratio. However, this difference in the amount of reduction is likely simply due to higher laser power, and thus higher temperature, required to induce morphological changes in the Pt-Fe₃O₄ HD system.

Table 1.1.

Tabulated values of the integral ratio of the Fe L₃ and L₂ edges of the heterodimers before and after laser irradiation with included Fe reference states.

Sample	Initial	Laser-Treated	% Difference
Fe ₂ O ₃	4.36 ± 0.44	-	-
Fe Ref.	3.18 ± 0.13	-	-
Pt-Fe ₃ O ₄ on Si ₃ N ₄ membrane	3.89 ± 0.33	2.03 ± 0.73	63.02 %
Au-Fe ₃ O ₄ on Si ₃ N ₄ membrane	3.29 ± 0.39	2.89 ± 0.23	13.03 %

1.5 Conclusions

In conclusion, we have probed the thermal behavior and stability of Pt-Fe₃O₄ HD and Au-Fe₃O₄ HD nanoparticles utilizing the *in situ* capabilities of an ILH-TEM. It was found that both Pt and Au nanoparticles undergo wetting onto Fe₃O₄, an indication of strong metal support bonding. *In situ* BF-TEM and SAED analyses,

ex situ HAADF-STEM imaging, and STEM-EELS spectroscopy were used to analyze the wetting/de-wetting process. Au-Fe₃O₄ HD nanoparticles undergo a partial de-wetting procedure that can be used as a way to produce Janus particles, which is not undergone by the Pt-Fe₃O₄ HD particles. Furthermore, reduction of Fe₃O₄ to Fe was detected when experiments were performed on both silicon nitride and carbon support membranes, and the extent of reduction was more rigorous for Pt heterodimer nanoparticles. The laser heating technique was shown to be a useful and novel method to undergo such *in situ* heating experiments to underpin future development of functional heterodimer nanoparticles.

1.6 Supporting Information

1.6.1 DRUV-Vis Characterization

Silicon nitride grids (Ted-Pella) and an amorphous carbon nanopowder (<50 nm via TEM, >99%, Aldrich) were selected as suitable samples to model light absorption behavior of the silicon nitride and amorphous carbon grids used for laser heating. Before diffuse reflectance UV-Vis spectra (DRUV-Vis) spectra were collected, the relevant samples were ground, pressed then sieved between 60 and 120 mesh for the sake of sample scattering uniformity in data collection. Spectra (Figure 1.6) were measured under ambient conditions with a UV-vis-NIR spectrophotometer (Agilent, CARY 5000) with Poly(tetrafluoroethylene) (PTFE, 200 μ m particle size, Aldrich) as a solid reference and background. The scans were reported in Kubelica-Munk units to be used as a pseudo absorbance for use in comparing the different spectra quantitatively. At a light wavelength of 532 nm, the Kubelica-Munk absorbance units for silicon nitride and amorphous carbon were 3.295 and 8.814 respectively, leading to a carbon/silicon nitride absorbance ratio of 2.675.

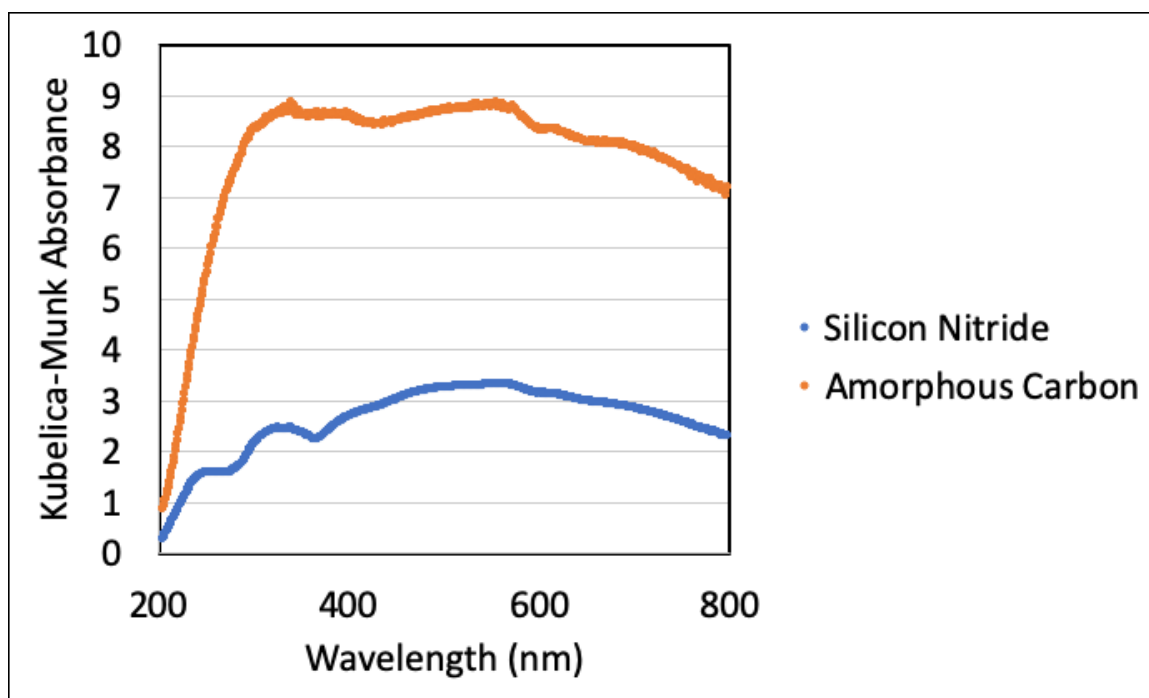


Figure 1.6. DRUV-Vis spectra of model samples silicon nitride and amorphous carbon

2. EFFECT OF COBALT ADDITION ON PLATINUM SUPPORTED ON MULTI-WALLED CARBON NANOTUBES FOR WATER-GAS SHIFT

Garrett M. Mitchell¹, Kaiwalya D. Sabnis¹, Fred G. Sollberger¹, Yanran Cui¹, Chang Wan Han², Paulami Majumdar¹, Zhenhua Zeng¹, Jeffrey T. Miller¹, Jeffrey Greeley¹, Volkan Ortolan³, Chao Wang⁴, W. Nicholas Delgass¹ and Fabio H. Ribeiro¹

¹Davidson School of Chemical Engineering, Purdue University, ²School of Materials Engineering, Purdue University, ³Department of Materials Science and Engineering, University of Connecticut, and ⁴Department of Chemical and Biological Engineering, Johns Hopkins University

2.1 Abstract

A series of cobalt-promoted Pt catalysts supported on multi-walled carbon nanotubes was synthesized, and their performance was evaluated for the water-gas shift (WGS) reaction. Compared to the monometallic Pt catalyst, the WGS turnover rate (TOR) at 300 °C was promoted by a factor of 10 at a Pt:Co molar ratio of 1:3. X-ray absorption spectroscopy and XRD showed the presence of a Pt₃Co alloy along with a partially oxidized cobalt and a free cobalt metal phase after reduction pretreatment. In order to determine the dominant active site over the Co-promoted catalysts, selective leaching of partially oxidized Co (designated as CoO_xH_y) and Co metal was performed with a 5 wt% acetic acid solution, while preserving the Pt-rich phases. The WGS TOR at 300 °C for the Co-promoted catalysts after leaching was observed to be even lower than that of the monometallic Pt catalyst. Thus, the alloy formation was determined to be inconsequential towards promotion in the WGS TOR, while the dominant active site was determined to be a PtCo alloy in intimate contact with

the CoO_xH_y phase. Combined Density Functional Theory (DFT) calculations and ab-initio thermodynamic phase diagrams point to a monolayer of CoOH being the most stable Co phase on Pt (111) under WGS conditions. Calculations of OH binding energies on Pt(111), $\text{Pt}_3\text{Co}(111)$, and at the interface between CoOH overlayers and Pt(111) shows that trends in the WGS activity of these catalysts are linked to the strength of OH binding, with the strongest OH binding found at the interface between CoOH and Pt, supporting the conclusion that a similar interface is the source of enhanced WGS activity in the PtCo bimetallic system.

2.2 Introduction

Supported noble metal catalysts such as Pt and Au are of great interest for the water-gas shift (WGS) reaction. These catalysts do not suffer from the disadvantages of the commercial Cu-based catalysts such as pyrophoricity, high sensitivity to moisture, and the requirement of a controlled reduction process [48]. The supported Pt catalysts have been shown to experience an increase in WGS rates with addition of various secondary metal promoters [49–53]. The exact role of secondary metals such as Re, Mo, or Co has, however, been a topic of debate in the literature. It is still unclear if a secondary metal alters the electronic properties of the Pt by forming an alloy or it helps by facilitating water activation during WGS [53]. Dietrich et al. [54, 55] showed, with the use of a series of PtCo bimetallic catalysts with varying Pt:Co ratios, that the rate of H_2 production in the aqueous phase reforming of glycerol increases with increasing amount of Co. It was also shown that the turnover rate of WGS over a series of PtCo samples correlates with the reforming rate of glycerol. However, the role of Co in promoting the WGS rate is still not well understood. A detailed study of PtCo alloys supported on silica as catalysts for propane dehydrogenation has also appeared in the literature [56]. It shows the formation of core/shell particles with the intermetallic compound Pt_3Co to be the dominant shell composition.

In this study, a series of PtCo bimetallic catalysts with increasing Co:Pt ratios was studied for the WGS reaction. Co was found to promote the WGS rate by

a factor of ten. Pt and Co were also observed to form an alloy after reduction, with some Co remaining isolated. Selective leaching of the isolated (unalloyed) Co from the catalysts was performed in such a way that much of the alloyed Co was retained in the PtCo catalyst. This leaching procedure was found to reduce activity up to a factor of 25.6. This dramatic decrease in rate was associated with removal of the Co oxyhydroxide layer, and showed clearly that the metal/ CoO_xH_y interface is the source of highest activity in this bimetallic system, As supported by DFT analysis. In order to further examine these catalysts, samples were characterized with multiple techniques to permit detailed correlations between atomic structure and WGS activity to be identified. X-ray absorption spectroscopy (XAS) and Extended X-ray Absorption Fine Structure (EXAFS) studies were performed to elucidate the structure of the PtCo alloys before and after leaching. Atomic resolution Scanning Transmission Electron Microscopy (STEM) analyses were also performed to map the distribution of Pt and Co within reference Pt_3Co bimetallic nanoparticles. DFT studies were performed to identify the most stable partially oxidized Co phase in contact with Pt and to understand its promotional effect as compared to pure Pt and the Pt_3Co alloy.

2.3 Experimental Methods

2.3.1 Catalyst Synthesis

Monometallic Pt and PtCo bimetallic catalysts supported on multi-walled carbon nanotubes (MWCNT's) were synthesized using a sequential incipient wetness impregnation method. The MWCNT support was purchased from Cheap Tubes Inc. The Pt weight loading was kept constant at ~ 5 wt%, while the Co target loading was varied from 1.6 wt% to 11.9 wt% i.e. a series of catalysts with varying target Pt:Co molar ratio (1:1, 1:2, 1:3, 1:5 and 1:8) were prepared. Aqueous solution of tetraammineplatinum(II) nitrate (Sigma Aldrich) was used as the Pt precursor. After Pt impregnation, the samples were dried overnight at 60 °C in air. Cobalt was

then added to each sample using an aqueous solution of cobalt nitrate hydrate (Alfa Aesar), followed by overnight drying at 150 °C in air.

Selective leaching of isolated Co was performed with a 5% acetic acid solution in a 10 mm × 6 mm × 200 mm (OD × ID × L) quartz tube plug flow reactor. A similar reactor system was used by Dietrich et al. [54] for performing aqueous phase reforming of glycerol, and a detailed description of it can be found in that reference. Catalysts with Pt:Co ratios of 1:3, 1:5 and 1:8, as well as a monometallic Pt catalyst, were subjected to this leaching process. Each of these as-prepared catalyst samples was loaded into a quartz tube reactor in between two quartz wool plugs. The catalyst was reduced at 450 °C (5 °C min⁻¹) for 2 hours in 100 sccm 5% H₂/Ar. Following the reduction, the catalyst was cooled to 25 °C under Ar. It was then exposed to an upward flow of the liquid 5% acetic acid solution. Liquid samples of the effluent solution were collected at fixed time intervals and were analyzed qualitatively for presence of Co with atomic absorption spectroscopy (AAS) using the Perkin Elmer AAnalyst 300 instrument.

The Pt₃Co/MWCNT catalyst was prepared by deposition of Pt₃Co alloy nanoparticles on to a MWCNT support. These spherical Pt₃Co nanoparticles were prepared by an organic solvothermal method, details of which can be found elsewhere [57]. Platinum acetylacetonate was reduced via the use of 1,2-tetradecanediol in the presence of 1-adamantanecarboxylic acid and an excess of oleamine as a capping agent, thermal decomposition of cobalt carbonyl was used to introduce Co. A desired amount of as synthesized Pt₃Co particles were kept in 10 mL of toluene. The MWCNT support was added to the solution, and the mixture was sonicated in an ultrasound bath for 1 hour. The solvent was removed by heating the vial at 50 °C. The catalyst was then further dried in static air inside an oven at 185 °C.

2.3.2 Measurements of Reaction Kinetics

The details of the differential plug flow reactor system used for WGS kinetic measurements can be found in the published literature [58]. The catalyst was loaded in

the plug flow reactor on top of a quartz wool plug. A K-type thermocouple protected by an SS sheath was inserted in the catalyst bed. As a pretreatment, all the catalysts were reduced in 25% H₂/Ar at 450 °C. For the Pt₃Co/MWCNT catalyst prepared using the organic solvothermal method, ligands such as acetylacetonate from the precursor Pt(acac)₂ (platinum acetylacetonate) can be retained from the synthesis [57]. In order to burn off these ligands prior to the reduction pretreatment, this catalyst was annealed in 50 sccm of air flow inside the reactor at 300 °C. Following the pretreatment, the catalysts were exposed to a standard WGS reaction mixture (7% CO, 8.5% CO₂, 21.9% H₂O, 37.4% H₂ and balance Ar). The reaction temperatures were adjusted such that CO conversion below 10% could be achieved in order to maintain differential conditions. The catalysts were stabilized at these temperatures for 20 hours before the apparent reaction orders and the apparent activation energies were measured. For the measurement of apparent reaction orders, one gas concentration was varied at a time (4–21% CO, 5–25% CO₂, 11–34% H₂O, and 14–55% H₂). The apparent activation energies were measured by varying the temperature over a range of 30 °C (around the test temperature), while keeping the gas concentrations fixed at standard conditions. To maintain a useful comparison between catalysts at differing reaction temperatures, the reaction rates were adjusted to 300 °C via this activation energy measurement.

2.3.3 Catalyst Characterization

CO chemisorption was used to measure the moles of exposed metal on the catalyst used for kinetic measurements. The CO uptake experiments were performed using a Micromeritics ASAP 2020 instrument. Prior to CO adsorption, the aforementioned reduction pretreatment at 450 °C was performed.

The Pt and Co contents were measured using inductively coupled plasma-atomic emission spectroscopy (ICP-AES) at Galbraith Laboratories. X-ray diffraction (XRD) was performed on the used catalysts using a Rigaku Smartlab X-ray Diffractometer.

The scans were performed between $2\theta = 30^\circ$ and $2\theta = 60^\circ$, at the scan speed of $0.1^\circ/\text{min}$ with a step size of 0.05° .

Ex situ X-ray absorption (XAS) experiments at the Pt L_{III} edge and the Co K edge were carried out at the MRCAT 10 ID (insertion device) beam line at the Advance Photon Source at Argonne National Laboratory. Due to the low-Z (atomic number) MWCNTs, all the XAS experiments could be carried out in the transmission mode. The XAS experiments were conducted in 1 in OD quartz tubes connected to Ultra-Torr fittings with welded ball valves (for gas inlet/outlet and sealing) and Kapton windows. The catalyst samples were pressed into a 6 well sample holder as self-supporting wafers. The catalysts were pre-reduced in the holder at 450°C in 5% H_2/Ar . Without exposing to air, the scans at Pt L_{III} edge and Co K edge were collected at RT in Helium. The XAS data was analyzed using WINXAS 3.1 software. The X-ray absorption near edge structure (XANES) data was energy-calibrated by computing the first derivative of the first peak of the spectra for Pt and Co metal foil standards and comparing them to the known edge position. The extended X-ray absorption fine structure (EXAFS) data was fit using experimental standards and references computed using the FEFF6 code. Phase shifts and amplitudes for Pt-Pt and Co-Co scatters were obtained from the foil standards of the respective elements. The phase and amplitude for the PtCo bimetallic alloys were obtained using FEFF6. From the least square fits for the first shell, average coordination numbers, bond distances and the Debye-Waller factors were obtained for all the tested catalysts.

Pt₃Co on MWCNT samples were characterized in ‘Z-contrast’ high-angle annular dark-field (HAADF) mode by using a probe aberration-corrected JEOL ARM200CF STEM equipped with a cold field emission gun and an Oxford XMAX100TLE windowless XEDS detector. The operation voltage of the microscope was 200 kV. The probe spot size (higher spot sizes will increase electron probe current but reduce resolution) was chosen as 5 to get a high signal to noise ratio for imaging and EDS analysis while still maintaining atomic spatial resolution. The Z-contrast STEM mode was chosen, because the atomic structure and the distribution of Co and Pt in a single

Pt₃Co particle can be readily visualized in this imaging mode. We also performed STEM-EDS analysis, including line-scan and mapping to quantify chemical composition of Pt₃Co particles and distribution of its comprising elements in the particles. EDS spectrum collection, processing, and quantifications were done using the Oxford AZtec software.

2.3.4 DFT Calculations

All calculations were performed with the Vienna Ab-initio Simulation Package (VASP) using Projector Augmented Wave (PAW) method [59–61]. The Generalized Gradient Approximation (GGA) method was employed with the Perdew-Burke-Ernzerhof (PBE) [62] functional for metals, while PBE+U [63] was employed for the inverse oxide/hydroxide structures. Selected calculations with the van der Waals-corrected opt-PBE+U [64] functional ($U = 3.0$ for Co [65]) showed identical trends (see Table 2.8). All calculations containing Co in the system were spin polarized. For Pt and Pt₃Co, a slab thickness of 4 layers was used with the bottom two layers constrained at bulk atomic distances. The structure of inverse Co oxide/hydroxide films on Pt(111) has been developed in a previous publication from our group [65]. To briefly summarize, the stability of multiple Moire patterns of Co oxide and hydroxide films having thickness of 1 ML on Pt was evaluated. Each of these films was oriented in a variety of registries on the Pt (111) substrate to minimize strain. For a given oxidation state and stoichiometry of Co film, the structure with lowest formation energy was then used to generate the ab-initio phase diagram, and the most stable Co film structure and oxidation state on Pt(111), under WGS conditions, was identified. A three-phase boundary interface was created by eliminating part of the film to construct a semi-infinite ribbon, such that distance between ribbons and their periodic images was maintained at ~ 10 Å to minimize image interactions. Adopting a semi-infinite structure for the inverse catalyst (oxide supported on the metal rather than the traditional metal on the oxide) permits minimization of finite size effects usually associated with models of small clusters of inverse catalysts. Multiple cuts

of the film were tested to identify the lowest energy ribbon structure. The structure thus generated had undercoordinated, partially oxidized Co atoms at the interface, which were subsequently analyzed for adsorption energy calculations.

The binding energy of OH (BEOH) was calculated as follows,

$$BE_{OH^*} = E_{OH^*} - E_{clean} - [E_{H_2O(g)} - \frac{1}{2}E_{H_2(g)}] \quad (2.1)$$

where E_i is the DFT calculated energy of the system i and $*$ denotes adsorption.

2.4 Results

2.4.1 Measurement of Reaction Kinetics

Figure 2.1 shows the WGS turnover rate (TOR, rate normalized by the moles of CO measured by chemisorption) plotted against the Co:Pt molar ratio. The values on the x-axis are computed from the Pt and Co contents measured using ICP-AES (Table 2.5). For simplicity, the samples are henceforth referred to by their targeted Pt:Co molar ratios. For the series of as-prepared samples: the TOR increased from 4.6×10^{-2} mol H₂ (mol CO ads.)⁻¹ s⁻¹ for the monometallic Pt sample to 46×10^{-2} mol H₂ (mol CO ads.)⁻¹ s⁻¹ for the PtCo 1:3 sample, an order of magnitude. For the PtCo 1:5 and 1:8 catalyst, there was a decrease in the TOR compared to the PtCo 1:3. The 1:3, 1:5, and 1:8 leached catalysts have TORs of 2.1×10^{-2} , 1.8×10^{-2} and 1.7×10^{-2} mol H₂ (mol CO ads.)⁻¹ s⁻¹, respectively. These were 18 to 22 times lower than for the as-prepared counterparts. The Pt₃Co/MWCNT catalyst had TOR of 1.8×10^{-2} mol H₂ (mol CO ads.)⁻¹ s⁻¹, which was similar to the leached PtCo catalysts prepared by sequential impregnation of Pt and Co.

Table 2.1 shows detailed kinetic parameters for all of the PtCo catalysts tested. The PtCo 1:3, 1:5, and 1:8 catalysts were tested at the same temperature (250 °C), and hence, the kinetic parameters can be directly compared. The apparent reaction orders and the apparent activation energies (~ 136 kJ mol⁻¹) were similar for these catalysts, within error. For the acetic acid leached counterparts of the 1:3, 1:5 and 1:8 catalysts, the kinetic parameters were also similar when these leached catalysts

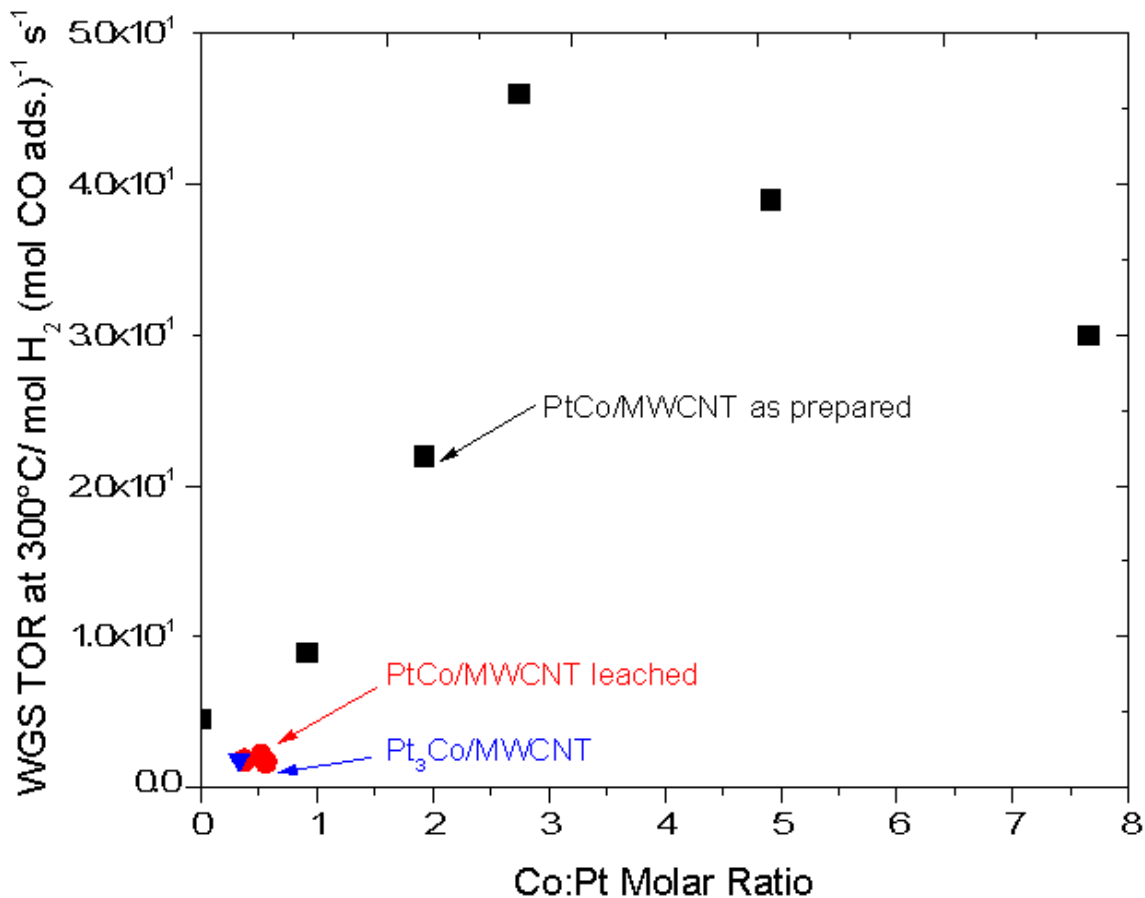


Figure 2.1. WGS TOR at 300 °C vs. Co:Pt molar ratio for the as prepared, leached and the Pt₃Co/MWCNT catalysts. Reaction conditions, 7% CO, 8.5% CO₂, 21.9% H₂O, 37.4% H₂ and balance Ar.

were tested at 310 °C. The Pt₃Co/MWCNT catalyst that was tested at the 330 °C also exhibited similar reaction orders and apparent activation energy as the leached catalysts. A comparison of the kinetic parameters of the as-prepared monometallic Pt/MWCNT and the Pt/MWCNT that had undergone the same acetic acid leaching treatment as the PtCo bimetallic catalysts was also made. The WGS TOR at 300 °C and the kinetic parameters (measured at 290 and 300 °C) were similar for these catalysts within experimental errors, although the amount of chemisorbed CO for the

Table 2.1.
Comparison of WGS TOR, E_{app} , and reaction orders for the as prepared and the acetic acid treated Pt/MWCNT monometallic catalysts.

Catalyst	WGS TOR at 300 °C ^a (10^{-2} mol H ₂ (mol CO ads) ⁻¹ s ⁻¹)	E_{app} (kJ mol ⁻¹) (±3)	H ₂ O (±0.04)	CO (±0.04)	CO ₂ (±0.04)	H ₂ (±0.04)
Pt/MWCNT	4.6	86	0.83	0.10	-0.08	-0.38
Pt/MWCNT Leached ^b	4.2	90	0.77	0.08	-0.06	-0.34
PtCo 1:1/MWCNT	9.0	96	0.90	-0.01	-0.11	-0.47
PtCo 1:2/MWCNT	22	114	1.10	-0.03	-0.07	-0.52
PtCo 1:3/MWCNT	46	137	1.10	-0.26	-0.01	-0.57
PtCo 1:5/MWCNT	39	142	1.10	-0.17	-0.01	-0.47
PtCo 1:8/MWCNT	30	136	0.90	-0.20	-0.01	-0.49
PtCo 1:3/MWCNT Leached ^b	2.1	118	1.00	-0.10	-0.05	-0.58
PtCo 1:5/MWCNT Leached ^b	1.8	116	1.00	-0.02	-0.02	-0.58
PtCo 1:8/MWCNT Leached ^b	1.7	118	0.75	0.00	-0.05	-0.59
Pt ₃ Co/MWCNT	1.8	113	0.87	-0.03	-0.04	-0.54

^aReaction conditions, 7% CO, 8.5% CO₂, 21.9% H₂O, 37.4% H₂ and balance Ar.

^bCatalysts subjected to acetic acid leaching at 25 °C.

as-prepared catalyst was as much as ~ 2.3 times higher than some of the catalysts treated with acetic acid solution (Table 2.6).

2.4.2 Catalyst Characterization

The selective leaching of cobalt was based on the previous reports of reaction of supported cobalt with acetic acid [66]. Dietrich et al. [54,55] also reported that during the aqueous phase reforming of glycerol over PtCo bimetallic catalysts, the presence of cobalt in the reactor effluent was detected and attributed to the leaching caused

by organic acids. Co and CoO possibly undergo the following reactions with acetic acid to form cobalt acetate and hydrogen/water.



The evolution of hydrogen during the leaching process was confirmed with gas chromatography and was visually observed as rapid evolution of bubbles during introduction of the solution to the reduced catalyst in the quartz reactor.

Figure 2.2 shows the XRD patterns for the Pt, Pt-Co as-prepared, and Pt-Co leached catalysts, all obtained post WGS reaction, and corrected for the MWCNT background. The peaks at 39.8° and 46.4° are present for all the catalysts and is assigned to a Pt or Pt₃Co phase, as these phases have similar X-ray diffraction patterns [56]. The full PtCo phase diagram is available in ref. [67]. The as-prepared Pt-Co 1:3, 1:5, and 1:8 catalysts have a peak at 44.4° , which is assigned to a metallic cobalt phase (PDF 00-001-1259). This same peak is absent from the patterns for the samples that were subjected to the acetic acid leaching process. The leached samples show a broad peak at 43° , which, using the ICDD database, is assigned to PtCo₄ (PDF 01-071-7412). This phase can also be evidenced by the presence of the shoulders at $\sim 41^\circ$ and $\sim 47.3^\circ$.

Ex situ XAS experiments at Pt L_{III} and Co K edge were performed to analyze the catalysts for the effect of the reduction pretreatment at 450 °C. The Co K edge XANES spectra for these catalysts are shown in Figure 2.3, along with reference spectra of Co foil and CoO powder. The XANES spectra qualitatively show that the Co is predominantly reduced. Quantification of the degree of reduction was made using the linear combination XANES tool available in the WINXAS 3.1 software to estimate the fraction of Co that stays oxidized after the 450 °C reduction pretreatment (Table 2.2). The as-prepared PtCo 1:1, 1:2, 1:3, 1:5, and 1:8 catalysts have about 9%, 11%, 13%, 14% and 20% cobalt in the oxidized state, respectively. This result is in agreement with the observation made by Dietrich et al. [54] on similar catalytic

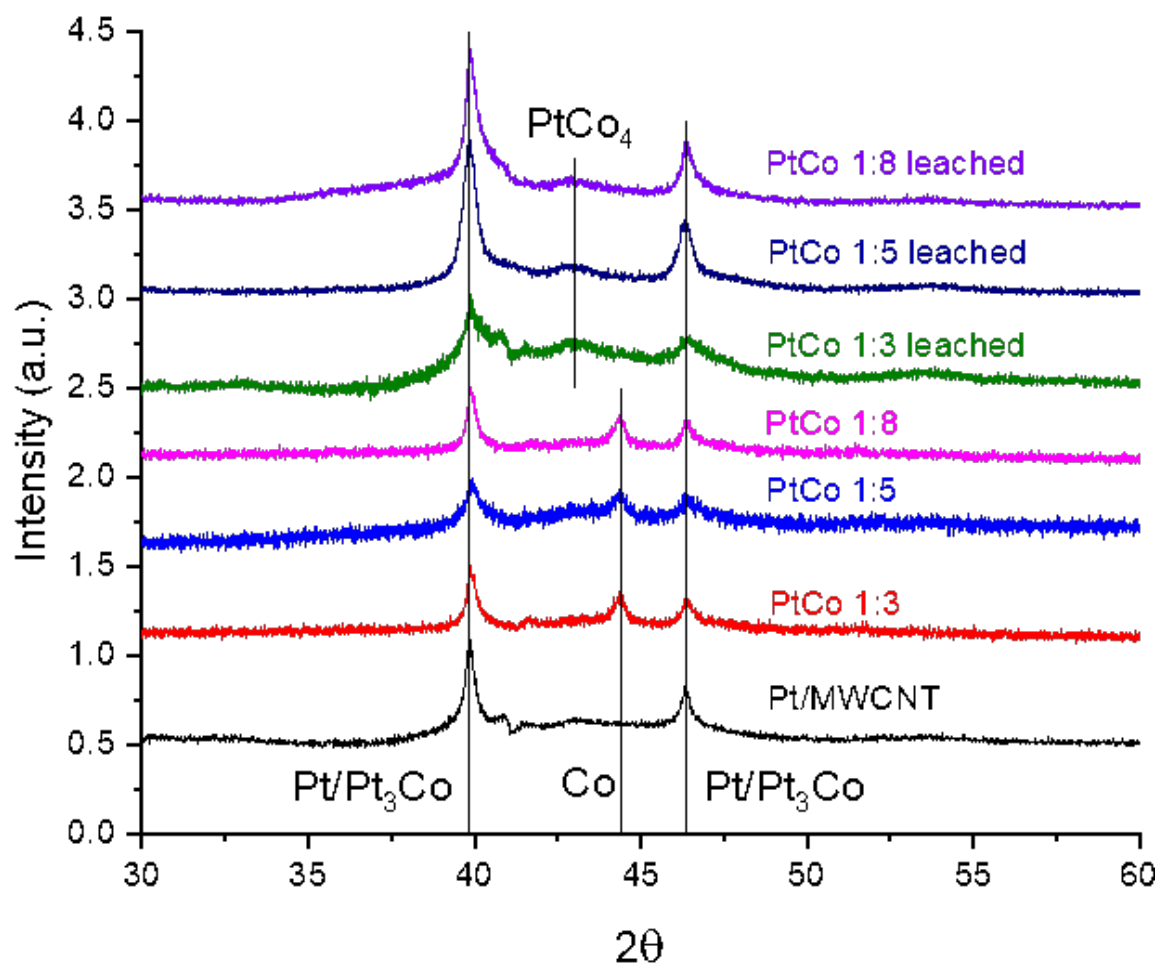


Figure 2.2. XRD patterns for Pt, PtCo as prepared and PtCo leached catalysts supported on MWCNT.

systems. For the catalysts subjected to the acetic acid leaching process, the amount of oxidized cobalt was below the detection limit for XANES fitting.

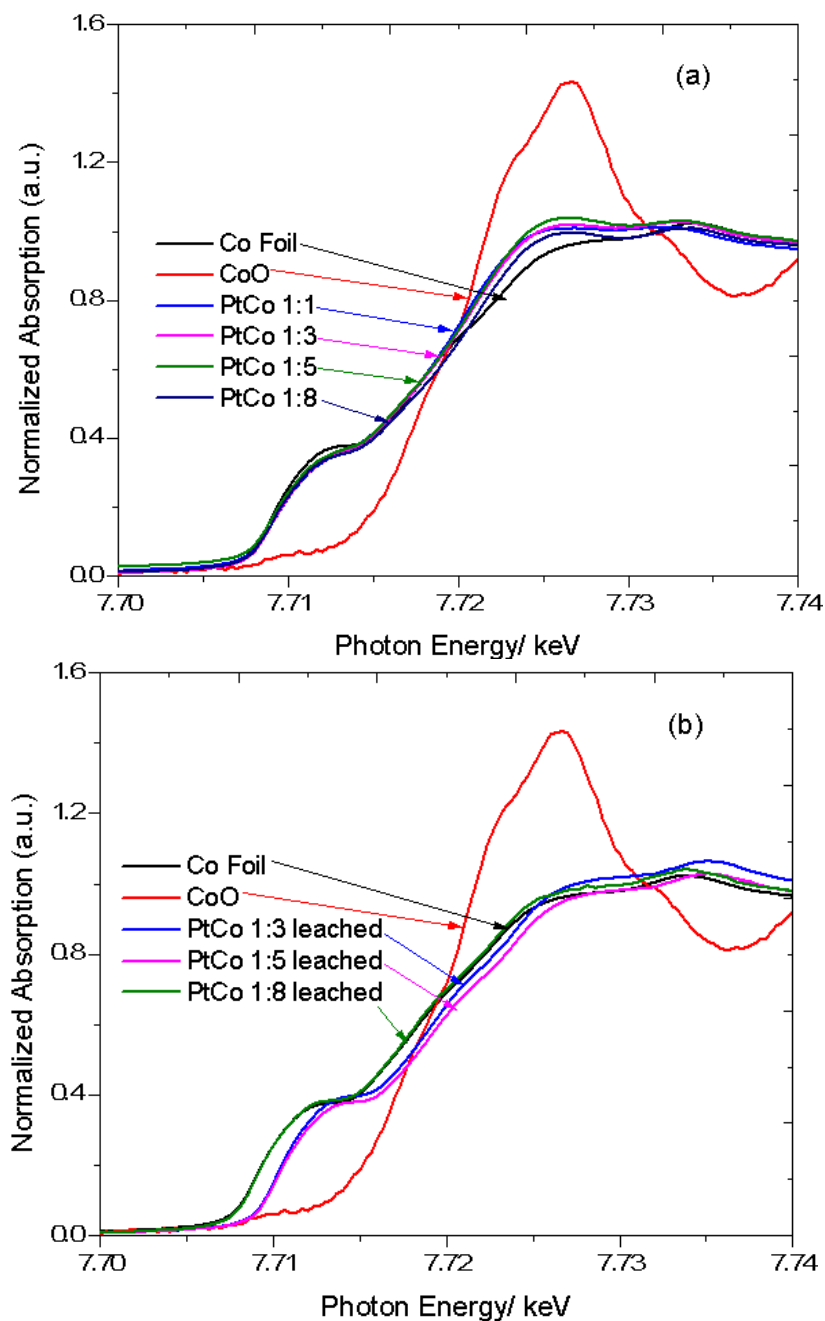


Figure 2.3. Co K edge XANES spectra at RT after 450 °C reduction for (a) as prepared and (b) leached PtCo catalysts.

Table 2.2.

Results of linear combination XANES fits of the Co K edge for the as-prepared leached PtCo/MWCNT catalysts. Co foil was used as a standard for metallic Co, while CoO powder was used as reference for Co^{2+} .

Catalyst	% Co^0	% Co^{2+}
PtCo 1:1 MWCNT	91	9
PtCo 1:2 MWCNT	89	11
PtCo 1:3 MWCNT	87	13
PtCo 1:5 MWCNT	86	14
PtCo 1:8 MWCNT	80	20
Leached PtCo 1:3 MWCNT	100	0
Leached PtCo 1:5 MWCNT	100	0
Leached PtCo 1:8 MWCNT	100	0

Figure 2.4 shows the Pt L_{III} edge EXAFS spectra for the as-prepared and leached PtCo/MWCNT catalysts. For the as-prepared catalysts, the spectra exhibit differences from the metallic Pt foil in terms of the peak shapes and the peak positions. These changes are due to the presence of a second scatter apart from Pt-Pt, i.e. Pt-Co [54, 55]. The Pt-Pt and the Pt-Co contributions were fitted at bond distances of 2.7 and 2.6 Å respectively. The average coordination numbers (CN) determined from the EXAFS fit parameters are listed in Table 2.3. The Pt-Pt CN does not change significantly with increasing Co:Pt ratio and remains between 5 and 6. Similarly, the Pt-Co CN stays between 2 and 3.5 for the as-prepared catalysts with various Co:Pt molar ratios. For the catalysts subjected to the acetic acid leaching process, the features assigned to Pt-Pt and Pt-Co at distances of 2.7 and 2.6 Å are still retained. Leaching also leads to an increase in the Pt-Pt CN to around 6.6. The Pt-Co CN decreases in comparison to the as-prepared counterparts (3.5 to 2.5 for 1:3, 2.9 to 1.4 for 1:5 and 2.5 to 1.7 for 1:8 catalysts). Nonetheless, some Pt-Co bonds are still retained after the leaching process, suggesting that the leached catalyst has bimetallic particles, albeit with lower Pt-Co CN compared to the as-prepared catalysts. The Pt₃Co/MWCNT catalyst also exhibits the features in the EXAFS spectrum that are similar to the catalysts prepared using the sequential impregnation method. The Pt-Pt and Pt-Co CNs for this catalyst were 6.2 and 3.4, respectively, which are similar to those of the leached samples.

The Co K-edge EXAFS fitting results are shown in Table 2.9. The Co-Co CN increases as the Pt:Co ratio increases and finally reaches 11.8 for the PtCo(1:8) catalyst and then decreases significantly to 1.3-2.6 after the acetic acid leaching process. On the contrary, the Co-Pt CN increases after the leaching process. The features assigned to Co-Co and Co-Pt at distances of 2.5 and 2.6 Å are still retained. The existence of Co-Pt bonds after the leaching process are consistent with the EXAFS results from Pt EXAFS results.

Figure 2.5 shows the STEM and X-ray EDS mapping results for a WGS used Pt₃Co/MWCNT catalyst. The zone axis was found via CrysTbox to be the $[\bar{1}10]$ zone

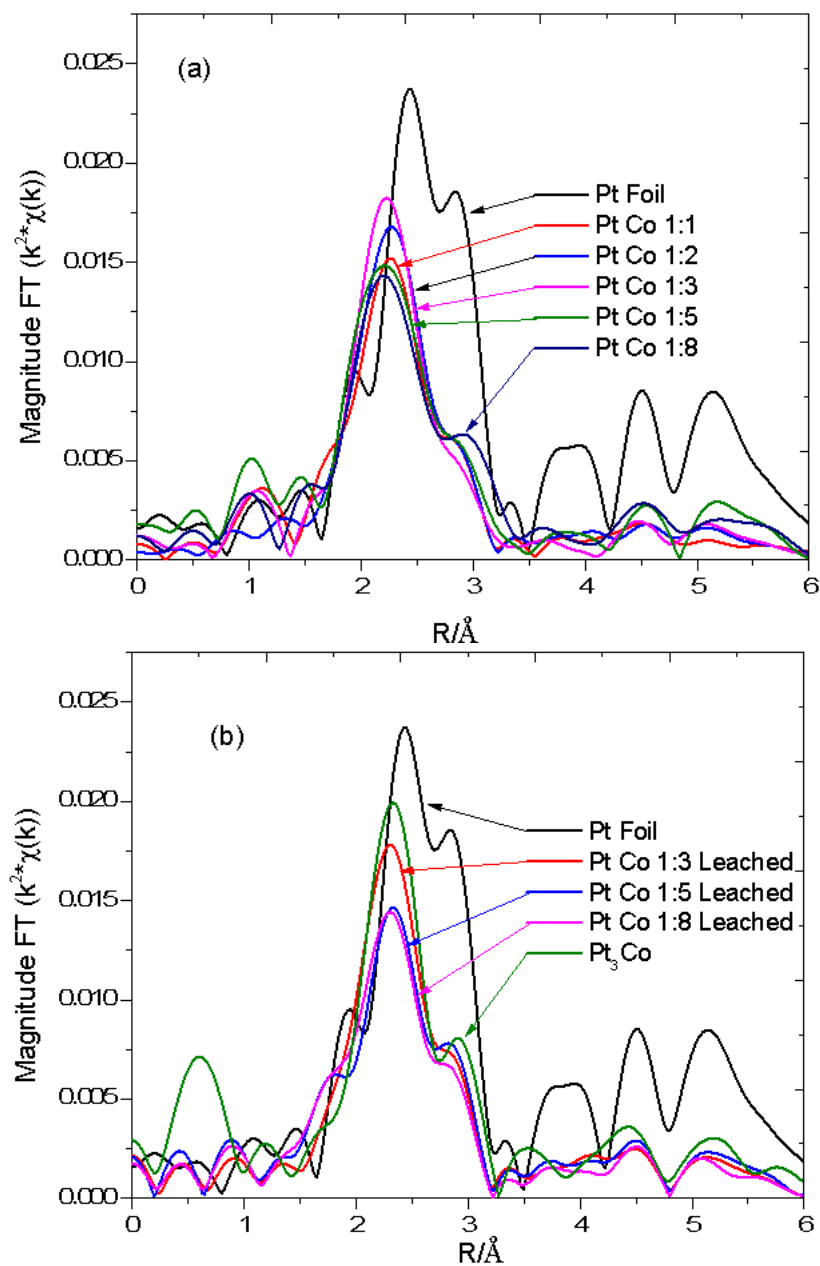


Figure 2.4. Pt L_{III} edge EXAFS spectra collected at RT after 450 °C reduction of PtCo/MWCNT catalysts (a) as prepared (b) leached and Pt₃Co/MWCNT.

Table 2.3.
Pt L_{III} edge EXAFS data fit parameters for the PtCo/MWCNT catalysts.

Catalyst	Pt-Pt				Pt-Co				Total CN	Pt-Co CN Pt-Pt CN
	CN	R	$\Delta\sigma^2$	E_0	CN	R	$\Delta\sigma^2$	E_0		
		(Å)	(Å ²)	(eV)		(Å)	(Å ²)	(eV)		
PtCo 1:1	5.9	2.71	0.002	-2.6	2.1	2.58	0.002	2.9	8	0.36
PtCo 1:2	6.0	2.72	0.002	-2.7	2.8	2.59	0.002	4.3	8.8	0.47
PtCo 1:3	5.0	2.71	0.002	-3.4	3.5	2.58	0.002	3.6	8.5	0.70
PtCo 1:5	5.9	2.71	0.002	-5.4	2.9	2.58	0.002	4.9	8.8	0.49
PtCo 1:8	5.9	2.71	0.002	-5.2	2.6	2.58	0.002	4.6	8.5	0.44
PtCo 1:3 Leached	6.7	2.74	0.002	0.0	2.5	2.61	0.002	3.4	9.2	0.37
PtCo 1:5 Leached	6.6	2.74	0.002	-1.0	1.4	2.61	0.002	0.7	8.0	0.21
PtCo 1:8 Leached	6.6	2.73	0.002	-2.3	1.7	2.60	0.002	2.9	8.3	0.26
Pt ₃ Co	6.2	2.73	0.002	-3.1	3.4	2.59	0.002	3.0	9.6	0.55

axis of Pt_3Co [68,69]. No separate Pt or Co phases were observed, demonstrating the value of this sample as a reference Pt_3Co alloy sample, with no Cobalt oxide phases. More detailed Z-contrast STEM results are shown in Figures 2.9 and 2.10. Both Pt and Co exist in the shell and core of the nanoparticle, which is also confirmed by the line-scan shown in Figure 2.11. X-Ray EDS analysis showed an atomic percentage of $67.6 \pm 13.6\%$ of Pt and $32.4 \pm 13.6\%$ of Co, resulting in a Pt to Co ratio about 2.1:1, within error of a 3:1 alloy. EDS mapping showed a random distribution of Pt and Co atoms within the nanoparticle. STEM results confirmed that after reaction, the Pt_3Co nanoparticles are random alloys.

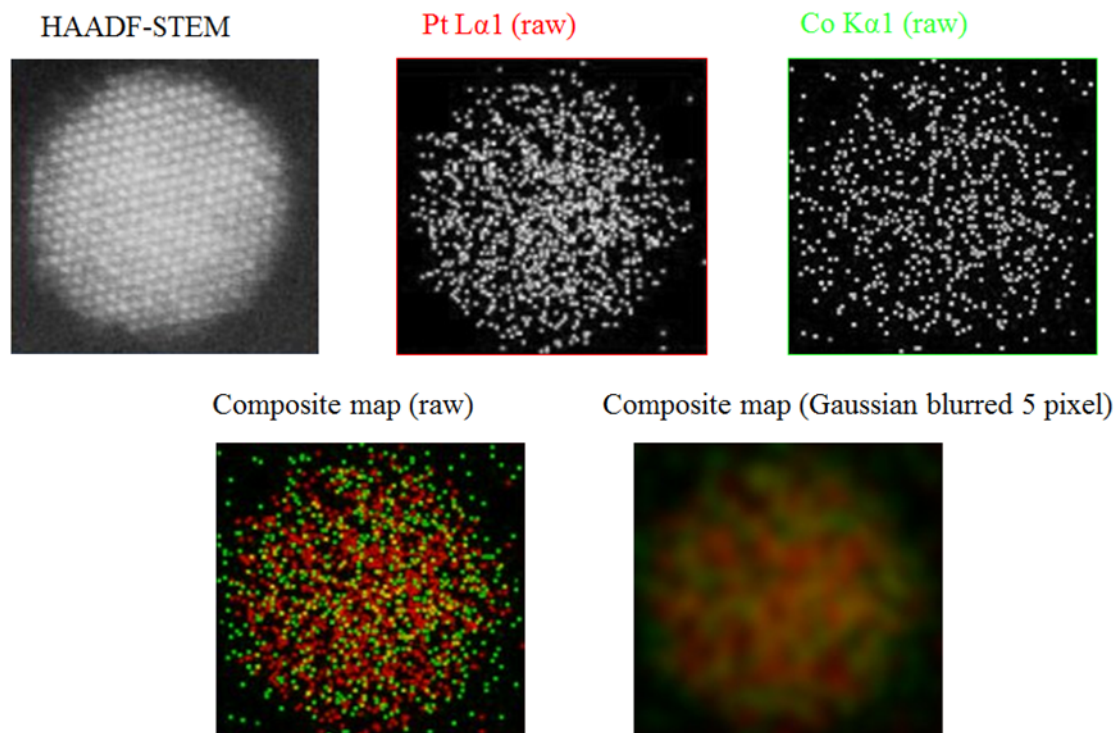


Figure 2.5. HAADF-STEM image and X-ray EDS mapping of the Pt_3Co /MWCNT catalyst after reaction. In the composite EDS map, Pt is shown in Red and Co is shown in green.

2.4.3 DFT Results

Figure 2.6 shows the calculated ab-initio phase diagram of various bulk Co and Co oxide films on Pt (111), with H_2O and H_2 chemical potentials corresponding to the indicated water-gas shift conditions. Figure 2.6a shows the phase diagram of bulk phases of Co at or near WGS conditions. Both metallic Co and CoO are similar in energy under these conditions and both of them could exist as metastable phases. At the contact region with Pt, however, Co can exist as a partially oxidized phase, modelled using inverse Co oxy/hydroxide films on Pt(111). Figure 2.6b shows the phase diagram of Co oxy/hydroxide films on Pt. Interestingly, CoOH, which is unstable in the bulk phase, is the most stable phase when in contact with Pt(111). The most stable CoOH film corresponded to a $(\sqrt{7}\times\sqrt{7})\text{CoOH}$ on $(3\times 3)\text{Pt}(111)$ [65]. Details of this structure are provided in ref. [65] and in Figure 2.12. The stabilization of CoOH on Pt can be straightforwardly attributed to strong binding of the CoOH film with Pt(111).

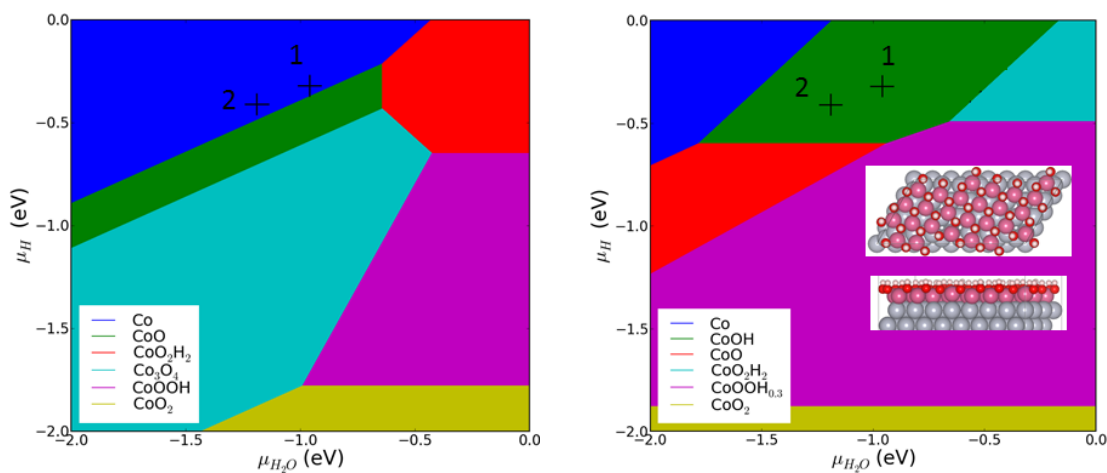


Figure 2.6. Phase diagram of (left) bulk Co oxides (right) 1 ML of Co oxide films on Pt. WGS conditions are highlighted with + symbol (1) $T = 227\text{ }^\circ\text{C}$ (2) $T = 327\text{ }^\circ\text{C}$. Inset in (right) shows the structure of most stable phase on Pt under WGS conditions. Green – CoOH. Grey-Pt, Pink-Co, White-H, Red – O

After identifying the most stable CoOH phase on Pt, a CoOH/Pt interface was generated by creating a semi-infinite ribbon from the film, wherein multiple cuts of the film were tested to identify the most energetically favorable ribbon structure, shown in Figure 2.7. This structure represents a thermodynamically stable model of the interface between Pt and CoOH.

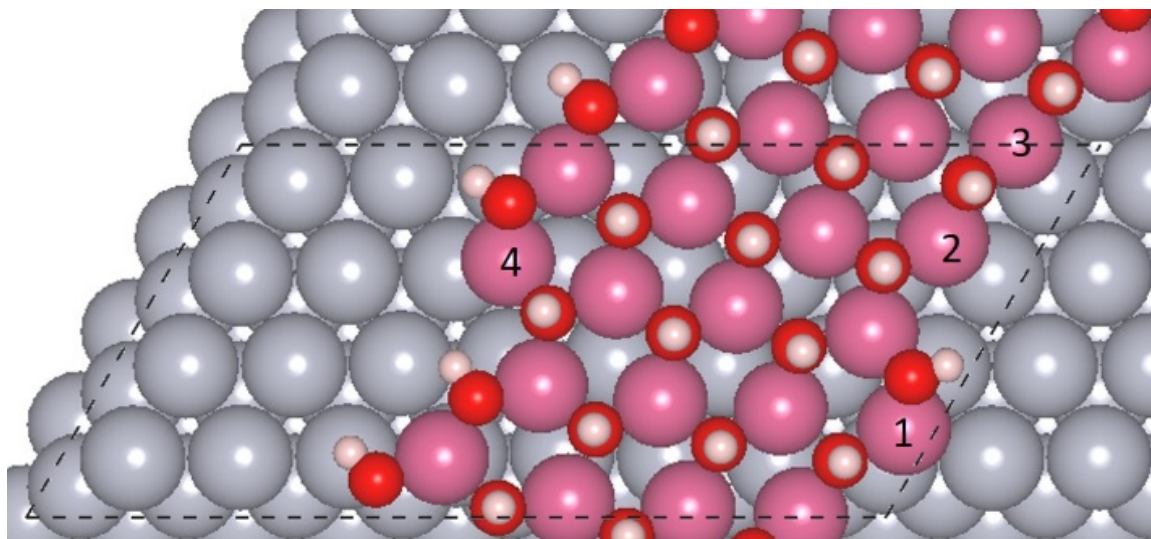


Figure 2.7. Semi-infinite CoOH ribbon on Pt. Grey - Pt, Pink - Co, White - H, Red - O of CoOH. The under-coordinated Co atoms at the interface are numbered. Adsorption energies of OH at these sites are provided in Table 2.8.

A number of prior studies have suggested that water dissociation is a kinetically significant step for WGS [70,71]. The energetics of this step, therefore, can be used as a plausible descriptor of activity. We investigated OH binding strengths for different catalysts (Pt, Pt₃Co alloy and CoOH/Pt interface) to understand the contribution of Co towards aiding water dissociation. BEOH* values at the under-coordinated interfacial sites of CoOH/Pt vary from 0.03 – 0.52 eV (where less positive values correspond to stronger binding – see Table 2.8, PBE+U), while the corresponding value on Pt₃Co is 0.47 eV (Table 2.9). Compared to pure Pt(111) (BEOH* of 0.87 eV), OH is more strongly stabilized at the CoOH/Pt interface than on the Pt₃Co

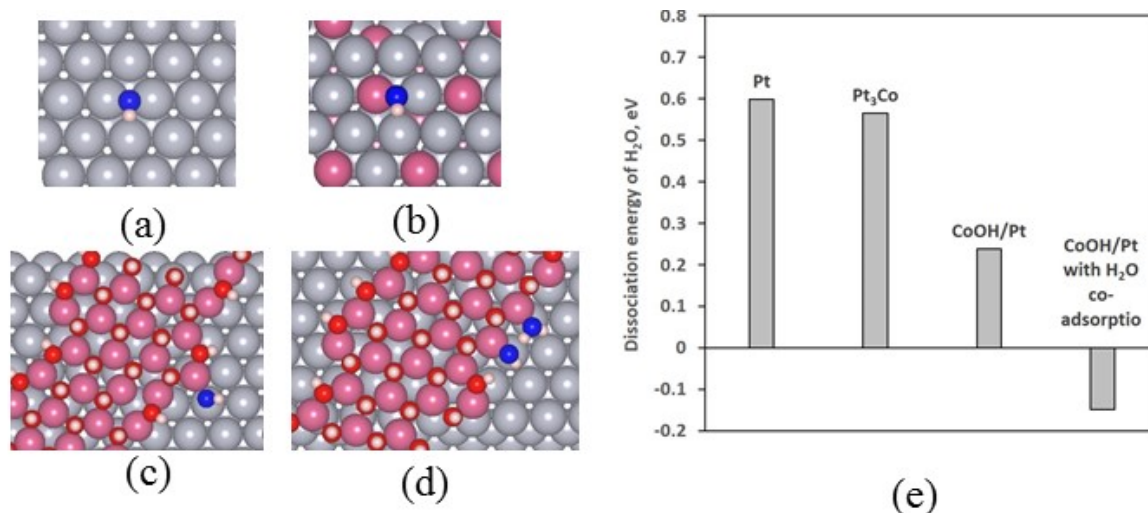


Figure 2.8. Stabilization effect of different systems of adsorbates: – Grey - Pt, Pink - Co, White - H, Red - O of CoOH, Blue - O; (a) OH on Pt (b) OH on Pt₃Co alloy (c) OH at CoOH/Pt interface (d) co-adsorbed OH and H₂O at CoOH/Pt interface (e) dissociation energy of H₂O for the different systems showing more favorable dissociation thermodynamics for CoOH/Pt system.

alloy surface. The stabilization of OH at the CoOH/Pt interface results not only from the under-coordination of partially oxidized Co sites at the interface but also from hydrogen bonding. In fact, coadsorbing H₂O at the interface results in further stabilization of OH due to hydrogen bonding with coadsorbed water, in which case the BEOH becomes -0.28 eV. The relevant adsorption geometries are given in Figures 2.8 and 2.13. The BEOH* therefore varies as CoOH/Pt < Pt₃Co < Pt. The stronger binding of OH, in turn, suggests that water will be more readily dissociated. In fact, interfaces between Pt and supported metal oxides in inverse catalysts have been shown to have considerably lower water dissociation barriers than pure Pt [72]. To verify this hypothesis, we compared the reaction energies for H₂O dissociating to H and OH on Pt, Pt₃Co and CoOH/Pt. Figure 2.8 shows that H₂O dissociation energies on Pt and Pt₃Co are similar, with Pt₃Co having only slightly more favorable dissociation. CoOH/Pt, on the other hand, has significantly more favorable dissociation by 0.36

eV compared to Pt. Coadsorbing OH and H₂O at the CoOH/Pt interface (Figure 2.8d), in turn, provides additional stabilization due to hydrogen bonding, while H₂O dissociation becomes exothermic and is 0.75 eV more favorable than on Pt. Note that water coadsorption also stabilizes reactant H₂O (Figure 2.13e) but not to the same extent as product OH. With water dissociation considered to be important for WGS, the trends in OH binding acts as a suitable descriptor. These results indicate that the promotion in WGS activity for PtCo catalysts is linked to increased stabilization of OH and consequent facile H₂O dissociation at the interface of CoOH and Pt.

2.5 Discussion

The PtCo/MWCNT catalysts synthesized with a similar method have been used for the aqueous phase reforming of glycerol [54]. It was suggested by Dietrich et al. [54] that some amount of Co from the catalysts was leached out into the product stream. The leaching was attributed to the presence of organic acids formed as a side product of reforming. Based on their observations, the leaching method in the present work was devised.

As shown in Figure 2.1, the WGS TOR increased by a factor of 10 with addition of Co, up to Co:Pt of 1:3. The promotion in the WGS rate led to the need for lower test temperatures with increasing amounts of Co, in order to limit the CO conversions below 10%. The 1:3, 1:5, and 1:8 catalysts exhibit similar kinetic parameters compared at the same test temperature of 250 °C. The apparent activation energies and reaction orders of all the catalysts containing Co, although unable to be directly compared because they were measured in different temperature regions, are significantly different from those of the monometallic Pt.

As seen in Table 2.1, the apparent activation energies were found to increase with increasing Co content, from monometallic Pt (86 kJ mol⁻¹), PtCo 1:1 (96 kJ mol⁻¹), PtCo 1:2 (114 kJ mol⁻¹), to the fully promoted PtCo 1:3 sample (137 kJ mol⁻¹). An increase in the apparent reaction order for water with increasing Co addition also occurs in this range. This suggests that as the Co amount is increased, an active site

for WGS which is chemically different from monometallic Pt is formed. A further decrease in the Pt:Co ratio after 1:3 does not lead to any noticeable changes in the apparent kinetic parameters, alluding to the statistical dominance of this new type of active site over the monometallic Pt sites, and also a sensitivity of the optimum site population to the amount of Co.

After the leaching process, all the bimetallic catalysts have similar kinetic parameters at 310 °C, and these are, in turn, similar to those of the Pt₃Co/MWCNT catalyst, which has all of the cobalt in the alloyed form [57]. Furthermore, the kinetic parameters for the leached catalysts and the Pt₃Co/MWCNT catalyst are significantly different compared to those of the monometallic Pt. For example, these catalysts exhibit higher apparent activation energies (~ 116 kJ mol⁻¹) compared to the monometallic Pt (86 kJ mol⁻¹) and the turnover frequencies are lower. This result implies that even though the WGS TOR over the leached catalysts is closer to the monometallic Pt than to the as-prepared bimetallic catalysts, the chemical nature of the active sites is discernably different compared to those of the monometallic Pt. This modification to Pt particles is likely to have been caused by the presence of Co in the particles, as will be discussed later.

The leaching process also caused a decrease in the number of exposed metal sites measured by CO chemisorption as indicated in Table 2.6. This is also explained with the presence of a PtCo₄ phase seen in the post leaching XRD (Figure 2.2), as the Co rich phase will lead to less CO chemisorption than a pure Pt phase. A further explanation of Pt and Co chemisorption is given below.

It should be noted that Co is active for CO chemisorption, which could interfere with quantification of active sites via this method [73]. However, with an increase in Co content from PtCo 1:1 to PtCo 1:8 the surface area increased from 51 $\mu\text{mol g}^{-1}$ to 71 $\mu\text{mol g}^{-1}$, which would lower the calculated TOR only by a factor of ~ 1.4 . Since the TOR is seen to actually increase with Co content from PtCo of 1:1 to PtCo 1:3 by a factor of ~ 5.1 , the effect of CO chemisorption on Co does not dramatically affect the result of Co-promotion, and the CO chemisorption on Co was found to be

minor compared to chemisorption on Pt. Comparison of Table 2.1 with Table 2.6, suggests, however, that CO chemisorption on Co could be the cause of TOR drop-off with increasing Co content relative to the CoPt 1:3 sample.

There was no significant change in the apparent kinetic parameters when the monometallic Pt was subjected to the leaching process. This experiment was performed to verify that the acetic acid treatment does not chemically alter the monometallic Pt active sites. However, sintering of Pt particles was observed for the monometallic catalyst, which is marked by a significantly lower CO chemisorption value (Table 2.6). The lower CO chemisorption also has a contribution that can be attributed to the decrease in Pt loading from 4.5% wt. to 3.8% wt, but the loss of Pt alone cannot account for total decrease in CO chemisorption, leading to the conclusion that the effect of the leaching treatment causes a loss of Pt that shifts the Pt particle size distribution toward larger particles.

Based on the XRD data (Figure 2.2), it is clear that with addition of Co, there is an isolated phase of metallic cobalt that is created on these catalysts. There was no observable peak for cobalt oxide. The absence of a cobalt oxide peak, in light of the XANES evidence for a cobalt oxide phase, indicates that CoO_xH_y clusters are small or that the oxide phase is a thin layer on larger metallic Co or PtCo alloy particles on the support. Such phases would not have sufficient long-range order to result in discernible XRD peaks. We note that in keeping with the Co XANES data, which indicate oxidized Co, and the DFT results that show the importance of a CoOH surface phase, we use CoO_xH_y to describe the oxidized Co phase. For the leached catalysts, the absence of the Co peak suggests that the metallic Co was leached to a level below detection limit of the XRD. A new XRD peak at $\sim 43^\circ$ demonstrates the appearance of a high Co PtCo alloy (PtCo_4). As can be seen in Table 2.5, the acetic acid treatment leaches Co, but will also leach Pt as well. These data suggest that redispersion from leached Pt and Co leads to the presence of Co rich alloys, as seen in the post-leaching XRD patterns. The presence of PtCo alloys is also confirmed with the EXAFS results as discussed further below.

Although the XRD could not identify a Co oxide phase, the Co K-edge linear combination XANES data indicated that there was an increasing fraction of oxidized cobalt as the Pt:Co molar ratio was decreased (Table 2.2). The absence of the CoO_xH_y phase in either XANES or XRD for the leached samples suggests that all of the residual Co is in the metallic state (likely due to alloying). The dramatic loss of TOR ($\sim 20\times$) after leaching, even with the presence of residual metallic Co, demonstrates that metallic Pt and Co interfaces or alloy formation do not play a significant role in catalytic activity. Thus, these data suggest that the $10\times$ increase in activity from Co addition is due to the presence of a CoO_xH_y phase, and not a metallic Co phase.

Based on the Pt L_{III} edge EXAFS data (Table 2.3), it was observed that the Pt-Pt and Pt-Co coordination numbers are relatively independent of the Co:Pt molar ratio for the as-prepared catalysts. It is known from the literature [56], that PtCo alloys form core-shell particles, which makes exact quantification of the relevant PtCo alloy phases involved difficult. However, relatively constant coordination numbers imply that a single PtCo alloy composition was formed at all the Co weight loadings. Furthermore, the Pt EXAFS data match best with the spectra assigned to the presence of a Pt_3Co alloy in ref. [56]. The relatively weak interaction of Co with the carbon support relative to that for the SiO_2 support and sequential impregnation here as compared to co-impregnation in [56] appear to promote formation of an isolated Co phase not seen in [56]. This scavenging of Co can thus account for the formation of only Pt-rich alloys. From the Pt edge EXAFS data, leached catalysts still have some the alloy structure of Pt_3Co preserved, although there is a decrease in the Pt-Co coordination numbers as compared to the as prepared counterparts. The XRD data, however, show the presence of a PtCo_4 phase formed from Pt and Co released during the leaching process. In short, the combination of the XRD, Co K edge XANES and the Pt L_{III} edge EXAFS data, shows that the majority of the isolated cobalt phase and the CoO_xH_y phases are selectively leached out during the acetic acid leaching, with some of the Co preserved in PtCo alloys. Thus, the leaching has enabled us to selectively remove one type of possible active site, i.e. the interface between the

PtCo alloy and the $\text{Co}/\text{CoO}_x\text{H}_y$ (partially oxidized cobalt) phase. The Co K-edge EXAFS results are also consistent with this claim (Table 2.7). As the Pt:Co ratio decreases, more Co exists in isolated Co or CoO_xH_y phases. The increase of Co-Co CN with the decrease in the Pt:Co ratio implies an increase in the amount of the Co or CoO_xH_y patches. After the leaching process, essentially all of the isolated Co or CoO_xH_y species are leached out. This is illustrated by the significant decrease in the Co-Co CN. The preservation of Co-Pt bonds suggests that Pt-Co bimetallic structures remained after the leaching process, consistent with Pt EXAFS results. There is an increase in the average Co-Pt CN after the leaching process, implying that the remaining Co exists in alloy form with Pt after leaching. We note that the increase in Co-Pt scattering in the Co EXAFS is consistent with the formation of the PtCo4 phase. This phase is not seen in the Pt EXAFS because it is overwhelmed by the dominant Pt rich phase, but it may contribute to the fraction of ~ 2 decrease in TOR for leached PtCo catalysts versus pure Pt catalysts. Based on both XANES and EXAFS results, PtCo alloy, isolated Co (metallic cobalt that is not alloyed with Pt) and CoO_xH_y phases exist before leaching. After leaching, mainly PtCo alloy structures are preserved.

Unlike the systematic change in WGS TOR and the kinetic parameters with decreasing Pt:Co ratio from monometallic Pt to the 1:3 for the as prepared catalyst, the structure of the Pt-Co alloy particles was independent of the Pt:Co molar ratio. This indirectly implies that even though the alloy of the same structure was formed at the lowest Co loading (1:1), the WGS TOR was not fully promoted until the ratio decreased to 1:3. However, there is a small but noticeable increase in the CoO_xH_y fraction estimated with linear combination XANES, with an increase in the Co:Pt ratio from 1 to 8. Thus, the kinetics, XRD and XANES results indicate that the presence of CoO_xH_y phases are required for promotion in the WGS reaction rate. Previous studies [52] on other bimetallic catalysts such as Pt-Re have made similar claims about the alloy formation being just a consequence of having reduced metals in close proximity. In that system, and we conclude for the PtCo system as well,

the partially oxidized secondary metal phases promote the rate by providing sites for activation of water.

The Pt₃Co/MWCNT catalyst has provided further evidence for our claims that leaching removes isolated Co and CoO_xH_y phases from the bimetallic catalysts to an extent where the WGS TOR is not promoted. The Pt₃Co nanoparticles synthesized by a reported organic solvothermal method have been shown to be homogeneous in composition [74]. One might argue that the catalysts synthesized using the sequential impregnation of Pt and Co would be inhomogeneous in structure [54], wherein monometallic Pt could coexist with the alloy particles. However, for the acetic acid leached catalysts, the similarity of WGS TOR and apparent kinetic parameters at between 310 °C and 330 °C to that of the homogeneous Pt₃Co alloy particles supported on MWCNT suggests that PtCo alloy particles must be statistically dominant in these catalysts after leaching. Furthermore, the Pt edge EXAFS data also shows that Pt is alloyed, confirming the retention of alloy after leaching. Thus, by benchmarking the kinetics and the EXAFS data for the leached catalysts against that for the Pt₃Co/MWCNT catalyst, it can be proposed that the formation of PtCo alloys is inconsequential towards Co promotion for the WGS TOR.

In order to rule out the dominance of one type of active site over the other for a given reaction on a given catalyst, it is desirable that the sites of one particular type are selectively removed and a significant effect is observed over the reaction rate. In the present case, the two candidates for the cause of promotion in the WGS rate were the Pt-Co alloy and the interface between the Pt/PtCo and the Co/CoO_xH_y phases. When the Co/CoO_xH_y phases were selectively removed, the WGS TOR decreased by ~20 times compared to a fully promoted PtCo/MWCNT as prepared bimetallic catalyst. This confirms, in agreement with the discussion above, that alloy formation, which results from the juxtaposition of reduced Pt and reduced Co, is a mere coincidence.

DFT calculations, in conjunction with ab-initio thermodynamic phase diagram analyses, show metallic Co and CoO phases to be similar in energy at or near WGS

reaction conditions. This indicates that these phases may exist as metastable phases and the oxidation of Co or the reduction of CoO_xH_y will be dictated by kinetic limitations. On the other hand, Co partially oxidized to CoOH becomes stable at the contact interface with Pt under the same conditions. The OH binding energies on Pt(111), $\text{Pt}_3\text{Co}(111)$ and at the CoOH/Pt interface show that OH is stabilized at the interface of CoOH and Pt. The extent of stabilization is unique to the interfacial structure and is caused by under-coordination of partially oxidized Co and hydrogen bonding and although a pure Pt_3Co alloy surface is not expected, it provides the same degree of stabilization. Nevertheless, the Pt_3Co alloy does adsorb the OH intermediate more strongly than monometallic Pt and could, therefore, be useful to give a qualitative picture of the effect of the secondary metal on reactivity trends. Trends in OH binding energies across a series of Pt_3M alloys, for example, would be expected to track corresponding trends at MOH/Pt(111) interfaces. The trend in H_2O dissociation energy agrees well with the experimental trend of observed promotion in WGS activity in these systems. Thus, we conclude that PtCo catalysts promote the WGS rate by allowing more facile H_2O dissociation at the interface between Pt and partially oxidized Co and designate the role of the pure Co metallic phase as secondary, further supported by the DFT result that a metallic Co overlayer on Pt is not stable at our reaction conditions (Figure 2.6).

The present study highlights the importance and indispensability of the sites formed by the partially oxidized secondary metal promoter towards understanding the WGS mechanism. As suggested by Azzam et al. [53] for Re promotion of Pt for WGS, the partially oxidized secondary metal (ReO_x) could directly take part in the reaction by activating water and the direct interaction of Pt and Re may be insignificant. The presence of an Au/MgO interface has also been shown by theory and experiment to promote WGS rate by promoting water dissociation [75, 76]. The results in the present study suggest that a similar conclusion can be drawn for Co-promoted Pt catalysts. Thus, using a combination of experimental and theoretical tools highlights the need to accommodate interfacial secondary metal oxide sites,

in addition to the electronic effects induced due to alloy formation, into theoretical design frameworks for better description of reactivity of such systems.

2.6 Conclusions

A series of PtCo bimetallic catalysts, as confirmed by XAS, was studied for the WGS reaction. Cobalt has been shown to promote the WGS TOR over Pt supported on MWCNT at 300 °C by an order of magnitude at a Co:Pt ratio of 1:3, measured under 7% CO, 8.5% CO₂, 21.9% H₂O, 37.4% H₂ and balance Ar. A fraction of Co was shown to be in a Co/CoO_xH_y phase (metallic Co and CoO_xH_y). This Co/CoO_xH_y phase was selectively removed by leaching with 5% acetic acid, while the Pt-Co alloy was preserved. The leaching process led to a decrease in the WGS TOR at 300 °C by 20 times as compared to the unleached catalysts. The WGS activation energies and reaction orders for the leached catalysts were similar to those for the Pt₃Co/MWCNT catalyst containing only homogeneous PtCo alloys, but the TORs were ~2 times lower than that for the monometallic Pt sample. Analysis of the kinetic data along with the spectroscopic characterization results show that the presence of the CoO_xH_y phase is essential for promoting the WGS rate with Co. DFT calculations show that water dissociation is more favorable at the interface between CoOH and Pt than for monometallic Pt. Furthermore, CoOH on Pt was identified to be a stable phase under WGS conditions. Thus, the DFT results strongly support the conclusion that the interface of CoO_xH_y with Pt is the source of promotion and that the role of such sites is to accelerate the dissociation of water.

2.7 Supporting Information

2.7.1 DFT Methods

The kinetic energy cutoff was fixed at 400 eV and a gamma point scheme was used to sample the Brillouin zone. The electronic convergence was set at 10⁻⁵ eV while ionic steps were converged to a force cutoff of 0.02 eV/Å. A Methfessel-Paxton

smearing of order one was used, with the smearing width specified using a sigma of 0.2. A Hubbard U correction was used to correct for self-interaction errors [77]. Inverse catalyst calculations were checked with the Van der Waals corrected opt-PBE functional to account for the weak binding sometimes found in thin films of hydroxides [78]. Structures of atoms and interfaces were constructed using the VESTA 3D visualization program [79].

Table 2.4.
WGS Kinetic data over the series of PtCo/MWCNT catalysts

Catalyst	Test Temp. (°C)	WGS Rate ^a (10^{-2} mol H ₂ (total mol Pt) ⁻¹ s ⁻¹)	E _{app} (kJ mol ⁻¹) (± 3)	H ₂ O (± 0.04)	CO (± 0.04)	CO ₂ (± 0.04)	H ₂ (± 0.04)
Pt	290	0.96	86	0.83	0.10	-0.05	-0.38
PtCo 1:1	275	1.9	96	0.90	-0.01	-0.11	-0.47
PtCo 1:2	260	4.4	114	1.10	-0.03	-0.07	-0.52
PtCo 1:3	250	9.3	137	1.10	-0.26	-0.01	-0.57
PtCo 1:5	250	9.4	142	1.10	-0.17	-0.01	-0.47
PtCo 1:8	250	8.4	136	0.90	-0.20	-0.01	-0.49
PtCo 1:3 Leached ^b	310	0.19	118	1.00	-0.10	-0.05	-0.58
PtCo 1:5 Leached ^b	310	0.34	116	1.00	-0.02	-0.02	-0.58
PtCo 1:8 Leached ^b	310	0.35	118	0.75	0.00	-0.05	-0.59
Pt ₃ Co	330	0.14	113	0.87	-0.03	-0.04	-0.54

^aRate extrapolated to 300°C

^bCatalysts subjected to acetic acid leaching at 25 °C.

Table 2.5.
ICP-AES data for PtCo/MWCNT catalysts

Catalyst	Pt wt%	Co wt%	Co:Pt Molar Ratio
Pt/MWCNT	4.49	-	-
Pt/MWCNT Leached	3.81	-	-
PtCo 1:1/MWCNT	4.76	1.21	0.8
PtCo 1:2/MWCNT	4.46	2.46	1.8
PtCo 1:3/MWCNT	4.21	3.47	2.7
PtCo 1:5/MWCNT	4.28	5.38	4.2
PtCo 1:8/MWCNT	4.16	8.72	6.9
PtCo 1:3/MWCNT Leached	3.98	0.62	0.5
PtCo 1:5/MWCNT Leached	4.12	0.40	0.3
PtCo 1:8/MWCNT Leached	4.61	0.69	0.5

Table 2.6.
CO Chemisorption (collected at 35 °C) and WGS TOR data for
PtCo/MWCNT Catalysts

Catalyst	Co Absorbed ($\mu\text{mol g}^{-1}$)	WGS TOR at 300 °C (10^{-2} $\text{mol H}_2 (\text{mol Co ads.})^{-1} \text{s}^{-1}$)
Pt/MWCNT	49	4.6
Pt/MWCNT Leached	21	4.2
PtCo 1:1/MWCNT	51	9.0
PtCo 1:2/MWCNT	57	22
PtCo 1:3/MWCNT	51	46
PtCo 1:5/MWCNT	62	39
PtCo 1:8/MWCNT	71	30
PtCo 1:3/MWCNT Leached	47	2.1
PtCo 1:5/MWCNT Leached	21	1.8
PtCo 1:8/MWCNT Leached	52	1.7
Pt ₃ Co/MWCNT	19	1.8

Table 2.7.
Co K edge EXAFS data fit parameters for the PtCo/MWCNT catalysts.

Catalyst	Co-Co				Co-Pt				Total CN
	CN	R (Å)	$\Delta\sigma^2$ (Å ²)	E_0 (eV)	CN	R (Å)	$\Delta\sigma^2$ (Å ²)	E_0 (eV)	
PtCo 1:1	7.3	2.51	0.002	-1.0	3.9	2.64	0.002	10.5	11.2
PtCo 1:2	6.1	2.50	0.002	-2.2	3.8	2.63	0.002	10.2	9.9
PtCo 1:3	9.8	2.50	0.002	0.9	-	-	-	-	9.8
PtCo 1:5	10	2.51	0.002	2.1	1.4	2.64	0.002	-9.7	11.4
PtCo 1:8	11.8	2.51	0.002	2.4	-	-	-	-	11.8
PtCo 1:3 Leached	2.4	2.51	0.002	-4.1	4.7	2.64	0.002	-4.5	7.1
PtCo 1:5 Leached	1.3	2.51	0.002	-5.1	5.6	2.64	0.002	-6.0	6.9
PtCo 1:8 Leached	2.6	2.51	0.002	-4.5	5.1	2.64	0.002	-4.1	7.7

Table 2.8.
DFT calculated binding energies of intermediates at the CoOH/Pt interface, the sites correspond to that shown in Figure 2.7

Site #	PBE+U (eV)		Opt PBE+U (eV)	
	OH	H ₂ O	OH	H ₂ O
1	0.03	-0.77	-0.25	-0.29
2	0.13	-0.63	-0.13	-0.27
3	0.52	-0.60	0.18	-0.18
4	0.21	-0.61	-0.08	-0.20

Table 2.9.
DFT calculated binding energies of intermediates on various Pt-containing structures

System	Binding Energy (PBE+U) (eV)		
	H ₂ O	OH	H
Pt	-0.23	0.87	-0.51
Pt ₃ Co	-0.44	0.47	-0.35
CoOH/Pt with co-adsorbed H ₂ O	-0.67	-0.28	-0.56 ^a

^aH adsorbs on Pt away from interface and no co-adsorption effect was considered here

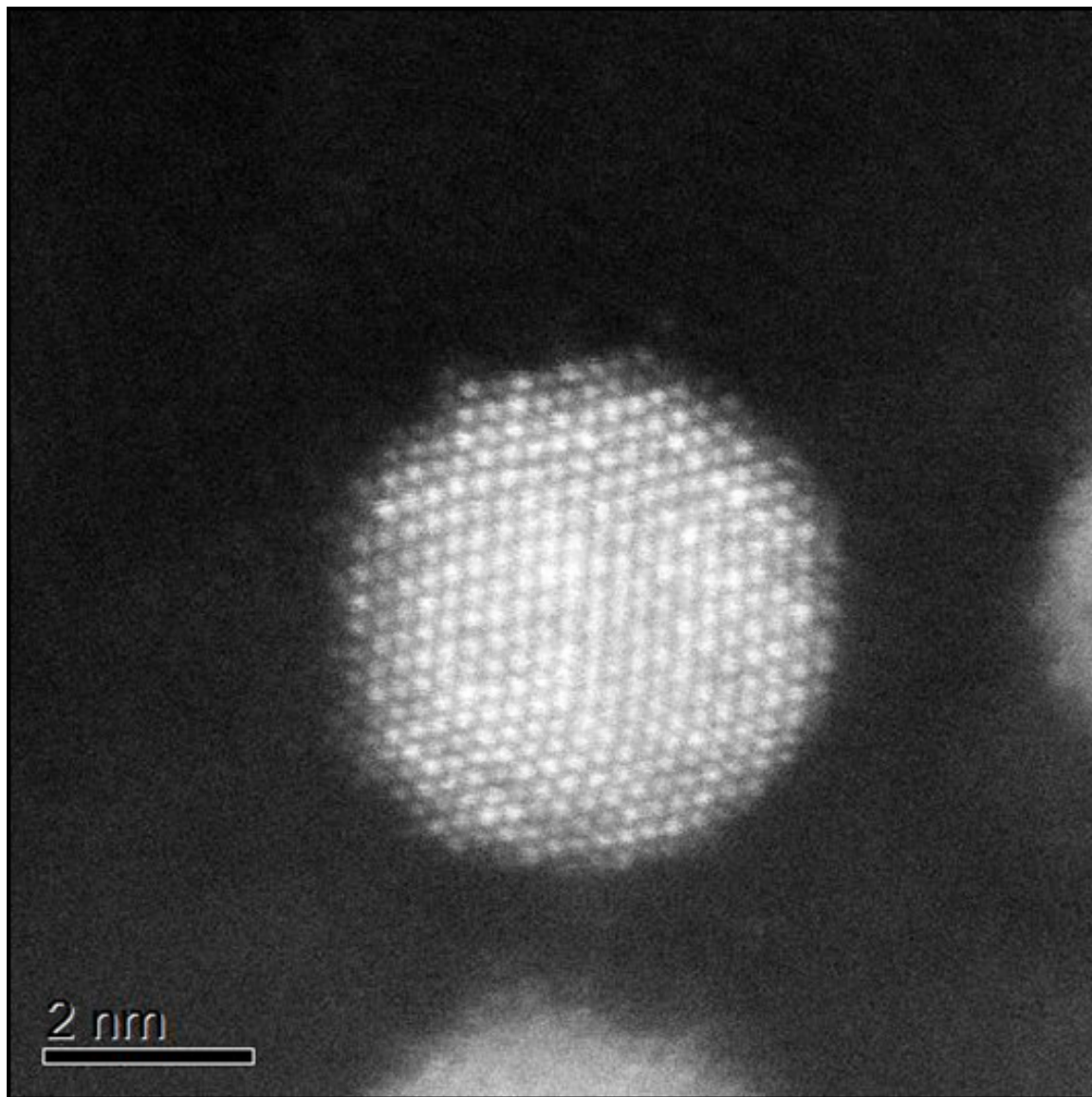


Figure 2.9. HAADF-STEM image of the $\text{Pt}_3\text{Co}/\text{MWCNT}$ catalyst after reaction.

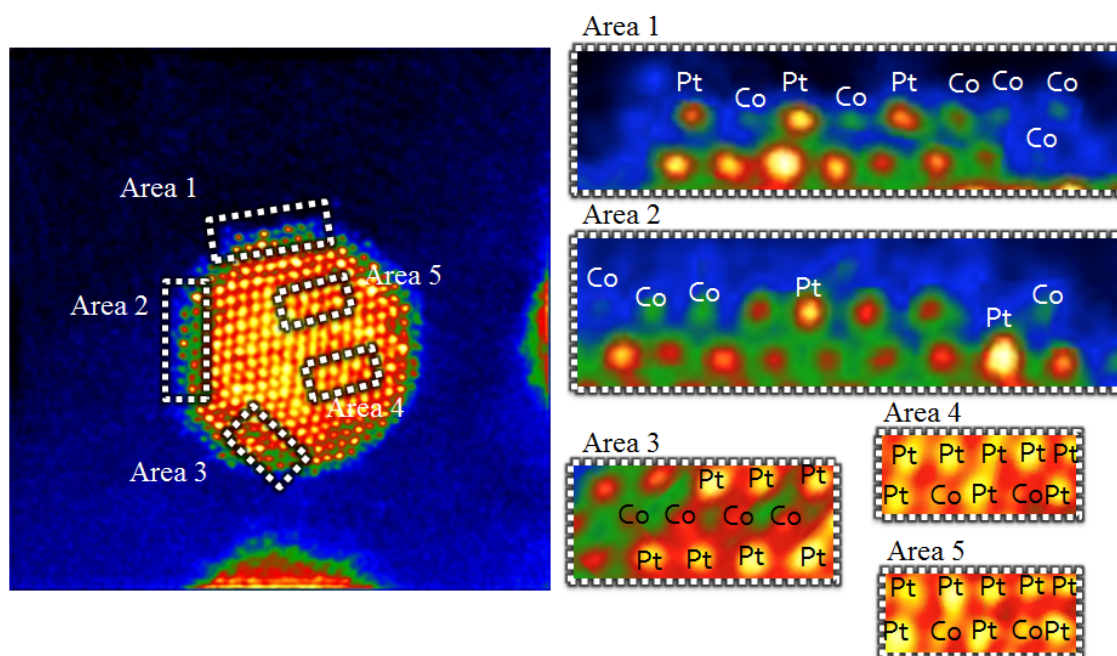


Figure 2.10. Colorized Z-contrast STEM image of the $\text{Pt}_3\text{Co}/\text{MWCNT}$ catalyst after reaction indicating placement of Pt and Co atoms.

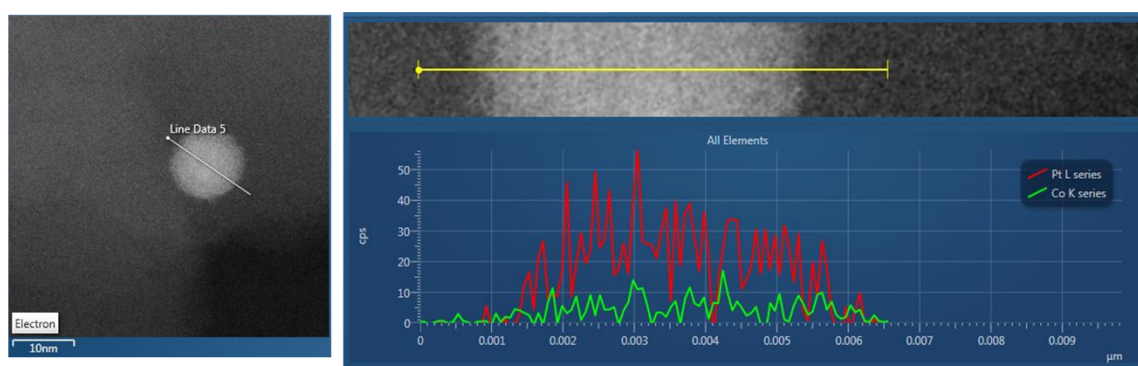


Figure 2.11. X-ray EDS line-scan of the $\text{Pt}_3\text{Co}/\text{MWCNT}$ catalyst after reaction

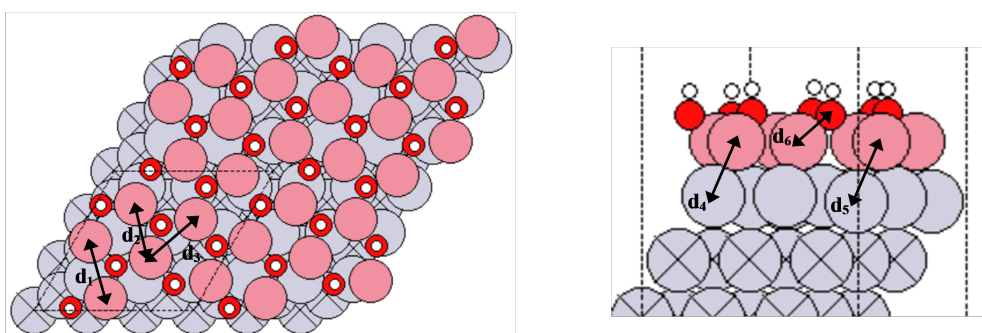


Figure 2.12. $(\sqrt{7} \times \sqrt{7})$ CoOH on (3×3) Pt(111) (left) top view (right) side view. Grey - Pt, Pink - Co, White - H, Red - O of CoOH. The unit cell boundaries are indicated using dashed lines. The height of the film from the top layer of Pt is 2.18 \AA [66]. Some of the bond lengths are indicated in \AA . $d_1 = 3.15$, $d_2 = 2.9$, $d_3 = 3.12$, $d_4 = 2.57$, $d_5 = 2.48$, $d_6 = 2.16$.

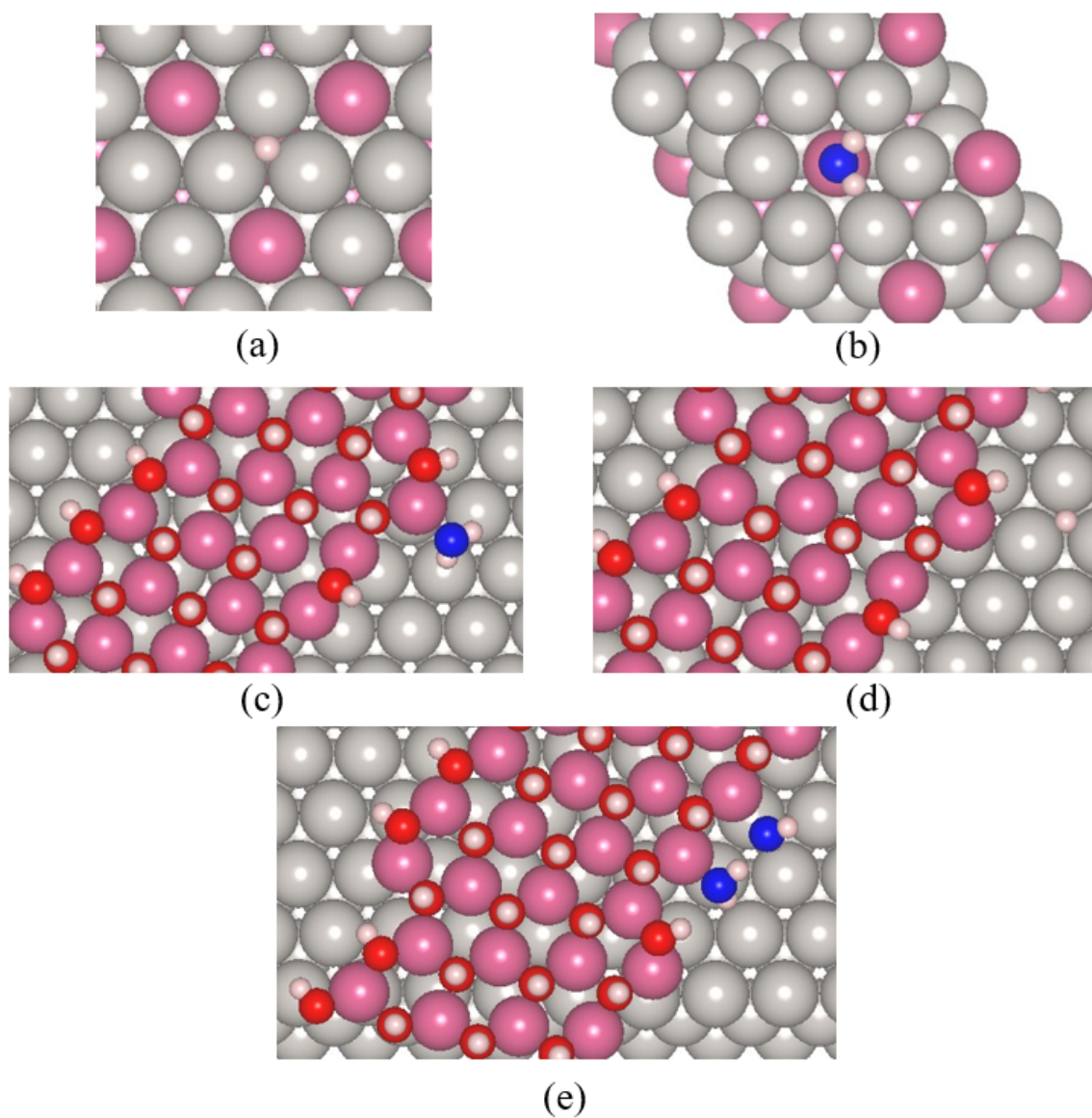


Figure 2.13. Adsorption geometries; Grey - Pt, Pink - Co, White - H, Red - O of CoOH, Blue - O of adsorbate; (a) H on Pt₃Co (b) H₂O on Pt₃Co (c) H₂O on CoOH/Pt (d) H on CoOH/Pt (e) two co-adsorbed H₂O on CoOH/Pt.

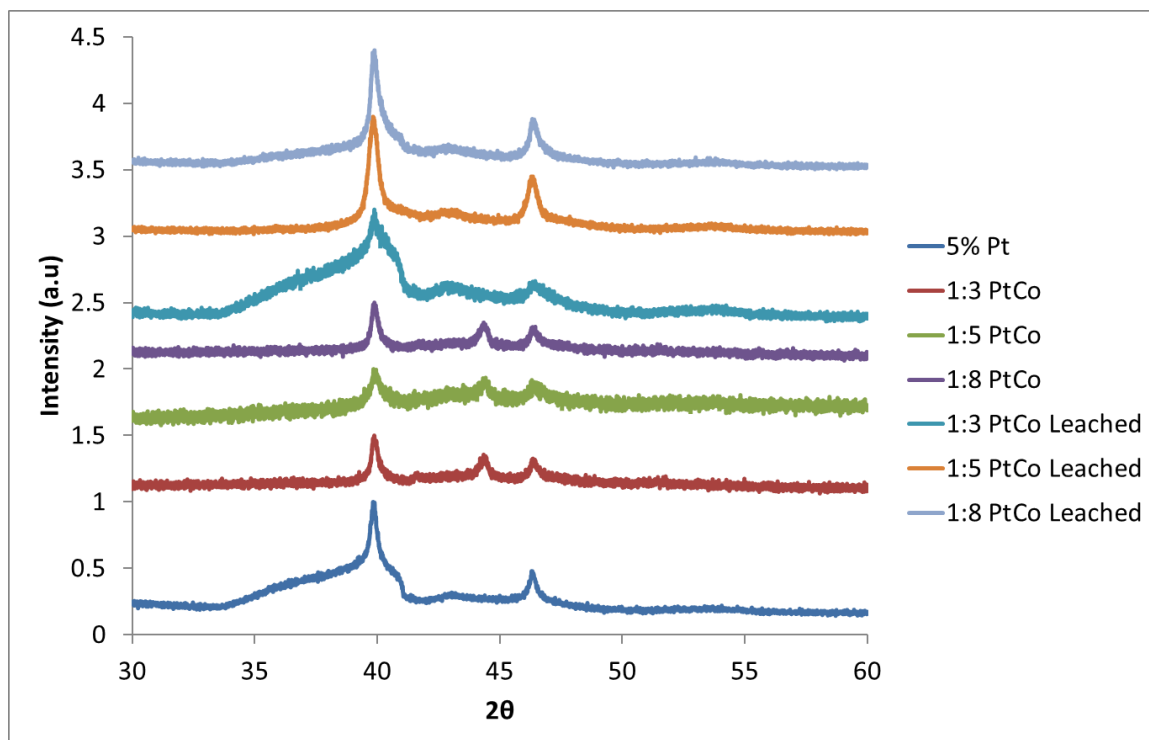


Figure 2.14. Raw XRD patterns correlated with Figure 2.2 before background selection.

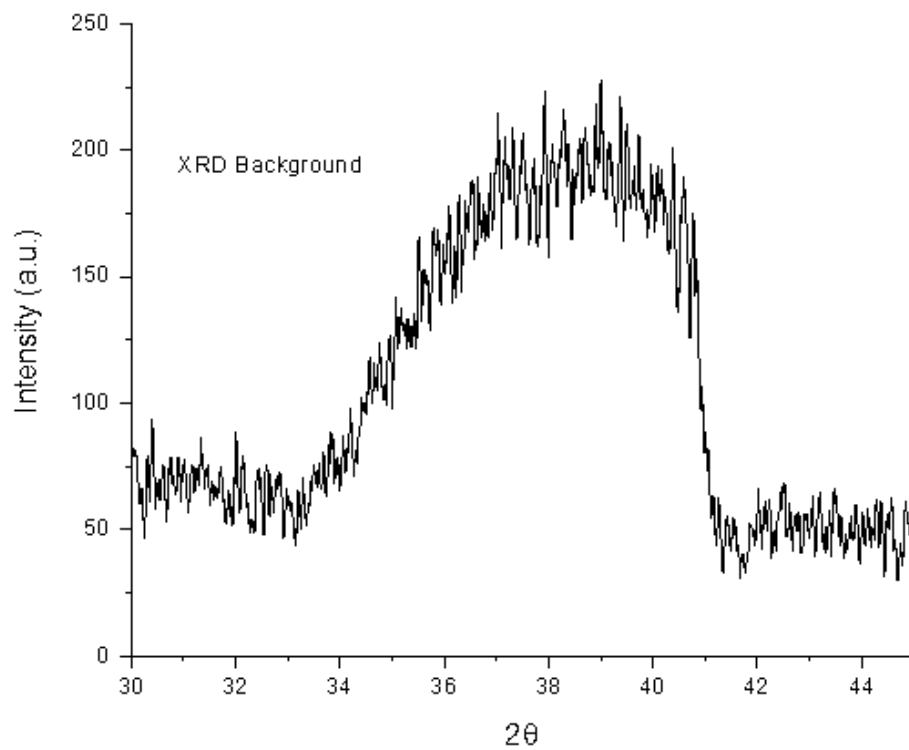


Figure 2.15. XRD background pattern collected on the MWCNT support used for correction of artifacts in the raw XRD patterns shown in Figure 2.14.

3. ORIGIN OF ELECTRONIC MODIFICATION OF PLATINUM IN A Pt₃V ALLOY AND ITS CONSEQUENCES FOR PROPANE DEHYDROGENATION CATALYSIS

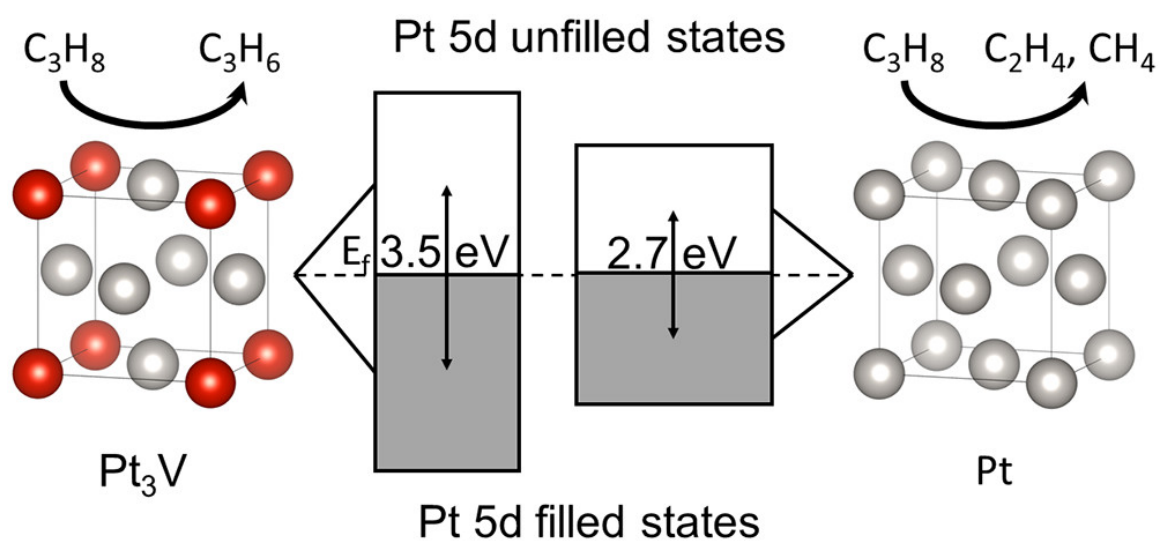
ACS Applied Energy Materials 2020, 3, 1410-1422. <https://doi.org/10.1021/acsaem.9b01373>

Stephen C. Purdy, Pushkar Ghanekar, Garrett Mitchell, A. Jeremy Kropf, Dmitry Y. Zemlyanov, Yang Ren, Fabio Ribeiro, W. Nicholas Delgass, Jeffrey Greeley, and Jeffrey T. Miller

Reprinted (adapted) with permission from (*ACS Appl. Energy Mater.* 2020, 3, 2, 1410-1422). Copyright (2020) American Chemical Society.

3.1 Abstract

We demonstrate the synthesis of a Pt₃V alloy and Pt/Pt₃V core/shell catalysts, which are highly selective for propane dehydrogenation. The selectivity is a result of the Pt₃V intermetallic phase, which was characterized by *in situ* synchrotron XRD and XAS. Formation of a continuous alloy surface layer 2–3 atomic layers thick was sufficient to obtain identical catalytic properties between a core–shell and full alloy catalyst, which demonstrates the length scale over which electronic effects pertinent to dehydrogenation act. Electronic characterization of the alloy phase was investigated by using DFT, XPS, XANES, and RIXS, all of which show a change in the energy of the filled and unfilled Pt 5*d* states resulting from Pt–V bonding. The electronic modification leads to a change in the most stable binding site of hydrocarbon fragments, which bind to V containing ensembles despite the presence of 3-fold Pt ensembles in Pt₃V. In addition, electronic modification destabilizes deeply dehydrogenated species thought to be responsible for hydrogenolysis and coke formation.



3.2 Introduction

Alloy catalysts have been extensively studied for many catalytic reactions due to their improved performance over their monometallic constituents. [80] In particular, alloy catalysts have seen extensive use for dehydrogenation of light alkanes for the production of olefins. Monometallic catalysts such as Pt suffer from low olefin selectivity due high hydrogenolysis activity. [81] Industrially, an alloy of Pt and Sn is often used for propane and butane dehydrogenation and offers improved selectivity and stability over a Pt only catalyst. [82] Interest in alloy catalysts for on-purpose light alkane dehydrogenation has also been fueled by decreased supply of propylene due to naphtha crackers switching to an ethane feedstock and the widespread production of shale gas which contains a significant fraction of C_2+ alkanes. [83] New alloy catalysts with higher selectivity will allow for more efficient utilization of the C_2+ fraction of shale gas which will increasingly be used in on-purpose dehydrogenation plants. A major goal in the research of alloy catalysts for dehydrogenation is to understand the electronic and geometric factors responsible for the increased selectivity to olefins.

The formation of an alloy between Pt and a second promoter metal leads to changes in the electronic and structural properties of the catalyst. The electronic effect is usually explained by extending Hammer and Nørskov's d-band theory to alloys, in which the promoter element shifts the d-band center away from the Fermi energy, leading to a decrease in binding strength of adsorbates. [84,85] Experimentally, it has been observed that alloy formation with Pt causes a decrease in the heat of adsorption of alkenes, resulting in the product desorption pathway becoming more favorable than deep dehydrogenation and coking. [86,87] Density functional theory (DFT) studies on Pt and Pt–Sn surfaces have come to similar conclusions. [88,89]

While the qualitative effect of shifting electronic states with respect to the Fermi energy is generally agreed upon, other aspects of how the promoter modifies the electronic properties of alloys, such as the effect of charge transfer, are still debated.

Spectroscopic changes between pure metals and alloys are often explained by electron transfer to or from the d-band driven by electronegativity difference. [90–92] An observed increase in the Pt L_3 edge X-ray absorption near edge structure (XANES) edge energy and decrease in the Pt 4d binding energy measured by X-ray photoelectron spectroscopy (XPS) seen in alloys has been interpreted as a donation of electron density from the promoter to Pt. The donation of electron density further fills the d-band, and the shift of the d-band center and the resulting decrease in the binding strength of alkenes are cited as being responsible for the improved selectivity. [90,91] While charge partitioning on alloys generally shows a subunity change in the total number of electrons between atoms in a pure metal and an alloy, alloys generally show a negligible change in the d-band filling, which would preclude electron transfer from significantly modifying adsorbate bonding. [84, 93, 94] Alternative explanations for the spectroscopic shifts not involving electron transfer have been suggested involving broadening of the d-band. [95,96] However, arguments both for and against charge transfer generally rely on theoretical calculations and a single spectroscopic technique that indirectly probes the filled valence d-states responsible for catalysis.

Recently, Cybulskis et al. used resonant inelastic X-ray scattering (RIXS) spectroscopy to experimentally measure the energy change of the 5d electrons between Pt and Pt in a Pt_1Zn_1 (AuCu structure) alloy. [97] They found that alloy formation with Zn leads to an upward shift in the energy of the unfilled states and a downward shift in the energy of the filled state. DFT results showed that the d-band center in Pt_1Zn_1 is minimally shifted (~ 0.1 eV) relative to Pt. The change in the energy of the filled and unfilled Pt 5d states was cited as responsible for observed changes in the turnover rate (TOR), while isolation of active sites by zinc was responsible for the increased selectivity.

Regardless of whether electron transfer or changing electron energy underlie the electronic effect, a Pt alloy with a large d-band shift should have a large electronic effect and should lead to improved performance over monometallic Pt. Additionally, an alloy with a large d-band shift should also show easily discernible spectroscopic

shifts relative to the pure metal, allowing for unambiguous trends among multiple spectroscopic techniques. Pt and V have a larger electronegativity difference than do other widely studied alloys such as Pt–Sn. Finally, computational and experimental studies on Pt–V alloys show large shifts in the d-band center, and thus should display large changes in the electronic properties of Pt. [84,98] Pt–V alloys, however, have not been previously studied as dehydrogenation catalysts, possibly because Pt–V alloys are difficult to synthesize, requiring oxygen free synthesis and strong reducing agents. [99]

Herein, we demonstrate that Pt₃V nanoparticles significantly improve selectivity to propylene as compared to unalloyed Pt. The structural ordering of the nanoparticles is confirmed by *in situ* X-ray absorption spectroscopy (XAS) and *in situ* synchrotron X-ray diffraction (XRD). The corresponding changes in the electronic properties are determined by using DFT, RIXS, XPS, and XANES. DFT calculations demonstrate that the binding strengths of prototypical intermediates involved in coking and dehydrogenation decrease appreciably due to presence of V promoter. Additionally, the electronic structure of Pt atoms also changes with increasing V incorporation as evidenced from projected density of states (pDOS) analysis of Pt d-states. In agreement with DFT, the XPS, XANES, and RIXS show that the electronic modification results from a decrease in the energy of the filled Pt 5d orbitals, rather than due to a change in the number of d-electrons.

3.3 Experimental Section

3.3.1 Catalyst Synthesis

Pt–V catalysts were supported on Davisil grade 646 silica (35–60 mesh, Sigma-Aldrich) and synthesized by sequential incipient wetness impregnation. Pt and V loadings are given in weight percent with respect to the total catalyst mass. V impregnation to give a 5% V on silica catalyst was done by using a solution of 1:2 molar ratio of ammonium metavanadate to oxalic acid. 0.574 g of ammonium metavanadate

and 0.884 g of oxalic acid dihydrate were dissolved in 4 mL of Millipore water. The oxalic acid/ammonium metavanadate solution was heated to 100 °C, refluxed for 1 h, and then added dropwise to 5 g of silica. The impregnated silica was dried overnight at 125 °C and then calcined at 350 °C for 3 h in flowing air.

Pt was added to the V-SiO₂ by incipient wetness impregnation of a pH adjusted solution of tetraamine platinum(II) nitrate. The solution pH was adjusted to 11 with ammonium hydroxide. After impregnation of the Pt salt, the catalyst was dried overnight at 125 °C and calcined at 250 °C for 3 h in flowing air. The mass of tetraamine platinum nitrate used in the impregnation solution was adjusted to give Pt loadings of 2% and 5% on the bimetallic catalysts and a separate monometallic Pt catalyst with a Pt loading of 3%. After calcination, catalysts were reduced in 5% H₂ with a slow heating ramp (2.5 °C/min) through 250 °C and a fast ramp to 550 °C with a 30 min dwell at temperature. The reduced catalysts were then cooled to room temperature in nitrogen and passivated in air. Other Pt-V catalysts were synthesized with different metal loadings of each component with full details given in Table 3.3 of the Supporting Information.

3.3.2 Electron Microscopy

Particle size distributions were measured by scanning transmission electron microscopy (STEM) and are reported as volume average particle sizes. Imaging was performed on a FEI Titan at an accelerating voltage of 300 keV in STEM mode by using a high angle annular dark field detector. Particle size distributions were measured by counting over 250 particles per sample. Energy-dispersive X-ray spectroscopy (EDS) maps were taken on a FEI Talos F200X S/TEM with an X-FEG high brightness electron source and a Super-X EDS system. The microscope was operated at an accelerating voltage of 200 keV and has a maximum STEM resolution of 1.2 Å and a maximum EDS mapping resolution of 1.6 Å.

3.3.3 Propane Dehydrogenation

Catalytic measurements were performed on a laboratory scale fixed bed microreactor. 0.025–0.25 g of catalyst was diluted to 1 g total mass with Davisil grade 646 (35–60 mesh) and loaded into a quartz tube for testing, creating a catalyst bed approximately 2–3 cm in length. A stainless-steel thermocouple well was inserted into the bottom of the catalyst bed to monitor temperature during reactions. Four mass flow controllers (Parker) were used to supply reactant gases to the reactor. Effluent gas was analyzed by an online HP 6890 gas chromatograph equipped with an FID detector and a Restek Alumina BOND/ Na_2SO_4 capillary column. Full separation of C_1 through C_3 products was accomplished in 5 min.

The selectivity to propylene and propane conversion were calculated on a carbon basis of gas phase products. Dehydrogenation turnover rates were normalized based on the fraction of surface Pt determined by surface oxidation difference extended X-ray absorption fine structure (EXAFS) (described below). Catalysts were pretreated at 550 °C in 5% H_2 , and the reactor was purged with N_2 before flowing reactant gases. A first-order exponential decay function was fit to time on stream data to determine selectivity and conversion for each test at zero deactivation. Each conversion, selectivity, and initial turnover rate reported was determined by using a fresh sample from the same respective batch of each prereduced catalyst.

3.3.4 X-ray Absorption Spectroscopy (XAS)

Pt L_3 edge *in situ* XAS was performed at the MRCAT bending magnet line (10BM) at Argonne National Laboratory's Advanced Photon Source. Measurements were taken in transmission mode using a set of three ion chambers for simultaneous measurement of a sample and an energy reference foil. Powder samples pressed into a stainless steel sample holder were treated and measured in a quartz tube reactor with X-ray transparent windows. Before measurement, samples were reduced at 550 °C in 3.5% H_2 for 30 min. The reactor was then purged with ultrahigh-purity helium

passed through an oxygen trap at temperature to desorb hydrogen and cooled to room temperature for measurement. Scans were also collected after exposing the reduced samples to air at room temperature.

To study the surface layer of the Pt–V nanoparticles, EXAFS difference spectra were used. EXAFS spectra of the catalyst oxidized in air at room temperature and that of the catalyst in the reduced state were subtracted to give the difference. Air exposure at room temperature oxidizes the surface layer of Pt nanoparticles. [100] The unchanged spectral features of the particle core common to both the reduced and surface oxidized samples are removed in the difference, leaving only the changes resulting due to the surface oxidation process. Details of the data processing for EXAFS difference spectra and EXAFS fitting are given in the Supporting Information.

3.3.5 Resonant Inelastic X-ray Scattering (RIXS)

RIXS measurements were performed at the MRCAT insertion device line (10ID). RIXS measurements were performed on catalyst wafers treated in an *in situ* fluorescence cell described elsewhere. [101] Measurements were conducted at 100 °C after a 30 min pretreatment at 550 °C in 3.5% H₂. The RIXS process measured was the L β_5 fluorescent emission (Pt 5d decay to 2p_{3/2} core hole) resonant about the Pt L₃ absorption edge (Pt 2p_{3/2} to 5d unfilled). X-ray absorption at the Pt L₃ edge was measured in transmission by using a set of ion chambers. Simultaneously, high-resolution X-ray emission spectra of the Pt L β_5 fluorescence line were collected by using a wavelength dispersive spectrometer based on a bent silicon crystal. Full details of the emission spectrometer and data processing are given in the Supporting Information.

3.3.6 X-ray Photoelectron Spectroscopy (XPS)

XPS analysis was performed by a Kratos Axis Ultra Imaging DLD spectrometer with an attached pretreatment chamber. The XPS spectra were collected by using a monochromatic Al K α (1486.69 eV) radiation and a hemispherical electron energy an-

alyzer operated with a constant pass energy of 20 eV. Charge neutralization was used to mitigate nonhomogeneous charging and to improve resolution. Prior to measurement, samples were pretreated at 550 °C in 5% hydrogen for 30 min. The pretreatment chamber was then evacuated, and the sample was transferred under ultrahigh vacuum to the analysis chamber. XPS spectra were processed by using CasaXPS software. The Pt 4f peaks were fit by using an asymmetric Lorentzian function (LF(a,b,c,d) function in CasaXPS) after subtraction of a Shirley background. Charge correction was performed by setting the Si 2p binding energy to 103.7 eV.

3.3.7 X-ray Diffraction (XRD)

In situ synchrotron XRD spectra were collected at the 11-ID-C beamline at the Advanced Photon Source. XRD experiments were performed in transmission geometry, using an X-ray energy of 106.257 keV (0.11684 Å) and a PerkinElmer large area detector. Pressed catalyst wafer samples were loaded into a water-cooled Linkam stage, which allowed for heating and cooling as well as gas flow. Samples were pretreated identically to XAS measurements. Scans of the empty Linkam cell and bare silica support were collected for background subtraction. The collected 2D diffraction patterns were calibrated by using a CeO₂ standard sample and integrated to give standard powder diffraction data by using Fit2D software. [102,103] Theoretical XRD patterns were calculated by using crystallographic references and the Materials Analysis Using Diffraction (MAUD) software. [104] Multiple peak fitting was performed with OriginPro software using a mixed Gaussian–Lorentzian peak profile.

3.3.8 Density Functional Theory (DFT)

Electronic structure calculations were performed using periodic, self-consistent DFT, as implemented within the Vienna ab Initio Simulation Package (VASP). [105–108] Projector augmented wave pseudopotentials [109] and the PBE functional for exchange and correlation [110] were used, which have been extensively benchmarked

for transition metals and have been shown to provide good predictions of trends in adsorption properties across different metal surfaces. Lattice constant optimization and bulk binary phase diagram calculations were performed using a plane wave cutoff energy of 600 eV and a $10 \times 10 \times 10$ Monkhorst–Pack \mathbf{k} -point grid and Methfessel–Paxton smearing. [111,112] Lattice constants were converged with a force criterion of $0.02 \text{ eV}/\text{\AA}$, giving a lattice constant of 3.98 \AA for Pt and 3.92 \AA for Pt_3V .

Surface calculations for adsorption energies were conducted on close-packed (111) facets with supercells of Pt and Pt_3V having side lengths of $\sqrt{12}$ times those of the primitive unit cell. A plane wave cutoff of 500 eV and a $4 \times 4 \times 1$ Monkhorst–Pack \mathbf{k} -point grid with Methfessel–Paxton smearing were used. The slabs were composed of five layers with the bottom two layers constrained to represent the bulk. For comparison, binding energies of CO and CH_3 species were also calculated on a smaller $2 \times 2 \times 5$ unit cell with the same number of layers relaxed, and no differences were found (see the Supporting Information for additional details). We note that although such single crystal models may not capture all quantitative aspects of the structure and reactivity of transition metal alloy nanoparticles, they provide reasonable descriptions of qualitative trends, which is the goal of this study. All calculations were spin polarized, and a dipole correction was employed perpendicular to slab surface to reduce periodic image interactions.

Projected density of states (pDOS) calculations were conducted on (111) close-packed surfaces with $2 \times 2 \times 5$ supercells and three layers relaxed. Pure Pt (111), bulk-terminated Pt_3V (111), and Pt (111) with one and two monolayers of Pt_3V skins on the surface were considered for the pDOS analysis. For these calculations, a plane wave cutoff of 800 eV, a denser \mathbf{k} -point grid of $13 \times 13 \times 1$, and tetrahedron Blöchl smearing were used. The density of states was projected according to the Wigner–Seitz radius provided by the PAW potential. The DOS was evaluated on 800 grid points in a range of $\pm 8 \text{ eV}$ from the corresponding Fermi energy for the system. Methfessel–Paxton smearing with a width of 0.2 eV was used to generate a smoother pDOS. The Pt d-band center was calculated as the first moment of the pDOS of

d-electrons for surface Pt atoms, and the d-band width was evaluated as the square root of its second moment.

Transition-state (TS) energy calculations were performed with CI-NEB where each optimized TS structure was checked with a normal-mode analysis to ensure that only a single imaginary frequency exists. [113] Gas phase species were calculated with a plane wave cutoff of 500 eV with Gaussian smearing and a gamma \mathbf{k} -point within a $20 \times 21 \times 22$ Å supercell. For setup, visualization, and analysis of atomistic simulations, Atomic Simulation Environment (ASE) was used. [114] Rendering of the atomic configuration was done using OVITO. [115]

3.4 Results

3.4.1 Structural Characterization

Metal nanoparticle sizes of the 3Pt, 5Pt-5V, and 2Pt-5V catalysts were determined by STEM imaging (Figure 3.10). The volume average particle sizes for 3Pt, 5Pt-5V, and 2Pt-5V were 2.6 ± 0.5 , 2.2 ± 0.5 , and 2.2 ± 0.7 nm, respectively. STEM EDS maps of 2Pt-5V (Figure 3.11) of Pt and V show a highly dispersed V on the support and particles containing both Pt and V. The TEM images do show some amount of particle size heterogeneity, likely due to sintering and coalescence resulting from the high-temperature reduction done as part of the synthesis process.

XAS was used to verify that V incorporates into the metallic Pt particles and forms a bimetallic phase. From the V K edge (Figure 3.12), only scattering from nearest-neighbor V-O and second shell V-O-V is evident after reduction of the 5Pt-5V catalyst, suggesting most of the V is present as oxide clusters. Figure 3.1 shows the R-space magnitude and imaginary components of the Pt L₃ EXAFS for 3Pt (black) and 2Pt-5V (blue). 3Pt shows the three peaks characteristic of scattering from metallic Pt. Compared to 3Pt, the first peak in the 2Pt-5V sample at 2 Å (phase uncorrected distance) increases slightly in intensity, and the third peak at 3 Å (phase uncorrected distance) decreases slightly in intensity. Additionally, the peaks

in 2Pt-5V shift to lower R compared to 3Pt. The changes in the first shell scattering peaks are due to Pt-V scattering, confirming that a Pt-V bimetallic forms. Fits of the first shell EXAFS and XANES edge energies are shown in Table 3.1.

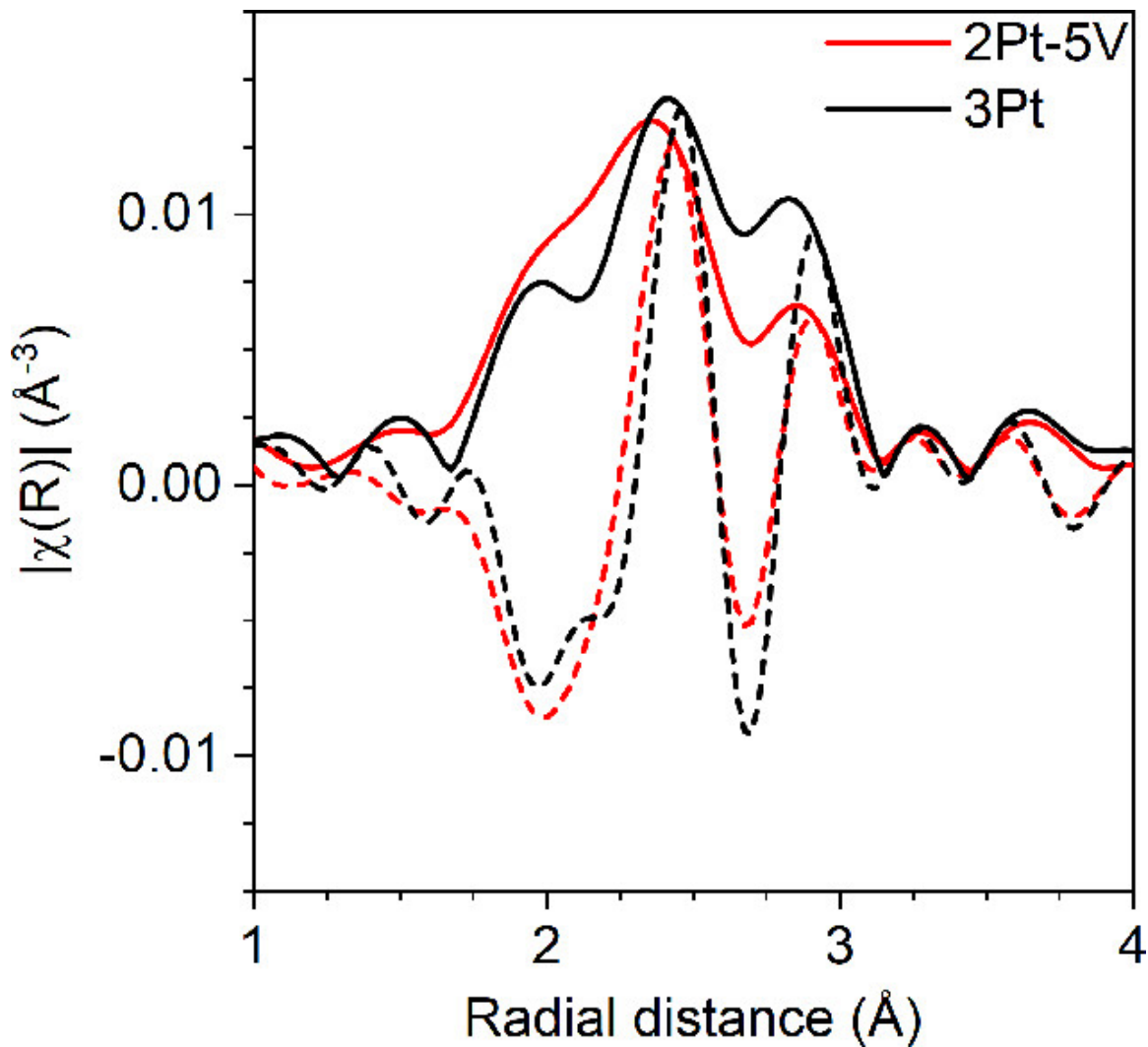


Figure 3.1. *In situ* Pt L_3 edge EXAFS magnitude (solid lines) and imaginary (dashed lines) of 3Pt (black) and 2Pt-5V (red) catalysts. Spectra were collected at room temperature in He after a 30 min reduction at 550 °C in 3.5% H_2

For 3Pt, a high-quality fit was obtained by fitting with a single Pt-Pt scattering path. To fit the Pt-V catalysts, it was necessary to include a second scattering

Table 3.1.
XANES Edge Energies and EXAFS Fitting Parameters for 3Pt, 5Pt-5V, and 2Pt-5V: Coordination Number (CN), Bond Distance (R), Debye-Waller Factor (σ^2), and E_0 Correction

Sample	XANES Edge Energy (eV)	Scattering Pair	CN	R (Å)	σ^2 (Å ²)	E_0 (eV)
3Pt	11564.0	Pt-Pt	8.8	2.74	0.002	-0.9
5Pt-5V	11564.2	Pt-Pt	6.5	2.73	0.003	-0.8
		Pt-V	2.0	2.71	0.003	2.6
2Pt-5V	11564.4	Pt-Pt	6.2	2.72	0.003	-1.6
		Pt-V	2.9	2.72	0.003	2.3

path (Pt-V) to fit the data. The total coordination number, which is correlated to the metal particle size, [116] of all three catalysts is close to 9, which agrees with the STEM results showing that all three catalysts have similar particle sizes (2–2.5 nm). The bond distance of 2.74 Å in the 3Pt sample is characteristic of small Pt nanoparticles, where the decrease in average coordination number causes a slight contraction of the Pt-Pt bond distance from the bulk value of 2.77 Å. [117] In the Pt-V catalysts, the Pt-Pt bond distance was also contracted, with 5Pt-5V having a bond distance of 2.73 Å and 2Pt-5V having a Pt-Pt bond distance of 2.72 Å. For both alloy samples, the Pt-V bond distance for each sample was the same as the respective Pt-Pt bond distance. Fit parameters and spectra for other Pt-V catalysts discussed in the Experimental Methods synthesis section are given in Table 3.4 and Figure 3.13, respectively and have bond distances and coordination numbers similar to the above-described Pt-V catalysts.

The ratio of Pt-V to Pt-Pt neighbors is related to the particle composition. By nature of their fixed composition, Pt-V intermetallic phases have fixed values of the neighbor ratio, and hence the ratio can be used to determine whether a sample has a

local Pt environment consistent with a given alloy phase. Of the possible Pt–V alloys only Pt₈V and Pt₃V have Pt–Pt bonds. Pt₈V has a Pt–V/Pt–Pt neighbor ratio of 0.2, and Pt₃V has a Pt–V/Pt–Pt neighbor ratio of 0.5. The 5Pt–5V catalyst had a Pt–Pt coordination number of 6.5 and a Pt–V coordination number of 2, leading to a ratio of Pt–V to Pt–Pt neighbors of 0.31, which is Pt rich with respect to Pt₃V. An intermediate neighbor ratio could be explained by a mixture of two phases as would be present in core–shell particles. The 2Pt–5V catalyst had a Pt–Pt coordination number of 6.2 and a Pt–V coordination number of 2.9, giving a Pt–Pt/Pt–V coordination number ratio of 0.47, which closely matches the ratio of Pt₃V.

In a 5Pt–5V catalyst reduced at 200 °C from the freshly calcined state the coordination number ratio closely matches that of 5Pt–5V reduced at 550 °C (Figure 3.14 and Table 3.4), albeit with a lower total coordination number. Based on the color change of the catalyst during reduction from brown to black, the onset of platinum reduction on silica supported Pt–V catalysts is close to 200 °C. The presence of Pt–V scattering in 5Pt–5V early in the reduction process suggests that vanadium reduction and incorporation occur early or simultaneously with the nucleation of metallic Pt. The similarity in composition between the 5Pt–5V catalyst reduced at 200 and 550 °C suggests that the particle size heterogeneity in the high-temperature reduction sample does not also accompany a compositional heterogeneity.

To study the long-range order and phase composition of the Pt–V nanoparticles, *in situ* synchrotron XRD was used. Synchrotron XRD provides several advantages over laboratory-based XRD, including improved signal-to-noise and the ability to use a high X-ray energy which further suppresses the contribution of the amorphous support for the spectrum. As a result of the high X-ray energy used (106.257 keV), diffraction peaks occur at a lower angle and a lower angular range than typical of a laboratory instrument.

Distinguishing between Pt and Pt₃V is difficult due to the small difference in their unit cell parameters: 3.92 Å for Pt and 3.87 Å for Pt₃V. [118] Additionally, below 10 nm, the lattice parameters of both Pt and Pt₃V change with particle size due to

the contraction of bond distance that occurs in nanoparticles. Leontyev et al. used synchrotron XRD to measure the lattice parameter contraction in Pt nanoparticles of different size. [119] At 2 nm in size, the lattice parameter of Pt nanoparticles decreased from the bulk value by 0.03 Å, a decrease comparable in size to the lattice parameter difference between Pt and Pt₃V (0.05 Å). Because both V incorporation and decreasing particle size each decrease the lattice parameter, changes cannot be solely attributed to composition unless a comparison is made between a Pt and Pt–V particle of similar size.

Figure 3.2a shows the *in situ* synchrotron XRD pattern of 3Pt and 5Pt–5V. The fundamental lines characteristic of an fcc metal are present, ruling out the presence of Pt–V phases without fcc symmetry, such as Pt₈V, PtV, or Pt₂V. The XRD peaks are broad and weak in intensity due to the small average particle size present in the sample, as described above. In the high Pt loading sample (5Pt–5V), no diffraction from a crystalline vanadium oxide phase is observed; while weak vanadium oxide diffraction peaks are seen in the sample with lower Pt loading. Both samples, however, have similar shifts in the position of fcc reflections (2Pt–5V, Figure 3.15). Figure 3.2b shows details of the 220 and 311 reflections for 3Pt and 5Pt–5V after a reduction treatment at 550 °C. While the peak shifts between 3Pt and 5Pt–5V are small (0.03° for the 220 peak), the shift is larger than the angular resolution of the instrument (0.005°) and is more apparent in the high index diffraction peaks. Particle size dependent lattice contraction is controlled for by measuring a monometallic and alloy catalyst of the same particle size, and the shift in peak position is attributed to formation of the Pt₃V phase. The peak positions of the 3Pt catalyst agree with the simulated Pt pattern with a lattice parameter of 3.89 Å. The peak positions of the 5Pt–5V catalyst are shifted to higher angle than the 3Pt catalyst. Simulating a Pt₃V pattern with a lattice parameter of 3.87 Å gives excellent agreement with the peak positions of the 5Pt–5V sample across the entire pattern. The lattice parameter for 5Pt–5V is larger than expected for a nanoparticle Pt₃V catalyst which would be contracted from the bulk lattice parameter of 3.87 Å. The difference is explained by the EXAFS

results for 5Pt–5V showing that it is Pt-rich with respect to Pt₃V, which would give a lattice parameter intermediate between Pt and Pt₃V. In other Pt–V catalysts that are more Pt-rich (Figure 3.16), XRD shows asymmetric peak shapes, indicating two phases are present. When fit with two components (Table 3.5), the peak and shoulder give lattice parameters matching that of Pt (3.89–3.90 Å) and Pt₃V (3.87–3.88 Å), respectively.

3.4.2 Electronic Characterization

As the 5Pt–5V sample was determined to be a phase mixture, further electronic characterization was carried out on the 2Pt–5V, which had a coordination number ratio closely matching Pt₃V, which suggests that 2Pt–5V is a pure phase Pt₃V alloy. Figure 3.3a shows the Pt L₃ edge XANES for 3Pt and 2Pt–5V after reduction in 3.5% H₂ at 550 °C. The edge energy (measured as the energy of the first zero crossing of the second derivative of the XANES) for the 3Pt catalyst was identical to the concurrently measured foil value of 11.5640 keV. The edge energy of 2Pt–5V was shifted 0.4 eV higher than the Pt foil. The white line shape of 2Pt–5V is also different than the 3Pt catalyst which has a similar particle size, becoming narrower and higher in intensity. The changes reflect the difference in the energy distribution of the unfilled states between the monometallic and alloy catalysts.

Figure 3.3b shows the Pt 4f high-resolution XPS spectra of 3Pt and 2Pt–5V. Fitting parameters for the Pt 4f high resolution XPS spectra are given in Table 3.6. The binding energies for 3Pt and 2Pt–5V from fitting were 70.9 and 71.3 eV, respectively. Pt metal has a Pt 4f_{7/2} binding energy of 71.0 eV with an asymmetric peak shape toward higher binding energy, while platinum oxides have higher binding energies between 73 and 75 eV with a symmetric peak shape. [120] The asymmetric peak shape and binding energy for both samples are consistent with Pt in the metallic state. The core level shift (CLS) for 2Pt–5V is calculated as the difference in binding energy between the pure metal (3Pt) and the alloy, giving an increase in binding energy of 0.4 eV.

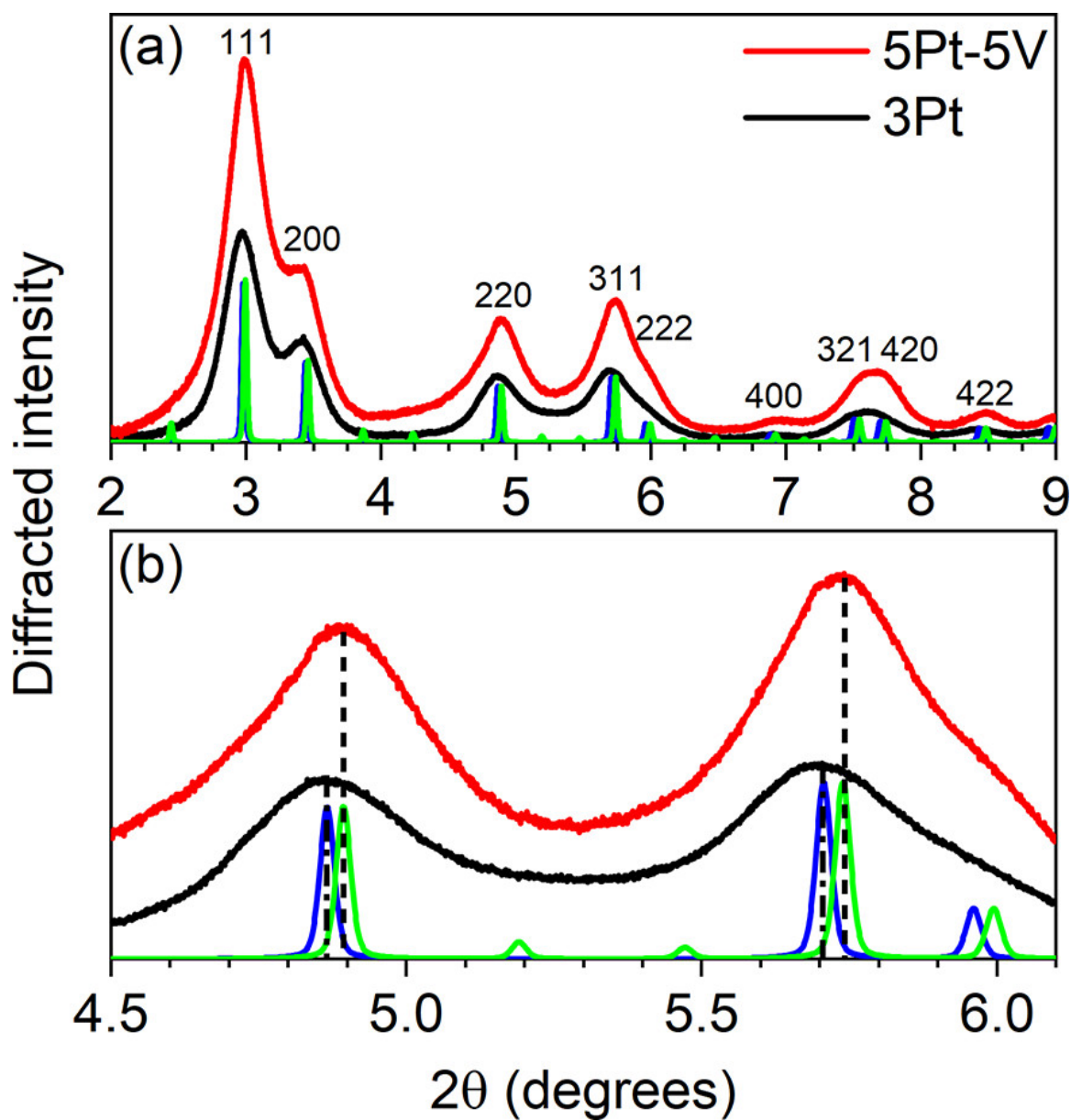


Figure 3.2. (a) *In situ* synchrotron XRD patterns of 3Pt (black), 5Pt-5V (red). Fundamental fcc lines are labeled in black. Simulated patterns of Pt with a lattice parameter of 3.89 Å (blue) and Pt₃V with a lattice parameter of 3.87 Å (green). (b) Expanded view of the 220 and 311 reflection for the above samples with vertical dashed lines denoting experimental peak positions. All experimental spectra were collected at 35 °C in 3.5% H₂ after reduction at 550 °C.

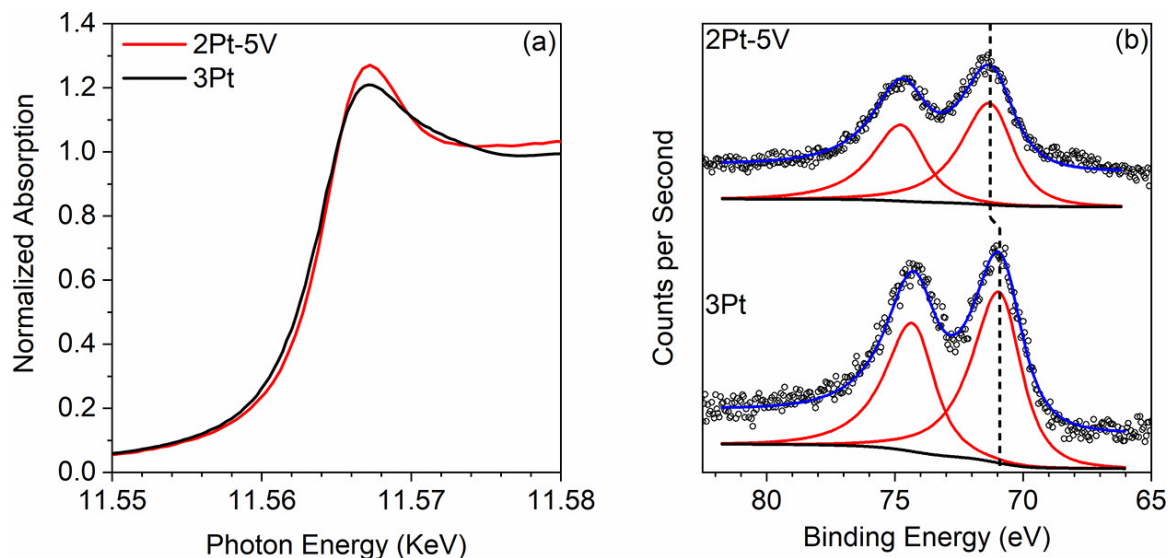


Figure 3.3. (a) *In situ* Pt L_3 edge XANES of 3Pt (black) and 2Pt-5V (red). Spectra were collected at room temperature in He after reduction at 550 °C in 3.5% H_2 for 30 min and a subsequent purge in He at 550 °C. (b) High-resolution Pt 4f XPS spectra of 2Pt-5V and 3Pt after a reduction treatment in 5% H_2 at 550 °C for 30 min. Black circles: raw data; black line: Shirley background; red lines: component fits; blue line: total fit. Background and components are offset for clarity. The vertical line denotes the peak position of the Pt $4f_{7/2}$ component of 3Pt and 2Pt-5V.

RIXS is a two-photon spectroscopy where an electron is photoexcited from a core state to a vacant valence state (here a Pt 5d unfilled state) and an emitted photon is measured arising from an electron in the filled valence state (Pt 5d filled state) filling the core hole. To probe the energy of the Pt 5d electrons, the $L\beta_5$ emission line, which corresponds to the decay of a 5d electron into a $2p_{3/2}$ core hole, is selectively measured. When the incident photon is scattered elastically (i.e., the photoexcited $2p_{3/2}$ electron decays back into the $2p_{3/2}$ core hole), the fluoresced photon energy is equal to the incident photon energy, which gives a peak at an energy transfer value of 0 eV. For clarity, the elastic scattering line has been subtracted from the RIXS plots in Figure 3.4. Intensity fluctuations around an energy transfer value of 0 eV

are artifacts from the subtraction of the elastic scattering line. Inelastic scattering occurs when the fluorescent decay into the $2p_{3/2}$ core hole occurs by an electron other than the excited $2p_{3/2}$ electron. This can occur by any symmetry allowed electron transition according to dipole selection rules.

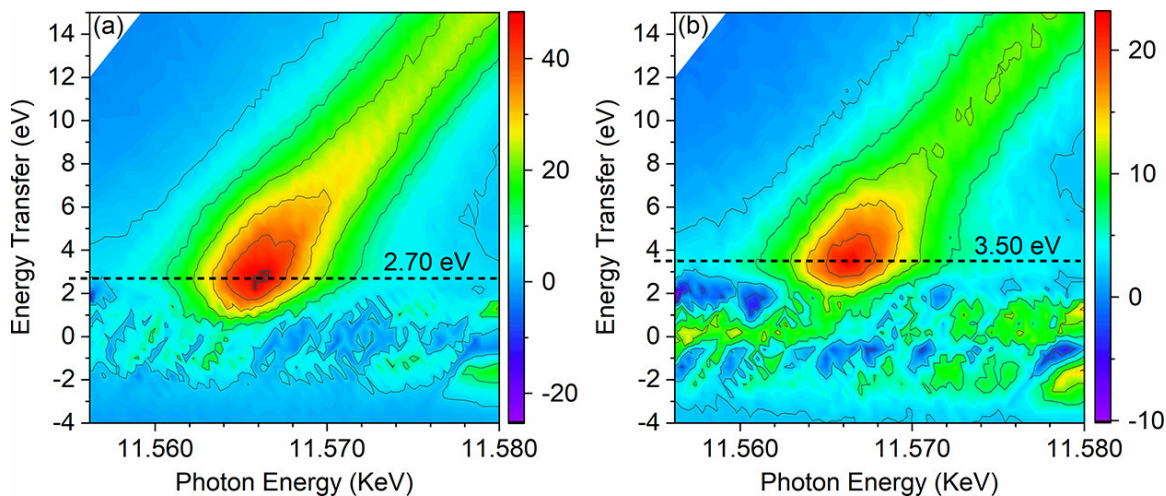


Figure 3.4. Pt L_3 - $L\beta_5$ RIXS maps of Pt (a) and Pt₃V (b). Spectra were collected after a reduction treatment at 550 °C in 3.5% H₂ for 30 min. Spectra were collected at 100 °C in 3.5% H₂. Horizontal dashed lines denote the maximum of the inelastic scattering peak for each sample.

RIXS spectra are plotted as the fluoresced intensity as a function of the incident photon energy on the abscissa and the energy difference between the incident and emitted photon (energy transfer) on the ordinate. The inelastic scattering peak manifests as a broad maximum centered at an incident energy value between the respective XANES edge energy and white line energy for each sample. Far from the XANES inflection point (~ 5 eV), the resonant enhancement of the $L\beta_5$ emission mode decays, leading to a low-intensity tail toward higher energy transfer values with increasing incident energy. For the Pt sample, the maximum of the inelastic scattering peak lies at an incident energy of 11.5640 keV and an energy transfer value of 2.7 eV. This corresponds to an energy separation of 2.7 eV between the average energy of the

filled and unfilled states. For Pt_3V , the maximum of the inelastic scattering peak lies at an incident energy of 11.5644 keV, with an energy transfer value of 3.5 eV. The energy separation between the filled and unfilled states in Pt_3V is 0.8 eV larger than Pt. From the XANES edge energy of pure phase Pt_3V (2Pt-5V) the 0.8 eV split can be separated into a 0.4 eV increase in the energy of the unfilled states and a 0.4 eV decrease in the energy of the filled 5d states relative to Pt.

3.4.3 Propane Dehydrogenation

Figure 3.5 shows propylene selectivity and propane conversion extrapolated to zero deactivation for 3Pt, 5Pt-5V, and, 2Pt-5V with each data point representing a separate sample of catalyst from the same synthetic batch. For all reactions, propylene was the main product; hydrogenolysis led to the formation of methane, ethane, and ethylene. Tests performed without cofed hydrogen are shown in Figure 3.5a. The selectivity of 2Pt-5V and 5Pt-5V were equivalent in tests without hydrogen, both showing above 95% propylene selectivity which did not decrease with increasing conversion. In comparison, 3Pt showed moderate selectivity which decreased as the conversion increased.

Figure 3.5b shows catalyst tests performed with cofed hydrogen. Dehydrogenation in the presence of H_2 is a more demanding test of the catalysts' selectivity as the latter is required for hydrogenolysis. The propane-to-hydrogen ratio was 1:1. Similar to the tests done without hydrogen, 3Pt decreased in selectivity with increasing conversion, but the selectivity at low conversion when tested with hydrogen was lower than when tested without. For the 2Pt-5V catalyst, cofeeding hydrogen did not change the selectivity noticeably from the values obtained without hydrogen. For 5Pt-5V, there was a 4% decrease in the selectivity with increasing conversion over the tested range when hydrogen was cofed.

To count the fraction of surface Pt in the alloy and properly normalize the propylene production rate, XAS data were collected for each sample in the reduced state and after exposing the sample to air at room temperature. The basis of measuring

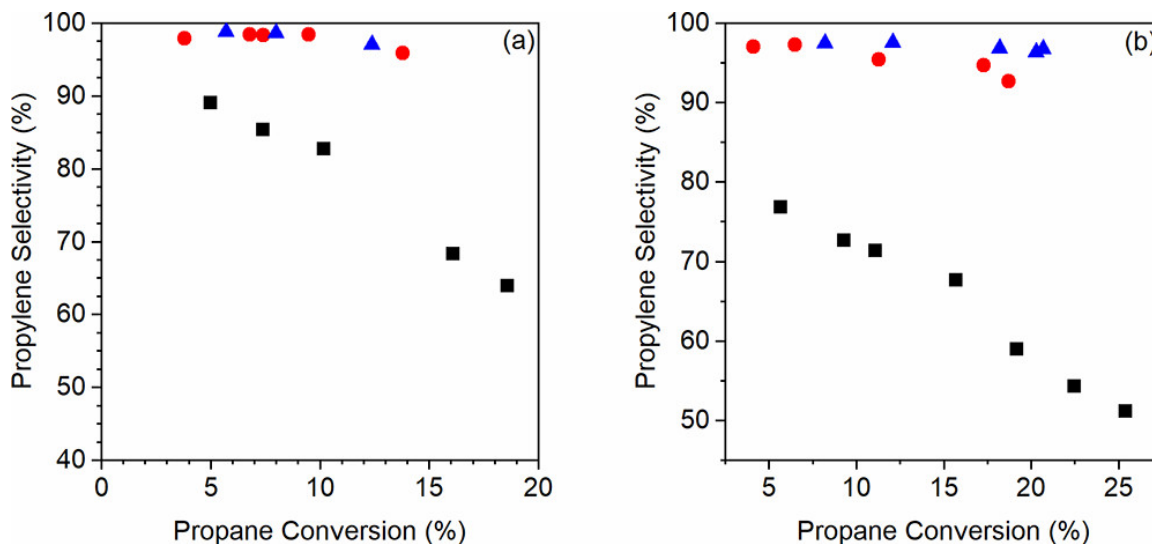


Figure 3.5. Propylene selectivity and propane conversion for 3Pt (black squares), 5Pt-5V (red circles), and 2Pt-5V (blue triangles) tested without (a) and with (b) cofed H₂. Reactions were performed at 550 °C at 3 psig with 2.5% propane balance N₂. For (b) the hydrogen concentration was 2.5%. Data points shown are at zero deactivation with each data point representing a separate test.

dispersion by this method comes from the fractional Pt-O coordination arising from surface oxidized Pt. In an oxidized particle with 100% dispersion, each Pt(II) ion will have four oxygen neighbors (platinum oxide). As the dispersion decreases from unity, the Pt-O coordination number represents the fraction of the sample that is oxidized and is proportional to the dispersion. The same methodology of surface oxidation is the basis of H₂-O₂ titration, but because of the element specificity of EXAFS, the confounding effect of V oxidation on the titration is avoided, and additional structural information about the surface can be obtained.

Figure 3.6 shows the EXAFS difference spectra for 2Pt-5V and 5Pt-5V; fitting parameters for the difference spectra are given in Table 3.2. Three peaks are present in the difference spectra. The first peak at low R (at about 1.5 Å phase uncorrected distance) is characteristic of Pt-O scattering. For the 2Pt-5V sample, fitting the

peak gave a bond distance of 2.05 Å and a gain in average Pt–O coordination number of 0.5, which corresponds to a dispersion of 0.13. The two peaks between 2 and 3.5 Å (phase uncorrected distance) are due to lost Pt–Pt and Pt–V scattering. Fitting these peaks in the 2Pt–5V sample gives a Pt–Pt bond distance of 2.72 Å with a coordination number of 0.9 and a Pt–V bond distance of 2.70 Å with a coordination number of 0.6. Within the error of the small features in the difference spectrum, the surface layer Pt–V:Pt–Pt neighbor ratio for 2Pt–5V matches the total sample neighbor ratio.

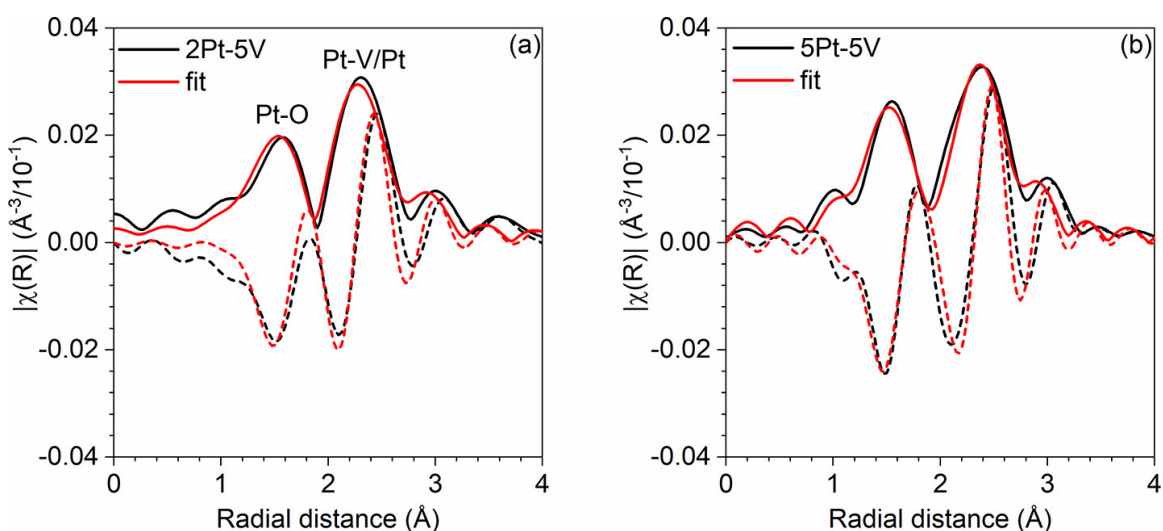


Figure 3.6. Pt L₃ edge EXAFS difference spectra for 2Pt–5V (a) and 5Pt–5V (b) (magnitude: solid black; imaginary: dashed black) and difference spectra fit (magnitude fit: solid red; imaginary fit: dashed red). A reduced scan of both 2Pt–5V and 5Pt–5V was taken at room temperature in He after reduction at 550 °C in 3.5% H₂; subsequently, the samples were exposed to air for 30 min and then scanned again.

The 5Pt–5V sample has a Pt–O coordination number of 0.6 at 2.03 Å, corresponding to a dispersion of 0.15. The bond distance for Pt–Pt and Pt–V was 2.74 Å with 1.2 and 0.7 Pt–Pt and Pt–V average coordination numbers, respectively, giving a Pt–V:Pt–Pt neighbor ratio close to 0.5. The surface ratio of 0.5 is significantly higher than the total sample neighbor ratio of 0.31, showing that the surface composition in

Table 3.2.
EXAFS Fit for Pt–V Difference Spectra

Sample	Path	CN	R (Å)	σ^2 (Å ²)	E_0 (eV)
5Pt–5V	Pt–O	0.6	2.03	0.002	–4.5
	Pt–Pt	1.2	2.74	0.002	–3.0
	Pt–V	0.7	2.74	0.002	4.4
2Pt–5V	Pt–O	0.5	2.05	0.002	–4.4
	Pt–Pt	0.9	2.70	0.003	2.1
	Pt–V	0.6	2.72	0.003	–3.2

the 5Pt–5V sample is different than that of the total sample. For both catalysts, the EXAFS difference analysis is consistent with a Pt₃V surface structure.

With the Pt dispersion from difference XAS, the initial propylene production turnover rates were calculated from catalyst test data. Note that dispersion values measured by CO chemisorption for both alloy samples were also below 20%, demonstrating the ability of the difference XAS technique to accurately determine dispersion; however, because of the possibility of metallic V adsorbing CO, dispersion values from difference XAS were used for rate normalization. The values obtained by difference XAS should be considered a lower bound on dispersion due to the possibility of surface vanadium oxide blocking chemisorption sites. Turnover rate measurements were conducted at 550 °C with differential propane conversion (<10%) and a propane concentration of 2.5%,. When hydrogen was cofed, the concentration was 2.5%. The pure Pt catalyst had a dispersion of 29% and a turnover rate of 0.36 s^{–1} when hydrogen was cofed and 0.03 s^{–1} without hydrogen. The 5Pt–5V catalyst had a dispersion of 15% and a turnover rate of 0.28 s^{–1}, while the 2Pt–5V catalyst had a dispersion of 13% and a higher turnover rate of 0.38 s^{–1}. When tested without hydrogen, 5Pt–5V had an initial TOR of 0.06 s^{–1} and 2Pt–5V had an initial TOR of

0.16 s⁻¹. The small differences between the samples under equivalent conditions are within the error generally assumed for the reproducibility of determining turnover rates. [121]

3.4.4 DFT

To better understand the electronic effect of V incorporation in Pt when forming Pt₃V alloys, DFT calculations were conducted on model Pt₃V (111) and Pt (111) surfaces. First, compositional phase stability of various Pt–V alloys was studied by constructing a 0 K isothermal–isobaric binary compositional phase diagram, shown in Figure 3.7. Finite temperature effects are not expected to significantly impact the formation energy of the concerned alloys and hence are not considered. Each point on the plot is the most thermodynamically stable bulk structure, considering fcc, hcp, and bcc crystal structures in each case, for the given composition of Pt–V. The most stable phases are connected through a convex hull and represented by red points. Unstable phases lie above the convex hull (plotted in blue) and would decompose into nearest stable phase on the convex hull, with compositions predicted by the lever rule. Apart from pure bulk Pt, the Pt₃V phase is the only stable close-packed fcc phase. This result is fully consistent with the experimental XRD and XAS measurements, which also point to the presence of a Pt₃V alloy phase with an fcc crystal structure.

The effect of V incorporation on the Pt electronic energy levels was studied by examining the calculated atom projected density of states of the Pt 5d band (Figure 3.8). Four geometries were modeled to represent pure Pt, a core–shell structure with two different shell thicknesses, and pure Pt₃V. For modeling of the core–shell structures, the topmost and top two layers of a Pt slab were replaced with Pt₃V, labeled as Pt₃V-1 ML-Pt and Pt₃V-2 ML-Pt, respectively. Starting from Pt, replacing subsequent layers of the slab with Pt₃V causes a decrease in the density of states at the Fermi level and the creation of new unoccupied states farther from the Fermi level. Pt occupied states broaden and shift to occupy lower energies with increasing V incorporation, with the most significant changes in density concentrated slightly

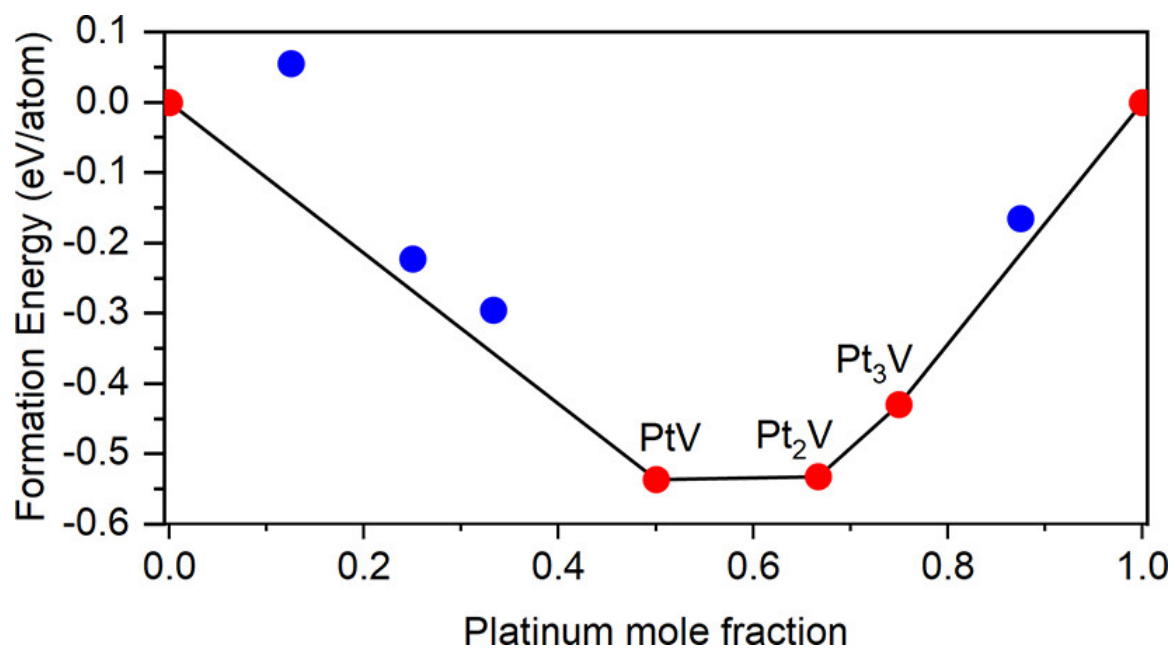


Figure 3.7. Binary compositional phase diagram for Pt-V. Red nodes are stable phases lying on the convex hull (black line). Blue nodes are the most stable phases for given Pt-V compositions which do not lie on the convex hull.

below the Fermi energy. This shift results in the Pt d-band center decreasing from -1.95 eV for pure Pt to -2.49 eV for bulk Pt_3V . The binding strength of CO and C_1 adsorbates (Table 3.7) on the four slabs decreased as the alloy layer was thickened, in line with shifts in the d-band center. The degree of band filling is nearly constant for all Pt atoms in the surface and bulk alloys studied, suggesting that charge transfer to or from the d-band in the system is minimal, in agreement with previous calculations on Pt bimetallics. [84, 95]

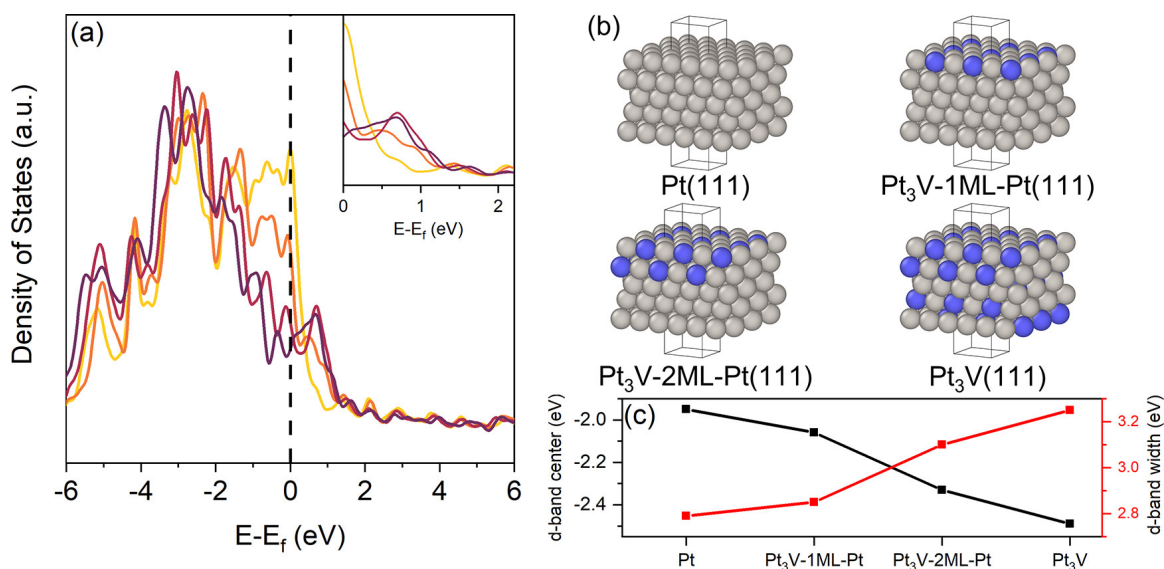


Figure 3.8. (a) pDOS for Pt (gold), Pt_3V (burgundy), and two epitaxial structures with one (orange) and two (crimson) layers of Pt_3V on Pt with the Fermi energy marked by a vertical dashed line. The inset graph shows an expanded view of near-Fermi energy unfilled states. (b) Structures corresponding to each model. (c) The d-band center and d-band width for the above structures.

The consequences of d-band modification from V incorporation can be seen in the weakening of binding energy of adsorbates important to the dehydrogenation reaction network. The binding energies for hydrocarbon adsorbates (C_1 – C_3) and hydrogen are shown in Tables 3.9 and 3.10, respectively. All hydrocarbons bind more weakly on Pt_3V as compared to Pt, and hydrogen no longer binds isoenergetically on all Pt

sites in the alloy. The strongest decreases are seen in adsorbates that involve bonding to multiple surface atoms, such as is the case with deeply dehydrogenated species such as C_3H_5 and ethynidyne. The strain contribution to the binding energy changes (Table 3.11), calculated by fixing the lattice parameter of a Pt slab to that of Pt_3V and repeating adsorption calculations, was found to be within DFT error. Adsorbates that bond at hollow sites also bond at V containing ensembles, despite the presence of structurally equivalent Pt-only hollow sites (Figure 3.17).

Additionally, an often-used selectivity descriptor for dehydrogenation, the energy difference between propylene desorption and propylene dehydrogenation (Figure 3.18), predicts that desorption of propylene is more energetically favorable than deep dehydrogenation on Pt_3V . The change in energetics is mainly due to the destabilization of propylene, as the barrier for propylene dehydrogenation between Pt and Pt_3V differs by only 0.1 eV. The propylene dehydrogenation transition state and C_3H_5 are also both destabilized relative to gas phase propylene.

3.5 Discussion

3.5.1 Structural Model

There are several possibilities for the arrangement of Pt and V in a bimetallic nanoparticle. The bulk Pt–V phase diagram lists five stable phases: Pt_8V , Pt_3V , Pt_2V , PtV, and PtV_3 . Pt can form a solid solution with V, but the solubility (which decreases with temperature) is limited to 15 at. % V at 400 °C. [122] From the isothermal–isobaric phase diagram, Pt_3V , Pt_2V , and PtV were identified as thermodynamically stable phases.

The primary reflections in XRD of the 5Pt–5V sample rule out the non-fcc Pt–V phases which include Pt_8V , Pt_2V , and PtV. The $AuCu_3$ form of PtV_3 can be ruled out based on the presence of Pt–Pt nearest neighbors seen in EXAFS, which are not present in PtV_3 . In samples that are Pt-rich with respect to Pt_3V , a phase mixture of Pt and Pt_3V form, rather than a solid solution based on asymmetric peak shapes seen

in XRD. Rather than separate particles of Pt and Pt₃V, the phase mixture takes the form of a core-shell structure with a Pt₃V shell and a Pt core based on the surface composition matching Pt₃V while the total composition was Pt-rich with respect to Pt₃V.

The atomic environment of Pt in Pt₃V is cuboctohedral with eight Pt neighbors and four V neighbors, both at a bond distance of 2.74 Å. As the particle size decreases, the total coordination number and bond distance both decrease, but the ratio of V to Pt neighbors will remain constant between nanophase and bulk Pt₃V because of the local Pt environment inherent to the phase. Thus, the Pt-Pt and Pt-V coordination numbers can be used to determine whether a sample has a stoichiometry consistent with the Pt₃V phase.

For the 5Pt-5V, the Pt-V:Pt-Pt neighbor ratio is lower than bulk Pt₃V, indicating that the sample is Pt-rich with respect to Pt₃V. Surface oxidation difference XAS and XRD demonstrated that the phase arrangement is a core-shell particle with a Pt core and a Pt₃V shell. Because Pt-V scattering arises from the formation of Pt₃V, the Pt-Pt coordination number can be separated into Pt-Pt coordination in the alloy and Pt-Pt coordination in the Pt core, as the ratio of Pt-V to Pt-Pt in the alloy is fixed at 0.5. This allows for the fraction of each phase to be derived from the total coordination number. For 5Pt-5V, the Pt-V coordination number of 2.0 gives a total Pt₃V coordination of 6 (2 Pt-V + 4 Pt-Pt); the total coordination of 8.5 gives an alloy phase fraction of 70% and a Pt core phase fraction of 30%. Given the volume average particle size (2.2 nm) and measured lattice parameter (3.88 Å), the alloy shell layer thickness can be estimated as in Ref [123], giving a shell layer thickness of 4 Å on a core 14 Å in diameter. A 4 Å shell layer corresponds to approximately 2-3 atomic layers of alloy.

In the 2Pt-5V, the Pt-V:Pt-Pt neighbor ratio matches bulk Pt₃V. Based on the XRD results for 5Pt-5V, the interpretation most consistent with the EXAFS would be that the 2Pt-5V sample is pure phase Pt₃V. The surface oxidation difference EXAFS data show that the surface stoichiometry also matches that of Pt₃V and demonstrates

that no surface segregation occurs under reducing conditions. Additionally, the surface EXAFS suggests that there are few, if any, unalloyed Pt nanoparticles in this sample.

The importance of phase purity in the measurement of electronic modifications is shown in Figure 3.9, which shows the Pt L_3 XANES edge energy shift relative to Pt foil as a function of the V:Pt neighbor ratio for 11 Pt–V catalysts of different composition. The neighbor ratio expected for Pt_3V is 0.5; values below this are phase mixtures of Pt and Pt_3V which have XANES edge energies lower than that of pure phase Pt_3V . In the pure phase, the XANES shift is 0.4 eV, which reflects an increase in the energy of the Pt 5d unfilled states in the alloy. Samples that are not phase pure then underestimate the electronic modification inherent to Pt_3V . Further electronic characterization was done only on the pure phase Pt_3V sample, 2Pt–5V, which allowed for more accurate comparison with the Pt_3V slab models. While this choice of a slab model neglects the contribution of corner and edge atoms in the electronic structure calculations, the experimental techniques used to characterize the catalysts are bulk sensitive and probe all Pt atoms. The majority of atoms in a 2 nm nanoparticle are terrace or interior atoms, and their electronic structure is properly captured in the slab model. While adsorption energies on terrace sites may vary significantly from corner and edge sites, scaling relationships on metals have been reported as a function of the adsorption sites' metal coordination number, and hence the trend in binding energy between Pt and Pt_3V can be captured without explicitly considering all sites. [124]

3.5.2 Nature of Electronic Modification

Frequently in the metal catalysis literature, the rigid band model is invoked to describe the mechanism of electronic modification of catalysts. [90–92, 125, 126] This model has been successfully used to describe thermal and electronic properties of alloys, which are properties dominated by conduction band s- and p-electrons, whereas in metal catalysis the localized d-electrons are responsible for catalytic behavior.

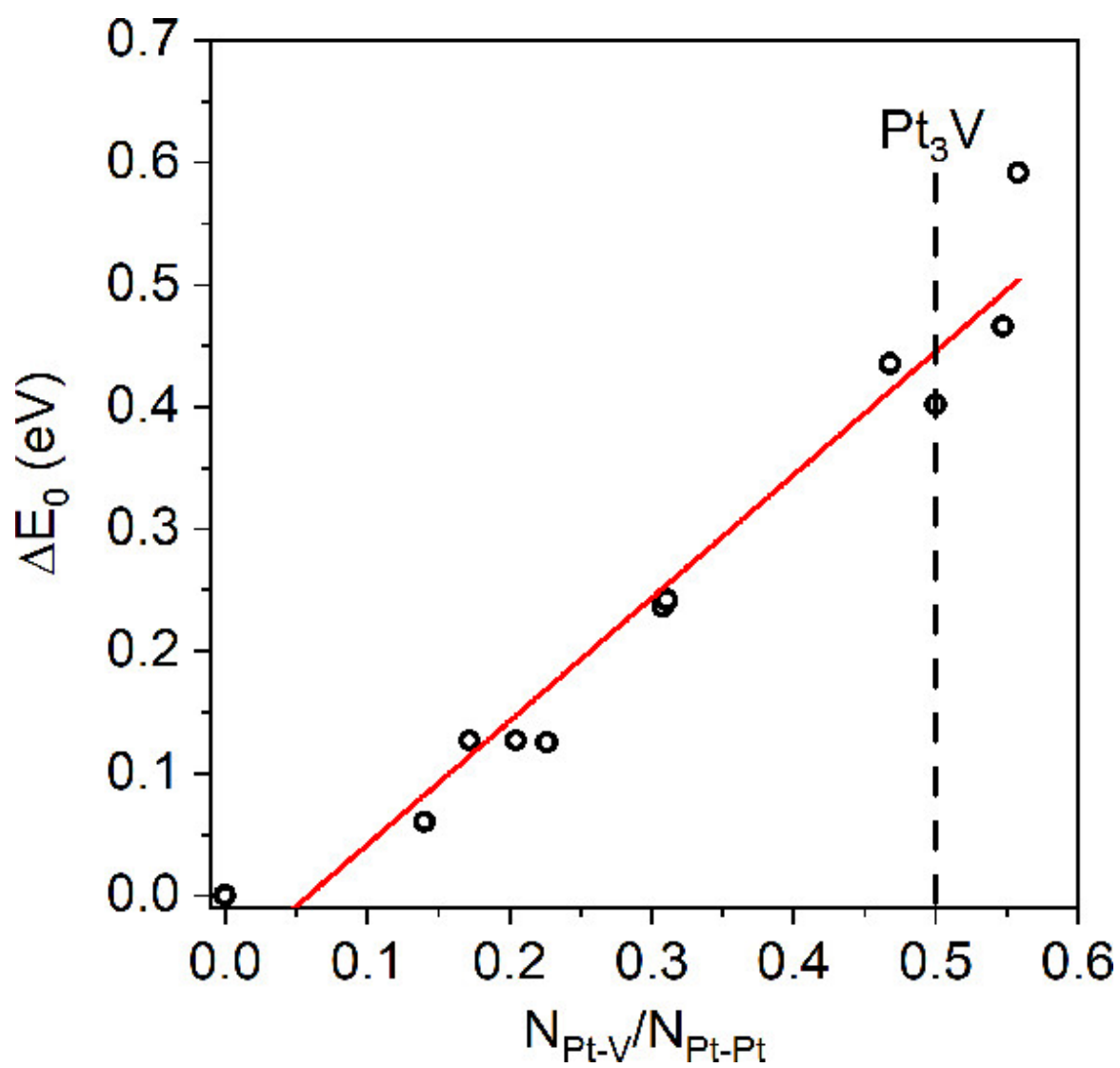


Figure 3.9. Pt L₃ edge XANES shift (vs Pt foil) plotted against the ratio of Pt-V to Pt-Pt coordination numbers for 3Pt and 10 Pt-V catalysts. The Pt-V to Pt-Pt ratio for the bulk Pt₃V phase is shown as a vertical dashed line. A linear fit of the data is shown in red.

[127] In the rigid band model, when two elements of different electronegativity are combined in an alloy, the atom with lower electronegativity transfers electron density to the other. [128, 129] This is interpreted to further fill the d-band, shifting the Fermi energy relative to the band while the shape and absolute energy of the band remain constant. The model of charge transfer has been extended to describe not only electronic changes in alloys [90, 91, 130] but also nanoparticle–support interactions [131] and particle size effects. [132] These observations of electronic modification are based on spectral changes seen in various techniques sensitive to valence d-electrons such as XPS, XANES, and ELNES, among others. Using this model, one could predict the direction and magnitude of electron transfer for a given alloy and hence the spectral changes in XPS, XANES, and RIXS. If electron transfer to the d-band accurately describes the mechanism of electronic modification of Pt, the direction of charge transfer predicted should be consistent among these methods.

The Pt L_3 edge XANES transition probability is proportional to the number of unfilled states, and changes in the intensity and broadness of the XANES white line reflect changes in the density of Pt 5d unfilled states. [133, 134] The rigid band model has also been used to describe these spectral changes in the XANES. [90, 129] In this interpretation, the transfer of electron density to Pt decreases the number of unfilled Pt 5d states (i.e., more d-electron density), leading to a lower white line intensity. Additionally, because of the increased filling of the d-band resulting from the electron transfer, the average energy of the unfilled states increases which causes an increase in the XANES edge energy. By the above model, the 0.4 eV increase in XANES edge energy seen for Pt_3V would mean that Pt in Pt_3V has gained electrons through electron transfer from V. The increase in the number of Pt electrons would also be expected to lead to a decrease in the white line intensity; however, the white line intensity increases relative to a Pt nanoparticle of the same size.

XPS binding energy shifts are also frequently used demonstrate electronic modification resulting from alloying. Chemical shifts in XPS are frequently interpreted based on electron transfer, as the energy required for photoemission is greater in a

positively charged atom and vice versa for a negatively charged atom. Based on this interpretation, the 0.4 eV core level shift to higher binding energy seen for Pt₃V is due to Pt in the alloy having transferred electrons to V. It should be noted that the orbital to which the electron is transferred is not specified, but unfilled states exist in the 5d or conduction band 6s or 6p orbitals. By use of the same electron transfer model, XANES and XPS come to opposite conclusions regarding the direction of the transfer.

While XANES and XPS allow for an indirect measurement of filled d-states, RIXS is a direct measurement. The inelastic scattering peak in RIXS represents the energy difference between the weighted average energy of the filled and unfilled states. By the rigid band model, any change in filling of the d-band would shift the average energy of the filled and unfilled states in the same direction. Hence, the separation in energy between the filled and unfilled states should be similar regardless of any electron transfer. Based on the separately collected XANES spectrum, the energy transfer value can be deconvoluted into a downward shift in the filled state energy and an upward shift in energy of the unfilled state energy, which cannot be explained by electron transfer.

The inconsistency between the predicted direction of electron transfer in XPS, XANES, and the increased separation energy between the filled and unfilled states by RIXS suggests that the rigid band model and electron transfer between the Pt d-band and the promoter atom is incorrect. For Pt and Pt₃V, the density of states calculations demonstrate that the alloy does not follow rigid band behavior. Instead, the d-band of Pt₃V is broadened with respect to Pt, resulting in changes the energy of the filled and unfilled 5d states. These energy changes are consistent with the spectral changes observed by XPS, XANES, and RIXS. For example, the broadening of the d-band causes the d-band center to shift away from the Fermi level, decreasing the average energy of the filled states, consistent with the RIXS results. The unfilled Pt 5d states also increase in energy due to the broadening of the band, resulting in an increase in the XANES edge energy in Pt₃V. Despite this modification in the density of

states, the filling of the d-band (and hence number of d-electrons) remains constant, as shown by the integration of the d-band density of states for Pt and Pt₃V. The increased splitting in the energy of the filled and unfilled d-states is a consequence of bonding interactions between Pt and V which form new d-states that differ in energy from those in a homoatomic bond. Thus, it is a change in the energy of the filled and unfilled d-states that gives rise to the changes in the XPS, XANES, and RIXS spectra of Pt₃V. While the above results do not preclude electron transfer to Pt s- and p-bands, these electrons are minimally involved in adsorbate binding, and hence transfer to these orbitals would be largely inconsequential as far as catalytic properties are concerned. Inferring changes to the d-band from XPS alone should be made with caution since core level shifts in alloys are sensitive to changes in energy, number, and orbital character of the valence electrons as well as extra-atomic relaxations and shifts in the Fermi energy. [135, 136] See Figure 3.19 and Table 3.12 as well as the supplemental discussion for a more comprehensive examination of the contribution of various effects to the XPS core level shifts and their interpretation.

The consequence of these electronic effects can be seen in decrease in binding strength of adsorbates on the Pt₃V alloy vs monometallic Pt surfaces (Table 3.9). All the model adsorbates considered, including CH_x, CCH₃, C₃H₆, and C₃H₅, showed weakening in binding energy compared to their binding strength on pure Pt. Because alloying decreases the average energy of the filled 5d states, the binding strength of adsorbates weakens as predicted by d-band theory. [85] It has been proposed that this weakening of adsorption strength leads to the desorption pathway being favored over deep dehydrogenation in DFT studies of Pt–Sn alloys. [137] As seen from Figure 3.18, a similar conclusion can be drawn for Pt₃V since the thermodynamics of deep dehydrogenation compared to desorption are competitive in the case of Pt₃V, while for monometallic Pt the deep dehydrogenation is clearly thermodynamically favored.

3.5.3 Effect of Structure on Catalytic Performance

The structural characterization explains why 5Pt–5V and 2Pt–5V have close to identical propylene selectivities and dehydrogenation turnover rates despite the particle composition being different in each catalyst. The reason is that the surface and near-surface layers which affect catalytic properties are compositionally the same. The geometric effect only requires the presence of V atoms in the surface layer, whereas the electronic effect is affected by both the surface and subsurface. The surface alloy layer in 5Pt–5V is 2–3 atomic layers thick, meaning that the nearest neighbors of surface atoms participating in catalysis, both surface and subsurface, are the same as in the pure alloy catalyst. The importance of the subsurface layer on catalytic properties was demonstrated in the difference in CO heat of adsorption between a Pt₃Mn full alloy and a Pt/Pt₃Mn core–shell catalyst. [138] The electronic effect occurs as a result of bonds between the active metal and the promoter. Because of this nature, electronic modification is necessarily a short-range effect, as demonstrated by surface Pt density of states, which showed a large change when first nearest neighbors were changed, as compared to the small change which occurred between the two monolayer slab and the full alloy where only second nearest neighbors of the surface Pt atoms are changed.

The geometric effect, or the decreasing the active metal ensemble size, requires the presence of the promoter metal in the surface layer of the nanoparticle. Difference XAS spectra on Pt–V alloys demonstrate that V is present in the surface layer. The geometric effect is often cited as the dominant factor in dehydrogenation selectivity in alloys where the active metal is isolated. [97,139,140] However, in the case of Pt₃V, the (111) surface is composed of interconnected groups of three Pt atoms. Despite the lack of total Pt isolation, Pt₃V still shows above 95% propylene selectivity, which suggests that total Pt isolation is not a requirement for high dehydrogenation selectivity. This conclusion is supported by DFT results, which show that Pt₃V alloys bind C₂ and C₃ intermediates more weakly on sites of different geometry as compared to pure Pt, in

spite of the presence of threefold Pt sites geometrically equivalent to Pt on the Pt₃V surface.

It is also worth mentioning that mechanisms proposed for the hydrogenolysis of alkanes vary in the number of metal sites required for the reaction from two to more than four. [141–144] DFT studies on various metals have shown that the barrier for C–C bond cleavage lowers as more hydrogen atoms are removed from the adsorbed hydrocarbon. [145] Based on these results, the mechanism for hydrogenolysis is suggested to occur through a deeply dehydrogenated species. For every hydrogen lost to dehydrogenation, the C–H bond is replaced with a metal–carbon bond. [146] Thus, the extent of dehydrogenation at which hydrogenolysis occurs determines the number of active metal atoms needed to catalyze the reaction. Even assuming the high-end ensemble size requirements for hydrogenolysis (4+ atoms), the (111) surface of Pt₃V should still have a large enough active metal ensemble to catalyze hydrogenolysis. A possible reason that these sites, which are important for stabilization of coke precursors on Pt, [147] do not cause low selectivity in Pt₃V may be due to the decreased binding strength and change of binding geometry of coke precursors shown in Figure 3.17 and Table 3.9. The surface and subsurface V atoms proximal to the 3-fold site electronically modify Pt destabilizing adsorption on this site.

3.6 Conclusions

The addition of V to a Pt catalyst leads to the formation of the Pt₃V intermetallic compound with the AuCu₃ structure. The formation of the Pt₃V phase, or an alloy surface layer on a Pt core, led to high propylene selectivity, demonstrating that total Pt site isolation, and full alloy formation, are not required for high dehydrogenation selectivity. Instead, it is only necessary to form an alloy layer 2–3 atomic layers thick to obtain the same performance as a pure phase alloy. Formation of the ordered alloy phase ensures that all Pt atoms in the nanoparticle experience similar electronic modification and that large Pt ensembles are eliminated. Other unexplored alloys with the AuCu₃ structure may also show high dehydrogenation selectivity based on

the high selectivity of both Pt_3Sn and Pt_3V despite very different bonding interactions between Pt and the promoting element. The magnitude of the electronic modification was shown to be dependent on the extent of alloy formation, demonstrating the importance of phase purity in determining the electronic modification inherent to a specific alloy phase. The source of electronic modification in Pt–V alloys is not caused by electron transfer to or from the Pt 5d orbitals, but rather a change in the energy of the orbitals. The consequences of the electronic modification were shown by DFT to be weakening of adsorbate bonding to Pt and changes in the most stable binding geometries in the alloy.

3.7 Supporting Information

3.7.1 Experimental

3.7.1.1 Catalyst Synthesis

Vanadium impregnation was also done using vanadyl acetylacetonate to study the effect of the vanadium precursor on the dispersion of the vanadium oxide on silica. For the synthesis of a second 2%Pt-5%V catalyst 1.30 g of vanadyl acetylacetonate was dissolved in 25 mL methanol and impregnated to the pore volume of 5 g of silica (davasil 646, Sigma Aldrich). Due to the low solubility of Vanadyl acetylacetonate, multiple rounds of impregnation and calcination were performed to achieve the desired 5% V weight loading. After each impregnation step, the catalyst was dried at room temperature for 3 hours, then at 125 °C overnight and finally calcined at 300 °C for 3 hours. Platinum was loaded on the 5V-SiO₂(AcAc) to 2% weight in the same manner as the 2Pt-5V catalyst prepared with ammonium metavanadate. The reduction procedure for 2Pt-5V(acac) was identical to the other Pt-V bimetallic catalysts. A full list of synthesized catalysts is given in Table 3.3.

Table 3.3.
Synthesis parameters for Pt and Pt-V catalysts

Name	Pt Loading (wt %)	V Loading (wt %)	V:Pt Atomic Ratio	Pt Calcination Temperature (°C)	V Calcination Temperature (°C)
3Pt	3	0	-	250	-
5Pt-2.5V	5	2.5	1.9	250	350
5Pt-5V	5	5	3.8	250	350
5Pt-5V-450C	5	5	3.8	450	350
5Pt-5V-500C	5	5	3.8	500	350
5Pt-5V-550C	5	5	3.8	550	350
5Pt-5V-600C	5	5	3.8	600	350
2Pt-5V	2	5	9.5	250	300
2Pt-5V(acac) ^{*†}	2	5	9.5	250	300
2Pt-10V [†]	2	10	19.1	250	300
1Pt-10V [†]	1	10	38.1	250	300
5Pt-5V-R200C [‡]	5	5	3.8	250	350

*Vanadyl acetylacetonate was used as the vanadium precursor. For synthetic details, see the supplemental information.

†Vanadium impregnation performed in multiple steps with drying and calcination steps between impregnations

‡Nonstandard reduction process: 200°C reduction instead of 550°C.

3.7.1.2 Electron Microscopy

The volume average particle size and standard deviation were calculated using equations 3.1 and 3.2, respectively, below.

$$\bar{d}\{4, 3\} = \frac{\sum d_i^4}{\sum d_i^3} \quad (3.1)$$

Where $\bar{d}\{4, 3\}$ is the volume average particle size and d_i is the diameter of particle i . The standard deviation of the volume average particle size is given by equation 3.2:

$$\bar{\sigma}\{4, 3\} = \sqrt{\frac{\sum (d_i - \bar{d}\{4, 3\})^2 d_i^3}{\sum d_i^3}} \quad (3.2)$$

3.7.1.3 X-ray Absorption Spectroscopy

Difference X-ray absorption spectroscopy was performed by subtracting surface oxidized and reduced catalyst spectra. The same edge energy was used for both the oxidized and reduced samples for conversion into k space. The extracted chi data of the oxidized sample was then subtracted from the reduced sample. The difference chi was then k^2 weighted and Fourier transformed over a k range of 3 to 10 \AA^{-1} . Because the Pt-O scattering present in the oxidized sample is subtracted from the reduced sample, the Pt-O scattering in the difference spectra is phase shifted by π radians with respect to the normal experimental phase function. To fit the phase shifted Pt-O scattering in the difference, the experimental reference Pt-O phase was aligned with the difference Pt-O scattering by adding π radians to the experimental phase function.

XAS data analysis was performed in WINXAS 3.1 software. Coordination numbers and bond distance were obtained using a least squares fit in R-space of k^2 weighted Fourier transformed data. Fourier transforms were taken from 2.7-11.5 \AA^{-1} and R-space fits were performed from 1.8-3.2 \AA . For Pt-O and Pt-Pt scattering, experimental phase and amplitude functions were extracted from bulk references: $\text{Na}_2\text{Pt}(\text{OH})_6$ (6 neighbors 2.05 \AA) and Pt foil (12 neighbors at 2.77 \AA). For Pt-V

scattering, an experimental phase and amplitude function was created using a Pt-Fe scattering (7.5 neighbors at 2.66 Å) obtained from pure phase PtFe₃ nanoparticles. The bond distance and phase purity of the PtFe₃ nanoparticles was verified by *in situ* synchrotron X-ray diffraction (XRD). The phase transference error in coordination number introduced by using Pt-Fe to fit Pt-V scattering was estimated using Pt-V and Pt-Fe phase and amplitude functions generated using FEFF 6 and gave coordination numbers 6% lower in magnitude. Fitting was accomplished on isolated first shell coordination in R space by fixing the Debye-Waller factor ($\Delta\sigma^2$) and allowing coordination number (CN), bond distance (R) and energy shift (E_0) to vary.

3.7.1.4 Resonant Inelastic X-ray Scattering

RIXS measurements were made by the simultaneous measurement of the Pt L³ absorption edge in transmission mode and the Pt L β_5 emission line. The wavelength dispersive spectrometer is based on a bent Laue silicon analyzer coupled to a Pilatus 100K (Dectris) 2D pixel array detector [148, 149]. The analyzer crystal is a 55- μ m thick Si(400) wafer, cylindrically bent to 0.5-m radius. We scatter from the Si(133) reflection with a calculated asymmetry angle of 13.76°. The analyzer was mounted to a rotation stage declined about 20° from horizontal to allow significant elastically scattered X-rays through the crystal analyzer to the detector for accurate calibration of the fluorescence energy scale. Elastic scattering was more than 5x stronger than the peak valence X-ray emission. To resolve the X-ray emission from the tails of the elastic peak, the elastic peak was removed by fitting a Gaussian curve to the truncated data and using a single pair of peak width and center values for the entire data set. The amplitude was varied using a linear function to simulate the effect of beam polarization on the elastic scatter amplitude as a function of emission angle.

3.7.2 Results

Figure 3.10 shows volume average particle size distributions and representative STEM images for 3Pt, 5Pt-5V and 2Pt-5V. All three particle sized distributions deviate from pure Gaussian shape with an asymmetric tail towards higher particle sizes. Similar asymmetry has been reported for Pt nanoparticles on alumina after a high temperature treatment due to sintering [150]. All three samples have a particle size within one standard deviation of one another. The particle sizes were 2.6 ± 0.5 nm, 2.2 ± 0.5 nm and 2.2 ± 0.7 nm for 3Pt, 5Pt-5V and 2Pt-5V respectively.

Figure 3.11a shows a HAADF STEM image of 2Pt-5V after reduction at 550 °C (and subsequent exposure to air) and is representative of all samples measured. All three catalysts have average particle sizes of 2-2.5 nm. Figure 3.11b shows overlaid EDS elemental maps of Pt (blue) and V (yellow) for 2Pt-5V. Both platinum and vanadium are present in the small particles. The vanadium oxide clusters, which were not distinguished strongly from the support in the STEM images, can be seen in the EDS maps. Pt particles present in the maps are close to or in intimate contact with vanadium, though the amount varies from particle to particle. Figure 3.11c shows a line scan taken from the EDS map pictured in S2b. The Magnitude of the V and Pt signals are comparable across the particle, demonstrating the incorporation of V throughout the platinum particle as opposed to only on the surface layer, though vanadium oxide cannot be distinguished from V in a bimetallic. To determine if a Pt-V bimetallic forms, XAS was used to probe the local environment of Pt and V.

Figure 3.12 shows the vanadium K edge R space EXAFS of 5Pt-5V after reduction at 550 °C in 3.5% H₂. The peak between 1-2 Å occurs due to scattering from vanadium oxygen pairs. The peak between 2-3 Å is due to scattering from second nearest neighbor V-O-V scattering. The lack of metallic scattering from V or Pt (V-V or V-Pt, respectively) shows that most of the vanadium in the sample remains an oxide after the reduction procedure. The large second shell scattering peak suggests that

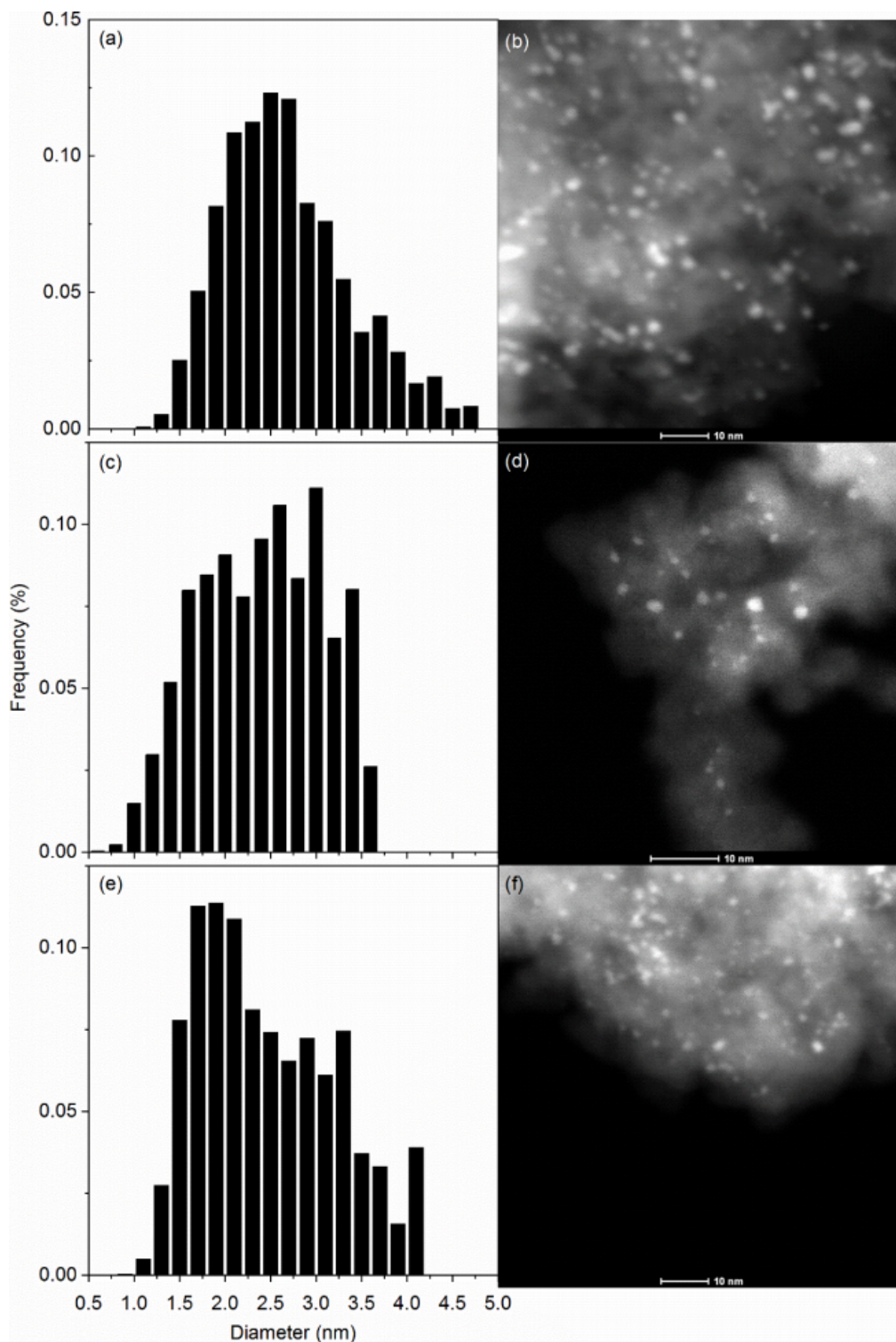


Figure 3.10. Volume average particle size distributions and representative STEM images for: (a,b) 3Pt, (c,d) 5Pt-5V, and (e,f) 2Pt-5V

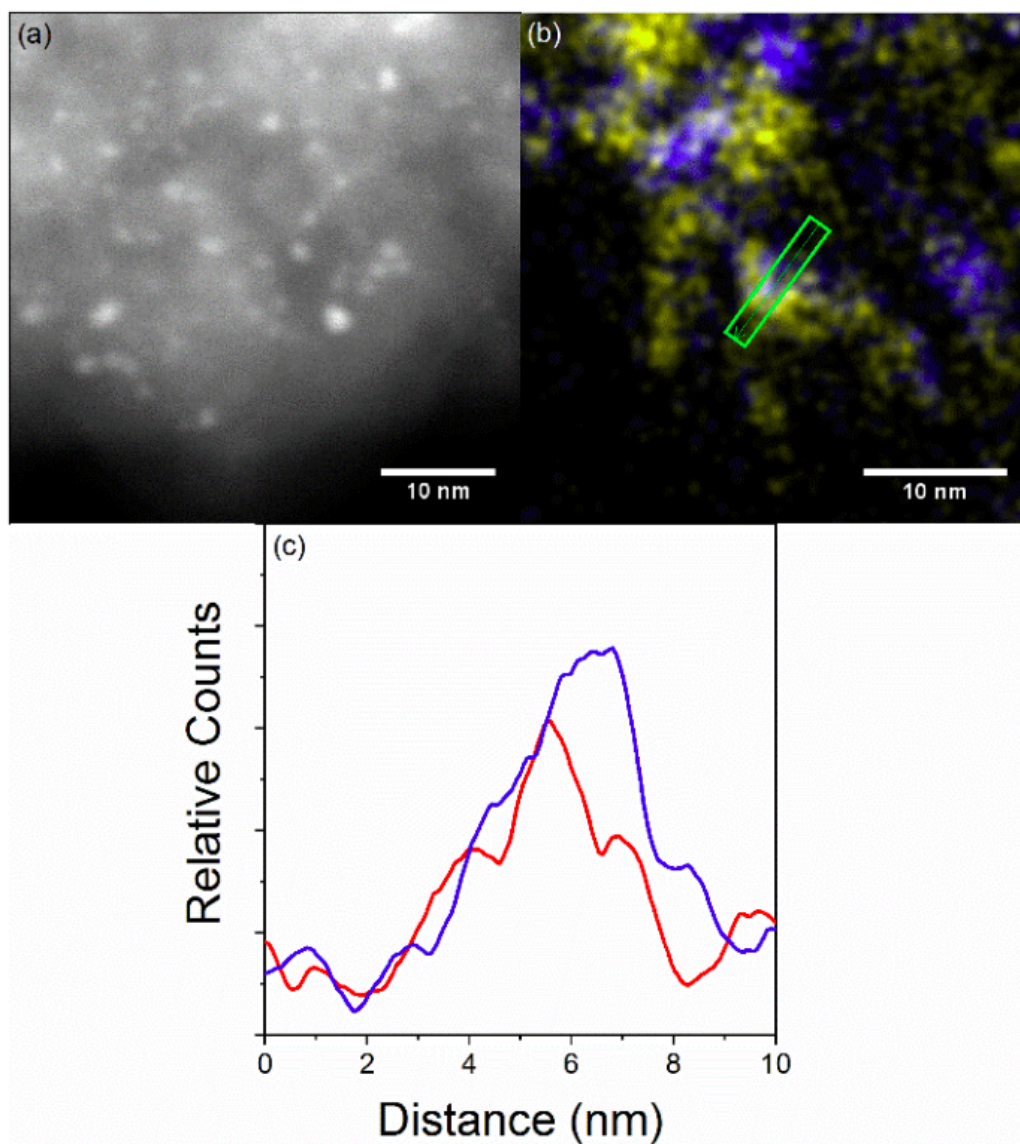


Figure 3.11. Pt-V catalyst characterization by electron microscopy. (a) HAADF STEM image of 2Pt-5V. (b) EDS map of 2Pt-5V with Pt in blue and V in yellow. (c) EDS line scan of green boxed area in b, with Pt in blue and V in Red.

vanadium is present as clusters of vanadium oxide, rather than single sites which would not have strong second shell scattering.

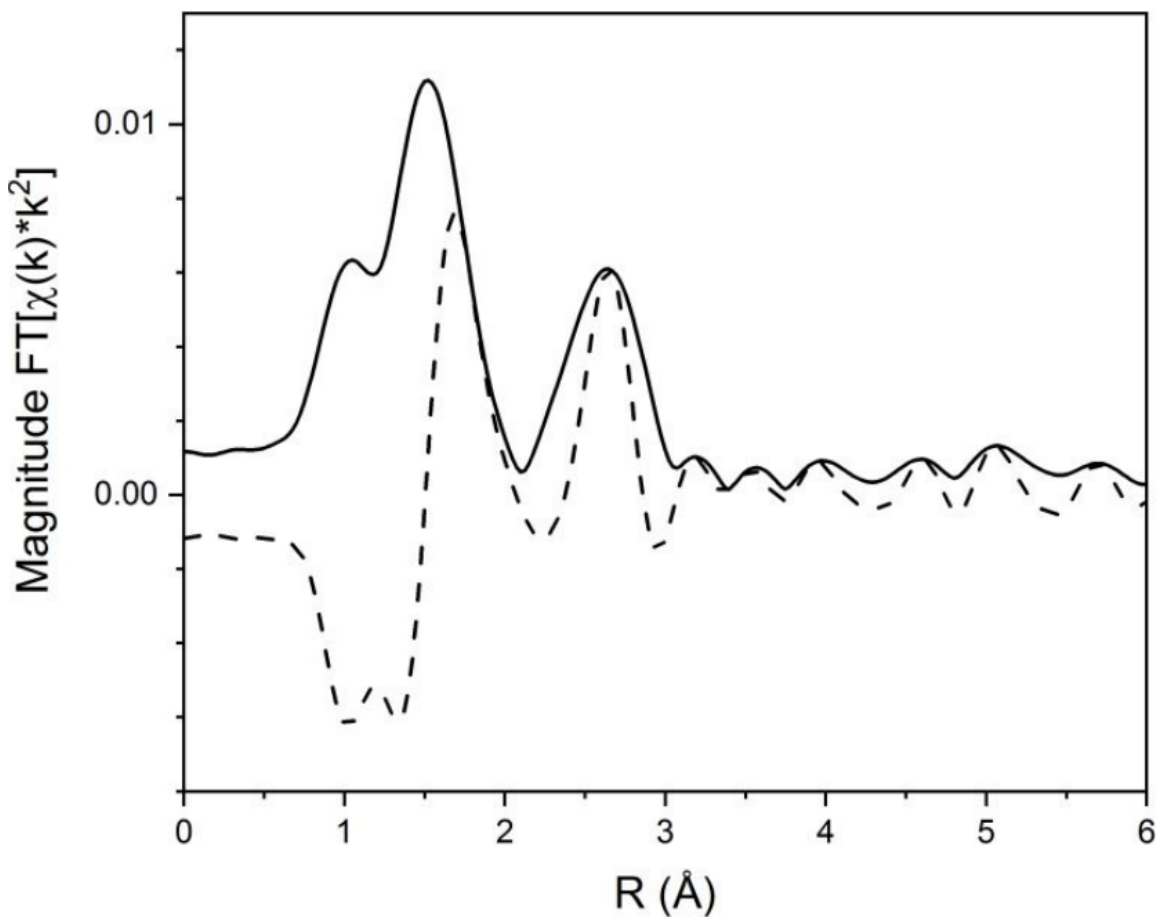


Figure 3.12. V K edge EXAFS of 5Pt-5V after reduction at 550°C in 3.5% H₂.

Figure 3.13 shows the Pt L₃ edge EXAFS of the 5Pt-5V catalysts calcined at different temperatures. As the calcination temperature increases, the FT magnitude increases showing that as the calcination temperature increases, the total coordination number, and hence particle size increases. The as the calcination temperature increases the most intense peak (ca. 2.5 Å) shifts to higher R and there is an increase in the ratio of the high (ca. 3 Å) to low (ca. 2 Å) R space peaks. Fits of the spectra in Figure 3.13 are shown in Table 3.4. For all Pt-V samples, the average Pt-V coordi-

nation number changes by only 0.5, whereas the Pt-Pt coordination number increases from 6.5 for the sample calcined at 250 °C to 10.6 for the sample calcined at 600 °C. The Pt-V:Pt-Pt neighbor ratio decreases as the calcination temperature is increased. For the sample calcined at 250 °C, the ratio is 0.31, and decreases to 0.22, 0.20, 0.17, and 0.14 for the 450 °C, 500 °C, 550 °C and 600 °C calcined samples respectively. In the sample calcined at 600 °C, the Pt-Pt bond distance is close to that of bulk Pt, whereas in the 250 °C sample, the Pt-Pt bond distance is contracted by 0.03 Å. The Pt-V bond distance for all samples does not change within the error of EXAFS.

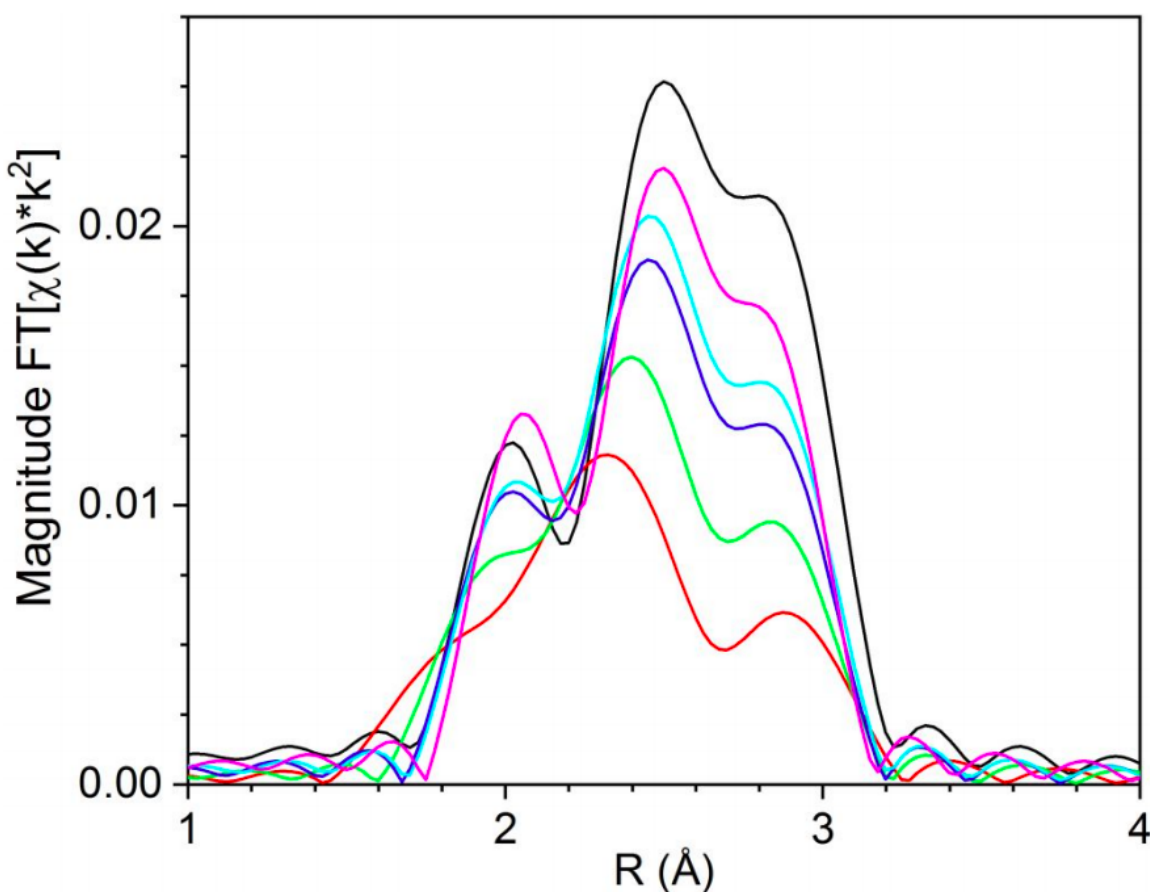


Figure 3.13. *In situ* Pt L_3 edge EXAFS of Pt foil (black) and 5Pt-5V catalysts calcined at 600°C (magenta), 550°C (cyan), 500°C (Blue), 450°C (green) and 250°C (Red). Scans were taken at room temperature in He after reduction at 550°C in 3.5% H_2 .

Figure 3.14 shows the R space Pt L₃ edge EXAFS of 5Pt-5V after reduction at 200 °C. No Pt-O scattering can be seen in the range of 1-2 Å, confirming that platinum in the sample totally reduces by 200 °C. Fits of the first shell scattering are given in Table 3.4. Fitting gave 5.7 Pt-Pt neighbors at 2.73 Å and 1.8 Pt-V neighbors at 2.69 Å. The presence of Pt-V scattering confirms that V incorporation starts at around the same temperature that platinum reduces to the metallic state. The similarity in neighbor ratio between the 200 °C sample and the same sample reduced at 550 °C suggests that the degree of vanadium incorporation is largely determined in the early stages of the reduction process.

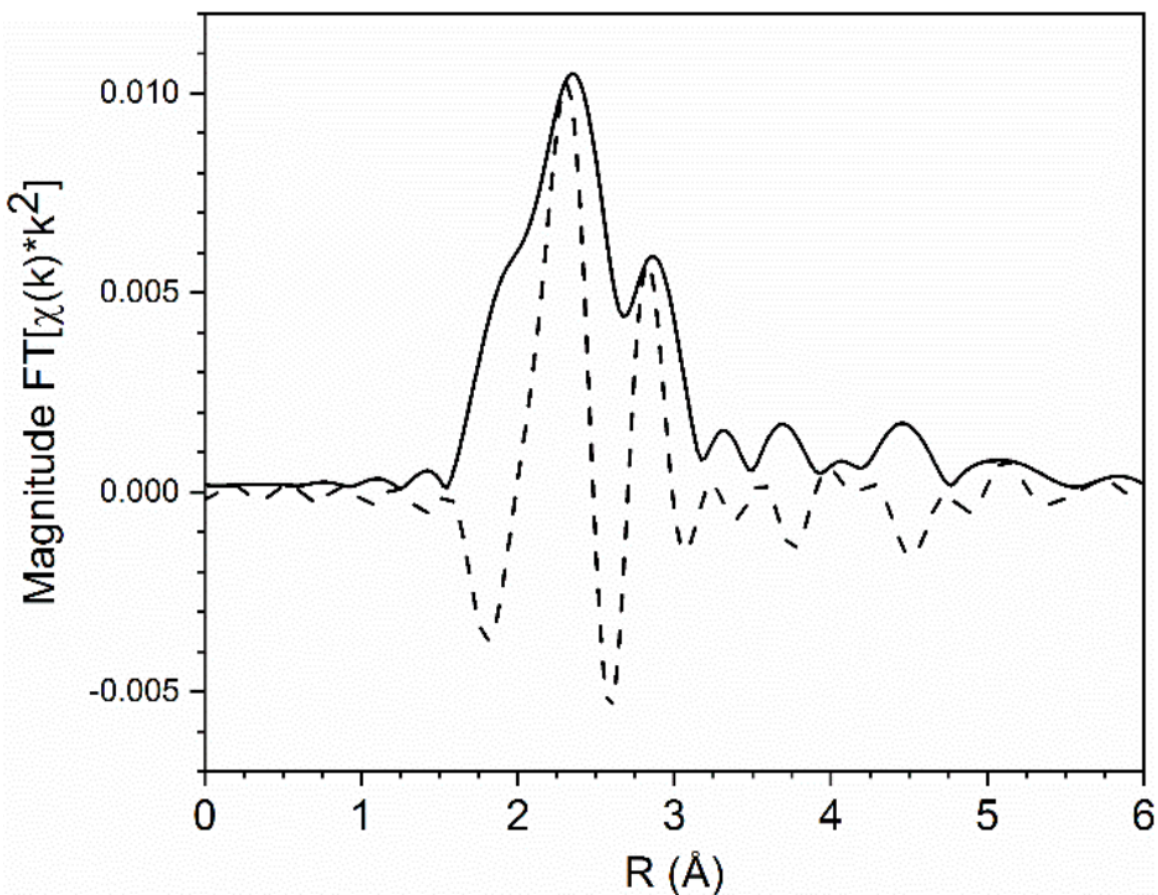


Figure 3.14. R space EXAFS magnitude (solid black) and imaginary (dashed black) components of 5Pt-5V reduced at 200°C in 3.5% H₂.

Table 3.4 shows EXAFS fits for four Pt-V catalysts synthesized with different ratios of V:Pt wt% loadings and non-standard calcination and reduction procedures. For all catalysts both the Pt-Pt and Pt-V bond distances were equivalent and were contracted from the bulk values of Pt (2.77 Å) and Pt₃V (2.74 Å). The magnitude of the contraction was larger for samples with lower total coordination numbers. For the lowest ratio, 5Pt-2.5V, the Pt-V:Pt-Pt neighbor ratio was 0.31, which is the same as 5Pt-5V, which has a higher vanadium loading and the same platinum loading. In both of these catalysts the vanadium loading is well in excess of the amount required for all Pt to form the Pt₃V phase. In 2Pt-5V(acac) the bond distance and coordination number ratios were very similar to the 2Pt-5V sample synthesized with ammonium metavanadate and oxalic acid. This can be attributed to the calcination procedure after impregnation which combusts the organic from both precursors and leaves vanadium oxide which aggregates similarly in both cases. For 2Pt-10V, the Pt-V:Pt-Pt coordination number only increases by 0.05 as compared to the 2Pt-5V sample despite doubling the vanadium loading. Silica can stabilize a limited surface concentration of V atoms before vanadium oxide clusters start to form which limits the number of V atoms in close proximity to a given Pt particle. Because both the 5% V loading and 10% V loading sample seem to be above this threshold (as evidenced by the 5% V K edge EXAFS showing VO_x clusters), doubling V loading from 5% to 10% loading does not meaningfully increase vanadium incorporation. Similarly, decreasing Pt loading from 2% to 1% also doesn't cause vanadium incorporation to increase far past the 0.5 neighbor ratio found for 2Pt-5V, however, the total particle size in the 1Pt-10V sample is lower than the bimetallic samples with 2% or 5% Pt loading as evidenced by the lower total coordination number in this sample.

Due to the small crystallite size of the particles being measured (ca. 2 nm), it was necessary to use *in situ* synchrotron XRD to collect data of sufficient quality for quantitative analysis. Due to the high energy of the X-rays used (106.257 keV), the diffraction peaks appear over a much smaller 2θ range (2-8 degrees) than a pattern obtained on a typical laboratory XRD instrument (20-80 degrees). Use of a high X-

Table 3.4.
First shell EXAFS fits and XANES edge energy of Pt-V catalysts

Catalyst	XANES Inflection Point (eV)	Pt-Pt				Pt-V			
		CN	R (Å)	DWF (Å ²)	E_0 (eV)	CN	R (Å)	DWF (Å ²)	E_0 (eV)
Pt Foil	11564.0	12	2.77	0	0	-	-	-	-
5Pt-5V-600C	11564.1	10.6	2.76	.001	-0.6	1.5	2.73	.001	2.2
5Pt-5V-550C	11564.1	9.9	2.76	.001	-0.7	1.7	2.73	.001	1.9
5Pt-5V-500C	11564.1	8.8	2.75	.001	-0.4	1.8	2.73	.001	1.9
5Pt-5V-450C	11564.1	8.1	2.74	.002	-1.1	1.8	2.72	.002	1.3
5Pt-5V-250C	11564.2	6.5	2.73	.003	-0.8	2.0	2.71	.003	2.6
5Pt-2.5V	11564.2	7.4	2.74	.003	-0.7	2.3	2.71	.003	1.6
2Pt-5V(acac)	11564.4	5.6	2.72	.003	-1.3	2.8	2.71	.003	1.9
2Pt-10V	11564.5	5.3	2.72	.003	-1.8	2.9	2.71	.003	2.0
1Pt-10V	11564.6	4.3	2.69	.004	-1.4	2.4	2.68	.004	1.1
5Pt-5V-R200C	11564.2	5.7	2.73	.003	-0.8	1.8	2.69	.003	1.1

ray energy above the Pt K absorption edge is necessary to resolve the small fraction of the sample that is metallic (<5%); at high energy, the difference in absorption cross section between the support and platinum is large enough to resolve metallic peaks from the amorphous signal from the support. The high flux provided by an insertion device coupled with a wide area detector also gives a signal to noise ratio high enough to resolve the weak, broad diffraction peaks resulting from nanoparticles less than 3 nm in diameter [151]. Finally, *in situ* measurement under reducing conditions ensures that the surface of the nanoparticle is metallic. Ex-situ XRD on small metal nanoparticles where the surface is oxidized can produce misleading results with respect to the observed lattice parameter and particle size [151]. Figure 3.15 shows a typical *in situ* XRD pattern of 2Pt-5V at 35 °C after reduction at 550 °C.

Vanadium present in the platinum nanoparticles could be arranged as a random solid solution or as an ordered intermetallic compound. To distinguish between the two possibilities, a series of 5Pt-5V samples were synthesized, where the calcination temperature after the impregnation of platinum tetraammine nitrate was increased from 250°C to 450 °C, 500 °C, 550 °C and 600 °C respectively. Higher calcination temperatures lead to larger platinum metal particle sizes after reduction [152]. Increasing the calcination temperature also decreases the dispersion of vanadium oxide on silica [153]. These combined effects should lead to a lower degree of vanadium incorporation as the calcination temperature is increased. This was confirmed by EXAFS, which showed an increase in the particle size and decrease in vanadium content with calcination temperature.

Figure 3.16 shows the 220 reflection for 5Pt-5V catalysts calcined at different temperatures. The increase in calcination temperature results in larger particles, which is reflected in the XRD spectra as a decrease in the peak full width at half maximum (FWHM). For the 5Pt-5V catalysts calcined at 450 °C and above, the main peak position matches that of the 3Pt catalyst at 4.866 2θ , whereas the catalyst calcined at 250 °C has a peak position at higher angle than the platinum catalyst. For the 5Pt-5V catalysts calcined at 450 °C, and 500 °C, the peak shape is asymmetric,

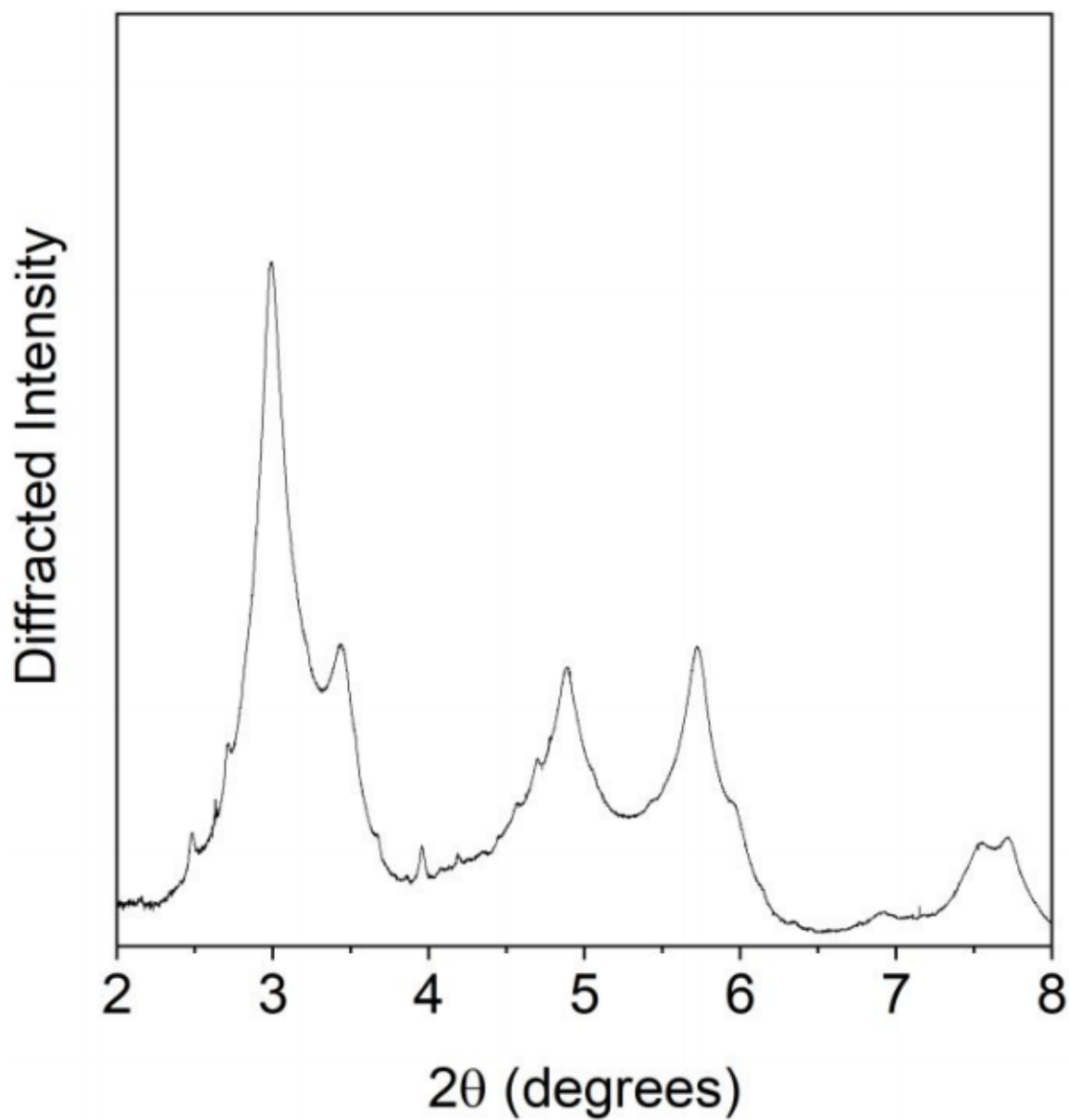


Figure 3.15. *In situ* synchrotron XRD pattern of 2Pt-5V at 35 °C in He after a reduction treatment in 3.5% H₂ at 550 °C for 30 minutes. The pattern was collected using an X-ray wavelength of 0.1173 Å.

with a shoulder at 4.896 and 4.899 2θ respectively. Asymmetric peaks are consistent with 2 phases, rather than a solid solution.

Fitting parameters for the 220 reflection for 3Pt and the four 5Pt-5V catalysts calcined at different temperatures are shown in Table 3.5. For the samples calcined at 250 °C and 600 °C, a single Lorentzian peak was sufficient to fit the spectra. For the samples calcined at 450 °C and 500 °C, a second Lorentzian was necessary to properly fit the high angle shoulder. The main peak for the 5Pt-5V catalysts calcined at 600 °C, 500 °C and 450 °C lies at 4.861, 4.861 and 4.865 2θ , respectively, and is attributed to diffraction from Pt. Using the Scherrer equation the particle size calculated using the FWHM of the main peak was 9, 11 and 16 nm for the sample calcined at 450 °C, 500 °C and 600 °C, respectively. In the 5Pt-5V samples calcined at 450°C and 500°C, the peak position of the shoulder was 4.896 and 4.899 2θ respectively. This peak is attributed to diffraction from Pt₃V based on the matching lattice parameter of 3.87 Å [154]. The particle size of the shoulder component peak was 3 and 4 nanometers for the 5Pt-5V samples calcined at 450°C and 500 °C respectively. The 5Pt-5V sample calcined at 250 °C has peak position 0.01 degrees lower than the shoulder component of the 450 °C and 500 °C samples at 4.887 2θ , which corresponds to a lattice parameter of 3.88 Å. In the 5Pt-5V-250C sample, the particle size is too small to separately fit diffraction from Pt and Pt₃V, and the resulting peak position is the average lattice parameter of both phases, which is 0.01 Å larger than that found for the Pt₃V shell layers in the 5Pt-5V samples calcined at 450 °C and 500 °C.

Table 3.7 shows the binding energy of CO and CH₃ on slab models with different alloy layer thicknesses. Binding energies were calculated according to Table 3.8. Platinum (111) shows the strongest binding energies with a CO binding energy 1.78 eV more stable than gas phase CO, and CH₃ being the least unstable of the surface methyl groups at 0.38 eV. When the first slab layer is replaced by Pt₃V, the binding energy for CO becomes 60 meV less stable and 30 meV less stable for CH₃, however these changes are within the error of DFT in determining differences in binding energy. As compared to the Pt surface, the slab with two monolayers of alloy shows significant

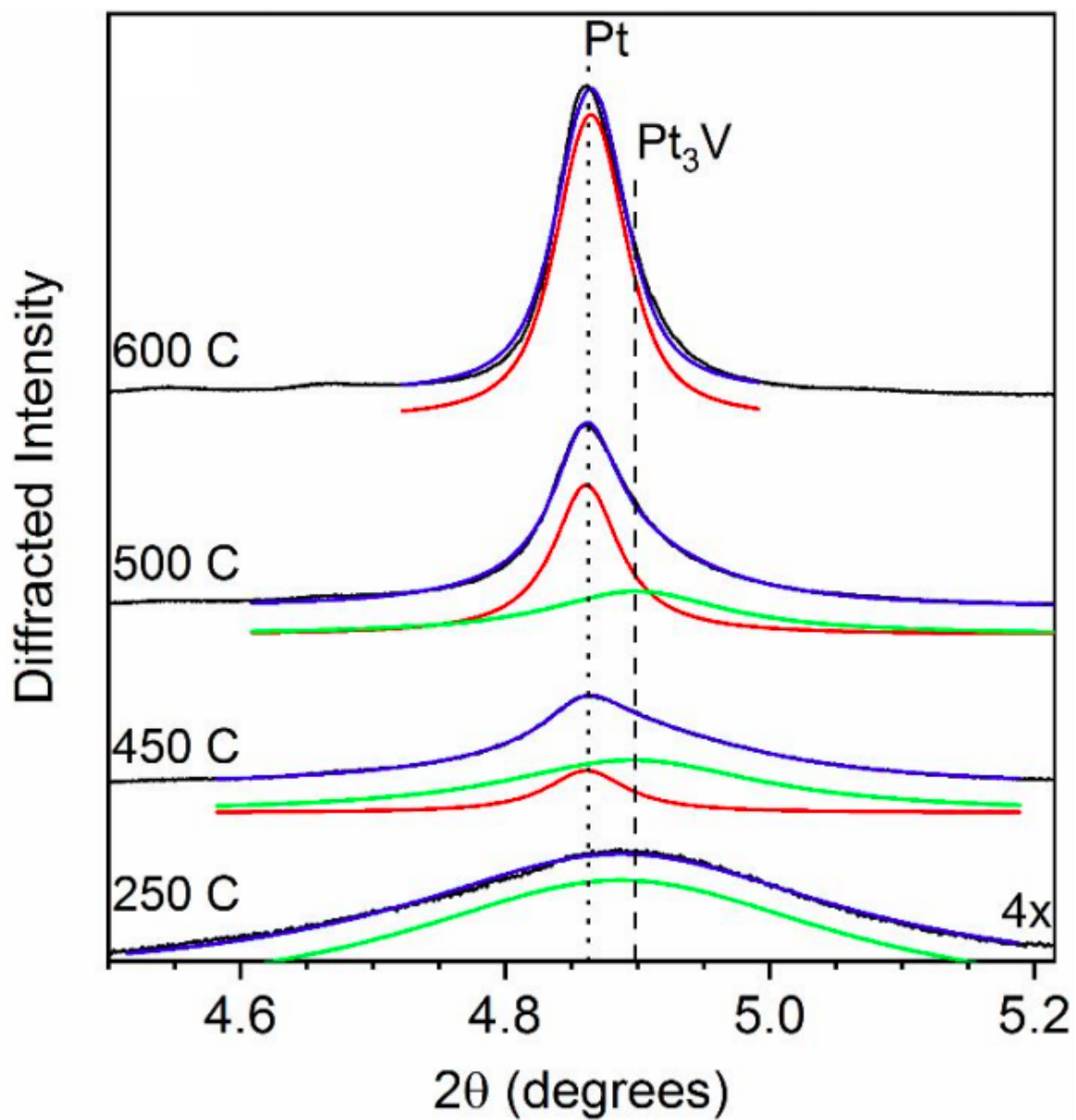


Figure 3.16. Multi component fits of the 220 XRD reflection for 5Pt-5V catalysts calcined at 250 °C, 450 °C, 500 °C, and 600 °C. Raw data is shown in black, component fits in red (Pt) and green (Pt₃V) and total fit (Pt+Pt₃V) in blue. Component fits have been offset for clarity. Spectra were collected at 35 °C in 3.5% H₂ after reduction in the same atmosphere at 550 °C.

Table 3.5.
Fits of the 220 reflection for 3Pt and 5Pt-5V catalysts calcined at different temperatures

Sample	Peak	FWHM (2θ)	Crystallite Size (nm)	Peak Position (2θ)	Unit Cell Parameter (\AA)	M-M Bond Distance (\AA)
3Pt	1 (Pt)	.315	2	4.866	3.89	2.75
5Pt-5V-250C	2 (Pt ₃ V)	.401	2	4.887	3.88	2.74
5Pt-5V-450C	1 (Pt)	.073	9	4.861	3.90	2.76
	2 (Pt ₃ V)	.241	3	4.896	3.87	2.74
5Pt-5V-500C	1 (Pt)	.060	11	4.861	3.90	2.76
	2 (Pt ₃ V)	.166	4	4.899	3.87	2.73
5Pt-5V-600C	1 (Pt)	.042	16	4.865	3.89	2.75

Table 3.6.
Pt 4f XPS fitting parameters for 3Pt and 2Pt-5V

Sample	Pt 4f _{7/2}	FWHM (eV)	Spin Orbital Splitting (eV)	LF Parameters			
	Binding Energy (eV)			a	b	c	d
3Pt	70.9	1.7	3.3	1	1.6	10	30
2Pt-5V	71.3	2.0	3.4	1	1.6	10	30

differences in stability of CO, with the CO binding energy decreasing to -1.56 eV and increasing to 0.59 for CH₃. The full alloy slab showed the weakest binding

energies but are within error equal to that of the slab with two atomic layers of alloy. These calculations suggest that electronic modifications that modify adsorbate binding strengths are limited to the nearest neighbors of the surface atoms. The change between the 1 and 2 monolayer slabs changes the subsurface neighbor identity and surface Pt atoms go from having 2 V neighbors to 3. In the full alloy slab, only second nearest neighbors are modified and the change in binding energy is minimal.

Table 3.7.

Binding energies of CO and CH₃ on Pt (111), Pt₃V-1ML-Pt, Pt₃V-2ML-Pt and Pt₃V (111). Binding energies were calculated according to Table 3.8

System	Binding Energy (eV)	
	CO	CH ₃
Pt (111)	-1.78	0.38
Pt ₃ V-1ML-Pt	-1.72	0.41
Pt ₃ V-2ML-Pt	-1.56	0.59
Pt ₃ V (111)	-1.60	0.62

Table 3.8.

Formalism used to calculate binding energies for CO and CH₃ on Pt, Pt₃V shell on Pt and Pt₃V alloy

$$BE_{CO} = E_{CO+slab} - E_{slab} - E_{CO(g)}$$

$$BE_{CH_x} = E_{CH_x+slab} + \frac{x}{2}E_{H_2(g)} - E_{slab} - E_{CH_4(g)}$$

Table 3.9 shows the binding energy and corresponding binding sites on Pt₃V (111) and Pt (111) surfaces for CO, C₁, C₂ and C₃ fragments. The effects of electronically modifying platinum by alloying are seen on the binding energetics of important intermediates which have been used to model propane dehydrogenation and coking networks [155–157]. All the intermediates modeled show weaker binding on Pt₃V

(111) compared to Pt (111). CH, CCH₃, and CH₃CCH₂ intermediates bind 0.97 eV, 0.52 eV, and 0.67 eV more weakly on Pt₃V compared to Pt. Additionally, Pt-Pt-Pt ensembles on Pt₃V are unstable compared to Pt-Pt-V 3-fold sites as seen from adsorption of CH and CHCCH₂ (see Figure 3.17). Hydrogen binds equally as strong on the HCP site on Pt and Pt₃V, where the HCP site is a Pt-Pt-V ensemble. In contrast to Pt, all Pt₃V surface sites no longer isoenergetically bind H as shown in Table 3.10.

Table 3.9.

Most stable binding configurations and their corresponding binding energies for CO, C₁, C₂, and C₃ hydrocarbon fragments adsorbed on Pt (111) and Pt₃V (111) surfaces.

Species	Most Stable Binding Location On		Binding Energy Relative to Pt (111) (eV)
	Pt ₃ V (111)	Pt (111)	
CO	Pt _{top} /V _{top}	FCC/HCP	0.19
CH	HCP/FCC (PtPtV)	FCC/HCP	0.97
CH ₂	HCP/FCC (PtPtV)	Pt bridge	0.51
CH ₃	Pt _{top}	Pt _{top}	0.24
C-CH ₃	FCC (PtPtV)	FCC	0.67
CH ₃ -CH-CH ₂	PtV Bridge	Pt Bridge	0.79
CH ₃ -CH-CH	HCP (PtPtV)	FCC	0.37
H ₃ -C-CH ₂	PtV Bridge-Pt _{top}	Pt Bridge-Pt _{top}	0.98

Figure 3.17 shows the most stable binding geometries and binding energies of C₁, C₂ and C₃ adsorbates on Pt₃V (111) and Pt (111) surfaces. For Pt (111), CH bond equivalently to the FCC and HCP sites, whereas on Pt₃V (111) CH bonds at a PtPtV HCP/FCC site, and is 1.36 eV less stable on the 3Pt ensemble of Pt₃V (111) as compared to the PtPtV ensemble which is in turn 0.97 eV less stable than CH on Pt (111). CH₃ bonds to equivalent Pt top sites in both Pt (111) and Pt₃V (111), but is 0.24 eV less stable on Pt₃V (111). Similar to CH, C₃H₅ (CH₃-C-CH₂) bonds to an

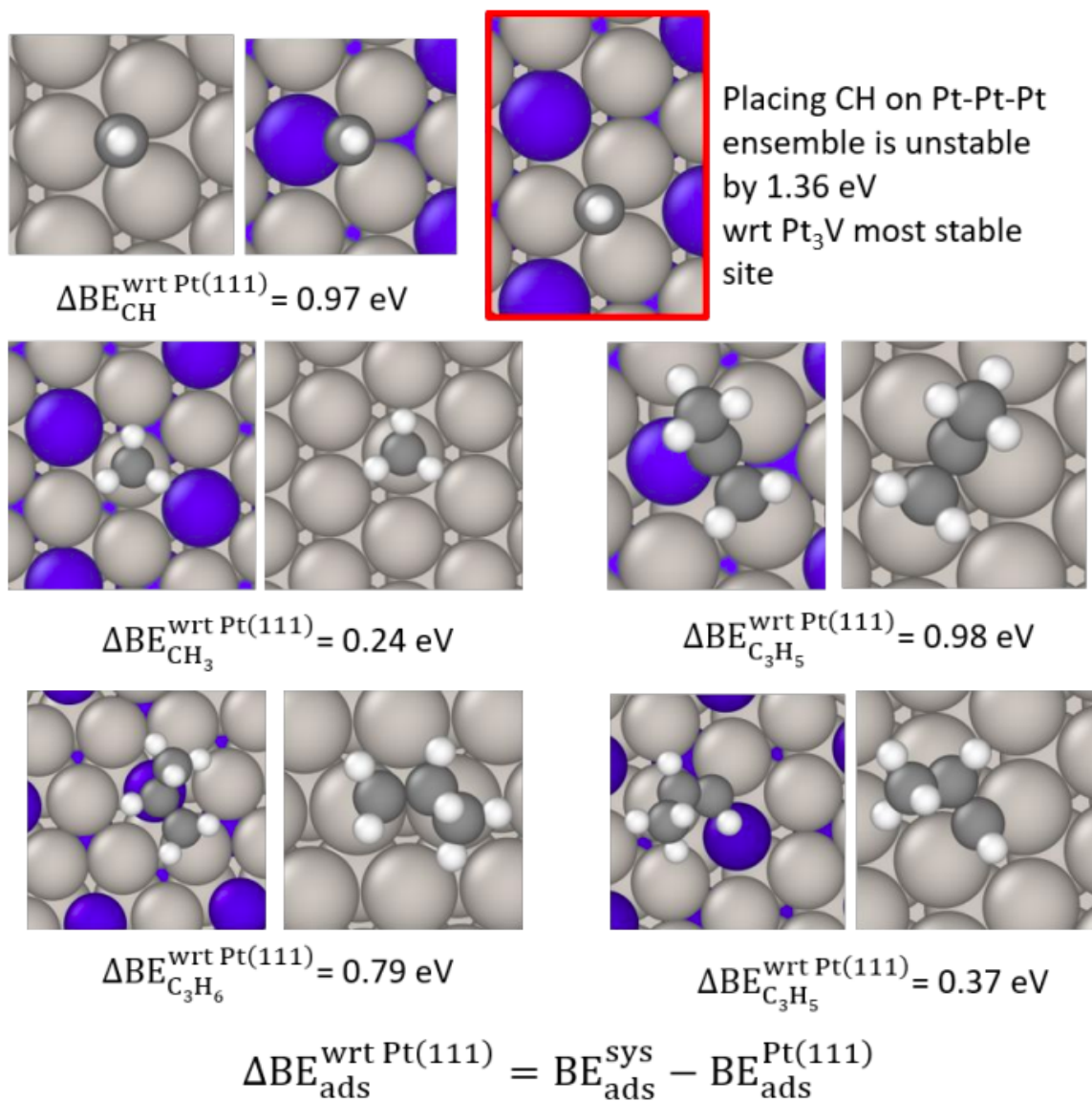


Figure 3.17. Schematics of most stable binding configurations and their corresponding binding energies (with respect to Pt (111)) for CO, C₁, C₂, and C₃ hydrocarbon fragments adsorbed on Pt₃V (111) and Pt (111) surfaces.

ensemble containing a V atom, here with the middle carbon on a Pt-V bridge site and the CH₂ carbon binding to the Pt top site and is 0.98 eV less stable than on Pt (111). On Pt (111) CH₃-C-CH₂ bonds to a Pt-Pt bridge and Pt top site. On Pt₃V

(111) CH₃-CH-CH binds to an HCP PtPtV ensemble, while on Pt it binds at the FCC site, and is 0.37 eV less stable on Pt₃V (111). Lastly surface propylene bonds to the PtV bridge site on Pt₃V (111) and is 0.79 eV less stable than on the Pt bridge site on Pt (111).

Table 3.10 shows the binding energy of adsorbed H on various Pt and Pt₃V adsorption sites on the (111) face. The binding energy on the most stable site on Pt and Pt₃V (HCP) are the same. For platinum case the binding energy surface is relatively isoenergetic with similar binding energies for H to bind at Pt-top, HCP, and within error also bridge and FCC sites. However, for Pt₃V (111) the HCP site made of Pt-Pt-V is the only site with stability comparable to Pt (111) with the Pt top site showing significantly weaker binding.

Table 3.10.
H binding energy on Pt (111) and Pt₃V (111) referenced to H₂ gas

Pt (111) Binding Site	Binding Energy (eV)	Pt ₃ V (111) Binding Site	Binding Energy (eV)
Pt top	-0.48	Pt top	-0.25
FCC	-0.44	V top	0.25
HCP	-0.48	HCP (Pt-Pt-V)	-0.43
Bridge	-0.44	-	-

The contribution of surface strain to the binding energy changes observed was evaluated by fixing the Pt lattice constant to that of Pt₃V and recalculating the adsorption energies. The effect is caused due to the Pt-Pt distance decreasing from 2.81 to 2.77 Å when vanadium is incorporated into the lattice. In all cases, the change in binding energy was within the error of DFT as shown in Table 3.11, demonstrating the preeminence of V in the modification of binding energies in the alloy even in cases where the adsorbate does not directly adsorb to a vanadium containing site.

Table 3.11.

Binding energies of CO, and CH_x, species as calculated on Pt₃V (111) and Pt (111) with the lattice constant of Pt₃V. The effect of changing the lattice constant of Pt (111) is minimal on the binding energy compared to the Pt slab constructed using the equilibrium lattice constant.

Species	Binding Energy Relative to Pt (111)	
	Pt with Pt ₃ V Lattice Constant	Pt ₃ V
CO	0.08	0.19
CH	0.09	0.97
CH ₂	0.07	0.51
CH ₃	0.07	0.24

A frequently used descriptor for selectivity of dehydrogenation is the energy difference between the first deep dehydrogenation step and the desorption energy for propylene [155]. The barrier for C-H bond cleavage in adsorbed propylene, shown in Figure 3.17, are similar on Pt and Pt₃V (111) surfaces. They differ by only about 0.1 eV, with the transition state on Pt₃V being higher in potential energy. However, there is appreciable difference in the stability of transition state (TS) with respect to the desorbed gas phase C₃H₆: the TS for Pt is 0.32 eV more stable than desorbed propylene while for Pt₃V the TS is 0.09 eV unstable. This suggests that for modeled (111) surfaces of Pt₃V the thermodynamics of desorbing and bond-breaking are competitive but for Pt (111) the deep dehydrogenation pathway is favorable.

Figure 3.19 shows the X-Y averaged electrostatic potential along the axis normal to the slab face for the (111) surface of Pt and Pt₃V. Table 3.12 shows the work function calculated from the electrostatic potential plots. The calculated work function for Pt (111) is close to what is measured experimentally [158]. Alloying with vanadium reduces the work function of the (111) face by 0.41 eV. This suggests a shift in the

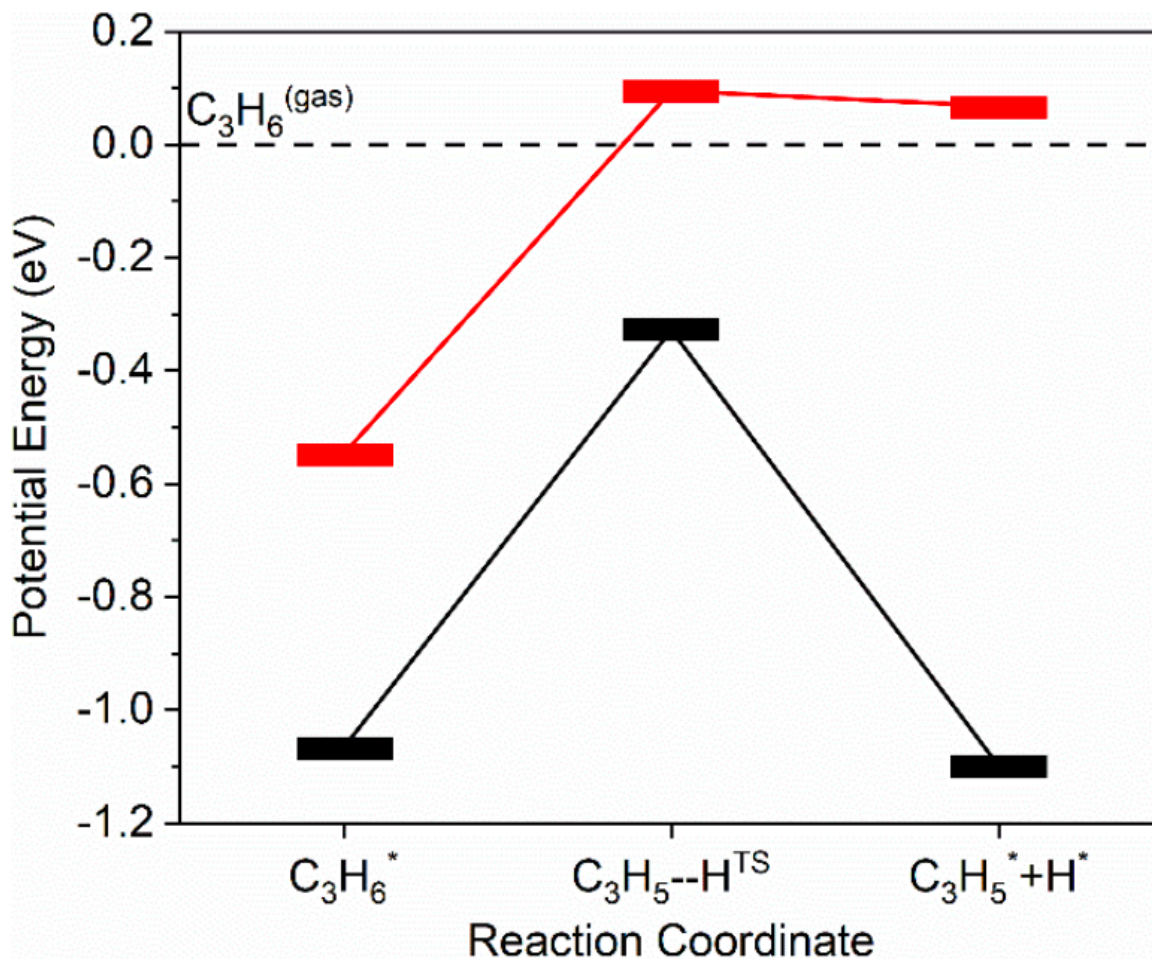


Figure 3.18. Calculated C-H bond breaking energy for adsorbed propylene on Pt (111) (solid black) and Pt₃V (111) (solid red) referenced to gas phase propylene (dashed black).

fermi level compared to the monometallic Pt (111) slab, demonstrating that changes in the fermi level cannot be neglected in interpretation of core level shifts between Pt and Pt₃V. However, a more rigorous model is needed to definitively assign the observed experimental core level shift to a specific effect.

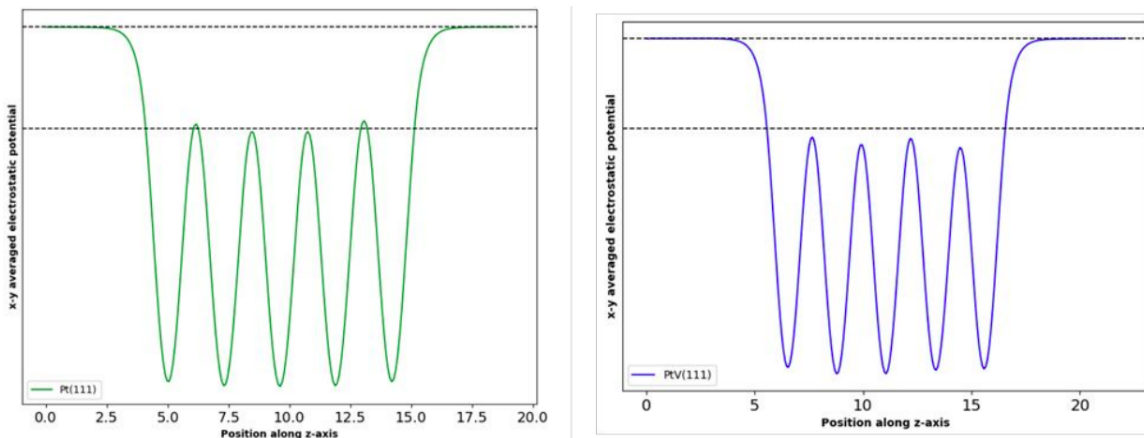


Figure 3.19. X-Y axis averaged electrostatic potential for Pt (111) and Pt_3V (111) slab plotted along Z-axis (perpendicular to the surface of the slab).

Table 3.12.

Work function values for the (111) face of Pt and Pt_3V .

	Pt (111)	Pt_3V (111)	Difference
Work function (eV)	5.68	5.27	0.41

3.7.3 Discussion

The interpretation of XPS shifts in alloys is complicated due to the sensitivity of core level binding energies to particle size, chemical environment (initial state effect), the screening character of the valence electrons (final state effect), and changes in the position of the Fermi level which is the binding energy reference. The potential model of XPS is frequently invoked to describe XPS core level shifts between pure metals and alloys [159]. In this model, the initial state effect is due to a change in the electrostatic potential in the ground state between pure element and the alloy. This change in potential has been related to a difference in electron density between the

two environments. If charge is removed from the atom, more energy is required to remove an electron from a more cationic atom and vice versa. The final state effect has intra-atomic and extra-atomic components and is caused by a change in the screening character of the valence electrons and a change in the electrical conductivity of the metal respectively. If one were to attribute a part, or the entirety of the 0.4 eV core level shift measured for 2Pt-5V to an initial state effect, the increase in binding energy by the above model would mean that platinum in Pt₃V has lost electrons through electron transfer to vanadium.

While XPS shifts are often interpreted as due to initial state effects, core level shifts have been shown to move in the same direction as the valence band center as measured by valence band photoelectron spectroscopy, indicating a correlation between energy changes in the valence band and core level shifts (CLS) [160, 161]. Therefore CLS in alloys cannot be explained solely by the initial state effect or a transfer of electrons from one element to another, and the final state effect must also be considered [162, 163]. The calculated work function of the Pt and Pt₃V (111) surface (see Table S9) are also different, which shows that changes in the fermi level between the two cannot be neglected as contributing to the core level shift. It has been demonstrated that the CLS in alloys may be due to the intra-atomic charge redistribution in the valence band [161, 164]. The 0.4 eV CLS for the 2Pt-5V catalyst is consistent with a shift of the d-band center away from the Fermi level caused by the redistribution of energy states in the d-band in agreement with DFT and RIXS. The present work on Pt₃V further demonstrates why assuming core level shifts are dominated by an initial state effect, or even that the core level shift occurs in the same direction as the initial state effect is not a safe assumption. Theoretical calculations of core level shifts in alloy systems as a function of composition by the complete screening model show in many systems, such as Pd-Ag, that the final state effect is non-negligible and that initial state effect shift and total CLS do not have the same sign [161]. Further, the initial state effect shift of both components in an alloy do

not always occur in opposite directions as would be expected in all cases if electron transfer explained the cause of the initial state effect for alloys [165].

Another consequence of non-rigid band behavior can be seen in the L_3 edge XANES of Pt_3V , where the white line increases in intensity and narrows compared to a platinum nanoparticle of the same size. Pt-Mo alloys also have a white line intensity higher than a similarly sized platinum nanoparticle despite Mo also being less electronegative than platinum [166, 167]. In the other direction gold-platinum alloys, where platinum is the more electropositive element have a Pt L_3 edge white line intensity is lower than that of the platinum foil and the XANES edge energy is shifted to a value higher than Pt [168]. The increase in XANES edge energy and white line intensity, therefore are not necessarily indicative of increased oxidation state, or electron transfer from Pt, as is often suggested. What is generally neglected in the interpretation of the white line intensity is that the broadness of the white line also changes. Thus, a small, broad white line can have the same area (and hence number of unfilled states) as a narrow, large white line. These spectral features reflect changes in the energy distribution of unfilled states (as seen in the d band DOS for Pt and Pt_3V), not necessarily the loss of states due to electron transfer. This was demonstrated by Schweitzer et al. based on the integrated area of experimental and calculated Pt L_3 edge XANES of platinum and platinum alloys [169]. The same conclusion was reached in nickel containing alloys using energy loss near edge structure (ELNES) and auger electron spectroscopy (AES) by Nikolla and coworkers [170].

In summary, interpretation of the shifts in the XPS, XANES and RIXS experimental measurements are all consistent with the DFT calculations, which indicate changes in the electronic properties due to alloy formation result from a lowering of the energy of the filled 5d orbitals and are responsible for weaker adsorbate energies, facile desorption of the olefin product, reduced hydrogenolysis and coke selectivities.

4. STRUCTURAL TRENDS IN THE DEHYDROGENATION SELECTIVITY OF PALLADIUM ALLOYS

Stephen C. Purdy, Ranga Rohit Seemakurthi, Garrett M. Mitchell, Mark Davidson, Brooke Lauderback, Siddharth Deshpande, Zhenwei Wu, Evan Wegener, Jeffrey P. Greeley, Jeffrey T. Miller

4.1 Abstract

Alloying is well-known to improve the dehydrogenation selectivity of pure metals, but there remains considerable debate about the structural and electronic features of alloy surfaces that give rise to this behavior. To provide molecular-level insights into these effects, a series of palladium intermetallic alloy catalysts with Zn, Ga, In, Fe and Mn promoter elements were synthesized, and the structures were determined using *in situ* X-ray absorption spectroscopy (XAS) and synchrotron X-ray Diffraction (XRD). The alloys all showed propane dehydrogenation turnover rates 5-8 times higher than monometallic Pd and selectivity to propylene of over 90%. Moreover, among the synthesized alloys, Pd₃M alloy structures are less olefin selective than PdM alloys which are, in turn, almost 100% selective to propylene. This selectivity improvement was interpreted by changes in the DFT calculated binding energies and activation energies for C-C and C-H bond activation, which are ultimately influenced by perturbation of the most stable adsorption site and changes to the *d*-band density of states. Furthermore, transition state analysis showed that the C-C bond breaking reactions require 4-fold ensemble sites, which are suggested to be required for non-selective, alkane hydrogenolysis reactions. These sites, which are not present on alloys with PdM structures, could be formed in the Pd₃M alloy through substitution of one M

atom with Pd, and this effect is suggested to be partially responsible for their inferior selectivity.

4.2 Introduction

Dehydrogenation is the first step in the activation of alkanes, and on-purpose catalytic dehydrogenation is becoming increasingly important with the widespread exploitation of shale gas reserves, which contain a significant fraction of C₂+ alkanes [171]. Further, light olefins such as ethylene and propylene produced from alkane dehydrogenation are important feedstocks for the petrochemical industry [172, 173]. However, dehydrogenation is an endothermic reaction, where high equilibrium conversion is favored by high temperature and low alkane pressure [174]. At the high temperature required for dehydrogenation of light alkanes, hydrogenolysis also occurs, forming methane and other lower carbon number species leading to low olefin selectivity [175, 176]. Rationally improving dehydrogenation catalyst selectivity, in turn, relies upon development of molecular-level understanding of these unselective hydrogenolysis pathways.

Hydrogenolysis is a structure sensitive reaction, implying that the turnover rate is a function of the surface structure and Pd ensemble size [177]. Modifications to the ensemble can occur by either changing the particle size or by diluting the active metal with a second inactive metal. In contrast, dehydrogenation is believed to be a relatively structure insensitive reaction, meaning it only requires a single active metal atom to be catalyzed, and hence the dehydrogenation turnover rate shows only modest variations with particle size and ensemble size [178–180]. To improve the selectivity of dehydrogenation catalysts, it is possible to exploit this difference in structure sensitivity between dehydrogenation and hydrogenolysis through alloying. By separating active metals with an inactive atom, termed a promoter, the turnover rate of hydrogenolysis can be decreased while the turnover rate of dehydrogenation is minimally changed, resulting in increased olefin selectivity [177]. Most of the early work on structure sensitivity in hydrogenolysis and dehydrogenation reactions was performed

on binary alloy systems that form solid solutions [181]. In these structures, a solute metal randomly substitutes for a solvent metal atom in the parent lattice. This leads to a distribution of active metal ensemble sizes, and high dehydrogenation selectivity is only achieved at very high dilutions of the active metal [182, 183]. Recent work has focused more on intermetallic compounds, which have a fixed (or narrow) composition range and can have crystal structures that differ from their pure components while possessing comparable or higher selectivities than solid solutions [184]. In these intermetallic compounds, the ensemble size is determined by the crystal structure and atomic plane, and in some materials, such as PtZn, the active metal atoms are completely isolated from one another by promoter atoms [185]. In other structures, there are still small active metal ensembles, such as in the case of Pt₃M alloys with the L1₂ structure [186, 187]. These well characterized ordered structures of intermetallics are useful in identifying the geometry of active metal ensembles that are required for selective performance of propane dehydrogenation chemistry, and this is indeed the primary objective of the present work.

Theoretical studies of dehydrogenation reactions, using density functional theory, have focused mainly on platinum and platinum alloys [188–196]. Early mechanistic studies on Pt₃Sn alloys [188, 197] showed that a simple thermodynamic selectivity descriptor, the energy difference between propylene desorption energy and the activation energy barrier of the first deep dehydrogenation reaction, correlates with the observed higher selectivity of platinum tin alloy as compared to pure platinum. This descriptor has been used to computationally estimate olefin selectivities in selected alloys [191, 192, 196]. In addition, recent work with microkinetic model analysis by Saerens et al. [193] on Pt (111) has shown that, along with the propylene dehydrogenation step, C-C bond breaking of propyne, which is a deeply dehydrogenated derivative of propylene, is also one of the relevant steps for byproduct formation and thereby adversely affects the selectivity of propylene production. Taken in aggregate, these studies suggest that both the simple selectivity descriptor, comparing desorption and further dehydrogenation of propylene, and C-C bond breaking of deeply dehydro-

generated species can be important for prediction of selectivity trends across alloys. The transition states of these steps are, further, strongly affected by the geometry and ensemble sizes of active atoms available on the catalyst surfaces.

As discussed above, most research on selective dehydrogenation catalysts has focused on Pt and its alloys, since pure Pt is shown to be more stable against deactivation and to have less hydrogenolysis activity than other metals [198]. Nonetheless, a few recent reports have also shown that alloys of palladium can have dehydrogenation selectivities comparable to platinum alloys [199, 200]. The ability of promoter metals to suppress hydrogenolysis in alloys in a way seemingly independent of the active metal's intrinsic hydrogenolysis activity motivates systematic study of alloy selectivity not only in platinum alloys, but also other less selective metals such as Pd. This strategy should give insight into the salient features of alloying that lead to improved selectivity, independent of the behavior of the active metal, and ultimately open up a larger space of catalyst compositions and structures for use as dehydrogenation catalysts. Hence, in this combined experimental and computational study, we synthesize a series of palladium alloy catalysts with five different promoters: indium, zinc, gallium, iron, and manganese. Alloy catalysts were synthesized as to be pure phase and of similar particle size to permit comparisons of selectivity based on differences in promoter identity and the crystal structure of the alloy phase. The formation of alloy phases was verified using *in situ* synchrotron XRD and *in situ* XAS. Catalytic tests show that propylene selectivities are highest for site-isolated alloys (1:1), while olefin selectivity of alloys with threefold Pd ensembles is slightly lower, and all of the alloys had significantly higher selectivities than pure Pd. The experimental trends in dehydrogenation selectivity are further compared with calculated trends in adsorbate binding energy and transition state energies for C-C and C-H bond activation. Fully consistent with the experimental results, the DFT calculated trends predict that site isolated alloys have higher olefin selectivity than do alloys without site isolation. Further, the improved olefin selectivity for the 1:1 alloys is found to be linked to weaker binding of propylene and to an increase in hydrogenolysis (C-C bond breaking) bond

breaking barriers which is driven by the structural dissimilarity of the active ensemble for hydrogenolysis compared to that in pure Pd. In contrast, the active hydrogenolysis ensembles in Pd₃M alloys are structurally similar to those of Pd, only requiring one atomic substitution to create an ensemble equivalent to Pd. This structural similarity is proposed to be partially responsible for their inferior selectivity compared to site isolated alloys.

4.3 Methods

4.3.1 Catalyst Synthesis

Monometallic and bimetallic catalysts were synthesized by sequential loading of the promoter and palladium on Davasil 646 silica (Sigma Aldrich). The loading was done either using incipient wetness impregnation or strong electrostatic adsorption with a calcination step between loadings. All catalysts were reduced after synthesis using a slow ramp through 250 °C and subsequently aged at 550 °C for 30 minutes to reduce the effect of sintering on rate data. The synthetic procedure for each catalyst is summarized below in Table 4.1, and full details are given in the supporting information.

Table 4.1.
Synthetic details of Pd and Pd alloy catalysts.

Catalyst	1Pd	2Pd	Pd-In	Pd-Fe	Pd-Ga	Pd-Zn	Pd-Mn
Promoter Loading (wt %)	-	-	3	3	2.5	3	5
Palladium Loading (wt %)	1	2	2	2	2.5	2	1

4.3.2 STEM/EDS

Scanning transmission electron microscopy (STEM) and energy dispersive X-ray spectroscopy (EDS) was performed on an FEI Talos F200X S/TEM with a Super-X

EDS system and a high brightness field emission electron source. The microscope was operated at 300 keV and STEM images were recorded using a high angle annular dark field (HAADF) detector. Ground catalyst powder was physically mixed with a copper 300 mesh lacey carbon coated TEM grid (SPI supplies). Reported particle size distributions are number average particle sizes and were determined by measuring more than 250 particles. Measurement of particles was done using the Fiji distribution of ImageJ [201].

4.3.3 *In Situ* Synchrotron X-ray Diffraction (XRD)

In situ synchrotron XRD was performed at the ID-11C beamline of the advanced photon source. XRD was performed in transmission geometry using an X-ray wavelength of 0.1173 Å (105.7 keV). Samples for XRD were ground into a fine powder and pressed into a self-supporting wafer. The sample wafers were then loaded into a water cooled linkam stage capable of gas flow and heating. The X-ray transparent windows on the cell were made of kapton film. The cell was purged with He before a flow of 3.5% H₂ in He was started and the temperature ramped to 550 °C at 10 °C/min. After a 30 minute dwell at temperature, the cell was cooled to 35 °C and a pattern was collected. Diffracted X-rays were measured using a Perkin-Elmer large area detector. Detector calibration was performed using a CeO₂ standard. Trace oxygen was removed from He using an oxygen trap made by Restek.

Detector calibration and pattern integration was performed using GSAS II software [202]. Background subtraction was done using patterns of the empty cell and the bare SiO₂ support. Pattern simulation was done using Materials Analysis Using Diffraction (MAUD) and phase references from ICSD [203–208]. Particle size broadening in simulated patterns was varied by changing the isotropic crystallite size.

4.3.4 *In Situ* X-ray Adsorption Spectroscopy (XAS)

Pd K edge XAS was performed at the MRCAT 10BM line of the advanced photon source. Samples were measured in transmission mode using 3 ion chambers which allowed for simultaneous measurement of a Pd foil reference. Samples were ground into a fine powder and pressed inside of a stainless-steel sample holder which was loaded into a quartz tube reactor. The reactor was sealed at each end by a 1-inch ultra-torr union modified with a gas flow port and a kapton window. The reactor was purged with He and then treated at 550 °C in 3.5% H₂ for 30 minutes. The cell was then purged at high temperature with He to desorb chemisorbed hydrogen and decompose any palladium hydride that may have formed during treatment. The samples were then cooled to room temperature in He and scanned. Samples were also scanned after exposure of the reduced samples to air at room temperature.

Extended X-ray adsorption fine structure (EXAFS) data on Pd and Pd alloys were fit using WinXAS software. The extracted chi was k^2 weighted and Fourier transformed over a k range of 2.9-12 Å⁻¹. Phase and amplitude functions for Pd-Pd scattering were extracted from Pd foil with a coordination number of 12 and a bond distance of 2.75 Å. Pd-O scattering was extracted from palladium (II) acetate (4 Pd-O bonds at 2.05 Å). Bimetallic scattering (Pd-Mn at 2.62 Å, Pd-Zn at 2.71 Å, and Pd-Ga at 2.6 Å) were constructed using FEFF with the amplitude reduction factor, Debye-Waller factor and E_0 correction fixed to the values fit to Pd foil. Fitting was performed in R space on isolated first shell scattering for each sample by allowing the coordination number, bond distance, Debye-Waller factor and E_0 correction to vary.

Reduction-Oxidation difference EXAFS was performed by subtracting unweighted chi data of the reduced and room temperature air exposed samples as in reference [209]. The core of the nanoparticle, which is unchanged during the surface oxidation process is subtracted out in the difference, and only the signal from surface scattering modified during the reduction-oxidation process remains. Metal-metal scattering, which are lost during oxidation remains in phase with experimental phase

and amplitude functions, while the new Pd-O scattering peak is phase shifted by π -radians with respect to the experimental reference due to the subtraction in the difference spectra. Fitting of the difference spectra was performed in R space on Fourier transformed k^2 weighted difference chi. Fourier transforms were taken over a k range of 2.9-10 \AA^{-1} and fit over an R range of 1-3 \AA . The fitting procedure was then identical to the above reduced samples.

4.3.5 Propane Dehydrogenation

Propane dehydrogenation was performed in a fixed bed microreactor. 50-150 mg of catalyst was mixed to a total mass of 1 g with Davasil 646 silica and loaded into a quartz tube reactor with an inner diameter of 9.5 mm. The catalyst bed was dried in flowing nitrogen at 100 °C for 15 minutes and then reduced in 5% H₂ in N₂ at 550 °C for 30 minutes. Before starting the flow of reactant gasses hydrogen was purged from the bed by flowing 100 ccm of nitrogen for 5 minutes. Propane dehydrogenation reactions were carried out at 550 °C at 3 psig with 2.5% propane and 2.5% hydrogen. Conversion was adjusted by changing the total flow rate and mass of catalyst used in a test. Conversion and selectivity were calculated on a carbon basis of gas phase products measured by an online HP 6890 gas chromatograph with a flame ionization detector and a Restek Alumina BOND/Na₂SO₄ column. A chromatogram was collected every 5 minutes for 90 minutes. The resulting time on stream data was fit with a first order exponential function to give the selectivity and conversion at zero deactivation.

Propylene production turnover rates were measured at differential conversion (>5%) in 2.5% propane and 2.5% hydrogen at 550 °C. Rates were normalized based on the fraction of exposed palladium determined by surface oxidation EXAFS using the Pd-O coordination number. 100% PdO has a Pd-O coordination number (CN) of 4; thus the dispersion was determined from the fit Pd-O CN divided by 4.

4.3.6 Density Functional Theory

Periodic density functional theory (DFT) calculations were performed using the Vienna Ab-initio Simulation Package (VASP) [210–213]. The Kohn-Sham equations were solved self-consistently using the Perdew, Burke, and Ernzerhof (PBE) functional [214], with the projected augmented wave (PAW) method [215, 216]. The converged bulk lattice constants for fcc Pd, Pd₃Fe and bcc PdIn were $a = 3.94\text{\AA}$, $a = 3.89\text{\AA}$, and $a = 3.3\text{\AA}$, respectively. The length of bulk tetragonal PdZn unit cell vectors were $a = 2.9\text{\AA}$ and $c = 3.42\text{\AA}$, while the vectors for orthorhombic Pd₂Ga unit cell were $a = 4.1\text{\AA}$, $b = 5.58\text{\AA}$ and $c = 7.82\text{\AA}$. To simulate the fcc (111) surfaces of Pd and Pd₃Fe, a 3x3x5 unit cell was used, while to simulate the core-shell structure of Pd₃Mn/Pd alloy surface, a 4x4x5 unit cell was used. For the 1:1 alloy surfaces of PdZn (101) and PdIn (110), a 2x3x5 unit cell was chosen. Finally, for the orthorhombic Pd₂Ga (010) surface, a 2x2x6 unit cell was simulated. The bottom two layers have been fixed for all alloy surfaces considered. A planewave energy cutoff of 400 eV was used with a 3x3x1 Monkhorst-Pack k-point grid for Pd (111), Pd₃Fe (111), PdIn (110), and PdZn (101) alloy surfaces, while a 2x2x1 k-point grid was used for Pd₃Mn/Pd (111) because of its larger unit cell size, and a 3x2x1 k-point grid was used for Pd₂Ga (010) due to its orthorhombic unit cell symmetry. These values were confirmed to converge the adsorption energies to within 0.05 eV. The adsorption properties and thermodynamic energy barriers on the surface were calculated using DFT geometry optimizations until the forces were converged within 0.02 eV/Å². All the calculations were spin polarized, and dipole corrections were used to cancel out the net dipole moment on the slab. The Methfessel–Paxton scheme was used with an energy smearing of 0.2 eV to determine the partial electron occupancies. Further, a vacuum of 20 Å was used to separate the two slabs in the z-direction. The activation barriers were determined with Climbing Image Nudged Elastic Band (CINEB) calculations using both the first and second order methods (QuickMin, LBFGS, and Dimer) developed by Henkelman and co-workers [217–220]. For the NEB calculations,

depending on the length of reaction coordinate, 6-8 images were used, and the images between initial and final states were generated using the Image Dependent Pair Potential (IDPP) method [221]. Finally, for the Density of States (DoS) calculations, an energy cutoff of 520 eV and a gamma-centered 9x9x1 k-point grid were used in conjunction with the tetrahedron method using Blöchl corrections.

The adsorption energies of open-shell species were calculated by referencing them to the corresponding gas phase closed-shell species energies and adding a stoichiometric amount of gas phase H₂. Therefore, the binding energies of dehydrogenated C₃, C₂, and C₁ species were estimated using gas phase propane, ethane, and methane energies, respectively. For each of these adsorbates, all the distinct binding configurations were generated using CatKit, a python based open-source framework developed by Boes et al. [222], and implemented with some modifications for binding of C₃ adsorbates. The geometry optimizations were then performed for all the sites and configurations, and the unique configurations were identified and databased for each adsorbate and catalyst surface using an in-house algorithm. The energies of the most stable structures were used for the analysis presented in this work.

4.4 Results

4.4.1 Structural Characterization

Detailed characterization of the particle size and phase composition of the Pd-In and Pd-Fe catalysts is detailed in references [199, 200], respectively. Herein, detailed characterization is given only for catalysts newly synthesized for this work: Pd-Ga, Pd-Mn and Pd-Zn though PdZn, which has been reported previously, was reproduced according to the synthesis given in reference [223].

Table 4.2 shows the number average particle size for the two monometallic Pd catalysts and five bimetallic Pd catalysts. Representative STEM and EDS maps are shown in Figure 4.10 of the supporting information and show the high dispersion of metal nanoparticles and the promoter. The 1% Pd catalyst was smaller in size than

the 2% Pd catalyst due to the high calcination temperature employed in the synthesis of the latter. The standard deviation of the 2% Pd catalyst was also larger due to the presence of both small particles and a significant number of large agglomerates likely resulting from the coalescence and sintering of smaller particles. The bimetallic samples all had particle sizes within one standard deviation of one another and were approximately 1.5-2 nm. Similar to the 2% Pd catalyst, the 2.5%Pd-2.5Ga catalyst contained both small 1.5 nm particles and larger (>5 nm) agglomerates, which is reflected in the larger standard deviation of the particle size.

Table 4.2.
Number average particle size for Pd and bimetallic catalysts

Sample	Number Average Particle Size (nm)
1Pd	1.4 ± 0.5
2Pd	3.7 ± 2.0
2Pd-3Zn	1.5 ± 0.7
2Pd-3In	1.8 ± 0.4
2.5Pd-2.5Ga	2.1 ± 1.6
2Pd-3Fe	1.5 ± 0.7
1Pd-5Mn	1.5 ± 0.5

Pd K edge EXAFS results for the Pd, Pd-Ga, Pd-Mn, and Pd-Zn catalysts are shown in Figure 4.1. For the monometallic Pd catalysts, the amplitude of the first shell scattering is attenuated relative to the Pd foil due to the large fraction of surface atoms in the sample which decreases the average coordination number below 12 for bulk fcc metals. No scattering from Pd-O is present, demonstrating that the catalyst is in the metallic state. Fitting the first shell scattering for 1Pd (shown in Table 4.3) gave a coordination number of 7.7 with a bond distance of 2.74 Å, which is consistent with a Pd nanoparticle. The 2Pd sample had a total coordination number of 10.4 at a bond distance of 2.74 Å.

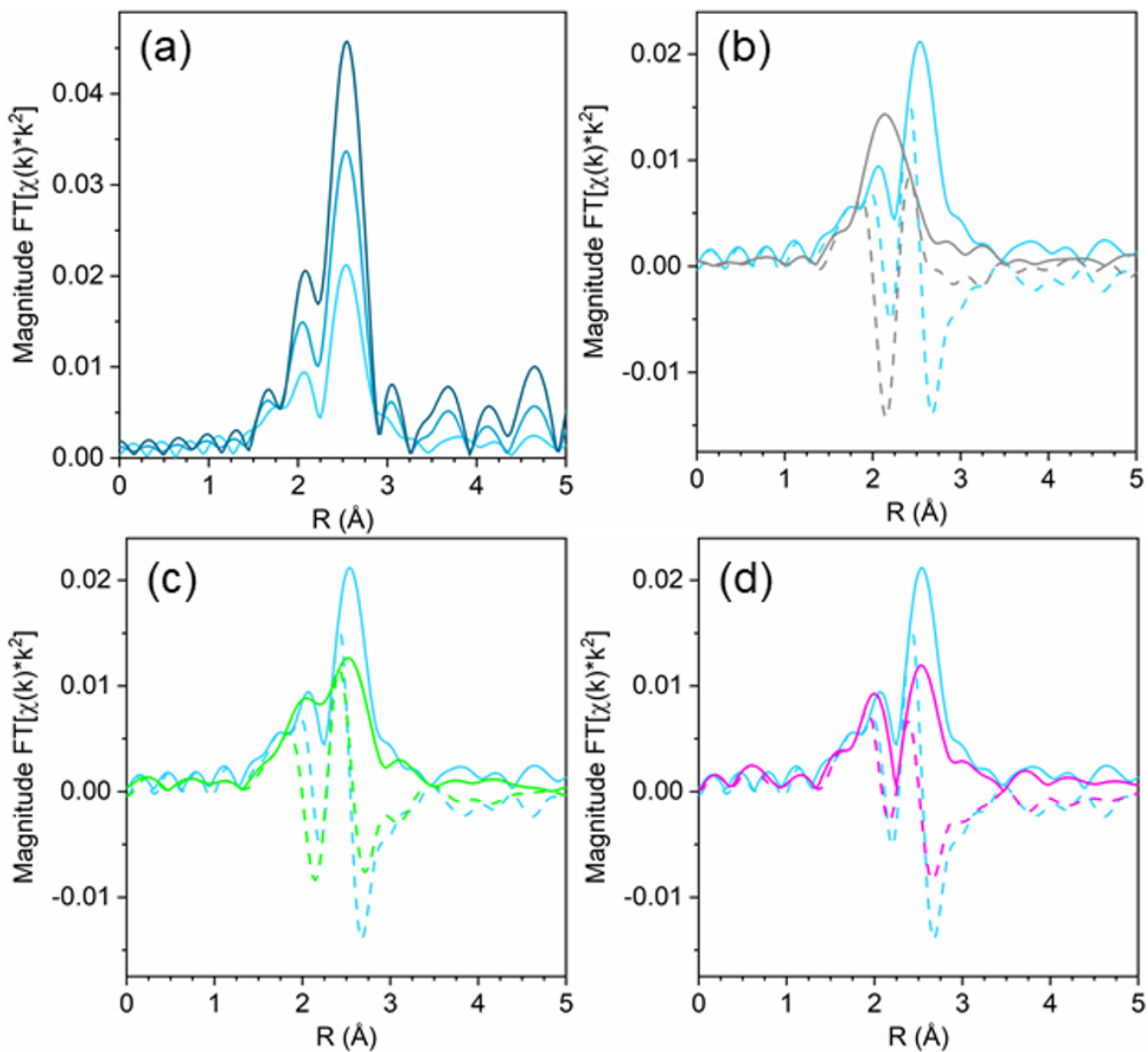


Figure 4.1. R space Pd K edge EXAFS magnitude (solid lines) and imaginary (dashed) components of Pd catalysts. (a) monometallic Pd catalysts: Pd foil (dark blue) 2Pd (blue) and 1Pd (light blue), (b) 2Pd-3Zn (grey) and 1Pd (light blue), (c) 2.5Pd-2.5Ga (green) and 1Pd (light blue), and (d) 1Pd-5Mn (magenta) and 1Pd (light blue). Spectra were collected at room temperature in He after reduction at 550 °C in 3.5% H_2 .

Table 4.3.
EXAFS fitting parameters for Pd foil, Pd, Pd-Mn, Pd-Ga, and Pd-Zn

Sample	Scattering Pair	CN	R (Å)	$\Delta\sigma^2$	E_0 (eV)
Pd Foil	Pd-Pd	12	2.75	0	0
1Pd	Pd-Pd	7.7	2.74	.0035	-1.3
2Pd	Pd-Pd	10.4	2.74	.0020	-1.8
1Pd-5Mn	Pd-Pd	6.1	2.71	.0050	-2.6
	Pd-Mn	1.4	2.66	.0050	-1.0
2.5Pd-2.5M	Pd-Pd	4.1	2.78	.0030	-3.6
	Pd-Ga	2.7	2.49	.0030	-3.7
2Pd-3Mn	Pd-Pd	1.0	2.81	.0020	-5.1
	Pd-Mn	4.1	2.54	.0020	-5.2

The first shell scattering envelope in 2Pd-3Zn, shown in Figure 4.1b, changes in shape relative to the monometallic Pd sample due to the formation of Pd-Zn bonds in the catalyst. The single R space peak is consistent with Pd having only nearest neighbor Zn. The broadness of the peak occurs due to an overlap between scattering from the first nearest neighbor zinc and single scattering from second nearest neighbor palladium. Fitting (shown in Table 4.3) gave 4.1 zinc neighbors at 2.54 Å and 1.0 Pd neighbors at 2.81 Å. The short Pd-Zn distance and long Pd-Pd distance is consistent with the structure expected for a 1:1 phase [206]. Two Pd-Zn phases with isolated Pd are known, differing only by a tetragonal distortion which changes the bond distance and coordination number of second nearest neighbor Pd. While the Pd-Pd bond under 3 Å is consistent with the β_1 phase, the ratio of Pd-Pd:Pd-Zn bonds is lower than expected for this phase (1:2), which would be consistent with a mixture of the structurally similar β (cubic CsCl) and β_1 (tetragonal CuTi) phases, though some departure from the bulk ratio should be expected due to the small particle size.

The first shell scattering envelope from 2.5Pd-2.5Ga bears resemblance to the monometallic Pd catalyst due to the presence of both Pd-Pd and Pd-Ga scattering. Pd-Pd scattering is comprised of three peaks, with the lowest intensity peak at the lowest R value and the highest peak at the highest R value. In the Pd-Ga catalyst, the second peak is much closer in intensity, relative to the third high R peak, as compared to the monometallic Pd sample due to scattering from Pd-Ga. Fitting of the 2.5Pd-2.5Ga catalyst gave a Pd-Pd coordination number of 4.1 at a bond distance of 2.78 Å and a Pd-Ga coordination number of 2.7 at a bond distance of 2.49 Å. The Pd-Ga: Pd-Pd coordination number ratio (0.66) is consistent with the local Pd environment in Pd₂Ga which has a Pd-Ga: Pd-Pd ratio of 5:8 (0.63).

Similar to the Pd-Ga catalyst, the 1Pd-5Mn catalyst also exhibited a change in shape of the first shell scattering envelope, showing two peaks close to the same intensity instead of three peaks of increasing intensity. The scattering resembles that of Pd-Fe [200], albeit with the first peak at low R being lower in intensity than the high R peak. Fitting the Pd-Mn catalyst gave a Pd-Pd coordination number of 6.1 with a bond distance of 2.71 Å and a Pd-Mn coordination number of 1.4 at a bond distance of 2.66 Å, indicating Pd-rich bimetallic particles.

The coordination number ratio in 1Pd-5Mn (0.23) does not match that of any bulk Pd-Mn phase. To further understand the structure of the catalyst, reduction-oxidation difference EXAFS was performed to examine the local Pd coordination in the surface layer of the nanoparticle [209]. Figure 4.2 shows the R space difference XAS spectra between the 1Pd-5Mn catalyst in the reduced state and after exposure to air at room temperature. Three peaks are present: the lowest R space peak is due to Pd-O scattering formed during the surface oxidation, while the two higher R peaks between 2-3 Å (phase uncorrected distance) are due to the loss of Pd-Mn and Pd-Pd bonds. Table 4.4 shows the fit of the difference spectra. The Pd-O coordination number was 0.4 at a bond distance of 2.05 Å, a bond distance typical for palladium (II) oxide. The surface Pd-Mn to Pd-Pd ratio from the difference is 0.56, significantly higher than the total nanoparticle ratio. The difference in Pd-Mn

to Pd-Pd ratio between the surface and fully reduced catalysts is consistent with a core-shell nanoparticle having a surface phase that is Mn rich with respect to the average particle composition [209].

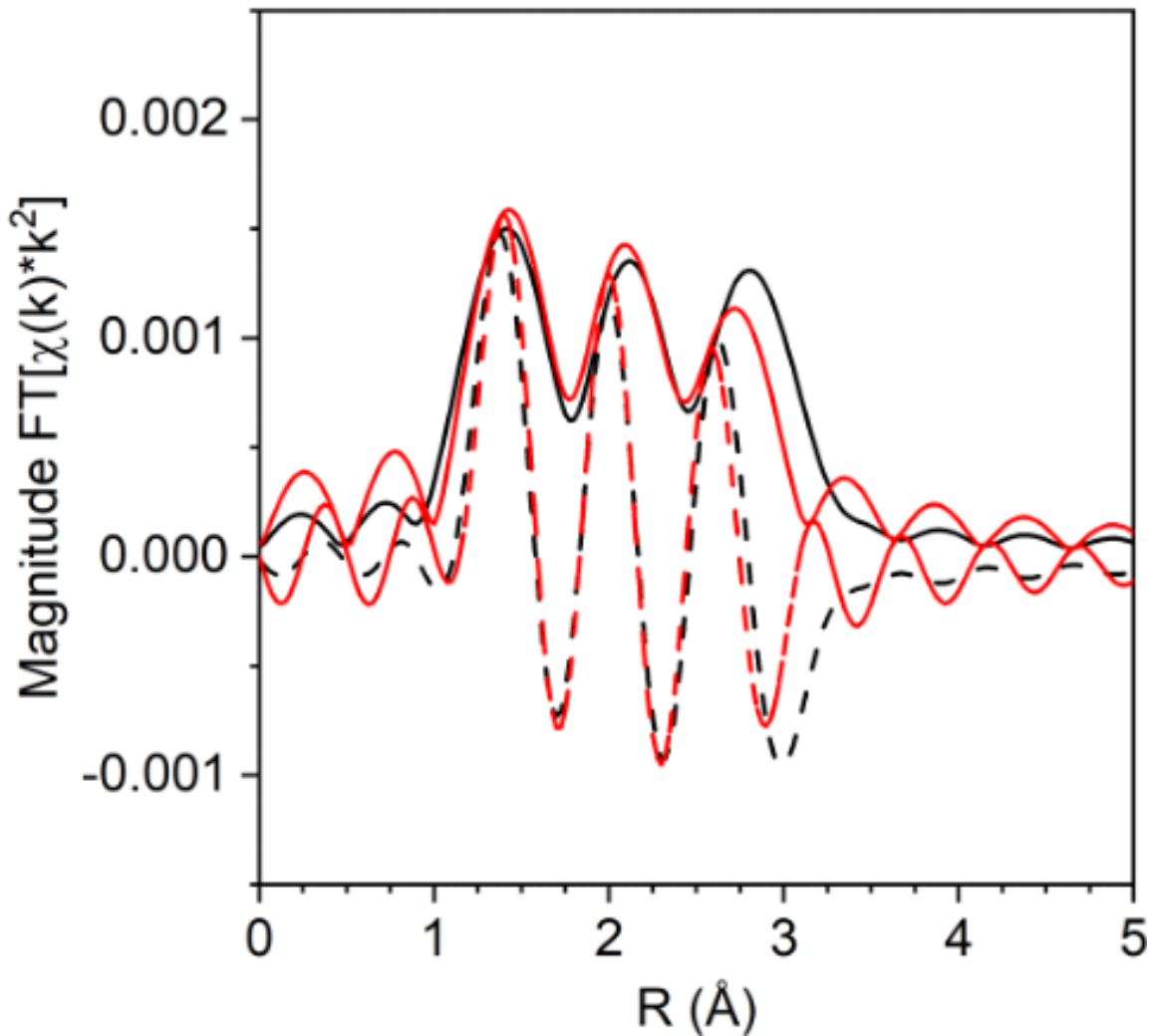


Figure 4.2. Reduction-Oxidation difference EXAFS of 1Pd-5Mn with the experimental difference magnitude (solid) and imaginary (dashed) shown in black and the difference fit shown in red.

To determine the phase composition of the catalysts suggested by the EXAFS fits, *in situ* synchrotron XRD was used. A high X-ray energy was used to maximize the difference in structure factor between the amorphous SiO₂ support and palla-

Table 4.4.
Reduction-Oxidation difference EXAFS fit of 1Pd-5Mn

Scattering Path	Coordination Number	Bond Distance (Å)	σ^2 (Å ²)	E_0 (eV)
Pd-O	0.4	2.05	0.002	2.3
Pd-Pd	0.9	2.73	0.004	-3.2
Pd-Mn	0.5	2.63	0.004	1.8

dium. The high flux provided by an insertion device allows for collection of data with sufficient signal-to-noise to resolve the small broad features from nanoparticles. Use of an *in situ* cell ensures that the entire nanoparticle remains in the metallic state during measurement; otherwise, the surface of the nanoparticle is oxidized during measurement, leading to misleading values of the particle size, NP structure, and lattice parameter [224].

Figure 4.3 shows the simulated patterns of known bulk Pd-Ga phases and the experimental pattern for the Pd-Ga catalyst. The experimental pattern, though significantly broadened due to the small particle size, matches that of Pd₂Ga, which has an orthorhombic Co₂Si structure. The pattern is inconsistent with monometallic Pd and other Pd-Ga alloy phases including Pd₅Ga₃, PdGa, and Pd₃Ga₇. The high X-ray energy used (105.7 keV) causes diffraction peaks to occur at lower 2θ and over a smaller 2θ range than is typical of a laboratory XRD instrument. The XRD result is consistent with the EXAFS results which show Pd having a neighbor ratio (Pd-Ga: Pd-Pd) consistent with that of Pd₂Ga, in which Pd has 5 Ga neighbors and 8 Pd neighbors. Simulated Pd₂Ga patterns with different crystallite sizes (Figure 4.11) estimate a particle size close to 3 nm.

Figure 4.4 shows simulations of the bulk Pd-Zn phases and the experimental pattern for 2Pd-3Zn. Similar to the Pd-Ga catalyst, the diffraction peaks in the Pd-Zn catalyst are broadened due to the small particle size. Four distinct peaks are resolved, though some are asymmetric due to peak overlap. The pattern largely matches that

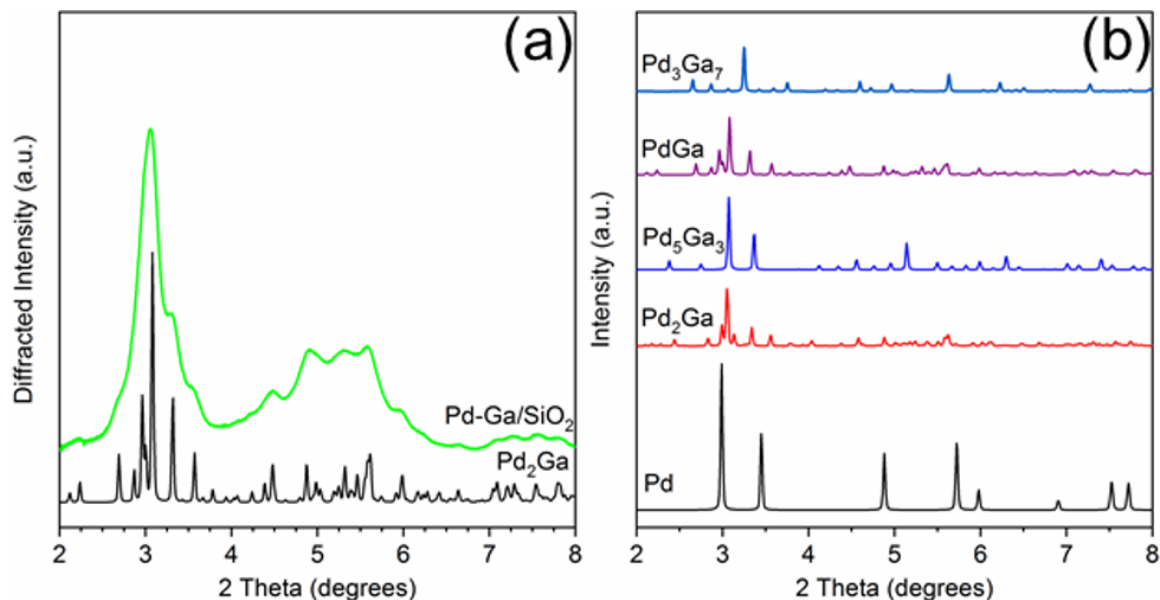


Figure 4.3. (a) *In situ* synchrotron XRD pattern for 2.5Pd-2.5Ga (green) after a reduction treatment at 550 °C in 3.5% H₂ with simulated Pd₂Ga pattern (black), and (b) simulated bulk patterns for Pd-Ga intermetallic compounds.

of the β_1 -PdZn phase, which has a tetragonal unit cell and body centered symmetry. However, there is some peak misalignment between 4-6 degrees which suggests some distortion from the a/c lattice parameter ratio expected for bulk β_1 Pd-Zn (1.147). Evidence of this is seen in the EXAFS bond distances, where the Pd-Pd bond distance is contracted 3.1% from the bulk value whereas Pd-Zn is contracted 3.8% giving a c/a ratio of 1.126. The tetragonal distortion also decreases when zinc partially substitutes at palladium sites, which leads to a cubic CsCl structure ($c/a = 1$) and a Pd-Zn/Pd-Pd coordination number ratio higher than 2 [206]. The poor separation and peak asymmetry in the diffraction peaks at 4.55 and 5.45 degrees is more consistent with the β_1 , which has multiple peaks in this region, in contrast to the β phase, which only has one weak peak. However, the β phase may be present as a minor impurity, or the particle composition may be off-stoichiometric (Zn rich) leading to a smaller tetragonal distortion than expected. Monometallic Pd and other non 1:1

Pd-Zn phases do not match the measured diffraction pattern of 2Pd-3Zn. The assignment of a 1:1 PdZn phase is consistent with the EXAFS results which show only zinc nearest neighbors and a second nearest neighbor Pd at a long bond distance. Previous reports of Pd-Zn bimetallics synthesized by sequential incipient wetness impregnation have also shown the formation of the β_1 -PdZn phase [225].

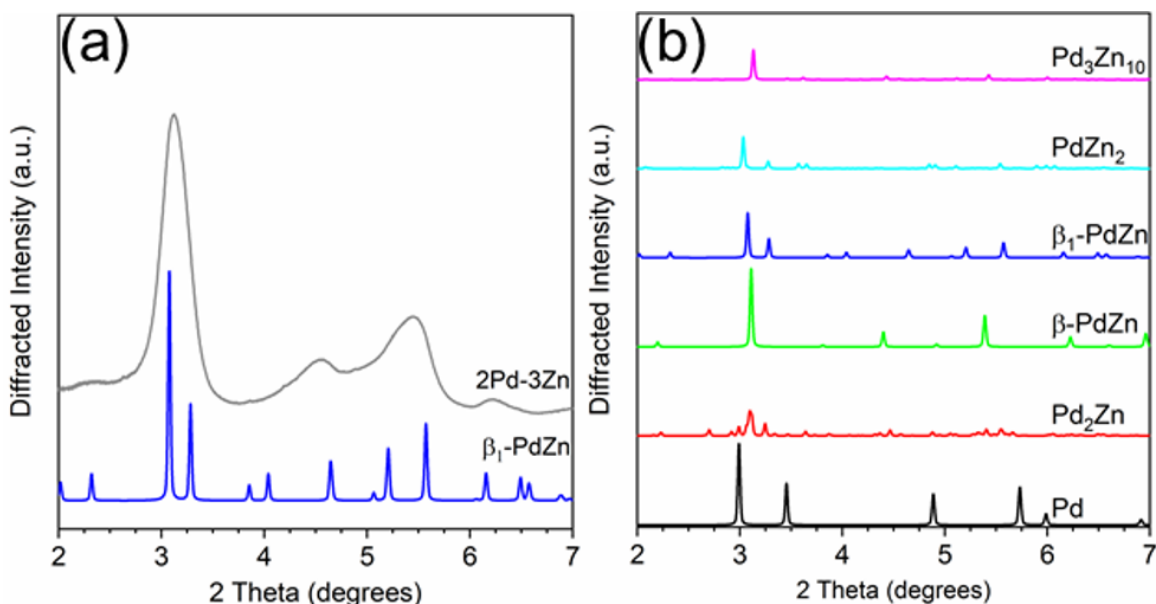


Figure 4.4. (left) simulations of bulk PdZn phases and (right) experimental in-situ synchrotron XRD pattern for the Pd-Zn catalyst (grey) along with simulated pattern for the β_1 -PdZn phase.

4.4.2 Propane Dehydrogenation

Figure 4.5 shows the initial propylene selectivity at different levels of initial propane conversion for Pd and Pd alloy catalysts reported on a carbon basis of gas phase products. Catalyst tests were performed with cofed hydrogen as a more demanding test of catalyst selectivity, since the latter is required for hydrogenolysis. It was also necessary to cofed hydrogen to improve the stability of the monometallic Pd catalysts which otherwise deactivated too rapidly to properly extrapolate conversion and selec-

tivity to zero time on stream. A 1:1 ratio of propane to hydrogen gave deactivation rate constants (Table 4.5) of the same order of magnitude for Pd and Pd alloy catalysts which allowed for initial conversion and selectivity to be properly determined. The main products were propylene, methane, ethane and ethylene, the latter three resulting from hydrogenolysis. For all alloy catalysts, the carbon balance was in excess of 98% for all tests, and hence the contribution of coke formation to selectivity has been neglected. For the palladium catalysts, the carbon balance decreased from 98% at <5% conversion to 83% at 20% conversion. For consistency, the selectivity and conversion for both palladium catalysts is reported for gas phase products, though this overestimates the selectivity at high conversions. The 2% Pd catalyst (4 nm) shows poor selectivity, 70%, at differential conversion, and as the conversion is increased, the selectivity quickly drops to around 25% at 20% conversion. The 1% Pd catalyst (1.5 nm) shows much higher selectivity at equivalent conversion compared to the 2% Pd catalyst which demonstrates the effect of particle size on the rate of hydrogenolysis. The selectivity of the 1% Pd catalyst is high ($\sim 100\%$) at differential conversion but decreases with increasing conversion, falling to 70% at 20% conversion.

Table 4.5.
Dehydrogenation rate, first order deactivation rate constants, and activity loss after 90 minutes of reaction for Pd and Pd alloy catalysts

Sample	Dispersion	Propylene TOR (s^{-1})	Selectivity at 20% Conversion	Deactivation Rate Constant (10^{-3} min^{-1})	Activity Loss After 90 Minutes (%)
2Pd-3Zn	0.13	0.30	100	3.3	52
2Pd-3In	0.15	0.25	96	2.3	39
2.5Pd-2.5Ga	0.08	0.20	92	4.0	64
2Pd-3Fe	0.08	0.40	91	6.0	62
1Pd-5Mn	0.10	0.26	91	6.3	48
2Pd	0.18	0.03	25	3.2	54
1Pd	0.35	0.05	70	8.6	80

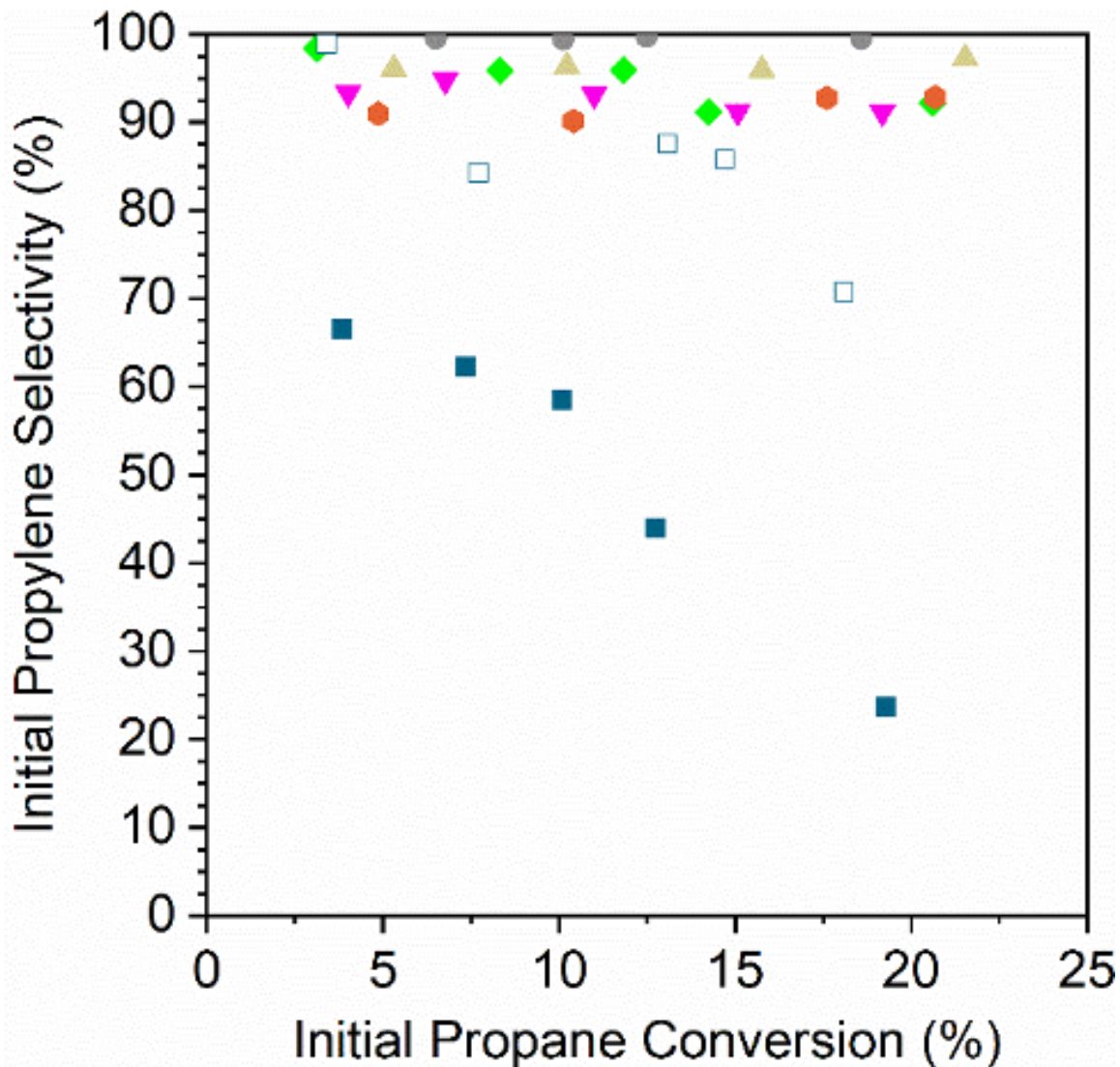


Figure 4.5. Initial propylene conversion for 2Pd-3Zn (grey circles), 2Pd-3In (tan triangles), 2.5Pd-2.5Ga (green diamonds), 1Pd-5Mn (magenta inverted triangles), 2Pd-3Fe (orange hexagons), 1Pd (open dark blue squares), and 2Pd (filled dark blue squares) plotted against the initial propane conversion. Tests were performed at 550 °C in 2.5% H₂ and 2.5% propane after pre-reducing in 550 °C in 5% H₂.

In comparison, the alloy catalysts have selectivity above 90% across the conversion range tested, and there is little change in selectivity with increasing conversion. For

2Pd-3Zn, the selectivity was above 99% up to 20% conversion. The 2Pd-3In catalyst selectivity also did not decrease with conversion, but the selectivity was slightly lower than the 2Pd-3Zn catalyst at 96%. The 2.5Pd-2.5Ga catalyst showed a small decrease in selectivity, falling from 98% at 3% conversion to 92% at 20% conversion. The 1Pd-5Mn catalyst had a lower selectivity than the Pd-Zn and Pd-In catalysts, between 95-91%. The 2Pd-3Fe catalyst also did not decrease in selectivity with increasing conversion, but the selectivity was constant at a lower value (91%).

In order to measure dehydrogenation turnover rates, the percentage of surface palladium was measured by surface oxidation difference XAS. Exposing the fully reduced catalyst to air at room temperature causes the surface Pd to oxidize, which can be seen by XAS as Pd-O scattering. In catalysts containing both metallic and Pd-O scattering, the Pd-O coordination number represents the phase fraction of surface Pd which is accessible to oxygen weighted by the natural coordination number of palladium oxide, which has 4 Pd-O bonds. Thus, the Pd-O coordination number divided by 4 gives the palladium dispersion without the confounding effects which would occur in H₂-O₂ titration or CO chemisorption caused by absorption or redox of the promoter. Fits of the oxidized catalysts are shown in Table 4.9 of the Supporting Information. The method closely matches the dispersion measured by CO chemisorption for the Pd-In catalyst as reported previously [199].

Table 4.5 shows the propylene turnover rate for the Pd and Pd alloy catalysts. The monometallic Pd catalysts have a low turnover rate: 0.03 s⁻¹ for the 2Pd catalyst, which has a large particle size, and 0.05 s⁻¹ for the 1Pd catalyst, which has the same particle size as the alloy samples. The alloy catalysts have propylene turnover rates 4-8 times higher than the monometallic Pd catalyst of the same size. Between the alloys, the propylene turnover rates only varied by a factor of two.

4.4.3 Density Functional Theory

To further understand the catalytic trends in the different alloys considered, Density Functional Theory (DFT) calculations were carried out on model surfaces of each

alloy. These calculations were performed on the most stable terrace surfaces corresponding to the respective bulk alloy structures found by XRD experiments. For alloy phases with fcc structures (Pd, Pd₃Fe), the (111) facet was used, for the body centered cubic (bcc) PdIn, the (110) surface was used, and for body centered tetragonal β_1 -PdZn, the (101) surface was used. Pd₂Ga has a low symmetry orthorhombic crystal structure composed of two symmetrically equivalent flat layers stacked along the $\langle 010 \rangle$ direction. These (010) terrace surfaces, which have a stoichiometry matching the bulk, were analyzed, and the same surface has been modeled previously for semi-hydrogenation of acetylene [226]. There are two crystallographically distinct Pd sites within Pd₂Ga (hereafter denoted Pd₁ and Pd₂), whereas all other alloys have a single crystallographic Pd site. To simulate the core shell structure of Pd₃Mn/Pd, Pd atoms were replaced with Mn atoms in the first two atomic layers of the slab, corresponding to the ordering of Pd₃Mn with AuCu₃ structure that is consistent with the surface EXAFS CN ratio. We note, in passing, that although the absolute values of turnover rates will vary between the terraces and other surface features, such as steps, the trends in binding energies, activation energies, and selectivities between alloys are likely to be similar on other surface features, assuming that Pd ensemble sizes are similar to the terraces.

Figure 4.6 shows the binding sites for the slab models. For monometallic Pd, four adsorption sites were considered: onefold ontop, twofold bridge, threefold hcp, and threefold fcc. In the fcc alloy systems, additional promoter ontop, Pd-M bridge, and threefold sites containing two Pd and one promoter atom were also considered. As the ratio of alloy composition changes from 3:1 to 1:1, the Pd atoms become completely surrounded by the promoter atoms, where Pd atoms now have promoter atoms as their only nearest neighbors (Zn, In). This leads to loss of Pd-only threefold sites for the 1:1 alloy surfaces; while all other sites are the same as the adsorption sites on 3:1 fcc alloys. Due to the low symmetry of the Pd₂Ga (010) surface, a relatively large number of distinct adsorption sites exist. On this surface, hollow sites can

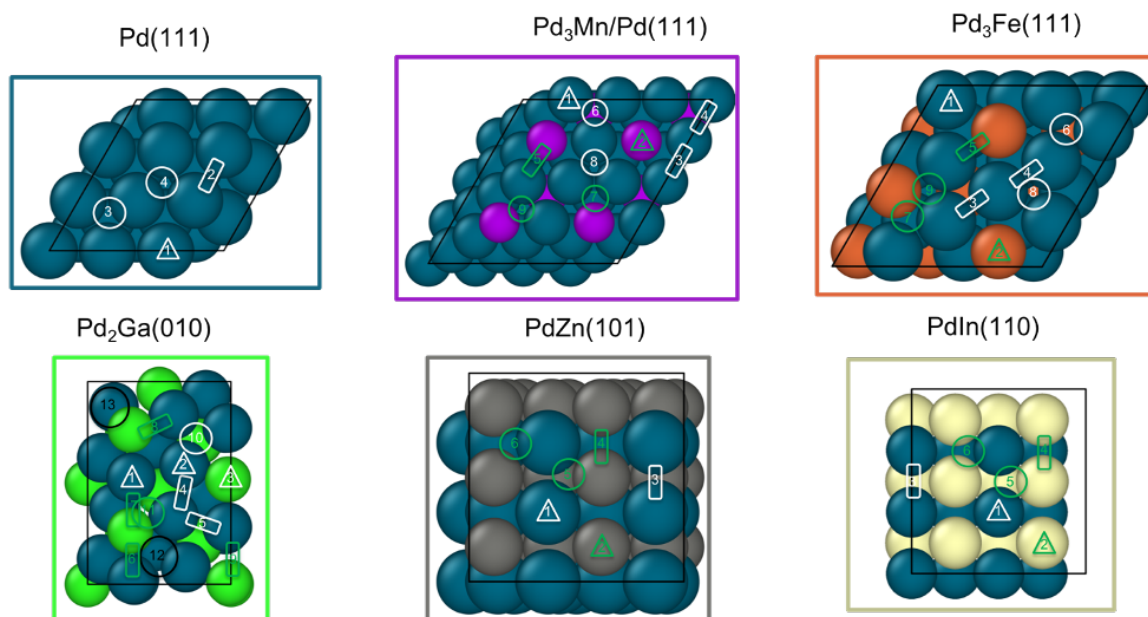


Figure 4.6. Adsorption sites for Pd and Pd alloy slabs. Ontop sites are denoted by triangles, bridge sites by rectangles, and adsorption sites involving three or more atoms by circles. Sites marked in white involve direct bonding only to Pd atoms, while those in green indicate that the site involves a promoter atom. The black circles in Pd₂Ga indicate bonding at a fourfold site.

additionally be formed by four atoms which leads to a total of three ontop sites, five bridge sites, two threefold hollow sites and two fourfold sites.

4.4.3.1 Adsorption Energies

Adsorption energies and geometries of selected intermediates, including propylene, hydrogen, and ethylidyne, are reported in Tables 4.6 and 4.7. These species are representative of both propylene and deeply dehydrogenated intermediates in the PDH reaction network (corresponding results for propyne, propynyl, methylidyne, and carbon are reported in Table 4.11). As is discussed further below, the energetics of these species closely track trends in the propylene selectivity across the space of considered Pd alloys.

Table 4.6.

Binding energies of adsorbates on Pd and Pd alloy surfaces, with more positive values indicating weaker adsorption. The binding energies of open-shell species (hydrogen, ethylidyne), are referenced to the corresponding gas phase species (H_2 , ethane).

Adsorbate Binding Energy (eV)	Pd (111)	Pd ₃ Mn/Pd (111)	Pd ₃ Fe (111)	Pd ₂ Ga (010)	PdZn (101)	PdIn (110)
Propylene	-0.79	-0.73	-0.49	-0.48	-0.13	-0.06
Hydrogen	-0.63	-0.55	-0.46	-0.43	-0.25	0.03
Ethylidyne	0.96	1.35	1.54	1.98	2.96	3.18

The adsorption energies of all the intermediates considered are weaker on the Pd alloys as compared to monometallic Pd. Propylene is most stable on the bridge site on the Pd (111) surface (binding energy of -0.79 eV), where it takes a di-sigma configuration (Figure 4.13). Compared to gas phase propylene, the carbon-carbon double bond is elongated from 1.34 Å to 1.45 Å, indicating that the propylene π bond is significantly weakened upon adsorption. On Pd₃Mn/Pd, the binding energy weakens slightly to -0.73 eV, while the most stable adsorption geometry remains

Table 4.7.
Most stable binding sites of adsorbates on Pd and Pd alloy surfaces.
The numbers in parentheses refer to sites as labeled in Figure 4.6.

Adsorbate	Binding Site	Pd (111)	Pd ₃ Mn/Pd (111)	Pd ₃ Fe (111)	Pd ₂ Ga (010)	PdZn (101)	PdIn (110)
Propylene		Pd-Pd bridge (2)	Pd-bridge (3)	Pd ontop (1)/ Pd-Pd bridge (3)	Pd ontop (2)	Pd ontop (1)	physisorbed
Hydrogen		fcc (4)	Pd-Pd-Pd hcp (6)	Pd-Pd-Pd (6)	hcp (10)	Pd-Pd bridge (3)	Pd-Pd bridge (3)
Ethylidyne		hcp (3)	Pd-Pd-Pd hcp (6)	Pd-Pd-Fe fcc (9)	Pd-Pd-Pd hcp (10)	Pd-Pd-Zn hcp (5)	Pd-Pd-In hcp (5)

di-sigma. The binding of propylene is weakened by 0.3 eV on Pd₃Fe and Pd₂Ga surfaces, while for the site isolated alloys PdZn and PdIn, the binding is weakened by 0.66 eV and 0.73 eV, respectively. On Pd₃Fe, propylene binds to both ontop-Pd and bridge Pd-Pd with similar stability, whereas the most stable configuration shifts from bridge Pd-Pd to ontop-Pd for the two post-transition metal alloy surfaces, Ga and Zn. On the PdIn (110) surface, propylene is physisorbed. These results show that the propylene binding energies and adsorption geometries are strongly affected by increases in the promoter content of the alloys.

The most stable adsorption site for the hydrogen atom on pure Pd (111) is the threefold fcc site. The binding energy of hydrogen is weakened by 0.1 eV on core-shell Pd₃Mn/Pd, while the corresponding weakening is approximately 0.2 eV on Pd₃Fe and Pd₂Ga surfaces. The most stable adsorption site for hydrogen is the hollow site composed of three Pd atoms for all alloy surfaces that contain such sites (Pd₃Mn, Pd₃Fe and Pd₂Ga). Similar to the case of propylene, the weakening in H binding for the 1:1 PdZn and PdIn surfaces, which do not contain threefold Pd sites, is even larger (0.38 eV and 0.66 eV, respectively), and the most stable binding site shifts to bridge Pd-Pd.

Ethylidyne, a dehydrogenated C_2 intermediate and product of propyne and propynyl hydrogenolysis, is most stable on the threefold hcp site on the Pd (111) surface (Figure 4.14). The binding energy is weakened by 0.39 eV, 0.58 eV, and 1.02 eV for Pd_3Mn/Pd , Pd_3Fe , and Pd_2Ga terraces, respectively. Ethylidyne is adsorbed on threefold Pd hcp sites on Pd_3Mn/Pd and Pd_2Ga , but on the Pd_3Fe terrace, the site preference changes to the fcc site that contains an iron atom and two palladium atoms (adsorption at the hcp hollow site composed of three palladium atoms is less favorable by 0.1 eV). The weakening in adsorption energies is considerably larger for the 1:1 $PdZn$ and $PdIn$ surfaces, at 2.22 and 2.00 eV, respectively. On these alloys, ethylidyne is most stable on the hcp Pd_2X sites where the unfavorable interaction of the adsorbate with the promoter atom (In, Zn) contributes to the weakened adsorption. The binding energy trends for propyne, propynyl, methylidyne and carbon on the alloy surfaces (Table 4.11) are similar to those observed for ethylidyne.

We note that unusual binding geometry of ethylidyne, which involves partial coordination to surface Fe atoms on the Pd_3Fe alloy surface, can be straightforwardly understood in terms of the affinity of deeply dehydrogenated carbon-containing species for Fe. To illustrate this point, adsorption energies on the bcc Fe (110) terrace surface (Table 4.12) have also been calculated. The binding of ethylidyne, along with other deeply dehydrogenated intermediates, was found to be 0.5-1 eV stronger than on Pd (111).

The trends in binding energy shifts are also influenced by electronic changes in the Pd atoms, consistent with the d -band model of metal and alloy surfaces [227,228], where the Pd alloys with the Pd d -band center shifted furthest from the fermi level ($PdZn$, $PdIn$) showed the largest shifts in adsorption energies. The first and second moments of the d -band for Pd and Pd alloys are given in Table 4.10. Experimental evidence for electronic modification of Pd was seen in the Pd L_3 and K edge XANES of the catalysts, which showed small changes in the edge energy and white line shape. In particular, the L_3 edge XANES, which probes the $4d$ and $5s$ unfilled states, gives direct evidence of this electronic modification which manifests as a

change in the whiteness shape in the alloys relative Pd. The modifications are a result of the heteroatomic bonds in each alloy which modify the Pd density of states, as was demonstrated computationally. Pd L_3 edge XANES spectra are given in Figure 4.12 of the supporting information.

4.4.3.2 C-H and C-C Bond Activation

A commonly used selectivity descriptor for alkane dehydrogenation reactions is the energy difference between the alkene desorption energy and the alkene dehydrogenation barrier, which has been linked to the selectivity trends for propane dehydrogenation on Pt alloys [197]. Propylene dehydrogenation barriers have been estimated on all the Pd alloy surfaces and are depicted in Figure 4.7 and Table 4.8. The dehydrogenation barrier is seen to increase as the promoter content in the alloy increases. The increase in barrier, as compared to Pd (111), is highest for the PdIn surface (~ 0.66 eV increase), while the smallest change is on Pd₃Mn/Pd (0.1 eV increase). The transition states for these C-H bond breaking steps are shown in Figure 4.15. On all of the alloy surfaces, the dissociated H atom is on the ontop site of Pd, which then shifts to either a hollow site or the bridge site at the final state, depending on the alloy composition. On the other hand, the product propenyl species are close to their most stable sites (a hollow site or a bridge site) and only require a small rotation towards their most stable configurations in the final state. Hence, the reaction coordinate involves a three atom Pd ensemble for the pure Pd, 3:1, and 2:1 Pd alloy surfaces, while a one atom Pd site is required on the 1:1 alloy surface.

An approximate selectivity descriptor was calculated from the difference between the propylene adsorption energy (Table 4.6) and the propylene dehydrogenation barrier (Table 4.8). More negative selectivity descriptor values indicate more favorable energetics for propylene desorption compared with further dehydrogenation. As the promoter content increases, the selectivity descriptor becomes more negative, suggesting higher selectivity on the indicated alloys. Monometallic Pd had the most positive value of the selectivity descriptor, corresponding to the lowest predicted selectivity,

in line with experimental results. In comparison, the Pd₃Fe and Pd₂Ga alloys have more negative values (change is ~ 0.5 eV in comparison to the Pd) which are reflected in the measured increase in selectivity to 92%. Interestingly, for the core-shell Pd₃Mn/Pd alloy, the selectivity descriptor increases by only 0.2 eV compared to Pd, but the selectivity increase is comparable to the other 3:1 alloy, Pd₃Fe. Finally, the largest negative values of the selectivity descriptor are for the 1:1 PdIn and PdZn alloys (change is ~ 1 eV in comparison to Pd), in agreement with highest selectivities (96%, 100%) obtained in our experiments. In general, the primary contributor to these trends in the selectivity descriptor is the change in binding energies of propylene. Changes in C-H bond breaking barriers are smaller; in all alloys except PdIn, the propylene dehydrogenation barriers differ from that of Pd by less than 0.3 eV.

Table 4.8.

Propylene dehydrogenation activation energy barrier, propylene selectivity descriptor, and activation energy barriers for C-C bond cleavage of propynyl for Pd and Pd alloys.

Surface	Propylene Dehydrogenation Barrier (eV)	Selectivity Descriptor (eV)	Propynyl C-C Bond Breaking Barrier (eV)
Pd (111)	0.98	-0.19	1.23
Pd ₃ Mn/Pd (111)	1.10	-0.37	1.97
Pd ₃ Fe (111)	1.23	-0.74	1.28
Pd ₂ Ga (010)	1.12	-0.64	2.30
PdZn (101)	1.29	-1.16	3.62
PdIn (110)	1.66	-1.60	3.13

In addition to the selectivity descriptor introduced above, recent work from Saerens et al. on Pt (111) suggests that C-C bond breaking in C₃ species formed from deep dehydrogenation of propylene is also kinetically relevant for unselective formation of byproducts, including methane, ethane, and ethylene [193]. To probe the significance of these reactions for Pd and Pd alloys, the C-C bond breaking barriers of propyne

(C_3H_4) and propynyl (C_3H_3) on the alloy and pure metal surfaces were calculated. The trends are very similar for both intermediates, and only the analysis for propynyl is discussed in the main text (the corresponding analysis for propyne is presented in Table 4.13).

C-C bond activation in propynyl leads to the formation of carbon (C_1) and ethynidyne (C_2) species which can further hydrogenate to form methane and ethane, respectively. Alternatively, the adsorbed C_1 and C_2 species can dehydrogenate or polymerize to form coke on the surface [229]. The trends in barriers (Table 4.7) show that, as the promoter content increases, the C-C bond breaking barrier also increases, except for Pd_3Fe (111), where the barrier is closer to that on the Pd (111) surface. This smaller change in barrier for Pd_3Fe can be attributed to the favorable binding of deeply dehydrogenated species in the threefold Pd_2X sites.

The transition states for propynyl C-C bond breaking for all the considered alloy surfaces (Figure 4.16) show that the product ethynidyne and carbon species are close to each other and are in the process of shifting towards their stable configurations on adjacent hollow sites. For the alloy surfaces, due to the extended nature of transition state, either carbon or ethynidyne must bond with a hetero-promoter atom at the transition state. Indeed, it appears that a four or five surface atom ensemble is involved at the transition state, which is in contrast to the C-H bond breaking in propylene (discussed above), where a one or three atom ensemble was involved. This increase in the number of surface ensemble atoms associated with the transition state, and the consequent contact between the transition state structure and heteroatoms on the alloys, offers an explanation for the larger increase in the C-C bond breaking barriers on alloy surfaces in comparison to the corresponding increases in C-H bond breaking barriers. A reaction coordinate of all selectivity-relevant elementary steps, including C-H and C-C bond cleavage, is shown in Figure 4.7.

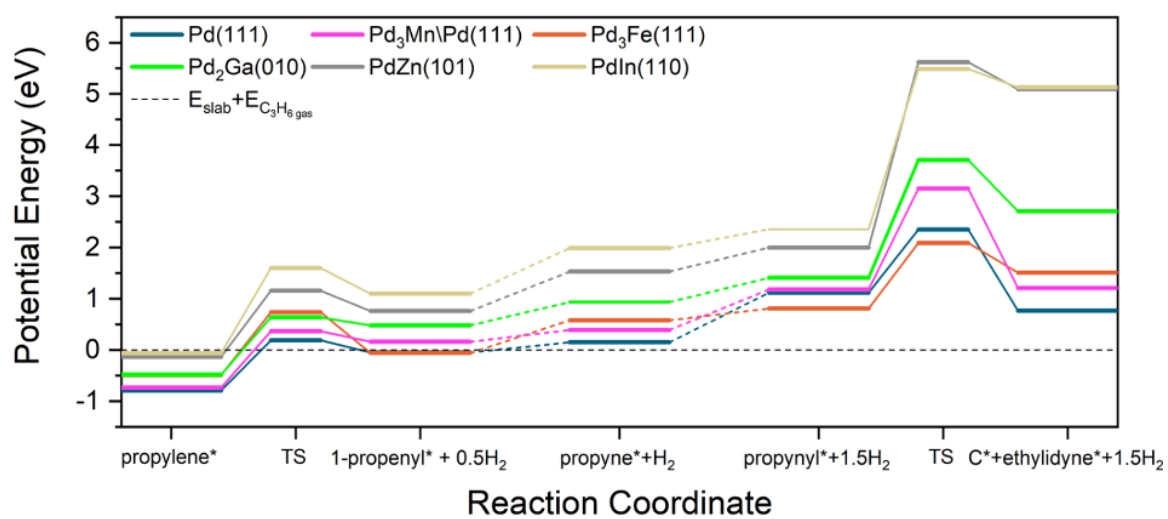


Figure 4.7. Reaction coordinate diagram for propylene dehydrogenation and propynyl hydrogenolysis.

4.5 Discussion

4.5.1 Catalyst Structure

The catalyst structure of 2Pd-3Fe and 2Pd-3In are detailed in references [199,200]. The 2Pd-3Fe catalyst is a pure phase Pd₃Fe alloy, based on the *in situ* synchrotron XRD pattern and matching atomic Pd environment measured by XAS. The Pd-In catalyst had a Pd core and alloy shell of the cubic PdIn phase with a CsCl structure. The XRD pattern for 2Pd-3Zn showed that palladium and zinc form the β_1 -PdZn alloy phase, though it may contain an impurity phase of the closely related β phase or be slightly Zn rich. The formation of the β_1 -PdZn phase in nanoparticle bimetallic Pd-Zn catalysts has been reported and is consistent with the present results [223,225]. Consistent with the XRD result, the Pd K edge EXAFS showed exclusively Pd-Zn nearest neighbors and Pd-Pd scattering at an elongated distance. The 2.5Pd-2.5Ga catalyst was verified to form the Pd₂Ga phase with the Co₂Si structure, consistent with other literature reports on Pd-Ga bimetals [230]. The Pd K edge EXAFS reflected the Pd₂Ga structure in the Pd-Ga: Pd-Pd coordination number ratio which closely matched that of Pd in Pd₂Ga. The 1Pd-5Mn formed a Pd-Mn bimetallic, as shown by EXAFS, but the low Pd loading and small particle size did not allow for collection of XRD spectra, even by synchrotron XRD. The catalyst was verified to have a core shell structure by difference XAS, which showed that the particle shell is manganese rich with respect to the total particle composition. The Pd-Mn/Pd-Pd neighbor ratio in the nanoparticle matched that of Pd₃Mn, which has an AuCu₃ structure. The formation of a shell layer of intermetallic also occurred in 2Pd-3In, and has been reported for other nanoparticle alloy systems [231,232]. The structural model, unit cell and slab model of each catalyst is summarized in Figure 4.8.

4.5.2 Selectivity Trends in Pd Alloys

Testing each catalyst under equivalent propane dehydrogenation conditions clearly distinguished between the rate and selectivity of Pd and the alloys and showed a

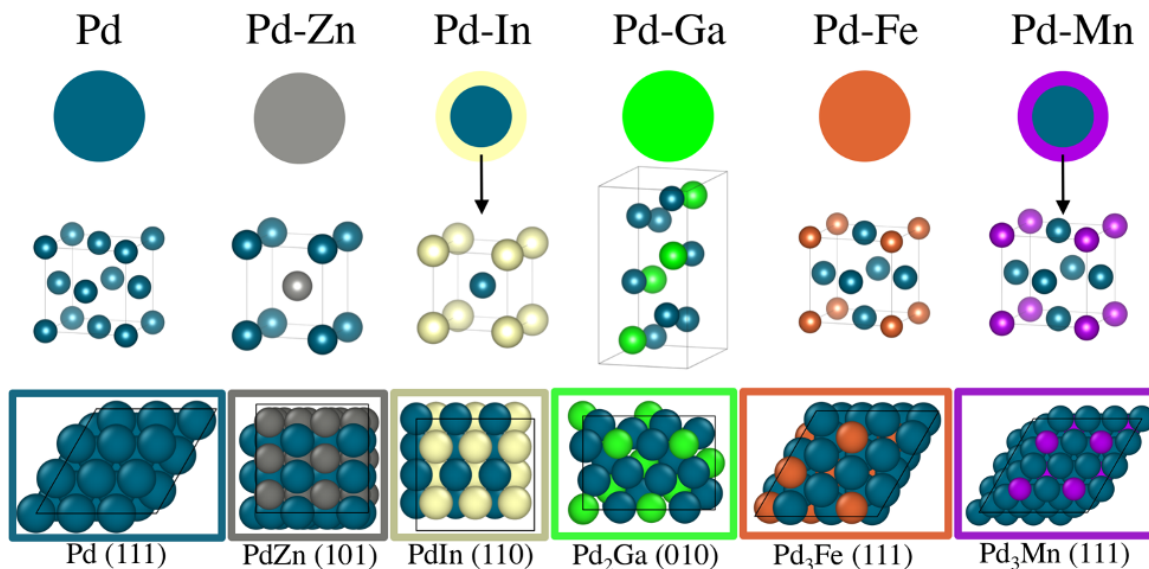


Figure 4.8. Structural model of Pd and Pd alloy catalysts. The PdIn and PdMn catalysts have alloy shells with a Pd core, while the PdZn, PdGa and PdFe catalysts are pure phases. The unit cell of each alloy structure and the lowest energy surface are pictured beneath the respective nanoparticle models.

smaller difference between the selectivity of alloys with and without Pd site isolation. Although all Pd alloy catalysts are significantly more selective than monometallic Pd, there are differences in selectivity depending on the structure and number of adjacent Pd atoms in the surface ensembles. Among the alloy catalysts, the site isolated alloys β_1 -PdZn and PdIn have the highest dehydrogenation selectivity. The selectivity of the Pd₂Ga, which has distorted threefold sites where the three atoms are no longer equidistant from one another (as is the case with Pd and the Pd₃M alloys), was close to that of the 3:1 alloys. The Pd₃Fe and Pd₃Mn alloys, with threefold Pd ensembles, show the lowest selectivity among the alloys. The difference in selectivity from the most selective alloy (PdZn) and the least selective alloys (Pd₃Mn, Pd₃Fe) was approximately 10%, with all alloys showing selectivity at 20% conversion above 90%. The initial dehydrogenation turnover rate for the alloys only varied by

a factor of two, and such a small difference should be considered within the error of reproducibly determining turnover rates in a reaction with fast deactivation [233]. Because all the dehydrogenation turnover rates for the alloys are similar, and carbon balances for the alloys showed a negligible amount of coke formation, the difference in selectivity comes from changes the rate of hydrogenolysis, which we define as all elementary steps involving reaction of propylene or more deeply dehydrogenated intermediates. An increase in selectivity from 90% to 99% requires that the rate of hydrogenolysis decrease by about an order of magnitude, with the dehydrogenation rate being constant. Thus, while the difference in selectivity between the site isolated alloys and those without is moderate, the difference in the hydrogenolysis rate is large.

As the hydrogenolysis rate largely determines the selectivity ranking of the alloys, DFT modeling efforts were focused on two different steps in the reaction. First, as discussed above, the previously established selectivity descriptor involving the propylene dehydrogenation barrier was determined (Table 4.8). The dehydrogenation of propylene is the first step in the hydrogenolysis reaction network, and the selectivity descriptor compares the relative favorability of propylene dehydrogenation and propylene desorption. Alloys with the highest promoter content (PdIn, PdZn) had the most negative value of the selectivity descriptor (predicting favorable propylene desorption over dehydrogenation), while the magnitude was lower for alloys with lower promoter content. Although the highest negative value of the selectivity descriptor is for the PdIn alloy, the experimentally observed selectivity is highest for PdZn. Additionally, the 0.2 eV decrease in the selectivity descriptor value from Pd to Pd₃Mn causes an increase in selectivity from 70% to 91%, yet a further 0.4 eV decrease from Pd₃Mn to Pd₃Fe does not alter the selectivity. These results suggest that the selectivity descriptor can qualitatively describe the trends in observed experimental selectivity, but the value should not be used to quantitatively rank alloys with similar structures. It can, however, clearly distinguish the selectivity changes observed experimentally between 3:1 and 2:1 (Pd-rich) alloys (91%-93%) with the 1:1 (site-isolated) alloys (97%-100%).

Another important elementary step in hydrogenolysis is the C-C bond cleavage step. C-C bond cleavage is irreversible and often assumed to be rate-limiting for hydrogenolysis [176, 234, 235]. The propynyl C-C bond breaking barriers calculated across the various Pd alloys have similar trends compared to the selectivity descriptor involving propylene dehydrogenation. The largest increase in barriers (corresponding to highest predicted selectivity for propylene production) is found for the 1:1 Pd alloys, and the barriers become smaller with decrease in promoter content for non-catalytic promoters. However, in contrast to the trend in the selectivity descriptor on 1:1 alloys, PdZn has the largest C-C bond breaking barrier, which is almost 0.49 eV greater than PdIn. This larger barrier on PdZn is also consistent with the greater selectivity observed in the experiments for the PdZn (100%) alloy than the PdIn alloy (97%). In aggregate, the trends in both C-C bond breaking barriers and the selectivity descriptors show good qualitative agreement with experimentally-determined selectivity patterns.

Additional insights into the factors driving propylene selectivity can be obtained by comparing differences in C-C bond breaking transition state structures across the various alloys (Figure 4.16). On pure Pd, the 3:1 alloys, and Pd₂Ga, hydrogenolysis occurs on two adjacent threefold sites across four atoms in a diamond shape (Figure 4.9). On the 3:1 and 2:1 alloy surfaces, this structure implies that the promoter element interacts with one of the dissociated product species (carbon or ethylidyne). In contrast, for the 1:1 alloys, the transition state for C-C bond breaking is slightly more extended, involving a five atom ensemble of which two atoms are promoter elements. Hence, in this case, both the dissociated carbon and ethylidyne interact with the promoter atoms (Figure 4.9). This larger interaction of the transition state with the promoter atoms for the 1:1 alloys than the alloys with threefold ensembles is one of the primary reasons for the higher C-C bond breaking barriers observed, thereby inhibiting the hydrogenolysis reactions on the site-isolated alloys. The modification of the C-C cleavage transition state ensemble also explains why site isolated alloys have high selectivity regardless of the intrinsic selectivity of the active metal. By changing

the crystal structure through alloying, sites that lead to unselective pathways are removed, and instead these pathways must occur on sites with higher reaction barriers, regardless of the affinity of the active metal for such reactions.

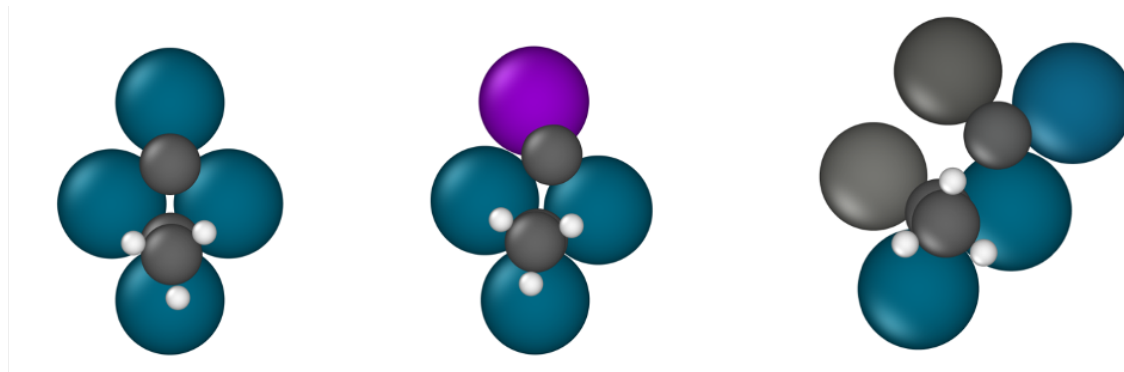


Figure 4.9. Representative ensembles of surface atoms involved in propynyl C-C bond breaking with corresponding transition state structures. (a) Pd (111) (b) Pd₃Mn/Pd (111) (c) PdZn (101)

To further probe the extent to which the structure of the metal ensembles, as opposed to the chemical identity of the promoter, is responsible for the large change in energetics in the 1:1 alloy systems, a theoretical Pd₃Zn alloy with the AuCu₃ crystal structure was simulated (Figure 4.17). This theoretical alloy contains the same four atom hydrogenolysis ensembles present in the other Pd₃M alloys, and if the chemical identity of zinc is predominantly responsible for selectivity, then its binding energies and activation energy barriers for C-C and C-H bond cleavage would fall closer those of the 1:1 PdZn alloys than those of the other 3:1 alloys. However, the calculated binding energies and activation energy barriers for the Pd₃Zn structure (Table 4.14) do indeed fall within the range of other Pd₃M alloys simulated. This result suggests that the structure of the metal ensembles, rather than identity of the promoter, that is predominantly responsible for the high dehydrogenation selectivity observed for 1:1 alloys.

Finally, we note that the superior selectivity of 1:1 alloys, as compared to the 3:1 or 2:1 alloys, at high reaction temperatures, can also be influenced by the lower sensitivity of the 1:1 alloy structures to surface segregation of Pd atoms. All of the 3:1 alloy structures studied herein (and more generally most $L1_2$ alloys) are stable over a narrow (2-5 at%) composition range, which is facilitated by partial occupancy of Pd at M lattice sites and vice versa. For example, this could allow metastable exchange of a surface M atoms with a subsurface Pd atom on a Pd_3M surface, leading to fourfold Pd ensembles with lower olefin selectivity. Formation of such a defect through surface pre-melting in nanoparticles at high temperature is well documented [236]. While the same partial occupancy can occur for similar reasons in 1:1 alloys, the occurrence of fourfold Pd ensembles by elemental exchange is less likely because multiple atom exchanges would need to occur in close proximity to produce atomic ensembles with maximum propensity for hydrogenolysis.

4.6 Conclusions

Simple synthetic methods, such as strong electrostatic adsorption and incipient wetness impregnation, allowed for the synthesis of 1-2 nm intermetallic compounds between palladium and five different promoters: Zn, Ga, In, Fe and Mn. All the alloys had higher dehydrogenation turnover rates and selectivities than that of an equivalently sized monometallic palladium catalyst. The site isolated alloys, PdIn and PdZn had the highest selectivity among the alloys due to an order of magnitude decrease in the rate of hydrogenolysis as compared to alloys without site isolation. The change in selectivity and turnover rate in all the alloys resulted from the heteroatomic bonds between palladium and the promoter metal atoms, which led to electronic modification of Pd and changes in the crystal structure of the alloy. Computed selectivity descriptors involving the energy difference between propylene desorption and propylene dehydrogenation qualitatively match the experimental trends that site isolated Pd alloys have higher selectivity than Pd_3M alloys. Modeling the C-C bond cleavage of propynyl, a representative C_3 species resulting from deep dehydrogenation

of propylene, showed a difference in the number of surface atoms involved in the hydrogenolysis reaction in the 1:1 alloys and in the alloys containing threefold ensembles, with implications for the design of new selective dehydrogenation catalysts. The relation of the selectivity descriptor to the reaction mechanism implies that it can be extended to other catalysts having the same dehydrogenation and hydrogenolysis mechanisms. This further implies that such an approach could be fruitful for other systems such as base metal alloys and metal phosphides.

4.7 Supporting Information

4.7.1 Methods

4.7.1.1 Catalyst Synthesis

Pd A Monometallic 2% Pd catalyst was prepared by strong electrostatic adsorption (SEA). 5 grams of Davasil 646 silica was dispersed in 50 mL of deionized (DI) water and the pH was adjusted to 11 with 32% ammonium hydroxide. 2.8 g of 10% palladium (II) tetraammine nitrate solution was diluted to a total volume of 25 mL and the pH was adjusted to 11 by the addition of 32% ammonium hydroxide. The silica suspension and the palladium solution were mixed for 15 minutes. The silica was then allowed to settle out of solution and removed by filtration. The Pd-SiO₂ was then washed 3 times with DI water and dried at room temperature for 3 hours and then overnight at 125°C. After drying the catalyst was calcined at 300 °C for 3 hours. The Pd-SiO₂ was then reduced in 5% H₂ in steps from 100 °C to 250 °C at a 2.5 °C/min ramp rate with 15 minute dwells every 25 °C and then a fast ramp (10 °C/min) to 550 °C and a 30 minute dwell. The catalyst was then cooled to room temperature and passivated in air. A second monometallic Pd catalyst was synthesized by the above method except the calcination temperature was 200°C for 3 hours and the mass of 10% palladium (II) tetraammine nitrate was adjusted to give a weight loading of 1%.

Pd-In A 2% Pd 3% In catalysts was synthesized according to the procedure for Pd-In 0.8 in reference [198]. Briefly, In-SiO₂ was synthesized by incipient wetness

impregnation of an $\text{In}(\text{NO}_3)_2$ and Citric acid solution pH adjusted to 11 with ammonium hydroxide. The In-SiO_2 was dried at 125 °C overnight and then calcined in air at 200 °C. Palladium was then added by incipient wetness impregnation of a pH 11 solution of palladium (II) tetraammine nitrate. The Pd-In-SiO_2 catalyst was then dried overnight at 125 °C and calcined at 200 °C. The catalyst was then reduced using a slow ramp to 200 °C and then a fast ramp to 600 °C in 5% H_2 (balance N_2). The catalyst was cooled to room temperature in nitrogen and then passivated in air.

Pt-Fe A 2% Pd 3% Fe catalyst was synthesized according to the procedure for “ Pd_3Fe small” in reference [199]. A 2:1 molar ratio of citric acid to iron (III) nitrate nonahydrate was pH adjusted to 11 using concentrated ammonium hydroxide. The solution was impregnated dropwise onto 5 g of SiO_2 and dried at 125 °C and then calcined at 400 °C for 3 hours. Pd loading was accomplished using a pH 11 solution of palladium (II) tetraammine nitrate. The Pd-Fe-SiO_2 catalyst was then dried at 125 °C and then calcined at 250 °C for 3 hours. Reduction was performed in 3% H_2 (balance Ar) at 200 °C for 30 minutes and then at 600 °C for 30 minutes. The catalyst was then cooled to room temperature and passivated in air.

Pd-Ga A 2.5% Pd 2.5% Ga catalysts was prepared by sequential incipient wetness impregnation of gallium and palladium on silica. 1.25 g of gallium (III) nitrate hydrate and 2 grams of citric acid were dissolved in DI water to a total volume of 5 mL. The pH was adjusted to 11 with 32% ammonia solution and subsequently impregnated into 5 g of Davasil 646 silica. The Ga-SiO_2 was dried at 125 °C overnight and then calcined at 400 °C for 3 hours. Pd impregnation was done using 3.3 g of 10% palladium (II) tetraammine nitrate diluted to 5 mL total volume and pH adjusted to 10 with 32% ammonia solution. The Pd solution was then impregnated to the pore volume of the 5 g of Ga-SiO_2 catalyst and then dried at 125 °C overnight. The Pd-Ga catalyst was then calcined at 250 °C for 3 hours and then subsequently reduced in 5% H_2 with a slow ramp (2.5 °C/min) through 200 °C and then a fast ramp (10 °C/min) to 600 °C

with a 30 minute dwell. The reduced catalyst was then cooled to room temperature in 5% H₂ and passivated in air.

Pd-Zn A 2% Pd 3% Zn catalyst was synthesized by sequential incipient wetness impregnation. 1.14 g of Zinc nitrate hexahydrate was dissolved in 2 mL of DI water and the pH was adjusted to 11 using 32% ammonia solution. Finally, the total volume of the Zn solution adjusted to 5 mL with the addition of DI water. The Zn solution was impregnated to the pore volume of 5 g of Davasil 646 silica and dried overnight at 125 °C. The Zn-SiO₂ catalyst was then calcined at 300 °C for 3 hours. 0.281 g of palladium (II) tetraammine nitrate was dissolved in 3.5 mL of DI water and the pH was adjusted to 11 using 32% ammonia solution. The palladium solution was then impregnated to the pore volume of the calcined Zn-SiO₂ and dried at 125 °C. The Pd-Zn-SiO₂ catalyst was calcined at 200 °C for 3 hours and then reduced in 5% H₂ (balance N₂) with a slow ramp (2.5 °C/min) through 250 °C and a fast ramp (10 °C/min) to 550 °C and a 30 minute dwell at temperature. The reduced catalyst was then cooled to room temperature in hydrogen and passivated in air.

Pd-Mn A 1% Pd 5% Mn catalyst was synthesized by sequential incipient wetness impregnation. 0.814 g of manganese (II) nitrate hydrate and 0.874 g of citric acid were dissolved in 5 mL of Millipore water to give a solution with a 2:1 molar ratio of citric acid to manganese nitrate. The pH of the solution was adjusted to 11 by the addition of 32% ammonium hydroxide. The solution was then added dropwise to 5 g of Davasil 646 silica. The Mn-SiO₂ was then dried at 125 °C overnight and calcined at 250 °C for 3 hours. Pd loading was done by diluting 1.4 g of 10% palladium (II) tetraammine nitrate to 5 mL total volume and adjusting the pH to 11 with 32% ammonium hydroxide. The solution was then added dropwise to the Mn-SiO₂ and dried at 125 °C overnight and calcined at 200 °C for 3 hours. The Pd-Mn-SiO₂ catalyst was then reduced in 5% H₂ (balance N₂) with a slow ramp (2.5 °C/min) through 250 °C and a fast ramp (10 °C/min) to 550 °C with a 30-minute dwell at

temperature. The reduced catalyst was then cooled to room temperature in 5% H₂ and passivated in air.

4.7.1.2 Pd L₃ Edge XANES

Pd L₃ edge X-ray adsorption near edge structure (XANES) were measured at the 9BM line of the advanced photon source. Measurements were performed in fluorescence mode using a vortex 4 element detector. The samples were ground and pressed into a steel sample holder with the catalyst wafer at a 45-degree angle relative to the beam. The reactor used for treatment has been described elsewhere [237], and is capable of heating and gas flow with Kapton windows for transmission and fluorescence measurements. Samples were treated by heating to 500 °C in 3.5% H₂ (balance He). After a 30-minute dwell at 500 °C, the gas flow was switched to He at high temperature to desorb hydrogen and decompose any palladium hydride formed during the reduction. The samples were then cooled to room temperature and multiple scans were collected and averaged. L₃ edge XANES spectra were normalized using first order polynomial for the pre-edge region and a second order polynomial for the post-edge region. Due to the close proximity of the L₃ to the L₂ edge, the data collection range for post edge normalization is limited and the third order polynomial typically fit to the post edge region fits poorly. The absolute energy scale was calibrated using bulk PdO with an L₃ edge energy of 3174.4 eV.

4.7.2 Results

Figure 4.10 shows STEM images and EDS maps of Pd and Pd alloy catalysts. Pictured in Figure 4.10a, the 1% Pd catalyst is monodisperse with small metal particles under 2 nm in diameter. In contrast, the 2% Pd catalyst, shown in Figure 4.10b, contains both small (1-2 nm) particles and large (>5 nm) particles. The high temperature calcination treatment used in the 2Pd catalyst results in agglomeration of the palladium oxide resulting in larger metallic particles after reduction. EDS was used

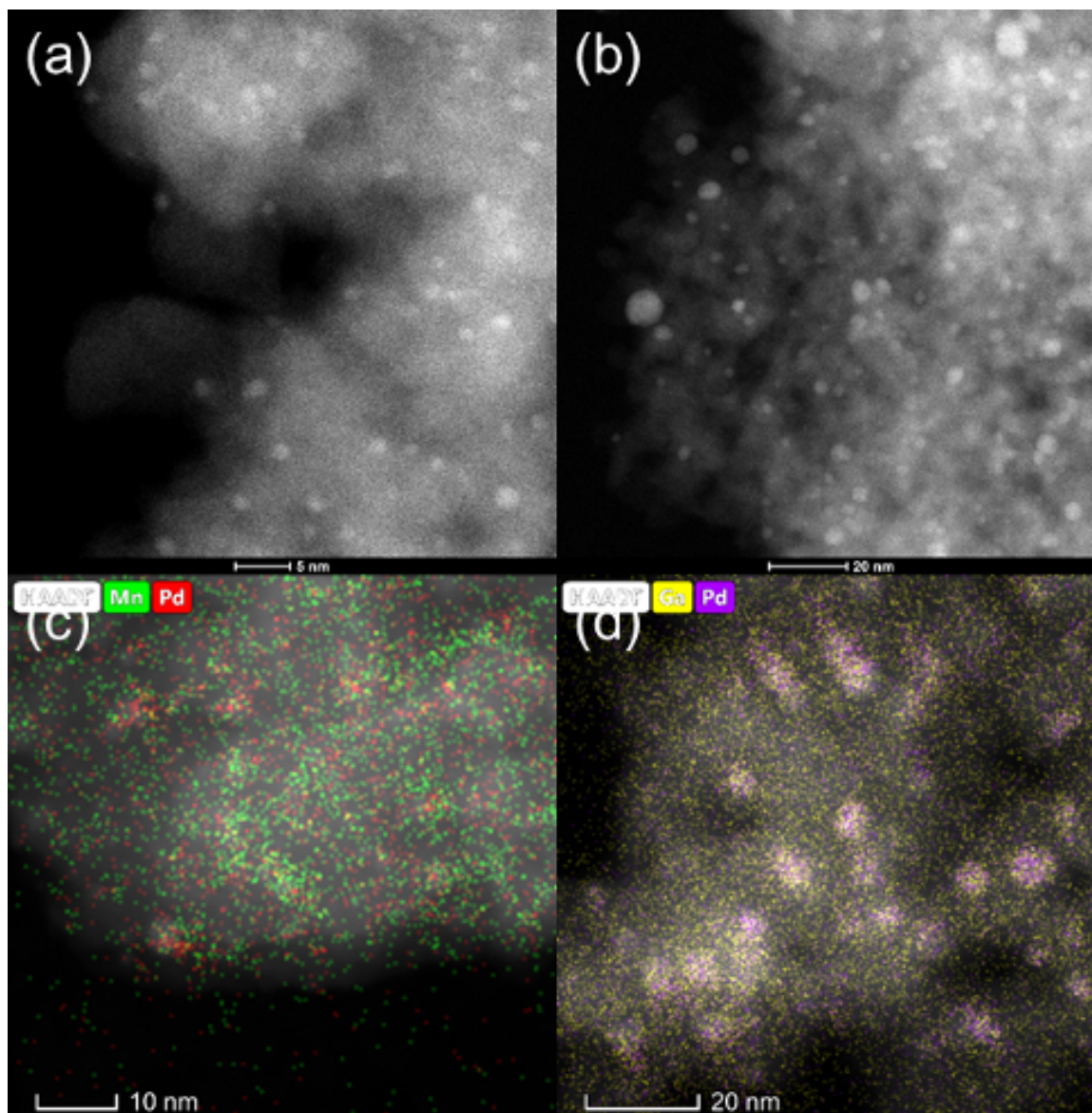


Figure 4.10. STEM images of Pd and bimetallic Pd catalysts: (a) 1Pd (b) 2Pd (c) STEM image of 1Pd-5Mn with overlaid EDS maps for Pd (red) and Ga (Green). (d) STEM image of 2.5Pd-2.5Ga with overlaid EDS maps for Pd (purple) and Ga (yellow).

to observe the dispersion of the second metal, which is difficult to distinguish from the support in STEM images. Figure 4.10c shows a STEM image of 1Pd-5Mn with overlaid EDS maps for manganese and palladium. The manganese is well dispersed across the support, small clusters containing both Pd and Mn can be seen, consistent with the formation of a Pd-Mn bimetallic. Ga in the Pd-Ga catalyst (Figure 4.10d) is also well dispersed on the support, but the bimetallic Pd-Ga clusters are better resolved owing to their slightly larger particle size.

Due to the large number of overlapping peaks and imperfect background subtraction, it was not possible to determine a lattice parameter using the XRD pattern in Figure 4.11. However, simulation of the particle size broadening, shown in Figure 4.14, gives an estimate of the particle size. The first major group of peaks, between 2.5-4 degrees, merges into a single asymmetric peak when the particle size is below 2 nm. In the 3 and 4 nm sized simulations, distinct shoulders start to emerge, and 4 major peaks can be resolved. In the 5 nm simulation, the most intense peak in the pattern around 3.1 degrees starts to split into two distinct peaks. In the Pd-Ga catalyst, the first cluster of peaks between 2.5-4 degrees most closely resembles the 3 nm simulation, which is larger than the TEM measured particle size of 2.1. The difference between the XRD determined value and the TEM determined value can be attributed to the presence of microstrain broadening and the volume averaging nature of the XRD measurement.

4.7.2.1 Electronic Characterization

In addition to changing the catalyst structure, alloying can also electronically modify palladium, which can be studied by XANES. Figure 4.12a shows the Pd K edge XANES collected for 2Pd-3Zn, 2.5Pd-2.5Ga, 1Pd-5Mn and 1Pd after reduction in 3.5% H₂ (balance He) for 30 minutes. The alloy catalysts show small changes in the edge shape which are indicative of alloying. The first peak in the XANES is lower in intensity for the three alloy samples and the edge position for each is shifted 0.2 eV lower in energy compared to the Pd foil value of 24350.0 eV. The close edge position

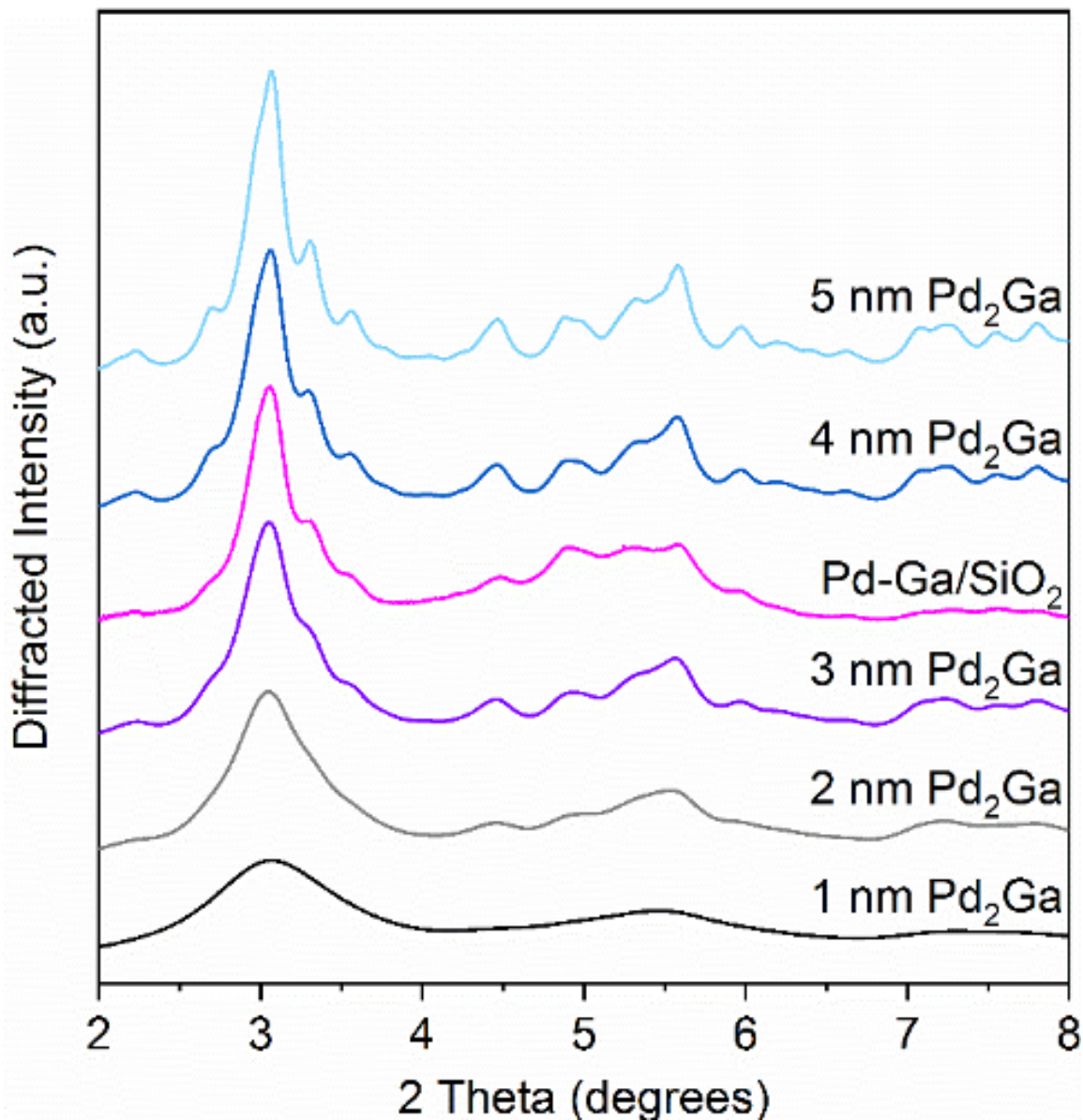


Figure 4.11. Simulated Pd₂Ga XRD patterns with different crystallite sizes (black, grey, purple, blue, light blue) compared with experimentally measured Pd-Ga catalyst (pink).

and white line intensity shows that the alloy sample and Pd nanoparticles are all in the metallic state. Because the final state in K edge absorption is a *p* electron, and transition metals bond and adsorb through *d* electron interactions, only small

Table 4.9.
Pd K edge EXAFS fits of Pd and Pd alloy catalysts after room temperature air exposure.

Sample	Scattering Pair	Coordination Pair	Bond Distance (Å)	Debye-Waller Factor (Å ²)	E ₀ (eV)
1Pd	Pd-Pd	5.6	2.71	0.0060	-3.2
	Pd-O	1.4	2.02	0.0020	0.4
2Pd	Pd-Pd	8.6	2.74	0.0018	-2.0
	Pd-O	0.6	2.01	0.0020	1.6
2Pd-3Zn	Pd-Pd	1.3	2.70	0.0030	-3.6
	Pd-Zn	2.2	2.52	0.0030	-9.6
	Pd-O	0.5	2.05	0.0020	2.1
2Pd-3In	Pd-M	4.9	2.70	0.0060	-3.3
	Pd-O	0.6	2.04	0.0020	0.4
2.5Pd-2.5Ga	Pd-Pd	3.6	2.75	0.0030	-1.8
	Pd-Ga	1.1	2.46	0.0030	-9.2
	Pd-O	0.3	2.01	0.0010	1.9
2Pd-3Fe	Pd-Pd	5.2	2.72	0.0040	-0.2
	Pd-Fe	1.6	2.60	0.0040	-4.4
	Pd-O	0.4	2.02	0.0020	-1.6

changes are evident at the Pd K edge. Larger modifications can be seen at the L₃ edge, which is more sensitive to adsorbates and heteroatomic bonding due to the final state involving unfilled valence *s* and *d* states.

Figure 4.12b shows the Pd L₃ edge XANES for 2Pd-3Zn, 2.5Pd-2.5Ga, 1Pd-5Mn and 1Pd after reduction at 500 °C in 3.5% H₂. The modification of the XANES due to alloying is evident in the intensity and broadness of the white line, demonstrating the sensitivity of the L₃ edge to heteroatomic bonding. The PdZn and PdGa catalysts look similar, both with white line intensities lower than and broader than Pd sample.

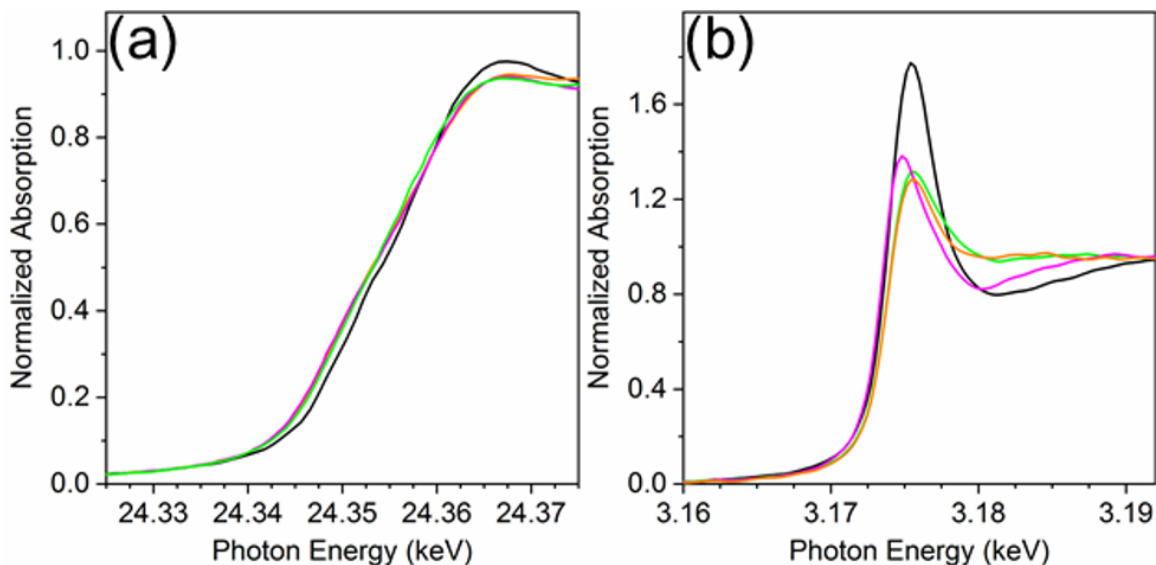


Figure 4.12. XANES of 1Pd (black), 2Pd-3Zn (orange), 2.5Pd-2.5Ga (green) and 1Pd-5Mn (magenta) at the K edge (a) and L₃ edge (b) after reduction at 550 °C in 3.5% H₂.

The PdGa sample white line is slightly broader and higher in intensity compared to the PdZn sample. Conversely, the PdMn sample has a white line that is narrower and lower in intensity compared to the Pd catalyst. The edge energy for the Pd and PdMn catalysts was 3173.6 eV. For PdGa and PdZn, the edge energy increased to 3173.9 eV. The dipole selection rule for Pd L₃ edge XANES allows for transition of a $2p_{3/2}$ electron into an unfilled $4d$ or $4d$ state. Since metallic Pd is d_{10} , there are no unfilled d states and the changes in the Pd L₃ XANES reflect the $4d$ unfilled density of states (conduction band) which are just above the $4d$ electrons in energy. The change in white line shape for the alloys represents a redistribution of the energy of the unfilled s states resulting from alloy formation.

4.7.2.2 Electronic Structure Calculations

The surface Pd-atom projected Density of States (DoS) have been calculated for all the alloy surfaces to quantify the electronic modification of palladium in the alloy

structures. Further, the 1st moment (d -band center) and 2nd moment (d -band width) are reported in Table 4.10. Apart from the Pd₂Ga surface, all the Pd atoms on the surface of the alloys are crystallographically identical. Pd₂Ga has two symmetrically distinct Pd atoms, hence an average of their moments has been reported.

Table 4.10.

The d -band center (first moment) and d -band width (second moment) calculated from the pDOS of surface Pd atoms in monometallic Pd and Pd alloys

Structure	d -band Center (First Moment) (eV)	d -band Width (Second Moment) (eV)
Pd (111)	-1.54	2.19
Pd ₃ Mn/Pd (111)	-1.67	2.30
Pd ₃ Fe (111)	-1.85	2.51
Pd ₂ Ga (010)	-1.95	2.55
PdZn (101)	-2.07	2.70
PdIn (110)	-2.16	2.66

The results show that as the promoter content increases the Pd d -band center shifts away from the fermi level leading to more negative d -band centers. The decrease in d -band center is also accompanied by a concomitant increase in d -band width. This inverse linear correlation has also been observed for Pt-skin alloys by Nikolla et al [238]. The changes are smallest for Pd₃Mn/Pd, which also showed the smallest changes in binding strengths. The alloys that had the largest binding energy shifts (PdIn and PdZn) also showed the largest movement in the d -band center, in agreement with the d -band theory. Both Pd and the Pd alloys had a negligible amount unfilled d states above the Fermi level which is consistent with palladium being d_{10} in all cases and the L₃ edge XANES modifications coming from s unfilled state modification.

4.7.2.3 Adsorption Energies of Deep Dehydrogenated Intermediates

(See Tables 4.11, 4.12, and 4.13)

Table 4.11.

Binding energies of deep dehydrogenated intermediates with respect to gas phase reference

Adsorbate	Pd (111)	Pd ₃ Mn/Pd (111)	Pd ₃ Fe (111)	Pd ₂ Ga (010)	PdZn (101)	PdIn (110)
Propyne	1.75	2.02	2.18	2.54	3.13	3.59
Propynyl	2.72	2.78	2.41	3.01	3.60	3.96
Methylidyne	1.30	1.67	1.86	2.19	3.20	3.13
Carbon	2.15	2.20	2.31	3.07	4.47	4.29

Table 4.12.

Binding energies of deep dehydrogenated intermediates on Fe (110) and their difference from Pd (111)

Fe (110)	Binding Energy (eV)	Difference from Pd (111)
Propyne	0.69	-1.06
Propynyl	1.40	-1.32
Methylidyne	0.72	-0.58
Carbon	1.22	-0.93
Ethylidyne	0.58	-0.38

4.7.2.4 Most Stable Adsorption Configurations for Reaction Intermediates

(See Figures 4.13 and 4.14)

Table 4.13.
 Activation energy barriers for C-C bond cleavage of propyne on Pd
 and Pd alloy surfaces

Alloy Surfaces	Kinetic Barrier (eV)
Pd (111)	1.10
Pd ₃ Mn/Pd (111)	1.50
Pd ₃ Fe (111)	0.92
Pd ₂ Ga (010)	1.84
PdZn (101)	2.55
PdIn (110)	2.58

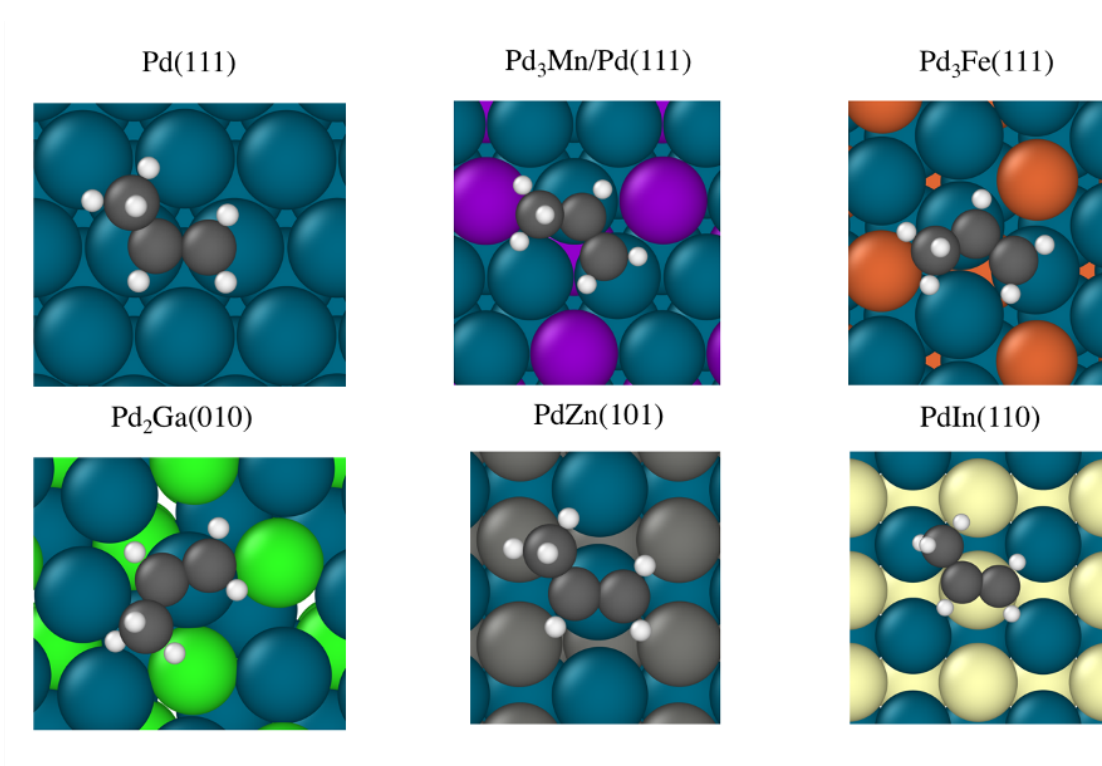


Figure 4.13. Propylene most stable configurations on alloy and pure Pd surfaces

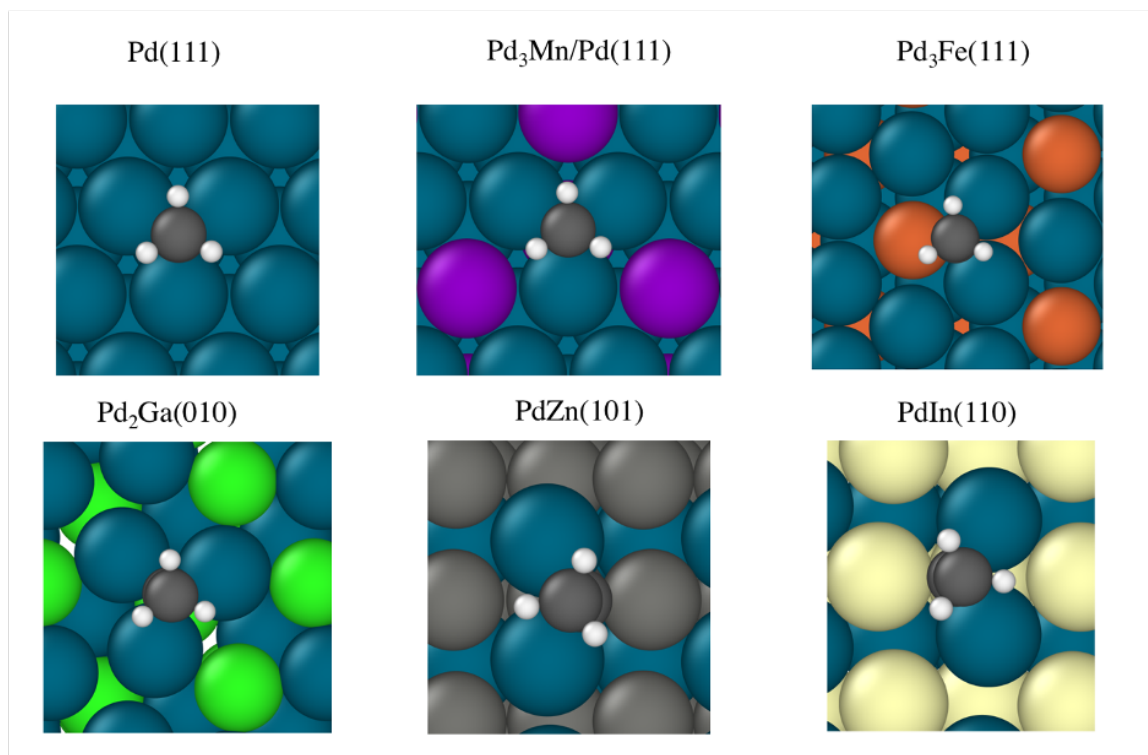


Figure 4.14. Ethylidyne most stable configurations on alloy and pure Pd surfaces

4.7.2.5 Transition States for C-H and C-C Bond Breaking

(See Figures 4.15 and 4.16)

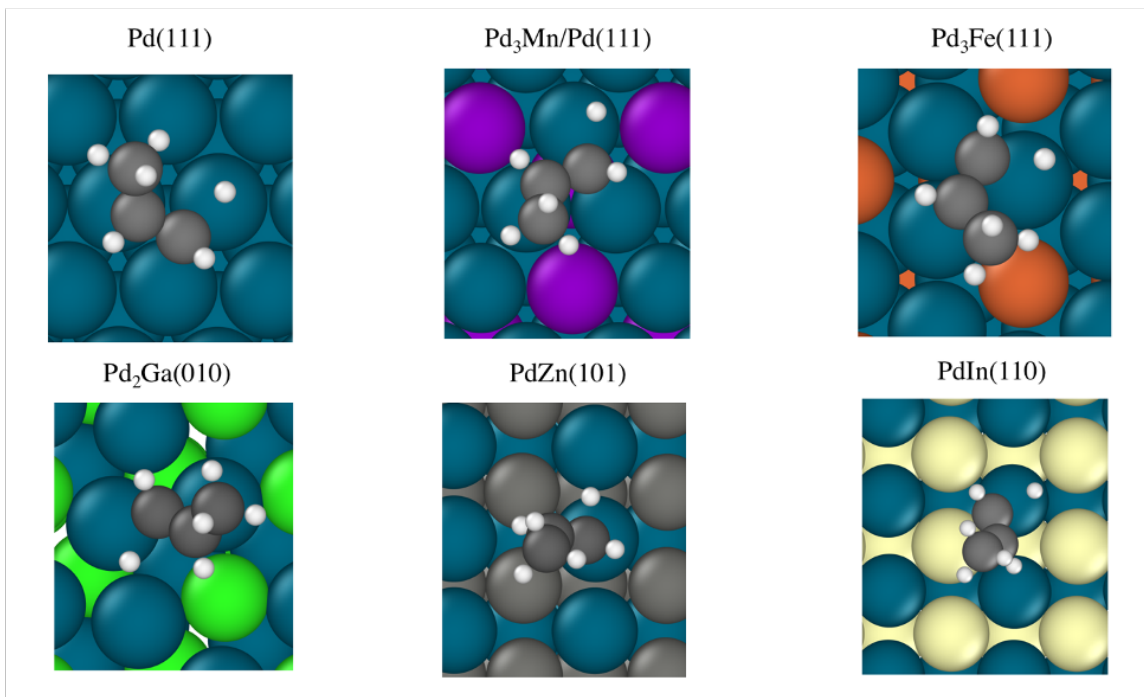


Figure 4.15. Transition states of propylene C-H bond breaking to form propenyl and hydrogen

4.7.2.6 Theoretical Pd₃Zn Alloy Results

(See Figure 4.17 and Table 4.14)

4.7.3 Discussion

Because the structure of the alloy determines the local Pd coordination in an intermetallic compound, it also determines the electronic effect, and the two effects cannot be decoupled. In addition to the difference in ensemble size between the alloys, they also differ in the number of surface Pd-Pd and Pd-promoter bonds. The

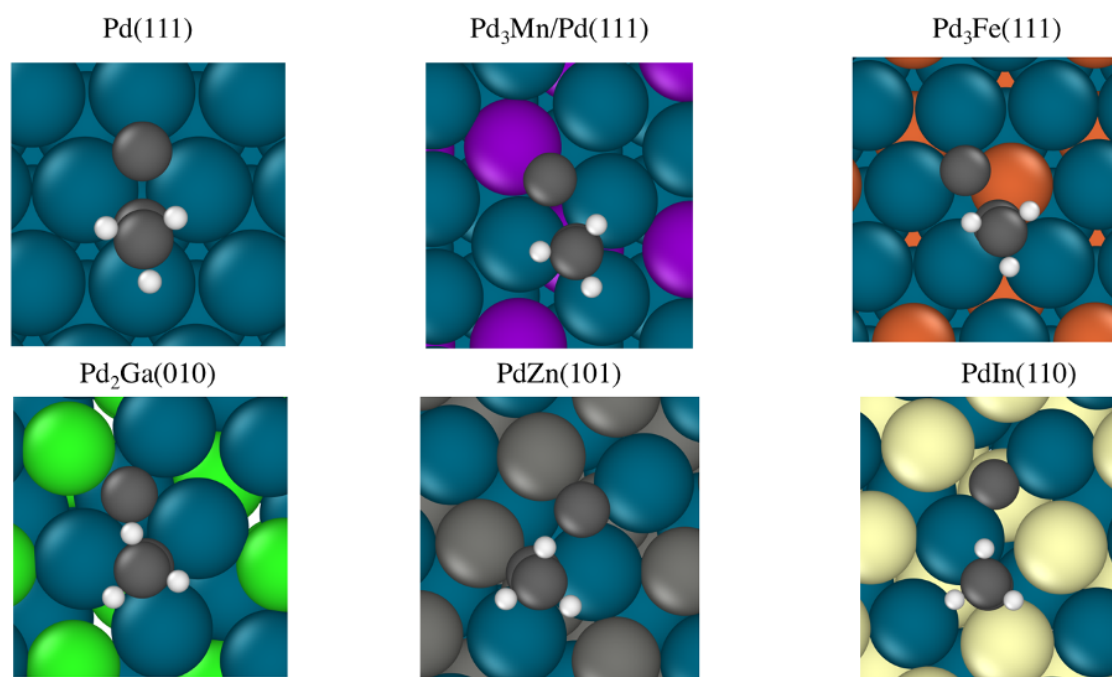


Figure 4.16. Transition states of propynyl C-C bond breaking to form carbon and ethylidyne

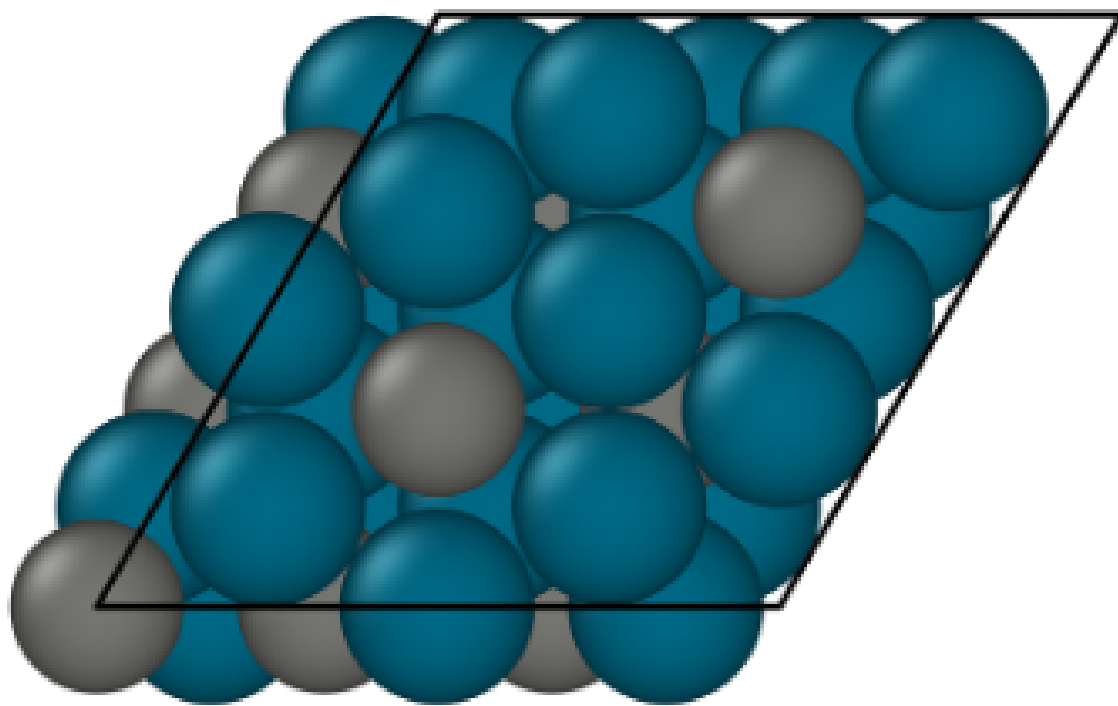


Figure 4.17. Top view of fcc Pd₃Zn (111) surface

Table 4.14.
 Calculated values of selectivity descriptor and propynyl C-C bond breaking barriers for Pd₃Zn (111) surface

Alloy Surface	Propylene Adsorption Energy (eV)	Propylene Dehydrogenation Barrier (eV)	Selectivity Descriptor (eV)	Propynyl C-C Bond Breaking Barrier (eV)
Pd ₃ Zn (111)	-0.60	1.28	-0.68	1.98

Electronic effect occurs due changes in the local coordination sphere of the surface atoms, and the number of bonds changes the strength of the electronic modification. This has been demonstrated in the Pt-Mn system, where the subsurface alloy or Pt layer of the catalyst changed the CO heat of adsorption of the Pt₃Mn surface [239]. In the site isolated PdZn alloy (Figure 4.8), each surface Pd atom on the lowest energy surface has 6 heteroatomic bonds (4 surface, 2 subsurface) and 2 Pd second nearest neighbors at a non-bonding distance (2.89 Å); PdIn has the same number of heteroatomic bonds but 6 Pd second nearest neighbors at 3.22 Å. Pd atoms on the (010) surface of Pd₂Ga have 3 Ga neighbors (2 surface, one subsurface) with 4 Pd nearest neighbors at an elongated bond distance (2.8, 2.85 Å). Lastly, surface atoms in the Pd₃M structures have 3 promoter nearest neighbors (2 surface, 1 subsurface) with 6 Pd-Pd bonds equal in length to the Pd-promoter bonds. As the local coordination changes, the *d*-band of palladium is modified, which is quantified in the first and second moments of the *d*-band. In general, as the number of Pd-promoter bonds increases, the *d*-band shifts away from the fermi level and increases in width (see Table 4.10).

While L₃ edge XANES is commonly used to demonstrate *d*-band modification in platinum, the same information cannot be gained at the Pd L₃ edge due to the electron configuration of Pd. Because Pd metal is *d*₁₀, there are no unfilled *d* states, and the L₃ edge XANES cannot give information about the *d*-band. The lowest energy unfilled state accessible by the dipole selection rules of XANES is the 5*s*

unfilled states. The change in whiteline shape observed for the alloys reflects the unfilled s states redistributing in energy due to overlap with neighboring promoter s orbitals, similar to how the $5d$ unfilled states in platinum are modified by promoters in platinum alloys [240].

5. REACTIVE METAL–SUPPORT INTERACTIONS AT MODERATE TEMPERATURE IN TWO-DIMENSIONAL NIOBIUM-CARBIDE-SUPPORTED PLATINUM CATALYSTS

Nature Catalysis 2018, 1, 349-355. <https://doi.org/10.1038/s41929-018-0067-8>

Zhe Li¹, Yanran Cui², Zhenwei Wu², Cory Milligan², Lin Zhou³, Garrett Mitchell², Biao Xu¹, Enzheng Shi¹, Jeffrey T. Miller², Fabio H. Ribeiro², and Yue Wu¹

¹Department of Chemical and Biological Engineering, Iowa State University, ²Charles D. Davidson School of Chemical Engineering, Purdue University, and ³Department of Energy, Ames Laboratory.

5.1 Abstract

Reactive metal–support interactions (RMSI) can have electronic, geometric and compositional effects that can be used to tune catalytic active sites. Generally, supports other than oxides are disregarded not able to produce RMSI effects. Here, we report an example of non-oxide-based RMSI between platinum and Nb₂CT_x MXene—a recently developed, two-dimensional metal carbide. The surface functional groups of the two-dimensional carbide can be reduced, and a Pt–Nb surface alloy is formed at a moderate temperature (350 °C). Such an alloy exhibits weaker CO adsorption than monometallic platinum. Water-gas shift reaction kinetics reveal that this RMSI stabilizes the relevant nanoparticles and creates alloy–MXene interfaces with higher H₂O activation ability compared with a non-reducible support or a bulk niobium carbide. This RMSI between platinum and the niobium MXene support can be extended to other members of the MXene family and opens new avenues for the facile design and manipulation of functional bimetallic catalysts.

5.2 Introduction

Supported bimetallic nanoparticles represent a wide range of catalysts with tunable compositions and electronic properties [241,242]. Common strategies for preparing bimetallic catalysts include impregnation, reductive deposition precipitation and atomic layer deposition [241,243]. Recently, a so-called reactive metal–support interaction (RMSI) has been shown to provide a facile route for preparing bimetallic alloys [244]. RMSI refers to a chemical reaction between a metal and the support that induces the formation of bimetallic structures that may not be easy to obtain by other synthetic methods. The reducibility of the support plays a crucial role in its RMSI activity. For instance, materials with RMSIs involving reducible oxides, such as TiO_2 and CeO_2 , can be prepared at lower temperatures than those involving hard-to-reduce oxides (such as SiO_2 and Al_2O_3) [245]. Until now, only oxide supports have been considered as candidates for RMSI, but high-temperature reductions ($>550^\circ\text{C}$) are often needed, which limits the compositional variety of catalysts available, and may lead to particle agglomeration and difficulty in controlling the size of the nanoparticles [246,247]. More reactive or reducible supports, such as carbides, represent an alternative that could be involved in RMSIs at lower temperatures and be prepared with well-dispersed active sites. Nonetheless, interactions between metals and supports other than oxides are not well understood even though they are key to establishing general rules for rational catalyst design via RMSI.

MXenes—a new family of two-dimensional (2D) metal carbides, nitrides or carbonitrides—are usually produced by selective extraction of the ‘A’ layers from layered ternary transition metal carbides called MAX phases [248]. This synthetic procedure generates surface termination groups within MXenes, including $-\text{OH}$, $-\text{O}$ and $-\text{F}$ groups. Thus, MXenes have the general formula $M_{n+1}X_nT_x$, where M represents an early transition metal, X is C or N, n varies from 1 to 3, T represents for the surface functional groups and x represents the uncertainty of the surface terminations [249]. To date, MXenes have been extensively developed as electrodes for batteries and

supercapacitors due to their good electrical conductivities [250]. Recently, MXenes have started to gain attention in photo- and electrochemical applications due to their unique surface functional groups [251, 252]. Functional groups on the surface of supports have been known to facilitate the adsorption of metal precursors by electrostatic interactions and thus serve as anchors for active sites [253–255]. Atomic concentrations of O and F on the surface of Ti_2CT_x MXene decreased after hydrogen annealing at low temperature (227 °C) [256]. Removal of the terminal groups on the surface of the MXenes also exposes new terminal metal sites (for example, Nb, Ti and V) that are redox active [252]. For MXene-supported catalysts, these sites can also form admetal–support interfaces that are catalytically active. Moreover, highly reducible and reactive surfaces make MXenes promising candidates for involvement in RMSIs with metal nanoparticles. Considering the reducibility of the 2D carbides, RMSIs may occur at lower temperatures (<550 °C) for MXene-supported catalysts.

Here, we report a platinum nanoparticle catalyst supported on Nb_2CT_x MXene exhibiting an RMSI after reduction in H_2 at moderate temperature (350 °C). Quasi *in situ* X-ray photoelectron spectroscopy (XPS) indicate that the surface of the Nb_2CT_x MXene is reducible based on the removal of the surface –O and –OH terminations, and enrichment of Nb_2O_5 on the reduced MXene surface upon subsequent air exposure. Electron energy-loss spectroscopy (EELS) and *in situ* X-ray absorption spectroscopy (XAS) show that a Pt–Nb surface alloy is formed as a result of the H_2 reduction. The water-gas shift (WGS) reaction was selected as a model reaction to understand the effects of RMSI on adsorbates and metal–support interfaces. WGS kinetics at 300 °C suggest that CO has a lower relative surface coverage on the Pt/ Nb_2CT_x , and the alloy nanoparticles form active interfaces for H_2O activation with the reduced Nb_2CT_x MXene surface, which exhibits enhanced H_2O dissociation activity compared with Pt/ Al_2O_3 . In contrast with Pt/ Nb_2CT_x , platinum supported by conventional bulk NbC was inert in the WGS reaction. The catalyst underwent significant particle agglomeration, and no alloy formation was observed. This work demonstrates that RMSI can be achieved on supports other than oxides, and 2D Nb_2CT_x MXene allows

the catalyst to become involved in RMSIs at 350 °C while retaining control of the particle size.

5.3 Methods

5.3.1 Synthesis of the Nb₂AlC phase

The Nb₂AlC powder was synthesized by spark plasma sintering of niobium, aluminium and graphite mixtures. Commercial powders of niobium (99.8%, 325-mesh), graphite (99%, 7–11 μm) and aluminium (99.5%, 325-mesh) were mixed in a molar ratio of Nb:Al:C = 2:1.4:0.9 in a graphite die coated with boron nitride. Excess aluminium and less than a full equivalent of graphite were added because aluminium is lost during high-temperature processing, and carbon deficiencies exist in most aluminium-containing MAX phases [257, 258]. Then, the material was loaded in a Fuji-2111x spark plasma sintering system and sintered at 1,500 °C under 30 MPa for 1 h. The resulting Nb₂AlC was then pulverized and sieved through a 325-mesh screen.

5.3.2 Preparation of Nb₂CT_x MXene

Approximately 1 g of the prepared Nb₂AlC powder was immersed in 10 ml of 50% aqueous hydrofluoric acid solution for approximately 3 days at 55 °C. The resulting MXene suspension was repeatedly washed with deionized water and centrifuged at 8,900 r.p.m. until the pH reached ~5. The final MXene was dried under vacuum at room temperature and stored in a glove box until usage.

5.3.3 Preparation of the Pt/Nb₂CT_x catalysts

Tetraamine platinum nitrate (99.995%; Sigma–Aldrich) was loaded on the Nb₂CT_x MXene and bulk NbC (99%; Sigma–Aldrich) supports by incipient-wetness impregnation. Specifically, a certain amount of platinum precursor was dissolved in deionized water to generate a solution with a concentration of 0.02 g Pt ml⁻¹. The solution was then added dropwise to the support until incipient-wetness impregnation (approximate

mately 0.5 ml g⁻¹ of support). The mixture was then dried under vacuum at ambient temperature. The procedure was repeated once so the final catalyst (referred to as Pt/Nb₂CT_x fresh) had an empirical platinum loading of approximately 1–2%.

5.3.4 Determination of the WGS reaction kinetics

The WGS reaction was monitored in a parallel plug flow reactor, which has been described previously [259]. The WGS reaction rates were measured under differential conditions; namely, the conversion was maintained below 10% and the products of the WGS reaction (CO₂ and H₂) were also co-fed into the reaction system. The WGS rate can be expressed by the power rate law given below:

$$r = A \exp\left(-\frac{E_{app}}{RT}\right) [CO]^a [CO_2]^b [H_2]^c [H_2O]^d (1 - \beta) \quad (5.1)$$

where r is the overall rate, A and E_{app} are the apparent pre-exponential factor and activation energy for the forward rate, R is gas constant, and T is reaction temperature, respectively, a , b , c and d are the forward reaction orders, $\beta = ([CO_2][H_2]) / (K_{eq}[CO][H_2O])$ is the approach to equilibrium, which measures the deviance from the equilibrium conditions, and K_{eq} is the equilibrium constant for the WGS reaction. Under the WGS conditions tested here, $\beta \ll 1$, implying the reaction is far from equilibrium.

For each measurement, approximately 300 mg of the as-prepared Pt/Nb₂CT_x catalyst was loaded into the reactor. The catalyst was pre-treated by reduction in 25% H₂/Ar at 350 °C for 2 h (the total flow rate was 50 ml min⁻¹ and the temperature ramping rate was 5 °C min⁻¹). After pre-treatment, the temperature was decreased to 300 °C and the catalysts were exposed to the WGS reaction mixture (standard conditions: 6.8% CO, 21.9% H₂O, 8.5% CO₂ and 37.4% H₂ balanced by argon) at a flow rate of 75.4 ml min⁻¹. The catalyst was stabilized at 300 °C for a period of approximately 20 h to reach initial stabilization. The apparent reaction orders were measured over the stabilized catalyst by varying the partial pressures of one component at a time over the range of 4–21% for CO, 5–25% for CO₂, 11–34% for H₂O and 14–55% for H₂. The WGS reaction rate under standard conditions was deter-

mined after evaluation of each apparent reaction order to measure the deactivation, if there was any. For this catalyst, after the initial stabilization period, no significant deactivation was observed during the full test period (approximately 50 h). The apparent activation energy was measured under standard conditions by varying the temperature between 290 °C and 320 °C. The WGS rate was normalized by the total platinum loading or by the number of surface platinum atoms as determined by CO chemisorption. After all measurements had been taken, the catalysts were passivated at room temperature in 30 ml min⁻¹ 2% O₂/Ar gas flow for 4 h before they were removed from the reactors.

5.4 Results

5.4.1 Preparation and characterizations of the Nb₂CT_x support

The preparation of few-layer niobium MXene (Nb₂CT_x) via hydrofluoric acid treatment is summarized in the Methods. The X-ray diffraction pattern of the prepared Nb₂CT_x support (Figure 5.6) shows that the (002) peak of the hydrofluoric acid-treated Nb₂AlC powder shifted to 2θ of 9.3°, which corresponds to a c-lattice parameter of 19 Å compared with that observed in the initial MAX (Nb₂AlC) phase (13.9 Å). XAS was performed to confirm the structure of the niobium carbide MXene. The results of niobium K-edge X-ray absorption near-edge structure (XANES) analysis are presented in Figure 5.1a and show that the shape of the XANES spectrum of Nb₂CT_x is similar to that of commercial NbC (Sigma–Aldrich) but different from those of Nb₂AlC and Nb₂O₅ (Sigma–Aldrich). The edge energy of the MXene (19,000.7 eV) is close to that of NbC (19,000.2 eV) but distinct from those of Nb₂AlC (18,998.7 eV) and Nb₂O₅ (19,003.3 eV), which confirms the removal of aluminium from the parent MAX phase. The edge energy of Nb₂CT_x is slightly higher than that of NbC, suggesting that the Nb₂CT_x is partially oxidized due to the terminal groups or Nb₂O₅ on its surface [260]. X-ray absorption fine-structure (EXAFS) spectra (Figure 5.1b) were also used to confirm the 2D structure of the material since

Nb_2CT_x showed first-shell (Nb–C) scattering similar to that of NbC but second-shell (Nb–C–Nb) scattering much lower than that of NbC due to the reduced dimensionality. Moreover, the typical lamellar structure of Nb_2AlC (Figure 5.7a) was converted to an accordion-like structure (Figure 5.1c), confirming the exposure of individual grains along the basal planes. After mildly sonicating the Nb_2CT_x MXene multilayers in deaerated ethanol, few-layered electron transparent nanosheets could be obtained, as shown in the transmission electron microscopy (TEM) image (Figure 5.1d).

5.4.2 Kinetics of the WGS reaction

Platinum was loaded onto the Nb_2CT_x support via incipient-wetness impregnation, as reported in ref. [261]. The platinum loading was estimated to be 1% by atomic absorption spectroscopy. The 1% Pt/ Nb_2CT_x catalyst was then tested for activity in the WGS reaction under standard conditions (see Methods). As shown in Figure 5.2a, the catalyst was stable under the conditions used for the WGS reaction kinetics tests. The WGS reaction rate per mole of platinum in 1% Pt/ Nb_2CT_x measured at 300 °C was $0.016 \text{ mol H}_2 \text{ mol Pt}^{-1} \text{ s}^{-1}$, and the apparent activation energy was $71 \pm 3 \text{ kJ mol}^{-1}$ (Figure 5.8). The spent 1% Pt/ Nb_2CT_x catalyst had an average particle size of approximately $2.6 \pm 0.6 \text{ nm}$ based on high-angle annular dark field scanning transmission electron microscopy (HAADF-STEM) (Figure 5.9), which showed that the MXene support stabilized small platinum nanoparticles. We selected the 1.5% Pt/ Al_2O_3 catalyst (Table 5.1) from our previous work [262] as the reference catalyst because the particle size (estimated by platinum dispersion) is comparable to that of the 1% Pt/ Nb_2CT_x catalyst. Moreover, Al_2O_3 is considered a non-reducible oxide at the moderate reduction temperature (350 °C) in contrast with the reducible Nb_2CT_x support. Although, according to CO chemisorption, 35% of the platinum was exposed on the surface of the 1.5% Pt/ Al_2O_3 catalyst, we did not observe any measurable CO uptake at ambient temperature or at -30 °C for the fresh 1% Pt/ Nb_2CT_x catalyst after it was reduced *in situ* at 350 °C (Supporting Methods). The suppressed CO chemisorption was not due to particle agglomeration, and

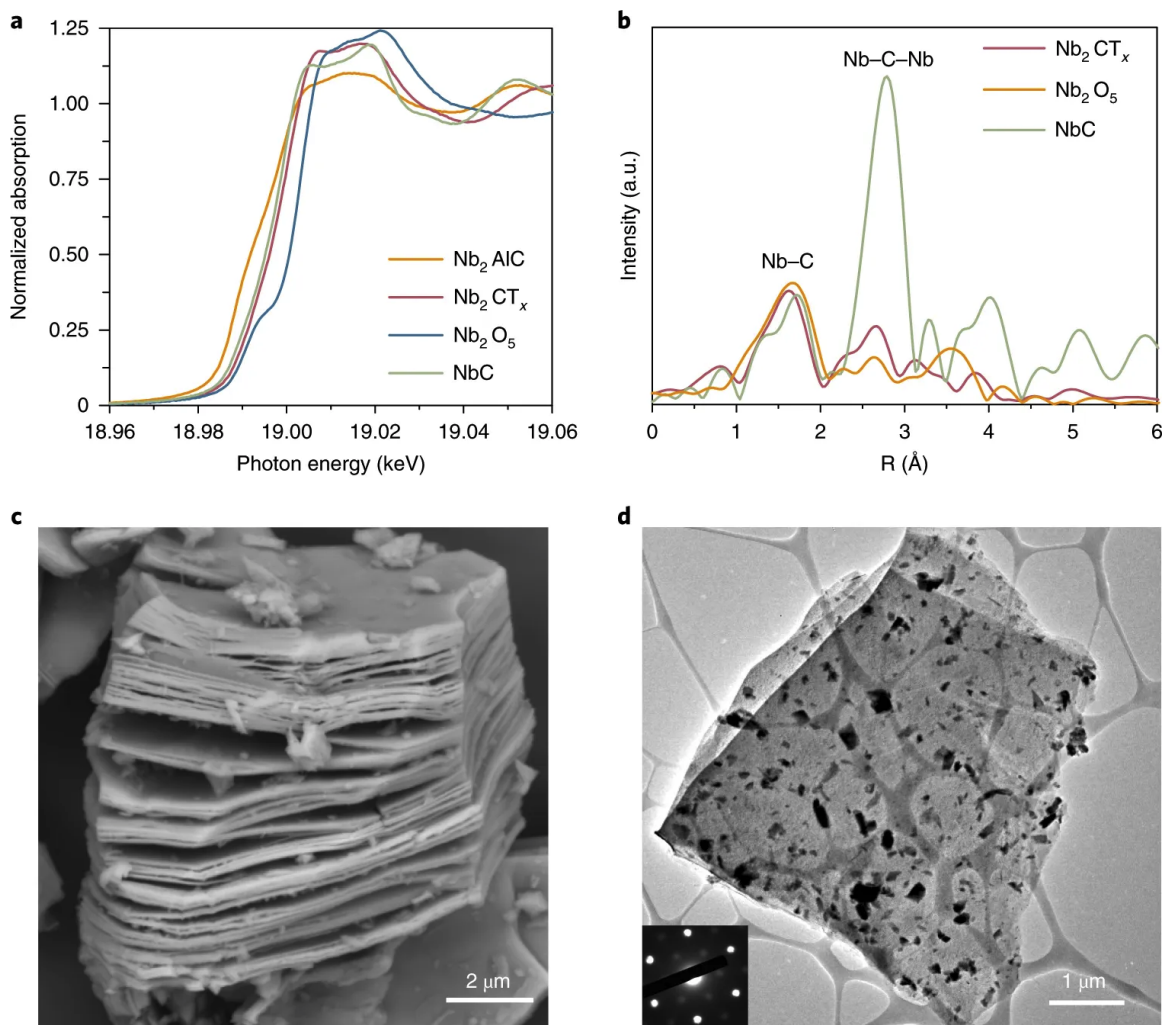


Figure 5.1. Characterization of Nb_2CT_x MXene support. (a) Niobium K-edge XANES of Nb_2AlC , Nb_2CT_x MXene, NbC and Nb_2O_5 . (b) Fourier transforms of the k^2 EXAFS of Nb_2CT_x compared with the references (NbC and Nb_2O_5). (c) Scanning electron microscopy micrograph of Nb_2CT_x MXene. (d) TEM image of Nb_2CT_x nanosheets. Inset: selected-area electron diffraction pattern showing hexagonal basal plane symmetry of the Nb_2CT_x nanosheets.

the average particle size of 1% Pt/ Nb_2CT_x should have corresponded to an estimated dispersion of 38%. This large discrepancy can be attributed to surface alloy formation due to the reducible surface of the niobium MXene-supported catalyst, which will be

discussed later. No measurable WGS conversion was observed for platinum supported by commercial NbC (bulk) under the same WGS test conditions. We found that the platinum particles had sintered significantly (average particle size: $\sim 13.8 \pm 9.6$ nm) in the Pt/NbC (bulk) catalyst (Figure 5.10). The agglomeration of nanoparticles substantially reduced the number of metal–support interface sites, which presumably led to the observed loss in WGS activity.

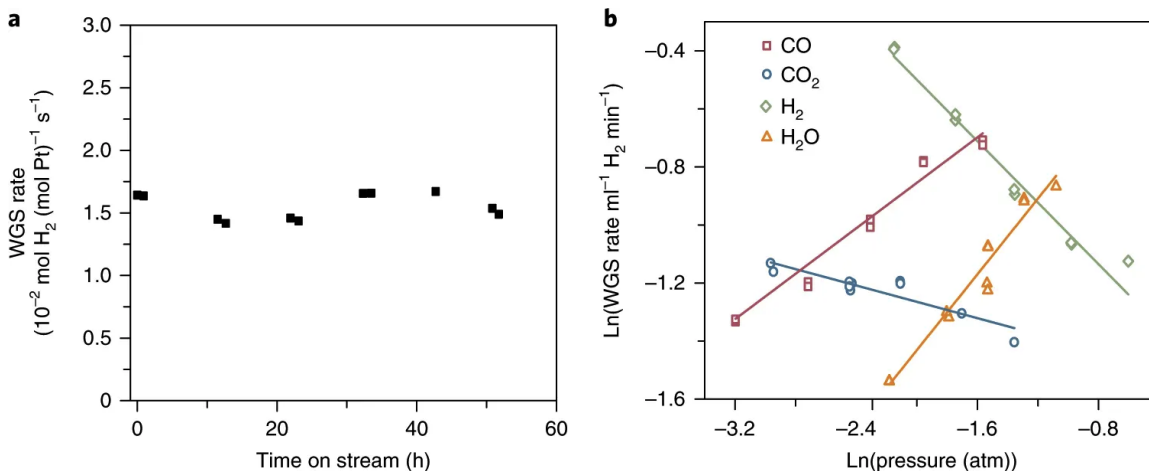


Figure 5.2. Kinetics of the WGS reaction over the 1% Pt/Nb₂CT_x MXene catalyst. (a) WGS rates normalized by the amount of platinum in the 1% Pt/Nb₂CT_x catalyst. The rates were measured at 300 °C with a feed composition of 6.8% CO, 21.9% H₂O, 8.5% CO₂ and 37.4% H₂ balanced by argon (standard conditions). (b) Apparent reaction orders for CO, CO₂, H₂ and H₂O for 1% Pt/Nb₂CT_x. Reaction orders were determined under standard conditions, with each component varying in the following range: 4–21% for CO, 5–25% for CO₂, 11–34% for H₂O and 14–55% for H₂.

The apparent reaction orders are shown in Figure 5.2b and Table 5.1. As the log derivative analysis of the Langmuir–Hinshelwood mechanism (Supporting Methods) shows, the apparent reaction order may be related to the relative surface coverage of the corresponding adsorbates. Lower apparent reaction orders with respect to certain reactants imply higher relative coverage of the adsorbed species [261]. Compared with the Pt/Al₂O₃ catalyst, Pt/Nb₂CT_x showed a higher apparent reaction order

Table 5.1.
WGS kinetics of Pt/Nb₂CT_x and Pt/Al₂O₃

Catalyst	WGS Rates at 300 °C (10 ⁻² mol H ₂ (mol Pt) ⁻¹ s ⁻¹)	TOR at 300 °C (10 ⁻² mol H ₂ (mol surface metal) ⁻¹ s ⁻¹)	E _a (kJ mol ⁻¹) (±3)	Reaction Orders (±0.03)				Percentage of Exposed Pt (%)
				H ₂ O	CO ₂	CO	H ₂	
1% Pt/Nb ₂ CT _x MXene	1.6	-	71	0.65	-0.09	0.39	-0.47	-
1.5% Pt/Al ₂ O ₃ (ref. [262])	1.4	4	96	0.90	-0.10	0.10	-0.50	35

E_a, activation energy; TOR, turnover rate

with respect to CO, which suggests that CO adsorption is weaker on the MXene-supported catalyst. At the same time, Pt/Nb₂CT_x had a lower apparent reaction order with respect to H₂O, indicating that the MXene support has a stronger H₂O adsorption affinity than that of Al₂O₃. Previous studies have also reported that the support surface plays a significant role in the activation of H₂O during the WGS reaction, and that the most active site of WGS is at the metal–support interface [263]. Here, Nb₂CT_x outperforms Al₂O₃ as a support for WGS catalysis due to its stronger interactions with H₂O or hydroxyl groups. The apparent reaction order for CO₂ was slightly negative and approached zero for both catalysts, which can be attributed to the weak interaction between the surface of the platinum and CO₂. The apparent reaction order with respect to H₂ was -0.47 for Pt/Nb₂CT_x, which is indicative of H₂ inhibition of the forward WGS reaction. The inhibition indicates that H₂ competes with CO for the limited number of active sites.

5.4.3 Reducibility of the Pt/Nb₂CT_x catalysts

To understand the change in the Nb₂CT_x MXene support after H₂ reduction, a series of quasi *in situ* XPS measurements were carried out (Supporting Methods). In the niobium 3*d* spectrum of a fresh Pt/Nb₂CT_x sample (top spectrum in Figure 5.3a), three pairs of peaks at 204.1/206.8 eV, 205.5/208.3 eV and 207.4/210.1 eV were identified as the 3*d*_{5/2}/3*d*_{3/2} doublets of Nb–C, NbC_xO_yF_z and Nb₂O₅, respectively [260]. The presence of surface terminations (–OH, –O and –F associated with

the $\text{NbC}_x\text{O}_y\text{F}_z$ species) on the fresh $\text{Pt}/\text{Nb}_2\text{CT}_x$ catalyst was also confirmed by high-resolution spectra in the O 1s and F 1s regions (bottom spectra in Figure 5.3b,c). The fresh $\text{Pt}/\text{Nb}_2\text{CT}_x$ catalyst was then reduced at 350 or 550 °C (designated as R350 °C and R550 °C, respectively) and the samples were analysed by XPS under ultrahigh vacuum conditions without exposure to air. Figure 5.3a shows the XPS spectra of the niobium 3d regions of the samples reduced at 350 and 550 °C, and the sample reduced at 350 °C and then exposed to air. The negligible change in the peaks corresponding to Nb–C (204.1 eV) indicates that the structure of Nb_2CT_x MXene was preserved after reduction at both 350 and 550 °C. However, after exposing the reduced sample to air, the intensity of the carbide peak decreased dramatically, and the Nb(V) oxide peak became better resolved (Figure 5.3a), which implies that the oxide species (Nb_2O_5) is enriched on the surface of the material, and the surface Nb–C partly decomposes. Moreover, after reduction at 350 °C (Figure 5.3b,c), the peaks for the adsorbed O and terminal OH/O groups that were present on the fresh $\text{Pt}/\text{Nb}_2\text{CT}_x$ surface disappeared, indicating that these surface OH/O terminations can be effectively removed. Following H_2 temperature-programmed reduction of Nb_2CT_x MXene, a peak indicative of H_2O at 340 °C appeared (Figure 5.11a), which was probably due to the removal of the O and OH functional groups. The atomic concentration of F terminations, as estimated by XPS analysis, decreased from 4 to 1.8% after reduction at 350 °C, but these were completely removed in the higher-temperature reduction (550 °C) (Figure 5.3c). The higher temperature required to remove the F moieties indicates that F groups bind more strongly than OH/O groups to the surface of the MXene. The results of the quasi *in situ* XPS analysis suggest that the surface of the catalyst is reduced under moderate temperature (350 °C). It is plausible that with the removal of surface functional groups from MXene, its coordinatively unsaturated surface is prone to oxidation in air, which suggests that the reduced surface is highly redox active.

$\text{Pt}/\text{Nb}_2\text{CT}_x$ samples with different treatments (fresh, 350 °C reduced and post-WGS) were also investigated by niobium K-edge XAS analysis (Figure 5.3d,e). In the

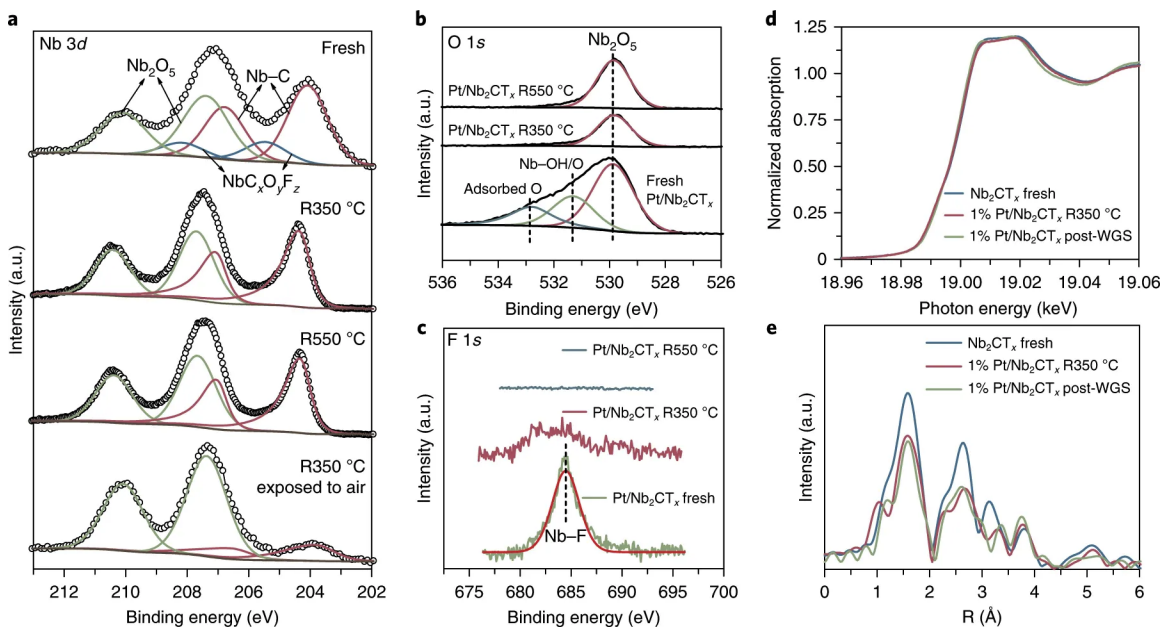


Figure 5.3. Niobium 3d XPS measurements and niobium edge XAS of Pt/Nb₂CT_x catalysts. (a) Niobium 3d region of *ex situ* XPS of a fresh 1% Pt/Nb₂CT_x sample, quasi *in situ* XPS of 1% Pt/Nb₂CT_x reduced at 350 and 550 °C, and *ex situ* XPS of 1% Pt/Nb₂CT_x reduced at 350 °C and exposed to air before analysis. (b) Quasi *in situ* XPS of the O 1s region of 1% Pt/Nb₂CT_x reduced at 350 °C and 550 °C. (c) Quasi *in situ* XPS of the F 1s region of 1% Pt/Nb₂CT_x reduced at 350 °C and 550 °C. (d) XANES spectra of the niobium K-edge of fresh Nb₂CT_x scanned in air, fresh 1% Pt/Nb₂CT_x treated with 3% H₂/He at 350 °C (*in situ*) and post-WGS reaction 1% Pt/Nb₂CT_x catalyst scanned in air. (e) Fourier transform magnitude of the k² EXAFS of fresh Nb₂CT_x, reduced fresh 1% Pt/Nb₂CT_x and post-WGS reaction 1% Pt/Nb₂CT_x catalyst. All treatments were the same as those used to collect the XANES spectra.

spent Pt/Nb₂CT_x catalyst and fresh Pt/Nb₂CT_x sample reduced by H₂ at 350 °C, the supports maintained the same carbide structure matrix as was present in the fresh Pt/Nb₂CT_x, based on the minimal changes observed in the XANES spectra. The scattering intensity in the EXAFS decreased slightly, which probably corresponded to the decrease in the number of ligands on the surface of Nb₂CT_x. The spent catalyst still showed the typical accordion-like structure of MXene (Figure 5.7b) and the

characteristic diffraction features of carbide (Figure 5.13), suggesting that the MXene support did not collapse during the WGS reaction. Therefore, our results indicate that the main structure of Nb_2CT_x remains intact during the reduction and WGS reaction, but the surface of Nb_2CT_x can be reduced at the moderate temperature (350 °C). The reducibility of the Nb_2CT_x support suggests that it can be used to introduce significant metal–support interactions to the catalyst.

5.4.4 RMSI

The interaction between platinum and the Nb_2CT_x support and the corresponding changes in the nanoparticles were further investigated by *in situ* platinum L_{III} edge XAS as well as platinum region XPS. For the platinum L_{III} edge XANES (Figure 5.4a), the whitenline of the 1% Nb_2CT_x catalyst reduced at 350 °C was more intense and narrower in shape than that of 2% Pt/ Al_2O_3 , which indicates the presence of non-platinum neighbours surrounding the platinum atoms. The change in the nanoparticle structure was also reflected by the altered EXAFS (Figure 5.4b) of the Nb_2CT_x catalyst compared with that of monometallic platinum on Al_2O_3 . The relative intensities of the peaks were different in the metal–metal distance region, suggesting that Pt–Nb interferes with Pt–Pt scattering; that is, through the formation of a bimetallic structure. Our fitting results of Nb_2CT_x reduced at 350 °C (7.4 Pt–Pt bond at 2.75 Å and 0.9 Pt–Nb bond at 2.76 Å) imply that a Pt-rich bimetallic surface alloy is formed at this moderate temperature, which indicates that RMSI occurs between the platinum nanoparticles and the Nb_2CT_x support.

Quasi *in situ* XPS analysis was also conducted to investigate the potential electronic effect of the formation of the bimetallic surface alloy. We used Pt/ SiO_2 as a reference instead of Pt/ Al_2O_3 because the aluminium $2p$ region overlaps with the platinum $4f$ region, and SiO_2 is a non-reducible oxide similar to Al_2O_3 . In previous works on Pt–M alloy systems (M = Sn, Co, Ru or Ti), the binding energies of platinum were reported to shift to higher values with respect to pure Pt [264–266]. In our XPS spectra (Figure 5.4c), the platinum $4f_{7/2}$ binding energy exhibited a positive shift (~ 0.5

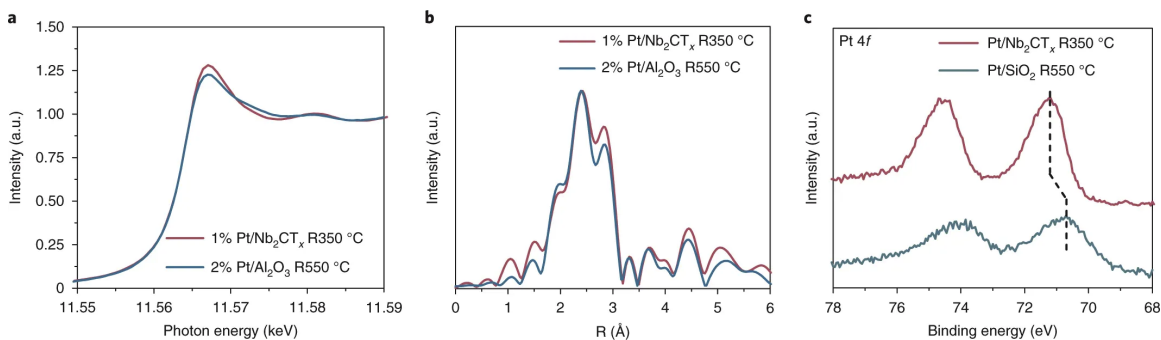


Figure 5.4. *In situ* XAS and quasi *in situ* XPS of the 1% Pt/Nb₂CT_x catalysts. (a) *In situ* XANES spectra of the platinum L_{III} edge of the 2% Pt/Al₂O₃ sample treated at 550 °C and fresh 1% Pt/Nb₂CT_x treated at 350 °C in 3% H₂/He. (b) Fourier transform magnitude of the k² EXAFS of the 2% Pt/Al₂O₃ sample treated at 550 °C and fresh 1% Pt/Nb₂CT_x treated at 350 °C in 3% H₂/He. (c) Quasi *in situ* XPS spectra of platinum 4f of Pt/SiO₂ reduced at 550 °C and 1% Pt/Nb₂CT_x reduced at 350 °C.

eV) for Pt/Nb₂CT_x compared with Pt/SiO₂, which is consistent with the literature and is indicative of the formation of a Pt–Nb bimetallic structure. When the reduction temperature was increased to 550 °C, similar changes of a greater magnitude were observed in the XPS and XAS analyses, and corresponded to a higher-degree alloy formation. We discuss this in more detail in Figure 5.14. Previous DFT studies suggest that the formation of alloys with transition metals modifies the electronic structure of platinum atoms and leads to shifts in the d-band centres, which could weaken CO adsorption [265,267,268]. This electronic effect resulting from the formation of the Pt–Nb surface alloy explains the suppressed CO chemisorption, as well as the altered relative coverage of CO on the Pt/Nb₂CT_x catalyst.

Although the *in situ* XAS and energy-dispersive spectroscopy (EDS) results (Figure 5.15) suggest that a uniform bulk alloy was not formed after reduction at the moderate temperature (350 °C), EELS in an aberration-corrected STEM was employed to provide a more direct characterization of the near-surface region of the Pt–Nb nanoparticles. Figure 5.5a shows typical Nb₂CT_x MXene-supported nanopar-

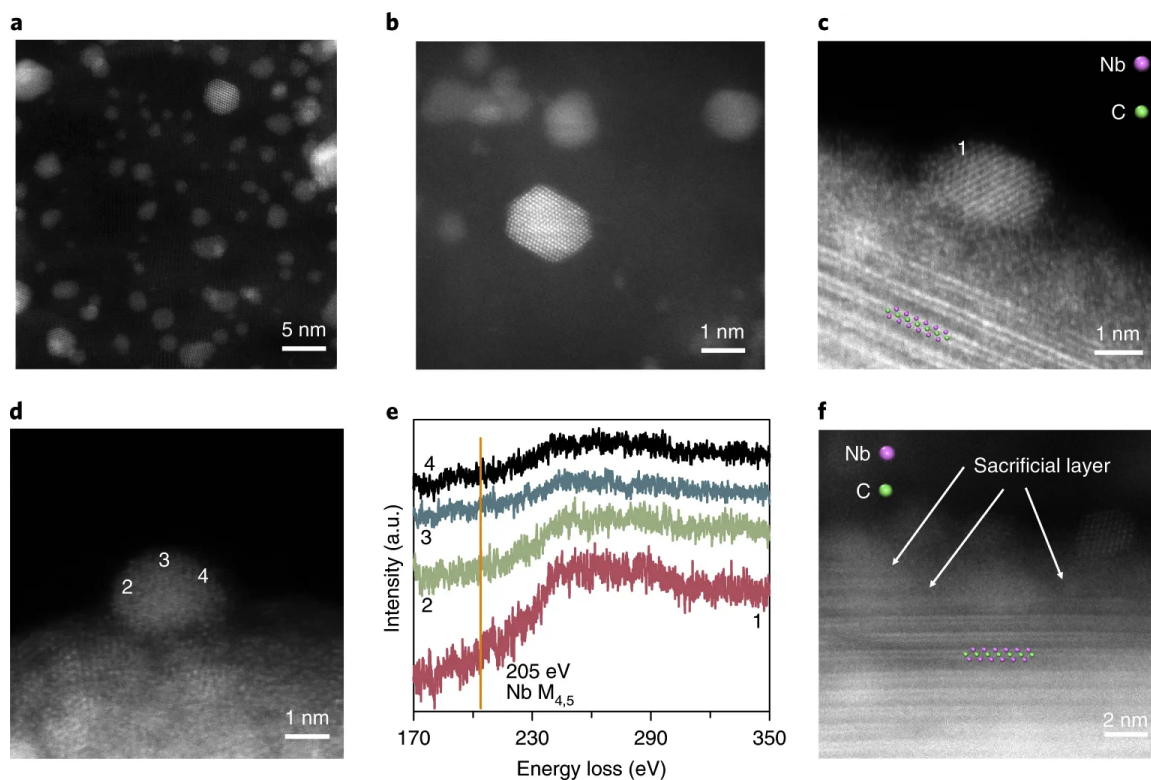


Figure 5.5. Electron microscopy and spectroscopy of the spent 1% Pt/Nb₂CT_x catalyst. (a,b) High-angle annular dark-field scanning TEM (HAADF-STEM) images of the post-WGS 1% Pt/Nb₂CT_x catalyst. (c,d) HAADF-STEM images of typical nanoparticles supported by Nb₂CT_x MXene. The majority of each particle is hanging over the vacuum to avoid niobium interference from the support. (e) EELS images acquired at several points on the particle surface, the locations of which are shown by corresponding numbers in (c) and (d,f) HAADF-STEM image showing discontinuous Nb₂CT_x MXene layers.

ticles with an average particle size of approximately 2.6 nm. The two-dimensionality of the MXene facilitates the STEM characterization of supported nanoparticles relative to conventional bulk carbide, so a twinned nanoparticle 3 nm in diameter can be atomically resolved (Figure 5.5b). Figure 5.5c,d shows Z-contrast STEM images of typical Pt–Nb alloy nanoparticles approximately 3 nm in diameter. The particles are only partially attached to the Nb₂CT_x MXene to avoid signals from the support.

Energy-loss spectra were taken with the electron beam scattering through several different points around the surface edge of the particles. The spectra from the edge of the nanoparticles provided electronic information primarily on near-surface atoms and exhibited a distinct 205 eV onset absorption band for niobium $M_{4,5}$ (Figure 5.5e), which indicates that niobium atoms are present on the surface of the particles. In comparison, we did not observe Pt–Nb alloy formation in the Pt/NbC (bulk) catalysts that were tested under the same conditions (Figure 5.16). This finding is consistent with previous work showing that platinum did not form an alloy with bulk carbide at moderate temperature, including Mo_2C that had been reduced at 450 °C [269], and these findings emphasize the significant role that the reducibility of MXenes plays in the RMSI.

Figure 5.5f shows nanoparticles supported by three-atom-thick Nb_2CT_x MXene layers. The MXene layers that were close to the nanoparticles decomposed (discontinued) and sacrificial layers were formed directly beneath the Pt–Nb particles. Taking the *in situ* XAS results in conjunction with the XPS results, this sacrificial layer may be the result of RMSI occurring at the interface between MXene and the nanoparticles. In addition, with the removal of surface terminations such as $-OH$, $-O$ and $-F$, exposed terminal niobium sites are generated on the surface of the Nb_2CT_x MXene support. These exposed niobium metal terminals are in contact with the Pt–Nb surface alloy and form interfaces that have strong affinities for H_2O or OH , as indicated by the WGS kinetics. The RMSI stabilizes and disperses the nanoparticles (~ 2.6 nm), which creates more interfaces than Pt/NbC (bulk) catalysts. Since the active sites of the WGS reaction are often thought to be the metal–support interfaces that are responsible for H_2O dissociation [270], the newly generated interfaces (with higher H_2O coverage than the Pt/ Al_2O_3) are presumed to make Pt/ Nb_2CT_x an active WGS catalyst. Thus, the Pt/ Nb_2CT_x catalyst becomes involved in RMSIs after reduction at the moderate temperature (350 °C), which probably tunes the catalytic properties through alloy formation, as well as modifying the admetal–support interface. Neither of these effects can be achieved using the conventional bulk niobium carbide.

Previous studies have shown that surface functional groups are not unique to Nb_2CT_x [249]. Considering the shared characteristics of the MXene family (prepared by etching) [250], such as reducible surface terminations and 2D structures, it is anticipated that RMSIs similar to the one between platinum and Nb_2CT_x MXene also apply to other MXene materials. We further investigated $\text{Ti}_3\text{C}_2\text{T}_x$ —another important member of the MXene family—as the support for platinum at 1% loading. EDS elemental mapping (Figure 5.17) was acquired in an area where nanoparticles were partially attached to the $\text{Ti}_3\text{C}_2\text{T}_x$ support to avoid the titanium signals from the MXene. The distribution of platinum and titanium overlapped through the nanoparticles, indicating the formation of Pt–Ti bimetallic structures. This result suggests that RMSIs can be extended to members of the MXenes family other than Nb_2CT_x , which showcases the generality of using MXenes as supports for preparing bimetallic catalysts.

5.5 Conclusions

In summary, we have demonstrated that 2D Nb_2CT_x MXene can be used as support for platinum and become involved in RMSIs after reduction at a moderate temperature (350 °C). The RMSI induces the formation of a bimetallic surface alloy and admetal– Nb_2CT_x interfaces that impact CO adsorption, H_2O activation and, ultimately, the kinetics of the WGS reaction. The highly reducible surface of Nb_2CT_x is vital to the introduction of the RMSI. The RMSI can be further extended to the Pt/ $\text{Ti}_3\text{C}_2\text{T}_x$ system with the formation of Pt–Ti bimetallic nanoparticles. Taken together, our results indicate that the RMSI between platinum and 2D carbides is probably a general phenomenon for members of the MXene family, which will open new avenues for designing bimetallic catalysts.

5.6 Supporting Information

5.6.1 Supporting Methods

Powder X-ray diffraction (XRD) was carried out on a Rigaku Ultima U4 diffractometer, with Cu K α radiation ($\lambda = 1.5418 \text{ \AA}$), at 40 kV and 44 mA. Scanning electron microscopy (SEM) was acquired on a FEI Quanta 250. Aberration-corrected high angle annular dark field scanning transmission electron microscopy (HAADF-STEM) images and electron energy loss spectroscopy (EELS) were acquired on a Titan Themis 300 probe corrected TEM equipped with a Super-X EDX detector at Sensitive Instrument Facility (SIF) of Ames Lab.

Pt loading of the Pt/Nb₂CT_x catalyst was determined by atomic absorption spectroscopy (AAS). Specifically, the catalyst was digested by aqua regia in a Nalgene[®] amber polyethylene bottle for 3 days and the solution was then diluted to desired concentration for the AAS measurement.

H₂ temperature programmed reduction (TPR) experiment was performed with an Autochem 2000 unit. About 70 mg of the Nb₂CT_x support was loaded in the unit and dried in 50 sccm He at 200 °C overnight. Then the catalyst was cooled to room temperature and purged with pure H₂. The temperature was ramped from room temperature to 900 °C under 50 sccm pure H₂. The products were analyzed by a mass spectroscopy.

CO chemisorption was measured with an ASAP 2020 unit. About 100 mg of the fresh Pt/ Nb₂CT_x catalyst was loaded and reduced at 350 °C in pure H₂ before measuring for CO chemisorption. CO/Pt stoichiometry factor of 1 was used to calculate the Pt dispersion.

Due to the low CO adsorption quantity on the catalyst, sub-ambient temperature CO pulse chemisorption was performed on a Micromeritics Autochem 2920 unit. Typically, about 100 mg of the fresh catalyst was loaded and reduced at 350 °C for 1 hour in 10% H₂/Ar with a total flow of 30 mL/min. Then the system was flushed

with He and the sample was cooled to $-30\text{ }^{\circ}\text{C}$. After reaching the stable temperature, CO pulse was introduced and the accumulated adsorption quantity was calculated.

XPS data were obtained using a Kratos Axis Ultra DLD spectrometer with monochromic Al $K\alpha$ radiation (1486.6 eV) at pass energy of 20 and 160 eV for high-resolution and survey spectra, respectively. A commercial Kratos charge neutralizer was used to avoid non-homogeneous electric charge of non-conducting powder and to achieve better resolution. The resolution measured as full width at half maximum of the curve fitted C 1s peak was approximately 1 eV. Binding energy (BE) values refer to the Fermi edge and the energy scale was calibrated using Au $4f_{7/2}$ at 84.0 eV and Cu $2p_{3/2}$ at 932.67 eV. XPS data were analyzed with CasaXPS. Curve-fitting was performed following a linear or Shirley background subtraction using Gaussian/Lorentzian peak shapes (GL and LF). The atomic concentrations of the elements in the near-surface region were estimated considering the corresponding Scofield atomic sensitivity factors and inelastic mean free path (IMFP) of photoelectrons using standard procedures in the CasaXPS software. For the quasi *in situ* XPS measurements, sample treatments were performed in a reaction cell ($\approx 30\text{ cm}^3$) connected to the XPS spectrometer and all samples were reduced in 5% H_2 at least for 30 minutes. Then the samples were moved between the reaction cell and the analysis chamber under ultrahigh vacuum (UHV) conditions without contact to air.

X-ray absorption measurements were acquired at the Nb K edge (18.9856 keV) and Pt L_{III} edge (11.5640 keV) on the bending magnet beam line of the Materials Research Collaborative Access Team (MRCAT) at the Sector 10 in the Advanced Photon Source, Argonne National Laboratory. Measurements were made in transmission step-scan mode. The ionization chambers were optimized for the maximum current with linear response with 10% absorption in the incident ion chamber and 70% absorption in the transmission detector. A third detector in series simultaneously collected a Nb or Pt metal foil reference spectrum with each measurement for energy calibration. Solid samples were pressed into a cylindrical sample holder consisting of six wells, forming a self-supporting wafer. The sample holder was placed in a quartz

reactor tube sealed with Kapton windows by two ultra-torr fittings through which gas could be flowed. Nb₂CT_x materials, parent Nb₂AlC and reference compounds Nb₂O₅, NbO₂, NbC (Sigma-Aldrich) were scanned in air. Fresh Pt on Nb₂CT_x catalyst were reduced in 3% H₂/He with a flow rate of 50 cm³ min⁻¹ at 350 °C or 550 °C for at least 30 min, then cooled to room temperature and flushed with He before they were scanned. The 1% Pt/Nb₂CT_x catalysts after water-gas-shift reaction were scanned in air.

The fits of the Extended X-ray Absorption Fine Structure (EXAFS) were evaluated using Artemis software [271]. The EXAFS coordination parameters were obtained by a least-squares fit in R-space of k²-weighted Fourier transform data together. The data range is from 3.0 to 12.0 Å⁻¹ in k space. For R space, the data was fitted from 1.0 to 3.0 Å in R space at the Nb edge and 1.6 to 3.2 Å at the Pt edge. The S₀² value was obtained at Nb edge by fitting the NbC standard and at Pt edge by fitting Pt foil. The bond distances were adjusted based on initial inputs from standard crystal structure information files of Nb₂AlC and Pt₃Nb for the fits of Nb edge and Pt edge, respectively [272, 273].

5.6.2 Langmuir-Hinshelwood mechanism

The detailed derivation of the Langmuir-Hinshelwood mechanism can be found in the book [274] Concepts of Modern Catalysis and Kinetics by I. Chorkendorff and J. W. Niemantsverdriet. Generally, for a mixture of reactant A and B:



$$\theta_A = \frac{K_A p_A}{1 + K_A p_A + K_B p_B + K_C^{-1} p_c} \quad (5.3)$$

$$\theta_B = \frac{K_B p_B}{1 + K_A p_A + K_B p_B + K_C^{-1} p_c} \quad (5.4)$$

Where θ_A and θ_B are the fraction of the available surface sites covered by species A or B at equilibrium, K_i is the adsorption equilibrium constant for species i and p_i is the partial pressure of species i . The dependence of K_i on temperature makes

θ_i temperature dependent. θ_i also depends on the heat of adsorption of species A and B. In turn, the apparent reaction orders with respect to such species involved in the reaction depend not only on the gas phase concentration but also on the reaction temperature. It is therefore necessary to measure the kinetic data over different catalysts at same temperature for objective comparison of relative surface concentrations of reactive species. If we assume the quasi-equilibrium assumption, which means only one elementary step determines the rate and all the other steps are in quasi-equilibrium state, then the apparent reaction orders can be derived as $n_A = 1 - \theta_A$ and $n_B = 1 - 2\theta_B$, where n_A and n_B are the apparent reaction orders with respect to A and B. Although it is a simplified estimation compared with our complex catalyst system here, it provides a quantitative picture about the relationship between the apparent reaction orders and the relative surface concentrations. The apparent reaction orders with respect to the reactants are thus negatively correlated with the corresponding relative surface coverage.

5.6.3 Supporting Figures

To test our hypothesis that only Pt-Nb surface alloy is formed for 1% Pt/Nb₂CT_x reduced at 350 °C, we further increased reduction temperature to 550 °C. Stronger evidence is observed from EXAFS of Pt/Nb₂CT_x sample reduced at higher temperature (550 °C), which is substantially different from that of Pt/Nb₂CT_x reduced at 350 °C because of the incorporation of larger amount of Nb in the nanoparticles. Fitting the spectra gives CN=6.7 for Pt-Pt bonds (2.77 Å) and CN=1.8 for Pt-Nb bonds (2.75 Å). Quasi *in situ* XPS spectra show Pt 4f_{7/2} components have binding energies equal to 70.7 eV, 71.2 eV and 71.6 eV for Pt/SiO₂ sample reduced at 550 °C and Pt/Nb₂CT_x sample reduced at 350 °C and 550 °C, respectively. Pt-Nb alloy with higher degree is presumably formed, as indicated by the further binding energy shift for Pt/Nb₂CT_x reduced at higher temperature (550 °C vs 350 °C). The alloy formation is further confirmed by HAADF-STEM with X-ray spectroscopy (EDS)

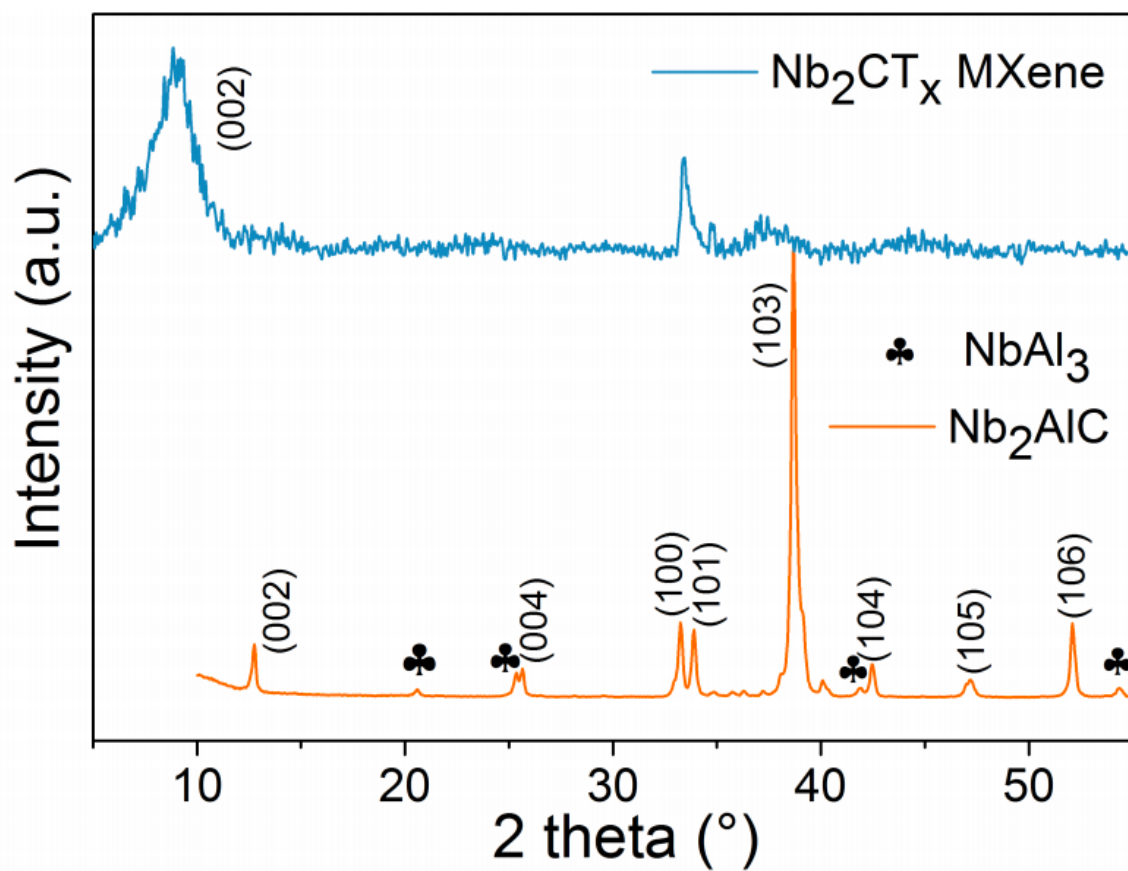


Figure 5.6. XRD patterns of Nb₂AlC MAX phase and Nb₂CT_x MXene

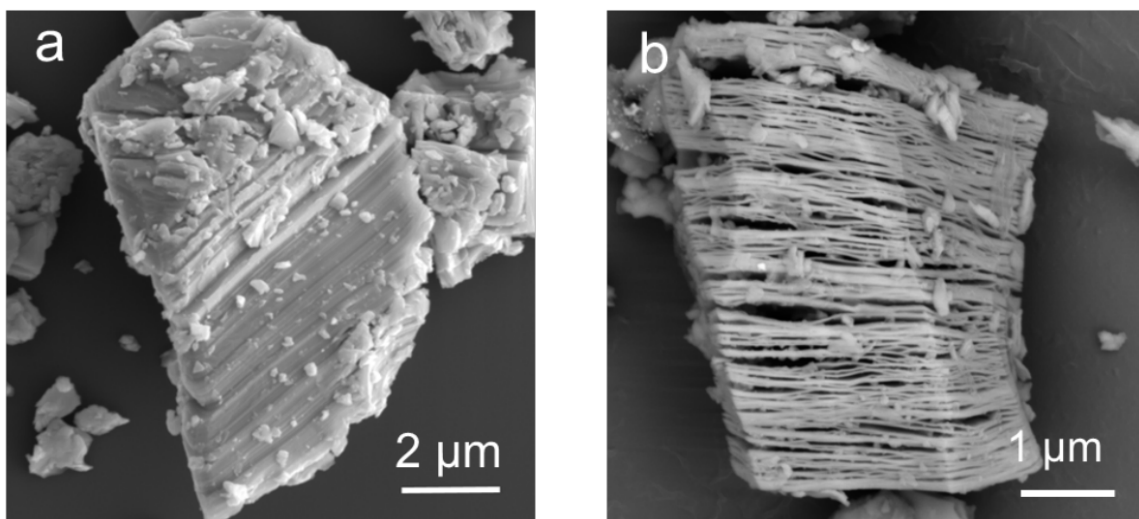


Figure 5.7. (a) SEM image of Nb₂AlC MAX. The as-synthesized Nb₂AlC shows the typical lamellar structure. (b) SEM image of 1% Pt/Nb₂CT_x after WGS reaction showing the Pt/Nb₂CT_x maintains the typical layered structure of MXene.

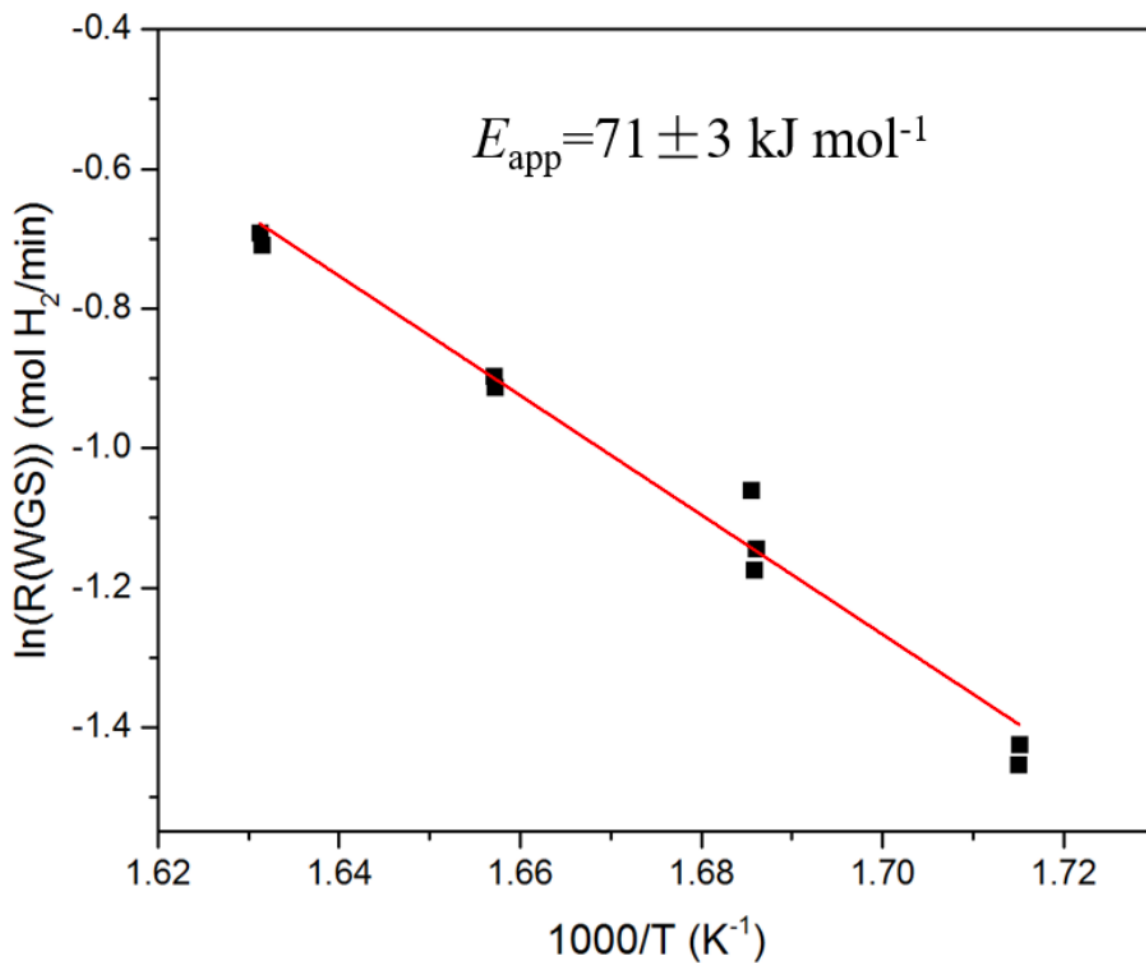


Figure 5.8. Arrhenius plots for WGS over 1% Pt/Nb₂CT_x-MXene catalyst. The WGS rates were measured in presence of 7% CO, 22% H₂O, 8.5% CO₂, 37% H₂, and balance Ar.

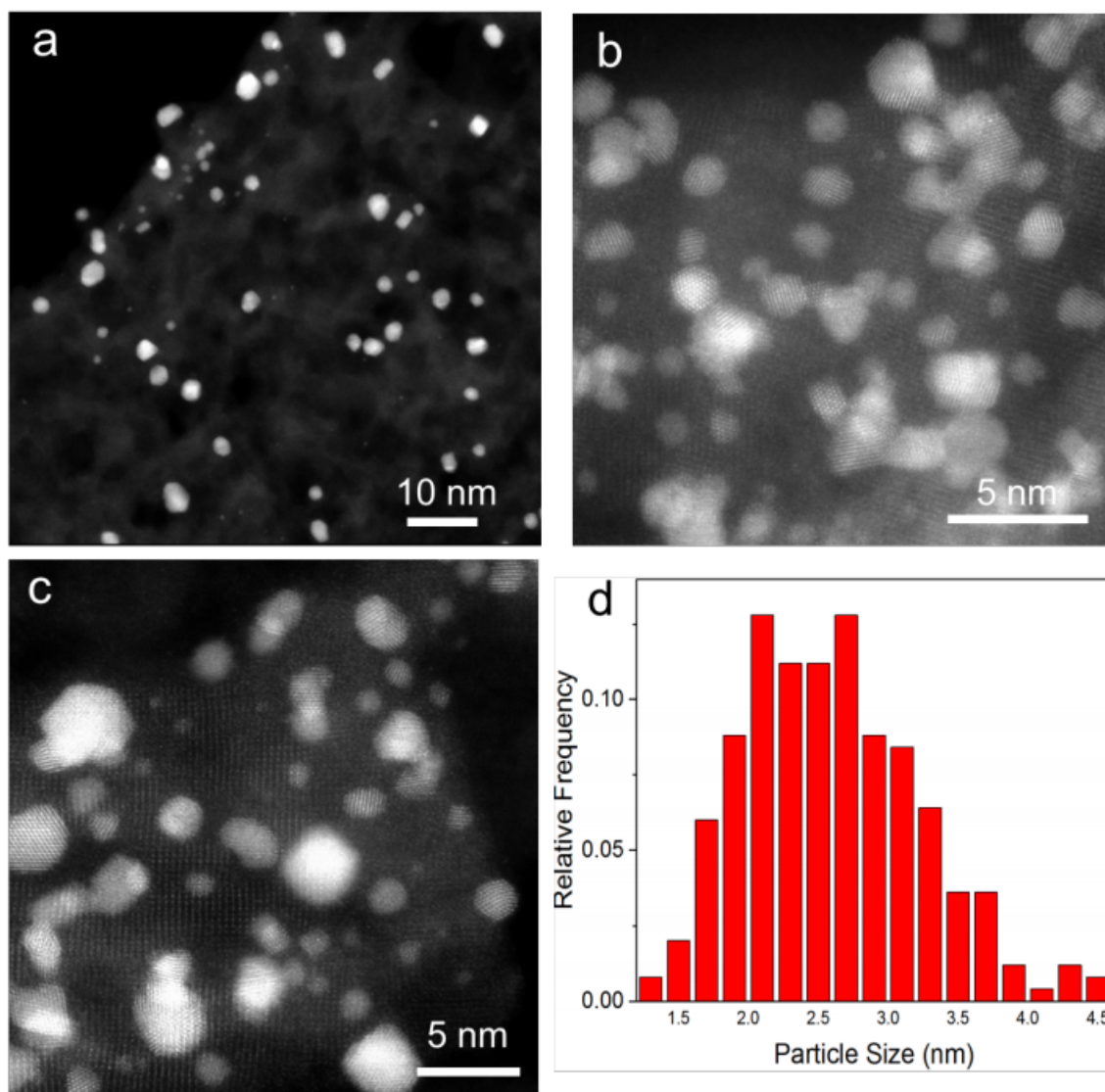


Figure 5.9. (a-c) HAADF-STEM images of 1% Pt/Nb₂CT_x after WGS reaction. (d) Particle size distribution statistics of used 1% Pt/Nb₂CT_x catalyst, and the average particle size is determined to be 2.6 ± 0.6 nm

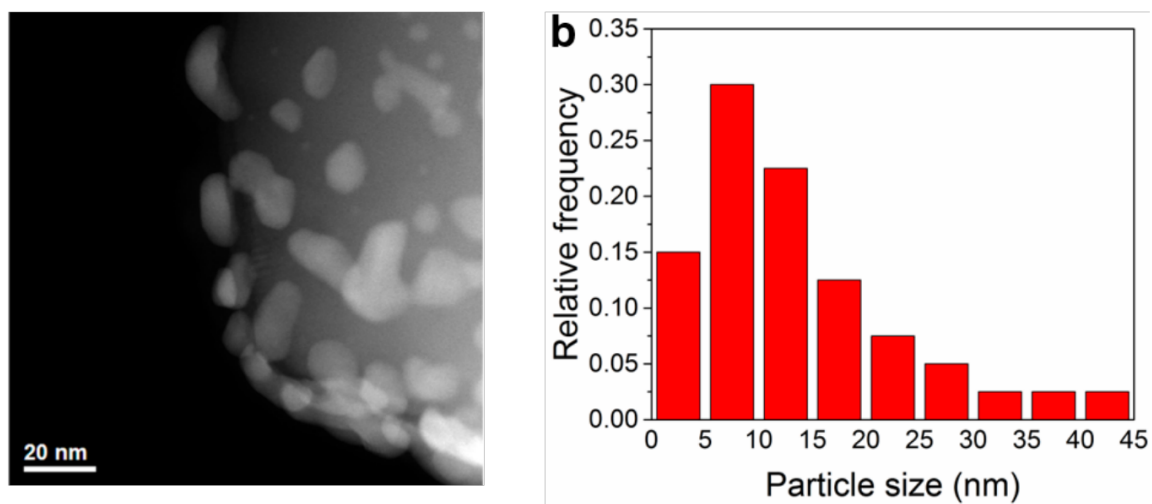


Figure 5.10. (a) HAADF-STEM image of 1% Pt/NbC (bulk) after WGS reaction. (b) Particle size distribution statistics of used 1% Pt/NbC (bulk), and the average particle size is determined to be 13.8 ± 9.6 nm.

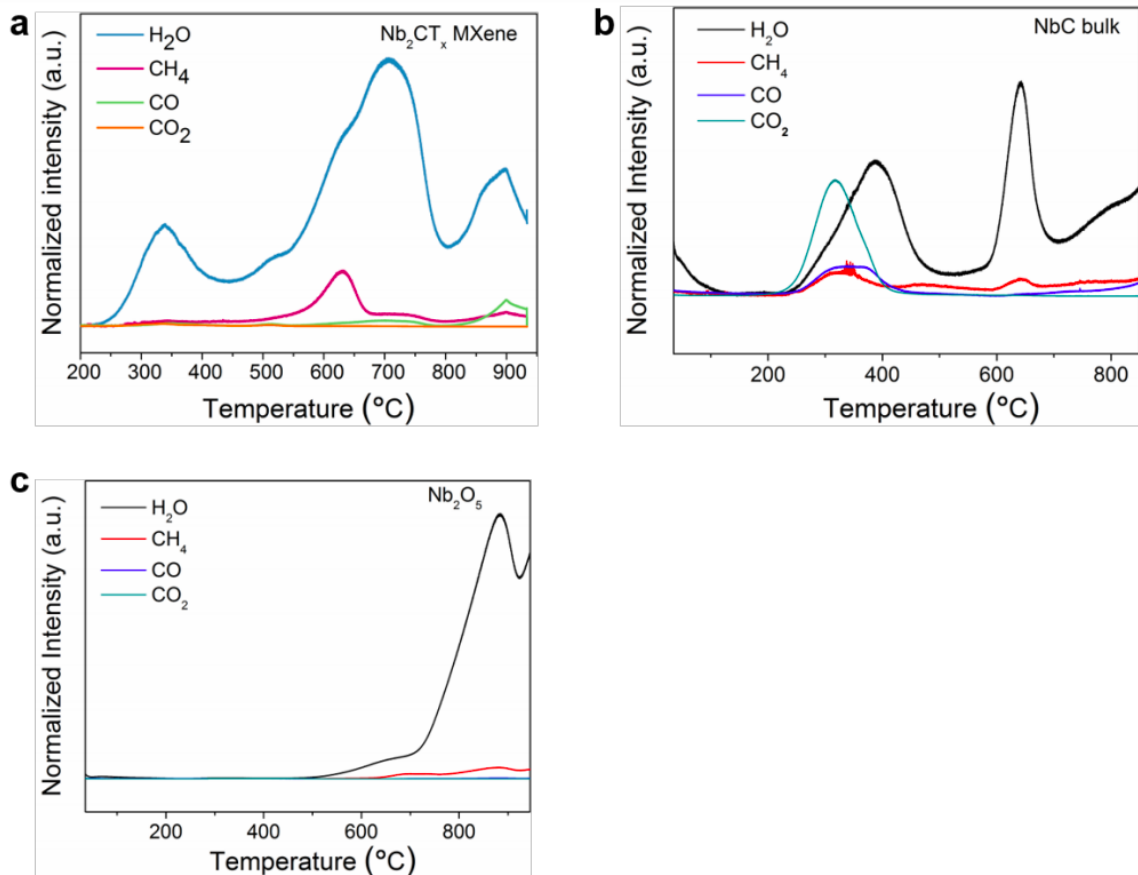


Figure 5.11. (a) Temperature programmed reduction (TPR) profile of Nb₂CT_x MXene. The H₂O peak around 340 °C can be attributed to the reduction of O and OH terminations on the surface of Nb₂CT_x MXene, which is consistent with the results of the quasi *in situ* XPS. Comparing with the TPR profile of Nb₂O₅, the additional H₂O peaks located above 600 °C can be assigned to the reduction of residual Nb₂O₅ after HF etching [275]. The residue oxygen on the surface also desorbs as CO and CO₂ [276] (b) TPR profile of commercial bulk NbC. The H₂O peaks at around 400 °C and 650 °C are likely due to the removal of the surface residue oxygen [277]. (c) TPR profile of commercial bulk Nb₂O₅. The peak between 800 °C and 900 °C is due to the reduction of Nb₂O₅ to NbO₂ [278].

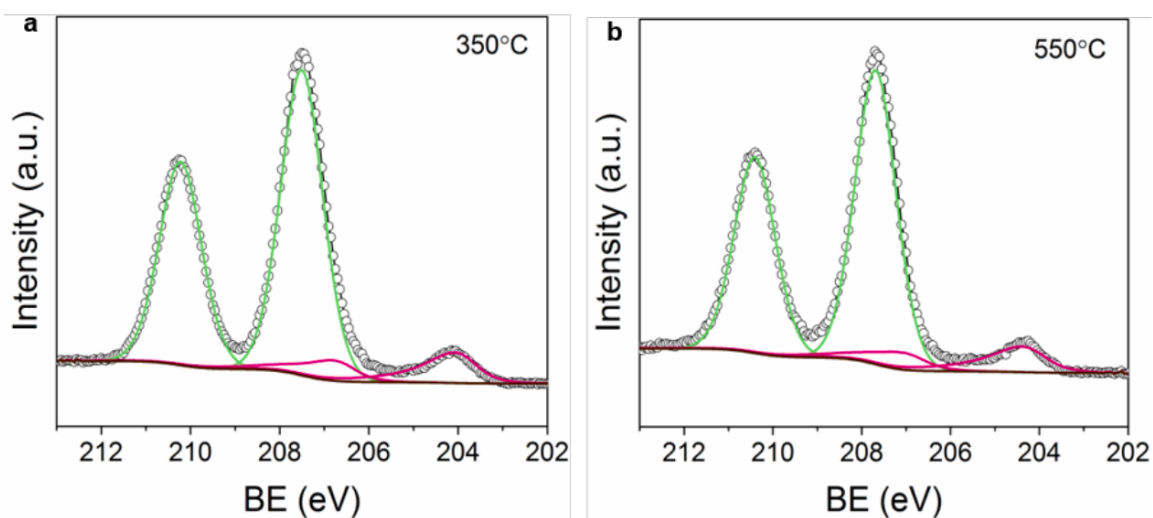


Figure 5.12. Quasi *in situ* XPS spectra of Nb 3d of pre-reduced 1% Pt/Nb₂CT_x sample (the fresh sample was reduced at 350 °C by H₂ and then exposed to air before the quasi *in situ* XPS measurement) reduced at 350 °C and 550 °C again. These results indicate the enriched Nb₂O₅ induced by subsequent air exposure is not reducible by H₂ at 550 °C.

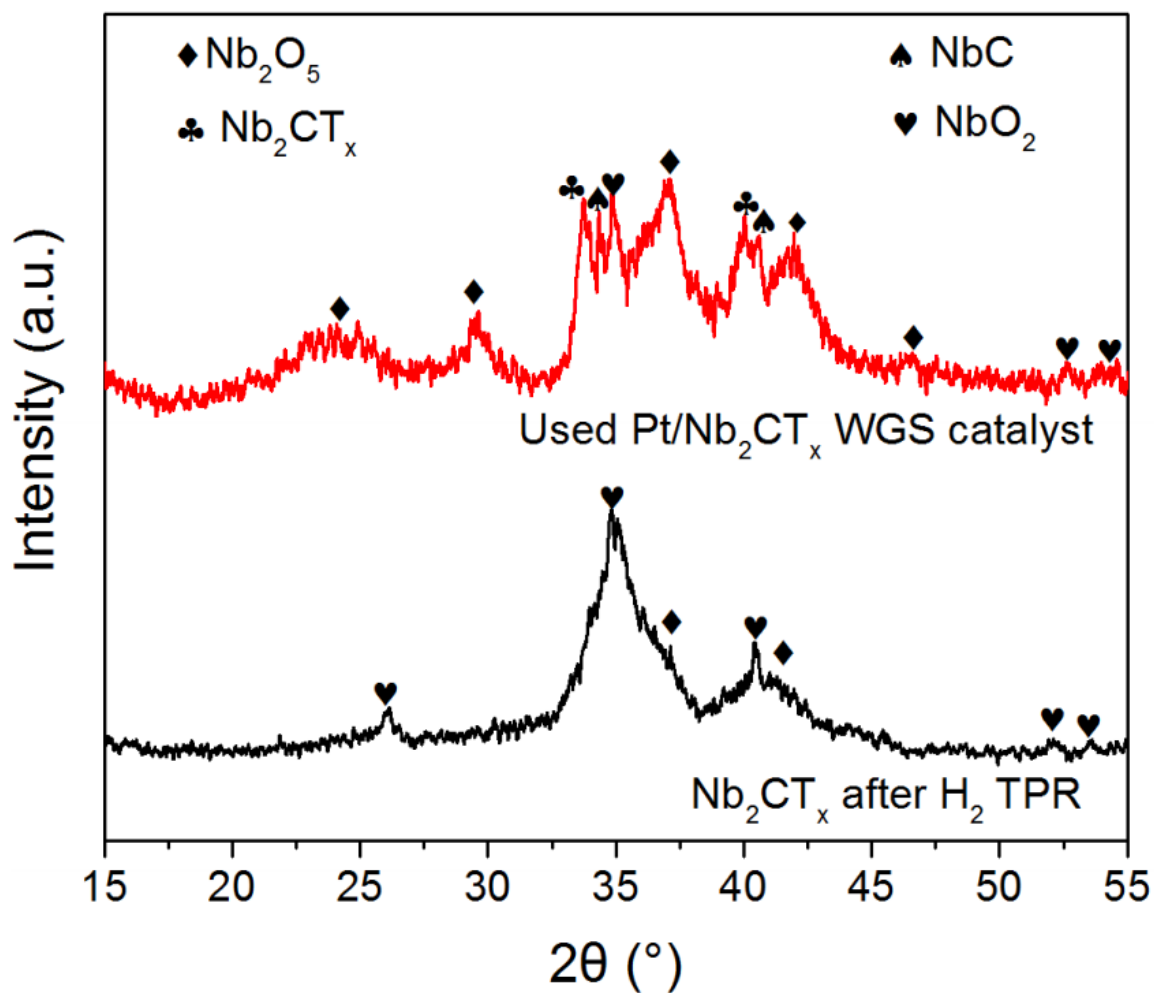


Figure 5.13. XRD patterns of spent 1% Pt/Nb₂CT_x catalyst after WGS reaction (red line) and Nb₂CT_x MXene after TPR treatment (black line).

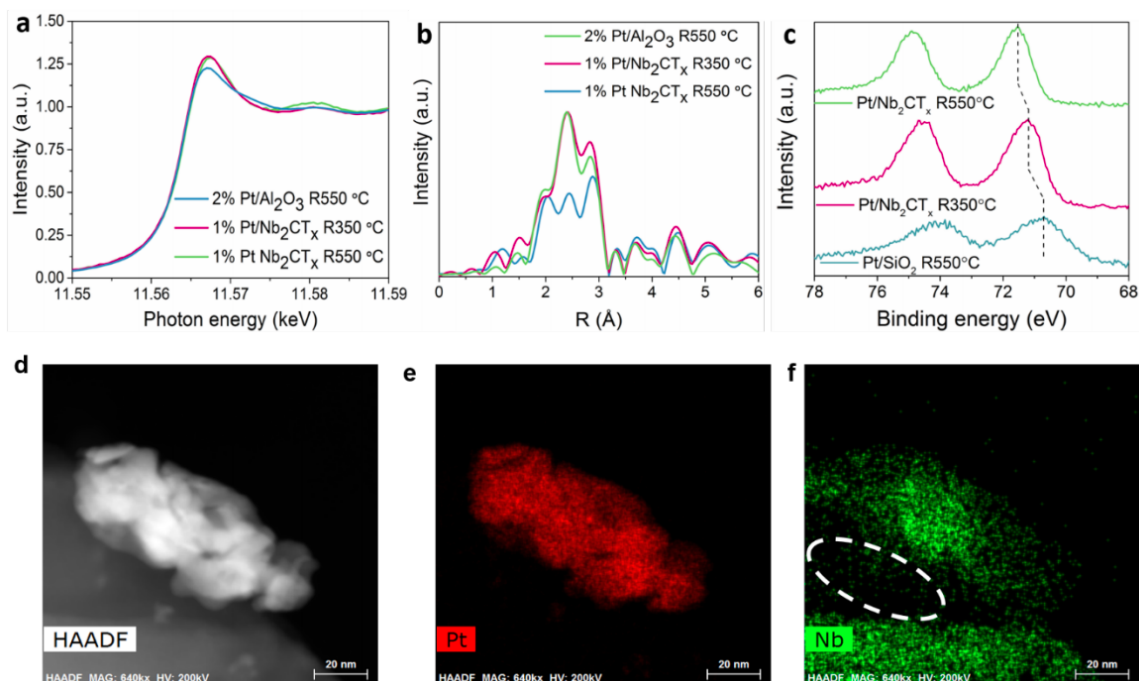


Figure 5.14. (a) *In situ* XANES spectra of Pt L_{III} edge of 2% Pt/Al₂O₃ sample treated at 550 °C and fresh 1% Pt/Nb₂CT_x treated at 350 °C and 550 °C in 3% H₂/He. (b) Fourier transform magnitude of the k² EXAFS of 2% Pt/Al₂O₃ sample treated at 550 °C and fresh 1% Pt/Nb₂CT_x treated at 350 °C and 550 °C in 3% H₂/He. (c) Quasi *in situ* XPS spectra of Pt 4f_{7/2} of Pt/SiO₂ reduced at 550 °C and Pt/Nb₂CT_x sample reduced at 350 °C and 550 °C. (d) HAADF-STEM image of fresh 1% Pt/Nb₂CT_x catalyst reduced in H₂ at 550 °C. Particle agglomerates after the high temperature (550 °C) reduction. (e) Elemental mapping of Pt. (f) Elemental mapping of Nb. A Nb deficient area is circled by the white dash line.

elemental mapping. Interestingly, a niobium deficient area is right beneath the alloy nanoparticle, which may imply diffusion of reduced Nb species.

Note the fitting results of XAS represent average numbers of the sample. The homogeneity and order of the alloys formed at 550 °C merit detailed study in the future.

Table 5.2.
Quantitative evaluation of the EXAFS fit (Artemis Software)

Sample	Scattering Pair	S_0^{2*}	CN*	Bond Length (Å)*	ΔE_0 (eV)*	σ^2 (Å ²)*
Pt/Nb ₂ CT _x Reduced at 350 °C	Pt-Pt	0.8	7.4	2.75	4.2	0.005
	Pt-Nb		0.9	2.76		0.010
Pt/Nb ₂ CT _x Reduced at 550 °C	Pt-Pt	0.8	6.7	2.77	5.5	0.005
	Pt-Nb		1.8	2.75		0.008

*The S_0^2 is fixed at the value obtained by fitting a Pt foil reference. The errors of all the fitted parameters are very close. The average error in CN (coordination number) is 0.5, in bond length is 0.02 Å, in ΔE_0 is 0.8 eV and in σ^2 is 0.002 Å².

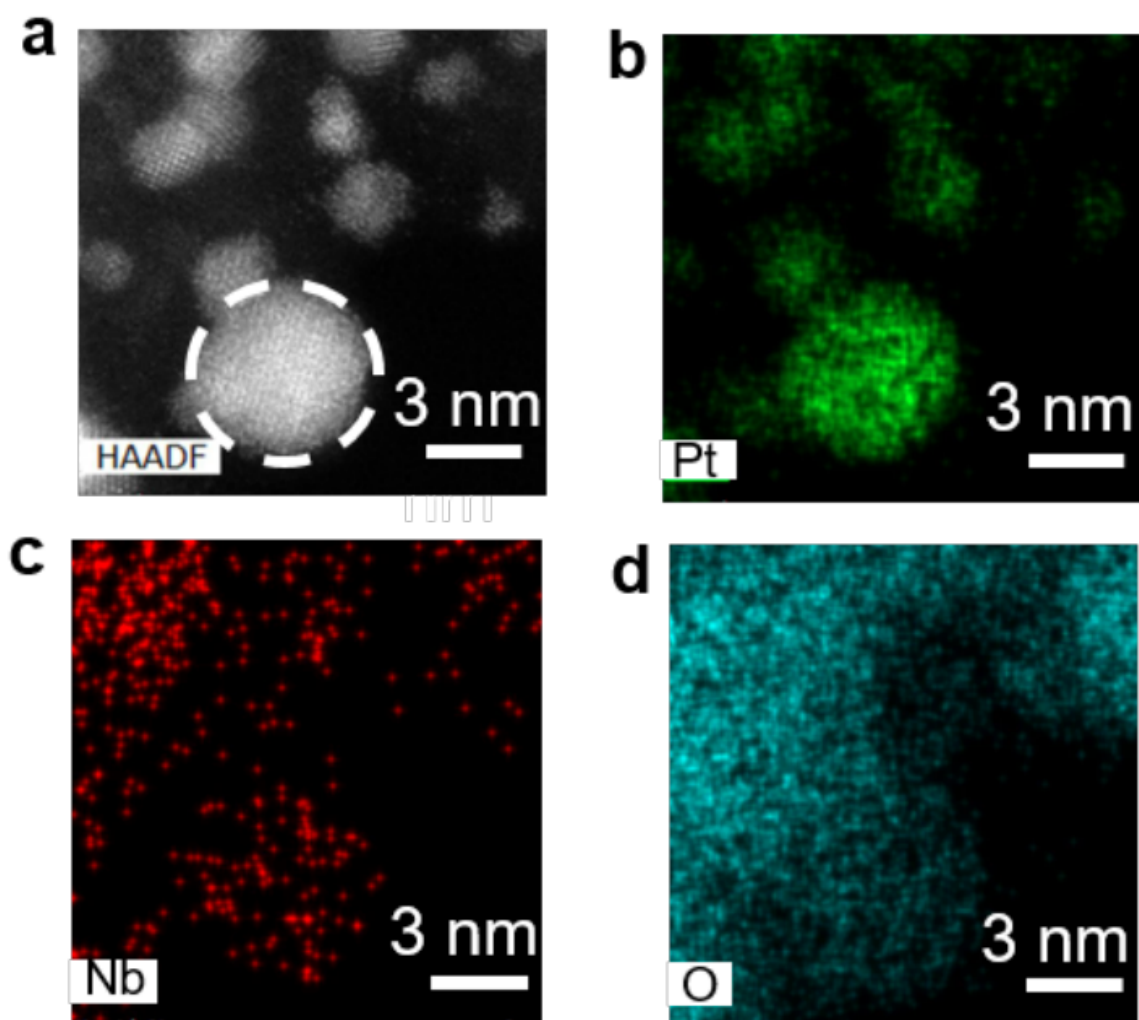


Figure 5.15. (a) HAADF-STEM image of used 1% Pt/Nb₂CT_x WGS catalyst. (b) Elemental mapping of Pt (c) Elemental mapping of Nb, (d) Elemental mapping of O. The area of interest (circled using white dash line) is a nanoparticle which is hanging over vacuum to avoid Nb signal from the Nb₂CT_x support. The EDS result suggests that uniform bulk Pt-Nb alloy is not formed.

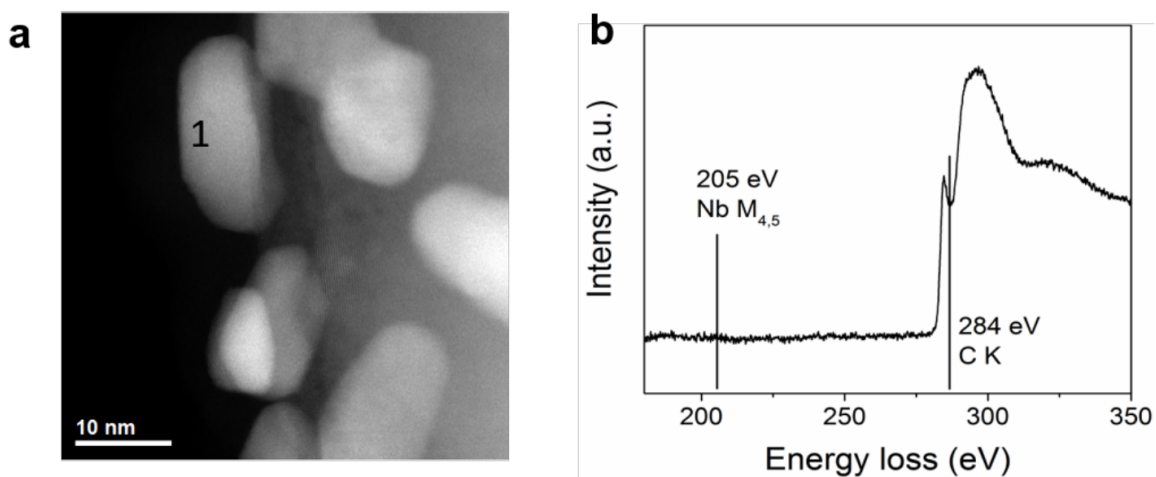


Figure 5.16. (a) HAADF-STEM image of used 1% Pt/NbC bulk catalyst. (b) Spectrum of electron-energy loss acquired at a point (marked as “1”) on the particle surface. The absence of Nb M_{4,5} absorption edge with onset at 205 eV indicates no Pt-Nb surface alloy is formed for Pt supported by bulk NbC. The signal of C can be caused by carbon lacey of the TEM grid or carbon contamination of the catalysts. Note the catalyst was synthesized and treated using the same procedure with 1% Pt/Nb₂CT_x WGS catalyst.

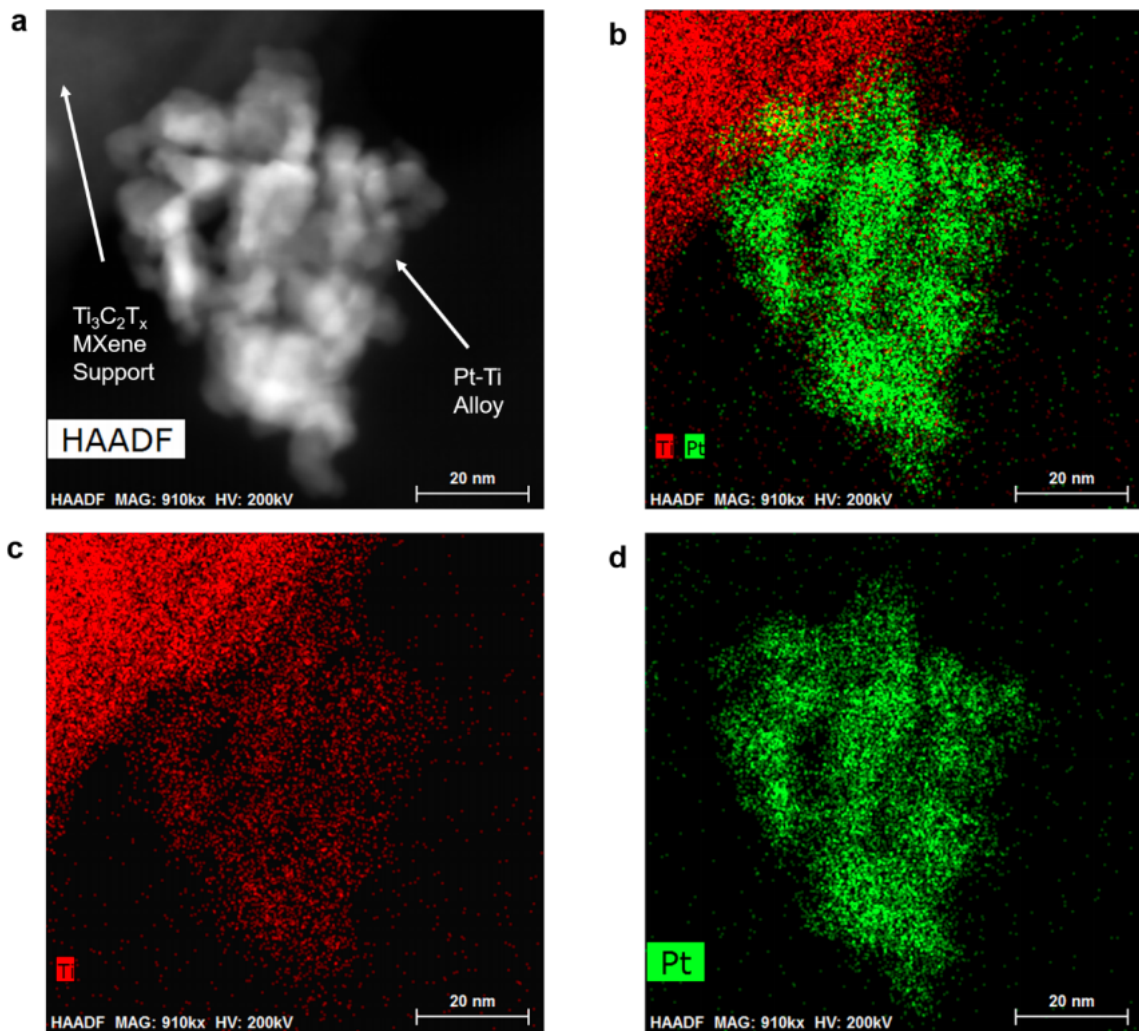


Figure 5.17. (a) HAADF-STEM image of fresh 1% Pt/Ti₃C₂T_x catalyst reduced in H₂ at 550 °C. Particles agglomerated after the high temperature (550 °C) reduction. (b) Elemental mapping of Pt and Ti. (c) Elemental mapping of Ti, (d) Elemental mapping of Pt.

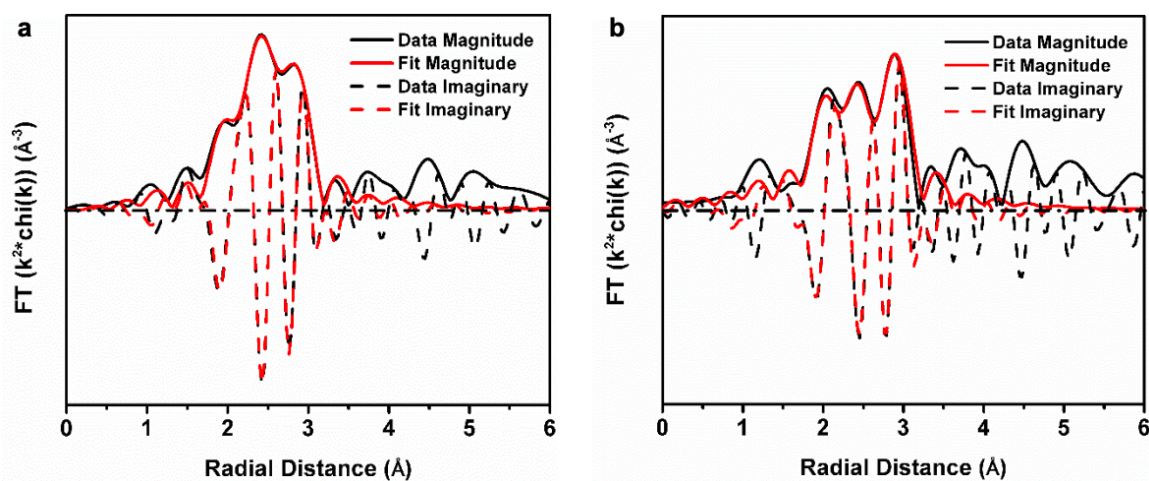


Figure 5.18. The magnitude and imaginary part of the Fourier Transform of the k^2 weighted EXAFS plot and corresponding first shell fit for Pt/Nb₂CT_x catalyst reduced at (a) 350 °C and (b) 550 °C. The fitting ranges are $\Delta k = 2.7\text{-}11.7 \text{\AA}^{-1}$ and $\Delta R = 1.6\text{-}3.2 \text{\AA}$. Corresponding fitting results are in Table 5.2

6. PROPYLENE OXIDE INHIBITS PROPYLENE EPOXIDATION OVER Au/TS-1

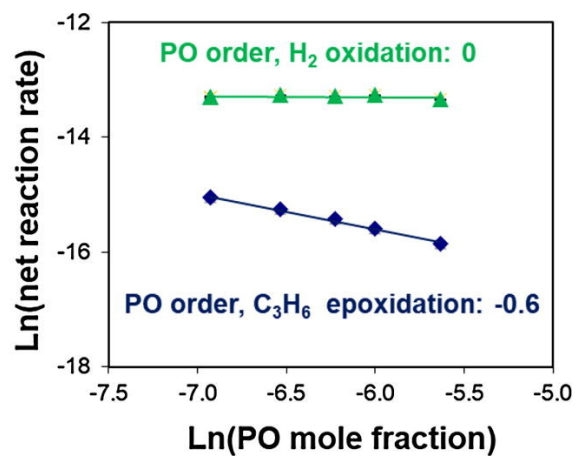
Journal of Catalysis, 2018, 365, 105-114. <https://doi.org/10.1016/j.jcat.2018.06.015>

James W.Harris, Jeremy Arvay, Garrett Mitchell, W. Nicholas Delgass, Fabio H. Ribeiro

6.1 Abstract

The kinetics of propylene epoxidation over Au supported on titanium silicalite-1 (Au/TS-1) catalysts were measured in a continuous stirred tank reactor (CSTR) free from temperature and concentration gradients. Apparent reaction orders measured at 473 K for H₂ (0.7 order), O₂ (0.2), and C₃H₆ (0.2) for a series of Au/TS-1 with varied Au (0.02–0.09 wt%) and Ti (Si/Ti: 75–143) contents were consistent with those reported previously. Co-feeding propylene oxide enabled measurement of the apparent reaction order in propylene oxide (−0.4 to −0.8 order) and the determination that relevant pressures of propylene oxide reversibly inhibit propylene epoxidation over Au/TS-1, while co-feeding carbon dioxide and water had no effect on the propylene epoxidation rate. Analysis of previously proposed two-site reaction mechanisms in light of reaction orders for O₂ (0.4), H₂ (1), and C₃H₆ (0.4), corrected to account for propylene oxide inhibition, provides further evidence that propylene epoxidation over Au/TS-1 occurs via a simultaneous mechanism requiring two distinct, but adjacent, types of sites, and not a sequential mechanism that invokes migration of H₂O₂ formed on Au sites to PO forming Ti sites. H₂ oxidation rates are not inhibited by propylene oxide, implying that the sites required for hydrogen oxidation are distinct from those required for propylene epoxidation.

Propylene epoxidation and hydrogen oxidation occur at distinct sites



6.2 Introduction

Propylene epoxidation is a critical step in industrial polyurethane production and has an estimated annual production of 8.6 million tons per year [279]. Since the first report of titania-supported Au catalysts for the partial oxidation catalysis by Haruta and co-workers [280], propylene epoxidation rates (per kg catalyst) over Au-Ti catalysts have increased dramatically. These increases have been achieved by limiting the TiO₂ domains to single Ti atoms by incorporation in SiO₂ substrates, particularly Ti-Si zeolites such as TS-1, leading to increased epoxidation rate (from ~ 11 g_{PO} kg_{cat}⁻¹ h⁻¹ over Au/TiO₂ at 323 K to ~ 150 g_{PO} kg_{cat}⁻¹ h⁻¹ over Au/TS-1 at 473 K) and with selectivity (from $\sim 70\%$ to $\sim 80\%$ [281]) that approaches that of Au/TiO₂ ($\sim 99\%$ [280]). Further steady-state rate and selectivity increases were achieved by judicious choice of promoters [282–288], resulting in steady state propylene oxide (PO) formation rates of ~ 300 g_{PO} kg_{cat}⁻¹ h⁻¹ with a PO selectivity of $\sim 80\%$ [282]. Similarly, reduction of zeolite crystal size and addition of mesoporosity resulted in steady state PO formation rates of ~ 140 g_{PO} kg_{cat}⁻¹ h⁻¹ over 50 h on stream with a propylene oxide selectivity of $\sim 95\%$ [289].

Despite increases in reaction rates, comparatively minor increases (from $\sim 10\%$ to 40%) [280,281] in hydrogen efficiency (S_{H_2} = mol PO produced per mol H₂ consumed) over Au/TS-1 catalysts compared to the industrially required value of $\sim 50\%$ continue to limit the utility of these catalysts [290]. While S_{H_2} values between 35 and 40% have been reported for Au/TS-1 with Si/Ti > 100 and Au loadings of 0.009–0.03 wt%, the steady state propylene epoxidation rates over these catalysts range from 22 to 80 g kg_{cat}⁻¹ h⁻¹ [281,287]. A S_{H_2} of 99% has been reported for a 0.005 wt% Au supported on TS-1 with a Si/Ti ratio of 170 (TS-1(170)), though the propylene epoxidation rate was 4.8 g kg_{cat}⁻¹ h⁻¹ [287]. The S_{H_2} values measured over 0.04 wt% Au catalysts supported on uncalcined TS-1 (U-TS-1) catalysts at steady state are $\sim 40\%$, compared to $\sim 25\%$ for their calcined counterparts at this Au loading [291]. While state-of-the-art Au-Ti catalysts for direct gas-phase epoxidation of propylene lack the combination of

PO selectivity, H₂ selectivity, and PO formation rate per mass of catalyst necessary to compete with existing processes, this catalyst system is of interest for the opportunity it presents to unravel the complex catalytic chemistry and kinetics of *in situ* hydrogen peroxide formation on coordinatively unsaturated Au clusters and epoxidation reactions of such species in proximity to isolated Ti atoms. In addition, understanding these Au-Ti catalysts may accelerate realization of the potential environmental and safety benefits of this approach to PO production. Without accurate measurement of the reaction kinetics, it is not tractable to determine whether the most active sites for propylene oxide production have inherently low S_{H₂}, or if there are separate, low epoxidation rate, high H₂ oxidation rate sites that could be limited during catalyst synthesis. Further, efforts to determine the most active Au-Ti sites in order to stabilize these sites via new synthetic procedures for operation at industrially relevant pressures [292] are not possible without first understanding the reaction kinetics.

Development of reaction mechanisms consistent with all data measured in the literature has lagged behind improvements in maximum propylene epoxidation rates and selectivities. Measured H₂/D₂ kinetic isotope effects on Au/TiO₂ catalysts [293] indicate the breaking of a bond to hydrogen in the rate determining step, consistent with kinetically relevant hydroperoxy intermediates observed spectroscopically over Au/TiO₂ catalysts previously [294]. Raman spectroscopy combined with measurement of H₂O₂ formation over colloidal palladium catalysts with either ¹⁶O₂ or ¹⁸O₂ reactants confirmed that oxygen was present as molecular oxygen during H₂O₂ formation over these catalysts [295]. An experimental study of activation energies and apparent reaction orders by Taylor et al. [296] determined reaction orders (H₂: 0.5, O₂: 0.3, C₃H₆: 0.2) across Au/TS-1 catalysts with a range of molar Si/Ti ratios (36–144), Au loadings (0.02–0.06 wt%), and at a range of feed partial pressures (H₂: 8–24 mol% O₂: 2–8 mol%; C₃H₆: 8–24 mol%) and temperatures (413–473 K), similar to those reported elsewhere [297, 298]. These findings are consistent with a simultaneous two-site mechanism, where a hydroperoxy intermediate forms on a Au site and reacts with propylene adsorbed on an adjacent framework Ti site in TS-1 [296, 299].

A second mechanism first proposed by Lu et al. [300] and reaffirmed by Kanungo et al. [301] includes two kinetically relevant steps, the first of which forms HOOH adsorbed at one of two Au sites required and the second involves decomposition of a $C_3H_6HOOH-Ti$ species into PO and water. The mechanism presented by Lu et al. and Kanungo et al. includes separate Au regions involved in either H_2 oxidation only or both H_2 oxidation and combustion [300,301]. This mechanism is consistent with reaction orders reported by Taylor et al. [296], and notably involves adsorption of C_3H_6 at Au rather than Ti sites. Additionally, the reaction orders reported by Taylor et al. [296] are inconsistent with a sequential two-site mechanism, in which H_2O_2 forms on Au particles prior to desorbing intact, co-adsorbing with propylene on Ti-defect sites ((OH)-Ti-(OSi)₃) and reacting, as has been proposed as the mechanism for liquid-phase epoxidation reactions over TiO_2 and TS-1 [302], since such a mechanism would result in reaction orders for hydrogen and oxygen being equal, which has not been observed [296].

Joshi et al. calculated lower energy barriers for the simultaneous mechanism than the sequential mechanism over Au clusters supported within TS-1 pores [299]. The predominance of the simultaneous mechanism over small Au clusters in the pores of TS-1 is also consistent with the observations of Lee et al., in which Au deposition on a TS-1 catalyst over-coated with an S-1 shell followed by measurement of propylene epoxidation rates leads to reaction rates (per kg TS-1) that are $\sim 4x$ higher than those measured over Au/TS-1, with similar measured apparent activation energy to conventional Au/TS-1 [303]. Furthermore, physical mixtures of TS-1 and Au supported on S-1 are not reactive [303]. These results demonstrate that the Au sites located within the pores of TS-1 are the active Au species for this reaction. Propylene epoxidation over Au supported on U-TS-1 results in reactivity that slowly increases with time on stream (over ~ 20 h at reaction temperature), concurrent with increases in BET surface area, suggesting that small Au ensembles can migrate into TS-1 pores excavated by removal of confined tetrapropylammonium cations in the presence of H_2O_2 , H_2O , and O_2 at 473 K [291]. Although the epoxidation rate appears to increase

over Au clusters confined in TS-1 pores, the H_2O_2 decomposition rate over Au/Ti O_2 catalysts has been reported to increase as Au cluster size decreases [304], suggesting that the desirable clusters for PO production may be undesirable for maintaining high hydrogen selectivity.

Despite these experimental and theoretical efforts to determine the gas-phase propylene epoxidation mechanism, accurate experimental measurement of kinetic parameters for reactions with product inhibition, as has been reported recently for liquid-phase cyclohexene epoxidation with H_2O_2 over Nb^{5+} , Ta^{5+} , and Ti^{4+} sites in Beta zeolites (313 K, [305]), requires either product co-feeding or correction of kinetic parameters for known product inhibition [306]. For gas-phase propylene epoxidation, inhibition has not been observed previously, though deactivation due to irreversible site-blockage by polymeric propylene oxide derivatives on Au/TS-1 was reported by Nijhuis et al. [307]. To our knowledge, neither propylene epoxidation experiments in a CSTR with correction for product inhibition, nor gas-phase propylene oxide co-feed experiments in plug-flow reactors has been reported.

Here, we report apparent activation energies and apparent reaction orders (measured by varying each component independently) for carbon dioxide, hydrogen, oxygen, propylene, propylene oxide, and water, and provide a clear demonstration that propylene oxide reversibly inhibits rates of propylene oxidation, but not hydrogen oxidation. We demonstrate that this product inhibition occurs at all space velocities measured, and that inhibition at low space velocity results exclusively from propylene oxide and not from the major reaction byproducts (CO_2 and water). A careful re-examination of the proposed mechanisms for direct gas-phase propylene epoxidation is presented, which accounts for inhibition by propylene oxide and provides evidence that propylene oxide binds to both sites invoked in the simultaneous mechanism. The reaction orders measured for hydrogen, oxygen, and propylene are consistent with the simultaneous mechanism for propylene epoxidation, and rule out a two-site sequential mechanism under the conditions studied here. The lack of propylene oxide inhibition

of H₂ oxidation rates implies that there are multiple sites or site-ensembles present on conventional Au/TS-1 catalysts.

6.3 Experimental Methods

6.3.1 Catalyst Synthesis

6.3.1.1 TS-1 Synthesis

Synthesis of titanium silicalite-1 (TS-1) was performed according to previously reported procedures [308]. Briefly, synthesis was performed by first mixing 3.85 g of polyoxyethylene 20-sorbitan monolaurate (Tween 20, Fischer Scientific, enzyme grade) and 61.56 g of deionized water (DI water) (Millipore, Synergy UV Water Purification System, 18.2 M Ω /cm resistivity) and stirring (\sim 300 RPM) for 900 s at ambient temperature. Then, 29.38 g of tetrapropylammonium hydroxide (TPAOH, Alfa Aesar, 40 wt%) and 70.00 g of tetraethylorthosilicate (TEOS, Sigma Aldrich, 98%) were added, followed by stirring (\sim 300 RPM) under ambient conditions for 1–2 h. In a separate 15 cm³ disposable centrifuge tube (VWR, sterile polypropylene), 1.14 g of titanium (IV) butoxide (TBOT, Alfa Aesar, 99%+) and 17.26 g of isopropyl alcohol (IPA, Sigma Aldrich, 99.5%) were combined and stirred with a vortex mixer (VWR Mini Vortex Mixer) and subsequently added dropwise to the synthesis gel, with stirring (\sim 300 RPM), under ambient conditions. The final molar ratio of the synthesis gel was 1 SiO₂/0.01 TiO₂/0.17 TPA⁺/13.1 H₂O/0.0093 Tween 20/0.04 C₄H₁₀O/0.85 C₃H₈O. The solution was then stirred (350 RPM), for at least 1 h at 313–318 K before addition to a Teflon-lined stainless-steel autoclave (45 cm³, Parr Instrument Company model 4744) and placement in an isothermal oven (Yamato DKN402C Constant Temperature Oven) and heated without agitation at 413 K for at least 18 h. The resulting solid was separated from the slurry via centrifugation (Thermo Scientific Heraeus Megafuge 16, 5000 RPM for 1800 s), and then washed twice with DI water, twice with acetone (Sigma Aldrich, 99.5%+), and one more time with DI water, with each wash using 15 cm³ of DI water or acetone per gram of TS-1 and a

vortex mixing time of ~ 30 s. Once washed, the solid was dried for approximately 48 h at 363 K. The dried TS-1 was then treated in flowing air ($100 \text{ cm}^3 \text{ min}^{-1} \text{ g}_{\text{cat}}^{-1}$) at 853 K for 10 h (1 K min^{-1} ramp).

6.3.1.2 Gold Deposition

A typical gold deposition onto TS-1 was performed according to previously published protocols [309]. First, approximately 0.040 g of hydrogen tetrachloroaurate(III) trihydrate ($\text{HAuCl}_4 \cdot 3\text{H}_2\text{O}$, Alfa Aesar, 99.99% (metals basis)) were mixed with 8.0 g of DI water followed by addition of 0.40 g of calcined TS-1. The slurry (water, gold precursor, and TS-1) was mixed under ambient conditions at 900 RPM for 1800 s. An appropriate amount of 0.5 M (1 N) sodium carbonate (Sigma Aldrich, 99.5%+) solution was then added to the slurry to bring the Na/Au molar ratio to a value chosen based on the desired final pH of the solution. Typically, this ratio was between 5.5 and 7.5 for a target final pH of the slurry was ~ 7 – 7.5 , measured via pH probe calibrated before each Au deposition (Mettler Toledo FiveEasy pH meter). The slurry was stirred at 900 RPM for another 10 h at ambient conditions. The Au/TS-1 was then separated from the slurry liquid via centrifugation (Thermo Scientific Heraeus Megafuge 16, 5000 RPM for 1800 s) and washed with approximately 25 cm^3 of DI water per g of Au/TS-1 for ~ 90 s with vigorous stirring. The resulting solid was then dried overnight under vacuum at room temperature.

6.3.2 Catalyst Characterization

Bulk elemental compositions of samples were determined using atomic absorption spectroscopy (AAS) performed with a Perkin Elmer AAnalyst 300 Atomic Absorption Spectrometer. 1000 ppm AAS standards (Alfa Aesar, TraceCERT, ± 4 ppm) for each metal were diluted to create calibration standards, and the instrument was calibrated for each element prior to collecting measurements. Au/TS-1 samples (typically 0.10 g) were dissolved in 2 g of HF (48 wt%, Alfa Aesar) and 2.5 g of aqua

regia (aqua regia prepared from a 2:1 v/v ratio of 37 wt% HCl, Mallinckrodt Chemicals and 70 wt% HNO₃, Mallinckrodt Chemicals) overnight and then further diluted with 30 g of deionized water. Absorbance values were measured at 399.9 nm in an acetylene/nitrous oxide flame for Ti, and at 267.6 nm in an air/acetylene flame for Au. Na content was determined by measuring absorbance values at 589.0 nm in an air/acetylene flame. Titanium AAS measurements were taken after calcination but before gold deposition. The Ti weight fraction was used along with the unit cell formula for zeolite MFI to calculate the Si/Ti ratios for each sample.

Powder X-ray diffraction (XRD) patterns were collected on a Rigaku Smartlab X-ray diffractometer equipped with an ASC-6 automated sample changer and a Cu K α X-ray source (1.76 kW). Typically, 0.01 g of sample were packed within zero background, low dead volume sample holders (Rigaku) and diffraction patterns were measured from 4° to 40° at a scan rate of 0.00417° s⁻¹ with a step size of 0.02°.

N₂ (77 K) adsorption isotherms were measured on samples (\sim 0.03 g, sieved to 180–250 μ m diameter particle size) using a Micromeritics ASAP2020 Surface Area and Porosity Analyzer. Prior to measurement of isotherms, samples were degassed under vacuum ($<$ 0.005 Torr) by heating to 393 K (0.0167 K s⁻¹) for 2 h, then heating under vacuum to 623 K (0.0167 K s⁻¹) for 8 h. Micropore volumes were determined from a semi-log derivative analysis of N₂ isotherms ($\partial(V_{\text{ads}}/g)/\partial(\log(P/P_0))$ vs. $\log(P/P_0)$) to identify the completion of micropore filling.

Diffuse reflectance UV–Vis (DRUV) spectra were collected on a Varian Cary 5000 UV–VIS–NIR using a Harrick Praying Mantis *in situ* diffuse reflectance cell. Spectra were collected on samples: (i) first exposed to ambient conditions and held in flowing dry He (4.17 cm³ s⁻¹ g_{zeolite}⁻¹) (“ambient” spectra) and (ii) after subsequent treatment to 523 K (\sim 0.5 K s⁻¹) for 1800 s in flowing dry He (4.17 cm³ s⁻¹ g_{zeolite}⁻¹) (“dehydrated” spectra). Spectra were collected at a scan rate of 10 nm s⁻¹, using poly(tetrafluoroethylene) (PTFE, 1 μ m powder, Sigma-Aldrich) as a 100% reflectance standard, and then converted to an absorption spectrum using the Kubelka-Munk

(F(R)) function. Absorption edge energies were calculated from the x-intercepts of Tauc plots of $[F(R)h\nu]^2$ vs. $h\nu$ (additional details in Section 6.6.4) [310–312].

6.3.3 Kinetic Studies of Propylene Epoxidation

The gas-phase reaction kinetic data were obtained in a continuous stirred tank reactor (CSTR), which ensures isoconcentration throughout the catalyst bed under all feed conditions and reactant conversions. This setup, detailed in Figure 6.6, facilitates quantitative study of orders of reaction, including product inhibition, as discussed for H₂O inhibition in the methane oxidation reaction by Cybulskis et al. [306]. The piping and instrumentation diagram (P&ID) shown on the right-hand side of Figure 6.6 shows that by choosing the proper valve configuration the reactor can be operated as a U-tube PFR, or, with the recirculating pump (Metal Bellows MB-21), as a CSTR, thus facilitating the advantages of the CSTR configuration and allowing direct comparison with our previous plug flow data.

Measurement of the kinetics was performed on as-deposited Au/TS-1 catalysts by sieving the Au/TS-1 samples to a 125–250 μm size range, followed by loading 0.080–0.400 g into a Pyrex U-tube reactor (diagram and photograph shown in Figure 6.7) equipped with a coiled inlet to allow for preheating the reaction gases, and placement of this reactor in a furnace controlled by a Eurotherm 2408 controller and protected by an over temperature thermocouple and controller (Omega CN9000A). Reaction temperature was measured by a thermocouple (Omega) inserted within a quartz thermowell that lies in the radial and vertical centers of the catalyst bed. The reactor is connected to the glass manifold that serves as a recirculating volume (Figure 6.6) using $\frac{1}{4}$ " ultra-torr fittings (Swagelok). The top of the furnace is insulated, and the reactor checked for leaks at ambient temperature by pressurizing to 3 PSI with N₂. The reactor was considered sealed when no change in pressure occurred over a period of 600 s. Next, flow of the reactant mixture, typically 10% H₂, 10% O₂, 10% C₃H₆, and 70% N₂ at a total flowrate of either 35 cm³ min⁻¹ during an initial day of catalyst activation or 65 cm³ min⁻¹ for kinetic experiments is started

using mass flow controllers connected to H₂ (Praxair, 99.999%), Air (Indiana Oxygen, Air Zero Grade, <1 ppm total hydrocarbon content), N₂ (Indiana Oxygen, 99.999%) and C₃H₆ (Matheson, Research Purity, 99.99%) cylinders. Care is taken such that hydrogen and propylene are introduced after nitrogen and air flow begins, and that H₂ and C₃H₆ never exceed 10 mol% of the flow to avoid operation in an explosive regime. After reactant flow begins and the total flowrate is confirmed using a bubble flowmeter, the reaction test is initiated by increasing the temperature to a standard temperature of 473 K (1 K min⁻¹ ramp rate) prior to an initial period of ~3 h, during which the catalyst deactivated to ~80% of its initial value, followed by a period of much slower deactivation. Kinetic studies are performed by independently varying either the H₂, O₂, air, or C₃H₆ flowrates while maintaining constant total flowrate by varying the N₂ flowrate. CO₂ and propylene oxide co-feed experiments are performed using a pure CO₂ (Indiana Oxygen) cylinder and a 1% PO/N₂ cylinder (Airgas, 1.032 ± 0.02% PO/N₂, Certified Standard Grade), while H₂O co-feed experiments are performed by flowing N₂ through a vapor-liquid-equilibrium (VLE) saturator at ambient temperature (295 K). To avoid creating a dangerous, explosive feed mixture, H₂, O₂, C₃H₆ order measurements are performed by decreasing the concentrations from the standard 10% flowrate in a non-monotonic fashion. Apparent activation energy measurements were performed starting from the standard 473 K reaction temperature by varying the temperature in a non-monotonic fashion from 443 to 483 K. In both apparent reaction order and apparent activation energy measurements, a minimum of three repeated GC injections were taken at each condition and the reported data represented the average of the last two (or more) of these injections.

Products were injected into an on-line Agilent 6890 GC equipped with a Supelcowax-10 capillary column (Agilent, 60 m × 530 μm × 1 μm) connected to a flame-ionization detector (FID) and a 60/80 Chromosorb 102 packed column connected to a thermal-conductivity detector (TCD) with N₂ used as the carrier gas for both columns and detectors. GC peak areas were quantified using pre-measured response factor calibrations for propylene, propanal, ethanal, acetone, acrolein, and propylene oxide on

the FID and H₂, O₂, and CO₂ for the TCD. Propylene conversions measured using the propylene peak were typically less than 5%, near the accuracy of the instrument. Thus, reported C₃H₆ conversions ($X_{C_3H_6}$) were calculated as moles of carbon containing products detected divided by the moles of C₃H₆ fed (Equation 6.1)

$$X_{C_3H_6} = \frac{\text{total moles carbon in products}}{\text{moles } C_3H_6 \text{ fed}} / 3 \quad (6.1)$$

The product carbon selectivity for a given product i ($S_{c,i}$) was defined on a carbon basis as:

$$S_{c,i} = \frac{\text{moles of product } i \text{ formed}}{\text{total moles C in products}} * \text{the number of carbon atoms in } i \quad (6.2)$$

while the hydrogen selectivity (S_{H_2}) was defined as:

$$S_{H_2} = \frac{\text{moles of PO formed}}{\text{total moles } H_2 \text{ consumed}} \quad (6.3)$$

The H₂ oxidation rate (r_{H_2O}) was defined as:

$$r_{H_2O} = \frac{\text{moles } H_2 \text{ consumed per second} - \text{moles of PO formed per second}}{g_{cat}} \quad (6.4)$$

assuming one mole of H₂ is consumed in water formation per mol of propylene oxide formed.

6.4 Results and Discussion

6.4.1 Structural Characterization of Titanosilicates

XRD patterns, N₂ isotherms, and UV–Visible spectra (523 K) after dehydration for all TS-1 samples used in this study are reported in Figures 6.8, 6.9, and 6.10, respectively. The XRD patterns and N₂ micropore volumes (Table 6.1) for all TS-1 samples were consistent with those reported previously for TS-1 (MFI micropore volumes 0.135–0.146 cm³ g⁻¹ [281]).

UV–VIS peak centers for dehydrated, isolated Ti⁴⁺ sites in TS-1 were between 215 nm and 225 nm, similar to those previously reported under ambient conditions for TS-1 synthesized in our lab [281] and for Ti-Beta-F zeolites reported previously [313]. The

Table 6.1.
Characterization data for all catalyst samples used in this study.

Catalyst	Si/Ti ^a	Au wt% ^b	Na wt% ^b	Au/Ti ^a	Na/Ti ^a	Na/Au ^a	V _{ads} (N ₂ , 77 K) (cm ³ g ⁻¹) ^c	DRUV Band Center (nm) ^d	DRUV Edge Energy (eV) ^d	PO Rate (10 ⁻⁷ mol PO g _{cat} ⁻¹ s ⁻¹) ^e
0.110Au/TS-1(81)	81	0.110	-	0.042	-	-	0.170	220	5.07	3.3
0.092Au/TS-1(75)	75	0.092	0.130	0.030	0.36	12	0.148	225	4.94	4.7
0.063Au/TS-1(75)	75	0.063	0.130	0.020	0.35	17	0.148	225	4.94	3.7
0.100Au/TS-1(143)	143	0.100	0.140	0.060	0.67	11	0.147	215	5.18	4.3
0.022Au/TS-1(143)	143	0.022	0.089	0.013	0.44	35	0.147	215	5.18	2.4
0.019Au/TS-1(143)	143	0.019	0.310	0.011	1.53	140	0.147	215	5.18	1.6
0.040Au/TS-1(81)	81	0.040	-	0.016	-	-	0.170	220	5.07	3.1
0.030Au/TS-1(81)	81	0.030	-	0.013	-	-	0.170	220	5.07	3.1
0.044Au/TS-1(81)	81	0.044	-	0.015	-	-	0.170	220	5.07	4.0
0.033Au/TS-1(143)	143	0.033	-	0.013	-	-	0.147	215	5.18	2.4
0.069Au/TS-1(143)	143	0.069	-	0.046	-	-	0.147	215	5.18	4.5
0.064Au/TS-1(143)	143	0.064	-	0.043	-	-	0.147	215	5.18	4.7

^aRatios reported are molar ratios determined by atomic absorption spectroscopy (AAS). Errors are $\pm 21\%$.

^bBulk composition determined by AAS. Errors are $\pm 15\%$.

^cMicropore volume determined from total N₂ uptake at the end of micropore filling in adsorption isotherms measured at 77 K (Section 6.6.3).

^dDiffuse reflectance UV-Vis spectra (band center at maximum F(R) intensity) and Tauc plots for samples after dehydration at 523 K (Section 6.6.4).

^eAverage PO rates are reported as the average values between 3rd and 5th hour on stream during the initial activation day (SV = 14,000 cm³ g_{cat}⁻¹ h⁻¹, T = 200°C, 10% C₃H₆/10% H₂/10% O₂/70% N₂ by volume). Multiply by 2.09×10⁸ to convert units to g_{PO} kg_{cat}⁻¹ h⁻¹.

UV–VIS edge energies of >4.9 eV for all dehydrated TS-1 samples (Tauc plots shown in Figure 6.11, edge energies reported in Table 6.1), are characteristic of primarily isolated, dehydrated Ti^{4+} sites in zeolites, but that does not exclude the possibility of a minority of nano-sized octahedral TiO_2 domains [314, 315] whose edge energies increase with decreasing domain size due to quantum confinement effects [316]. The lack of distinct peaks at 25.7° , 27.9° , and 31° is characteristic of TS-1 XRD patterns without larger (>3 nm [317]) TiO_2 domains [318]. Bulk Ti, Au, and Na contents measured by atomic absorption spectroscopy (AAS) for Au-loaded TS-1 samples are reported in Table 6.1, and demonstrate the low Au loadings typical of Au/TS-1 catalysts performed by careful deposition-precipitation procedures [281]. Despite the use of $\sim 4\text{--}5$ mol Na per mol Au for pH control during the Au DP step, the final Na/Au ratios measured using AAS range from 11 to 140 for the samples reported in Table 6.1. Na contents for samples prepared by this method have not been reported previously, and may underlie the low Au efficiency during the DP procedure as well as the possibility of Na covered Au particles, Ti defect sites, or Na exchanged SiOH groups in Au/TS-1 catalysts reported here. Na exchange on TS-1 (Na/Ti ~ 3.5) eliminates oxidation and epoxidation activity, as well as hydroperoxo complex formation, for epoxidation of n-octane over TS-1 in the presence of aqueous H_2O_2 at 353 K [319]. No clear effects of Na were observed in this work, but we note that the Na/Au ratio is a variable worth monitoring in future work.

6.4.2 Measurement of Reaction Kinetics of Over Au/TS-1 Catalysts

6.4.2.1 Propylene Epoxidation

Figure 6.1 shows the typical time on stream behavior for Au/TS-1 catalysts under reactant flow (10% H_2 /10% O_2 /10% C_3H_6 /70% N_2 by volume at 473 K). After reaching reaction temperature, the catalyst shows an initial rapid deactivation ($k_{\text{deactivation}} = 0.029 \text{ h}^{-1}$) which decelerates to $\sim 0.002 \text{ h}^{-1}$ after $\sim 3\text{--}4$ h on stream (Figure 6.12). Measurement of reaction orders was performed after the temperature ramp and initial

deactivation, with measured reaction rates corrected for the slow deactivation thereafter, enabled by intermittent measurements at the standard conditions and assuming first order exponential decay (example shown in Figure 6.13).

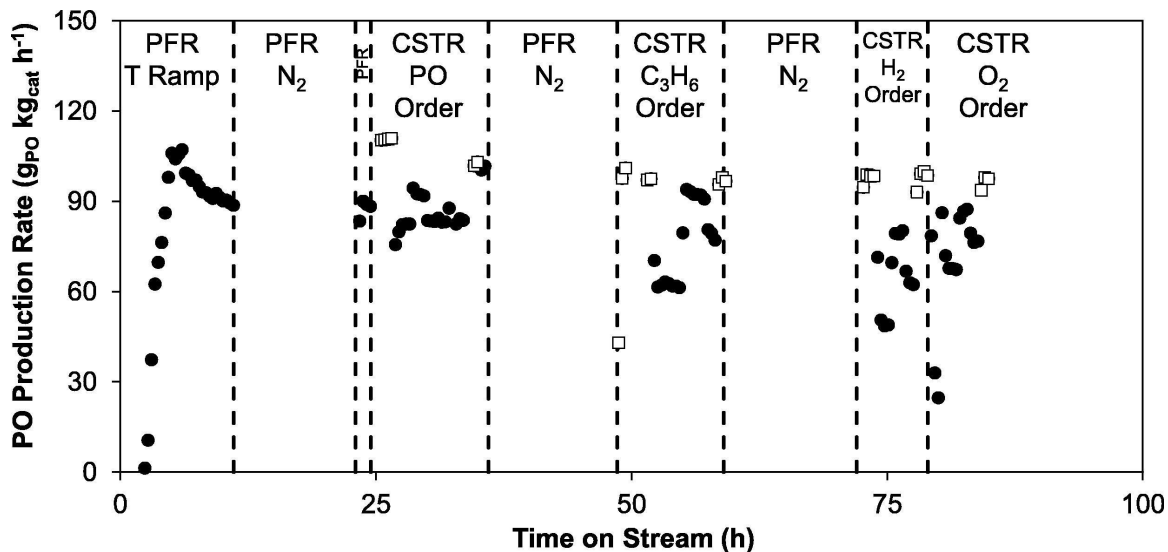


Figure 6.1. Time on stream (TOS) profile for 0.092Au/TS-1(75). Initial rate increase occurs during temperature ramp (0.0083 K s^{-1}) until reaction temperature (473 K) is reached. Returns to 10% H_2 /10% O_2 /10% C_3H_6 /70% N_2 (by volume) are represented by white boxes after the initial activation under these conditions. Reaction orders are measured by non-monotonically varying the reactant (or product) flowrate of interest while keeping the total flowrate constant ($\text{SV} = 14,000 \text{ cm}^3 \text{ g}_{\text{cat}}^{-1} \text{ h}^{-1}$ up to 25 h, then 26,000 for TOS > 25 h) and varying the balance N_2 flow rate to compensate. N_2 flow at reaction temperature maintained between each experiment to maintain O_2 and moisture-free atmosphere.

Measurement of apparent H_2 , O_2 , and C_3H_6 reaction orders in the absence of products in the feed resulted in similar reaction orders as those reported elsewhere (Table 6.2, example data shown in Figure 6.14), of 0.6, 0.2, and 0.2 respectively, while measured apparent activation energies were also similar to those reported elsewhere ($\sim 30 \text{ kJ mol}^{-1}$, Figure 6.15, vs. 28 kJ mol^{-1} [303]). The similarity of reaction orders measured on various supports (TS-1 and Ti-TUD), at various Au loadings (0.02–0.10

Table 6.2.
Measured reaction orders compared to those reported in literature.

Source	Molar Si/Ti Ratio	SV ($\text{cm}^3 \text{g}_{\text{cat}}^{-1} \text{h}^{-1}$)	Au Loading (wt%)	H ₂ Order	O ₂ Order	C ₃ H ₆ Order	PO Order ^e
[297] ^a	33	7000	0.11	0.5	0.2	0.4	-
[296]	36, 143	7000	0.02 - 0.06	0.6	0.3	0.2	-
[298] ^b	33	7000	0.02	0.5	0.3	0.2	-
Au/TS-1	75 - 143	26,000	0.02 - 0.09	0.6 ± 0.08^c	0.2 ± 0.01^c	0.2 ± 0.08^c	-0.6 ± 0.2
Au/TS-1, corrected for inhibition	75 - 143	26,000	0.02 - 0.09	1.0 ± 0.2^d	0.4 ± 0.06^d	0.4 ± 0.1^d	-0.6 ± 0.2

^aCatalyst used was Au/Ti-TUD.

^bOrders measured in packed-bed catalytic membrane reactor with Au/TS-1 at higher O₂ and H₂ partial pressures (up to 40 vol% each, respectively).

^cAverage values for our measured reaction orders (H₂, O₂, and C₃H₆ not PO corrected). Errors determined from standard deviation of the measured reaction orders across eight TS-1 samples listed in Table 6.1.

^dAverage values for our measured reaction orders (H₂, O₂, and C₃H₆ corrected by 1.6 to account for dependence of the rate on $[\text{PO}]^{-0.6}$). Errors determined from standard deviation of the measured reaction orders across eight TS-1 samples listed in Table 6.1.

^eAverage value of measured PO orders.

wt%), a range of space velocities ($7000\text{--}26,000 \text{ cm}^3 \text{g}_{\text{cat}}^{-1} \text{h}^{-1}$), and in both PFR and CSTR configurations implies that these reaction orders are not measured under mass transfer limited conditions.

The space velocity employed here is in a similar range to that used previously ($\sim 7000\text{--}14,000 \text{ cm}^3 \text{g}_{\text{cat}}^{-1} \text{h}^{-1}$), conditions under which the external mass transfer limitations were negligible (Mears criterion $\ll 0.15$) and the presence of internal mass transfer limitations was excluded by estimation of a Thiele modulus between 10^{-1} and 10^{-3} [296, 303] (Derivation shown in Section 6.6.5). Further, these results

suggest similar active Au/Ti species across the range of titanosilicate topologies and Au weight loadings tested.

Measurement of the PO reaction order while co-feeding controlled amounts of PO (0.06–0.30 vol% PO) and correcting for deactivation yielded a reaction order of, for example, -0.6 ± 0.02 (0.030Au/TS-1(81), Figure 6.2) or, on average for all Au/TS-1 samples, -0.6 ± 0.2 (Table 6.2). We note that we measured a range of PO orders from -0.4 to -0.8 over samples with varying Au loading and Si/Ti ratios, apparently reflecting a change in PO coverage, but have not yet been able to establish a clear correlation to catalyst properties. The active site geometry may vary from catalyst to catalyst due to differences in Au-Ti proximity, Au particle size, and Au location, resulting in the observed variations in the measured PO order. The inverse dependence of PO production rate on PO concentration implies substantial surface coverage of PO on kinetically relevant catalytic sites. The decrease in PO rate with PO concentration observed on all catalysts included in this study, including data collected without PO co-feeds at propylene conversions as low as 0.6%, demonstrates that operation of plug flow reactors at low reactant conversion ($<1\%$) in the absence of co-fed products does not guarantee such reactors can be considered differential. Varying the space velocity from 5200 to 62,000 $\text{cm}^3 \text{g}_{\text{cat}}^{-1} \text{h}^{-1}$ by varying the mass of catalyst loaded to the reactor and the total flowrate led to the trend reported in Figure 6.3a, where the rate of PO production decreases with increased space time. The effect of space time on rate was reported previously by Nijhuis et al., but was not considered as an effect of product inhibition but rather of irreversible site-blocking due to formation of propylene oxide-derived oligomers [307]. The H_2 oxidation rate is independent of space time as expected for a lack of inhibition for H_2 oxidation. The high scatter at low conversion, i.e. low space time, results from quantification of H_2 oxidation rates via subtraction of PO formation rates from H_2 consumption rates which are more difficult to quantify at low conversion, but the values average to the more accurate value at high conversion. The trend in H_2 oxidation rate is also complicated by changes in H_2 selectivity (from 41% to 19%) across this data set.

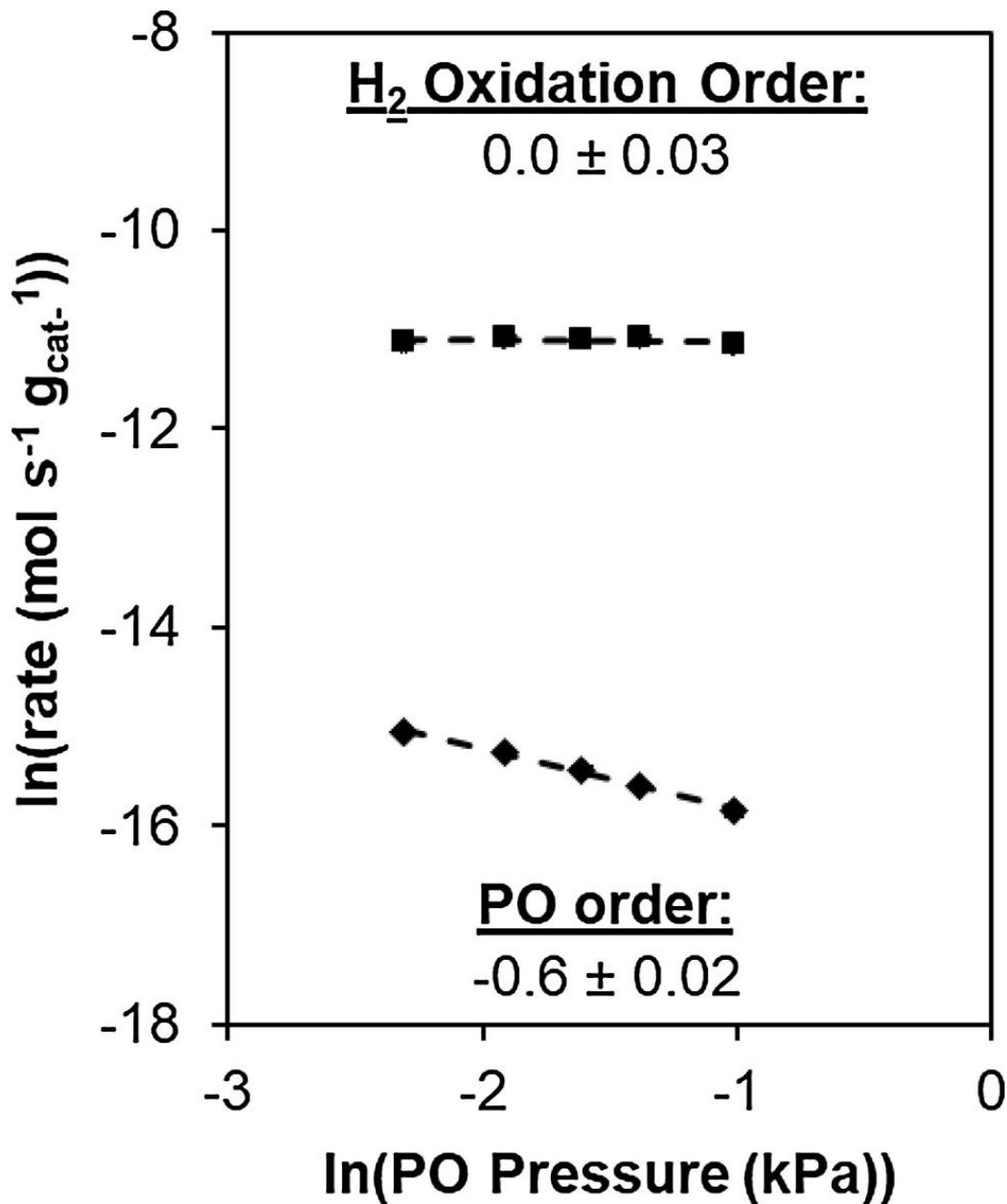


Figure 6.2. Natural log of the net PO rate ($\text{mol g}_{\text{cat}}^{-1} \text{s}^{-1}$ total minus $\text{mol g}_{\text{cat}}^{-1} \text{s}^{-1}$ fed) (diamonds) and natural log of the H_2 oxidation rate ($\text{mol g}_{\text{cat}}^{-1} \text{s}^{-1}$ H_2 consumed minus net $\text{mol g}_{\text{cat}}^{-1} \text{s}^{-1}$ PO formed) (squares) as a function of the natural log of the total gas phase PO mol fraction over 0.030Au/TS-1(81) at 473 K with gas composition 10% H_2 /10% O_2 /10% C_3H_6 , balance N_2 and PO (PO mol fraction in feed 0–0.003) at a SV of $26,000 \text{ cm}^3 \text{ g}_{\text{cat}}^{-1} \text{ h}^{-1}$. The solid lines show the linear regressions to the data resulting in the reported reaction orders. Error bars represent one standard deviation.

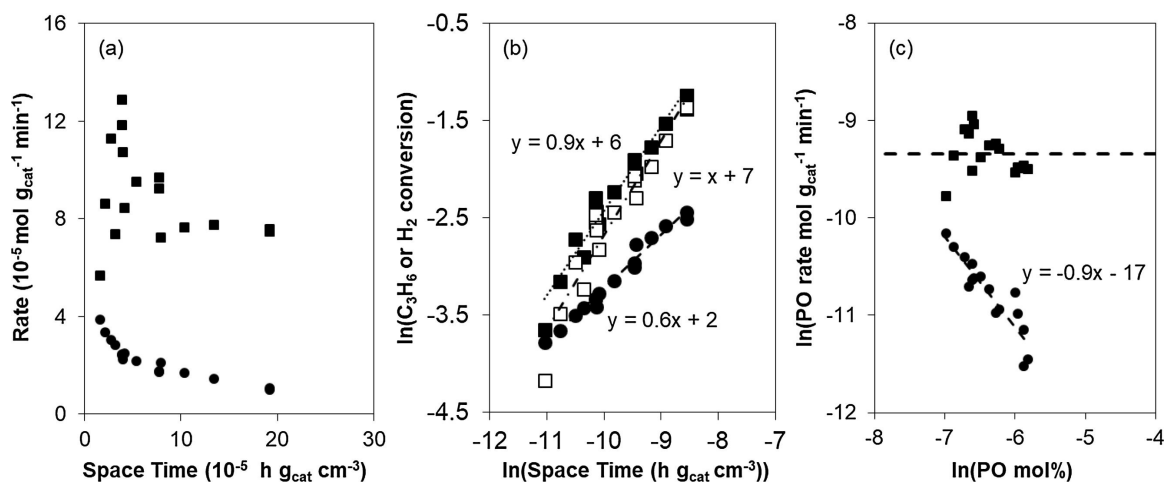


Figure 6.3. (a) PO production rate (circles) and H_2 oxidation rate (squares) in a gas-phase CSTR as a function of space time (b) natural log of C_3H_6 conversion (circles), natural log of H_2 conversion (filled squares), and natural log of H_2 oxidation computed from the H_2 conversion by subtracting PO formation (open squares) as functions of the natural log of space time (c) natural log of PO production rate (circles) and natural log of H_2 oxidation rate (squares) as functions of the natural log of the total gas phase PO mol%. Dotted lines in (b) and (c) are linear trendlines fit to the data resulting in the reported equations, while the thick dotted line in (c) is the average of the natural log of the H_2 oxidation rates included to guide the eye. Mass of catalyst ranged from 0.080 to 0.400 g 0.10Au/TS-1(143), 473 K, 10% H_2 /10% O_2 /10% C_3H_6 / 70% N_2 (vol%) and the total flow rate was varied from 0.6 to 1.4 $\text{cm}^3 \text{ s}^{-1}$, resulting in a range of space times from 1.6 to $19 \times 10^5 \text{ h g}_{\text{cat}} \text{ cm}^{-3}$.

To test for product inhibition, we invoke the following simple analysis. A mole balance on a CSTR produces the relation:

$$r_A = -C_{A_0}X/\tau \quad (6.5)$$

where X is the conversion of A and τ is the space time (reactor volume divided by the volumetric flow rate, the inverse of the space velocity). If we then assume a power law rate expression for the general reaction:



we determine that the forward rate is equal to:

$$r_A = -k C_A^a C_B^b C_C^c C_D^d \quad (6.7)$$

where a , b , c , and d are the orders of reaction for A, B, C, and D for the forward reaction. We can then express the concentrations in terms of conversion, X , to derive:

$$r_A = -k((C_{A_0}(1 - X))^a(C_{B_0}(1 - \frac{C_{A_0}X}{C_{B_0}}))^b(C_{C_0} + C_{A_0}X)^c(C_{D_0} + C_{A_0}X)^d) \quad (6.8)$$

If we then assume that X is small with respect to 1, as is usually done when the reactor is assumed to be running at differential conversion and that $C_{C_0} = C_{D_0} = 0$, then

$$r_A = -C_1 X^{c+d} \quad (6.9)$$

where C_1 is a constant equal to $kC_{A_0}^{a+c+d}C_{B_0}^b$. This expression shows the often-overlooked conclusion that when there is product influence on the forward rate, the rate is not independent of conversion even at low values typical of expected differential behavior. This leads to the final result,

$$\frac{C_{A_0}X^{1-c-d}}{\tau} = C_1 \quad (6.10)$$

or:

$$X = C_2 \tau^{1/(1-c-d)} \quad (6.11)$$

where $C_2 = (C_1/C_{A_0})^{1/(1-c-d)}$.

If there is no product inhibition, then c and d will be zero and X will be a linear function of τ with a slope equal to unity. Thus, the presence or absence of product effects on the forward rate are easily detected in a plot of $\ln(X)$ versus $\ln(\tau)$. For our data on PO, the slope of the plot in Figure 6.3b is 0.55 ± 0.02 , giving $c + d = -0.8 \pm 0.03$ and showing clear product inhibition. A plot of the natural log of the PO rate with respect to PO concentration across the entire data set for the 0.10Au/TS-1(143) catalyst gives an apparent PO reaction order of -0.9 ± 0.1 (Figure 6.3c), consistent with the result of Figure 6.3b (-0.8 ± 0.03). Co-feeding 16% CO₂ in the inlet had no effect on the measured PO formation rate, suggesting that CO₂ does not inhibit the PO production rate (See Figure 6.17). Co-feeding 0.3–0.9% H₂O during measurement of the H₂O reaction order over various samples (See Table 6.7, Figure 6.18) confirms that H₂O does not inhibit the rate of PO production. While these data do not exclude the possibility of reversible inhibition by propylene glycol or another species derived from reaction of propylene oxide, we note that we have not seen evidence for any such potential species in the product distribution. Figure 6.3b shows that the predicted inhibition of H₂ conversion is ~ -0.1 order, though if the H₂ conversion is replaced by H₂ oxidation alone (determined from the rate of H₂ consumption less the rate of PO formation) is considered, this inhibition is removed (slope for H₂ conversion in Figure 6.3b changes from -0.9 to -1). Some inhibition to H₂ conversion with increasing space time is expected, as formation of PO requires consumption of H₂, and we have demonstrated that PO formation, and not H₂ oxidation, is inhibited by increasing PO concentration via co-fed PO (Figure 6.2). Finally, Figure 6.3c shows that while there is a clear linear dependence of the natural log of the PO formation rate as a function of the natural log of the PO pressure when space time is varied, there is no clear monotonic trend in the log-log plot of the H₂ oxidation rate as a function of PO pressure. The scatter in these data reflects the convolution of decreased H₂ oxidation rates with decreased H₂ pressure (Section 6.4.2.2), changes in H₂ selectivity with increasing space time (from 40% to

17%), and scatter resulting from quantification of H₂ oxidation rates by measurement of H₂ consumption rather than H₂O formation.

The average values for the apparent reaction orders (0.6, 0.2, and 0.2 for H₂, O₂, and C₃H₆, respectively, Table 6.2) are all non-integer and difficult to rationalize mechanistically for a single-site Langmuir-Hinshelwood mechanism, but they are also not the intrinsic reaction orders, because they do not account for product inhibition. Assuming a power rate law (Equation 6.12), the true (PO inhibition corrected) reaction orders for H₂, O₂, and C₃H₆ require multiplication of the orders observed in absence of PO by the factor $1 - \delta$, or in this case 1.6 [306].

$$r_{PO} = k[H_2]^\alpha[O_2]^\beta[C_3H_6]^\gamma[PO]^\delta \quad (6.12)$$

Taking into account correction of the reaction orders for PO inhibition is also shown in Table 6.2. The corrected reaction orders for H₂, O₂, and C₃H₆ (1 ± 0.2 , 0.4 ± 0.06 , and 0.4 ± 0.1 , respectively) are near 1 for H₂ but non-integer for O₂ and C₃H₆. These are the values that must be reconciled with any proposed mechanism.

The mechanism proposed by our group previously [296] involves HOOH formation on Au sites (denoted as S₁ sites in Figure 6.4) that reacts in a single step with C₃H₆ adsorbed at the interface between small Au clusters and framework Ti atoms (denoted as S₂ sites in Figure 6.4). Pulido et al. [320] proposed a similar H-Au-OOH species during gas-phase propylene epoxidation over isolated Au atoms supported on graphene. The interface site as the binding location for C₃H₆ is consistent with DFT calculations that predict stronger adsorption of C₃H₆ at the interface between small Au clusters and framework Ti atoms ($\Delta E_{\text{ads}} \sim -20 \text{ kcal mol}^{-1}$) than at framework Ti atoms alone ($\Delta E_{\text{ads}} \sim -10 \text{ kcal mol}^{-1}$) [299]. The exact nature of the Ti site is not known, and could include titanium atom with three Si–O–Ti bonds and one –OH ligand, with a neighboring Si–OH group (i.e., $\equiv(\text{SiO})_3\text{–Ti–OH–HO–Si}\equiv$) in addition to framework Ti atoms with four Si–O–Ti bonds. Our previously proposed mechanism was consistent with the observed D₂ kinetic isotope effect for PO formation on Au/TiO₂ catalysts [293], DFT calculations of sequential and simultaneous mechanisms [299], and the measured apparent reaction orders from multiple

research groups (Table 6.2), but it did not account for PO inhibition. Figure 6.4 adds steps 8 and 9 for adsorption of PO at Au and Ti sites to correct this omission. We note that the kinetic relevance of H–H bond breaking is assumed on the basis of DFT predictions of a predominant “simultaneous” epoxidation mechanism involving H-Au-OOH intermediates over Au/Ts-1 [299] as well as the kinetic isotope effect seen for Au/TiO₂ [295].

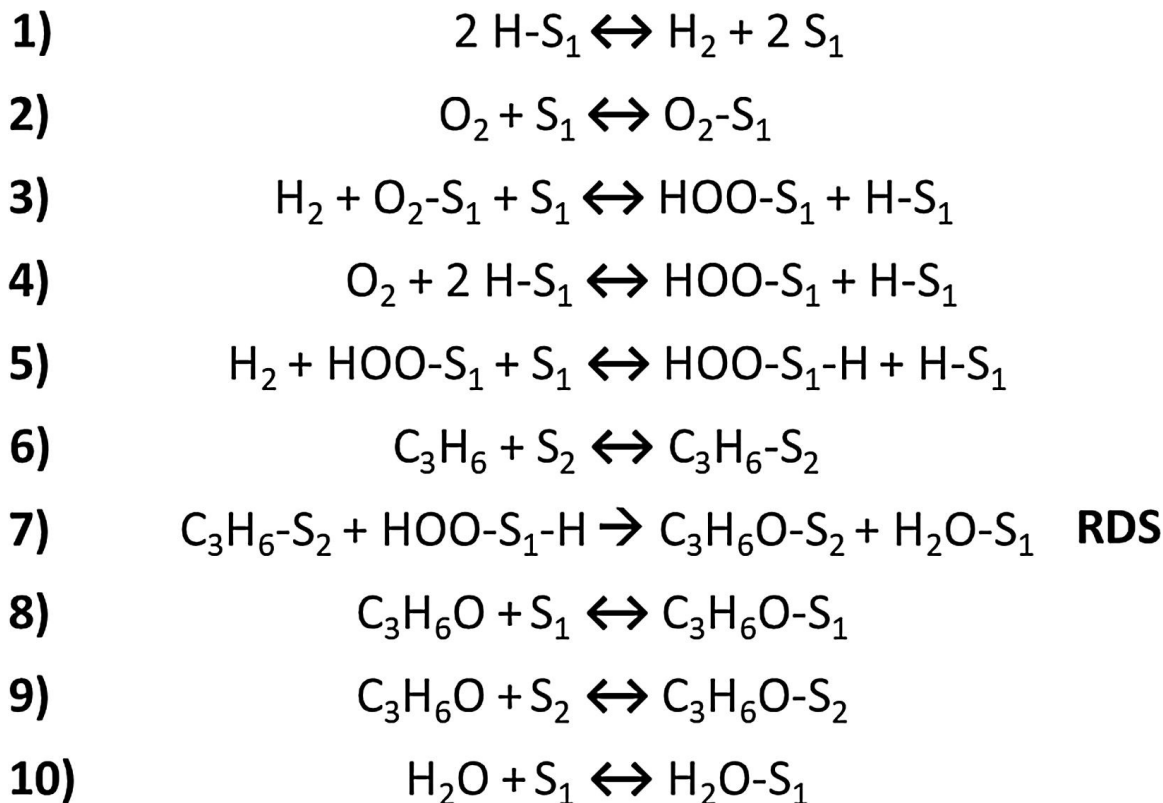


Figure 6.4. Proposed reaction mechanism for propylene oxide synthesis over Au/Ts-1 catalysts. S₁ is a Au site, S₂ is an Au-Ti interfacial site, and that they are neighboring sites.

If we take step 7 as the sole rate determining elementary step, in agreement with theoretical calculations that suggest the free energy barriers are lower for this step

than for the equivalent step in the sequential reaction pathway (discussed in the ensuing paragraphs) [299], we arrive at the following rate expression:

$$r_{PO} = k_7(C_3H_6 - S_2) \frac{HOO - S_1 - H}{L_1} \quad (6.13)$$

If all other steps are considered quasi-equilibrated, and if empty S_1 sites, O_2 - S_1 , PO - S_1 , and HOO - S_1 - H , are the most abundant surface species (MASIs) for S_1 , then $[HOO$ - S_1 - $H]$ becomes:

$$\frac{HOO - S_1 - H}{L_1} = \frac{K_5 K_4 P_{H_2} P_{O_2}}{1 + K_2 P_{O_2} + K_8 P_{PO} + K_5 K_4 P_{O_2} P_{H_2}} \quad (6.14)$$

where L_1 is the total number of covered plus empty S_1 sites, each K_i represents the equilibrium constant for elementary step i , and P_j represents the bulk gas phase partial pressure of a species j . The $[C_3H_6$ - $S_2]$ term can be derived by assuming that step 6 is quasi-equilibrated, that only empty S_2 sites, C_3H_6 - S_2 and PO - S_2 are MASIs on S_2 , and that L_2 is the total number of covered and empty S_2 sites:

$$C_3H_6 - S_2 = \frac{K_6 P_{C_3H_6} L_2}{1 + K_6 P_{C_3H_6} + K_9 P_{PO}} \quad (6.15)$$

Combining Equations 6.13, 6.14, and 6.15 yields the rate expression:

$$r_{PO} = \frac{k_7 K_6 K_5 K_4 P_{C_3H_6} P_{O_2} P_{H_2} L_2}{(1 + K_2 P_{O_2} + K_5 K_4 P_{O_2} P_{H_2} + K_8 P_{C_3H_6 O})(1 + K_6 P_{C_3H_6} + K_9 P_{C_3H_6 O})} \quad (6.16)$$

The numerator of 6.16 is directly proportional to the gas phase pressures of hydrogen, oxygen, and propylene, resulting in maximum apparent reaction orders of unity for each reactant. Depending on the coverage of S_1 and S_2 , any of the three reactants can have an apparent reaction order less than one. By taking the derivative of the natural log of the rate with respect to the natural log of the gas phase pressure of each species in the rate expression, one can derive relationships between the apparent reaction order and the surface coverage of each species (derivation shown in Section 6.6.5.1), resulting in the expressions for each reaction order are shown in Table 6.3.

Thus, in order to match the average measured reaction orders (Table 6.2), the coverage of $HOOH$ on S_1 is approximately zero, the coverage of O_2 on S_1 is 0.6, the

Table 6.3.

Relation between the true reaction order and the coverages of the most abundant surface species, according to the mechanism shown in Figure 6.4 and the mechanistic assumptions resulting in Equation 6.16.

Reaction Order	Function
H ₂	$1 - \theta_{\text{HOO-S}_1\text{-H}}$
O ₂	$1 - \theta_{\text{S}_1\text{-O}_2} - \theta_{\text{HOO-S}_1\text{-H}}$
C ₃ H ₆	$1 - \theta_{\text{C}_3\text{H}_6\text{-S}_2}$
C ₃ H ₆ O	$-(\theta_{\text{PO-S}_1} + \theta_{\text{PO-S}_2})$

coverage of C₃H₆ on S₂ is 0.6, and the coverage of C₃H₆O is $0.2 \leq \theta_{\text{PO-S}_1} \leq 0.4$ on S₁ and $0.2 \leq \theta_{\text{PO-S}_2} \leq 0.4$ on S₂, with the sum of $\theta_{\text{PO-S}_1} + \theta_{\text{PO-S}_2} = 0.6$, resulting in an apparent C₃H₆O reaction order of -0.6 . This analysis confirms that the observed orders could reasonably arise from the rate expression derived from Equations 6.5, 6.6, and 6.7 without violating the requirement that the coverage must be ≤ 1 on each of the two active sites. The mechanism reported here is consistent with the observed reaction orders for H₂, O₂, C₃H₆, and PO. An alternative mechanism reported by Kanungo et al. [301] invokes two kinetically relevant steps, the first of which forms HOOH over two types of non-competing Au sites, which then migrates to an adjacent Ti site and reacts with C₃H₆ adsorbed at an adjacent Au site to form C₃H₆-HOOH-Ti, which produces PO and H₂O in a second kinetically relevant step. This mechanism assumes C₃H₆ will not adsorb directly to a Ti site, and thus C₃H₆ must adsorb on Au adjacent to Ti-HOOH before formation of C₃H₆HOOH-Ti and subsequent formation of PO and H₂O. Adsorption of C₃H₆ at Au sites is consistent with C₃H₆ inhibition of H₂ oxidation over Au sites reported by Kanungo et al. [301] and observed in this study (*vide infra*). We note however that we have previously found adsorption of C₃H₆ on a Au-Ti interfacial site to be a feasible elementary step on the basis of density-functional theory calculations [299]. Whether or not there are three sites and

multiple kinetically relevant steps and migration of HOOH from Au to Ti prior to adsorption of C₃H₆ at a Au site neighboring the HOOH-Ti species and subsequent reaction, or two sites and a reaction of a Au-HOOH species with C₃H₆-(Au-Ti) in a single kinetically relevant step (as reported here, Figure 6.4) cannot be determined on the basis of kinetics alone and requires additional spectroscopic and/or computational evidence. Another difference in the two mechanisms that remains to be resolved is pathway for HOOH formation. Kanungo et al. [301] accommodate the experimental observation that the hydrogen order is roughly double that for oxygen by invoking an independent oxygen adsorption site. Our mechanism has been guided by both DFT [299] and our reluctance to invoke additional sites unless required. Given that both mechanisms are consistent with observed kinetic measurement data and our previous DFT results support the mechanism described in Figure 6.4, we report this mechanism in the present study. Our continuing efforts will attempt to differentiate between these two plausible mechanisms.

In the two-site sequential mechanism, hydrogen peroxide forms on a Au site prior to desorbing intact and adsorbing at a Ti-OH site where C₃H₆ has already adsorbed. This latter step mimics the proposed steps for liquid-phase epoxidation over TS-1 and TiO₂ [302]. In the sequential mechanism, assuming the epoxidation of propylene is the rate-limiting step, the numerator of the rate expression will be first order in C₃H₆, H₂, and O₂, and the denominator can contain coverage terms for C₃H₆, C₃H₆O, and H₂O₂. This results in apparent reaction orders for hydrogen and oxygen that are equal, which was not observed for any sample in this study (Table 6.2, Table 6.7). The equivalence of the hydrogen and oxygen reaction orders is a direct result of the desorption from Au and readsorption on Ti of H₂O₂, and therefore any mechanism which includes this step can be removed from consideration on the basis of the kinetic data presented in this study (Table 6.2, Table 6.7). Thus, from the kinetic results presented here, it is clear that the two-site sequential mechanism is ruled out by the measured kinetic parameters, and that the two-site simultaneous mechanism occurring over adjacent

Au-Ti sites, proposed by previous experimental and theoretical reports, can explain the measured kinetics.

6.4.2.2 Measurement of Reaction Orders and Activation Energies for Hydrogen Oxidation over Au/TS-1

The H₂ oxidation rate was indirectly calculated according to Equation 6.4, which assumes that all hydrogen consumed other than for PO formation (which produces one mole of H₂O per mole of PO) is consumed in direct H₂ oxidation to H₂O, as it was not possible in our experimental apparatus to quantify water in the reactor effluent via GC. Considering that the side products observed in this reaction do not include saturated oxygenates (e.g., alcohols) or hydrocarbons (e.g., ethane, propane), this assumption is reasonable. The highest H₂ oxidation rate measured here (3×10^{-6} mol H₂ consumed g_{cat}⁻¹ s⁻¹ (0.069Au/TS-1(143)), 10.1 kPa H₂, 10.1 kPa O₂, 2.53 kPa C₃H₆, T = 473 K) was significantly lower than that measured by Barton and Podkolzin over 0.15Au/TS-1(51) (1.5×10^{-1} mol H₂O formed g_{cat}⁻¹ s⁻¹, 2.5 kPa O₂, 5.0 kPa H₂, 433 K). As reported in Table 6.4, the apparent reaction orders for H₂ oxidation are 0.9 ± 0.1 for H₂, 0.3 ± 0.1 for O₂, -0.3 ± 0.07 for C₃H₆, and 0.0 ± 0.2 for PO, apparent orders that are markedly different from those for PO production reported here and elsewhere (Table 6.2). Barton and Podkolzin reported apparent orders for H₂O synthesis over Au catalysts of 0.7–0.8 for H₂, 0.1–0.2 for O₂, and zero for H₂O over Au/SiO₂ and Au/TS-1 catalysts at 433 K [321], while experiments over solid gold found orders of 1 for H₂ and 0.5 for O₂, and over gold gauze found orders of 1 for H₂ and zero for O₂ [322, 323]. The hydrogen and oxygen orders measured over Au/TS-1 in this study are similar to those reported by Barton and Podkolzin, but the vast difference in rate and the differences in Au loading and deposition method between their catalyst in the absence and ours in the presence of propylene and propylene oxide make it difficult to draw meaningful comparisons. The O₂ order for H₂ oxidation over Au/TS-1 reported here suggests that the sites for this reaction are partially covered with O₂. The apparent propylene order that is slightly

below zero can be explained by a small coverage of adsorbed propylene on the active sites for hydrogen oxidation.

Table 6.4.

Apparent and PO-inhibition-corrected reaction orders and activation energies for propylene oxide formation and H₂ oxidation determined by averaging the measured kinetic parameters for eight separate Au/Ts-1 samples (0.092Au/Ts-1(75), 0.019Au/Ts-1(143), 0.040Au/Ts-1(81), 0.030Au/Ts-1(81), 0.044Au/Ts-1(81), 0.033Au/Ts-1(143), 0.069Au/Ts-1(143), and 0.064Au/Ts-1(143)).

Product	Reaction Orders						E _{app} (kJ mol ⁻¹)
	H ₂	O ₂	C ₃ H ₆	PO	CO ₂	H ₂ O	
PO ^a	0.6 ± 0.08	0.2 ± 0.01	0.2 ± 0.08	-0.6 ± 0.2	0	0	33 ± 0.9
PO ^b	1.0 ± 0.20	0.4 ± 0.06	0.4 ± 0.10	-0.6 ± 0.2	0	0	52 ± 6.0
H ₂ O ^a from H ₂ oxidation	0.9 ± 0.10	0.3 ± 0.10	-0.3 ± 0.07	0.0 ± 0.2	0	-0.1 ± 0.07	31 ± 10

^aNot corrected for inhibition.

^bReactant orders and E_{app} corrected by a factor of 1.6 to account for PO inhibition [306].

Figure 6.5 shows the mechanism for hydrogen oxidation over Au/Ts-1 catalysts proposed by Barton and Podkolzin [321]. In agreement with observations over 3-atom Au particles simulated by Wells et al. [324], H₂ dissociation proceeds with assistance by adsorbed molecular oxygen (reaction (4), Figure 6.5). However, Barton and Podkolzin also included unassisted dissociative hydrogen adsorption (reaction (2), Figure 6.5) in order to simplify the definition of kinetic model parameters and the derivation of rate expressions [321]. H₂O₂ decomposition proceeds through breakage of the O–O bond to form 2 –OH species on the surface (reaction (5), Figure 6.5). The OH surface species can then react with adsorbed H to form water (reaction (6), Figure 6.5). Adsorbed OOH and H species were reported to be more stable on smaller Au particles [321], rendering these particles unreactive for hydrogen oxidation but active in oxygen-assisted hydrogen dissociation. H₂O₂ decomposition on intermediate-

size (13–55 Au atoms) and large Au particles (>55 Au atoms) was predicted to occur by breaking an O–O bond (reaction (5), Figure 6.5) [321]. This mechanism results in a hydrogen and oxygen reaction orders of 1 assuming exclusively empty sites, and can result in a hydrogen order of ~ 1 and oxygen order of ~ 0.3 , as reported here (Table 6.4), if O_2^* has a coverage of ~ 0.7 .

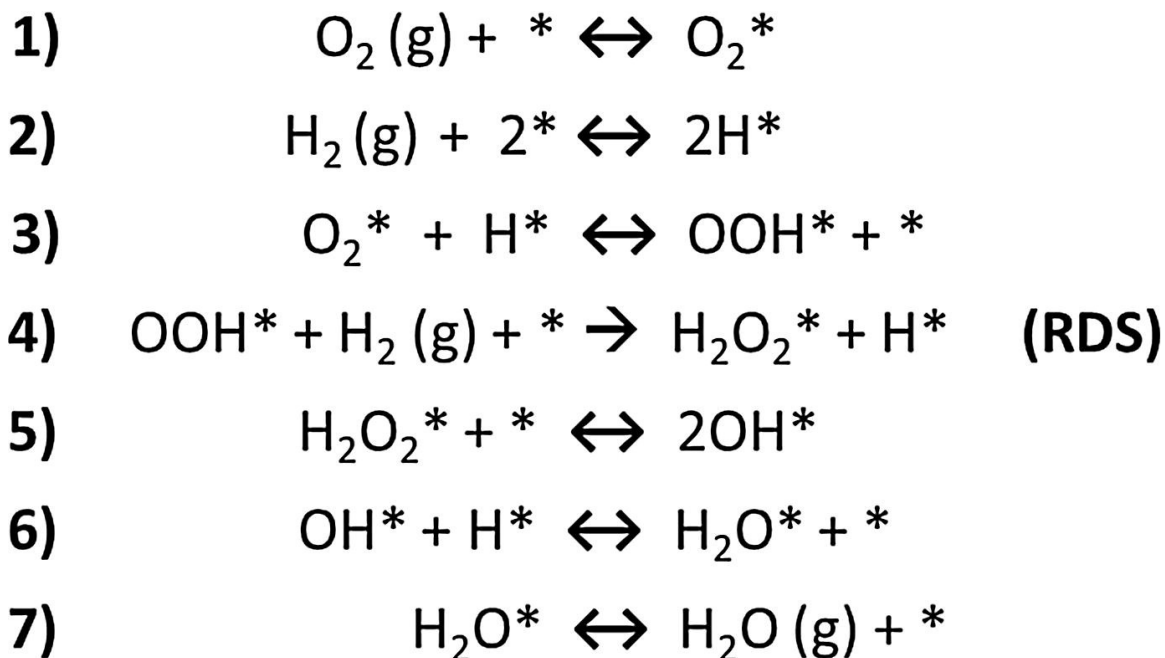


Figure 6.5. Single-site reaction mechanism proposed by Barton and Podkolzin for hydrogen oxidation over Au/TS-1 catalysts [321].

Nijhuis et al. observed that propylene adsorbed to Au sites in Au/SiO₂ catalysts during pre-adsorption experiments at 353 K, partially poisoning the hydrogen oxidation reaction, though to a lesser extent than when propylene was co-fed with hydrogen and oxygen (conditions under which PO was formed) over Au/TiO₂ catalysts [325], similar to the observation of Hayashi and Haruta that the presence of C₃H₆ in the feed stream decreased the rate of H₂ consumption over Au/TiO₂/SiO₂ catalysts between 273 and 400 K [280]. These results imply that propylene adsorbs to active sites for H₂ oxidation in Au-Ti catalysts at 353 K and are consistent with the observed slightly

negative apparent reaction order in propylene for hydrogen oxidation reported here. While the H_2 and O_2 order differences compared to those for PO formation could be explained by different kinetically relevant steps over the same active sites involved from the PO formation mechanism, the lack of PO inhibition for the H_2 oxidation reaction(s), a surface intermediate which occupies the surface on both sites in the PO formation mechanism (Section 6.4.2.1), suggests that H_2 oxidation occurs primarily on a site that is not involved in PO formation. A distribution of Au and Ti sites over Au/Ti-SiO₂ that form PO and water over Au sites in the vicinity of Ti sites and that form H₂O over Au sites that are not near Ti sites was proposed by Kanungo et al. [301]. The data presented here suggest a similar collection of sites is present over Au/TS-1, wherein Au sites that form water from H_2 oxidation must be distinct from those that form water along with PO, as the coverages of PO and C₃H₆ required for the observed reaction orders in PO and C₃H₆ would exceed 1 if PO were only bound to Ti sites and propylene and oxygen were only bound to Au sites. Thus, PO apparently binds to Au sites that are relevant for PO formation, but not those that are relevant for H₂O formation by H_2 oxidation, resulting in a zero order dependence on PO pressure for H_2 oxidation. The data presented here do not exclude the possibility that a minority of the H_2 oxidation events could occur over PO formation sites, but the dominant sites for H_2 oxidation must be distinct from those involved in formation of PO.

6.5 Conclusions

Apparent reaction orders and activation energies consistent with those reported previously over titanosilicate-supported Au catalysts were measured for a series of Au/TS-1 catalysts in a gas-phase CSTR reactor. Measurement of product inhibition by co-feeding propylene oxide has revealed significant inhibition by propylene oxide in the Au/TS-1 system, while CO₂ and H₂O do not inhibit propylene epoxidation rates. Previous reports of apparent reaction orders have not accounted for product inhibition, and thus these reaction orders for propylene oxide formation over Au/TS-1

and similar catalysts reported in the literature are incorrect by substantial amounts (a factor of ~ 1.6) and, therefore, can lead to incorrect mechanistic interpretations. We have found, however, that reaction orders corrected for propylene oxide inhibition are consistent with the previously proposed two-site simultaneous mechanism in which an $\text{HOO-S}_1\text{-H}$ species reacts with propylene adsorbed on a neighboring site, but rule out a two-site sequential mechanism in which H_2O_2 formed on Au sites desorbs and reacts with propylene adsorbed on Ti sites. The precise nature of the active species that we designate as $\text{HOO-S}_1\text{-H}$ is not yet clear and is a subject of continuing study. H_2 oxidation is not inhibited by propylene oxide, suggesting this reaction occurs on sites other than the sites responsible for PO formation. This finding implies the possibility of improved catalyst formulations in which the H_2 oxidation sites are minimized while the epoxidation sites are maximized, resulting in a catalyst with high epoxidation rates and H_2 selectivity, as required for industrial application of this reaction. Without accurate measurement of kinetics, in this case enabled by use of a gas-phase CSTR, discovering the physical identity of the active site, the use of mechanistic conclusions to guide new catalyst formulations, and the pairing of molecular-level theory with experiments would all not be possible.

6.6 Supporting Information

6.6.1 Reactor Apparatus

(See Figures 6.6 and 6.7)

6.6.2 XRD Patterns

(See Figure 6.8)

6.6.3 Nitrogen Isotherms

(See Figure 6.9)

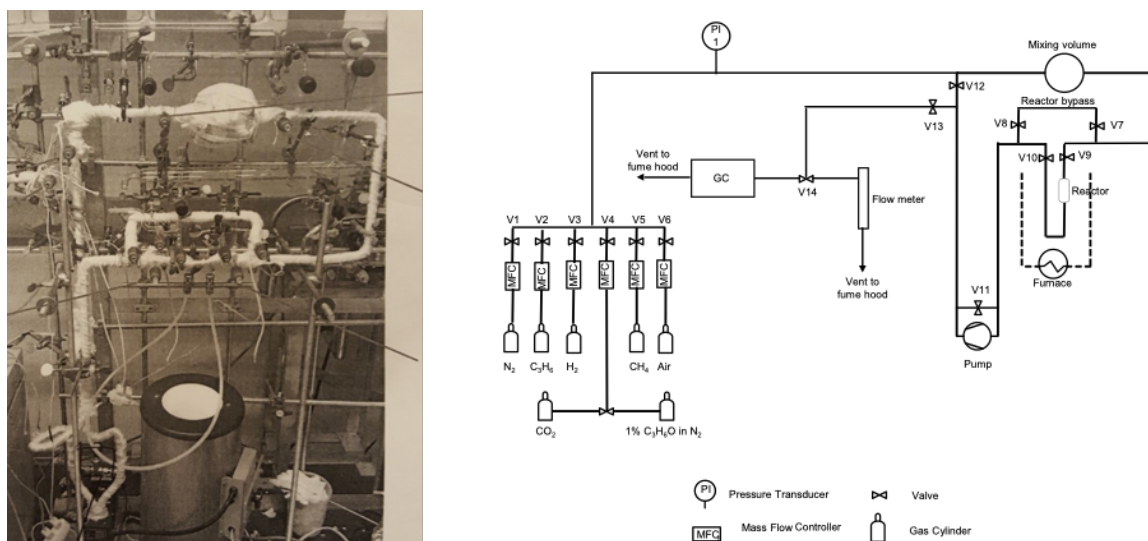


Figure 6.6. Photograph of gas-phase CSTR system with heat-traced recirculation loop (left). P&ID diagram for gas-phase PFR/CSTR system (right).

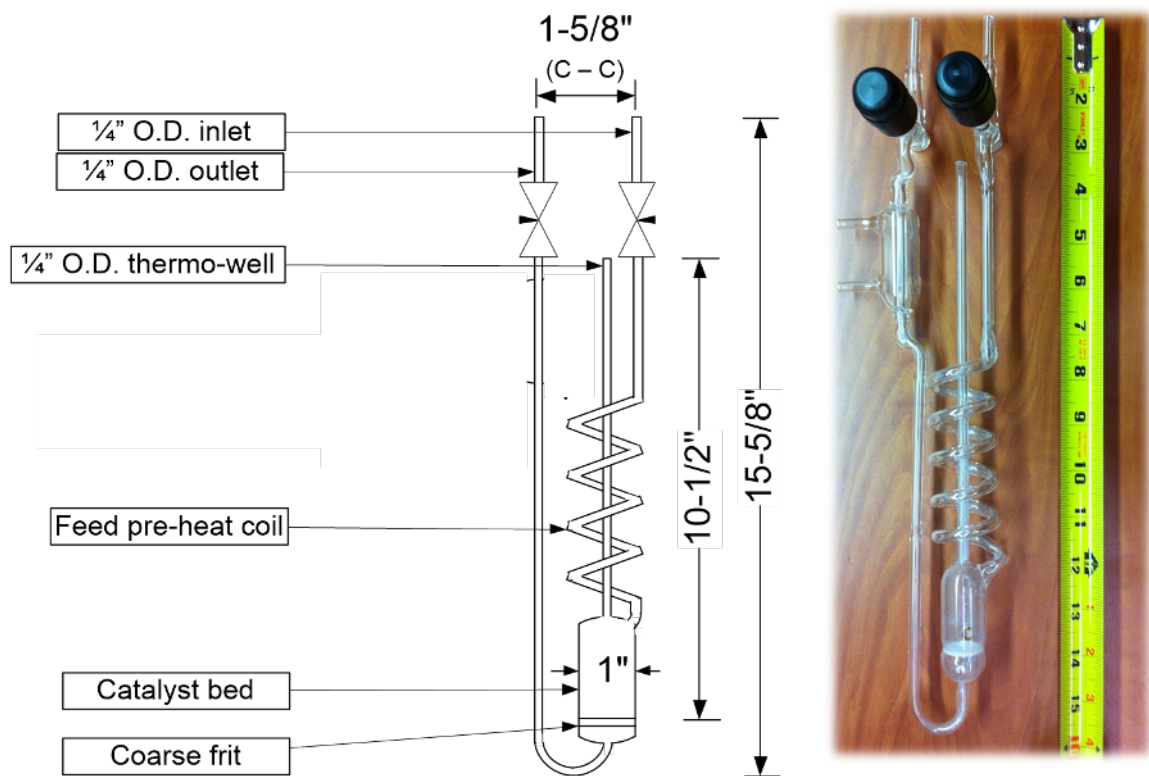


Figure 6.7. Diagram of Pyrex reactor (left). Photograph of Pyrex reactor (right).

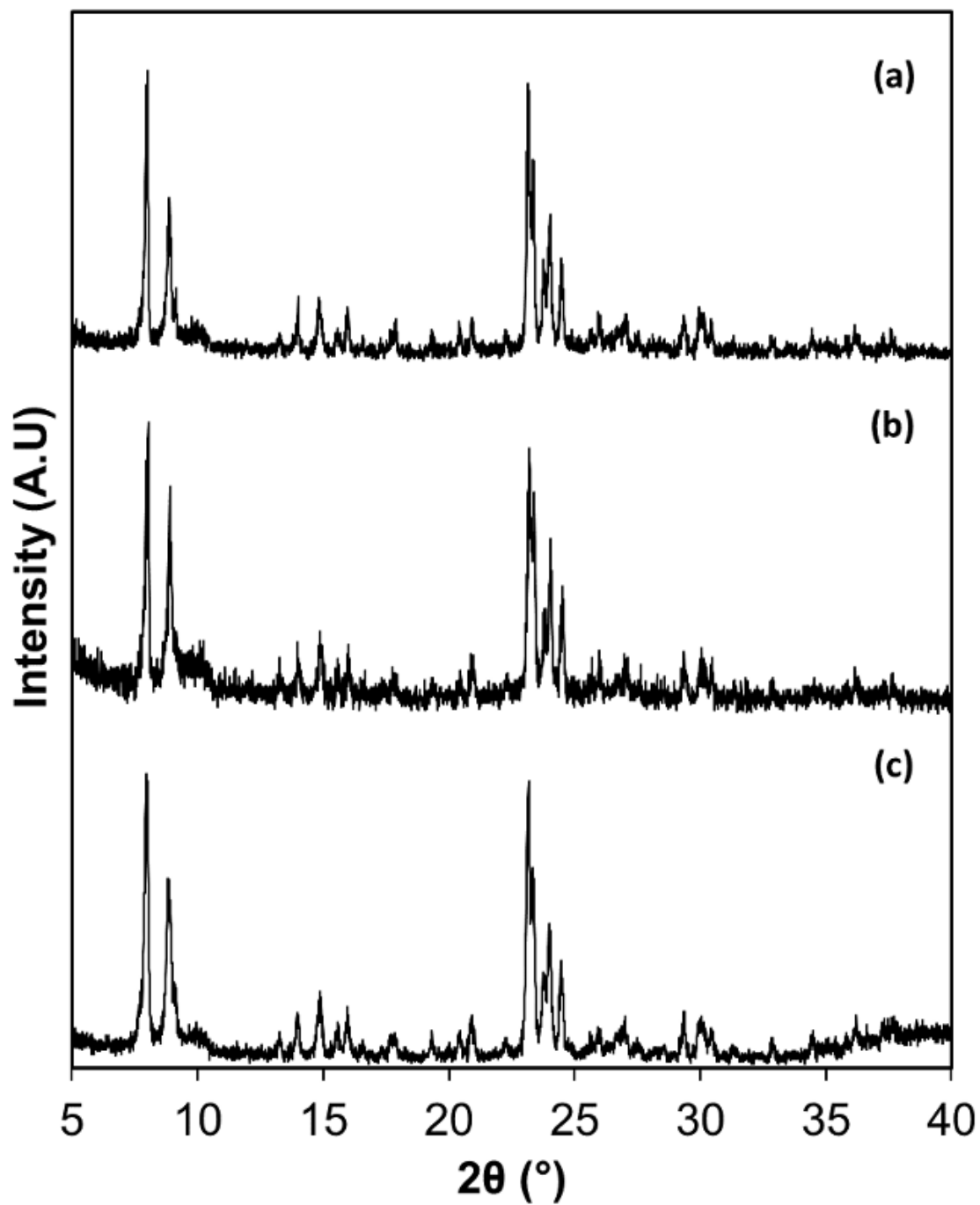


Figure 6.8. XRD patterns for calcined (a) TS-1(75) and (b) TS-1(81) and (c) TS-1(143). Patterns are normalized to their maximum intensity and offset vertically for clarity.

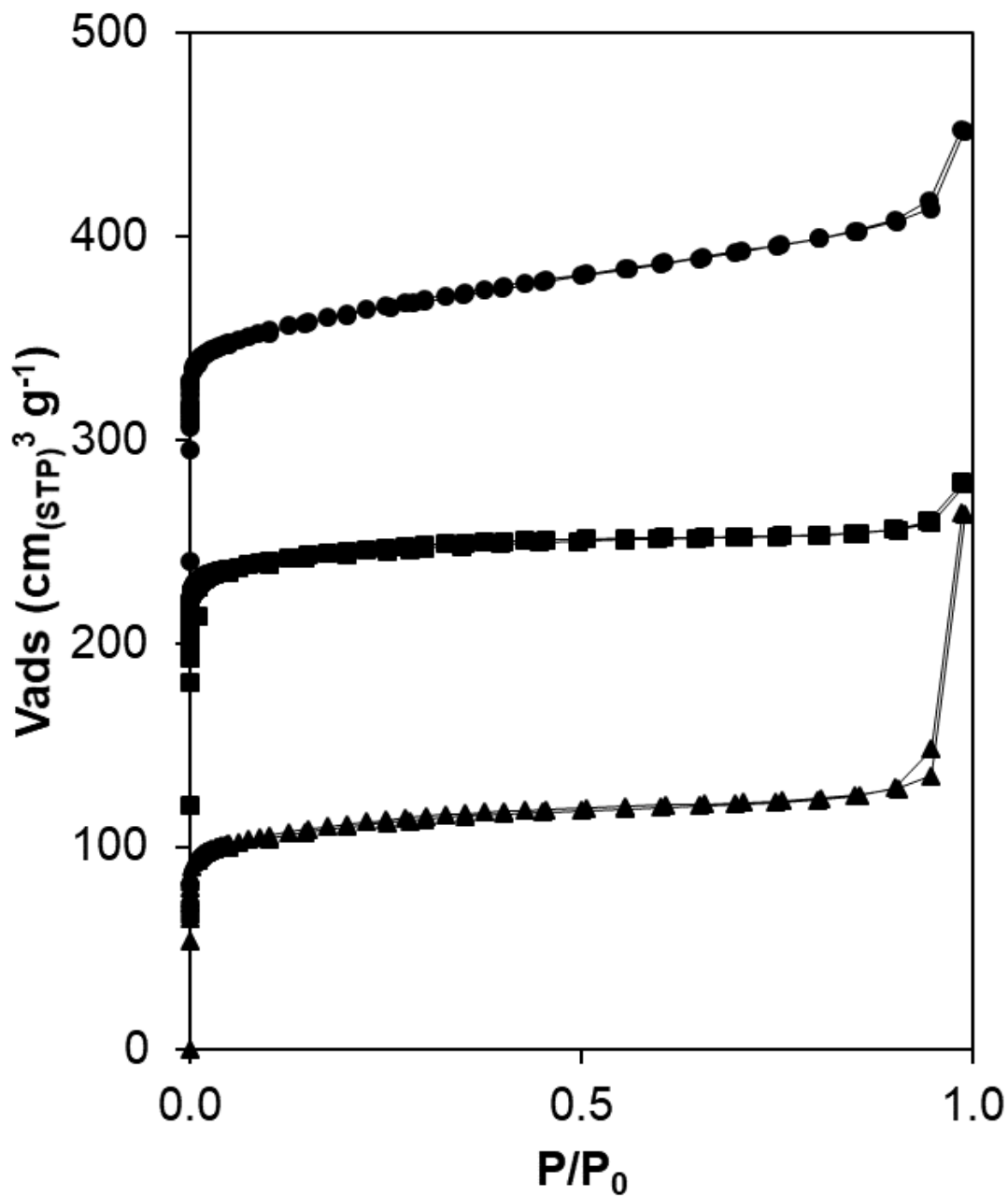


Figure 6.9. N₂ adsorption isotherms for TS-1(75) (circles) and TS-1(81) (squares) TS-1(143) (triangles). Isotherms are offset by 120 cm_{STP}³ g⁻¹ for clarity. Micropore volumes are reported in Table 6.1.

6.6.4 Diffuse Reflectance UV Visible Spectroscopy

DRUV spectra of dehydrated TS-1 samples (Figure 6.10) were used to produce the Tauc plots shown in Figure 6.11 for each TS-1 sample. The lowest energy x-intercepts of these plots (~ 5 eV) correspond to the Ti edge energies [326–328] and are reported in Table 6.1.

6.6.5 Additional Kinetic Data and Derivations

The absence of diffusion limitations was confirmed by calculation of the Mears' criterion and the Thiele Modulus for the Au/TS-1 catalysts studied here, as adapted from the derivation in Lee et al. [329]. The absence of external diffusion limitations is confirmed if the Mears' criterion (Equation 6.17) is met, specifically that:

$$\frac{-r_{A_{obs}}\rho_b R * n}{k_c C_{A_b}} < 0.15 \quad (6.17)$$

where $-r_{A_{obs}}$ is the observed reaction rate ($\text{kmol kg}_{\text{cat}}^{-1} \text{s}^{-1}$); R is the catalyst pellet radius (m); n is the reaction order of reactant A; C_{A_b} is the concentration of reactant A in the bulk gas phase at 473 K (kmol m^{-3}); and k_c is the mass transfer coefficient for reactant A (m s^{-1}). Finally, ρ_b is the catalyst bed density (kg m^{-3}), defined as:

$$\rho_b = (1 - \Phi)\rho_c \quad (6.18)$$

where ρ_c is the pellet bulk density (kg m^{-3}) and Φ is the porosity of the catalyst bed. The Reynolds number for this system is defined as:

$$Re = 2U * R * \frac{\rho}{\mu} \quad (6.19)$$

where U is superficial velocity (m s^{-1}), ρ is the density of the reactant mixture (kg m^{-3} , approximated by air at 473 K), μ is the viscosity of the reactant mixture (kg (m-s)^{-1} , approximated by air at 473 K). Since the Reynolds number is much smaller than 1, the mass transfer coefficient (k_c) can be estimated by assuming that the Sherwood number, Sh , defined as:

$$Sh = k_c \frac{2R}{De} \quad (6.20)$$

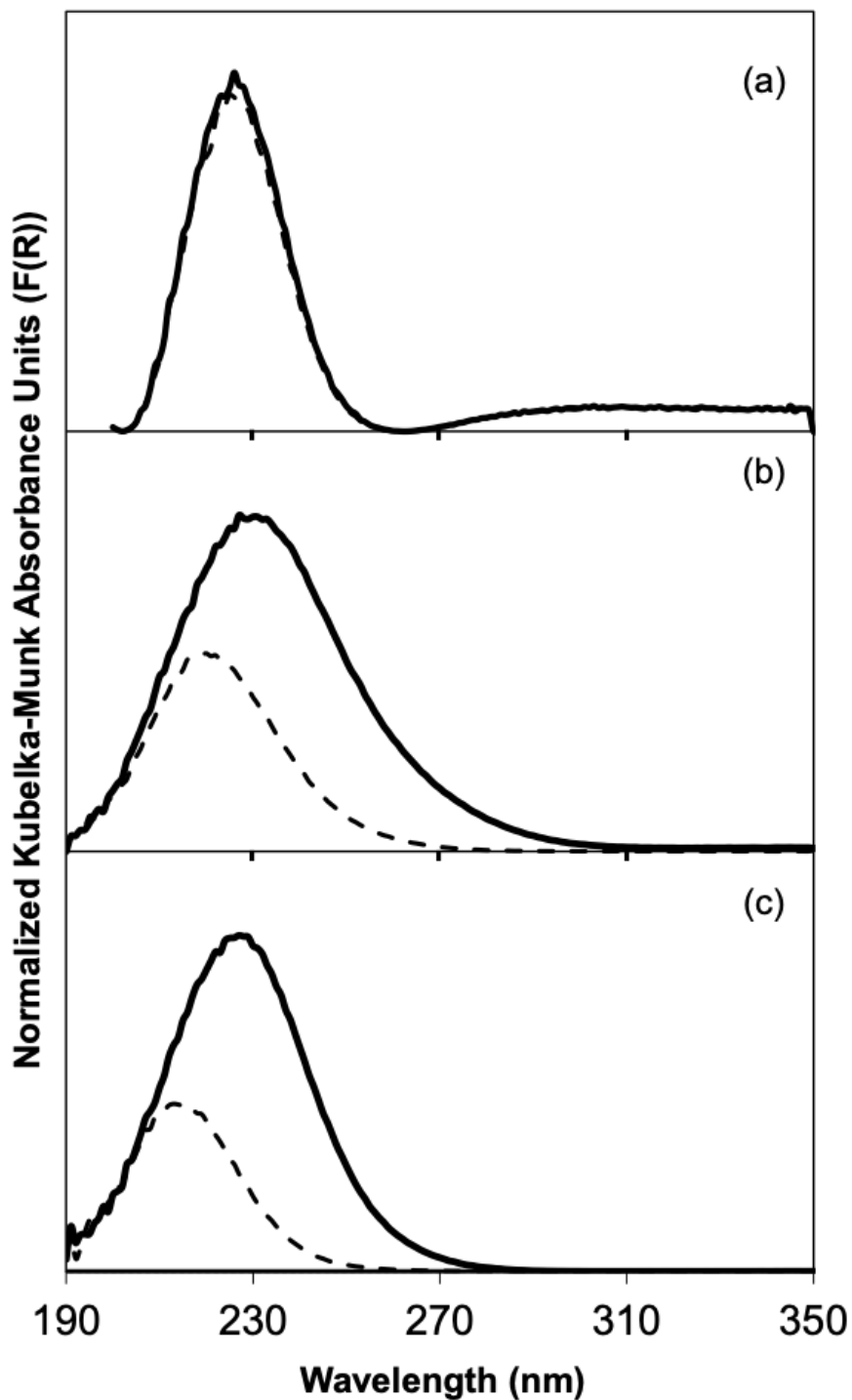


Figure 6.10. DRUV spectra in Kubelka-Munk units (normalized to the maximum $F(R)$ intensity) for (a) TS-1(75) (b) TS-1(81) and (c) TS-1(143), collected (i) under ambient conditions (solid line), (ii) after dehydration at 523 K (dashed line).

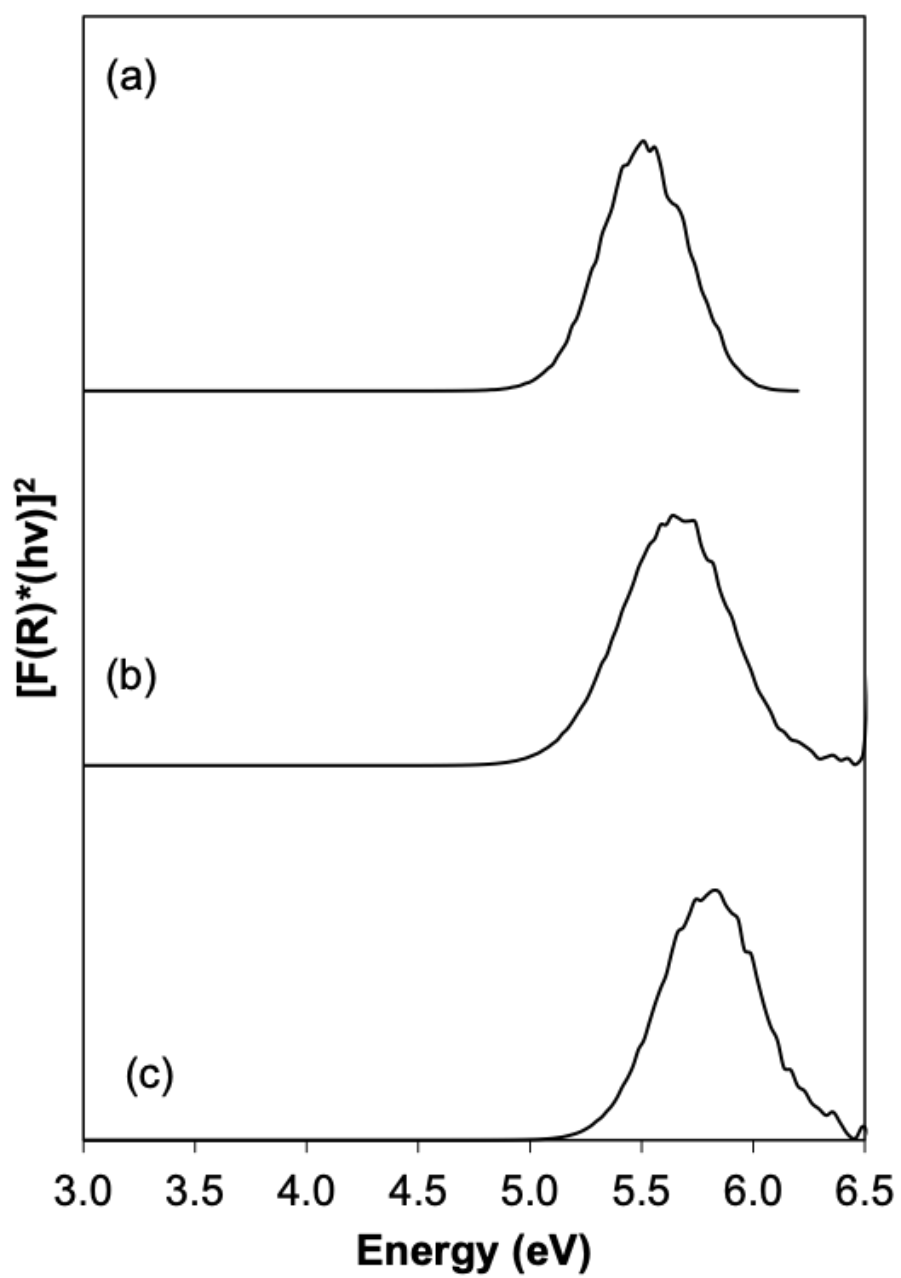


Figure 6.11. Tauc plots for (a) TS-1(75) and (b) TS-1(81) and (c) TS-1(143) measured under dehydrated conditions (He flow, 523 K).

is equal to 2, where De is estimated diffusivity of reactant A in the bulk gas phase [330]. All parameters used in these equations are listed in Table 6.5.

Table 6.5.
Parameters used to calculate the Mears' criterion for Au/Ts-1 catalysts used in this study.

Parameter	Value	Units
Highest observed PO rate at 473 K	$\sim 7.2 \times 10^{-7}$	$\text{kmol kg}_{\text{cat}}^{-1} \text{s}^{-1}$
Density of catalyst pellet	500	kg m^{-3}
Catalyst bed density (estimated bed porosity 0.3)	~ 350	kg m^{-3}
Radius of catalyst pellet	7.5×10^{-5}	m
Bulk gas concentration of propylene at 473 K	2.6×10^{-3}	kmol m^{-3}
Reynolds number ^a	$\sim 1.3 \times 10^{-2}$	unitless
Estimated gas phase diffusivity of propylene in air at 473 K [329, 330]	$\sim 3 \times 10^{-5}$	$\text{m}^2 \text{s}^{-1}$
Mass transfer coefficient for propylene ^b	0.4	m s^{-1}
Reaction order of C_3H_6	~ 0.5	unitless
Estimated Mear's criterion	9.1×10^{-6}	unitless

^aSuperficial velocity = 0.0021 m s^{-1} (flow rate = $65 \text{ cm}^3 \text{ min}^{-1}$ through a reactor with inner diameter $\sim 0.025 \text{ m}$), estimated fluid kinematic viscosity (\sim air at 473 K): $\sim 3.7 \times 10^{-5} \text{ (m}^2 \text{ s}^{-1})$

^bSince $\text{Re} \ll 1$, mass transfer coefficient was estimated by assuming Sh (Sherwood number) = 2 (Equation 6.20)

The absence of internal diffusion limitations was confirmed by estimating the Thiele modulus for the Au/Ts-1 catalysts used here under the standard reaction conditions employed. The catalysts were sieved to pellets of approximately $150 \mu\text{m}$ diameter, but each pellet contains many TS-1 crystallites with an average diameter of $\sim 200 \text{ nm}$, as shown in Figure 6.17. Thus, calculations related to internal mass

transfer assumed that this diameter was the relevant characteristic diameter. The Thiele modulus is defined as:

$$\Phi = \frac{-r_{A_{obs}} \rho_c R^2}{D_e C_{A_s}} = \eta \phi^2 \quad (6.21)$$

where $-r_{A_{obs}}$ is the observed reaction rate ($\text{kmol kg}_{\text{cat}}^{-1} \text{s}^{-1}$), ρ_c is the TS-1 crystallite density (kg m^{-3}), R is TS-1 crystallite radius (m), D_e is the effective gas-phase diffusivity at 473 K (estimated from the Knudsen equation assuming that the constriction factor, tortuosity and pellet porosity were 0.8, 6 and 0.3 respectively [330], assuming a pore radius of ~ 0.25 nm for the TS-1 crystallites), ($\text{m}^2 \text{s}^{-1}$), C_{A_s} is the gas concentration of A at the catalyst surface (kmol m^{-3}), η is the internal effectiveness factor and ϕ is the Thiele modulus. If $\phi \ll 1$, then $\eta \approx 1$ and ϕ is easily calculated. The parameters used for the Thiele modulus estimation are listed in Table 6.6.

Table 6.6.

Parameters used to calculate the Mears' criterion for Au/TS-1 catalysts used in this study.

Parameter	Value	Units
Density	1.7×10^3	kg m^{-3}
TS-1 crystallite size	1.0×10^{-7}	m
<i>Effective</i> gas phase diffusivity	3.3×10^{-9}	$\text{m}^2 \text{s}^{-1}$
Estimated Thiele modulus	1.2×10^{-3}	-

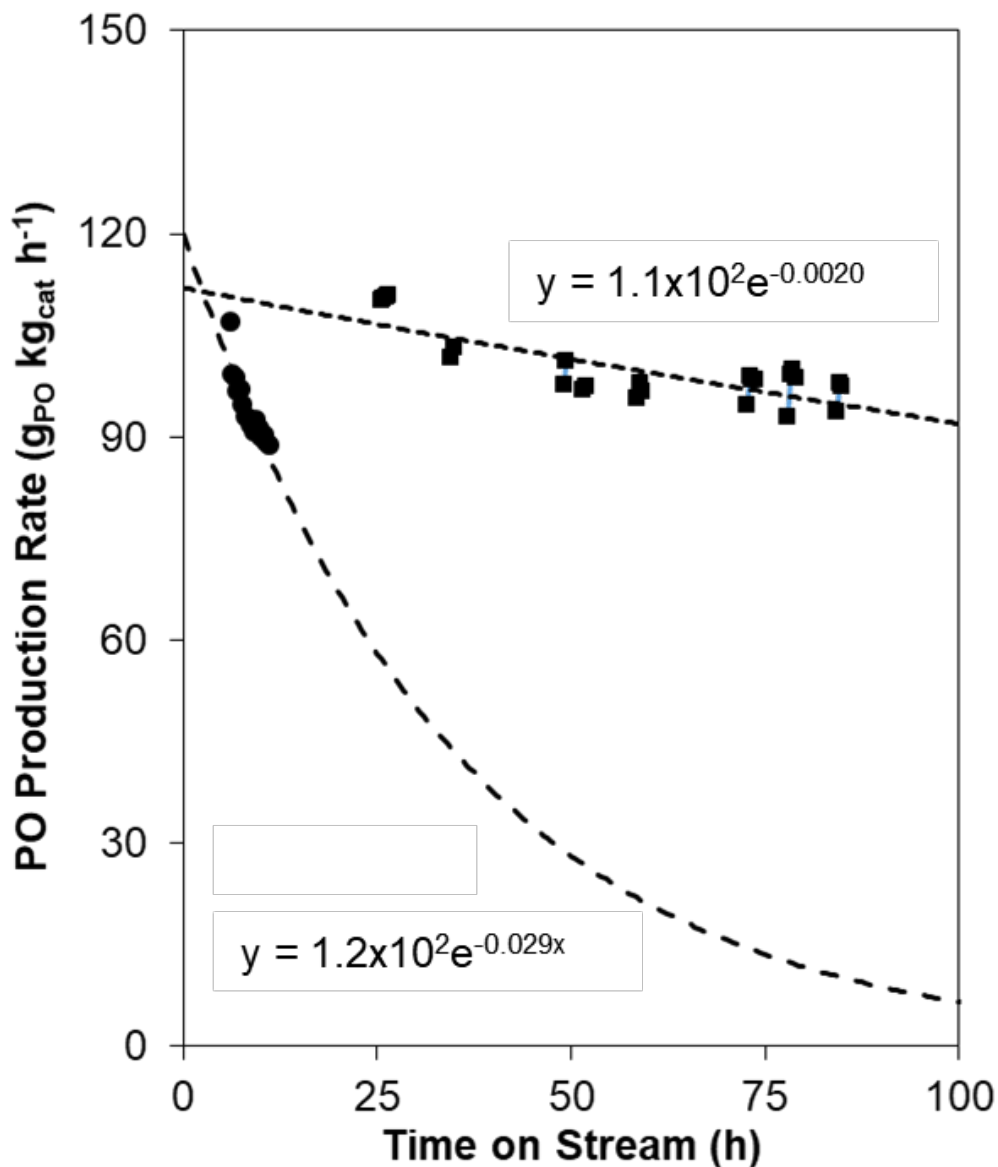


Figure 6.12. Determination of the deactivation rate constants in the initial deactivation (large dashed line, circles) and the steady-state deactivation (small dashed lines, squares) regimes for 0.092Au/TS-1(75). Note that after 24 h time on stream, the space velocity was changed from 14,000 to 26,000 cm³ g_{cat}⁻¹ h⁻¹ and the reactor operating mode changed from PFR to CSTR, resulting in an increased reaction rate at 25 h time on stream. (T = 473 K, feed was 10% H₂/10% O₂/10% C₃H₆/70% N₂ by volume).

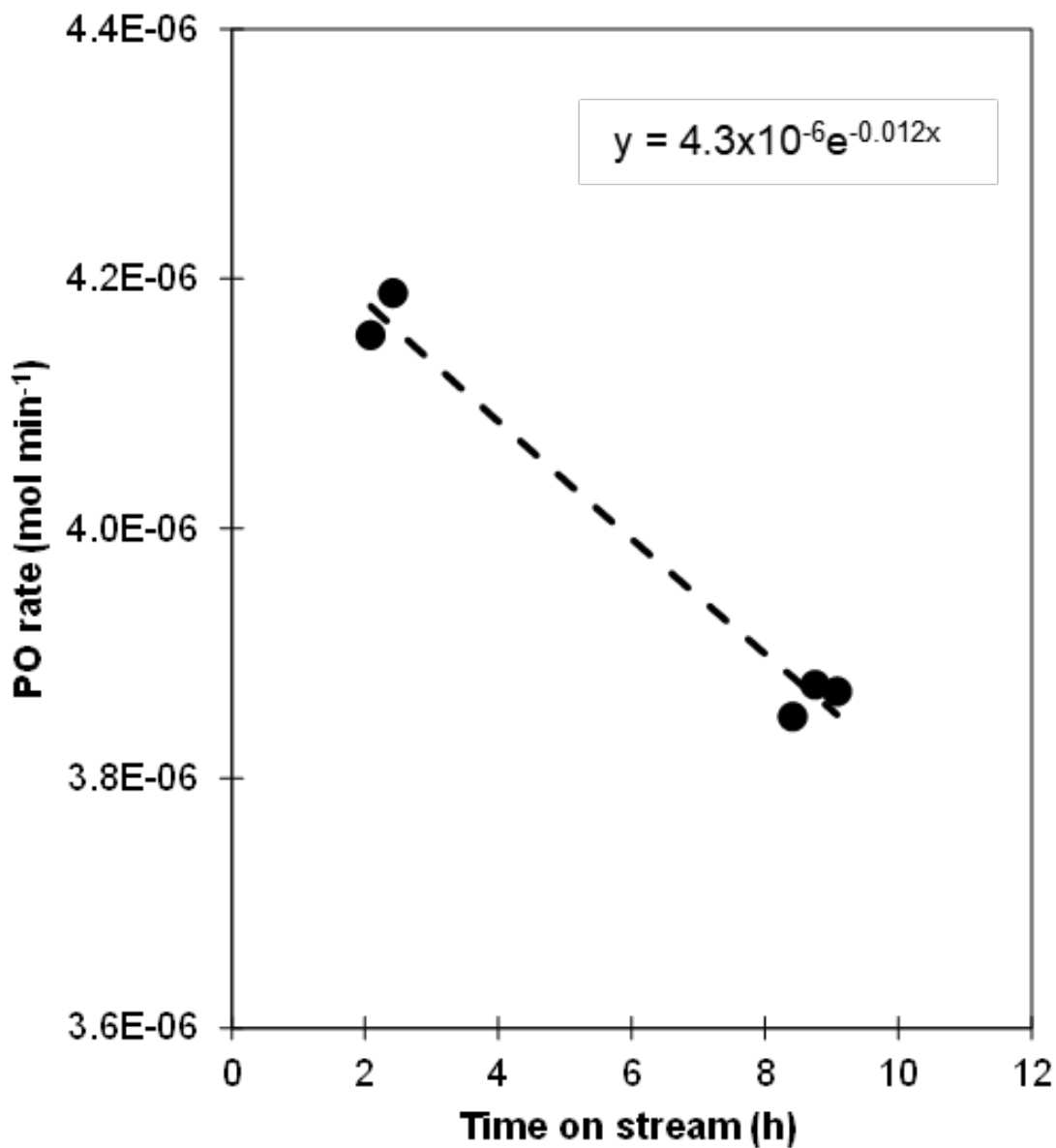


Figure 6.13. Example determination of the first-order exponential decay constant for correction of steady-state reaction rates during PO order measurement on 0.063Au/TS-1(75). Data collected in CSTR mode, $SV = 26,000 \text{ cm}^3 \text{ g}_{\text{cat}}^{-1} \text{ h}^{-1}$, $T = 473 \text{ K}$, feed = 10% H_2 /10% O_2 /10% C_3H_6 /0%-0.012% PO/Balance N_2 over 0.063Au/TS-1(75) and represent returns to the standard condition with 0% PO co-feed. Over the time scale studied, the deactivation is approximately linear.

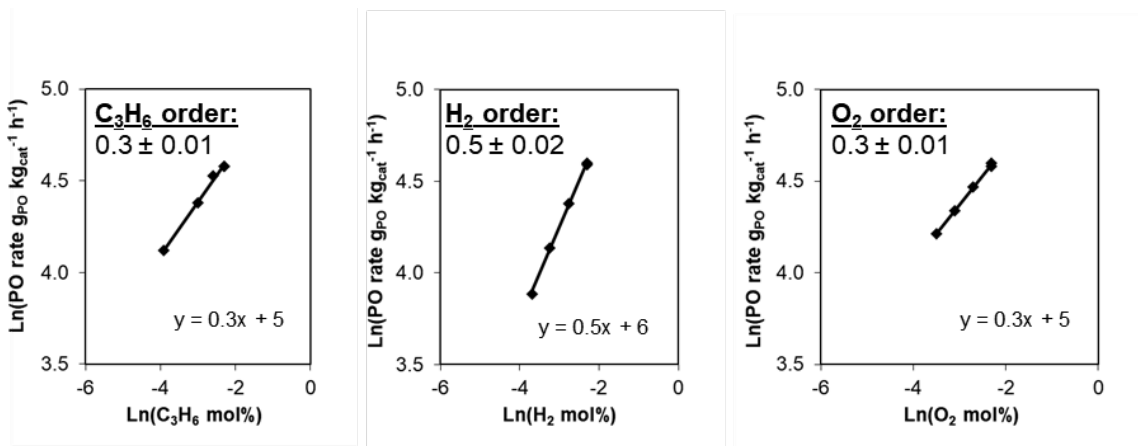


Figure 6.14. Apparent (a) H₂, (b) O₂, and (c) C₃H₆ reaction orders measured over 0.092Au/TS-1(75) at 473 K and a space velocity of 26,000 cm³ g_{cat}⁻¹ h⁻¹ in a gas-phase CSTR.

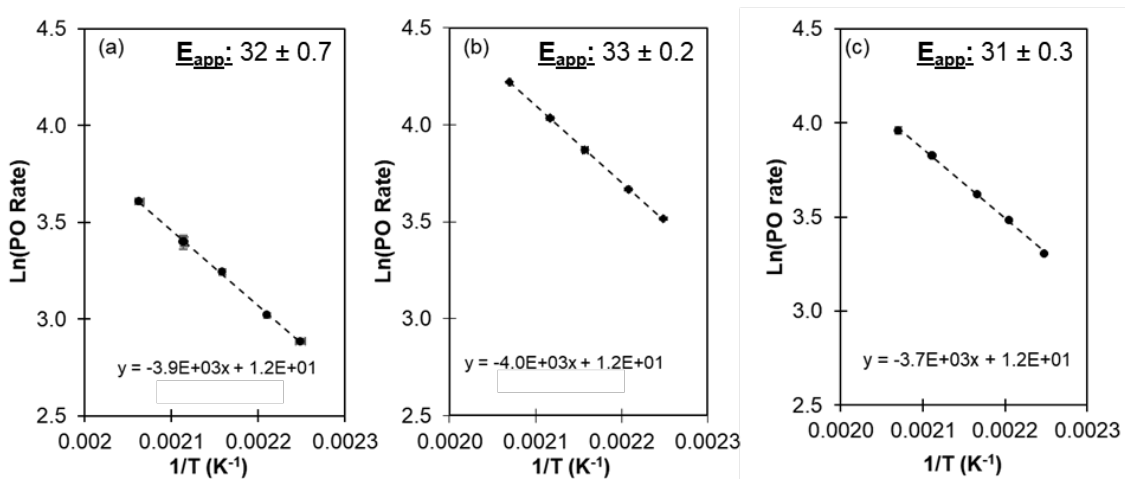


Figure 6.15. Apparent activation energies (deactivation corrected, not PO corrected) for PO formation measured over (a) 0.019Au/TS-1(143), (b) 0.040Au/TS-1(81), and (c) 0.022Au/TS-1(143) from 443-483 K with a feed composition of 10% H₂/ 10% O₂/ 10% C₃H₆/ 70% N₂ and a space velocity of 26,000 cm³ g_{cat}⁻¹ h⁻¹ in a gas-phase CSTR.

Table 6.7.

Apparent reaction orders and activation energies for PO formation measured over all catalysts in this study. Activation energies were measured in the temperature range 443-483 K with a feed composition of 10% H₂/ 10% O₂/ 10% C₃H₆/ 70% N₂ and a space velocity of 26,000 cm³ g_{cat}⁻¹ h⁻¹ in a gas-phase CSTR. Reaction orders were measured at 473 K with a feed composition of 2.5-10% H₂/ 2.5-10% O₂/ 2.5-10% C₃H₆/ 0-0.3% PO/ Balance N₂ and a space velocity of 26,000 cm³ g_{cat}⁻¹ h⁻¹ in a gas-phase CSTR.

Catalyst	Reaction Orders						E _{app} (kJ mol ⁻¹)
	H ₂	O ₂	C ₃ H ₆	PO	CO ₂	H ₂ O	
0.092Au/TS-1(75)	0.5	0.2	0.3	-0.8	-	-	-
0.019Au/TS-1(143)	0.7	0.2	0.2	-0.5	-	-	32
0.040Au/TS-1(81)	0.7	0.2	0.2	-0.8	-	-	33
0.030Au/TS-1(81)	0.7	0.2	0.1	-0.6	-	-	34
0.044Au/TS-1(81)	0.7	0.2	0.2	-0.7	-	-	34
0.033Au/TS-1(143)	0.7	0.2	0.2	-0.4	-	0.0	34
0.069Au/TS-1(143)	0.6	0.2	0.3	-0.4	-	0.0	32
0.064Au/TS-1(143)	0.6	0.2	0.3	-0.5	-	0.0	33

Table 6.8.

Apparent reaction orders and activation energies for propylene oxide, acrolein, acetone, ethanal, propanal, carbon dioxide, and H₂ oxidation determined by averaging the measured kinetic parameters for eight separate Au/TS-1 samples (0.092Au/TS-1(75), 0.019Au/TS-1(143), 0.040Au/TS-1(81), 0.030Au/TS-1(81), 0.044Au/TS-1(81), 0.033Au/TS-1(143), 0.069Au/TS-1(143), 0.064Au/TS-1(143)).

Product	Reaction Orders						E _{app} (kJ mol ⁻¹)
	H ₂	O ₂	C ₃ H ₆	PO	CO ₂	H ₂ O	
PO	0.6 ± 0.08	0.2 ± 0.01	0.2 ± 0.08	-0.60 ± 0.20	0	0.02 ± 0.03	33 ± 0.9
PO ^a	1.0 ± 0.20	0.4 ± 0.06	0.4 ± 0.10	—	0	—	52 ± 6.0
Acrolein	0.0 ± 0.09	0.4 ± 0.90	0.3 ± 0.04	-0.06 ± 0.04	0	-0.05 ± 0.08	72 ± 9.0
Acetone	0.3 ± 0.20	0.3 ± 0.20	0.0 ± 0.10	0.20 ± 0.20	0	-0.01 ± 0.03	40 ± 20
Ethanal	0.7 ± 0.08	0.2 ± 0.05	-0.2 ± 0.04	0.10 ± 0.05	0	0.02 ± 0.04	57 ± 4.0
Propanal	0.4 ± 0.04	0.1 ± 0.03	0.1 ± 0.02	0.40 ± 0.06	0	0.03 ± 0.04	63 ± 9.0
CO ₂	0.2 ± 0.07	0.1 ± 0.03	-0.10 ± 0.04	0.03 ± 0.06	0	0.04 ± 0.01	20 ± 5.0
H ₂ oxidation	0.9 ± 0.10	0.3 ± 0.10	-0.30 ± 0.07	-0.01 ± 0.20	0	-0.14 ± 0.07	31 ± 10

^aCorrected for PO inhibition (-0.6 order)

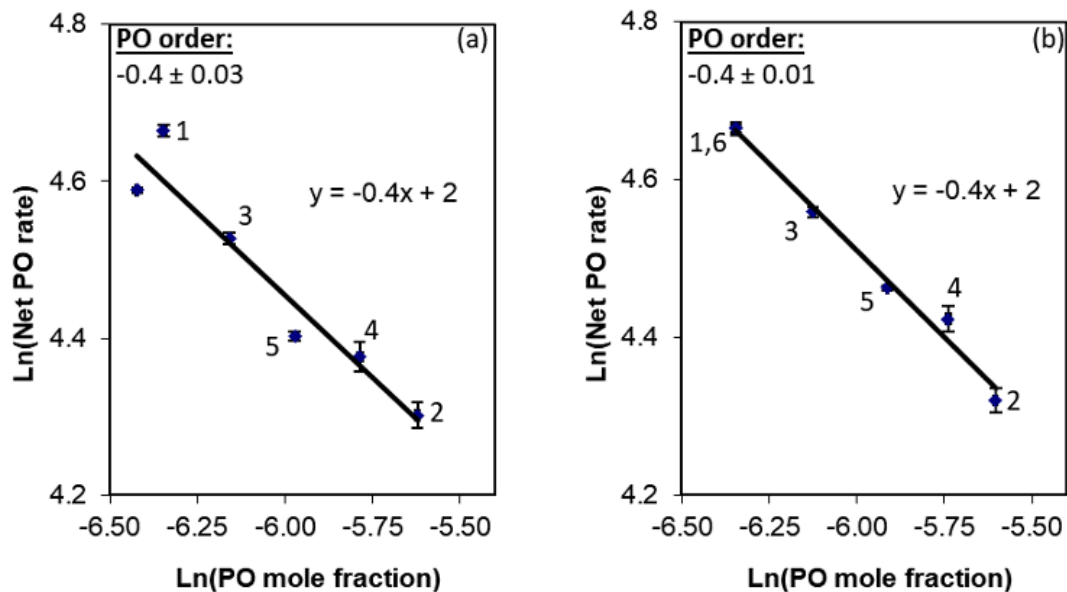


Figure 6.16. Example PO order measurement (a) before and (b) after correction for deactivation over time on stream. Numbers near each data point represent the non-monotonic order in which the data were collected (data points 1 and 6 represent no PO co-feed). Data collected in CSTR mode, $SV = 26,000 \text{ cm}^3 \text{ g}_{\text{cat}}^{-1} \text{ h}^{-1}$, $T = 473 \text{ K}$, feed = 10% H_2 /10% O_2 /10% C_3H_6 /0%-0.024% PO/Balance N_2 over 0.069Au/TS-1(143).

The reaction orders measured for each of the minor products are reported in Table 6.8, along with the reaction orders for propylene oxide and H_2 oxidation for comparison. Of the products, acetone, ethanal, propanal, and CO_2 had average measured H_2 reaction orders of 0.3, 0.7, 0.4, and 0.2 respectively, while the acrolein rate was not affected by changing the H_2 inlet pressure.

The oxygen reaction orders are similar to that for PO formation (0.2) for acrolein, acetone, and ethanal (0.4, 0.3, 0.2, respectively), while the reaction orders for propanal (0.1) and CO_2 (0.1) formation are notably lower.

Differences in apparent propylene orders, from slightly positive to slightly negative, were observed over all species and imply differences in common intermediates or

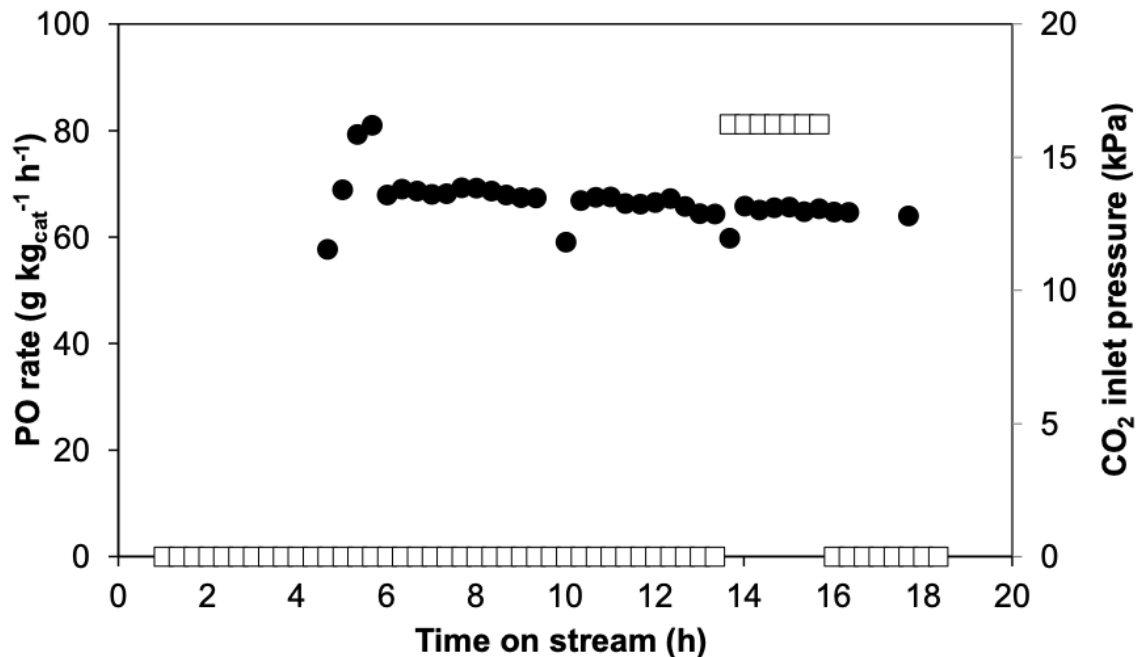


Figure 6.17. Propylene oxide formation rate as a function of time on stream (filled circles) and CO₂ inlet pressure (open squares) over 0.11Au/TS-1(81) with 10% H₂/10% O₂/10% C₃H₆/Balance N₂ flow (SV = 14,000 cm³ g_{cat}⁻¹ h⁻¹, T = 473 K).

differences in the sites in which side products are formed. For instance, acrolein (0.3 order) and propanal (0.1 order) were promoted by increased propylene pressure, while acetone (~ 0), ethanal (-0.2), and CO₂ (-0.1) were unaffected or slightly inhibited by propylene, similar to the observed kinetics for H₂ oxidation (-0.3 order).

Differences in apparent propylene oxide orders, from slightly positive to slightly negative, were observed over all species and imply differences in common intermediates or differences in the sites in which side products are formed. Propanal (0.4 order) in particular appears to be a series product from propylene oxide similar to acetone (0.2 order), as might be expected for these two ring opening products. In contrast, acrolein (~ 0), CO₂ (~ 0), and ethanal (0.1) formation rates were less de-

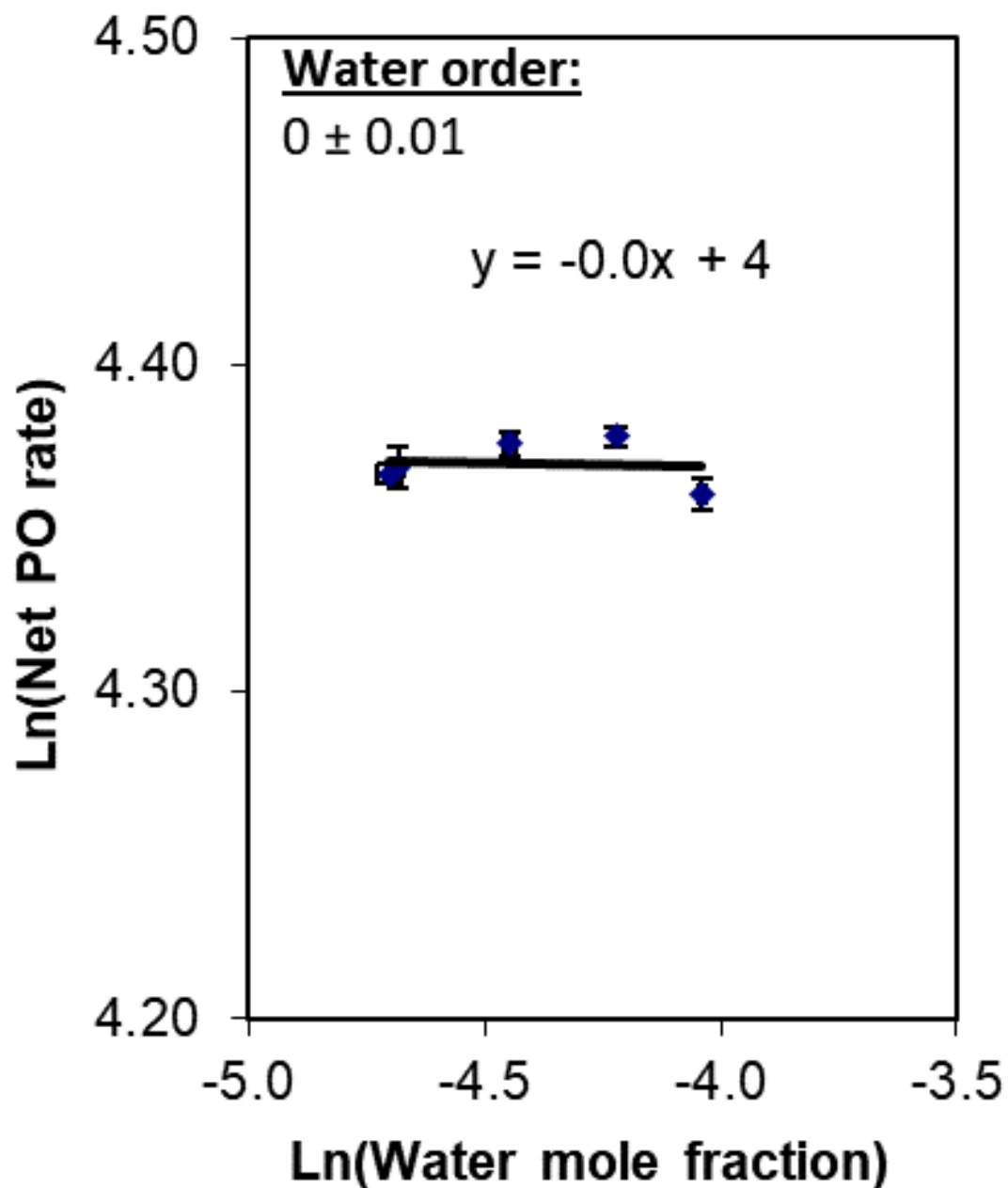


Figure 6.18. Apparent water order measured over 0.069Au/TS-1(143) at 473 K, $SV = 26,000 \text{ cm}^3 \text{ g}_{\text{cat}}^{-1} \text{ h}^{-1}$, 10% H_2 , 10% O_2 , 10% C_3H_6 , 0-0.86% H_2O /Balance N_2 in a gas phase CSTR.

pendent on PO pressure, suggesting the possibility of alternate pathways to forming these products than via propylene oxide.

The apparent activation energies for acrolein, acetone, ethanal, and propanal (72, 40, 57, and 63 kJ mol⁻¹, respectively) were distinct from that for CO₂ (~20 kJ mol⁻¹). Those for acrolein, ethanal, and propanal were higher, outside of experimental error, than those for propylene oxide formation (~33 kJ mol⁻¹) and H₂ oxidation (31 kJ mol⁻¹).

6.6.5.1 Example Log Derivative Derivation

As derived in Section 6.4.2.1, the rate of PO formation is:

$$\frac{r_{PO}}{L_2} = \frac{k_7 K_6 K_5 K_4 P_{C_3H_6} P_{O_2} P_{H_2}}{(1 + K_2 P_{O_2} + K_5 K_4 P_{O_2} P_{H_2} + K_8 P_{C_3H_6O})(1 + K_6 P_{C_3H_6} + K_9 P_{C_3H_6O})} \quad (6.22)$$

For example, to arrive at the equivalence of the H₂ reaction order with $1 - \theta_{HOOH}$, we first note that:

$$\frac{\partial \ln(r_{PO}/L_2)}{\partial \ln(P_{H_2})} = \frac{P_{H_2}}{r_{PO}/L_2} * \frac{\partial(r_{PO}/L_2)}{\partial P_{H_2}} \quad (6.23)$$

For convenience, we define:

$$r_{PO,L_2} \equiv \frac{r_{PO}}{L_2} \quad (6.24)$$

Then, taking the derivative of the rate expression with respect to hydrogen pressure results in:

$$\begin{aligned} & \frac{k_7 K_6 K_5 K_4 P_{C_3H_6} P_{O_2}}{(1 + K_2 P_{O_2} + K_5 K_4 P_{O_2} P_{H_2} + K_8 P_{C_3H_6O})(1 + K_6 P_{C_3H_6} + K_9 P_{PO})} \\ & * \left(1 - \frac{K_5 K_4 P_{H_2} P_{O_2}}{1 + K_2 P_{O_2} + K_5 K_4 P_{O_2} P_{H_2} + K_8 P_{PO}}\right) \end{aligned} \quad (6.25)$$

And thus:

$$\frac{P_{H_2}}{r_{PO,L_2}} * \frac{\partial(r_{PO,L_2})}{\partial P_{H_2}} = 1 - \frac{K_5 K_4 P_{H_2} P_{O_2}}{1 + K_2 P_{O_2} + K_5 K_4 P_{O_2} P_{H_2} + K_8 P_{PO}} \quad (6.26)$$

Or equivalently:

$$\frac{\partial \ln(r_{PO,L_2})}{\partial \ln(P_{H_2})} = 1 - \theta_{1,HOOH} \quad (6.27)$$

6.6.5.2 Sequential Mechanism, Rate Law, and Log Derivatives

In general, the sequential mechanism (Figure 6.19) features hydrogen peroxide production on gold sites (S_1), which then desorbs and adsorbs to titanium sites (in this case, S_2 -OH) to form a hydroperoxy species, which then epoxidizes propylene.

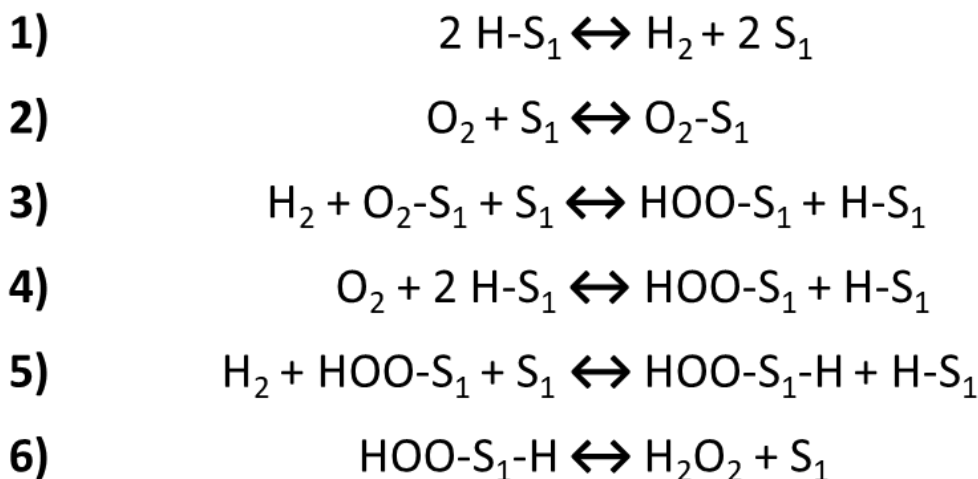
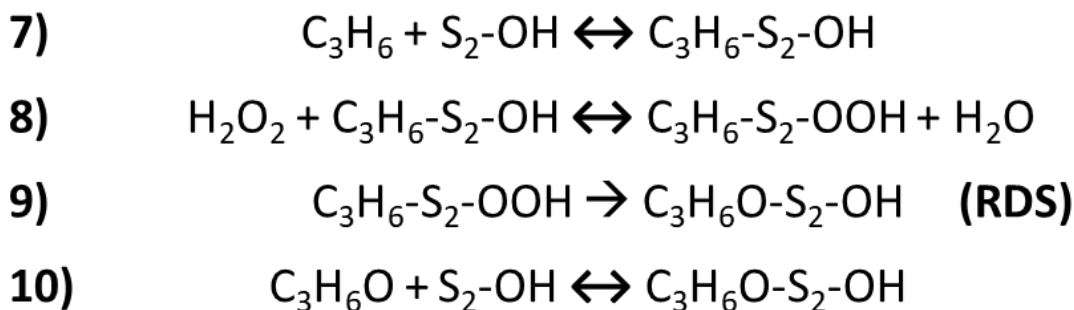
(HOOH Production)**(PO Production)**

Figure 6.19. One variation of the sequential mechanism. In this mechanism, S_1 refers to a Au site, and S_2 refers to a Ti site.

Assuming steps 1-8 and 10 are quasi-equilibrated, step 9 is the rate determining step, and that the MASIs on the Ti site (in order of appearance in the denominator

of the rate law) are empty sites (S_2 -OH), C_3H_6 - S_2 -OH, C_3H_6 - S_2 -OOH, and C_3H_6O - S_2 -OH results in the rate expression shown in equation 6.28.

$$r = \frac{r_{PO}}{L_2} = \frac{k_9 K_8 K_7 K_6 K_5 K_4 P_{C_3H_6} P_{H_2} P_{O_2}}{P_{H_2O} + K_7 P_{C_3H_6} P_{H_2O} + K_8 K_7 K_6 K_5 K_4 P_{C_3H_6} P_{H_2} P_{O_2} + K_{10} P_{PO} P_{H_2O}} \quad (6.28)$$

Where k_{11} is the forward rate constant for step 11, K_i is the equilibrium constant for step i , P_j is the partial pressure of component j , and L_2 is the number of Ti sites.

This rate law results in the following log derivative relationships (Equations 6.29-6.32), describing the relationship between surface coverages and reaction orders. An example derivation is shown above (Equations 6.23-6.27). Based on these log derivatives, the coverages required for the sequential model to reproduce the measured kinetics presented in this study (Table 6.2, Table 6.7.) necessitate a coverage on the Ti-OH site that is greater than 1.

$$\frac{\partial \ln(r)}{\partial \ln(P_{O_2})} = 1 - \theta_{C_3H_6-S_2-OOH} \quad (6.29)$$

$$\frac{\partial \ln(r)}{\partial \ln(P_{H_2})} = 1 - \theta_{C_3H_6-S_2-OOH} \quad (6.30)$$

$$\frac{\partial \ln(r)}{\partial \ln(P_{C_3H_6})} = 1 - \theta_{C_3H_6-S_2-OH} - \theta_{C_3H_6-S_2-OOH} \quad (6.31)$$

$$\frac{\partial \ln(r)}{\partial \ln(P_{C_3H_6O})} = -\theta_{C_3H_6O-S_2-OH} \quad (6.32)$$

7. THREE-DIMENSIONAL ANTIMONY NANOCHAINS FOR LITHIUM-ION STORAGE

ACS Applied Nano Materials 2019, 2, 5351-5355. <https://doi.org/10.1021/acsanm.9b01316>

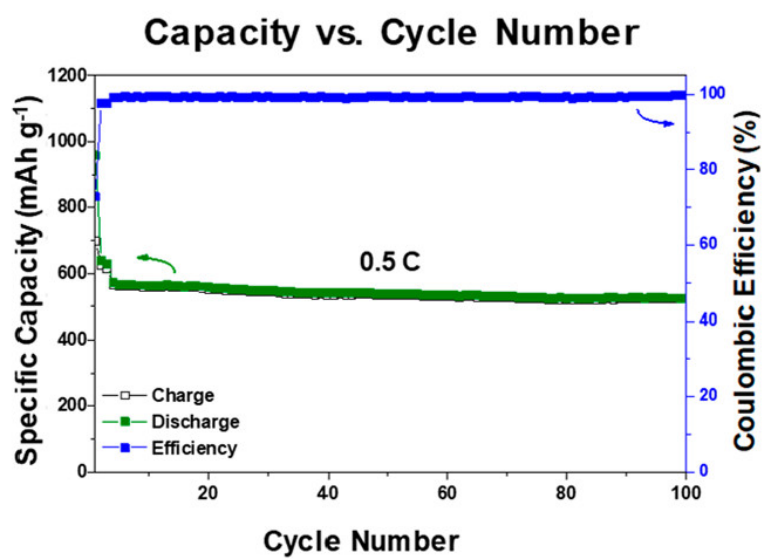
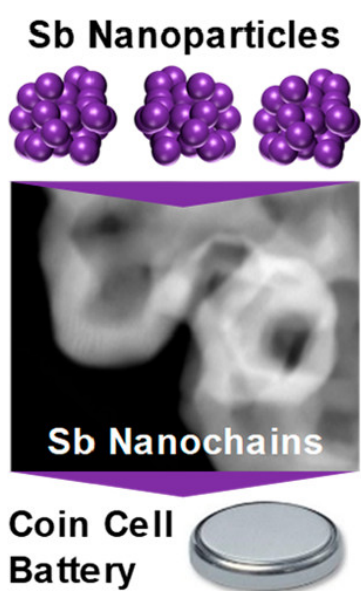
Jassiel R. Rodriguez¹, Henry J. Hamann², Garrett M. Mitchell¹, Volkan Ortalan^{3,4}, Vilas G. Pol¹, and P. Veeraraghavan Ramachandran²

¹Davidson School of Chemical Engineering, Purdue University, ²Herbert C. Brown Center for Borane Research, Department of Chemistry, Purdue University, ³School of Materials Engineering, Purdue University, and ⁴Birck Nanotechnology Center, Purdue University.

Reprinted (adapted) with permission from (*ACS Appl. Nano Mater.* 2019, 2, 9, 5351-5355). Copyright (2020) American Chemical Society.

7.1 Abstract

Three-dimensional antimony nanochain architectures with a rhombohedral phase, possessing particle sizes of ~ 30 nm, have been prepared via ammonia–borane reduction of SbCl_3 in an aqueous medium, followed by nucleation and capping processes. These offer adequate space to abate the large volumetric expansion during lithiation. Lithium-ion batteries fabricated with these antimony nanochains exhibited a stable specific charge capacity of 523 mAh g^{-1} at a C rate of $0.5 C$ with a Coulombic efficiency of 99.8% and a capacity retention of 92% after 100 cycles.



7.2 Introduction

Lithium-ion batteries (LIBs) remain a device of choice for electrochemical energy storage three decades after their commercialization. [331] An extensive demand for transportation, portable electronics, and multifarious stationary and grid energy storage systems has brought considerable attention on improving LIBs, particularly their anodes. [332–334] Currently, the commercial graphite anode offers a specific capacity of $\sim 330 \text{ mAh g}^{-1}$ (theoretical capacity, LiC_6 , 372 mAh g^{-1}) with a moderate rate of C/5. Nevertheless, the use of a graphitic anode leads to lithium (Li) plating at low electrochemical potential, making it unsafe because of the instability of lithiated graphite and hindering high-power applications [335]. Alternate negative electrode materials with improved characteristics, such as moderate, safe electrochemical negative potentials (0.2–0.5 V) and high specific capacities ($>350 \text{ mAh g}^{-1}$) with prolonged cycling stability, are desired to implement next-generation LIBs. Recently, materials chemists have devoted their attention to alloy-based anode materials, such as tin, antimony (Sb), silicon, etc., for LIBs. [336–340] However, such alloy-based anode materials suffer a large volume expansion during the lithiation process, which promotes a decrement of electronic conduction, because of the degradation of active particles and the loss of Li-ion host species. [341] All of these factors lead to a rapid loss of capacity and limit the charge–discharge cycling of the LIBs. [341]

Sb is considered to be a potentially superior anode material for LIBs because of its high theoretical specific capacity (Li_3Sb , 660 mAh g^{-1}) and good reversibility at moderate current density. [342] However, its large volumetric expansion, $\sim 147\%$, during the lithiation and delithiation reactions, promotes a continuous loss of specific capacity and therefore a lack of cycling performance. [343] One approach to dealing with this problem is to prepare Sb nanoparticles supported on or confined in carbon materials. [344] Another possibility is the design and preparation of new hollow Sb nanoarchitectures, such as nanotubes and interconnected nanoparticles. [345–348] The synthesized Sb alloy anodes incorporating these proposed strategies should lead to

the alleviation of mechanical strain, [349] resulting in a high retention of the specific capacity and prolonged cycling stability. [350, 351]

The preparation of tailored metallic nanoparticles with desired size and shape has become a topic of active investigation in several areas of research. Several methods have been reported for the reduction of different metal salts to prepare metallic nanoparticles, using hydrogen, hydrazine, sodium borohydride, etc., as reducing agents with fast kinetic rates. Control of the particle size and shape, particularly with the use of capping agents, has also been reported. Recently, amine–boranes with mild reducing characteristics have garnered attention because they provide much better control of the particle size distribution of the nanoparticles. [352, 353] Over a decade, we have been involved in the synthesis [354] and chemistry [355] of amine–boranes and have developed several efficient protocols for the preparation of amine–boranes, particularly ammonia–borane (AB). [356] Our expertise in this chemistry provides an exclusive opportunity to study the effect of a variety of amine–boranes on the reduction of metal salts, and we initiated a program to prepare Sb nanoparticles with a desirable morphology that can function as superior Li-ion anodes. Reported herein is the preparation of unique 3D Sb nanochain architectures, via AB reduction, offering wide and abundant pores to withstand the large volume expansion of Sb during the insertion and extraction of Li ions (Figure 7.1).

7.3 Results and Discussion

7.3.1 Nanoparticle Synthesis

Different Sb salts, SbCl_3 and SbF_3 , were reduced with AB, methylamine–borane, piperidine–borane, and triethylamine–borane in water for 2 h, followed by treatment with either tri-*n*-octylphosphine (TOP)/oleylamine (OA) or TOP/poly(vinyl alcohol) as a cosurfactant/capping agent at 230 °C for 2 h. The morphology of the obtained Sb nanoparticles was compared with those obtained via reduction with sodium borohydride. [357] Transmission electron microscopy (TEM) analysis of the morphology

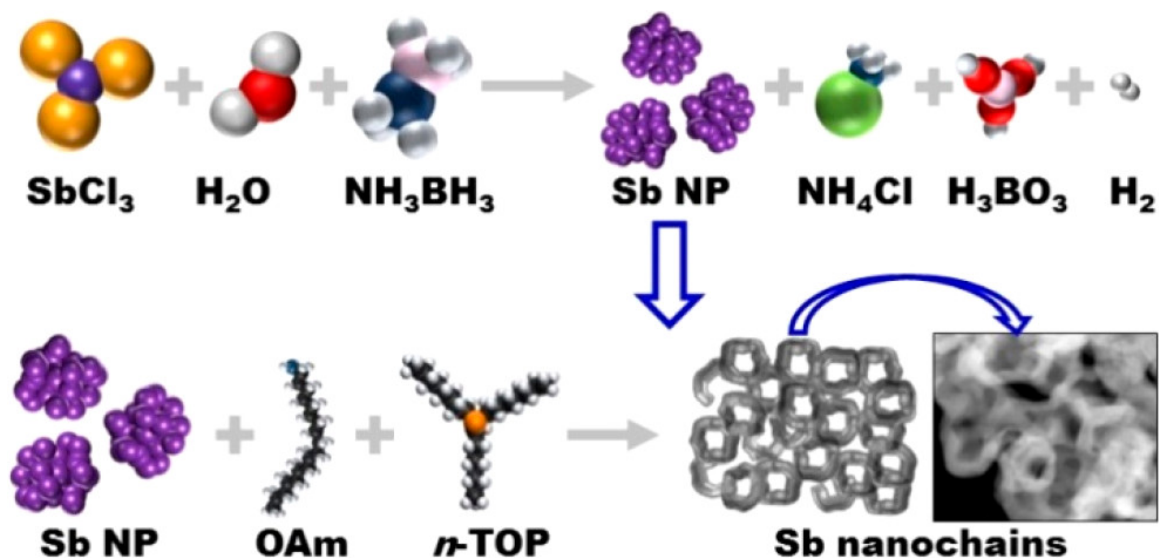


Figure 7.1. Illustration of the Formation of Sb Nanochains

and size distribution of the resulting nanomaterials (Figure 7.9 and Figure 7.10) revealed that the reduction of antimony trichloride with AB afforded the most uniform 3D Sb nanochain morphology and has the potential to exhibit enhanced performance as an anode material in LIBs. The above two-stage synthetic process involving the reduction, followed by nanoparticle growth and capping, resulted in a superior level of self-assembly with the formation of ~ 30 nm Sb nanoparticles (Figure 7.1).

7.3.2 Structural Characterization

The crystalline structure of the Sb nanochains was examined using powder X-ray diffraction (XRD) and Raman spectroscopy. Figure 7.11a shows the XRD patterns of Sb nanoparticles having 3D nanochains. The diffraction peaks observed at the 2θ positions of 23.7, 28.7, 40.1, 41.9, 47.1, 48.5, 51.7, 59.4, 62.8, 65.9, and 68.8 correspond to the Miller indices of (003), (012), (104), (110), (015), (006), (202), (024), (107), (116), and (122), respectively, which agree with JCPDS 01-071-1173, revealing the rhombohedral Sb phase. The additional peaks at the 2θ positions of 13.7, 27.6,

32.0, 35.0, 46.0, 54.5, 57.3, and 67.2 correspond to the Miller indexed planes (003), (020), (130), (131), (022), (231), (113), (171), and (271), respectively, related to the orthorhombic Sb_2O_3 phase, which is in tune with JCPDS 00-001-0729. Moreover, Raman scattering measurement analysis confirmed that the Sb nanoparticles contain traces of antimony oxide (Figure 7.11b), corroborating the analysis with the obtained powder XRD pattern. Some weak active bands can be observed near 192 cm^{-1} (F_{2g}), 254 cm^{-1} (A_{1g}) and 453 cm^{-1} (A_{1g}), which are related to the Raman active mode of Sb_2O_3 . Meanwhile, the strong vibrations around 112 and 150 cm^{-1} are associated with the A_g mode and the degenerated E_g band of the rhombohedral Sb phase. [358,359]

(Scanning) transmission electron microscopy (STEM) imaging was performed on a FEI Talos F200X S/TEM microscope with an X-FEG high brightness electron source and a Super-X EDS system to determine the morphology of the homogeneous 3D Sb nanochains. Energy-dispersive X-ray spectroscopy (EDS) was also performed on this instrument to confirm the identity of the Sb nanoparticles (Figure 7.2d–f). The EDS spectrum (Figure 7.11c) displayed an oxygen (O) peak, confirming the presence of Sb_2O_3 as well as revealing the presence of nearly equal amounts of carbon and Sb. This seems to indicate that the TOP/OA cosurfactant system might be incorporated into the final nanochain architecture. Figure 7.12a–c shows the presence of homogeneous 3D Sb nanochain morphology with higher crystallinity (Figure 7.12d). This indicates microdomains of agglomerated particles with random organization and without a clear particle shape, pointing to nanometric Sb particles. These observations indicate that the use of AB as a reducing agent allows the precipitation of metallic Sb as interconnected 3D nanochains (Figure 7.2a) containing voids and cavities in the formed chains. These chains appear to be porous nanostructures, as indicated in Figure 7.2b. Additionally, the crystalline nature of the 3D Sb nanochains was confirmed by the presence of lattice fringes (Figure 7.2c) and the fast Fourier transform [FFT; inset (#) in Figure 7.2c]. Detailed peak assignments are shown in Figure 7.13c,d for clarity. The relative positions and atomic distances of 0.11, 0.19, 0.22, and 0.34 nm were found, via the use of the CrysTbox program, to correspond with the (208),

($1\bar{1}5$), (105), and (01 $\bar{1}$) (of known distances of 0.112, 0.192, 0.224, and 0.354 nm, respectively). [360] Thus, the zone axis of Figure 7.2c was found to be the $[4\bar{1}1]$ Sb zone axis. [361] Matching of the lattice structure with known Sb diffraction analysis was verified by the analysis of multiple high-resolution TEM (HRTEM) images. From the high-angle annular dark-field (HAADF)-STEM image reference (Figure 7.2d) and elemental mapping (Figure 7.2e,f), the presence of Sb (yellow in Figure 7.2e) and O (cyan in Figure 7.2f) can be seen. Clearly, the impurity phase Sb_2O_3 is much less intense than the overall Sb concentration, which can be shown in the EDS spectrum (Figure 7.11c).

7.3.3 Electrochemical Studies

Electrochemical studies were carried out by fabricating working electrodes that contain a 8:1:1 weight ratio of Sb nanochains, Super P as the conductive material, and carboxymethyl cellulose as the binder. The mixture was coated on copper foil, with a loading density of the active material of $\sim 2 \text{ mg cm}^{-2}$. The resultant film was dried at $80 \text{ }^\circ\text{C}$ for 12 h in vacuo and cut into circular disks for use in CR-2032 coin cells. A Li metal foil was used as the reference-counter electrode with 1 M LiPF_6 in a 1:1 volumetric mixture of ethylene carbonate and diethyl carbonate as the electrolyte. The Li cells were assembled under an argon atmosphere in a glovebox using a disk of Celgard 2500 as the separator. Cyclic voltammetric analysis was performed between 0.01 and 2.5 V at a scan rate of 0.1 mV s^{-1} using a Gamry 600 potentiostat/galvanostat/ZRA. Galvanostatic discharge-charge cycling studies were carried out between 0.01 and 2.5 V versus Li/Li $^+$ at $25 \text{ }^\circ\text{C}$ using an Arbin battery cycler.

The electrochemical performance of the LIBs using the 3D Sb nanochain material as the anode is shown in Figure 7.3. Figure 7.14 (first, second, and fifth cycles) and the inset of Figure 7.3a (second cycle) show the cyclic voltammograms of the 3D Sb nanochains between 0.01 and 2.50 V at a scan rate of 0.1 mV s^{-1} with respect to Li metal used as reference and counter electrodes. During the first cycle of the

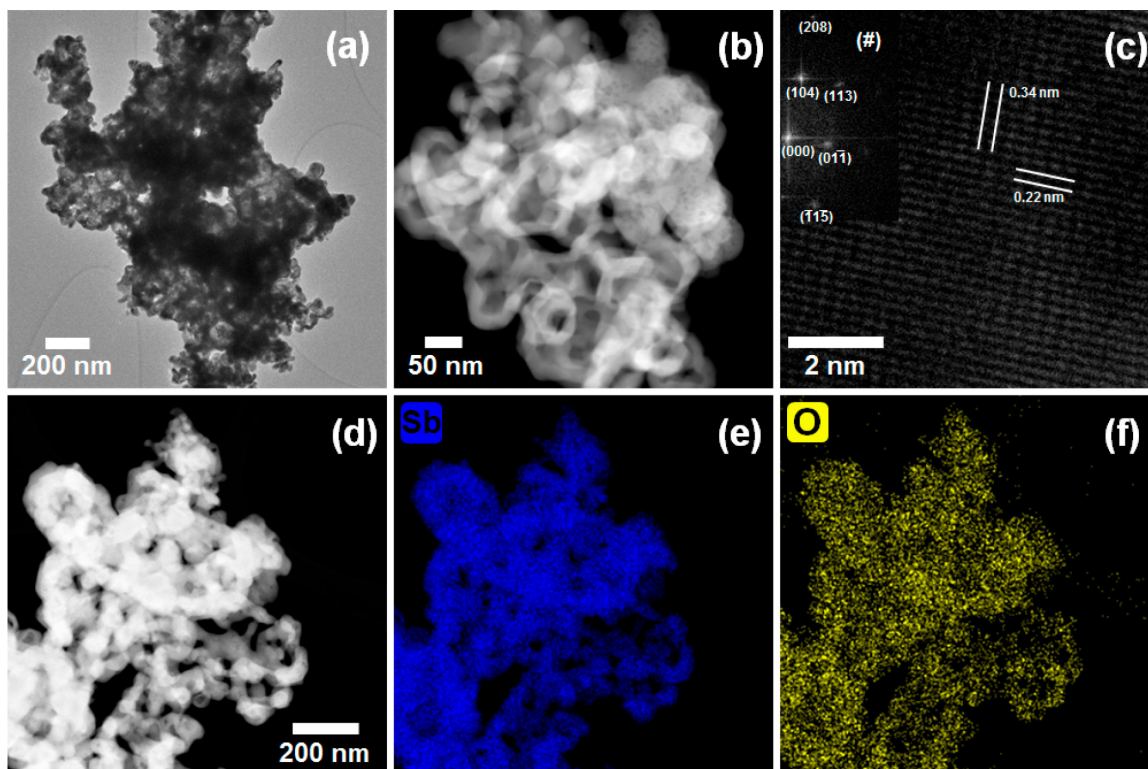


Figure 7.2. Micrographs of the Sb nanochains: (a) conventional TEM image displaying the connected Sb nanochain structure; (b) HAADF-STEM image showing the hollow structure of the Sb nanochains; (c) FFT bandpass-filtered HRTEM image displaying the crystal lattice of Sb with the corresponding FFT inset (#) relating to the $[4\bar{1}1]$ Sb zone axis; (d–f) STEM–EDS elemental maps with (d) a reference HAADF-STEM image with (e) the Sb elemental map in blue and (f) the O elemental map in yellow revealing an O impurity phase.

negative scan (Figure 7.14), irreversible broad peaks were obtained at ~ 1.53 , 1.17, 0.63, and 0.35 V versus Li/Li⁺, which are related to solid electrolyte interphase (SEI) film formation and the lithiation process. The cathodic reversible peak at 0.82 V is related to lithiation reactions: (i) $Sb_2O_3 + Li \rightarrow Sb + Li_2O$ and (ii) from crystalline Sb to Li₃Sb. [343, 362, 363] The corresponding first cycle anodic peak at 1.14 V (vs Li/Li⁺), related to the delithiation reaction, [343, 362, 363] overlaps with the subsequent CV curves, as shown in the inset of Figures 7.3a and 7.14. This shows

a reversible electrochemical redox reaction, displaying a stable performance as the Li-ion host anode material. Another anodic peak (Figure 7.14) at 1.37 V versus Li/Li⁺ corresponds to the reaction $Li_2O + Sb \rightarrow Sb_2O_3 + Li$. [363]

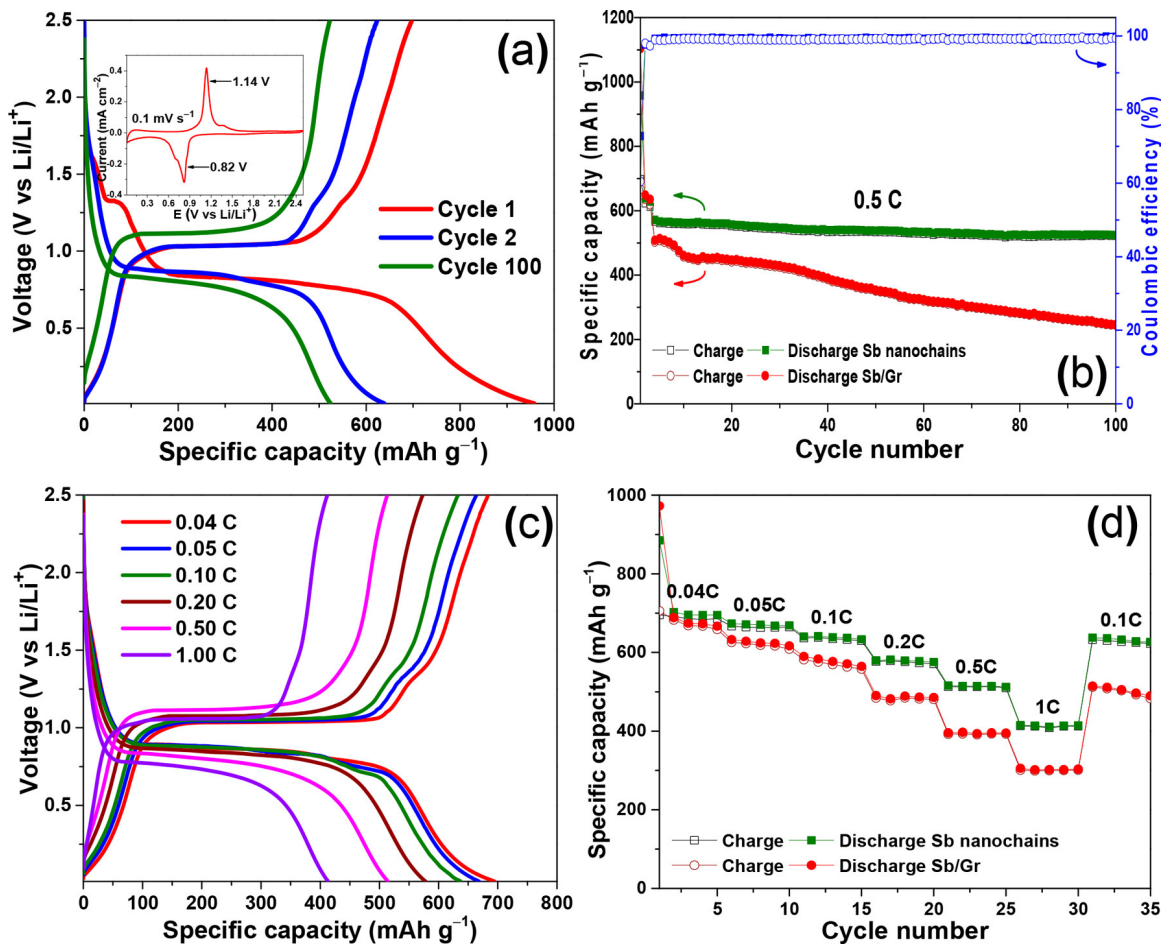


Figure 7.3. Electrochemical performance of Li-ion cells fabricated using a 3D Sb nanochain anode material: (a) voltage versus (dis)charge capacity profiles (the inset corresponds to the cyclic voltammetric analysis acquired between 0.01 and 2.5 V versus Li/Li⁺ at 0.1 mV s⁻¹); (b) capacity versus cycling performance for 100 cycles at 0.5 C, with a comparison between Sb nanochains and Sb supported on graphene; (c) rate capability studies of voltage versus (dis)charge capacity profiles; (d) comparison of the rate capability between Sb nanochains and Sb supported on graphene.

The galvanostatic cycling performance and rate capability studies of the 3D Sb nanochains were carried out between 0.01 and 2.5 V versus Li/Li⁺ at 25 °C, where all of the capacities were calculated based on the mass of Sb. The charge–discharge profiles of 3D Sb nanochains for the 1st, 2nd and 100th cycles show the typical plateau associated with the lithiation and delithiation processes and are depicted in Figure 7.3a. The Sb nanochain delivers an initial specific discharge capacity of ~ 956 mAh g⁻¹ at 0.05 C that is higher than its theoretical specific capacity (660 mAh g⁻¹) because of SEI layer formation during the first discharge cycle of the anodic electrode. This is in line with the first discharge cycle of the cyclic voltammetric analysis (inset of Figures 7.3a and 7.14). After the first cycle, the interconnected Sb nanoparticles show a stable and high specific charge capacity of ~ 523 mAh g⁻¹ at a *C* rate of 0.5 C, with a Coulombic efficiency of $\sim 99.8\%$, and an excellent cycle retention of $\sim 92\%$ after 100 cycles (Figure 7.3b). A recent publication utilizing Sb nanosheets as the anode material achieved a slightly higher specific charge capacity of ~ 584 mAh g⁻¹ at a *C* rate of 0.5 C. [348] The obtained higher specific discharge–charge capacity of the 3D Sb nanochains and the reported nanosheets could be attributed to the presence of voids, cavities, or pores that accommodate the continuous volumetric changes resulting from the lithiation and delithiation processes (Figure 7.15). Traces of Sb₂O₃ also might contribute with a certain capacity (~ 70 mAh g⁻¹) via a reversible conversion reaction of Sb₂O₃ and Li that occurs from ~ 1.5 to 0.9 V versus Li/Li⁺. [343,362,363] In contrast, Sb nanoparticles (80 wt %) supported on multilayer graphene (Sb/Gr; Figure 7.16) deliver a capacity of 236 mAh g⁻¹ at a *C* rate of 0.5 C, with a Coulombic efficiency of $\sim 98\%$, and lose more than 50% of their capacity after 100 cycles.

The rate performance of the 3D Sb nanochains was also investigated at various *C* rates, as shown in Figure 7.3c,d. These materials deliver a reversible specific discharge with capacities of ~ 762 , 705, 673, 611, 542, and 430 mAh g⁻¹, recover to 665 mAh g⁻¹ at *C* rates of 0.04, 0.05, 0.1, 0.25, 0.5, and 1 C, respectively, and then fall back to 0.05 C. These capacities are higher than that delivered by Sb/Gr under similar experimental condition (Figure 7.3d).

Figure 7.17 presents the Nyquist plots of fresh and cycled Sb nanochains and Sb/Gr anodes, wherein the cycled Sb nanochains show a stable electrode/electrolyte interface layer formation and its charge-transfer resistance does not change dramatically from 2 to 100 (dis)charge cycles. In contrast, the Sb/Gr anode shows a continuous increase of its charge-transfer resistance, which indicates a constant growth of the SEI layer during cycling. The enhanced cycling performance and rate capability of the 3D Sb nanochains could be associated with their porous structure, which aids in the prevention of nanoparticle pulverization, resulting in the maintenance of a good electric contact between the Sb nanoparticles in the electrode. As a result, a high capacity retention is achieved by abating volume expansion during Li cycling.

7.4 Conclusions

In conclusion, we have reported the preparation of novel 3D Sb nanochains by AB reduction of SbCl_3 in water. This nanoarchitecture offers considerable voids, providing sufficient space to accommodate the large volumetric changes of Sb during the discharge and charge cycles of the LIBs. The fabricated 3D Sb nanochain anode delivers a specific charge capacity of about 523 mAh g^{-1} at a C rate of 0.5 C, with a high Coulombic efficiency of $>99\%$ and a capacity retention of $\sim 92\%$ after 100 cycles. The cycling studies of the 3D Sb nanochains anode have also been extended to high C -rate capability, delivering $\sim 430 \text{ mAh g}^{-1}$ at a C rate of 1.0 C.

7.5 Supporting Information

7.5.1 Synthesis and NMR Characterization

7.5.1.1 General Information

^{11}B and ^1H NMR spectra were recorded at room temperature, on a Varian INOVA 300 MHz NMR spectrophotometer. Chemical shifts (δ values) are reported in parts per million relative to $\text{BF}_3 \cdot \text{Et}_2\text{O}$ for ^{11}B NMR respectively. Data are reported as: δ value, multiplicity (s=singlet, d=doublet, t=triplet, q=quartet, p=pentet, h=hextet,

m=multiplet, br=broad) and integration. All solvents for routine isolation of products were reagent-grade. Sodium borohydride (powder, purity >99% by hydride estimation [364]) was purchased in bulk from Dow Chemical Co. (Rohm and Haas). Ammonium sulfate (ACS reagent >99.0%, Fisher Chemical), was powdered prior to use. Tetrahydrofuran (THF, ACS reagent >99.0% containing 0.004% water and 0.025% BHT) was purchased from Sigma-Aldrich. Antimony (III) chloride (Crystalline ACS reagent >99.0%, Alfa Aesar), antimony (III) fluoride (Crystalline ACS reagent >99.8%, Alfa Aesar), polyvinyl alcohol (PVA) 13-23k (ACS reagent 86-89% hydrolyzed, Alfa Aesar), methanol (Anhydrous, Macron), tri-n-octylphosphine (97%, Sigma-Aldrich), oleylamine (98%, Sigma-Aldrich), acetone (ACS reagent >99.0%, Mallinckrodt Chemicals) were purchased from the respective commercial sources and used without further purification. Piperidine borane and triethylamine borane were prepared in accordance with literature reports, and methylamine borane was prepared from the hydrochloride salt of methylamine [365].

7.5.1.2 Procedure for the Preparation of Ammonia-Borane [366]

Sodium borohydride (SBH) (18.91 g, 0.5 mol, 1 eq.) and powdered ammonia sulfate (66.07 g, 0.5 mol, 1 eq.) were transferred to a dry 2 L round bottom flask containing a large magnetic stir bar. The flask was then cooled in an ice-water bath followed by the addition of 495 mL of reagent-grade tetrahydrofuran. With vigorous stirring 4.5 mL of water was then added dropwise over a period of 5 minutes to limit frothing. Once all water is added the flask is moved to room temperature and stirred vigorously. The reaction is monitored using ^{11}B NMR until completion (~5 h) as judged by the absence of sodium borohydride peaks in the ^{11}B NMR. (Prior to running the ^{11}B NMR experiments, a drop of dimethyl sulfoxide is added to the aliquot to solubilize any sodium borohydride present.) Once complete, the reaction mixture is filtered through celite and the filter cake thoroughly rinsed with tetrahydrofuran. The solvents were removed from the combined filtrates via rotary

evaporation, followed by drying *in vacuo* for 12 h to obtain ammonia borane (AB) as a white solid. A hydride analysis [364] revealed this to be >98% chemically pure.

7.5.1.3 ^{11}B NMR Spectroscopic Monitoring of Ammonia-Borane Synthesis

(See Figure 7.4)

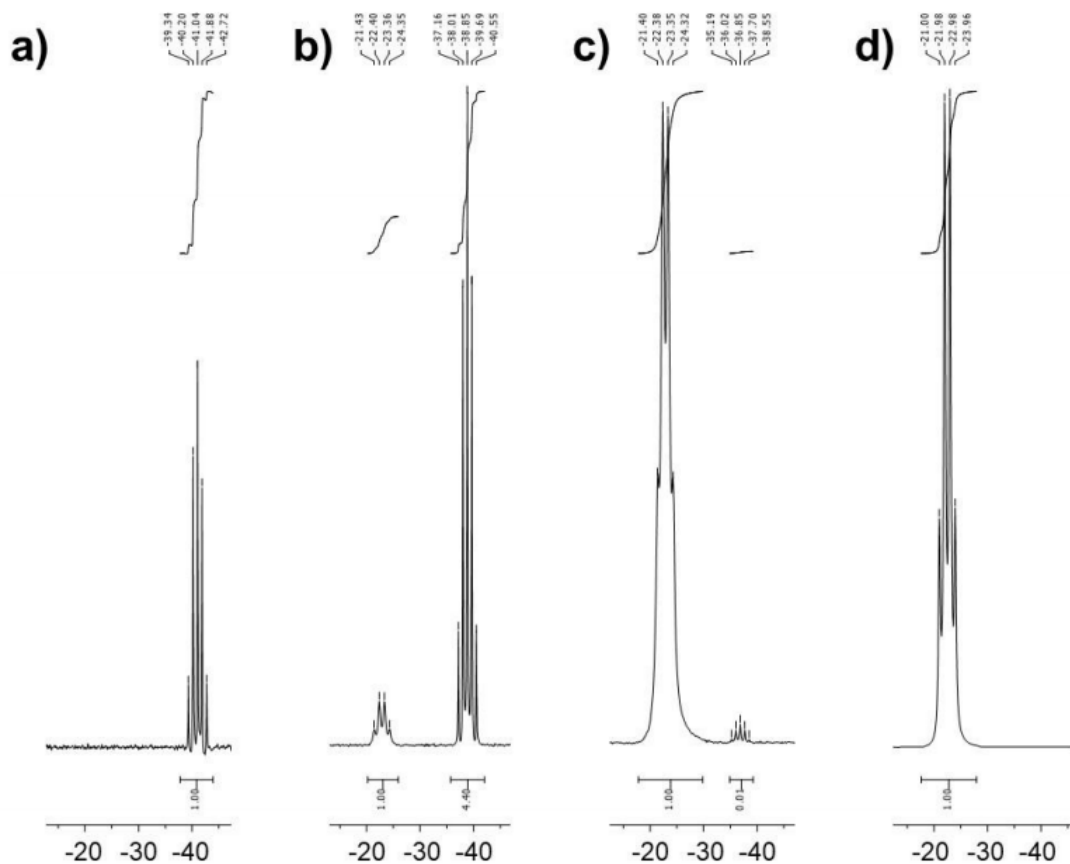


Figure 7.4. ^{11}B NMR spectrum of the progress of ammonia-borane synthesis: (a) prior to water addition (SBH: AB, 1:0); (b) 15 min. after addition of water (SBH: AB, 4.4:1.0); (c) 4 h after addition of water (SBH: AB, 0.01:1.00); and (d) 5 h after addition of water (SBH: AB, 0:1).

7.5.1.4 Characterization of Ammonia-Borane

^1H NMR (300 MHz, Tetrahydrofuran-*d*8) δ 4.26 – 3.69 (m, 3H, NH_3), 2.08 – 0.74 (m, 3H, BH_3) (see Figure 7.5)

^{11}B NMR (96 MHz, Tetrahydrofuran-*d*8) δ -22.04 (q, $J = 95.6$ Hz) (see Figure 7.6)

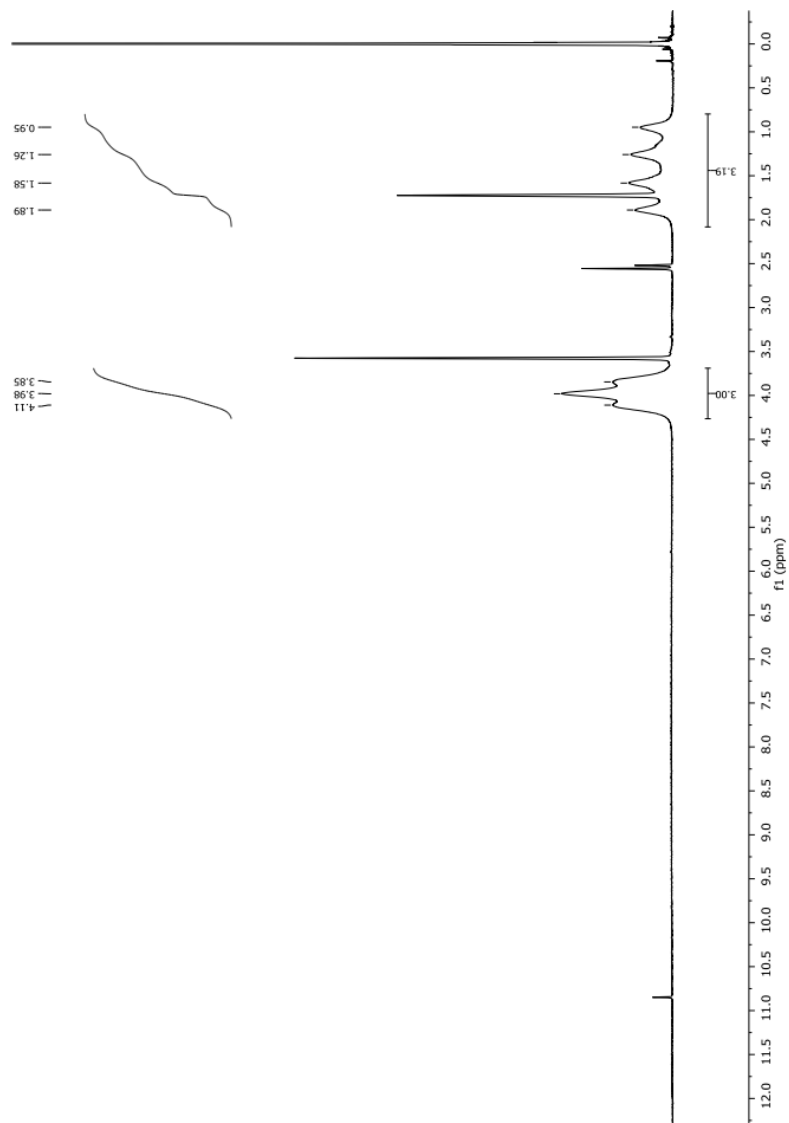


Figure 7.5. ^1H NMR (300 MHz, Tetrahydrofuran- d_8) Ammonia- d_8

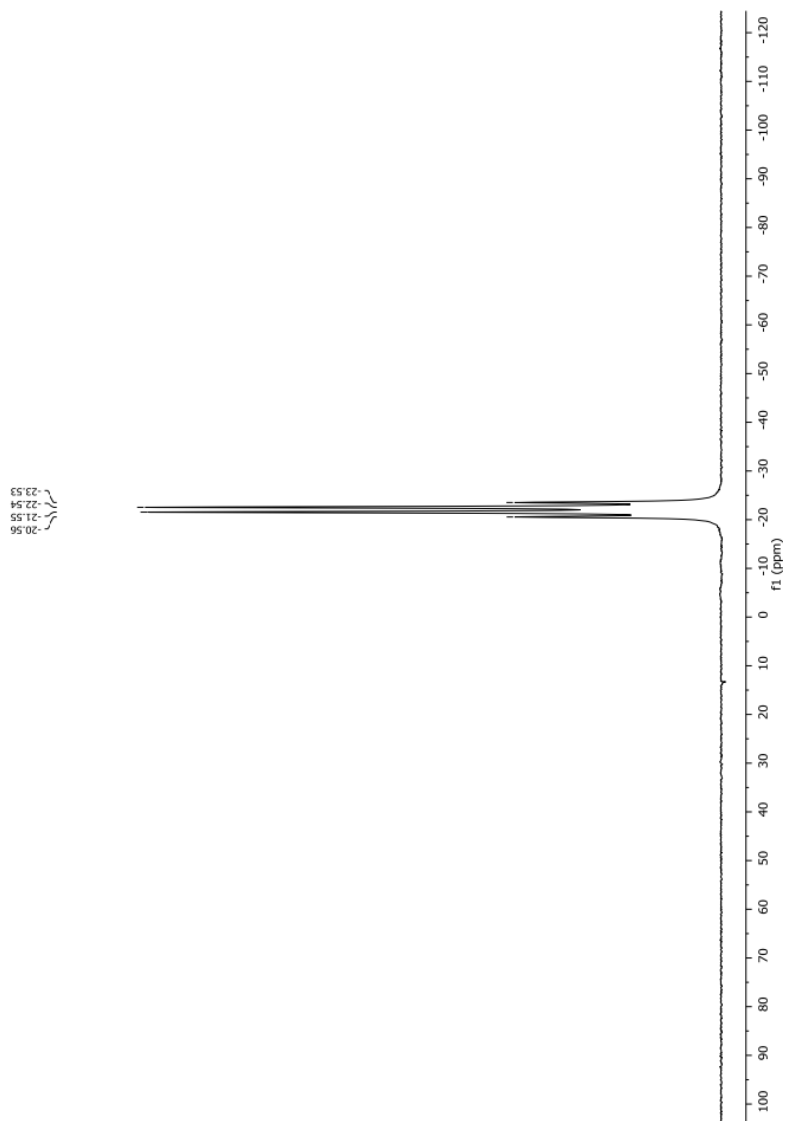


Figure 7.6. ^{11}B NMR (96 MHz, Tetrahydrofuran- d_8) Ammonia-borane

7.5.1.5 Procedure for the Preparation of Antimony Nanoparticles and Nanochains [367]

Antimony trichloride (0.080 g, 0.35 mmol, 1 eq.) or antimony salt (0.35 mmol, 1 eq.) was dissolved in 10 mL of deionized water in a 50 mL round bottom flask. Ammonia-borane (0.054 g, 1.75 mmol, 5 equiv.) or reducing agent (1.75 mmol, 5 equiv.) was dissolved in 10 mL of deionized water in a 25 mL round bottom flask. The metal salt/water solution was then quickly added to the ammonia borane/water solution. The flask was then sealed with a rubber septum and kept under nitrogen and stirred at room temperature for 2 h, followed by the addition of 10 mL methanol. The resultant solution was centrifuged, and the supernatant was decanted. The nanoparticles were then dispersed in tri-*n*-octylphosphine (6.0 mL, 13.5 mmol) and carefully added to a flask containing oleylamine (6.0 g, 50.0 mmol) or other capping agent (for PVA 6.0 g with 10 mL water) kept at 230 °C and stirred for 2 h, after which the reaction was cooled to room temperature, followed by the immediate addition of 10 mL of methanol. The resultant solution was then centrifuged and the supernatant decanted. When using PVA as a capping agent, the solution obtained after methanol addition was added to 100 mL of dichloromethane prior to centrifugation. The nanoparticles were resuspended in acetone. The centrifugation, decantation, and resuspension were repeated twice more and the nanoparticle/acetone solution was transferred to a 20 mL vial and sealed.

7.5.2 Discussion of Antimony Nanoparticles Synthesis via Ammonia Borane Reduction

Our synthesis of antimony nanochains, based on the procedure developed by Revaprasadu and co-workers for the synthesis of alkylamine capped antimony nanoparticles, was modified by the use of ammonia-borane as a reducing agent instead of sodium borohydride. The first stage involves the reduction of antimony trichloride using ammonia-borane, and in the second stage the nanoparticle growth and capping takes place. It has been previously observed [367,368] that antimony trichloride

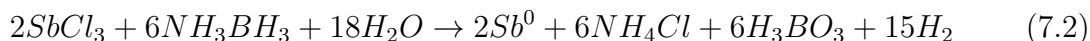
reduced using sodium borohydride can produce nanoparticles in the same diameter range as produced by the ammonia-borane reduction (10-20 nm). They have also been observed to undergo some self-assembly to higher order nanostructures, particularly when using alkylamine or other capping agents and hot-injection methods. However, the NPs produced with SBH do not form nanoarchitecture to the same extent that was produced when using ammonia-borane as a reducing agent (Figure 7.10e). It is postulated that the more extensive 3-dimensional nanochain architecture is critical for the results observed during our electrochemical study.

Some mechanistic information for the methods involving NaBH_4 reduction [367, 368], sodium hydride reduction [369], and metal amide reduction [370], has been proposed. The cation of the reducing agent forms a salt with the anion of the metal salt. This happens with a concurrent release of hydrogen gas, the formation of the neutral metal, and usually the production of a secondary byproduct containing the cation of the reducing agent.

Ammonia-borane, a compound with a dative bond between the borane and ammonia moieties, does not contain any ‘cationic’ species and is expected to undergo a related, but altered mechanism. When antimony trichloride dissolves in water it can be hydrolyzed to form antimony oxychloride and hydrogen chloride as shown in equation 7.1 below [371]. It was observed during our synthesis that the pH of the water dramatically decreased after the dissolution of the antimony trichloride (to approximately 1 from 5).



Upon combination of the antimony trichloride solution and ammonia-borane solution, there was a vigorous release of hydrogen and an immediate darkening of the mixture, indicative of the reduction of the metal salt. It is assumed that the overall reaction proceeds as in equation 7.2.



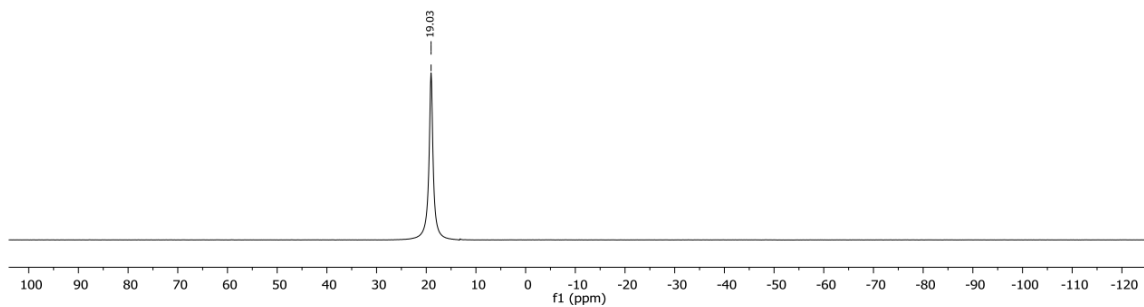


Figure 7.7. Reaction Solution, prior to the addition of methanol. ^{11}B NMR (96 MHz, water) δ 19.03. (s).

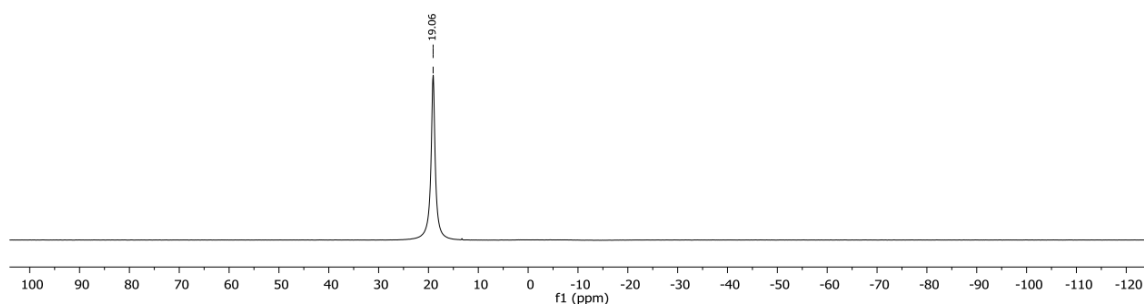


Figure 7.8. ^{11}B NMR of boric acid (96 MHz, water) δ 19.06. (s).

The hydrogen chloride produced through antimony trichloride hydrolysis is presumed to be involved in two processes, (i) having a role in the formation of the ammonium chloride byproduct by capture of the ammonia released from ammonia borane and (ii) as a driving force for the formation of boric acid, which is the only boron species observed in the reaction mixture prior to the addition of methanol (Figure 7.7). The ^{11}B NMR spectra matches almost exactly with a commercial sample of boric acid (Figure 7.8). Previous work by the Ramachandran group has also shown that in the presence of RuCl_3 that ammonia borane is dehydrogenated to produce ammonium tetraborate, [372] a compound which forms boric acid in the presence of HCl.

Once the water soluble byproducts are removed through centrifugation and water decantation, the reduced antimony is suspended in tri-n-octylphosphine (TOP) and injected into hot (230 °C) oleylamine (OA). The TOP/OA combination acts as a co-surfactants and capping agents, providing an environment which has been shown to be conducive to more controlled and stable nanoparticle growth [367,373]. The overall schematic for this stage of the nanoparticle synthesis is described in equation 7.3.



7.5.3 Effect of the Sb Salt, Reducing and Capping Agents on the Architecture of Sb Nanoparticles

(See Figure 7.9 and Figure 7.10)

7.5.3.1 Analysis of the Effect of the Sb salt, Reducing and Capping Agents on the Nanoarchitecture

In reference to Figure 7.9 and Figure 7.10: (a) The nanochain architecture is shown nicely in the TEM micrograph and the nanoparticles appear to be uniform. HAADF shows noticeable lower Z, potentially from a surface layer of carbon. Overall the material appears to be composed of single crystals, not polycrystalline. (b) The nanochain architecture is apparent here as well, but the size distribution appears to be more bimodal, with both smaller and larger chains being visible. Numerous hollow pockets or pores can be seen, and overall the bulk material looks to be composed of single crystals with a few regions of polycrystallinity and sharp surface facets. (c) Again, nanochains are apparent, and display a bimodal distribution, but there is a smaller disparity between the two general size categories. A less HAADF intense surface layer is also present, most likely a carbon surface layer. Visible pockets are smaller and less numerous than the previous materials. While low polycrystallinity is again present, with even the corners and turns of the nanochain being within the same zone axis, some small crystals do appear on the surface of the material. (d)

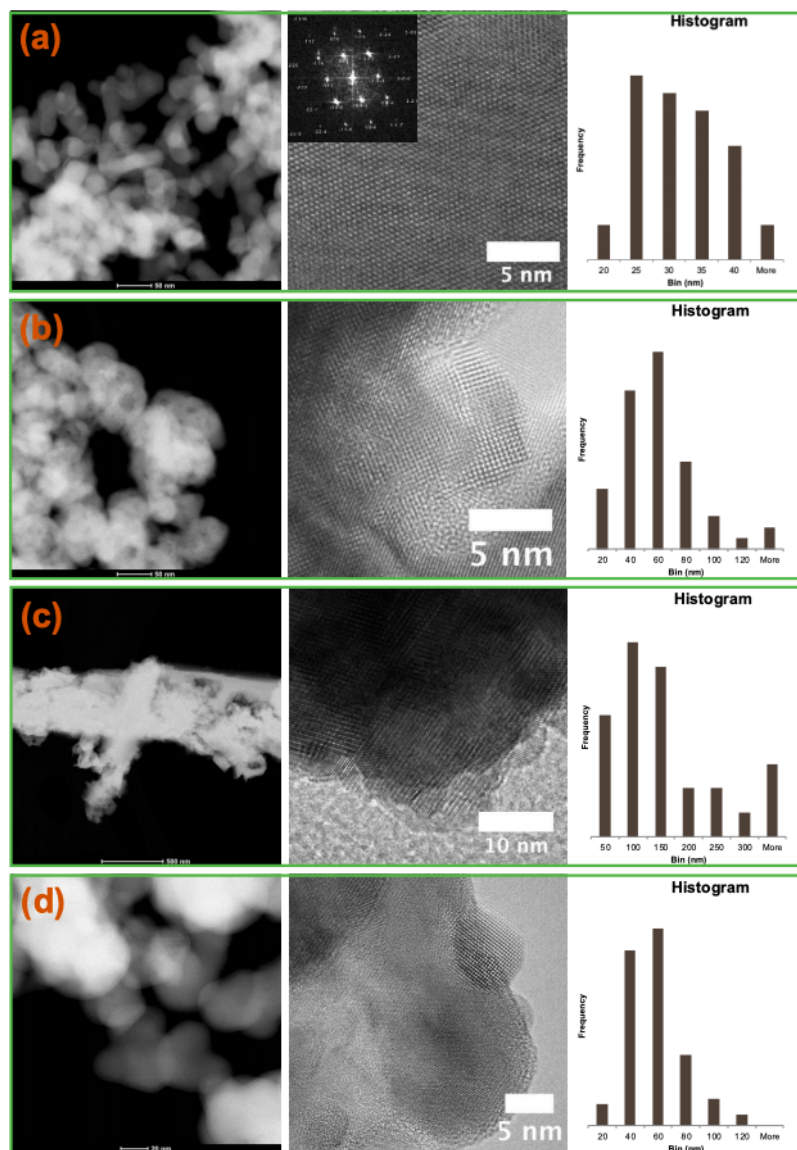


Figure 7.9. TEM analysis of antimony nanoparticles synthesized using; antimony salt, reducing agent, capping agent: (a) SbCl_3 , ammonia borane, oleylamine; (b) SbCl_3 , methylamine borane, oleylamine; (c) SbCl_3 , triethylamine borane, oleylamine; (d) SbCl_3 , piperidine borane, oleylamine

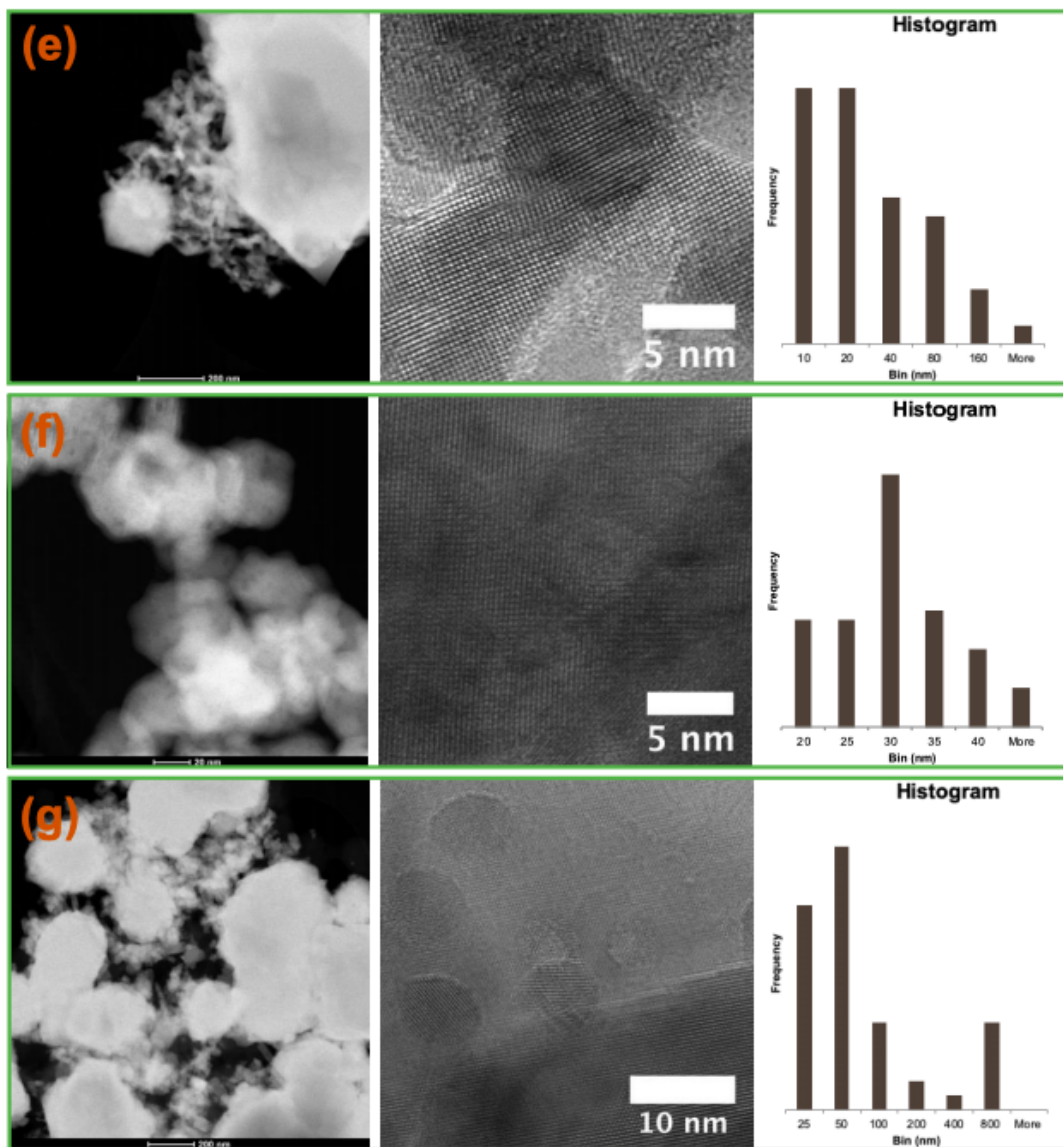


Figure 7.10. Continued from Figure 7.9: (e) SbCl₃, sodium borohydride, oleylamine; (f) SbF₃, ammonia borane, oleylamine; (g) ammonia borane, SbCl₃, PVA.

The bulk of the volume of this material is presented as large crystals, with only as estimated 20% showing nanochain-like structure. What nanochains are presents are nonuniform in size and appear to have grown on the large crystals. (e) A uniform nanochain is present in this material, and it seems to be clusters of spherical particles with narrow bridges between them. Pockets of varying sizes are again visible, and while small amounts of polycrystallinity appear near the pockets the material looks crystalline overall. A surface layer is again visible, likely an amorphous carbon layer. (f) No nanochain are apparent in this material, only what appear to be agglomerates of massive crystals with small crystals creating a rough surface layer. (g) Large, uniform crystals are present in this material, with a highly polycrystalline surface layer.

7.5.4 Structural Characterization

7.5.4.1 Powder XRD, Raman, and EDS Spectrographic Crystallinity and Compositional Analysis

The crystalline structure of antimony nanochains were examined using powder X-ray diffraction (XRD) technique equipped with Rigaku diffractometer. Subsequently, the Raman spectroscopic measurement was carried out for structural analysis using a LASER Raman spectrometer. (See Figure 7.11)

7.5.4.2 Transmission Electron Microscope Images

The morphology and 3D antimony nanochains were examined using scanning electron microscopy (JEOL NeoScope JCM6000 Benchtop, SEM) and transmission electron microscopy (TEM) at 300 kV on a FEI Titan ETEM 80-300 with fast Fourier transform (FFT) analysis to further confirm the crystallographic orientation of antimony nanochains under its simulated diffraction patterns obtained by the CrysTBox software. (See Figure 7.12)

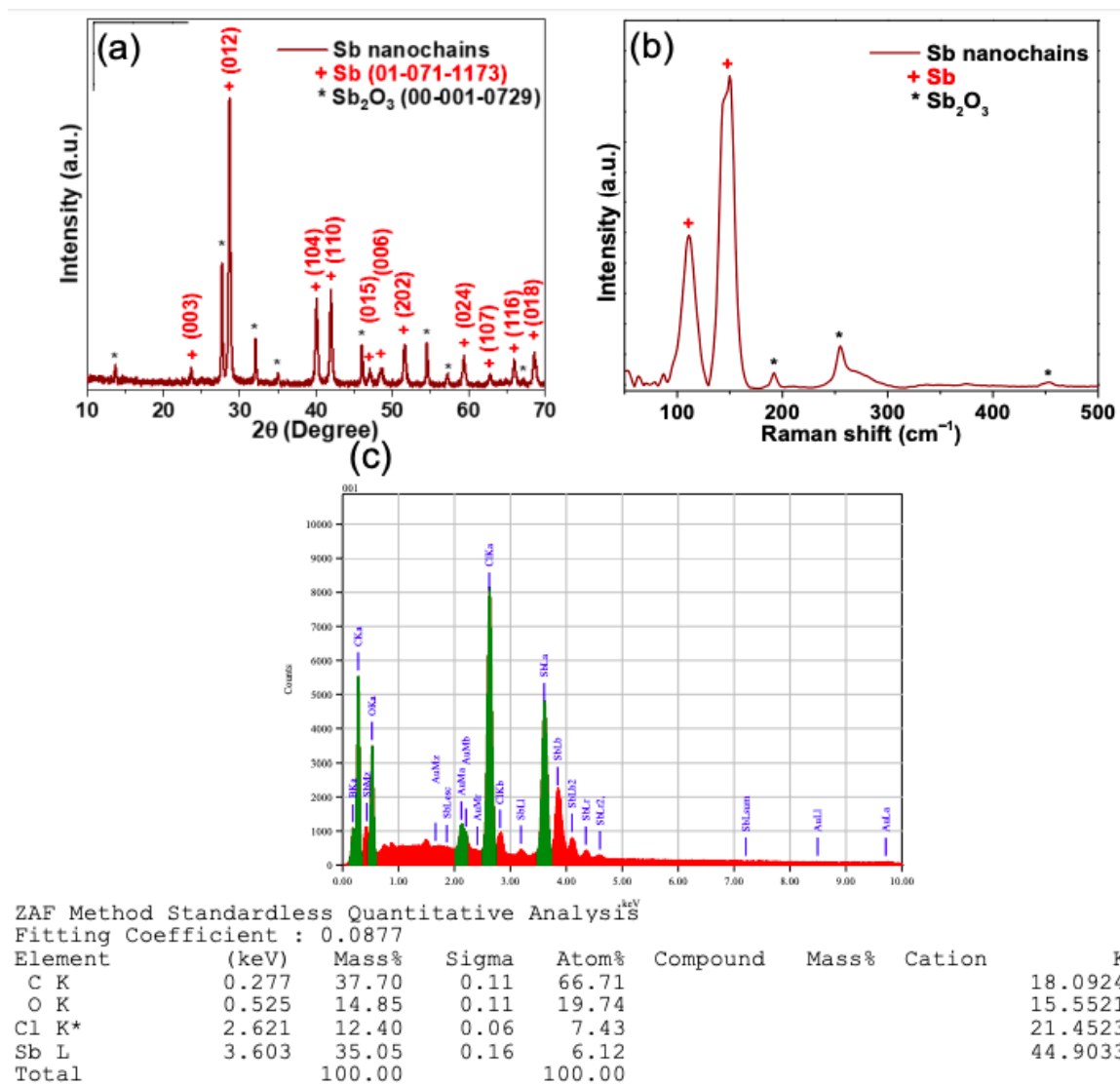


Figure 7.11. The crystalline structure and composition of 3D antimony-nanochains investigated using (a) powder X-ray diffraction, (b) Raman spectroscopic measurements, and (c) energy dispersive X-ray spectroscopy.

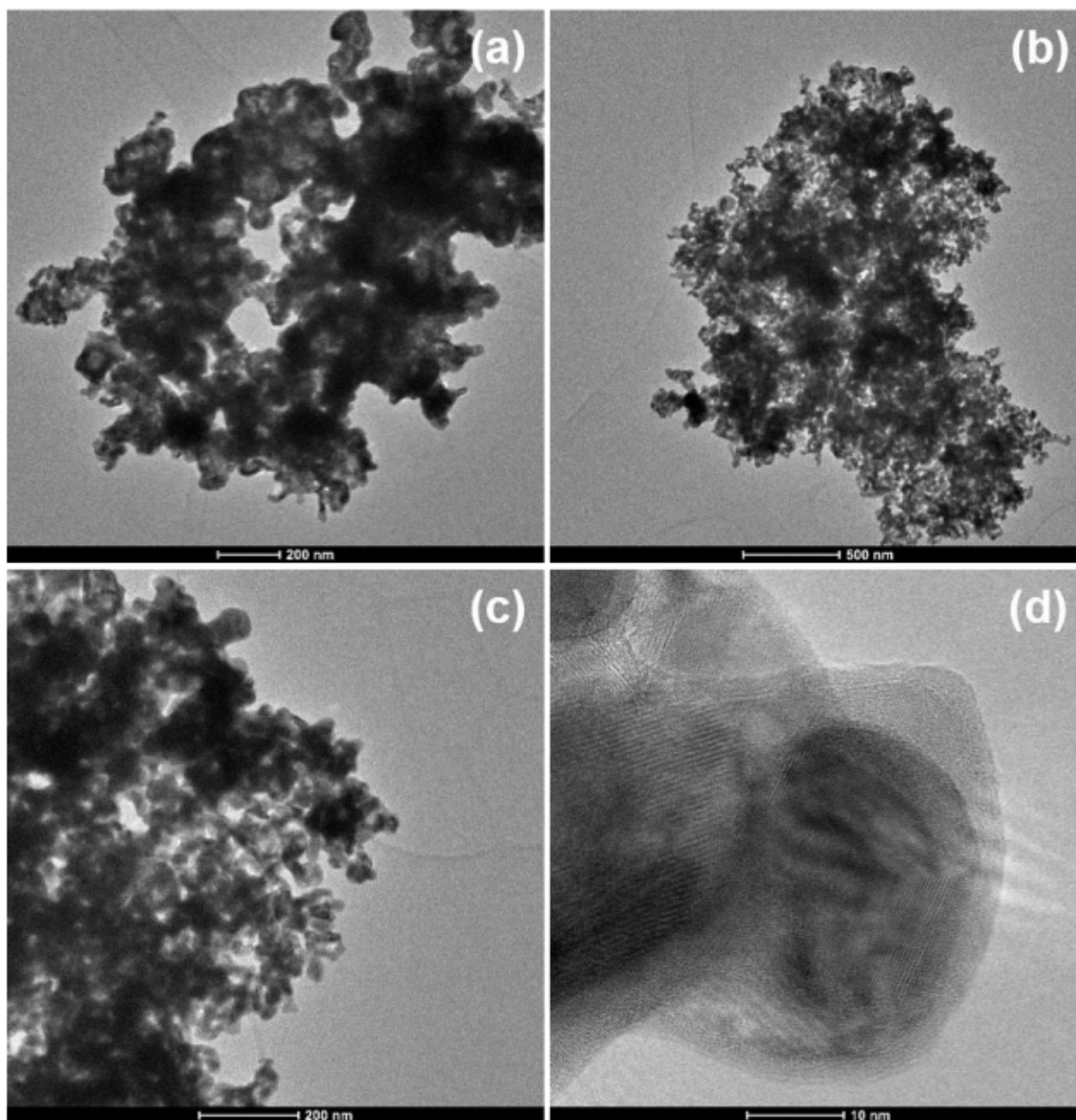


Figure 7.12. Homogeneous morphological investigation of 3D antimony nanochains (a), (b), (c) and crystallinity (d) examined using transmission electron microscopic technique.

7.5.4.3 High Resolution Transmission Electron Microscope Images

(See Figure 7.13)

7.5.5 Electrochemical Studies

7.5.5.1 Cyclic Voltammetric Analysis

(See Figure 7.14)

7.5.5.2 Li-ion Insertion into and Extraction from Antimony Nanochains

TEM images of the antimony nanochains demonstrate that the interconnected nano-architecture remains after (de)lithiation process (Figure 7.15 below). (a) shows the nanochains prior to lithiation, (b) is while the nanochains are lithiated, and (c) is after delithiation. (a) Large nanochains are visible in this material with some larger crystals also present, and large pockets appear throughout. There are also some parts of the structure which have the appearance of nanochains, but with less intensity than the crystal, possibly the results of antimony leaching into the larger crystals, leaving a less dense structure. (b) This material appears to be mixture of larger crystals and nanochains, and close-up the nanochains show a ‘fuzzy’, possibly polycrystalline, structure which looks like agglomerated crystals. A low-Z material is covering the particles, most probably binder added during the assembly of the battery cell. (c) The same low-Z material is present, again mostly likely binder present from the battery assembly process. The material also possesses many structures with a hollow appearance, with pockets that are larger and more exaggerated than previous samples. The material has a rougher appearance overall compared to the charged material, but with the same external ‘fuzzy’, polycrystalline appearance. It is noteworthy that the average particle size shifts towards lower values while going from lithiated to delithiated state. This indicates that the cycling process allows the existence of small nanoparticles within the electrode. Filling the pores of the

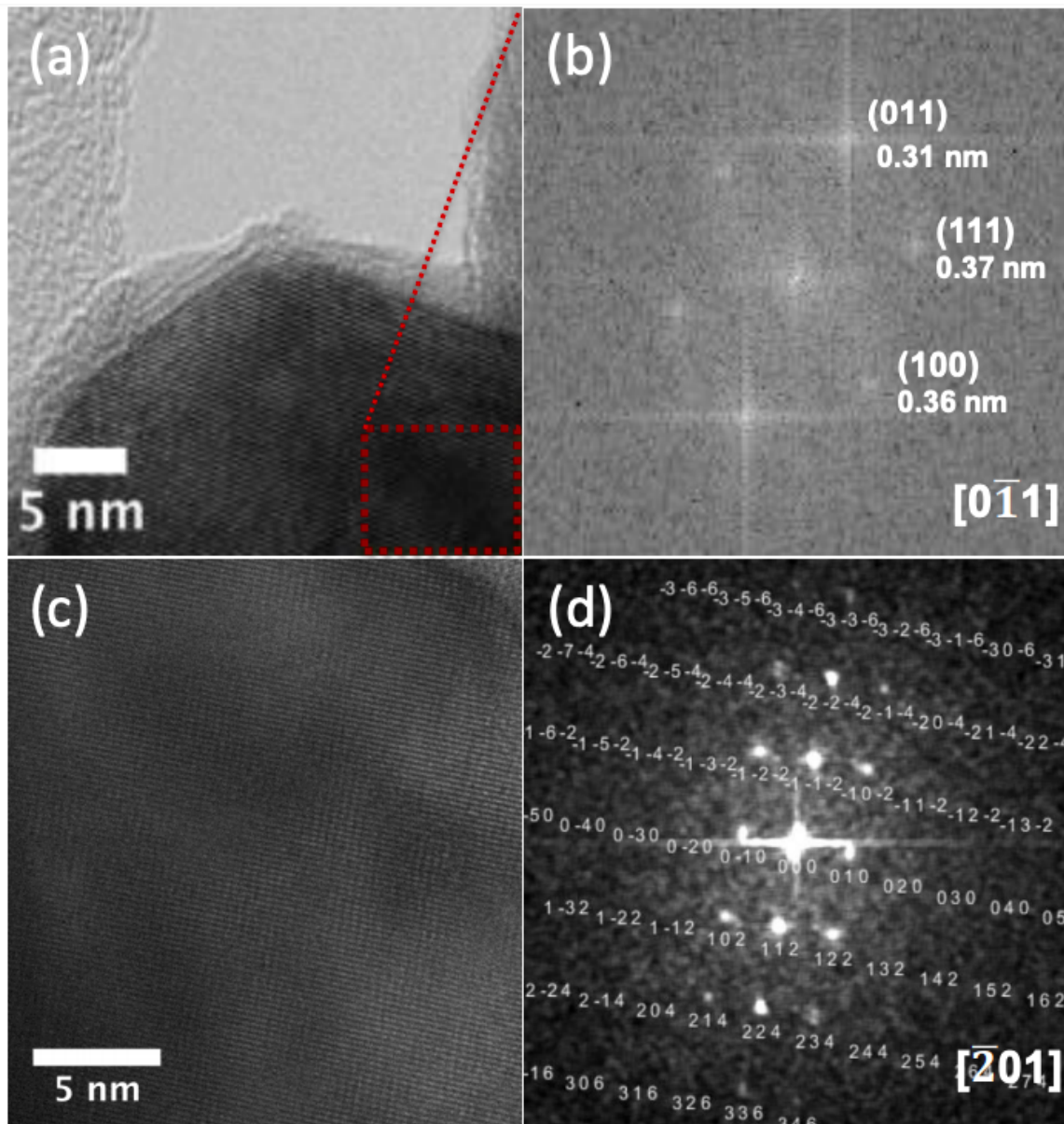


Figure 7.13. High resolution transmission electron microscope image displays (a) & (c) the lattice fringes of crystalline antimony and (b) & (d) the corresponding fast Fourier transform of 3D antimony nanochains of the characteristic zone axes $[0\bar{1}1]$ & $[\bar{4}11]$ of the rhombohedral antimony phase, respectively.

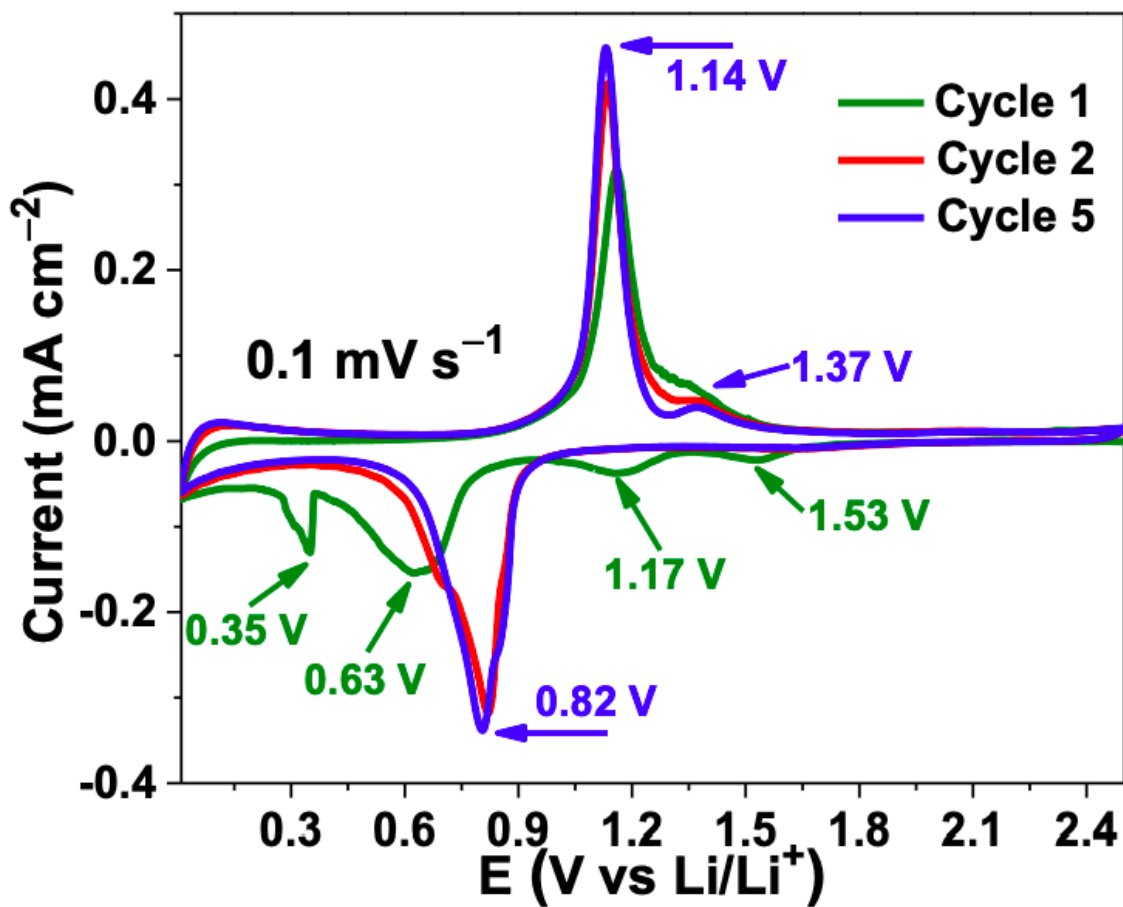


Figure 7.14. Cyclic voltammetric analysis of the 3D antimony nanochains anode material between 0.01 – 2.5 V at 0.1 mV s^{-1} using 1 M LiPF_6 in ethylene carbonate (EC) and diethyl carbonate (DEC) in the volume ratio of 1:1 as electrolyte and CelgardTM 2500 separator.

antimony nanochains with Carbon Super P, which is present in the electrode, could act to stabilize the architecture of the active material.

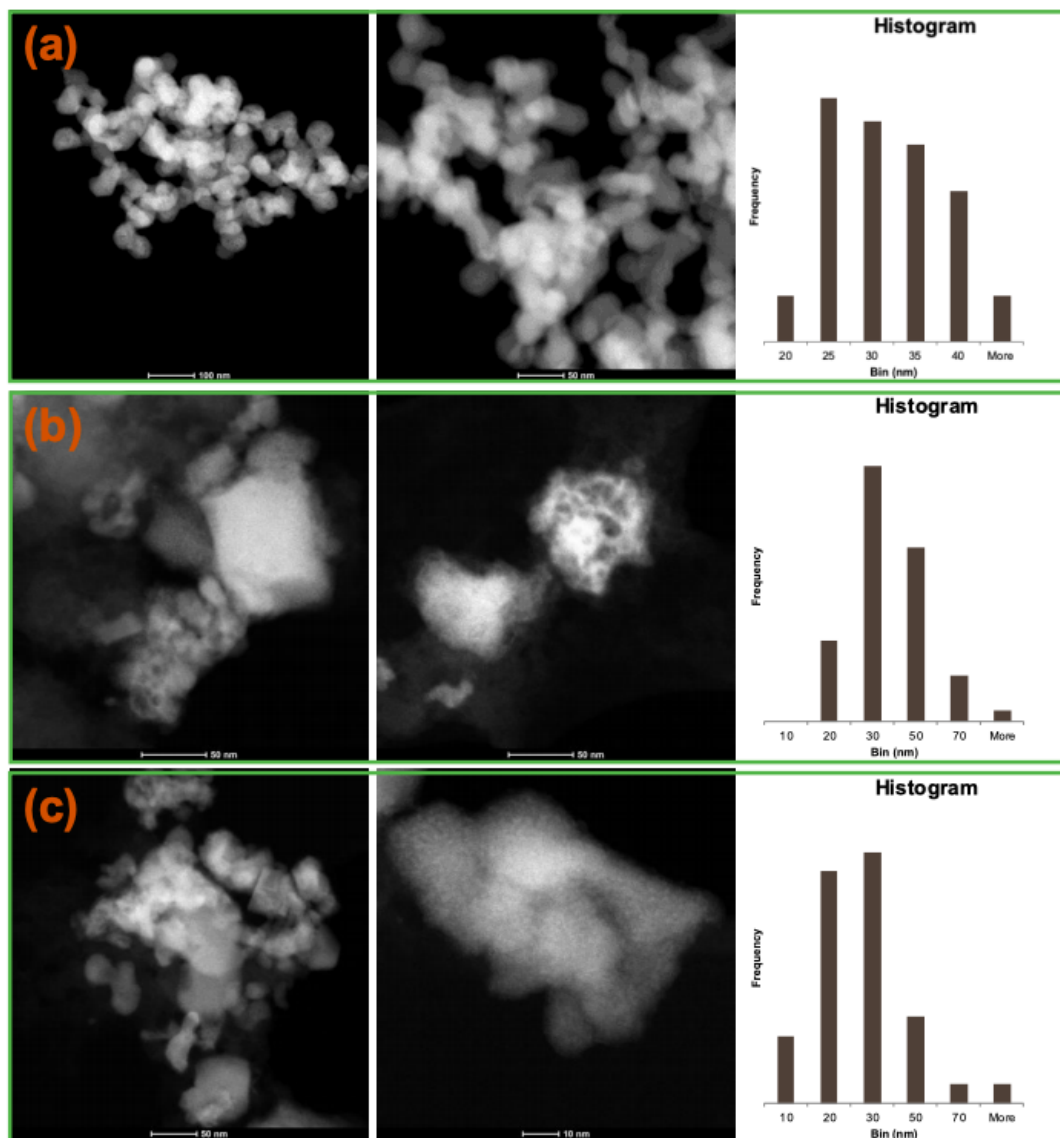


Figure 7.15. TEM analysis of (a) pristine, (b) lithiated and (c) delithiated antimony nanochains.

7.5.5.3 Preparation and Physical/Chemical Characterization of Graphene Supported Antimony

Antimony nanoparticles supported on graphene nanosheets were prepared via impregnation of graphene with antimony acetate solution. Using an antimony:graphene weight ratio of 9, graphene (0.2 grams) and antimony acetate (1.8 grams) were combined in 50 ml of acetic acid. The mixture was then heated at 80 °C overnight to remove the solvent. The resultant material was pyrolyzed at 650 °C for 2 h under inert atmosphere. After pyrolysis antimony nanoparticles supported on graphene were obtained as a dark powder. (Shown in Figure 7.16)

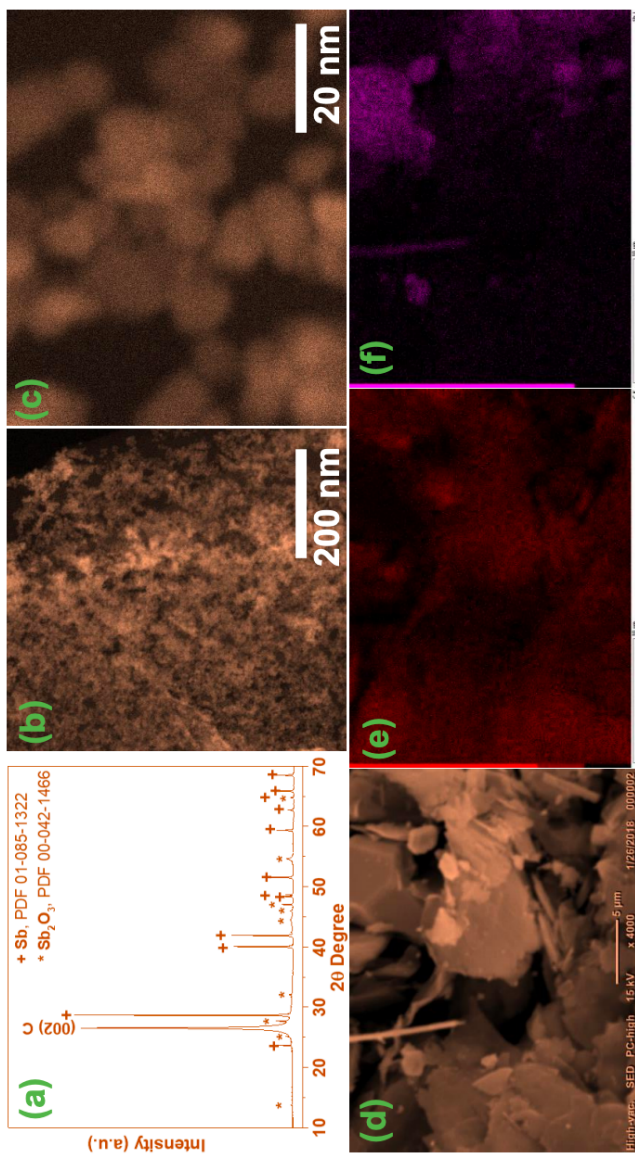


Figure 7.16. Physical and chemical characterization of Sb/Gr composite. (a) XRD pattern; (b,c) TEM micrographs; (d) SEM image; and EDX mapping of (e) carbon and (f) Sb.

7.5.5.4 Electrochemical Impedance Spectroscopic Analysis

(See Figure 7.17)

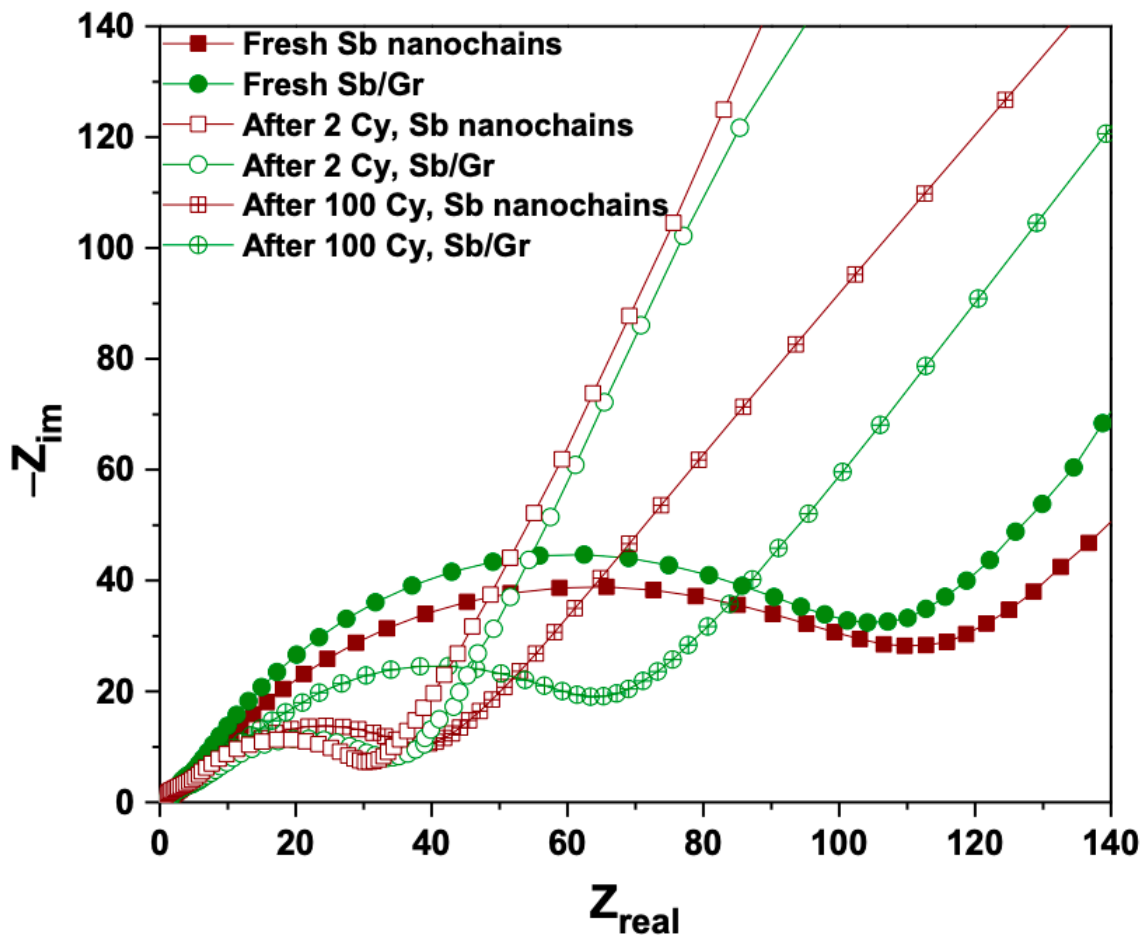


Figure 7.17. Electrochemical impedance spectroscopy information of 3D antimony nanochains and Sb/Gr before and after 2nd, 100th cycles.

8. EFFECT OF SYNTHESIS METHOD, USING VARYING TYPES OF MICROPORE LEVEL SULFUR INFILTRATION, ON ELECTROCHEMICAL PERFORMANCE IN LITHIUM-SULFUR BATTERIES

Energy Technology 2019, 7, 1900194-1900194. <https://doi.org/10.1002/ente.201900194>

Arthur Dence Dysart, Neal Amadeus Cardoza, Garrett Mitchell, Volkan Ortalan, and Vilas Ganpat Pol

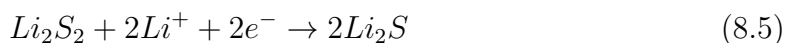
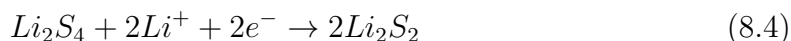
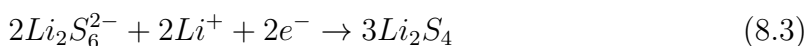
8.1 Abstract

The role of physically restrained, noncrystalline sulfur species in rechargeable lithium–sulfur batteries is examined by electrochemical and high-resolution material characterizations. Carbon–sulfur composites are created by melting and sublimation of sulfur in an isochoric reactor via the autogenic process. These noncrystalline sulfur cathodes demonstrate a high specific capacity of $\approx 1000 \text{ Ah kg}^{-1}$ after 100 cycles with a gravimetric current of 557 A kg^{-1} . Interestingly, this high-performance sulfur allotrope lacks a long-range structural order: high-resolution X-ray diffraction, performed at the Advanced Photon Source, indicates the lack of crystalline (i.e., orthorhombic or monoclinic) sulfur in the nanoscale domain. Electrochemical and material characterizations suggest that noncrystalline sulfur is a consequence of synthesis and not necessarily evidence of electrochemical efficacy. Rather, a high rate capacity depends on sulfur distribution, in turn, controlled by synthesis pathway. At higher sulfur content, the performance of carbon–sulfur composites is limited by the available surface area in which crystalline sulfur coincides with reduced gravimetric capacity and greater charge transport impedance, suggesting suboptimal sulfur containment.

8.2 Introduction

The progress of electric transportation and portable electronics necessitates better energy storage. In particular, petroleum-free electric vehicles require a gravimetric energy of $\approx 350 \text{ Wh kg}^{-1}$ [374, 375] unachieved by modern commercial batteries operating with lithium cobalt oxide and graphite electrochemistry. In response, there has been increasing interest and research upon the rechargeable lithium–sulfur battery, whose theoretical gravimetric energy of 2509 Wh kg^{-1} and practical estimate of 502 Wh kg^{-1} exceed viability requirements for electric vehicles. [374–378] Yet, after decades of research, the lithium–sulfur battery remains in the research sector due to inherent challenges of its multistage electrochemistry and inherent resistivity.

The lithium–sulfur battery operates on reversible electrochemistry between elemental sulfur and lithium. During discharge, orthorhombic crystalline sulfur S_8 reduces to soluble intermediate polysulfide species (Li_2S_n $4 < n < 8$) and insoluble dilithium sulfide Li_2S through chemical intermediates known as lithium polysulfides [379, 380] (see equations below).



These inorganic species are soluble in conventional glyme electrolytes: unrestricted polysulfide dissolution and migration are behind most of the major technical challenges facing the Li–S technology (i.e., low columbic efficiency, self-discharge, sulfur electrode dissolution, and dendrite growth). [376, 378, 380–383] In addition, the repeated dissolution and deposition of these active materials on electrode surfaces accelerate dendrite formation. Recent advances suggest that the full redox mechanism is an intricate network of elementary steps dependent on local thermodynamic properties.

With this knowledge, reported approaches to polysulfide suppression include optimized and engineered morphologies, electrolytes, binders, and separators. [382–389]

Electrode substrates produced via morphological approaches increase effective cathode conductivity and suppress polysulfide migration away from the cathode. Various morphology approaches have been demonstrated in the literature: the work of Ji et al. [390] demonstrated that the microporous carbon substrate CMK-3 effectively restrains polysulfide migration, with a high gravimetric capacity and long-term cycling performance. [391] Similarly, Li et al. demonstrated a great gravimetric capacity of $\approx 800 \text{ Ah kg}^{-1}$ using the high-temperature heating synthesis. [392] Work done by Zhang et al. [393] and Chen et al. [394] showed a stable capacity for 400–500 cycles via simple melt diffusion, due to sulfur encapsulation. Additional work done by Zhang showed that different surface level initial mixing of sulfur does not have an appreciable change on the initial performance of the cell and that more performance gain can be extracted from electrolyte control. [395] However, work done on sulfur and polysulfide deposition shows that a large portion of the conductive surface was left unoccupied, due to that the spatial homogeneity improves the electrochemical performance. [396] This leads to more performance gained via working with polysulfide mitigation via electrolyte changes.

Electrolyte control uses tailored electrolytes and additives to reduce the solubility of polysulfides to suppress the migration away from the cathode. The work of Park et al. [397] demonstrated that polysulfides were effectively suppressed using unique lithium salts with anions bis(trifluoromethanesulfonyl)amide [TFSA][−], bis(pentafluoroethanesulfonyl)amide [BETA][−], and hexafluorophosphate [PF₆][−]; however, low Li⁺ ion diffusivity in these electrolytes hinders the applications of these electrolytes. The addition of Li⁺ salts mitigates the low diffusivity issue, as demonstrated by Tachikawa et al. [398] Solid electrolytes improved safety and ionic conductivity, showing that the nanosized lithium sulfide allows increased ionic conductivity. [399]

This work implements autogenic synthesis to examine the infiltration process of creating carbon–sulfur composites. Autogenic synthesis, studied by Pol et al., [400]

enables chemical processes through thermal pressurization of isochoric reactor volumes. Typical applications of the autogenic process include the synthesis of inorganic nanoparticles (i.e., vanadium oxide [401]), amorphous carbons (polyethylene-derived carbon nanotubes [402]), and biphasic composites (i.e., silicon carbide nanospheres [403]). In this work, autogenic heating drives homogeneous distribution of sulfur throughout carbon substrate Ketjenblack EC-600JD, a high conductivity and high surface area carbon black. Autogenic carbon-sulfur composites demonstrate a great gravimetric capacity at a high gravimetric current $C/3$, values almost twice that of their mechanically synthesized counterpart. High-resolution X-ray powder diffraction and scanning transmission electron microscopy of noncrystalline sulfur species suggest that electrochemical performance is determined by the efficacy of sulfur distribution throughout the composite, not necessarily the presence of noncrystalline sulfur. At greater sulfur loadings, autogenic composites exhibit crystalline orthorhombic sulfur, suggesting the significance of the autogenic loading of the carbon pores. This point where crystalline orthorhombic sulfur is detected is theorized because the pores that are full noncrystalline orthorhombic sulfur can now sublime on the surface of the carbon. There is a possibility that crystalline orthorhombic sulfur does exist in the pores of the carbon, and due to carbon shielding, it shows up as noncrystalline. However, even high-energy X-ray powder diffraction fails to detect crystalline orthorhombic sulfur signals, therefore leading to the occurrence of noncrystalline orthorhombic sulfur within the carbon pore. This work, therefore, examines not only the effect of different autogenic settings on the overall electrochemical performance of the material but also the effect of using high sulfur loadings with autogenic synthesis and its characterization.

8.3 Experimental Section

8.3.1 Synthesis of Autogenic Carbon–Sulfur Composites

Carbon–sulfur composites were produced using the autogenic synthesis process [402] (Figure 8.1). Any air-sensitive processes were carried out in a glove box (Nexus II, Vacuum Atmospheres Co.) that was filled with 99.999% argon gas (Indiana Oxygen Co.). In a given mass ratio, orthorhombic sulfur (Sigma Aldrich Corp.) and Ketjenblack EC-600JD carbon (Akzo Nobel N.V.) precursors were gently homogenized using a mortar and pestle. The stainless-steel autogenic reactor (reactor volume of ≈ 5 mL) was loaded with the carbon–sulfur mixture and sealed under argon atmosphere (Indiana Oxygen Co.). The loaded autogenic reactor was placed within a horizontal steel tube furnace (MTI). The steel tube furnace was heated to a prespecified temperature at a constant temperature rate of 5°C min^{-1} . Similar cooling rates were used to cool the furnace chamber down to room temperature. Heating profiles included temperatures of 155 and 445°C for a total dwell time of 7 h. Autogenic samples are termed vaporization percentages, that is to say autogenic 30% refers to 4.9 h at 155 and 2.1 445°C . The collected products, termed autogenic carbon–sulfur composites, were used as is without any other modifications as active materials.

8.3.2 Synthesis of Mechanical Carbon–Sulfur Composites

Mechanically synthesized carbon–sulfur composites were produced using a vibration ball mill (Quantachrome Instruments). All reactor preparations were carried out in a glove box (Nexus II, Vacuum Atmospheres Co.) that was filled with 99.999% argon gas (Indiana Oxygen Co.). In a given mass ratio, orthorhombic sulfur (Sigma Aldrich) and carbon Ketjenblack EC-600JD carbon (Akzo Nobel) precursors were gently homogenized using a mortar and pestle. The stainless steel milling jar (reactor volume of ≈ 50 mL) was loaded with the carbon–sulfur mixture, and then, the stainless steel ball (Quantachrome) was sealed under argon atmosphere (Indiana Oxygen Co.). The loaded milling jar was placed within the vibrating ball mill and processed

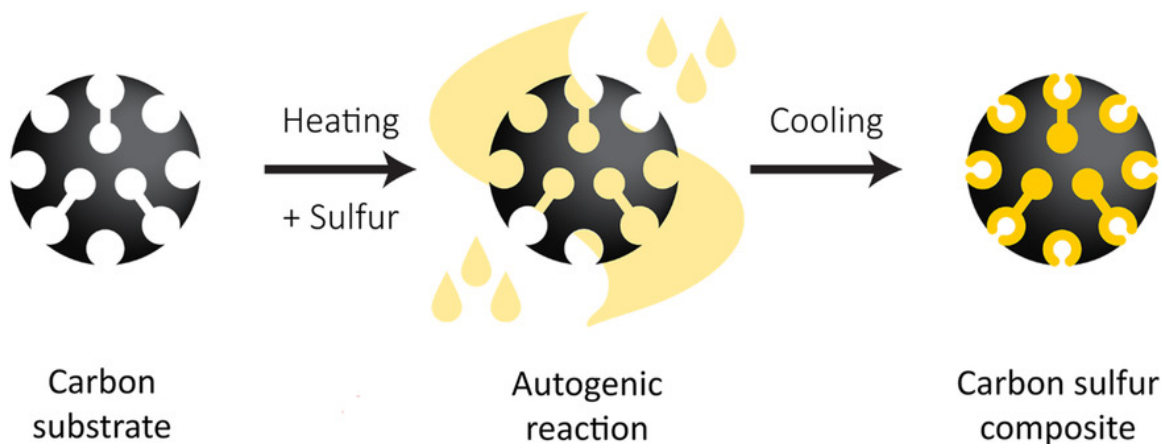


Figure 8.1. Autogenic synthesis of carbon–sulfur composites. Carbon–sulfur composites are synthesized by controlled deposition of sulfur vapor. Heating carbon and sulfur within the autogenic reactor distributes sulfur vapor throughout the carbon substrate. Upon cooling, solid sulfur deposits on the available surface area of the carbon substrate.

for 7 h at a vibration frequency of 10 Hz. The collected products, termed mechanical carbon–sulfur composites, were used as is without any other modifications as active materials.

8.3.3 Battery Fabrication and Assembly

The slurry mixture was comprised of 85 wt% autogenic sulfur composite, 15 wt% polyvinyl-pyrrolidone (Sigma Aldrich), and Type 1 water (Thermo Fisher Corp.) in polypropylene cups (Flacktec Inc.) with zirconium oxide mixing balls (MTI). This mixture was then homogenized in the same polypropylene cups (Flacktec Inc.) with the zirconium oxide mixing balls (MTI) in a planetary mixer (Thinky Corp.). This slurry was then coated on a carbon-laminated aluminum foil that is 18 μm thick, battery grade (MTI). To create the thin film lamination, the slurry was coated using a film applicator “doctor’s blade” (Gardco Inc.) using an automatic film coater unit (MTI). The resulting coating was dried for at least 12 h at the tem-

perature of 30 °C. To create the electrodes, the now dried thin film lamination was cut with a 0.25 in. diameter arch punch (General Tools Co.) and placed into stainless steel CR2032 coin cells (MTI). The electrolyte utilized in all cells comprised 1.0 m bis(trifluoromethane)sulfonimide lithium salt (LITFSI, Sigma Aldrich) in a solution of 1,3-dioxolane (DOL) and 1,2-dimethoxyethane (DME) in a volume ratio of 1:1 with 0.1 m lithium nitrate (LiNO_3) additive. A reference electrode of lithium metal (MTI) and polypropylene separator (Celgard 2500, Celgard LLC) were also used. The cells were sealed in the glove box (Nexus II, Vacuum Atmospheres Co.) that was filled with 99.999% argon gas (Indiana Oxygen Co.) under a hydraulic pressure of $\approx 1000 \text{ lb in}^{-2}$. The assembly of these cells was also carried out in the same glove box (Nexus II, Vacuum Atmospheres Co.) that was filled with 99.999% argon gas (Indiana Oxygen Co.).

8.3.4 Electrochemical Characterization

The newly fabricated batteries were left resting for ≈ 12 h at their open cell voltage (OCV). After this rest period, galvanostatic testing was performed on a multichannel battery cycler (Arbin Instruments Inc.). The initial rest period was performed to improve electrode wetting. All cells were tested in the voltage window of 2.6–1.7 V, which was the cutoff voltage, without any additional conditioning.

The reference electrode was considered when defining the charge and discharge processes: lithiation of sulfur was the discharge when the voltage approached 1.7 V, whereas the charge was defined as delithiation of sulfur when the potential approached 2.6 V. [376, 390] All reported gravimetric variables, such as specific capacity, were determined with basis or reference to the sulfur mass. The potentials here were relative to lithium metal 's ionization potential versus $\text{Li}^{0/+}$.

8.3.5 Characterization of Carbon–Sulfur Composites

High-resolution X-ray diffraction (XRD) experiments were performed at beamline 11-BM of the Advanced Photon Source (APS). Around 2 mg of the material was packed into polyimide capillaries (Kapton, 3M Corp.) mounted into custom aluminum sample holders. Diffraction patterns were produced using a hard X-ray beam with an energy range of ≈ 15 –35 keV and wavelengths of 0.34–1 Å. Spectral patterns were produced in the 2θ scattering range of 2–50° at a scanning rate of 0.5° min⁻¹. Reported spectral patterns were not smoothed or reduced for background. Control materials (viz., carbon and sulfur) and reference standards (viz., polyimide sample holder, aluminum sample mount, and air scattering) were performed or reproduced from beamline 11-BM at Advanced Photon Source, ANL. Reference standards were not corrected for runtime calibration.

The thermogravimetric analysis (TGA) was performed using a simultaneous thermal analyzer (Q600, TA Instruments Inc). The sample was loaded into an aluminum oxide crucible (TA Instruments), and this was tared prior to loading the sample. The crucible now loaded was placed inside the machine, in the horizontal furnace chamber. The furnace chamber was run with a continuous compressed air flow of 100 mL min⁻¹. The mass of the sample was recorded continuously during the heating, done at a rate of 10 °C min⁻¹ to a temperature of 1000 °C. Synthesis efficiency was calculated as the ratio of the precursor sulfur mass fraction and product sulfur mass fraction.

Scanning electron microscopy (SEM) was performed using a scanning electron microscope (Nova 200 DualBeam, FEI Co.). Around 5 mg of the material was placed on a double-sided carbon tape (3M), and the tape was used to secure the material on the aluminum sample stage. The stage was then placed inside the microscope chamber, which was then evacuated down to ≈ 2.6 nbar for a high vacuum. Micrographs were recorded at different levels of magnification, after the optimization of the parameters, such as stigmation, focus, brightness, and beam alignment. Energy dispersive X-ray spectroscopy (EDXS) was performed using an 80 mm² area silicon

drift detector (Oxford Instruments PLC) at an energy level of 10 keV. Electron pixel maps were produced using the AZTEC analysis software suite (Oxford Instruments).

Scanning transmission electron microscopy (STEM) was performed using an environmental transmission electron microscope (Titan, FEI). Dispersion was created by suspending 5 mg of the sample in anhydrous ethanol (Decon Labs). The dispersion was then loaded onto a 200-mesh carbon TEM grid (Pelco, Ted Pella Inc.). The ethanol was then evaporated at a temperature of 30 °C. The sample-loaded grid was then loaded into the specimen chamber, which was then evacuated to high vacuum (i.e., <2.6 nbar). Micrographs were recorded at different levels of magnification, after the optimization of the parameters, such as stigmation, focus, brightness, and beam alignment.

Adsorption and desorption isotherms for nitrogen gas were measured using a surface area and pore-size analyzer (Nova 2200e, Quantachrome). A quartz sample tube cell was dehydrated and then loaded with a sample. The sample was then degassed at 300 °C for 24 h in a vacuum on a heating mantle. The loaded sample cell, cooled by a dewar bath of liquid nitrogen, was subsequently loaded into the gassing chamber for sorption measurements. Measurements were recorded in the relative pressure range of 0.005–0.999 with a minimum equilibration time of 60 s. Masses of the quartz sample tube cell, both with and without sample, were measured using an analytical balance (Sartorius).

8.4 Results and Discussion

8.4.1 Influence of Synthesis on Material Properties of Carbon–Sulfur Composites

The results of this work show that the applied synthesis method controls sulfur distribution and structural order in carbon–sulfur composites. With Ketjenblack EC-600JD high porosity carbon substrates at a moderate sulfur loading of ≈ 40 wt%, autogenic and intensive mechanical synthesis processes produce composites with noncrystalline sulfur. In their composite products, the autogenic and mechanical processes

differ according to sulfur mass percentage and physisorption surface area. These differences suggest more homogeneous sulfur distribution in the autogenic composite compared with that in its mechanically produced counterpart (Figure 8.2).

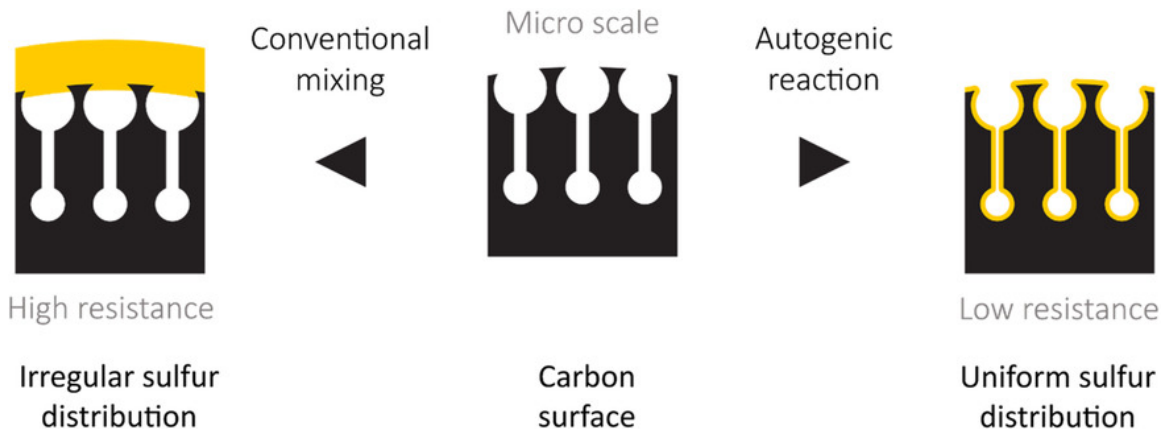


Figure 8.2. Sulfur distribution in carbon–sulfur composites. Deposition of fluid sulfur phases encourages homogeneous sulfur distribution. In the autogenic process, sulfur vapor can access and deposit onto the large surface area of small carbon micropores. In the mechanical mixing process, solid sulfur species are unable to penetrate or access pores beyond particle surfaces.

Autogenic synthesis produces noncrystalline sulfur composites by pressurizing the vapor phase of the heated isochoric reactor. In the first step, carbon and sulfur precursors are heated within the isochoric autogenic reactor under inert atmosphere. [401] During heating, local temperature governs phase transitions of the precursor mixture. At atmospheric pressure, high purity carbon does not experience significant phase transition at temperatures below 4800 K. [404] In contrast, orthorhombic sulfur experiences three phase transitions: [405] orthorhombic-monoclinic solid phase transition at a temperature of 373 K, monoclinic solid–liquid phase transition at 388 K, and liquid–vapor phase transition at 723 K. The extent of heating at solid–liquid and liquid–vapor transition temperatures controls fluid sulfur viscosity and, subsequently, sulfur distribution within carbon substrates. In the second step, sulfur vapor fuses or

deposits as solid sulfur upon cooling to room temperature at ≈ 300.15 K. [405] Within carbon micropores, sulfur deposits or fuses as noncrystalline species. Interestingly, sulfur does not recrystallize after prolonged storage.

Product sulfur mass fraction is sensitive to applied synthesis pathway. A thermogravimetric analysis (Figure 8.3), heating in an advective inert gas stream, measures composition of carbon–sulfur products. Here, synthesis efficiency measures sulfur mass conservation; greater efficiency implies greater sulfur retention through the given synthesis pathway. For the autogenic pathway, synthesis efficiency increases toward unity as a sulfur mass fraction increases. For the mechanical pathway, synthesis efficiency is constant at ≈ 96 wt% sulfur and generally independent of the sulfur mass fraction. Efficiency differences among autogenic and mechanical synthesis are attributed to the underlying pathway mechanism. Autogenic synthesis uses thermal pressurization to mobilize sulfur and homogenize distribution in the composite. With significant vaporization, a fraction of sulfur vapor may remain thermodynamically stable in the vapor phase and not deposit in the composite. In contrast, mechanical synthesis operates on inelastic collisions with stainless steel surfaces to combine precursors. This process does not induce appreciable vaporization, permitting synthesis efficiencies very close to unity.

Structural disorder of the bulk sulfur phase occurs in both the autogenically and mechanically derived composites. Hard X-ray diffraction (Figure 8.4a), performed at the Advanced Photon Source, enables long penetration depth (i.e., mean X-ray energy of ≈ 30 keV with wavelengths of ≈ 1.0 – 0.34 Å) and resolution (i.e., differential vector magnitude 2×10^{-4}): ideal facilities for crystallinity measurements at the nanometer scale. Interestingly, carbon–sulfur composites exhibit diffractogram features of disordered carbon but not those of crystalline sulfur. For bare carbon, low intensity and significant breadth of diffractogram features suggest a short-range structural order as nanocrystallites [406] and long-range disorder. Bare carbon exhibits diffractogram bands [407] at scattering angles of $\approx 6.38^\circ$, 11.32° , and 19.74° corresponding to principle reflections of the 002, 100, and 110 carbon lattice facets, respectively. Crystalline

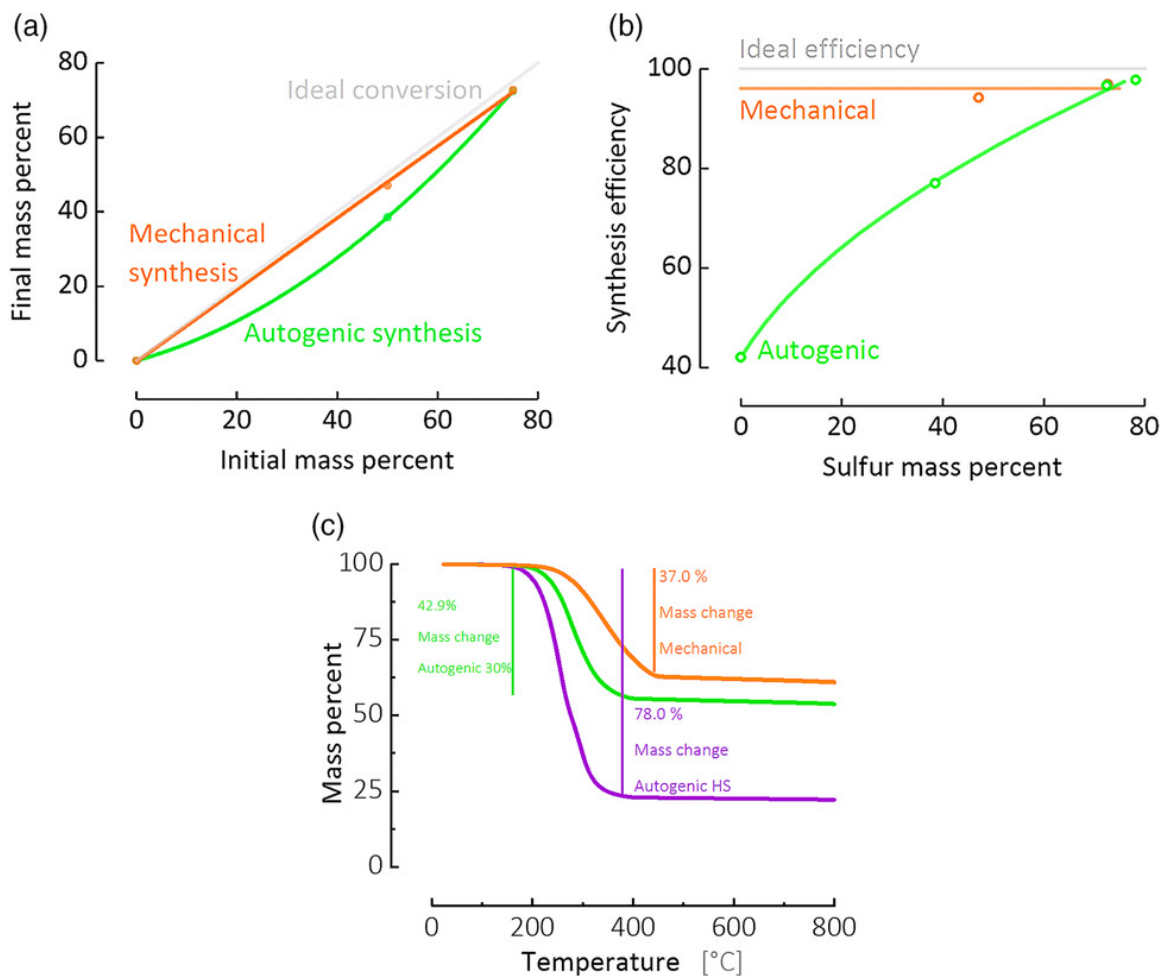


Figure 8.3. Controlled sulfur loading for autogenic carbon-sulfur composites. (a) As sulfur-carbon precursor ratio increases, the efficiencies of sulfur loading for the autogenic and mechanical mixing processes converge toward unity. (b) While it is constant for mechanical process, synthesis efficiency for the autogenic process is a monotonic function of final sulfur mass percent. (c) Targeted sulfur loading for different weight percent sulfur.

orthorhombic sulfur exhibits several high intensities and narrow diffractogram bands in a scattering angle range of $\approx 3\text{--}20^\circ$. Rigorous diffractogram accuracy, afforded by high-energy synchrotron X-rays, confirms a long-range disorder in synthesized composites containing $\approx 40\text{ wt}\%$ sulfur and Ketjenblack EC-600JD carbon.

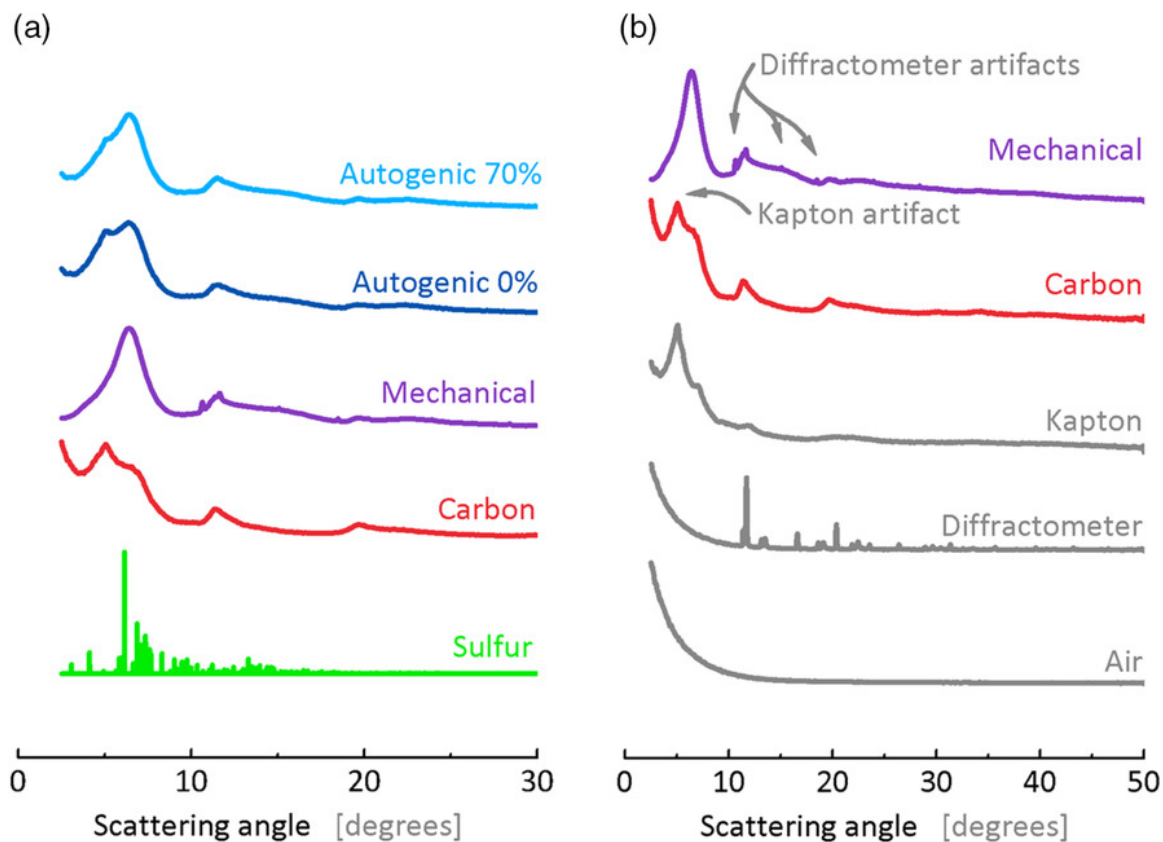


Figure 8.4. High-resolution X-ray powder diffraction of autogenic carbon–sulfur composites. (a) The characteristic diffraction features of orthorhombic sulfur (green) are absent in diffractograms of carbon–sulfur composites. (b) Diffractogram features not associated with amorphous carbon are likely attributable to experimental artifacts. High-resolution X-ray powder diffraction was conducted at beamline 11-BM at Argonne National Laboratory with a wavelength of 1–0.34 Å.

In addition, diffractograms exhibit additional intensity features not associated with carbon or sulfur; these features are caused by experimental artifacts (Figure 8.4b). Typically, diffractogram features of experimental artifacts are negligible when compared with those of ordered materials (e.g., orthorhombic sulfur; Figure 8.4a). [408] However, artifact features and disordered materials produce diffractogram features of comparable intensity. There are three principle diffraction artifacts observed across the studied materials. In all diffractograms, ambient air produces the diffuse band between 0° and 10° . This broad feature occurs at a low scattering angle due to air molecules. [409] In the autogenic, mechanical, and bare carbon diffractograms, the polyimide capillary produces features between $\approx 5^\circ$ and 9° . Polyimide films exhibit scattering bands at 5.1° and 6.9° corresponding to intrachain polyimide reflections and diffuse bands between 10.9° and 26.8° corresponding to interchain reflections. [410] In the mechanical composite, narrow features in a scattering range of $\approx 11.1\text{--}37^\circ$ are attributed to the aluminum sample mount. [411] The relative intensities of features centered at 10.6° , 15.0° , 18.5° , and 28.4° match the relative peak intensity profile of the diffractometer reference. Overall, experimental artifacts well describe the appearance of intense diffractogram features unrelated to bare carbon or synthesized composites. Therefore, high-resolution hard X-ray diffraction justifies the absence of orthorhombic sulfur in high porosity carbons.

The autogenic method produces more homogeneous carbon–sulfur composites than the mechanical method. Following the synthesis, the change in material surface area quantifies sulfur distribution. Isothermal nitrogen sorption (Figure 8.5) measures physisorption surface area before and after synthesis. [412] Differences in the surface area suggest that autogenically deposited sulfur does not greatly obstruct nitrogen sorption, whereas mechanically deposited sulfur significantly hinders subsurface porosity access. Autogenic synthesis produces composite with a gravimetric surface area of $263\text{ m}^2\text{ g}^{-1}$, whereas mechanical synthesis produces composite with a gravimetric surface area of $10\text{ m}^2\text{ g}^{-1}$. Prior to synthesis, bare carbon black exhibits a high gravimetric surface area of $1338\text{ m}^2\text{ g}^{-1}$. Modal micropore radii, calculated

using a nonlinear density functional theory, of the bare carbon substrate are 3.63 and 1.18 nm; the autogenically derived composites are 3.79 and 1.23 nm, and the mechanically derived composite is 4.15 nm. For each material, a gravimetric surface area is proportional to differential volume at modal micropore radii. Low differential volume and singular modal pore radius in the mechanically derived composite evidence micropore blockage.

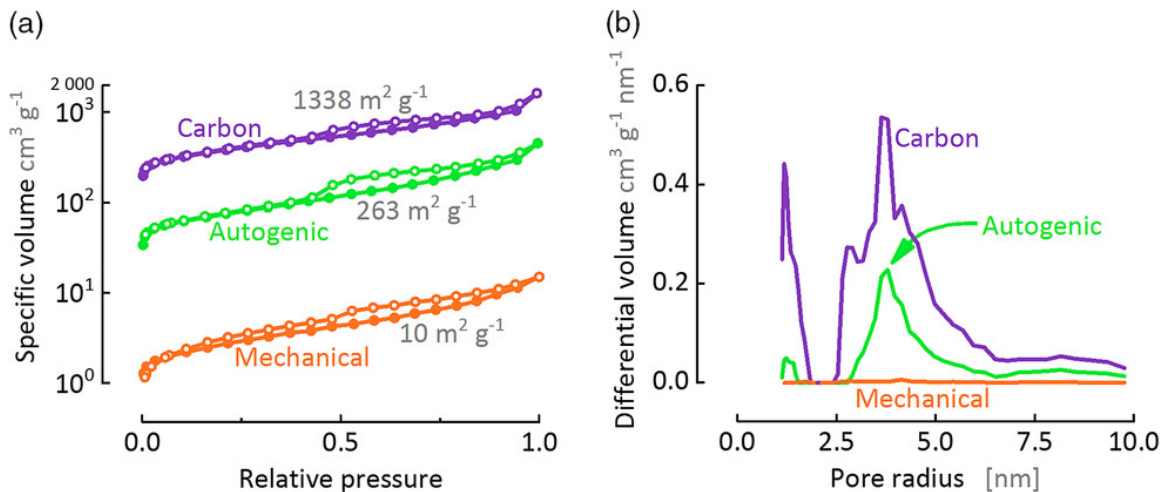


Figure 8.5. Isothermal nitrogen sorption of autogenic carbon-sulfur composites. (a) Specific volume of carbon precursor compared with the specific volumes of composites postsynthesis. Showing mechanical synthesis possibly has a high amount of surface sulfur. (b) Pore distribution of carbon precursor compared with the pore distributions of carbon-sulfur composites post synthesis.

Electron microscopy (Figure 8.6) further suggests homogeneous distribution of sulfur throughout autogenically synthesized carbon-sulfur composites. Scanning electron micrographs show a large sample of autogenically derived composite particles with carbon and sulfur distributed throughout the composite. At deeper magnification, scanning transmission electron micrographs (Figure 8.7) show a great morphological similarity of the carbon-coated sulfur and bare carbon black. The particle geometry appears branched, without a significant change in particle morphology be-

fore or after sulfur loading. Even after optimization, the sulfur-loaded carbon shows poor contrast, likely attributable to the loaded sulfur.

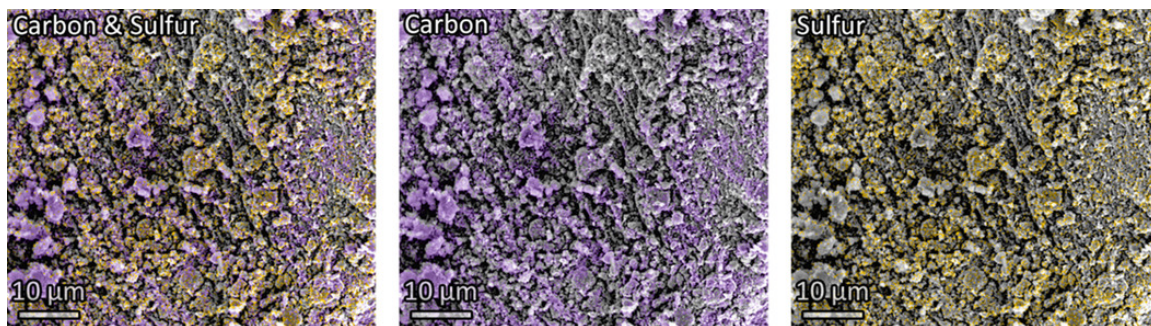


Figure 8.6. Scanning electron micrographs of autogenic carbon–sulfur composites. Autogenic carbon–sulfur composites (left) show carbon (middle) and sulfur (right) species distributed throughout the composites.

In summary, a high-resolution characterization demonstrates that sulfur lacks a long-range order when loaded into microporous carbon. Ultimately, applied synthesis pathway controls sulfur efficiency—that is, the final sulfur mass loading and spatial arrangement. While both synthesis routes produce noncrystalline sulfur, the distribution of sulfur is less obstructive to molecular probes in the autogenic composite. This critical feature has significant implications on the rate-dependent gravimetric capacity of these amorphous sulfur-containing composites.

8.4.2 Influence of Synthesis on Electrochemical Performance of Carbon–Sulfur Composites

Material characterization of autogenically and mechanically derived carbon–sulfur composites suggest that noncrystalline sulfur allotropes are not present in microporous carbons with appreciable sulfur loading. The chemical storage of nonorthorhombic sulfur is seemingly independent of the synthesis method, producible in carbon–sulfur composites synthesized by all studied synthesis methods. Though all materials con-

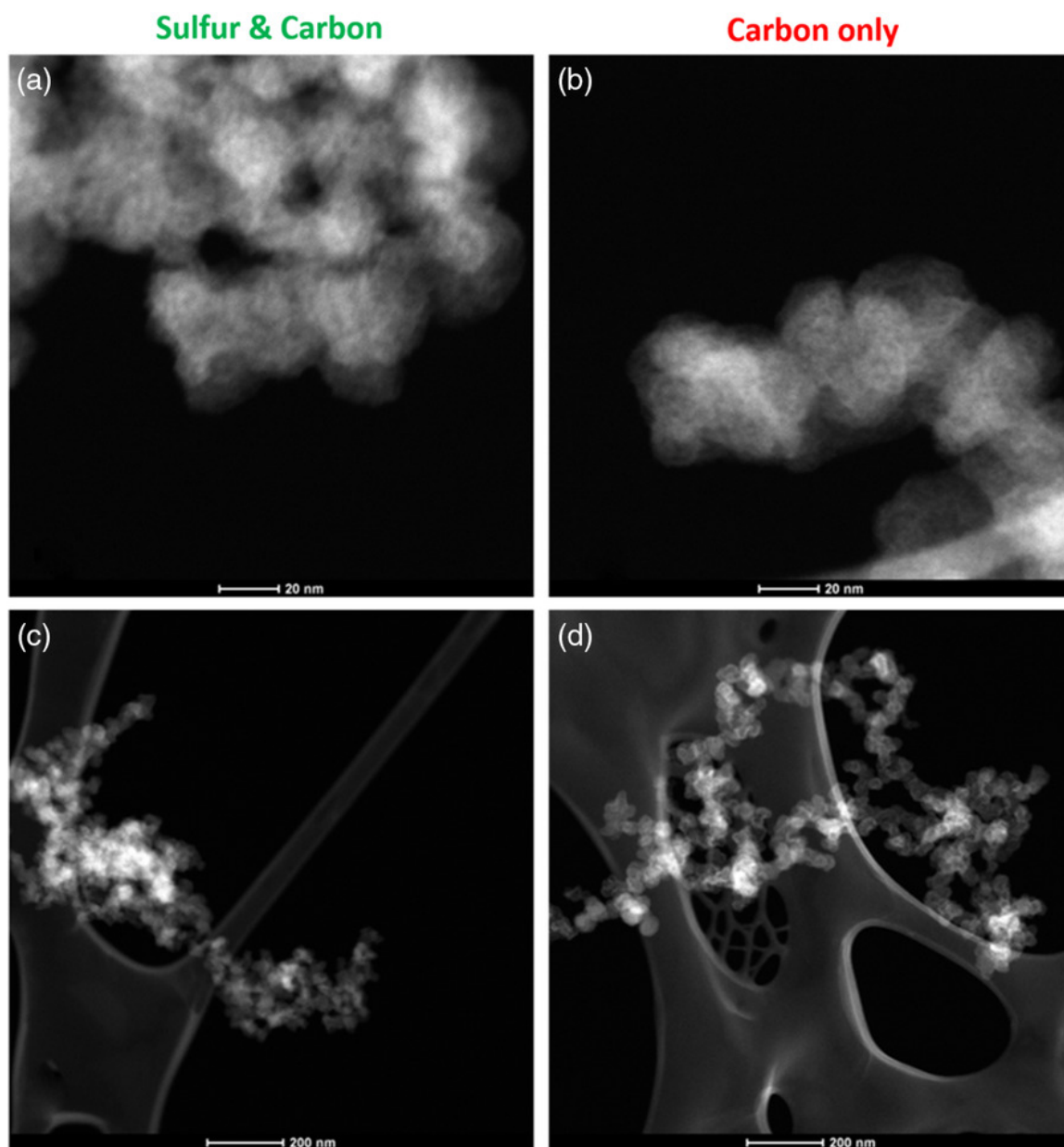


Figure 8.7. Scanning transmission electron micrographs of autogenic carbon–sulfur composites. (a,c) Autogenic composites and (b,d) pure carbon generally appear the same in scanning transmission microscopy.

tain amorphous sulfur, the electrochemical performance of autogenically derived composites surpasses that of its mechanically derived counterpart.

Between the autogenically and mechanically derived composites, a gravimetric surface area is directly proportional to gravimetric capacity. A gravimetric capacity of $\approx 1000 \text{ Ah kg}^{-1}$ is measured after extended gravimetric cycling of the autogenically derived carbon–sulfur composite with 40 wt% sulfur loading (Figure 8.8). The performance of a conventional sample derived via ball milling is shown for comparison. When cycled at various cycling rates, the autogenically derived carbon–sulfur composite shows a greater capacity of around 1100 Ah kg^{-1} after extended cycling. However, all materials demonstrate unstable coulombic efficiency (Figure 8.9), in which a gravimetric capacity decreases to $\approx 700 \text{ Ah kg}^{-1}$ following 100 cycles at the rate C/3. In comparison, the ball milled composite shows a much lower capacity of $\approx 300 \text{ Ah kg}^{-1}$ at similar rates. When analyzing the coulombic efficiency, the autogenic composite demonstrates better efficiency closer to unity ($\approx 100\%$) during the rate cycles corresponding to 836, 1672, and 3344 Ah kg^{-1} .

Following the testing at C/3 for 100 cycles, cells were cycled at C/2, 1C, 2C, C/5, C/10, and C/2 for 10 cycles each, respectively. Chronopotentiograms of carbon–sulfur composites show improved capacity profiles compared with mechanical mixing (Figure 8.10). In cycle 130, all autogenic composites show voltage profiles with a great specific capacity and less hysteresis than the mechanically mixed composite. Interestingly, voltage profiles show two characteristic sulfur voltage plateaus: the high voltage plateau near 2.3 V and the low plateau near 2.1 V. The presence of the high voltage plateau during discharge suggests the reduction of high-order polysulfides to species of the form Li_2S_6 , which eventually leads to the reduction of low-order polysulfides and lithium sulfide Li_2S . The sloping transition and activation overpotential observed at $\approx 350 \text{ Ah kg}^{-1}$ are due to high-order polysulfide salvation. [413] Note that the overpotential feature, which occurs during charging, is negligible in the autogenic materials but prevalent in the mechanically derived composite. This overpotential feature is attributed to activation barriers for lithium–sulfide dissolution. [414] The

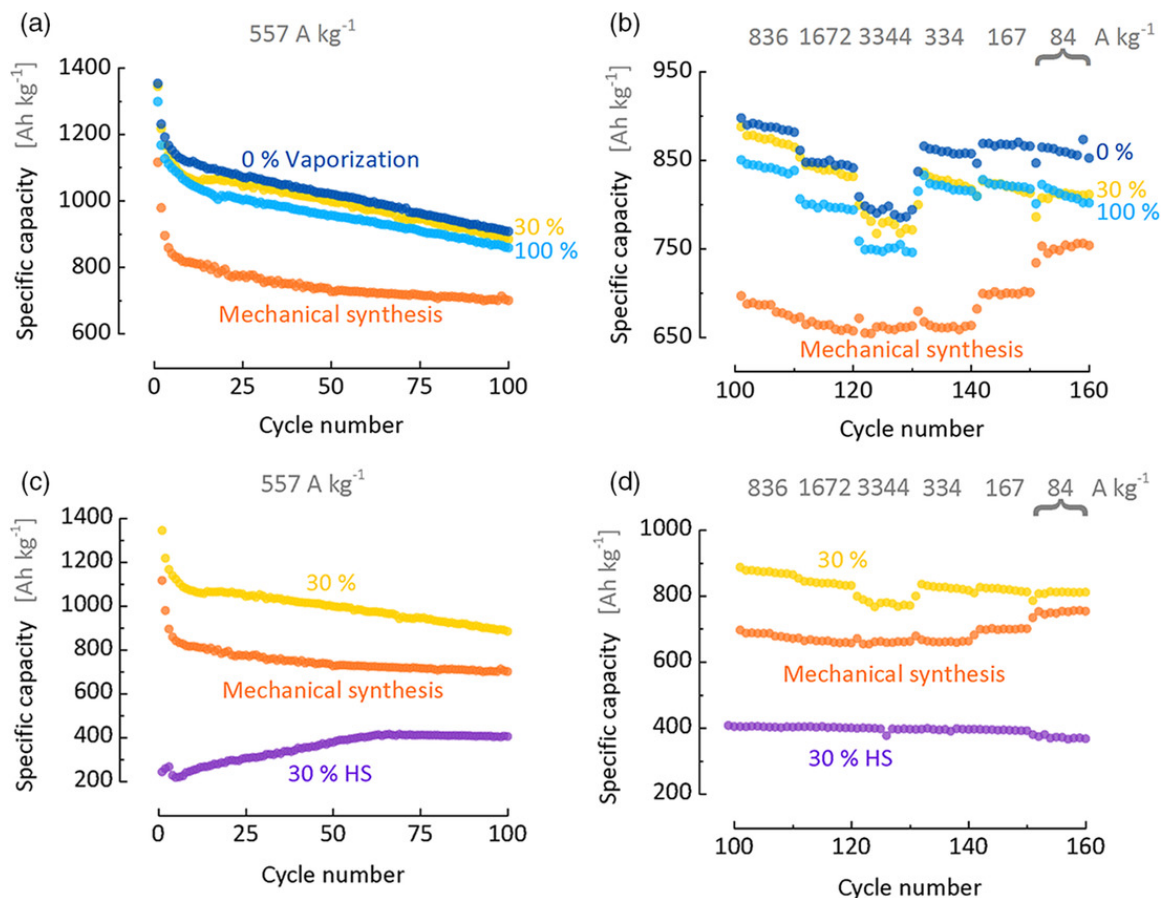


Figure 8.8. Extended galvanostatic cycling of autogenic carbon-sulfur composites. Autogenic carbon-sulfur composites, under various extent of vaporization time at a temperature of 445 °C, demonstrate a high specific capacity compared with mechanical mixing synthesis, in addition, to the high capacity demonstrated by the 30% vaporization high sulfur loading (HS) at 80 wt%. Autogenic samples are termed vaporization percentages, that is to say autogenic 30% refers to 4.9 h at 155 °C and 2.1 h at 445 °C.

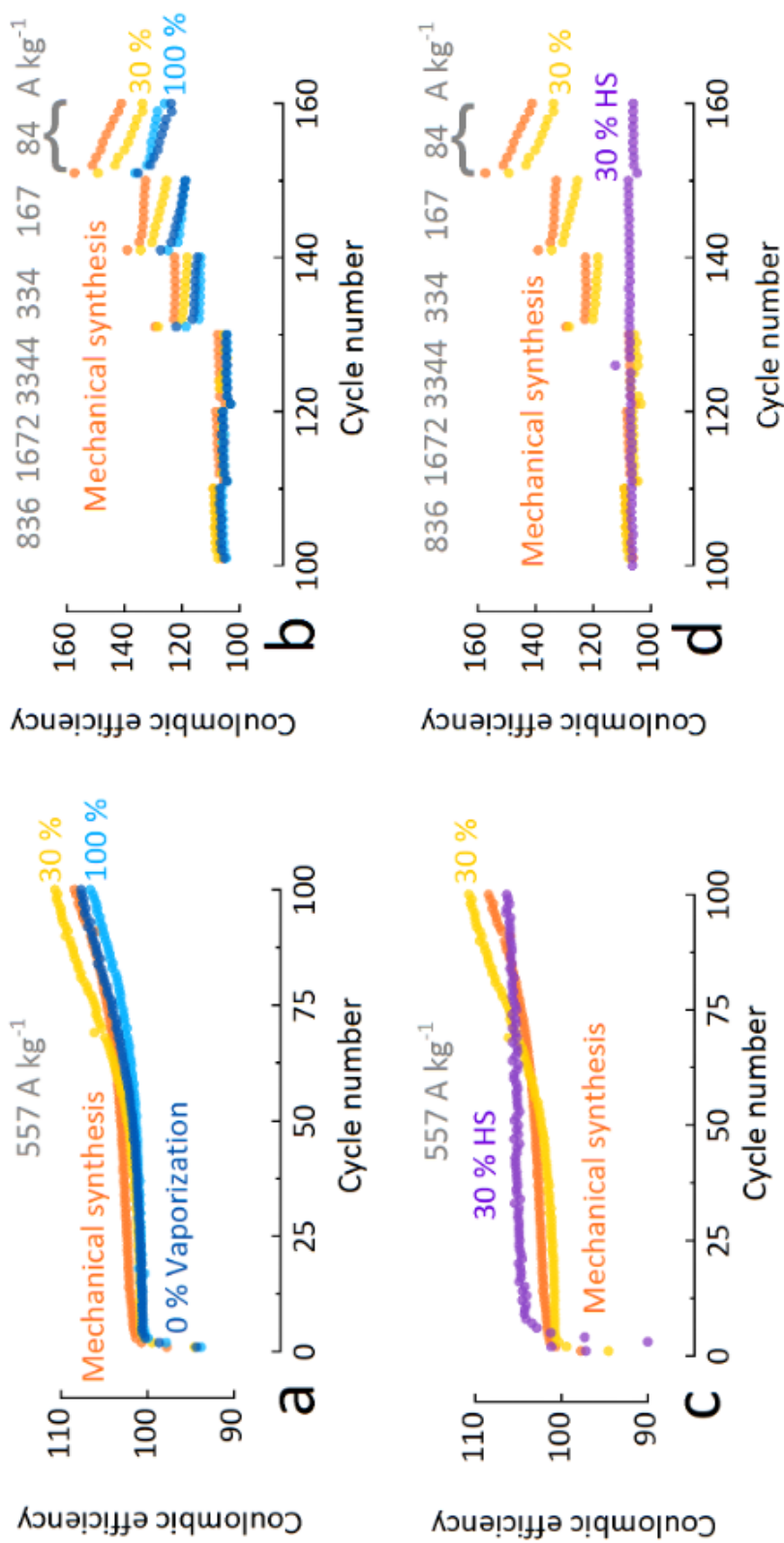


Figure 8.9. Coulombic efficiencies of extended galvanostatic cycling of autogenic carbon sulfur composites. Autogenic carbon sulfur composites, under various extent of vaporization time at temperature 445 °C, demonstrate unstable columbic efficiencies.

high sulfur case of the 30% vaporization, where the sulfur is loaded at 80 wt%, has an initial activation period. After 50 cycles, the capacity stops increasing. Lending to the hypothesis that at high sulfur loadings, sulfur deposition occurs on the surface of carbon in an orthorhombic crystalline form. In addition, this high sulfur loading typically results in low specific capacity at high C rates. [376,387,413,415] However, this material even at high C rates maintains $\approx 400 \text{ Ah kg}^{-1}$ even after 160 cycles.

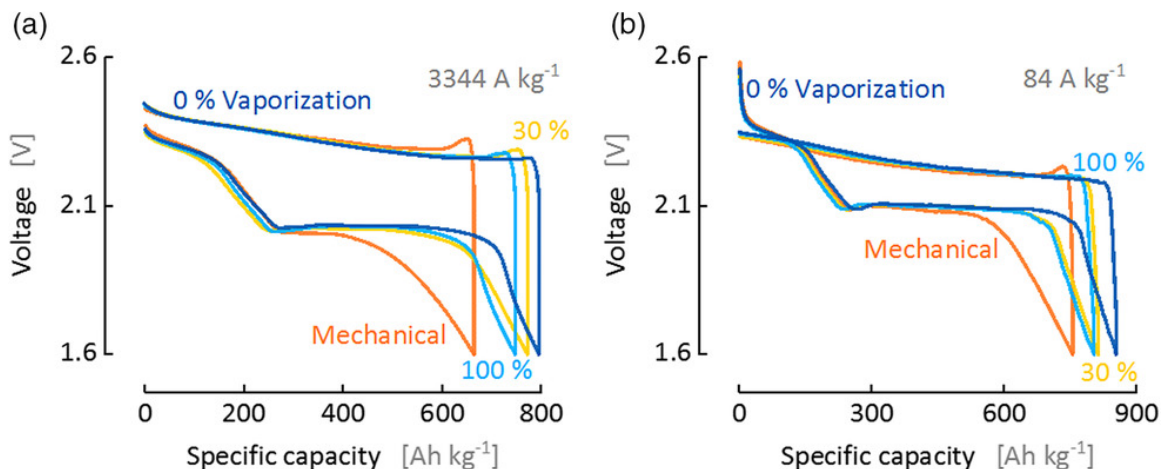


Figure 8.10. Chronopotentiograms for autogenic carbon–sulfur composites. (a) After ten cycles at a current density of 3344 A kg^{-1} (corresponding to cycle 130), which was the last cycle at that current density. (b) Similarly, ten cycles at a current density of 84 A kg^{-1} (corresponding to cycle 160), which was the last cycle for that current density. Autogenic carbon–sulfur composites demonstrate high capacity and greater energy efficiency than mechanically synthesized composites.

8.5 Conclusions

Homogeneity of sulfur distribution, within carbon substrates supporting morphological polysulfide control, dictates electrochemical performance and lifetime of carbon–sulfur composites. This property is most sensitive to synthesis pathway rather than the structural order of the sulfur phase. The effective interfacial surface area

(e.g., measured by isothermal nitrogen sorption) of the bare carbon substrate governs the maximum sulfur loading in which morphological polysulfide control can apply. Electrochemical experiments suggest that available surface area governs the maximum extent of constrained sulfur loading, in which high sulfur loading approaches the electrochemical performance of mechanically synthesized composites with less sulfur. That is $\approx 400 \text{ Ah kg}^{-1}$ for 80 wt% sulfur loading compared with $\approx 750 \text{ Ah kg}^{-1}$ for 40 wt% sulfur in mechanical milling.

The pathway of synthesis determines the electrochemical performance of the carbon–sulfur composite performance. Synthesis methods, which encourage homogeneous distribution of sulfur (i.e., with thinner effective sulfur coating thickness), produce composites with better electrochemical performance and less resistance features. In particular, specific capacity and capacity retention were found to increase for composites as homogeneity of sulfur distribution via the production process.

REFERENCES

- [1] Ribeiro F. H. Avalos-Borja M. & Iglesia E. Fujimoto, K. Structure and reactivity of pdox/zro2catalysts for methane oxidation at low temperatures. *J. Catal.*, 179:431–442, 1998.
- [2] Idakiev V. Tabakova T.-Andreev A. & Giovanoli R. Andreeva, D. Low-temperature water-gas shift reaction on au α -fe2o3 catalyst. *Appl. Catal. A Gen.*, 134:275–283, 1996.
- [3] Mul G.-Makkee M. & Moulijn J. A. Silberova, B. A. A. Drifts study of the water–gas shift reaction over au/fe 2 o 3. *J. Catal.*, 243:171–182, 2006.
- [4] Kiely C. J.-Carley A. F. Landon P. & Hutchings G. J. Herzing, A. A. Identification of active gold nanoclusters on iron oxide supports for co oxidation. *Science*, 321:1331–1335, 2008.
- [5] Qiao B. Wang J.-Zhang Y. & Zhang T. Zhao, K. A highly active and sintering-resistant au/feo x–hydroxyapatite catalyst for co oxidation. *Chem. Commun.*, 47:1779–1781, 2011.
- [6] Leelavathi A. Madras G. & Ravishankar N. Kundu, S. Room temperature growth of ultrathin au nanowires with high areal density over large areas by in situ functionalization of substrate. *Langmuir*, 30:12690–12695, 2014.
- [7] R. Lin, F. & Doong. Bifunctional au– fe3o4 heterostructures for magnetically recyclable catalysis of nitrophenol reduction. *J. Phys. Chem. C*, 115:6591–6598, 2011.
- [8] C. T. Farmer, J. A. & Campbell. Ceria maintains smaller metal catalyst particles by strong metal-support bonding. *Science*, 329:933–936, 2010.
- [9] Saltsburg H. & Flytzani-Stephanopoulos M. Fu, Q. Active nonmetallic au and pt species on ceria-based water-gas shift catalysts. *Science*, 301:935–938, 2003.
- [10] Weber A. & Flytzani-Stephanopoulos M. Fu, Q. Nanostructured au–ceo2 catalysts for low-temperature water–gas shift. *Catal. Letters*, 77:87–95, 2001.
- [11] Goergen S. Yi-N. & Flytzani-Stephanopoulos M. Boucher, M. B. ‘shape effects’ in metal oxide supported nanoscale gold catalysts. *Phys. Chem. Chem. Phys.*, 13:2517–2527, 2011.
- [12] I. et al. Laoufi. Size and catalytic activity of supported gold nanoparticles: An in operando study during co oxidation. *J. Phys. Chem. C*, 115:4673–4679, 2011.
- [13] Wang A.-Q.-Zheng M.-Y.-Wang X.-D. & Zhang T. Tu, C.-H. Factors influencing the catalytic activity of sba-15-supported copper nanoparticles in co oxidation. *Appl. Catal. A Gen.*, 297:40–47, 2006.

- [14] M. Kreibig, U. & Vollmer, editor. *Theoretical considerations. in Optical Properties of Metal Clusters*. Springer, 1995.
- [15] D. R. Bohren, C. F. & Huffman, editor. *Theoretical considerations. in Optical Properties of Metal Clusters*. Wiley-VCH, 2004.
- [16] A. et al. Leelavathi. Absorption and scattering of light by small particles. *RSC Adv.*, 3:20970–20977, 2013.
- [17] Y. Li, D. & Xia. Nanomaterials: Welding and patterning in a flash. *Nat. Mater.*, 3:753–754, 2004.
- [18] M. O’regan, B. & Grätzel. A low-cost, high-efficiency solar cell based on dye-sensitized. *Nature*, 353:737–740, 1991.
- [19] Vayssieres L. & Durrant J. R. Tachibana, Y. Artificial photosynthesis for solar water-splitting. *Nat. Photonics*, 6:511–518, 2012.
- [20] C. M. Morales, A. M. & Lieber. A laser ablation method for the synthesis of crystalline semiconductor nanowires. *Nat. Photonics*, 279:208–211, 1998.
- [21] H. et al. Zeng. Nanomaterials via laser ablation/irradiation in liquid: a review. *Adv. Funct. Mater.*, 22:1333–1353, 2012.
- [22] A. H. Zewail. 4d ultrafast electron diffraction, crystallography, and microscopy. *Annu. Rev. Phys. Chem.*, 57:65–103, 2006.
- [23] Penfold T. J. & Zewail A. H. van der Veen, R. M. Ultrafast core-loss spectroscopy in four-dimensional electron microscopy. *Annu. Rev. Phys. Chem.*, 2:024302, 2015.
- [24] A. H. Flannigan, D. J. & Zewail. 4d electron microscopy: principles and applications. *Acc. Chem. Res.*, 45:1828–1839, 2012.
- [25] A. H. Shorokhov, D. & Zewail. Perspective: 4d ultrafast electron microscopy—evolutions and revolutions. *Acc. Chem. Res.*, 144:080901, 2016.
- [26] A. H. Zewail. Four-dimensional electron microscopy. *Science*, 328:187–193, 2010.
- [27] A. H. Barwick, B. & Zewail. Photonics and plasmonics in 4d ultrafast electron microscopy. *ACS Photonics*, 2:1391–1402, 2015.
- [28] Baskin J. S. Kwon O.-H. & Zewail A. H. Park, H. S. Atomic-scale imaging in real and energy space developed in ultrafast electron microscopy. *Nano Lett.*, 7:2545–2551, 2007.
- [29] H. et al. Yu. Dumbbell-like bifunctional au– fe₃o₄ nanoparticles. *Nano Lett.*, 5:379–382, 2005.
- [30] Garcia M. A. Frey Huls N. A. & Sun S. Lee, Y. Synthetic tuning of the catalytic properties of au-fe₃o₄ nanoparticles. *Angew. Chemie*, 122:1293–1296, 2010.
- [31] H. et al. Yin. Colloidal deposition synthesis of supported gold nanocatalysts based on au–fe₃o₄ dumbbell nanoparticles. *Chem. Commun.*, 36:4357–4359, 2008.

- [32] J. Kunze, editor. *Nitrogen and carbon in iron and steel thermodynamics*. Akademie Verlag, 1990.
- [33] C. W. et al. Han. A discovery of strong metal-support bonding in nano-engineered au-fe₃o₄ dumbbell-like nanoparticles by in-situ transmission electron microscopy. *Nano Lett.*, 17:4576–4582, 2017.
- [34] E. Gatel, C. & Snoeck. Epitaxial growth of au and pt on fe₃o₄ (111) surface. *Surf. Sci.*, 601:1031–1039, 2007.
- [35] E. Gatel, C. & Snoeck. Comparative study of pt, au and ag growth on fe₃o₄ (001) surface. *Surf. Sci.*, 600:2650–2662, 2006.
- [36] N. Singh-Miller, N. E. & Marzari. Surface energies, work functions, and surface relaxations of low-index metallic surfaces from first principles. *Phys. Rev. B*, 80:235407, 2009.
- [37] Ruban A. V. Skriver H. L. & Kollár J. Vitos, L. The surface energy of metals. *Surf. Sci.*, 411:186–202, 1998.
- [38] W. M. Haynes, editor. *CRC handbook of chemistry and physics*. CRC press, 2014.
- [39] Helfensteyn S. Luyten J. & Schurmans M. Creemers, C., editor. *Synergy between material, surface science experiments and simulations*. Springer US, 2007.
- [40] Koshizaki N. Ishikawa Y. & Swiatkowska-Warkocka Z. Fuse, H. Determining the composite structure of au-fe-based submicrometre spherical particles fabricated by pulsed-laser melting in liquid. *Nanomaterials*, 9:198, 2019.
- [41] Bondi J. F. & Schaak-R. E. Buck, M. R. A total-synthesis framework for the construction of high-order colloidal hybrid nanoparticles. *Nanomaterials*, 4:37–44, 2012.
- [42] F. et al. Hu. Smart liquid sers substrates based on fe₃o₄/au nanoparticles with reversibly tunable enhancement factor for practical quantitative detection. *Sci. Rep.*, 4:7204, 2014.
- [43] Roy P. K. & Prins-R. Pirngruber, G. D. The role of autoreduction and of oxygen mobility in n₂o decomposition over fe-zsm-5. *J. Catal.*, 246:147–157, 2007.
- [44] C.C. Ahn. *Transmission electron energy loss spectrometry in materials science and the EELS atlas*. John Wiley & Sons, 2006.
- [45] Verbeeck J. Abakumov A. & Van Tendeloo G. Tan, H. Oxidation state and chemical shift investigation in transition metal oxides by eels. *Ultramicroscopy*, 116:24–33, 2012.
- [46] B. van Aken, P. A. & Liebscher. Quantification of ferrous/ferric ratios in minerals: new evaluation schemes of fe 123 electron energy-loss near-edge spectra. *Phys. Chem. Miner.*, 29:188–200, 2002.
- [47] R.F. Egerton. *Electron energy-loss spectroscopy in the electron microscope*. Springer Science & Business Media, 2011.

- [48] J.P. Wagner C. Ratnasamy. Water gas shift catalysis. *Catal. Rev.*, 51:325–440, 2009.
- [49] J.T. Miller W.N. Delgass F.H. Ribeiro W.D. Williams, L. Bollmann. Effect of molybdenum addition on supported platinum catalysts for the water-gas shift reaction. *Appl. Catal. B Environ*, 125:206–214, 2012.
- [50] P.M. Patterson L. Williams D. Sparks G. Thomas B.H. Davis G. Jacobs, E. Chenu. Water-gas shift: Comparative screening of metal promoters for metal/ceria systems and role of the metal. *Appl. Catal. A Gen.*, 258:203–214, 2004.
- [51] K. Seshan L. Lefferts K.G. Azzam, I.V. Babich. Role of re in pt-re/tio₂ catalyst for water gas shift reaction: A mechanistic and kinetic study. *Appl. Catal. B Environ.*, 80:129–140, 2008.
- [52] S. Hasegawa T. Miyao S. Naito Y. Sato, K. Terada. Mechanistic study of water-gas-shift reaction over tio₂ supported pt-re and pd-re catalysts. *Appl. Catal. A Gen.*, 296:80–89, 2005.
- [53] K. Seshan B.L. Mojet L. Lefferts K.G. Azzam, I. V. Babich. Stable and efficient pt-re/tio₂ catalysts for water-gas-shift: On the effect of rhenium. *Chem-CatChem.*, 5:557–564, 2013.
- [54] F.G. Sollberger E.A. Stach J.T. Miller W.N. Delgass F.H. Ribeiro P.J. Dietrich, M.C. Akatay. Effect of co loading on the activity and selectivity of ptco aqueous phase reforming catalysts. *ACS Catal.*, 4:480–491, 2014.
- [55] M.C. Akatay E.A. Stach W.N. Delgass J.T. Miller F.H. Ribeiro P.J. Dietrich, F.G. Sollberger. Structural and catalytic differences in the effect of co and mo as promoters for pt-based aqueous phase reforming catalysts. *Appl. Catal. B Environ.*, 156–157:236–248, 2014.
- [56] Z. Lu Y. Ren G. Zhang J.T. Miller L.G. Cesar, C. Yang. Identification of a pt₃co surface intermetallic alloy in pt-co propane dehydrogenation catalysts. *ACS Catal.*, 9:5231–5244, 2019.
- [57] K.C. Chang H. You D. Strmcnik J.A. Schluter N.M. Markovic V.R. Stamenkovic C. Wang, D. Van Der Vliet. Monodisperse pt₃co nanoparticles as a catalyst for the oxygen reduction reaction: Size-dependent activity. *J. Phys. Chem. C.*, 113:19365–19368, 2009.
- [58] A.M. Joshi W.D. Williams J. Pazmino Y. V. Joshi J.T. Miller A.J. Kropf W.N. Delgass F.H. Ribeiro L. Bollmann, J.L. Ratts. Effect of zn addition on the water-gas shift reaction over supported palladium catalysts. *J. Catal.*, 257:43–54, 2008.
- [59] J. Hafner G. Kresse. Ab initio molecular-dynamics simulation of the liquid-metalamorphous- semiconductor transition in germanium. *Phys. Rev. B.*, 49:14251–14269, 1994.
- [60] J. Furthmüller G. Kresse. Efficiency of ab-initio total energy calculations for metals and semiconductors using a plane-wave basis set. *Comput. Mater. Sci.*, 6:15–50, 1996.

- [61] D. Joubert G. Kresse. From ultrasoft pseudopotentials to the projector augmented-wave method. *Phys. Rev. B - Condens. Matter Mater. Phys.*, 59:1758–1775, 1999.
- [62] M. Ernzerhof J.P. Perdew, K. Burke. Generalized gradient approximation made simple. *Phys. Rev. Lett.*, 77:3865–3868, 1996.
- [63] S. Savrasov C.J. Humphreys A. Sutton S. Dudarev, G. Botton. Electron-energy-loss spectra and the structural stability of nickel oxide: An lsd+u study. *Phys. Rev. B - Condens. Matter Mater. Phys.*, 57:1505–1509, 1998.
- [64] A. Michaelides J. Klimes, D.R. Bowler. Van der waals density functionals applied to solids. *Phys. Rev. B - Condens. Matter Mater. Phys.*, 83:195131, 2011.
- [65] J. Kubal N.M. Markovic J. Greeley Z. Zeng, K.C. Chang. Stabilization of ultrathin (hydroxy)oxide films on transition metal substrates for electrochemical energy conversion. *Nat. Energy.*, 2:17070, 2017.
- [66] F. Fajula E. Fache I. Belkhir, A. Germain. Role of cobalt molecular sieves in the liquid-phase oxidation of cyclohexane to adipic acid. *J. Chem. Soc. - Faraday Trans.*, 94:1761–1764, 1998.
- [67] H. Okamoto. Co-pt (cobalt-platinum). *J. Phase Equilibria.*, 22:591, 2001.
- [68] M. Klinger. Iucr, more features, more tools, more crystbox. *J. Appl. Crystallogr.*, 50:1226–1234, 2017.
- [69] D.L. Martin A.H. Geisler. A new superlattice in co-pt alloys. *J. Appl. Phys.*, 23:375, 1952.
- [70] P. Liu. Water-gas shift reaction on oxidecu(111): Rational catalyst screening from density functional theory. *J. Chem. Phys.*, 133:204705, 2010.
- [71] W.N. Delgass F.H. Ribeiro W.D. Williams, J.P. Greeley. Water activation and carbon monoxide coverage effects on maximum rates for low temperature water-gas shift catalysis. *J. Catal.*, 347:197–204, 2017.
- [72] Z. Zeng C. Lin M. Giroux L. Jiang Y. Han J. Greeley C. Wang J. Jin L. Wang, Y. Zhu. Platinum-nickel hydroxide nanocomposites for electrocatalytic reduction of water. *Nano Energy.*, 31:456–461, 2017.
- [73] R.M. Lambert M.E. Bridge, C.M. Comrie. Chemisorption studies on cobalt single crystal surfaces. i. carbon monoxide on co(0001). *Surf. Sci.*, 67:393–404, 1977.
- [74] D. Li D. Van Der Vliet G. Wang Q. Lin J. F. Mitchell K.L. More N.M. Markovic V.R. Stamenkovic C. Wang, M. Chi. Synthesis of homogeneous pt-bimetallic nanoparticles as highly efficient electrocatalysts. *ACS Catal.*, 1:1355–1359, 2011.
- [75] Z. Zhao V.J. Cybulskis K.D. Sabnis C.W. Han V. Ortalan W.F. Schneider J. Greeley W.N. Delgass F.H. Ribeiro Y. Cui, Z. Li. Participation of interfacial hydroxyl groups in the water-gas shift reaction over au/mgo catalysts. *Catal. Sci. Technol.*, 7:5257–5266, 2017.

- [76] Y. Cui H. Zhu W.F. Schneider W.N. Delgass F. Ribeiro J. Greeley Z.-J. Zhao, Z. Li. Importance of metal-oxide interfaces in heterogeneous catalysis: A combined dft, microkinetic, and experimental study of water-gas shift on au/mgo. *J. Catal.*, 345:157–169, 2017.
- [77] S. Savrasov C.J. Humphreys A. Sutton S. Dudarev, G. Botton. Electron-energy-loss spectra and the structural stability of nickel oxide: An lsd+u study. *Phys. Rev. B - Condens. Matter Mater. Phys.*, 57:1505–1509, 1998.
- [78] A. Michaelides J. Klimes, D.R. Bowler. Van der waals density functionals applied to solids. *Phys. Rev. B - Condens. Matter Mater. Phys.*, 83:195131, 2011.
- [79] F. Izumi K. Momma. Vesta 3 for three-dimensional visualization of crystal, volumetric and morphology data. *J. Appl. Crystallogr.*, 44:1272–1276, 2011.
- [80] T. Furukawa, S.; Komatsu. Intermetallic compounds: Promising inorganic materials for well-structured and electronically modified reaction environments for efficient catalysis. *ACS Catal.*, 7:735– 765, 2017.
- [81] D. J. C. Sinfelt, J. H.; Yates. Catalytic hydrogenolysis of ethane over the noble metals of group viii. *J. Catal.*, 8:82–90, 1967.
- [82] J.; Vora B.; Imai T.; Pujadó P. Bhasin, M.; McCain. Dehydrogenation and oxydehydrogenation of paraffins to olefins. *Appl. Catal., A*, 221:397–419, 2001.
- [83] J.; Santillan-Jimenez E.; Weckhuysen B. M. Sattler, J. J. H. B.; Ruiz-Martinez. Catalytic dehydrogenation of light alkanes on metals and metal oxides. *Chem. Rev.*, 114:10613– 10653, 2014.
- [84] J. K.; Barteau M. A.; Chen J. G. Kitchin, J. R.; Nørskov. Modification of the surface electronic and chemical properties of pt(111) by subsurface 3d transition metals. *J. Chem. Phys.*, 120:10240– 10246, 2004.
- [85] J. K. Hammer, B.; Nørskov. Electronic factors determining the reactivity of metal surfaces. *Surf. Sci.*, 343:211– 220, 1995.
- [86] S. G.; Cortright R. D.; Dumesic J. A. Natal-Santiago, M. A.; Podkolzin. Microcalorimetric studies of interactions of ethene, isobutene, and isobutane with silica-supported pd, pt, and ptsn. *Catal. Lett.*, 45:155– 163, 1997.
- [87] J. A. Cortright, R. D.; Dumesic. Microcalorimetric, spectroscopic, and kinetic studies of silica supported pt and pt/sn catalysts for isobutane dehydrogenation. *J. Catal.*, 148:771– 778, 1994.
- [88] K. Nykänen, L.; Honkala. Density functional theory study on propane and propene adsorption on pt(111) and ptsn alloy surfaces. *J. Phys. Chem. C*, 115:9578– 9586, 2011.
- [89] K. Nykänen, L.; Honkala. Selectivity in propene dehydrogenation on pt and pt 3 sn surfaces from first principles. *ACS Catal.*, 3:3026– 3030, 2013.
- [90] G.; Vining W. C.; Chi M.; Bell A. T. Sun, P.; Siddiqi. Novel pt/mg(in)(al)o catalysts for ethane and propane dehydrogenation. *J. Catal.*, 282:165– 174, 2011.

- [91] J. M.; Casella M. L.; Fierro J. L. G.; Requejo F. G.; Ferretti O. A. Siri, G. J.; Ramallo-López. Xps and exafs study of supported ptsn catalysts obtained by surface organometallic chemistry on metals. *Appl. Catal., A*, 278:239– 249, 2005.
- [92] T. E.; Beeg S.; Zwiener L.; Scherzer M.; Girgsdies F.; Piccinin S.; Armbrüster M.; Knop-Gericke A.; Schlögl R. Greiner, M. T.; Jones. Free-atom-like d states in single-atom alloy catalysts. *Nat. Chem.*, 10:1008, 2018.
- [93] W. F.; Wolverton C. Chen, W.; Schneider. Trends in atomic adsorption on pt 3 m(111) transition metal bimetallic surface overlayers. *J. Phys. Chem. C*, 118:8342– 8349, 2014.
- [94] A.; Grin Y.; Armbrüster M. Friedrich, M.; Ormeci. Pdzn or znpd: Charge transfer and pd-pd bonding as the driving force for the tetragonal distortion of the cubic crystal structure. *Z. Anorg. Allg. Chem.*, 636:1735– 1739, 2010.
- [95] H.; Nikolla E.; Miller J. T.; Linic S. Schweitzer, N.; Xin. Establishing relationships between the geometric structure and chemical reactivity of alloy catalysts based on their measured electronic structure. *Top. Catal.*, 53:348– 356, 2010.
- [96] J.; Linic S. Nikolla, E.; Schwank. Measuring and relating the electronic structures of nonmodel supported catalytic materials to their performance. *J. Am. Chem. Soc.*, 131:2747– 2754, 2009.
- [97] B. C.; Tseng H. T.; Gallagher J. R.; Wu Z.; Wegener E.; Kropf A. J.; Ravel B.; Ribeiro F. H.; Greeley J.; Miller J. T. Cybulskis, V. J.; Bukowski. Zinc promotion of platinum for catalytic light alkane dehydrogenation: Insights into geometric and electronic effects. *ACS Catal.*, 7:4173– 4181, 2017.
- [98] M.; Rossi M.; Stamenkovic V.; Markovic N. M.; Ross P. N. Mun, B. S.; Watanabe. A study of electronic structures of pt3m (m = ti,v,cr,fe,co,ni) polycrystalline alloys with valence-band photoemission spectroscopy. *J. Chem. Phys.*, 123:204717, 2005.
- [99] H.; Zhao M.; Marshall D.; Yu Y.; Abruña H.; DiSalvo F. J. Cui, Z.; Chen. Synthesis of structurally ordered pt 3 ti and pt 3 v nanoparticles as methanol oxidation catalysts. *J. Am. Chem. Soc.*, 136:10206– 10209, 2014.
- [100] M. Benson, J.; Boudart. Hydrogen-oxygen titration method for the measurement areas of supported. *J. Catal.*, 4:704– 710, 1965.
- [101] T.; Schweitzer N.; Lobo-Lapidus R.; Kropf A. J.; Wang H.; Hu Y.; Miller J. T.; Heald S. M. Bolin, T. B.; Wu. In situ intermediate-energy x-ray catalysis research at the advanced photon source beamline 9-bm. *Catal. Today*, 205:141– 147, 2013.
- [102] A. P. Hammersley. *FIT2D: An Introduction and Overview*. European Synchrotron Research Facility, 1997.
- [103] S. O.; Hanfland M.; Fitch A. N.; Hausermann D. Hammersley, A. P.; Svensson. Two-dimensional detector software: From real detector to idealised image or two-theta scan. *High Pressure Res.*, 14:235– 248, 1996.

- [104] L. Lutterotti. Total pattern fitting for the combined size-strain-stress-texture determination in thin film diffraction. *Nucl. Instrum. Methods Phys. Res., Sect. B*, 268:334– 340, 2010.
- [105] J. Kresse, G.; Furthmüller. Efficiency of ab-initio total energy calculations for metals and semiconductors using a plane-wave basis set. *Comput. Mater. Sci.*, 6:15– 50, 1996.
- [106] J. Kresse, G.; Furthmüller. Efficient iterative schemes for ab initio total-energy calculations using a plane-wave basis set. *Phys. Rev. B: Condens. Matter Mater. Phys.*, 54:11169– 11186, 1996.
- [107] J. Kresse, G.; Hafner. Ab initio molecular dynamics for liquid metals. *Phys. Rev. B: Condens. Matter Mater. Phys.*, 47:558– 561, 1993.
- [108] J. Kresse, G.; Hafner. Ab initio molecular-dynamics simulation of the liquid-metal–amorphous-semiconductor transition in germanium. *Phys. Rev. B: Condens. Matter Mater. Phys.*, 49:14251– 14269, 1994.
- [109] P. E. Blöchl. Projector augmented-wave method. *Phys. Rev. B: Condens. Matter Mater. Phys.*, 50:17953– 17979, 1994.
- [110] K.; Ernzerhof M. Perdew, J. P.; Burke. Generalized gradient approximation made simple. *Phys. Rev. Lett.*, 77:3865– 3868, 1996.
- [111] J. D. Monkhorst, H. J.; Pack. Special points for brillouin-zone integrations. *Phys. Rev. B*, 13:5188– 5192, 1976.
- [112] A. T. Methfessel, M.; Paxton. High-precision sampling for brillouin-zone integration in metals. *Phys. Rev. B: Condens. Matter Mater. Phys.*, 40:3616– 3621, 1989.
- [113] B. P.; Jónsson H. Henkelman, G.; Uberuaga. A climbing image nudged elastic band method for finding saddle points and minimum energy paths. *J. Chem. Phys.*, 113:9901– 9904, 2000.
- [114] J.; Blomqvist J.; Castelli I. E; Christensen R.; Duřak M.; Friis J.; Groves M. N; Hammer B.; Hargus C.; Hermes E. D; Jennings P. C; Bjerre Jensen P.; Kermode J.; Kitchin J. R; Leonhard Kolsbjerg E.; Kubal J.; Kaasbjerg K.; Lysgaard S.; Bergmann Maronsson J.; Maxson T.; Olsen T.; Pastewka L.; Peterson A.; Rostgaard C.; Schiøtz J.; Schutt O.; Strange M.; Thygesen K. S; Vegge T.; Vilhelmsen L.; Walter M.; Zeng Z.; Jacobsen K. W Hjorth Larsen, A.; Jørgen Mortensen. The atomic simulation environment - a python library for working with atoms. *J. Phys.: Condens. Matter*, 29:273002, 2017.
- [115] A. Stukowski. Visualization and analysis of atomistic simulation data with ovito-the open visualization tool. *Modell. Simul. Mater. Sci. Eng.*, 18:015012, 2010.
- [116] A. J.; Zha Y.; Regalbuto J. R.; Delannoy L.; Louis C.; Bus E.; van Bokhoven J. A. Miller, J. T.; Kropf. The effect of gold particle size on auau bond length and reactivity toward oxygen in supported catalysts. *J. Catal.*, 240:222– 234, 2006.

- [117] J. A. Bus, E.; Van Bokhoven. Electronic and geometric structures of supported platinum, gold, and platinum-gold catalysts. *J. Phys. Chem. C*, 111:9761– 9768, 2007.
- [118] R. M. Waterstrat. The vanadium-platinum constitution diagram. *Metall. Trans. A*, 4:455– 466, 1973.
- [119] A. B.; Leontyev N. G.; Hennet L.; Rakhmatullin A.; Smirnova N. V.; Dmitriev V. Leontyev, I. N.; Kuriganova. Size dependence of the lattice parameters of carbon supported platinum nanoparticles: X-ray diffraction analysis and theoretical considerations. *RSC Adv.*, 4:35959– 35965, 2014.
- [120] W. F.; Sobol P. E.; Bomben K. D. Moulder, J. F.; Stickle. *Handbook of X-Ray Photoelectron Spectroscopy*. Perkin-Elmer Corporation, 1995.
- [121] A. E.; Bartholomew C. H.; Somorjai G. A. Ribeiro, F. H.; Schach Von Wittenau. Reproducibility of turnover rates in heterogeneous metal catalysis: Compilation of data and guidelines for data analysis. *Catal. Rev.: Sci. Eng.*, 39:49– 76, 1997.
- [122] A. Q.; Liu X. J. Wang, C. P.; Zheng. Thermodynamic assessments of the v-ge and v-pt systems. *Intermetallics*, 16:544– 549, 2008.
- [123] C.; Ren Y.; Zhang G.; Miller J. T. LiBretto, N. J.; Yang. Identification of surface structures in pt3cr intermetallic nanocatalysts. *Chem. Mater.*, 31:1597, 2019.
- [124] D.; Koper M. T. M.; Sautet P. Calle-Vallejo, F.; Loffreda. Introducing structural sensitivity into adsorption-energy scaling relations by means of coordination numbers. *Nat. Chem.*, 7:403– 410, 2015.
- [125] J. A.; Vilella I. M. J.; Cazorla-Amorós D.; Yamashita H. Román-Martínez, M. C.; Maciá-Agulló. State of pt in dried and reduced ptin and ptsn catalysts supported on carbon. *J. Phys. Chem. C*, 111:4710– 4716, 2007.
- [126] G. F.; Giovanetti L.; Casella M. L.; Ferretti-O. A.; Requejo F. G. Ramallo-López, J. M.; Santori. Xps and xafs pt l 2,3 -edge studies of dispersed metallic pt and ptsn clusters on sio 2 obtained by organometallic synthesis: Structural and electronic characteristics. *J. Phys. Chem. B*, 107:11441– 11451, 2003.
- [127] J. K. Nørskov. Covalent effects in the effective-medium theory of chemical binding: Hydrogen heats of solution in the 3d metals. *Phys. Rev. B: Condens. Matter Mater. Phys.*, 26:2875– 2885, 1982.
- [128] H. Mott, N. F.; Jones. *The Theory of the Properties of Metals and Alloys*. Clarendon Press: Oxford, 1936.
- [129] E. A. Stern. Rigid-band model of alloys. *Phys. Rev.*, 157:544– 551, 1967.
- [130] T.; Teramura K.; Tanaka T. Deng, L.; Shishido. Effect of reduction method on the activity of pt-sn/sio2for dehydrogenation of propane. *Catal. Today*, 232:33– 39, 2014.
- [131] L. K.; Mostafa S.; Croy J. R.; Shafai G.; Hong-S.; Rahman T. S.; Bare S. R.; Roldan Cuenya B. Behafarid, F.; Ono. Electronic properties and charge transfer phenomena in pt nanoparticles on γ -al₂o₃: Size, shape, support, and adsorbate effects. *Phys. Chem. Chem. Phys.*, 14:11766, 2012.

- [132] M. G. Mason. Electronic structure of supported small metal clusters. *Phys. Rev. B: Condens. Matter Mater. Phys.*, 27:748–762, 1983.
- [133] J. W.; Sayers D. E. Mansour, A. N.; Cook. Quantitative technique for the determination of the number of unoccupied d-electron states in a platinum catalyst using the L_{2,3} x-ray absorption edge spectra. *J. Phys. Chem.*, 88:2330–2334, 1984.
- [134] B. L.; Garriga Oostenbrink M. T.; Miller J. T.; Koningsberger D. C. Ramaker, D. E.; Mojet. Contribution of shape resonance and Pt–H EXAFS in the Pt L_{2,3} x-ray absorption edges of supported Pt particles: Application and consequences for catalyst characterization. *Phys. Chem. Chem. Phys.*, 1:2293–2302, 1999.
- [135] R. E. Weinert, M.; Watson. Core-level shifts in bulk alloys and surface adlayers. *Phys. Rev. B: Condens. Matter Mater. Phys.*, 51:17168–17180, 1995.
- [136] C.; Pourvskii L. V.; Johansson B.; Abrikosov I. A. Olovsson, W.; Göransson. Core-level shifts in fcc random alloys: A first-principles approach. *Phys. Rev. B: Condens. Matter Mater. Phys.*, 72:1–12, 2005.
- [137] Y. A.; Zhou X. G.; Sui Z. J.; Chen D. Yang, M. L.; Zhu. First-principles calculations of propane dehydrogenation over PtSn catalysts. *ACS Catal.*, 2:1247–1258, 2012.
- [138] B. C.; Li Z.; Milligan C.; Zhou L.; Ma T.; Wu Y.; Ren Y.; Ribeiro F. H.; Delgass W. N.; Greeley J. P.; Zhang G.; Miller J. T. Wu, Z.; Bukowski. Changes in catalytic and adsorptive properties of 2 nm Pt₃Mn nanoparticles by subsurface atoms. *J. Am. Chem. Soc.*, 140:14870, 2018.
- [139] E. C.; Tseng H.-T.; Gallagher J. R.; Harris J. W.; Diaz R. E.; Ren Y.; Ribeiro F. H.; Miller J. T. Wu, Z.; Wegener. Pd–In intermetallic alloy nanoparticles: Highly selective ethane dehydrogenation catalysts. *Catal. Sci. Technol.*, 6:6965–6976, 2016.
- [140] N. M.; Shahari-S. M. K.; Rioux R. M.; Miller J. T.; Meyer R. J. Childers, D. J.; Schweitzer. Modifying structure-sensitive reactions by addition of Zn to Pd. *J. Catal.*, 318:75–84, 2014.
- [141] G. A. Martin. The kinetics of the catalytic hydrogenolysis of ethane over Ni/SiO₂. *J. Catal.*, 60:345–355, 1979.
- [142] M. D.; Rekoske-J. E.; Cardona-Martinez N.; Dumesic J. A. Goddard, S. A.; Amiridis. Kinetic simulation of heterogeneous catalytic processes: Ethane hydrogenolysis over supported group VIII metals. *J. Catal.*, 117:155–169, 1989.
- [143] D. D.; Gürbüz-E. I.; Iglesia-E. Flaherty, D. W.; Hibbitts. Theoretical and kinetic assessment of the mechanism of ethane hydrogenolysis on metal surfaces saturated with chemisorbed hydrogen. *J. Catal.*, 311:350–356, 2014.
- [144] D. Almithn, A.; Hibbitts. Effects of catalyst model and high adsorbate coverages in ab initio studies of alkane hydrogenolysis. *ACS Catal.*, 8:6375–6387, 2018.
- [145] J. H. Sinfelt. Specificity in catalytic hydrogenolysis by metals. *Adv. Catal.*, 23:91–119, 1973.

- [146] R. D.; Nørskov-J. K.; Dumesic-J. A. Watwe, R. M.; Cortright. Theoretical studies of stability and reactivity of c 2 hydrocarbon species on pt clusters, pt(111), and pt(211). *J. Phys. Chem. B*, 104:2299–2310, 2000.
- [147] J. D.; Celik F. E. Hook, A.; Massa. Effect of tin coverage on selectivity for ethane dehydrogenation over platinum-tin alloys. *J. Phys. Chem. C*, 120:27307–27318, 2016.
- [148] B. C.; Tseng H. T.; Gallagher-J. R.; Wu Z.; Wegener E.; Kropf A. J.; Ravel B.; Ribeiro F. H.; Greeley J.; et al. Cybulskis, V. J.; Bukowski. Zinc promotion of platinum for catalytic light alkane dehydrogenation: Insights into geometric and electronic effects. *ACS Catal.*, 7:4173–4181, 2017.
- [149] A. J.; Yang D.; Wang M.; Topsakal-M.; Lu D.; Stennett M. C.; Hyatt N. C. Ravel, B.; Kropf. Nonresonant valence-to-core x-ray emission spectroscopy of niobium. *Phys. Rev. B*, 97:1–7, 2018.
- [150] I.; Dahl S.; Skoglundh M.; Sehested-J.; Helveg S. Simonsen, S. B.; Chorkendorff. Direct observations of oxygen-induced platinum nanoparticle ripening studied by in situ tem. *J. Am. Chem. Soc.*, 132:7968–7975, 2010.
- [151] T.; Zhao H.; Liu J.; Lei-Y.; Zhang X.; Ren Y.; Elam J. W.; Meyer R. J.; Winans R. E.; et al. Gallagher, J. R.; Li. In situ diffraction of highly dispersed supported platinum nanoparticles. *Catal. Sci. Technol.*, 4:3053–3063, 2014.
- [152] M.; Kropf A. J.; Regalbuto J. R. Miller, J.; Schreier. A fundamental study of platinum tetraammine impregnation of silica₂. the effect of method of preparation, loading, and calcination temperature on (reduced) particle size. *J. Catal.*, 225:203–212, 2004.
- [153] A.; Bell A. T.; Iglesia E. Olthof, B.; Khodakov. Effects of support composition and pretreatment conditions on the structure of vanadia dispersed on sio₂, al₂o₃, tio₂, zro₂, and hfo₂. *J. Phys. Chem. B*, 104:1516–1528, 2000.
- [154] R. M. Waterstrat. The vanadium-platinum constitution diagram. *Metall. Trans.*, 4:455–466, 1973.
- [155] K. Nykänen, L.; Honkala. Selectivity in propene dehydrogenation on pt and pt 3 sn surfaces from first principles. *ACS Catal.*, 3:3026–3030, 2013.
- [156] Y. A.; Zhou X. G.; Sui-Z. J.; Chen D. Yang, M. L.; Zhu. First-principles calculations of propane dehydrogenation over ptsn catalysts. *ACS Catal.*, 2:1247–1258, 2012.
- [157] K. Nykänen, L.; Honkala. Density functional theory study on propane and propene adsorption on pt(111) and ptsn alloy surfaces. *J. Phys. Chem. C*, 115:9578–9586, 2011.
- [158] N. Singh-Miller, N. E.; Marzari. Surface energies, work functions, and surface relaxations of low-index metallic surfaces from first principles. *Phys. Rev. B*, 80:235407, 2009.
- [159] U. Gelius. Binding energies and chemical shifts in esca. *Phys. Scr.*, 9:133–147, 1974.

- [160] G. Goyhenex, C.; Trégli a. Unified picture of d -band and core-level shifts in transition metal alloys. *Phys. Rev. B*, 83:075101, 2011.
- [161] W.; Johansson B. Abrikosov, I. A.; Olovsson. Valence-band hybridization and core level shifts in random ag-pd alloys. *Phys. Rev. Lett.*, 87:2–5, 2001.
- [162] R. E. Weinert, M.; Watson. Core-level shifts in bulk alloys and surface adlayers. *Phys. Rev. B*, 51:17168–17180, 1995.
- [163] C.; Pourovskii L. V.; Johansson B.; Abrikosov-I. A. Olovsson, W.; G oransson. Core-level shifts in fcc random alloys: A first-principles approach. *Phys. Rev. B - Condens. Matter Mater. Phys.*, 72:1–12, 2005.
- [164] K. Y.; Chung Y. D.; Whang-C. N.; Jeon Y. Lee, Y. S.; Lim. Xps core-level shifts and xanes studies of cu-pt and co-pt alloys. *Surf. Interface Anal.*, 30:475–478, 2000.
- [165] X.; Xiao Q.; Hu Y.; Wang Z.; Yiu Y. M.; Sham T. K. Wang, D.; Cui. Electronic behaviour of au-pt alloys and the 4f binding energy shift anomaly in au bimetallics- xray spectroscopy studies. *AIP Adv.*, 8:065210, 2018.
- [166] H. J.; Mehta D. D.; Dietrich P. J.; Detwiler M. D.; Akatay C. M.; Stach E. A.; Miller J. T.; Delgass W. N.; Agrawal R.; et al. Yohe, S. L.; Choudhari. High-pressure vapor-phase hydrodeoxygenation of lignin-derived oxygenates to hydrocarbons by a ptmo bimetallic catalyst: Product selectivity, reaction pathway, and structural characterization. *J. Catal.*, 344:535–552, 2016.
- [167] M. C.; Cui Y.; Sollberger F. G.; Stach E. A.; Miller J. T.; Delgass W. N.; Ribeiro F. H. Sabnis, K. D.; Akatay. Probing the active sites for water-gas shift over pt/molybdenum carbide using multi-walled carbon nanotubes. *J. Catal.*, 330:442–451, 2015.
- [168] J. A. Bus, E.; Van Bokhoven. Electronic and geometric structures of supported platinum, gold, and platinum-gold catalysts. *J. Phys. Chem. C*, 111:9761–9768, 2007.
- [169] H.; Nikolla E.; Miller J. T.; Linic S. Schweitzer, N.; Xin. Establishing relationships between the geometric structure and chemical reactivity of alloy catalysts based on their measured electronic structure. *Top. Catal.*, 53:348–356, 2010.
- [170] J.; Linic S. Nikolla, E.; Schwank. Measuring and relating the electronic structures of nonmodel supported catalytic materials to their performance. *J. Am. Chem. Soc.*, 131:2747–2754, 2009.
- [171] J. N. Armor. Emerging importance of shale gas to both the energy & chemicals landscape. *J. Energy Chem.*, 22:21–26, 2013.
- [172] J. J. Siirola. The impact of shale gas in the chemical industry. *AIChE J.*, 60:810–819, 2014.
- [173] D.; El-Halwagi M. M. Al-Douri, A.; Sengupta. hale gas monetization – a review of downstream processing to chemicals and fuels. *J. Nat. Gas Sci. Eng.*, 45:436–455, 2017.

- [174] J.; Santillan-Jimenez E.; Weckhuysen B. M. Sattler, J. J. H. B.; Ruiz-Martinez. Catalytic dehydrogenation of light alkanes on metals and metal oxides. *Chem. Rev.*, 114:10613–10653, 2014.
- [175] J. H. Sinfelt. Catalytic hydrogenolysis on metals. *Catal. Letters*, 9:159–171, 1991.
- [176] D. D.; Gürbüz E. I.; Iglesia E. Flaherty, D. W.; Hibbitts. Theoretical and kinetic assessment of the mechanism of ethane hydrogenolysis on metal surfaces saturated with chemisorbed hydrogen. *J. Catal.*, 311:350–356, 2014.
- [177] J. L.; Yates D. J. C. Sinfelt, J. H.; Carter. Catalytic hydrogenolysis and dehydrogenation over copper-nickel alloys. *J. Catal.*, 24:283–296, 1972.
- [178] S. A.; Rekoske J. E.; Dumesic J. A. Cortright, R. D.; Goddard. Kinetic study of ethylene hydrogenation. *J. Catal.*, 127:342–353, 1991.
- [179] P. E.; Dumesic J. A. Cortright, R. D.; Levin. Kinetic studies of isobutane dehydrogenation and isobutene hydrogenation over pt/sn-based catalysts. *Ind. Eng. Chem. Res.*, 37:1717–1723, 1998.
- [180] M. L.; Yu Y.; Zhu Y. A.; Sui Z. J.; Zhou X. G.; Holmen A.; Chen D. Zhu, J.; Yang. Size-dependent reaction mechanism and kinetics for propane dehydrogenation over pt catalysts. *ACS Catal.*, 5:6310–6319, 2015.
- [181] V. Ponec. Selectivity in catalysis by alloys. *Catal. Rev.*, 11:41–70, 1975.
- [182] Z.; Mu R.; Zha S.; Li L.; Chen S.; Zang K.; Luo J.; Li Z.; Purdy S. C.; et al. Sun, G.; Zhao. Breaking the scaling relationship via thermally stable pt/cu single atom alloys for catalytic dehydrogenation. *Nat. Commun.*, 9:4454, 2018.
- [183] Z.; Miller J. T. Ma, Z.; Wu. Effect of cu content on the bimetallic pt–cu catalysts for propane dehydrogenation. *Catal. Struct. React.*, 3:43–53, 2017.
- [184] T. Furukawa, S.; Komatsu. Intermetallic compounds: Promising inorganic materials for well-structured and electronically modified reaction environments for efficient catalysis. *ACS Catal.*, 7:735–765, 2017.
- [185] B. C.; Tseng H.-T.; Gallagher J. R.; Wu Z.; Wegener E.; Kropf A. J.; Ravel B.; Ribeiro F. H.; Greeley J.; et al. Cybulskis, V. J.; Bukowski. Zinc promotion of platinum for catalytic light alkane dehydrogenation: Insights into geometric and electronic effects. *ACS Catal.*, 7:4173–4181, 2017.
- [186] B. C.; Li Z.; Milligan-C.; Zhou L.; Ma T.; Wu Y.; Ren Y.; Ribeiro F. H.; Delgass W. N.; et al. Wu, Z.; Bukowski. Changes in catalytic and adsorptive properties of 2 nm pt₃mn nanoparticles by subsurface atoms. *J. Am. Chem. Soc.*, 140:14870–14877, 2018.
- [187] Z.; Tseng H.-T.; Gallagher J. R.; Ren Y.; Diaz R. E.; Ribeiro F. H.; Miller J. T. Wegener, E. C.; Wu. Structure and reactivity of pt–in intermetallic alloy nanoparticles: Highly selective catalysts for ethane dehydrogenation. *Catal. Today*, 299:146–153, 2017.
- [188] K. Nykänen, L.; Honkala. Selectivity in propene dehydrogenation on pt and pt 3 sn surfaces from first principles. *ACS Catal.*, 3:3026–3030, 2013.

- [189] D. G. Chen, Y.; Vlachos. Hydrogenation of ethylene and dehydrogenation and hydrogenolysis of ethane on pt(111) and pt(211): A density functional theory study. *J. Phys. Chem. C*, 114:4973–4982, 2010.
- [190] M. A.; Chen-J. G. Goda, A. M.; Barteau. Correlating electronic properties of bimetallic surfaces with reaction pathways of c2 hydrocarbons. *J. Phys. Chem. B*, 110:11823–11831, 2006.
- [191] F. E. Hook, A.; Celik. Predicting selectivity for ethane dehydrogenation and coke formation pathways over model pt – m surface alloys with ab initio and scaling methods. *J. Phys. Chem. C*, 121:17882–17892, 2017.
- [192] G.; Wu T.; Zhao-J.; Zhao Z. J.; Gong J. Zha, S.; Sun. Identification of pt-based catalysts for propane dehydrogenation: Via a probability analysis. *Chem. Sci.*, 9:3925–3931, 2018.
- [193] M. K.; Galvita V. V; Redekop E. A.; Reyniers M.; Marin G. B. Saerens, S.; Sabbe. The positive role of hydrogen on the dehydrogenation of propane on pt(111). *ACS Catal.*, 7:7495–7508, 2017.
- [194] Y. A.; Zhou X. G.; Sui Z. J.; Chen D. Yang, M. L.; Zhu. First-principles calculations of propane dehydrogenation over ptsn catalysts. *ACS Catal.*, 2:1247–1258, 2012.
- [195] D.; Dumesic J. A. Peng, G.; Gerceker. Catalysis science & technology ethane dehydrogenation on pristine and alox decorated pt stepped surfaces†. *Catal. Sci. Technol.*, 8:2159–2174, 2018.
- [196] J. K.; Bligaard T. Hangaard, M.; Nørskov. First principles micro-kinetic model of catalytic non-oxidative dehydrogenation of ethane over close-packed metallic facets. *J. Catal.*, 374:161–170, 2019.
- [197] Y.-A.; Fan C.; Sui Z.-J.; Chen D.; Zhou X.-G. Yang, M.-L.; Zhu. Dft study of propane dehydrogenation on pt catalyst: Effects of step sites. *Phys. Chem. Chem. Phys.*, 13:3257–3267, 2011.
- [198] D. J. C. Sinfelt, J. H.; Yates. Catalytic hydrogenolysis of ethane over the noble metals of group viii. *J. Catal.*, 8:82–90, 1967.
- [199] E. C.; Tseng H.-T.; Gallagher J. R.; Harris J. W.; Diaz-R. E.; Ren Y.; Ribeiro F. H.; Miller J. T. Wu, Z.; Wegener. Pd-in intermetallic alloy nanoparticles: Highly selective ethane dehydrogenation catalysts. *Catal. Sci. Technol.*, 6:6965–6976, 2016.
- [200] Z.; Zhang G.; Sheng-H.; Tian J.; Duan Z.; Sohn H.; Kropf-A. J.; Wu T.; Krause T. R.; et al. Yang, C.; Wu. Promotion of pd nanoparticles by fe and formation of a pd 3 fe intermetallic alloy for propane dehydrogenation. *Catal. Today*, 323:123–128, 2019.
- [201] I.; Frise E.; Kaynig V.; Longair M.; Pietzsch T.; Preibisch S.; Rueden C.; Saalfeld S.; Schmid B.; et al. Schindelin, J.; Arganda-Carreras. Fiji: An open-source platform for biological-image analysis. *Nat. Methods*, 9:676–682, 2012.
- [202] R. B. Toby, B. H.; Von Dreele. Gsas-ii: The genesis of a modern open-source all purpose crystallography software package. *J. Appl. Crystallogr.*, 46:544–549, 2013.

- [203] L. Lutterotti. Total pattern fitting for the combined size-strain-stress-texture determination in thin film diffraction. *Nucl. Instruments Methods Phys. Res. Sect. B Beam Interact. with Mater. Atoms*, 268:334–340, 2010.
- [204] Y.; Tellgren R.; Nordblad P. Öennerud, P.; Andersson. The magnetic structure of ordered cubic pd₃mn. *J. Solid State Chem.*, 128:109–114, 1997.
- [205] V. P.; Urvachev V. P. Savitskii, E. M.; Polyakova. An investigation of the polythermal pd in - pd sc cross section. *Izv. Akad. Nauk SSSR, Met.*, pages 226–230, 1980.
- [206] H. Nowotny, H.; Bittner. Die kristallstruktur von pdzn. *Monatshefte fuer Chemie*, 81:679–680, 1950.
- [207] E. Jääskeläinen, J.; Suoninen. Structure and ordering of solid solutions of iron in palladium. *Phys. Status Solidi*, 63:241–245, 1981.
- [208] M.; Waurisch C.; Armbrüster M.; Prots Y.; Grin Y. Kovnir, K.; Schmidt. Refinement of the crystal structure of dipalladium gallium, pd₂ga. *Zeitschrift für Krist. - New Cryst. Struct.*, 223:7–8, 2008.
- [209] C.; Ren Y.; Zhang G.; Miller J. T. LiBretto, N. J.; Yang. Identification of surface structures in pt₃cr intermetallic nanocatalysts. *Chem. Mater.*, 31:1597–1609, 2019.
- [210] J. Kresse, G.; Furthmüller. Efficient iterative schemes for ab initio total-energy calculations using a plane-wave basis set. *Phys. Rev. B - Condens. Matter Mater. Phys.*, 54:11169–11186, 1996.
- [211] J. Kresse, G.; Hafner. Ab initio molecular-dynamics simulation of the liquid-metalamorphous- semiconductor transition in germanium. *Phys. Rev. B*, 49:14251–14269, 1994.
- [212] J. Kresse, G.; Hafner. Ab initio molecular dynamics for liquid metals. *Phys. Rev. B*, 47:558–561, 1993.
- [213] J. Kresse, G.; Furthmüller. Efficiency of ab-initio total energy calculations for metals and semiconductors using a plane-wave basis set. *Comput. Mater. Sci.*, 6:15–50, 1996.
- [214] K.; Ernzerhof M. Perdew, J. P.; Burke. Generalized gradient approximation made simple. *Phys. Rev. Lett.*, 78:1396–1396, 1996.
- [215] P. E. Blöchl. Projector augmented-wave method. *Phys. Rev. B*, 50:17953–17979, 1994.
- [216] D. Kresse, G.; Joubert. From ultrasoft pseudopotentials to the projector augmented-wave method. *Phys. Rev. B*, 59:1758–1775, 1999.
- [217] R.; Henkelman G. Sheppard, D.; Terrell. Optimization methods for finding minimum energy paths. *J. Chem. Phys.*, 128:1–10, 2008.
- [218] H. Henkelman, G.; Jónsson. Improved tangent estimate in the nudged elastic band method for finding minimum energy paths and saddle points. *J. Chem. Phys.*, 113:9978–9985, 2000.

- [219] B. P.; Jónsson H. Henkelman, G.; Uberuaga. A climbing image nudged elastic band method for finding saddle points and minimum energy paths. *J. Chem. Phys.*, 113:9901–9904, 2000.
- [220] H. Henkelman, G.; Jo. A dimer method for finding saddle points on high dimensional potential surfaces using only first derivatives. *J. Chem. Phys.*, 111:7010, 1999.
- [221] A.; Stokbro K.; Jónsson H. Smidstrup, S.; Pedersen. Improved initial guess for minimum energy path calculations. *J. Chem. Phys.*, 140:214106, 2014.
- [222] O.; Winther K.; Bligaard T. Boes, J. R.; Mamun. Graph theory approach to high-throughput surface adsorption structure generation. *J. Phys. Chem. A*, 123:2281–2285, 2019.
- [223] N. M.; Shahari S. M. K.; Rioux R. M.; Miller J. T.; Meyer R. J. Childers, D. J.; Schweitzer. Modifying structure-sensitive reactions by addition of zn to pd. *J. Catal.*, 318:75–84, 2014.
- [224] T.; Zhao H.; Liu J.; Lei Y.; Zhang X.; Ren Y.; Elam J. W.; Meyer R. J.; Winans R. E.; et al. Gallagher, J. R.; Li. In situ diffraction of highly dispersed supported platinum nanoparticles. *Catal. Sci. Technol.*, 4:3053–3063, 2014.
- [225] D. J.; Zhao H.; Winans R. E.; Meyer R. J.; Miller T. Gallagher, J. R.; Childers. Structural evolution of an intermetallic pd – zn catalyst selective for propane dehydrogenation†. *Catal. Sci. Technol.*, 42:28144–28153, 2015.
- [226] J. Krajčí, M.; Hafner. Semihydrogenation of acetylene on the (010) surface of gapd2: Ga enrichment improves selectivity. *J. Phys. Chem. C*, 118:12285–12301, 2014.
- [227] J. K.; Barteau M. A.; Chen J. G. Kitchin, J. R.; Nørskov. Modification of the surface electronic and chemical properties of pt(111) by subsurface 3d transition metals. *J. Chem. Phys.*, 120:10240–10246, 2004.
- [228] J. K. Hammer, B.; Norskov. Theoretical surface science and catalysis — calculations and concepts. *Adv. Catal.*, 45:71–129, 2000.
- [229] P. Guisnet, M.; Magnoux. Organic chemistry of coke formation. *Appl. Catal. A Gen.*, 212:83–96, 2001.
- [230] E. L.; Kasatkin I.; Groppo E.; Ferri D.; Poceiro B.; Navarro Yerga R. M.; Behrens M. Ota, A.; Kunkes. Comparative study of hydrotalcite-derived supported pd 2ga and pdzn intermetallic nanoparticles as methanol synthesis and methanol steam reforming catalysts. *J. Catal.*, 293:27–38, 2012.
- [231] Z.; Zhang X.; Choi S.; Xiao Y.; Varma A.; Liu W.; Zhang G.; Miller J. T. Zhu Chen, J.; Wu. Identification of the structure of the bi promoted pt non-oxidative coupling of methane catalyst: A nanoscale pt3bi intermetallic alloy. *Catal. Sci. Technol.*, 9:1349–1356, 2019.
- [232] Z.; Liu W.; Ren Y.; Zhang G. Ye, C.; Wu. Structure determination of a surface tetragonal pt 1 sb 1 phase on pt nanoparticles. *Catal. Sci. Technol.*, 30:4503–4507, 2018.

- [233] A. E.; Bartholomew C. H.; Somorjai G. A. Ribeiro, F. H.; Schach Von Wittenau. Reproducibility of turnover rates in heterogeneous metal catalysis: Compilation of data and guidelines for data analysis. *Catal. Rev.*, 39:49–76, 1997.
- [234] D. Almithn, A.; Hibbitts. Comparing rate and mechanism of ethane hydrogenolysis on transition-metal catalysts. *J. Phys. Chem. C*, 123:5421–5432, 2019.
- [235] R. M.; Dumesic J. A. Cortright, R. D.; Watwe. Ethane hydrogenolysis over platinum selection and estimation of kinetic parameters. *J. Mol. Catal. A Chem.*, 163:91–103, 2000.
- [236] X.; Hoffmann R. Liu, X.; Wen. Surface activation of transition metal nanoparticles for heterogeneous catalysis: What we can learn from molecular dynamics. *ACS Catal.*, 8:3365–3375, 2018.
- [237] T.; Schweitzer N.; Lobo-Lapidus R.; Kropf A. J.; Wang H.; Hu Y.; Miller J. T.; Heald S. M. Bolin, T. B.; Wu. In situ intermediate-energy x-ray catalysis research at the advanced photon source beamline 9-bm. *Catal. Today*, 205:141–147, 2013.
- [238] J.; Linic S. Nikolla, E.; Schwank. Measuring and relating the electronic structures of nonmodel supported catalytic materials to their performance. *J. Am. Chem. Soc.*, 131:2747–2754, 2009.
- [239] B. C.; Li Z.; Milligan-C.; Zhou L.; Ma T.; Wu Y.; Ren Y.; Ribeiro F. H.; Delgass W. N.; et al. Wu, Z.; Bukowski. Changes in catalytic and adsorptive properties of 2 nm pt3mn nanoparticles by subsurface atoms. *J. Am. Chem. Soc.*, 140:14870–14877, 2018.
- [240] H.; Nikolla E.; Miller J. T.; Linic S. Schweitzer, N.; Xin. Establishing relationships between the geometric structure and chemical reactivity of alloy catalysts based on their measured electronic structure. *Top. Catal.*, 53:348–356, 2010.
- [241] Porosoff M. D. Yu, W. and J. G. Chen. Review of pt-based bimetallic catalysis: from model surfaces to supported catalysts. *Chem. Rev.*, 112:5780–5817, 2012.
- [242] M. et al. Sankar. Designing bimetallic catalysts for a green and sustainable future. *Chem. Soc. Rev.*, 41:8099–8139, 2012.
- [243] Wang C. Yan H. Yi H. Wang, H. and J. Lu. Precisely-controlled synthesis of au@pd core-shell bimetallic catalyst via atomic layer deposition for selective oxidation of benzyl alcohol. *J. Catal.*, 324:59–68, 2015.
- [244] M. Armbrüster. *Intermetallic Compounds in Catalysis, Encyclopedia of Catalysis*. Wiley, 2011.
- [245] S. Penner and M. Armbrüster. Formation of intermetallic compounds by reactive metal-support interaction: a frequently encountered phenomenon in catalysis. *ChemCatChem*, 7:374–392, 2015.
- [246] D. et al. Wang. Silicide formation on a pt/sio2 model catalyst studied by tem, eels, and edxs. *J. Catal.*, 219:434–441, 2003.
- [247] S. et al. Penner. Platinum nanocrystals supported by silica, alumina and ceria: metal-support interaction due to high-temperature reduction in hydrogen. *Surf. Sci.*, 532:276–280, 2003.

- [248] M. R. et al. Lukatskaya. Cation intercalation and high volumetric capacitance of two-dimensional titanium carbide. *Science*, 341:1502–1505, 2013.
- [249] Mochalin V. N. Barsoum M. W. Naguib, M. and Y. Gogotsi. 25th anniversary article: Mxenes: a new family of two-dimensional materials. *Adv. Mater.*, 26:992–1005, 2014.
- [250] Lukatskaya M. R. Anasori, B. and Y. Gogotsi. 2d metal carbides and nitrides (mxenes) for energy storage. *Nat. Rev. Mater.*, 2:16098, 2017.
- [251] Cao J. L. Jaroniec M. Ma, T. Y. and S. Z. Qiao. Interacting carbon nitride and titanium carbide nanosheets for high-performance oxygen evolution. *Angew. Chem. Int. Ed.*, 55:1138–1142, 2016.
- [252] J. et al. Ran. Ti₃C₂ mxene co-catalyst on metal sulfide photo-absorbers for enhanced visible-light photocatalytic hydrogen production. *Nat. Commun.*, 8:13907, 2017.
- [253] M. Schreier and J. R. Regalbuto. A fundamental study of pt tetraammine impregnation of silica: 1. the electrostatic nature of platinum adsorption. *J. Catal.*, 225:190–202, 2004.
- [254] S. et al. Lambert. Synthesis of very highly dispersed platinum catalysts supported on carbon xerogels by the strong electrostatic adsorption method. *J. Catal.*, 261:23–33, 2009.
- [255] Zhang X. Bravo-Suarez J. J. Fujitani T. Lu, J. and S. T. Oyama. Effect of composition and promoters in au/ts-1 catalysts for direct propylene epoxidation using h₂ and o₂. *Catal. Today*, 147:186–195, 2009.
- [256] Ahmed B. Hedhili-M. N. Anjum D. H. Rakhi, R. and H. N. Alshareef. Effect of postetch annealing gas composition on the structural and electrochemical properties of ti₂ctx mxene electrodes for supercapacitor applications. *Chem. Mater.*, 27:5314–5323, 2015.
- [257] C. et al. Hu. In situ reaction synthesis, electrical and thermal, and mechanical properties of nb₄alc₃. *J. Am. Ceram. Soc.*, 91:2258–2263, 2008.
- [258] X. Wang and Y. Zhou. Microstructure and properties of ti₃alc₂ prepared by the solid–liquid reaction synthesis and simultaneous in-situ hot pressing process. *Acta Mater.*, 50:3143–3151, 2002.
- [259] L. et al. Bollmann. Effect of zn addition on the water-gas shift reaction over supported palladium catalysts. *J. Catal.*, 257:43–54, 2008.
- [260] M. et al. Naguib. New two-dimensional niobium and vanadium carbides as promising materials for li-ion batteries. *J. Am. Chem. Soc.*, 135:15966–15969, 2013.
- [261] K. D. et al. Sabnis. Water-gas shift catalysis over transition metals supported on molybdenum carbide. *J. Catal.*, 331:162–171, 2015.
- [262] M. Shekhar. *Water-Gas Shift Catalysis Over Supported Gold and Platinum Nanoparticles, PhD Thesis*. Purdue Univ., 2012.

- [263] K. D. et al. Sabnis. Probing the active sites for water-gas shift over pt/molybdenum carbide using multi-walled carbon nanotubes. *J. Catal.*, 330:442–451, 2015.
- [264] K. Balakrishnan and J. Schwank. A chemisorption and xps study of bimetallic pt–sn/al₂o₃ catalysts. *J. Catal.*, 127:287–306, 1991.
- [265] M. et al. Wakisaka. Electronic structures of pt–co and pt–ru alloys for co-tolerant anode catalysts in polymer electrolyte fuel cells studied by ec-xps. *J. Phys. Chem. B*, 110:23489–23496, 2006.
- [266] B. C. Beard and P. N. Ross. Platinum–titanium alloy formation from high-temperature reduction of a titania-impregnated platinum catalyst: implications for strong metal–support interaction. *J. Phys. Chem.*, 90:6811–6817, 1986.
- [267] Morikawa Y. Hammer, B. and J. K. Nørskov. Co chemisorption at metal surfaces and overlayers. *Phys. Rev. Lett.*, 76:2141–2144, 1996.
- [268] Y. et al. Gauthier. Adsorption sites and ligand effect for co on an alloy surface: a direct view. *Phys. Rev. Lett.*, 87:036103, 2001.
- [269] Schweitzer N. M. Ajenifujah O. T. Schaidle, J. A. and L. T. Thompson. On the preparation of molybdenum carbide-supported metal catalysts. *J. Catal.*, 289:210–217, 2012.
- [270] Y. et al. Cui. Participation of interfacial hydroxyl groups in the water-gas shift reaction over au/mgo catalysts. *Catal. Sci. Technol.*, 7:5257–5266, 2017.
- [271] A. Athena. Hephaestus: data analysis for x-ray absorption spectroscopy using ifeffit. *J. synchrotron rad.*, 12:537–541, 2005.
- [272] Nowotny H. Jeitschko, W. and F. Benesovsky. Kohlenstoffhaltige ternäre verbindungen (h-phase). *Monatshefte für Chemie und verwandte Teile anderer Wissenschaften*, 94:672–676, 1963.
- [273] Gelato L. Zhao, J. and E. Parthé. Structure refinement of monoclinic 12-layer tani₃ with β -nbpt₃ type. new crystallographic descriptions of this type and of the nb₃rh₅ type based on smaller unit cells. *Acta Crystallogr., Sect. C: Cryst. Struct. Commun.*, 47:479–483, 1991.
- [274] I. Chorkendorff and J. W. Niemantsverdriet. *Concepts of modern catalysis and kinetics*. John Wiley & Sons, 2017.
- [275] I. Nowak and M. Jaroniec. “hard” vs. “soft” templating synthesis of mesoporous nb₂o₅ catalysts for oxidation reactions. *Top. Catal*, 49:193–203, 2008.
- [276] Dalla Betta R. Guskey G. Ribeiro, F. and M. Boudart. Preparation and surface composition of tungsten carbide powders with high specific surface area. *Chem. Mater.*, 3:805–812, 1991.
- [277] Schlatter J. C. Metcalfe III J. E. Oyama, S. T. and J. M. Lambert Jr. Preparation and characterization of early transition metal carbides and nitrides. *Ind. Eng. Chem. Res.*, 27:1639–1648, 1988.

- [278] Schmal M. Da Silva, V. T. and S. Oyama. Niobium carbide synthesis from niobium oxide: study of the synthesis conditions, kinetics, and solid-state transformation mechanism. *J. Solid State Chem.*, 123:168–182, 1996.
- [279] A. Forlin L.H. Pottenger J. Lindner H. Baer, M. Bergamo. *Propylene oxide*. Ullmann's Encyclopedia of Industrial Chemistry, 2012.
- [280] M. Haruta T. Hayashi, K. Tanaka. Selective vapor-phase epoxidation of propylene over au/tio₂ catalysts in the presence of oxygen and hydrogen. *J. Catal.*, 178:566–575, 1998.
- [281] E.A. Stach F.H. Ribeiro W. Nicholas Delgass W.-S. Lee, M. Cem Akatay. Reproducible preparation of au/ts-1 with high reaction rate for gas phase epoxidation of propylene. *J. Catal.*, 287:178–189, 2012.
- [282] E.A. Stach F.H. Ribeiro W. Nicholas Delgass W.-S. Lee, M. Cem Akatay. Enhanced reaction rate for gas-phase epoxidation of propylene using h₂ and o₂ by cs promotion of au/ts-1. *J. Catal.*, 308:98–113, 2013.
- [283] J.H. Zhang D.Y. Wang W.H. Ma Z.S. Li, Y.N. Wang. Better performance for gas-phase epoxidation of propylene using h-2 and o-2 at lower temperature over au/ts-1 catalyst. *Catal. Commun.*, 90:87–90, 2017.
- [284] Y.B. Liu C.H. Yang X.G. Zhou Z.N. Song, X. Feng. Advances in manipulation of catalyst structure and relationship of structure performance for direct propene epoxidation with h-2 and o-2. *Prog. Chem.*, 28:1762–1773, 2016.
- [285] T. Akita H. Ohashi M. Haruta J.H. Huang, T. Takei. Gold clusters supported on alkaline treated ts-1 for highly efficient propene epoxidation with o-2 and h-2. *Appl. Catal. B-Environ.*, 95:430–438, 2010.
- [286] T. Akita A. Guzman C.X. Qi T. Takei M. Haruta J.H. Huang, E. Lima. Propene epoxidation with o-2 and h-2: Identification of the most active gold clusters. *J. Catal.*, 278:8–15, 2011.
- [287] J.J. Bravo-Suarez T. Fujitani S.T. Oyama J.Q. Lu, X.M. Zhang. Effect of composition and promoters in au/ts-1 catalysts for direct propylene epoxidation using h-2 and o-2. *Catal. Today*, 147:186–195, 2009.
- [288] S.T. Oyama-M.F. Luo X.R. Pan J.Q. Lu T. Liu, P. Hacırlıoğlu. Enhanced reactivity of direct propylene epoxidation with h-2 and o-2 over ge-modified au/ts-1 catalysts. *J. Catal.*, 267:202–206, 2009.
- [289] Y.B. Liu-X.B. Chen D. Chen C.H. Yang X.G. Zhou X. Feng, N. Sheng. Simultaneously enhanced stability and selectivity for propene epoxidation with h-2 and o-2 on au catalysts supported on nano-crystalline mesoporous ts-1. *Acc Catal.*, 7:2668–2675, 2017.
- [290] S. Tsubota-M. Haruta A.K. Sinha, S. Seelan. A three-dimensional mesoporous titanosilicate support for gold nanoparticles: Vapor-phase epoxidation of propene with high conversion. *Angew. Chem. Int. Ed.*, 43:1546–1548, 2004.
- [291] E.A. Stach F.H. Ribeiro W.N. Delgass W.-S. Lee, M.C. Akatay. Gas-phase epoxidation of propylene in the presence of h-2 and o-2 over small gold ensembles in uncalcined ts-1. *J. Catal.*, 313:104–112, 2014.

- [292] R.C. Schroden K.J. Watson E.E. Stangland, D.J. Barton. *Deactivation of Au/TS-1 catalysts during the epoxidation of propylene in the presence of H₂/O₂*. AIChE Annual Meeting, 2015.
- [293] R.P. Andres W.N. Delgass E.E. Stangland, K.B. Stavens. Characterization of gold-titania catalysts via oxidation of propylene to propylene oxide. *J. Catal.*, 191:332–347, 2000.
- [294] L.L. Daemen J. Eckert D.W. Goodman C. Sivadinarayana, T.V. Choudhary. The nature of the surface species formed on au/tio₂ during the reaction of h-2 and o-2: An inelastic neutron scattering study. *J. Am. Chem. Soc.*, 126:38–39, 2004.
- [295] J.H. Lunsford D.P. Dissanayake. The direct formation of h₂o₂ from h-2 and o-2 over colloidal palladium. *J. Catal.*, 214:113–120, 2003.
- [296] G.E. Blau W.N. Delgass B. Taylor, J. Lauterbach. Reaction kinetic analysis of the gas-phase epoxidation of propylene over au/ts-1. *J. Catal.*, 242:142–152, 2006.
- [297] J.J. Bravo-Suarez S. Tsubota J. Gaudet S.T. Oyama J.Q. Lu, X.M. Zhang. Kinetics of propylene epoxidation using h-2 and o-2 over a gold/mesoporous titanosilicate catalyst. *Catal. Today*, 123:189–197, 2007.
- [298] J.Q. Lu-Y.F. Gu T. Fujitani S.T. Oyama, X.M. Zhang. Epoxidation of propylene with h-2 and o-2 in the explosive regime in a packed-bed catalytic membrane reactor. *J. Catal.*, 257:1–4, 2008.
- [299] K.T. Thomson A.M. Joshi, W.N. Delgass. Mechanistic implications of au-n/ti-lattice proximity for propylene epoxidation. *J. Phys. Chem. C*, 111:7841–7844, 2007.
- [300] J.J. Bravo-Suárez S. Tsubota J. Gaudet S.T. Oyama J. Lu, X. Zhang. Kinetics of propylene epoxidation using h₂ and o₂ over a gold/mesoporous titanosilicate catalyst. *Catal. Today*, 123:189–197, 2007.
- [301] F. Neira d'Angelo J.C. Schouten T.A. Nijhuis S. Kanungo, D.M. Perez Fernandez. Kinetic study of propene oxide and water formation in hydro-epoxidation of propene on au/ti-sio₂ catalyst. *J. Catal.*, 338:284–294, 2016.
- [302] U. Romano M.G. Clerici, G. Bellussi. Synthesis of propylene-oxide from propylene and hydrogen-peroxide catalyzed by titanium silicalite. *J. Catal.*, 129:159–167, 1991.
- [303] M.C. Akatay E.A. Stach F.H. Ribeiro W.N. Delgass W.-S. Lee, L.-C. Lai. Probing the gold active sites in au/ts-1 for gas-phase epoxidation of propylene in the presence of hydrogen and oxygen. *J. Catal.*, 296:31–42, 2012.
- [304] K. Yamaguchi T. Akita S. Tsubota M. Haruta M. Okumura, Y. Kitagawa. Direct production of hydrogen peroxide from h-2 and o-2 over highly dispersed au catalysts. *Chem. Lett.*, 32:822–823, 2003.
- [305] D.W. Flaherty D.T. Bregante. Periodic trends in olefin epoxidation over group iv and v framework-substituted zeolite catalysts: a kinetic and spectroscopic study. *J. Am. Chem. Soc.*, 139:6888–6898, 2017.

- [306] Y. Zvinevich R. Gounder W.N. Delgass F.H. Ribeiro V.J. Cybulskis, A. Smeltz. Learning the fundamentals of kinetics and reaction engineering with the catalytic oxidation of methane. *Chem. Eng. Educ.*, 50:202–210, 2016.
- [307] M. Makkee J.A. Moulijn T.A. Nijhuis, B.J. Huizinga. Direct epoxidation of propene using gold dispersed on ts-1 and other titanium-containing supports. *Ind. Eng. Chem. Res.*, 38:884–891, 1999.
- [308] A. Paraskar S.R. Sainkar R.B. Khomane, B.D. Kulkarni. Synthesis, characterization and catalytic performance of titanium silicalite-1 prepared in micellar media. *Mat. Chem. Phys.*, 76:99–103, 2002.
- [309] W.N. Delgass B. Taylor, J. Lauterbach. Gas-phase epoxidation of propylene over small gold ensembles on ts-1. *Appl. Catal. A-Gen.*, 291:188–198, 2005.
- [310] J. Tauc. Optical properties and electronic structure of amorphous ge and si. *Mater. Res. Bull.*, 3:37–46, 1968.
- [311] A. Vancu J. Tauc, R. Grigorovici. Optical properties and electronic structure of amorphous germanium. *Phys. Status Solidi(b)*, 15:627–637, 1966.
- [312] N.F. Mott E.A. Davis. Conduction in non-crystalline systems v. conductivity, optical absorption and photoconductivity in amorphous semiconductors. *Philos. Mag.*, 22:0903–0922, 1970.
- [313] M.E. Davis R. Gounder. Titanium-beta zeolites catalyze the stereospecific isomerization of d-glucose to l-sorbose via intramolecular c5–c1 hydride shift. *ACS Catal.*, 3:1469–1476, 2013.
- [314] G. Dealberti F. Genoni G. Leofanti M. Padovan G. Papparatto P. Roffia G. Petrini, A. Cesana. *Deactivation Phenomena on Ti-Silicalite*. Elsevier Science Publ B V, 1991.
- [315] J.L.G. Fierro M.A. Banares I.E. Wachs X.T. Gao, S.R. Bare. Preparation and in-situ spectroscopic characterization of molecularly dispersed titanium oxide on silica. *J. Phys. Chem. B*, 102:5653–5666, 1998.
- [316] Z. Mao H.J. Mao Y. Wang X. Wang W.D. Ruan B. Zhao J.R. Lombardi X.X. Xue, W. Ji. Raman investigation of nanosized tio2: effect of crystallite size and quantum confinement. *J. Phys. Chem. C*, 116:8792–8797, 2012.
- [317] R. Schlögl M. Behrens. *Characterization of Solid Materials and Heterogeneous Catalysts: From Structure to Surface Reactivity*. Wiley, 2012.
- [318] J.F. Banfield H.Z. Zhang. Understanding polymorphic phase transformation behavior during growth of nanocrystalline aggregates: Insights from tio2. *J. Phys. Chem. B*, 104:3481–3487, 2000.
- [319] J.A. Labinger M.E. Davis C.B. Khouw, C.B. Dartt. Studies on the catalytic-oxidation of alkanes and alkenes by titanium. *J. Catal.*, 149:195–205, 1994.
- [320] A. Corma A. Pulido, M. Boronat. Propene epoxidation with h2/h2o/o2 mixtures over gold atoms supported on defective graphene: a theoretical study. *J. Phys. Chem. C*, 116:19355–19362, 2012.

- [321] S.G. Podkolzin D.G. Barton. Kinetic study of a direct water synthesis over silica-supported gold nanoparticles. *J. Phys. Chem. B*, 109:2262–2274, 2005.
- [322] R.V. Wheeler W.A. Bone. The combination of hydrogen and oxygen in contact with hot surfaces. *Philos. Trans. R. Soc. Lond. A-Contain. Pap. Math. Phys. Character*, 206:1–67, 1906.
- [323] J.C. Elgin A.F. Benton. The catalytic synthesis of water vapor in contact with metallic gold. *J. Am. Chem. Soc.*, 49:2426–2438, 1927.
- [324] K.T. Thomson D.H. Wells, W.N. Delgass. Evidence of defect-promoted reactivity for epoxidation of propylene in titanosilicate (ts-1) catalysts: A dft study. *J. Am. Chem. Soc.*, 126:2956–2962, 2004.
- [325] A.M. Beale A.M.J. van der Eerden J.C. Schouten B.M. Weckhuysen T.A. Nijhuis, E. Sacaliuc. Spectroscopic evidence for the adsorption of propene on gold nanoparticles during the hydro-epoxidation of propene. *J. Catal.*, 258:256–264, 2008.
- [326] N.F. Mott E.A. Davis. Conduction in non-crystalline systems v. conductivity, optical absorption and photoconductivity in amorphous semiconductors. *Philosophical Magazine*, 22:0903–0922, 1970.
- [327] J. Tauc. Optical properties and electronic structure of amorphous ge and si. *Materials Research Bulletin*, 3:37–46, 1968.
- [328] A. Vancu J. Tauc, R. Grigorovici. Optical properties and electronic structure of amorphous germanium. *Physica Status Solidi (b)*, 15:627–637, 1966.
- [329] M.C. Akatay E.A. Stach F.H. Ribeiro W.N. Delgass W.-S. Lee, L.-C. Lai. Probing the gold active sites in au/ts-1 for gas-phase epoxidation of propylene in the presence of hydrogen and oxygen. *J. Catal.*, 296:31–42, 2012.
- [330] E.N. Lightfoot R.B. Bird, W.E. Steward. *Transport Phenomena, 2nd Ed.* John Wiley & Sons, 2002.
- [331] W. T.; Son D. Y.; Ono L. K.; Qi Y. B. Kim, T.; Song. Lithium-ion batteries: outlook on present, future, and hybridized technologies. *J. Mater. Chem. A*, 7:2942–2964, 2019.
- [332] J. G.; Liu R.; Yue M.; Huang Y. Y.; Yuan G. H. Huang, S.; Ren. The progress of novel binder as a non-ignorable part to improve the performance of si-based anodes for li-ion batteries. *Int. J. Energy Res*, 42:919–935, 2018.
- [333] J. L.; Kintner-Meyer M. C. W.; Lu X. C.; Choi D. W.; Lemmon J. P.; Liu J. Yang, Z. G.; Zhang. Electrochemical energy storage for green grid. *Chem. Rev.*, 111:3577– 3613, 2011.
- [334] R.; Zhao C. Z.; Zhang Q. Cheng, X. B.; Zhang. Toward safe lithium metal anode in rechargeable batteries: A review. *Chem. Rev.*, 117:10403– 10473, 2017.
- [335] Y. C.; Hu L. Y.; Zhou X. S.; Li Y. F.; Dai Z. H.; Bao J. C. Liu, X.; Du. Understanding the effect of different polymeric surfactants on enhancing the silicon/reduced graphene oxide anode performance. *J. Phys. Chem. C*, 119:5848–5854, 2015.

- [336] P.; Scrosati B.; Tarascon J. M.; Van Schalkwijk W. Arico, A. S.; Bruce. Nanostructured materials for advanced energy conversion and storage devices. *Nat. Mater.*, 4:366– 377, 2005.
- [337] D.; Tarascon J. M. Lepoivre, F.; Larcher. Electrochemical activation of silica for enhanced performances of si-based electrodes. *J. Electrochem. Soc.*, 163:A2791– A2796, 2016.
- [338] F. X.; Lee J. T.; Yushin G. Nitta, N.; Wu. Li-ion battery materials: present and future. *Mater. Today*, 18:252– 264, 2015.
- [339] V. L. Obrovac, M. N.; Chevrier. Alloy negative electrodes for li-ion batteries. *Chem. Rev.*, 114:11444– 11502, 2014.
- [340] Z. W.; Xiang C. S.; Ruan G. D.; Yan Z.; Natelson D.; Tour J. M. Lin, J.; Peng. Graphene nanoribbon and nanostructured SnO_2 composite anodes for lithium ion batteries. *ACS Nano*, 7:6001– 6006, 2013.
- [341] A. Manthiram. An outlook on lithium ion battery technology. *ACS Cent. Sci.*, 3:1063– 1069, 2017.
- [342] Y. Q.; Zhai T. Y.; Li H. Q. He, J.; Wei. Antimony-based materials as promising anodes for rechargeable lithium-ion and sodium-ion batteries. *Mater. Chem. Front.*, 2:437– 455, 2018.
- [343] K.; Walter M.; Kovalenko M. V. He, M.; Kravchyk. Monodisperse antimony nanocrystals for high-rate li-ion and na-ion battery anodes: Nano versus bulk. *Nano Lett.*, 14:1255– 1262, 2014.
- [344] J. G.; Miller D. J.; Thackeray M. M. Pol, V. G.; Wen. Sonochemical deposition of sn, SnO_2 and sb on spherical hard carbon electrodes for li-ion batteries. *J. Electrochem. Soc.*, 161:A777– A782, 2014.
- [345] J.; Nyholm L.; Herranen M.; Alm O.; Edstrom K. Bryngelsson, H.; Eskhult. Electrodeposited sb and sb/ SnO_2 nanoparticle coatings as anode materials for li-ion batteries. *Chem. Mater.*, 19:1170– 1180, 2007.
- [346] L. T.; Wu C.; Wen Y. R.; Yin K. B.; Chiang F. K.; Hu R. Z.; Liu J. W.; Sun L. T.; Gu L.; Maier J.; Yu Y.; Zhu M. Liu, J.; Yu. New nanoconfined galvanic replacement synthesis of hollow sb@c yolk-shell spheres constituting a stable anode for high-rate li/na-ion batteries. *Nano Lett.*, 17:2034– 2042, 2017.
- [347] T.; Chen J. S.; Shi W. H.; Zhang X. J.; Lou X. W.; Mhaisalkar S.; Hng H. H.; Boey F.; Ma J.; Yan Q. Y. Zhu, J. X.; Sun. Controlled synthesis of sb nanostructures and their conversion to CoSb_3 nanoparticle chains for li-ion battery electrodes. *Chem. Mater.*, 22:5333– 5339, 2010.
- [348] W. F.; Huo C. X.; Zhang K.; Guo S. Y.; Zhang S. L.; Song X. F.; Jiang L. F.; Huo K. F.; Zeng H. B. Gao, Y. J.; Tian. Tailoring natural layered beta-phase antimony into few layer antimonene for li storage with high rate capabilities. *J. Mater. Chem. A*, 7:3238– 3243, 2019.
- [349] O.; Pol V. G.; Sominski E.; Koltypin Y.; Gedanken A. Zhou, G. T.; Palchik. Microwave-assisted solid-state synthesis and characterization of intermetallic compounds of Li_3Bi and Li_3Sb . *J. Mater. Chem.*, 13:2607– 2611, 2003.

- [350] H. J. Park, C. M.; Sohn. Novel antimony/aluminum/carbon nanocomposite for high-performance rechargeable lithium batteries. *Chem. Mater.*, 20:3169– 3173, 2008.
- [351] A. Allcorn, E.; Manthiram. Fesb₂-al₂o₃-c nanocomposite anodes for lithium-ion batteries. *Appl. Mater. Interfaces*, 6:10886– 10891, 2014.
- [352] U.; Jagirdar B. R. Babu Kalidindi, S.; Sanyal. Chemical synthesis of metal nanoparticles using amine-boranes. *ChemSusChem*, 4:317– 324, 2011.
- [353] J.; Stucky G. D. Zheng, N.; Fan. One-step one-phase synthesis of monodisperse noble-metallic nanoparticles and their colloidal crystals. *J. Am. Chem. Soc.*, 128:6550– 6551, 2006.
- [354] A. S.; Zhao Y.; Mei J. G. Ramachandran, P. V.; Kulkarni. Amine-boranes bearing borane-incompatible functionalities: application to selective amine protection and surface functionalization. *Chem. Commun.*, 52:11885– 11888, 2016.
- [355] M. P.; Kulkarni A. S. Ramachandran, P. V.; Drolet. A non-dissociative open-flask hydroboration with ammonia borane: ready synthesis of ammonia-trialkylboranes and aminodialkylboranes. *Chem. Commun.*, 52:11897– 11900, 2016.
- [356] A. S. Ramachandran, P. V.; Kulkarni. Water-promoted, safe and, scalable preparation of ammonia borane. *Int. J. Hydrogen Energy*, 42:1451– 1455, 2017.
- [357] M. D.; Mlowe S.; Revaprasadu N. Mntungwa, N.; Khan. A simple route to alkylamine capped antimony nanoparticles. *Mater. Lett.*, 145:239– 242, 2015.
- [358] X. F.; Liu J. Z.; Yan Z.; Huo C. X.; Zhang S. L.; Su M.; Liao L.; Wang W. H.; Ni Z. H.; Hao Y. F.; Zeng H. B. Ji, J. P.; Song. Two-dimensional antimonene single crystals grown by van der waals epitaxy. *Nat. Commun.*, 7:XXX, 2016.
- [359] L.; Santamaria-Perez D.; Vilaplana R.; Manjon F. J.; Errandonea D.; Nalin M.; Beltran A. Pereira, A. L. J.; Gracia. Structural and vibrational study of cubic sb₂o₃ under high pressure. *Phys. Rev. B: Condens. Matter Mater. Phys.*, 85:XXX, 2012.
- [360] P.; Haefner K. Barrett, C. S.; Cucka. Crystal structure of antimony at 4.2, 78 and 298 degrees k. *Acta Crystallogr.*, 16:451, 1963.
- [361] M. Klinger. More features, more tools, more crystbox. *J. Appl. Crystallogr.*, 50:1226– 1234, 2017.
- [362] C.; Sougrati M. T.; Fraisse B.; Stievano L.; Monconduit L. Darwiche, A.; Marino. Better cycling performances of bulk sb in na-ion batteries compared to li-ion systems: An unexpected electrochemical mechanism. *J. Am. Chem. Soc.*, 134:20805– 20811, 2012.
- [363] C. H.; Wang H.; Yang J.; Hu P. F.; Guo L. Zhou, J.; Zheng. 3d nest-shaped sb₂o₃/rgo composite based high-performance lithium-ion batteries. *Nanoscale*, 8:17131– 17135, 2016.
- [364] H. C. Brown. *Organic Syntheses Via Boranes*. Wiley: New York, 1975.

- [365] Kulkarni A. S. Ramachandran P. V. Water-promoted, safe and scalable preparation of ammonia borane. *Int. J. Hydrogen Energy*, 42:1451, 2017.
- [366] Zhao Y. Mei J. Ramachandran P. V., Kulkarni A. S. Amine–boranes bearing borane-incompatible functionalities: application to selective amine protection and surface functionalization. *Chem. Commun.*, 52:11885, 2016.
- [367] M.; Mlowe S.; Revaprasadu N. Mntungwa, N.; Khan. A simple route to alkyamine capped antimony nanoparticles. *Mater. Lett.*, 145:239–242, 2015.
- [368] Rajasekhar Pullabhotla V.S.R. Revaprasadu N. Mntungwa, N. A simple route to bismuth nanoparticles in the form of dots, branched nanorods and self assembled cubes. *Mater Lett.*, 92:635–647, 2013.
- [369] A. et al. Houdayer. Activated hydride-mediated solution phase synthesis of crystallized antimony(0) nanoparticles. *Materials Chemistry and Physics*, 101:404–409, 2007.
- [370] M. et. al. He. A general synthesis strategy for monodisperse metallic and metalloid nanoparticles (in, ga, bi, sb, zn, cu, sn, and their alloys) via in situ formed metal long-chain amides. *Chem. Mater.*, 27:635–647, 2015.
- [371] Alan Greenwood, Norman N.; Earnshaw. *Chemistry of the Elements*. Oxford: Pergamon Press., 1975.
- [372] Gagare P D Ramachandran P V. Preparation of ammonia borane in high yield and purity, methanolysis, and regeneration. *Inorganic Chemistry*, 46:7810–7817, 2007.
- [373] Walter M Kovachenko M V. He M, Kravchyk K. Monodisperse antimony nanocrystals for high-rate li-ion and na-ion battery anodes: Nano versus bulk. *Nano Lett.*, 14:1255–1262, 2014.
- [374] U.S.A. B.C. LLC. *Advanced Batteries for Electric Vehicles—2020 Commercialization Goals*. USCAR, 2015.
- [375] L. J. Hardwick J.-M. Tarascon P. G. Bruce, S. A. Freunberger. Li–o₂ and li–s batteries with high energy storage. *Nat. Mater.*, 11:19–29, 2011.
- [376] S. H. Chung C. Zu Y. S. Su A. Manthiram, Y. Fu. Rechargeable lithium–sulfur batteries. *Chem. Rev.*, 114:11751–11787, 2014.
- [377] H.-X. Yang X.-P. Gao. Multi-electron reaction materials for high energy density batteries. *Energy Environ. Sci.*, 3:174–189, 2010.
- [378] P. Novák S. Urbonaitė, T. Poux. Progress towards commercially viable li-s battery cells. *Adv. Energy Mater.*, 5:XXX, 2015.
- [379] G. Salitra D. Aurbach A. Garsuch F. F. Chesneau A. Rosenman, E. Markevich. Review on li-sulfur battery systems: an integral perspective. *Adv. Energy Mater.*, 5:XXX, 2015.
- [380] L. F. Nazar X. Ji. Advances in li-s batteries. *J. Mater. Chem.*, 20:9821–9826, 2010.

- [381] K. Patel. Lithium-sulfur battery: Chemistry, challenges, cost, and future. *J. Undergrad. Res. Univ. Illinois Chicago*, 9:39–42, 2016.
- [382] F. Meng A. Xing J. Liu X. Fan, W. Sun. Advanced chemical strategies for lithium–sulfur batteries: A review. *Green Energy Environ.*, 3:2–19, 2018.
- [383] J. Ju Q. Li D. Wu X. Ma L. Li M. Naebe B. Cheng W. Kang, N. Deng. A review of recent developments in rechargeable lithium-sulfur batteries. *Nanoscale*, 8:16541–16588, 2016.
- [384] M.-C. Lin C.-J. Pan H.-L. Chou H.-A. Chen M. Gong Y. Wu C. Yuan M. Angell Y. J. Hsieh D.-Y. Wang, C.-Y. Wei. Advanced rechargeable aluminium ion battery with a high-quality natural graphite cathode. *Nat. Commun.*, 8:14283, 2017.
- [385] S. Trabesinger E. J. Berg. Viability of polysulfide-retaining barriers in li-s battery. *J. Electrochem. Soc.*, 165:A5001–A5005, 2018.
- [386] A. Manthiram S.-H. Chung, C.-H. Chang. Progress on the critical parameters for lithium–sulfur batteries to be practically viable. *Adv. Funct. Mater.*, 28:1801188, 2018.
- [387] R. Shah P. Qi L. Miao M. Chen-X. Zhao Y. Peng Z. Deng A. Abdul Razzaq, Y. Yao. High-performance lithium sulfur batteries enabled by a synergy between sulfur and carbon nanotubes. *Energy Storage Mater.*, 16:194–202, 2019.
- [388] H.-J. Peng M.-M. Titirici R. Xiang-R. Chen Q. Liu Q. Zhang H. Yuan, J.-Q. Huang. A review of functional binders in lithium-sulfur batteries. *Adv. Energy Mater.*, 8:1802107, 2018.
- [389] P. Johansson J. Scheers, S. Fantini. A review of electrolytes for lithium-sulphur batteries. *J. Power Sources*, 255:204–218, 2014.
- [390] L. F. Nazar X. Ji, K. T. Lee. A highly ordered nanostructured carbon-sulphur cathode for lithium-sulphur batteries. *Nat. Mater.*, 8:500–506, 2009.
- [391] Y. Yin Y. Guo J. Zhang, H. Ye. Core-shell meso/microporous carbon host for sulfur loading toward applications in lithium-sulfur batteries. *J. Energy Chem.*, 23:308–314, 2014.
- [392] L. Liu L. Chen G. Li, W. Zhao. Effects of electrolyte concentration and synthesis methods of sulfur/carbon composites on the electrochemical performance in lithium-sulfur batteries. *RSC Adv.*, 5:54293–54300, 2015.
- [393] G. R. Li X. P. Gao B. Zhang, X. Qin. Enhancement of long stability of sulfur cathode by encapsulating sulfur into micropores of carbon spheres. *Energy Environ. Sci.*, 3:1531–1537, 2010.
- [394] G.-L. Xu Y.-X. Jiang D.-Y. Zhao J.-T. Li L. Huang S.-G. Sun S.-R. Chen, Y.-P. Zhai. Ordered mesoporous carbon/sulfur nanocomposite of high performances as cathode for lithium-sulfur battery. *Electrochim. Acta*, 56:9549–9555, 2011.
- [395] S. S. Zhang. Does the sulfur cathode require good mixing for a liquid electrolyte lithium/sulfur cell? *Electrochem. Commun.*, 31:v10–12, 2013.

- [396] X.-Y. Liu X.-B. Cheng W.-T. Xu C.-Z. Zhao F. Wei Q. Zhang H.-J. Peng, J.-Q. Huang. Healing high-loading sulfur electrodes with unprecedented long cycling life: Spatial heterogeneity control. *J. Am. Chem. Soc.*, 139:8458–8466, 2017.
- [397] N. Tachikawa-K. Dokko M. Watanabe J.-W. Park, K. Ueno. Ionic liquid electrolytes for lithium-sulfur batteries. *J. Phys. Chem. C*, 117:20531–20541, 2013.
- [398] E. Takashima J. W. Park K. Dokko M. Watanabe N. Tachikawa, K. Yamauchi. Reversibility of electrochemical reactions of sulfur supported on inverse opal carbon in glyme-li salt molten complex electrolytes. *Chem. Commun.*, 47:8157–8159, 2011.
- [399] T. T. Fister J. W. Elam X. Meng, D. J. Comstock. Vapor-phase atomic-controllable growth of amorphous li₂s for high-performance lithium-sulfur batteries. *ACS Nano*, 8:10963–10972, 2014.
- [400] A. Gedanken S. V. Pol, V. G. Pol. Reactions under autogenic pressure at elevated temperature (rapet) of various alkoxides: Formation of metals/metal oxides-carbon core-shell structures. *Chem. - A Eur. J.*, 10:4467–4473, 2004.
- [401] S. V. Pol M. Koltypin A. Gedanken D. Aurbach A. Odani, V. G. Pol. Testing carbon-coated vox prepared via reaction under autogenic pressure at elevated temperature as li-insertion materials. *Adv. Mater.*, 18:1431–1436, 2006.
- [402] P. Thiyagarajan V. G. Pol. Remediating plastic waste into carbon nanotubes. *J. Environ. Monit.*, 12:455–459, 2010.
- [403] A. Gedanken V. G. Pol, S. V. Pol. Novel synthesis of high surface area silicon carbide by rapet (reactions under autogenic pressure at elevated temperature) of organosilanes. *Chem. Mater.*, 17:1797–1802, 2005.
- [404] P. Gustafson. An evaluation of the thermodynamic properties and the p,t phase diagram of carbon. *Carbon N. Y.*, 24:169–176, 1986.
- [405] L. Q. Lobo A. G. M. Ferreira. The low-pressure phase diagram of sulfur. *J. Chem. Thermodyn.*, 43:95–104, 2011.
- [406] E. A. Belenkov. Formation of graphite structure in carbon crystallites. *Inorg. Mater.*, 37:928–934, 2001.
- [407] B. E. Warren. X-ray diffraction in random-layer lattices. *Phys. Rev.*, 59:693–698, 1941.
- [408] L. E. Alexander H. P. Klug. *X-Ray Diffraction Procedures: For Polycrystalline and Amorphous Materials*. Wiley, 1974.
- [409] S. J. Van Der Gaast. A method to eliminate the background in x-ray diffraction patterns of oriented clay mineral samples. *Clay Miner.*, 16:383–393, 1981.
- [410] G. S. Cargill R. F. Boehme. *Polyimides*. Springer, 1984.
- [411] Argonne National Laboratory. Standards data for advanced photon source beamline 11-bm-a, 2014.

- [412] A. V. Neimark J. P. Olivier F. Rodriguez-Reinoso J. Rouquerol K. S. W. Sing M. Thommes, K. Kaneko. Physisorption of gases, with special reference to the evaluation of surface area and pore size distribution (iupac technical report). *Pure Appl. Chem.*, 87:1051–1069, 2015.
- [413] C. Y. Kwok L. F. Nazar Q. Pang, X. Liang. Advances in lithium-sulfur batteries based on multifunctional cathodes and electrolytes. *Nat. Energy*, 1:16132, 2016.
- [414] S. Misra J. Nelson M. F. Toney Y. Cui Y. Yang, G. Zheng. High-capacity micrometer-sized li₂s particles as cathode materials for advanced rechargeable lithium-ion batteries. *J. Am. Chem. Soc.*, 134:15387–15394, 2012.
- [415] J. Liu J. Zheng Y. Wang S. Ferrara J. Xiao J.-G. Zhang J. Liu D. Lu, Q. Li. Enabling high-energy-density cathode for lithium-sulfur batteries. *ACS Appl. Mater. Interfaces*, 10:23094–23102, 2018.
- [416] C.B. Carter D.B. Williams. *Transmission Electron Microscopy, 2nd Edition*. Springer, 2009.
- [417] P.D. Nellist S.J. Pennycook, editor. *Scanning Transmission Electron Microscopy*. Springer, 2011.
- [418] R.F. Egerton. *Electron energy-loss spectroscopy in the electron microscope*. Springer Science & Business Media, 2011.
- [419] C.C. Ahn. *Transmission electron energy loss spectrometry in materials science and the EELS atlas*. John Wiley & Sons, 2006.

A. A SHORT DESCRIPTION OF (S)TEM IMAGING

Since there are many different kinds of electron microscopy images shown in this dissertation, a short description of the differences between techniques is given. In conventional Transmission Electron Microscopy (TEM), parallel beams are transmitted through the sample, and are partially diffracted and partially transmitted without interference. In conventional TEM, both the diffracted beams and the direct beam have to be in focus or artifacts in the imaging will be seen. This focus-condition leads to extreme low-contrast imaging, as well as increased image artifacts since it is difficult to keep the entire image in focus due to z-height differences. In bright-field TEM (BF-TEM), seen in Figure A.1, an objective aperture is inserted to block the diffracted beams and thus allow slight defocusing (Scherzer defocus) to the end of slightly increasing contrast and therefore create a more interpretable image [416]. BF and conventional TEM can be recognized by a high-intensity (white) background, intensity in this kind of imaging (and TEM in general) is not strictly related to the amount of mass, and the simple orientation of the sample can greatly change the intensity in the images, leading to difficulties in image interpretation.

It is also possible to tilt the electron beam and place the objective aperture in such a way so as to collect an image only from some of the diffracted patterns. This technique, called dark field (DF) imaging (see Figure A.1) is useful for collecting information such as the orientation of the crystal planes of the particles in view. DF imaging will therefore often be similar to a negative image of a BF image, but since only diffraction information is collected by this kind of imaging, different information is found. Since DF-TEM images are not shown in this article, the reader is directed to an excellent TEM book [416], for additional information if desired. DF images are characterized by a low intensity (black) background.

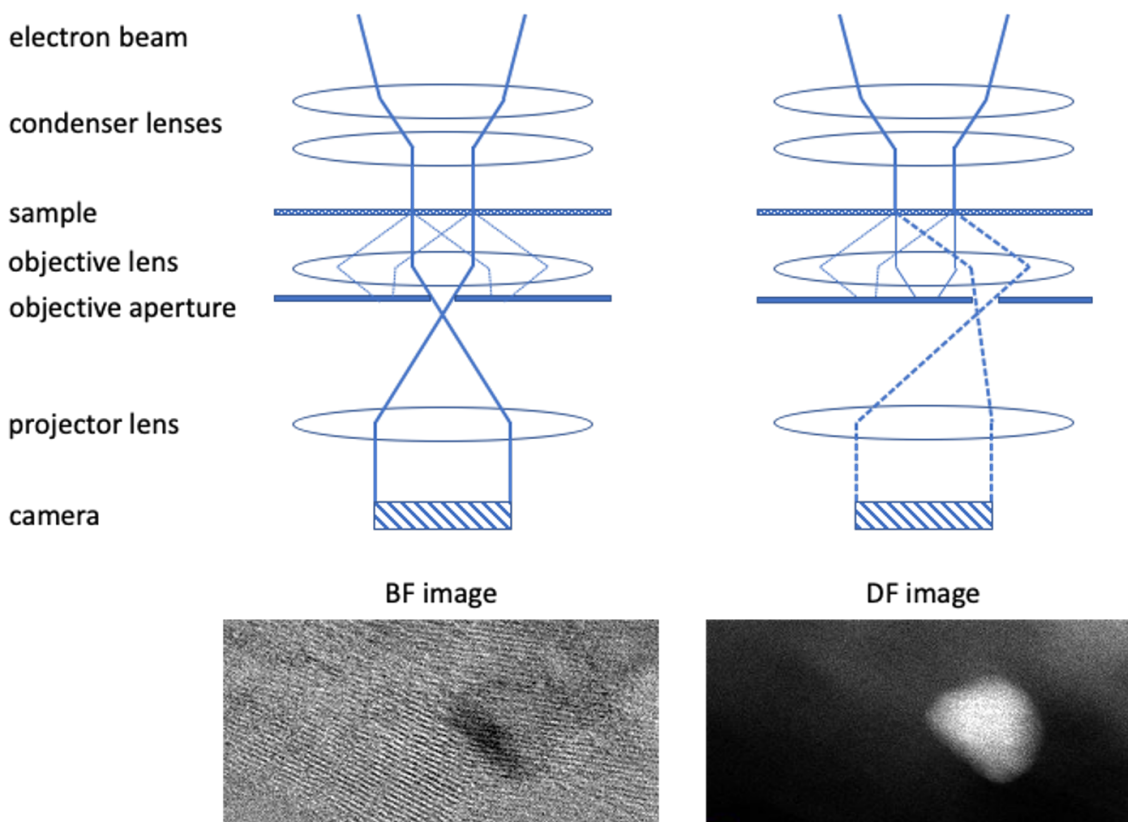


Figure A.1. Ray diagrams and sample TEM images demonstrating BF and DF TEM imaging. Dashed lines indicate electrons scattered or diffracted by the sample. Note the position of the objective aperture.

Scanning Transmission Electron Microscopy (STEM) imaging is another form of electron microscopy, where the electron beam is focused into a small point, or probe at the height of the sample and rastered, via scan coils, across a section of the sample to form an image (see Figure A.2 for clarification). In STEM imaging, detectors are used (no inherent spatial resolution) at each pixel location to create images. In essence, for each pixel in an image, the electron probe must rest on that spot in the sample, while a detector simply integrates the total intensity of electrons it's area for that point in time. Therefore, a STEM image collects pixels sequentially, since it is the moving of the electron probe, not the detector itself, that creates an image [417].

This is in contrast to TEM imaging, where a near parallel beam interacts with the sample creating an image at the camera (depending on focusing), that can be collected simultaneously [416].

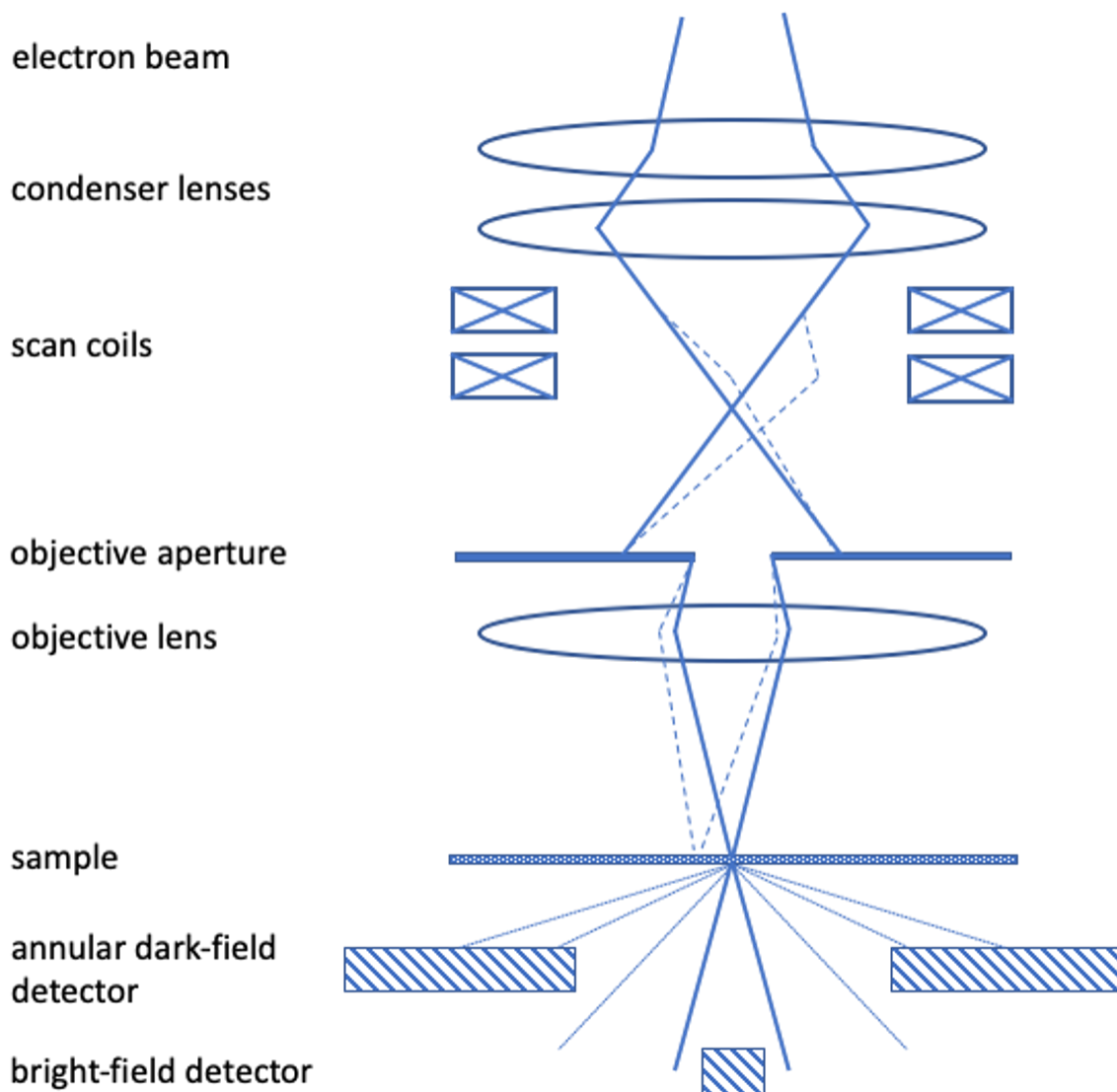


Figure A.2. A ray diagram showing the elements of the electron beam in STEM mode. Dashed lines indicate deflection of the beam path by the scan coils in order to raster the electron probe across the sample surface. Faint lines indicate electrons scattered or diffracted from the sample.

An important advantage of STEM imaging is that since detectors are used to collect information about the sample, techniques without an inherent spatial resolution such as electron energy loss spectroscopy (EELS) and energy dispersive spectroscopy (EDS) can be used to gain spatial resolution. Also, high angle annular dark field (HAADF) imaging is possible with a detector located at large angles >40 mrad from the incident electron beam, which is difficult to achieve in TEM imaging without long imaging times and specialized apertures [417]. The use of STEM mode also allows the ability to do many different kinds of imaging at the same time, simultaneous HAADF, ADF, EELS and EDX acquisition is possible, depending on the setup of the software and equipment.

STEM-HAADF imaging, the most commonly used type of imaging in this report, is novel in that the intensity is directly related to the atomic number squared (Z^2) of the sample via Rutherford scattering by the electrons near the nucleus. This Z^2 contrast makes images readily understandable, as there are no diffraction effects that can confuse the reader. For this clarity, and since the samples characterized in this paper are mostly high Z nanoparticles on a low Z support, perfect for HAADF imaging, this is the main imaging technique utilized in this report.

STEM imaging still has its drawbacks though, as it can be more damaging to the sample due to the intense localization of the electron beam. STEM imaging also usually suffers from a lower resolution when compared to TEM imaging ($\sim 5x$ in the old on-campus TITAN, $\sim 1.3x$ on the on-campus TALOS). The resolution can be dramatically improved via the use of aberration-corrected microscopes, at the cost of availability, lower focus depths, and dramatically increased intensities. The last two side-effects can be benefits depending on the experiment [417].

On a final note, S/TEM imaging results in a 2D projection of a 3D object, so care should be taken to avoid confusion by phenomena such as two particles lying on top of each other. Such confusing artifacts are inherently common in S/TEM imaging, so care should be taken to understand and ignore them.

B. ELECTRON ENERGY-LOSS SPECTROSCOPY (EELS) AND ENERGY DISPERSIVE SPECTROSCOPY (EDS)

EELS is a very powerful method to determine the electron binding energies of a sample. To first understand this method, it is necessary to first show the mechanism by which electrons are inelastically scattered by the sample.

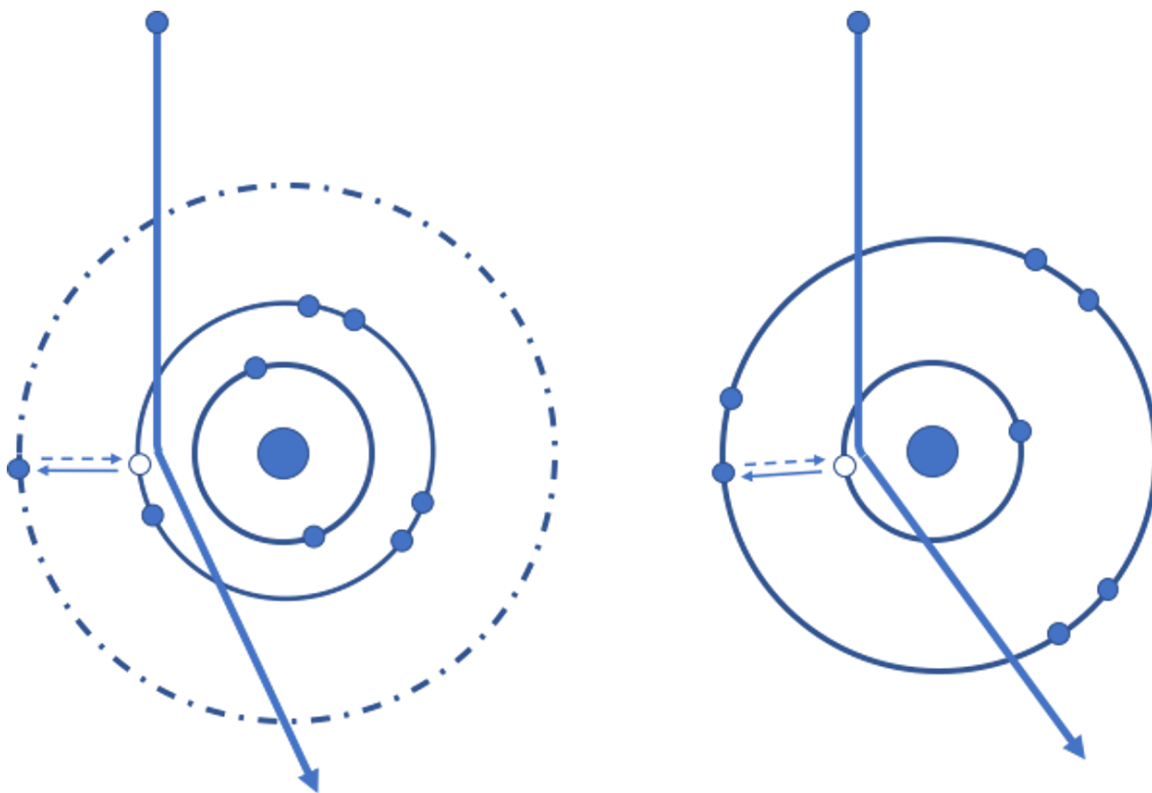


Figure B.1. Cartoon depicting the mechanism of incident electron deflection via excitation of an electron in an atom.

In Figure B.1, it is shown that interaction of the high-energy electrons in the microscope electron beam with the electrons in the target atoms will deflect the in-

coming high-energy electron. This deflection is inelastic in nature, as the electron in the atom is raised to an excited state. In EELS, since this mechanism will reduce the energy of the incoming electron by the amount that the atomic electron is excited, this leads to a powerful technique which can be used to investigate binding energies of the electrons in the sample [418]. Signals are generated by collecting the electrons that pass through the sample and measuring the energy difference between those electrons and the unaffected transmitted electron beam, called the zero-loss peak (ZLP). Since peaks for different elements are tabulated and well-known [419], elemental analysis is possible. Via the use of a microscope in STEM mode, spectrum imaging (SI) is possible, where an image is taken with each pixel containing the data for an entire spectrum. This leads to the possibility of creating chemical maps of different elements. EELS can be used to obtain a variety of information, such as chemical shifts, oxidation states, and fine-structure analysis with a spatial resolution. EELS is very dependent on having a high-quality electron beam (narrow energy distribution), and a thin sample, where multiple collisions causing erroneous electron-energy readings are negligible [416, 418].

EDS is very similar to EELS in method of signal-generation. After the sample electrons are excited by the incident high-energy electron beam, they relax into the ground state quickly, creating X-rays of energies related to the energy levels of the different atomic orbitals. These X-rays are collected, with the use of STEM mode imaging, to spectrum images that can be used to create chemical maps. For this purpose, EDS is superior to EELS for high Z elements ($Z > 13$), where EELS is the better for lower Z elements. It is also noted that EELS has a higher energy resolution due to current technology, making it the choice technique for fine-structure analysis [416–418]

VITA

I was raised in Buena Park, CA and I obtained my B.S. in Chemical Engineering at California State Polytechnic University, Pomona in 2015. My education at Purdue has taught me how to be a more independent, curious, and focused researcher as well as learning how to deal with the pain that is failure; a pain I was not as familiar with in undergrad. My time here has also given me an opportunity to experience the joy that is TEM, and I am glad to pursue TEM after my time here at Purdue.

In my off hours, I enjoy bouncing between many different hobbies such as computer building, target shooting, computer building, 3D printing, and D&D. I appreciate looking up sometimes and seeing the beautiful clouds that we have here at Purdue. When the weather is good, I enjoy walks with my beautiful wife, Lillian, and our dogs Bean and Poppy.